Physics of the Solid State, Vol. 47, No. 7, 2005, pp. 1191–1200. Translated from Fizika Tverdogo Tela, Vol. 47, No. 7, 2005, pp. 1153–1161.
Original Russian Text Copyright © 2005 by Zavitaev, Yushkanov.

METALS AND SUPERCONDUCTORS

Effect of the Character of Conduction Electron Reflection on the Electromagnetic Properties of an Inhomogeneous Cylindrical Particle

É. V. Zavitaev and A. A. Yushkanov
Moscow State Forestry University, Mytishchi, Moscow oblast, 141005 Russia
e-mail: yushkanov@mtu-net.ru

Received March 17, 2004; in final form, August 2, 2004

Abstract—The cross section of magnetic absorption of a small elongated cylindrical particle with a dielectric core and metallic shell is calculated. The general case of an arbitrary value of the ratio of the dielectric core radius to the radius of the particle is considered. The condition of mixed (mirror–diffuse) reflection of conduction electrons from the boundaries of the metal layer of the particle is chosen as the boundary condition to the problem. The limiting cases are considered, and the results obtained are discussed. *© 2005 Pleiades Publishing, Inc.*

1. INTRODUCTION

The electromagnetic properties of small metal particles exhibit a number of distinctive features [1]. These features are related to the fact that the electron mean free path in small particles is comparable to their linear size. Therefore, nonlocal effects begin to play an important role. In metals with good conductivity (aluminum, copper, silver, etc.), the electron mean free path Λ at room temperature is typically 10–100 nm. The size of experimentally studied particles can be as small as several nanometers; i.e., this situation is indeed realized. In this case, the classical theory of interaction of electromagnetic radiation with metal particles (the Mie theory) [2] based on the local equations of macroscopic electrodynamics is not valid.

In [3, 4], the theory of interaction of electromagnetic radiation with a spherical particle was developed. Somewhat earlier, a result similar to that in [3] was obtained in [5, 6] in the limiting case of low frequencies (far IR range). In those studies, the approach based on the solution of the transport Boltzmann equation for conduction electrons in a metal was used. An alternative approach to the problem was proposed in [7, 8].

In [9–11], it was conjectured that the specular reflection of conduction electrons from the surface can have a substantial effect on the electromagnetic properties of small metal particles.

Recently, interest in the problem of interaction of electromagnetic radiation with nonspherical particles has increased [12]. We also note studies in which an attempt was made to account for quantum-mechanical effects in this problem; these effects are especially important at low temperatures [13, 14].

In [15–18], the magnetic dipole absorption of IR radiation by cylindrical particles was investigated. To describe the electromagnetic response of a particle, the standard transport theory of a degenerate Fermi gas of conduction electrons in metals was used [19]. In [15, 16, 18], the approach was restricted to the case of purely diffuse reflection of conduction electrons from the inner surface of a particle, and in [17] a detailed study of the magnetic dipole absorption of a cylindrical particle was performed for the case where the reflection of electrons from the particle surface has a mixed (mirror–diffuse) character [19]. In all the studies cited above, only homogeneous particles were considered; i.e., the problem of the inner structure of absorbing particles did not arise.

However, experimental studies of particles with a complicated structure have recently been reported [20, 21]. Such particles consist of a dielectric (or metallic) core surrounded by a metallic shell, which, naturally, affects the optical properties of these particles. The importance of the investigation of particles with complicated inner structure was pointed out, e.g., in [22].

In this study, which is a logical continuation of [17], the theory of interaction of electromagnetic radiation with a nonuniform cylindrical particle (a metallic particle with a dielectric core) is constructed under the assumption that the reflection of conduction electrons inside the cylindrical metallic layer has a mixed (mirror–diffuse) character.

2. STATEMENT OF THE PROBLEM

We consider a metallic cylinder of length L with a dielectric core placed in the field of a plane electromagnetic wave. We denote the radius of the cylindrical core by R_1 and the radius of the cylindrical shell by R_2 and assume that $L \gg R_2$. The wave frequency is assumed to be bounded from above by the frequencies of the near IR range ($\omega < 2 \times 10^{15}$ s^{-1}). In the frequency range considered, the contribution from dipole electric polarization currents is small in comparison with the contribution of vortex currents induced by the external magnetic field of the wave in the metallic shell of the particle [3]. Therefore, the effect of the external electric field of the wave is disregarded. In the dipole approximation, neglecting the skin effect (we assume that $R_2 < \delta$, where δ is the skin depth), the vortex electric field inducing vortex currents is

$$\mathbf{E} = \frac{1}{2c}\left[\mathbf{r}, \frac{\partial \mathbf{H}}{\partial t}\right] = \frac{\omega}{2ic}[\mathbf{r}, \mathbf{H}_0]\exp(-i\omega t), \tag{1}$$

where $\mathbf{H} = \mathbf{H}_0\exp(-i\omega t)$ is the magnetic field, $\mathbf{r}$ is the radius vector (the origin is chosen to be on the axis of the particle), $\mathbf{H}_0$ is the amplitude of the magnetic field of the wave, ω is the angular frequency of the wave, and c is the velocity of light.

The average power $\bar{Q}$ dissipated in the particle is given by [23]

$$\bar{Q} = \int \overline{(\mathrm{Re}\,\mathbf{E})(\mathrm{Re}\,\mathbf{j})}d^3r = \frac{1}{2}\mathrm{Re}\int \mathbf{j}\mathbf{E}^* d^3r, \tag{2}$$

where a bar denotes time averaging, the asterisk denotes complex conjugation, and $\mathbf{j}$ is the vortex current density.

In the case where the particle radius R_2 is comparable to (or smaller than) the electron mean free path Λ in the metal, the relation between $\mathbf{E}$ and $\mathbf{j}$ appears to be substantially nonlocal. To derive this relation, we apply the transport equation (in the relaxation time approximation) to the degenerate Fermi gas of conduction electrons in the cylindrical metallic shell of the particle.

For sufficiently weak external fields, this equation can be linearized with respect to the external field $\mathbf{E}$ and to small deviations $f_1(\mathbf{r}, \mathbf{v})$ from the equilibrium Fermi distribution function f_0:

$$-i\omega f_1 + \mathbf{v}\frac{\partial f_1}{\partial \mathbf{r}} + e(\mathbf{v}\cdot\mathbf{E})\frac{\partial f_0}{\partial \varepsilon} = -\frac{f_1}{\tau}, \tag{3}$$

where e and $\mathbf{v}$ are the charge and velocity of conduction electrons, respectively, and τ is the electron relaxation time.

In what follows, we assume that the velocity dependence of the electron energy ε is quadratic, $\varepsilon = mv^2/2$ (m is the electron effective mass), and use a step approximation to the equilibrium function $f_0(\varepsilon)$ for the electron energy distribution [24]:

$$f_0(\varepsilon) = \theta(\varepsilon_f - \varepsilon) = \begin{cases} 1, & 0 \le \varepsilon \le \varepsilon_f \\ 0, & \varepsilon_f < \varepsilon, \end{cases}$$

where $\varepsilon_f = mv_f^2/2$ is the Fermi energy (v_f is the Fermi velocity). We assume that the Fermi surface of the cylindrical metal layer of the particle is spherical in shape and that the velocities of all electrons at the Fermi surface are equal to v_f.

The electron distribution function is

$$f(\mathbf{r}, \mathbf{v}) = f_0(\varepsilon) + f_1(\mathbf{r}, \mathbf{v}), \quad \varepsilon = \frac{m\mathbf{v}^2}{2}.$$

The deviation $f_1(\mathbf{r}, \mathbf{v})$ of the electron distribution function $f(\mathbf{r}, \mathbf{v})$ from the equilibrium function $f_0(\varepsilon)$ arising under the action of a vortex electric field induces a vortex current inside the particle,

$$\mathbf{j} = en_0\langle\mathbf{v}\rangle = en_0\left[\int f_0 d^3v\right]^{-1}\int f_1\mathbf{v}d^3v. \tag{4}$$

The electron concentration n_0 in the metallic layer of the particle can be determined using the standard formula

$$n_0 = 2\frac{m^3}{h^3}\int f_0 d^3v = 2\frac{m^3}{h^3}\frac{4\pi v_f^3}{3}, \tag{5}$$

where h is the Planck constant.

Substituting the field $\mathbf{E}$ in the form of Eq. (1) into Eq. (3), we can find $f_1(\mathbf{r}, \mathbf{v})$ as a solution to this equation. Then, using Eqs. (4) and (2), we find the current in the metallic shell and the absorption cross section of the energy of the external electromagnetic field for the particle:

$$\sigma = \frac{8\pi\bar{Q}}{cH_0^2}. \tag{6}$$

The solution of this problem is unique if we impose boundary conditions on the unknown function $f_1(\mathbf{r}, \mathbf{v})$ at the cylindrical surfaces of the metal shell and the dielectric core of the particle. We choose the boundary conditions corresponding to mirror–diffuse reflection of electrons from these surfaces [17]. Since electrons can be reflected from the inner (R_1) and outer (R_2) boundaries of the metallic layer, we write two boundary conditions:

$$f_{11}(\mathbf{r}_\perp, \mathbf{v}_\perp, \mathbf{v}_z) = q_1 f_{11}(\mathbf{r}_\perp, \mathbf{v}'_\perp, \mathbf{v}_z) \quad \text{for} \begin{cases} |\mathbf{r}_\perp| = R_1 \\ \mathbf{r}_\perp\mathbf{v}_\perp > 0, \end{cases} \tag{7}$$

$$f_{12}(\mathbf{r}_\perp, \mathbf{v}_\perp, \mathbf{v}_z) = q_2 f_{12}(\mathbf{r}_\perp, \mathbf{v}'_\perp, \mathbf{v}_z) \quad \text{for} \begin{cases} |\mathbf{r}_\perp| = R_2 \\ \mathbf{r}_\perp\mathbf{v}_\perp < 0. \end{cases} \tag{8}$$

Here, $\mathbf{r}_\perp$ and $\mathbf{v}_\perp$ are the components of the radius vector $\mathbf{r}$ and velocity $\mathbf{v}$ of an electron, respectively, in the plane normal to the axis of the inhomogeneous cylinder;

$$\mathbf{v}'_\perp = \mathbf{v}_\perp - \frac{2\mathbf{r}_\perp(\mathbf{r}_\perp \cdot \mathbf{v})}{R^2}$$

is the velocity vector, which transforms into $\mathbf{v}_\perp$ upon specular reflections from the inner or outer surface of the metallic layer at a point $\mathbf{r}_\perp$ ($|\mathbf{r}_\perp| = R_1$ or $|\mathbf{r}_\perp| = R_2$); $\mathbf{v}_z$ is the component of the electron velocity along the particle axis; and q_1 and q_2 are the reflectivities of a smooth surface (probabilities of specular reflection):

$$0 \le q_1 \le 1, \quad 0 \le q_2 \le 1.$$

The case of $\mathbf{r}_\perp\mathbf{v}_\perp > 0$ ($\mathbf{r}_\perp\mathbf{v}_\perp < 0$) corresponds to electrons moving away from the core (towards the core).

For $q_1 = 0$ ($q_2 = 0$), we have the conditions of diffuse reflection of conduction electrons from the inner or outer surface of the metallic layer of the particle, and for $q_1 = 1$ ($q_2 = 1$) we have the conditions of purely specular reflection. At $q \neq 0$ and $q \neq 1$, various types of mixed (mirror–diffuse) reflection of electrons are realized.

3. DISTRIBUTION FUNCTION

Transport equation (3) can be solved using the method of characteristics [25]. The variation of f_1 along a trajectory (characteristic)

$$d\mathbf{r} = \mathbf{v}dt$$

is determined by the equation

$$df_1 = -\left(\nu f_1 + e(\mathbf{v}\cdot\mathbf{E})\frac{\partial f_0}{\partial \varepsilon}\right)dt, \tag{9}$$

where

$$\nu = \frac{1}{\tau} - i\omega$$

is the complex scattering frequency.

Boundary conditions (7) and (8) determine the variation in the function $f_1(\mathbf{r}_\perp, \mathbf{v}_\perp, \mathbf{v}_z)$ along the specularly reflected trajectory. At the point $t = t_n$ of reflection (from any surface), the function $f_1(t)$ is discontinuous:

$$f_1(t_n + 0) = qf_1(t_n - 0). \tag{10}$$

The plus and minus sign denotes the limits (with respect to the time of flight) immediately after and before a reflection, respectively, of the function $f_1(\mathbf{r}_\perp, \mathbf{v}_\perp, \mathbf{v}_z)$ at the reflection point t_n.

For specular reflection, the angular momentum $[\mathbf{r}_\perp, \mathbf{v}_\perp] = [\mathbf{r}_\perp, \mathbf{v}'_\perp]$ is conserved; therefore, on the trajectory in question, we have

$$[\mathbf{r}_\perp, \mathbf{v}_\perp] = \text{const}.$$

The difference $t_n - t_{n-1}$ does not depend on the number n of the reflection point:

$$t_n = nT + \text{const}, \quad n \in Z,$$

where T is the transit time of an electron with velocity $\mathbf{v}_\perp$ from the point $\mathbf{r}_{n-1\perp}$ to the point $\mathbf{r}_{n\perp}$ and

$$T = -\frac{2(\mathbf{v}_{n\perp}\cdot\mathbf{r}_{n\perp})}{\mathbf{v}_\perp^2}.$$

The quantity $\mathbf{v}\cdot\mathbf{E}$ is also constant on the trajectory:

$$\mathbf{v}\cdot\mathbf{E} = \frac{\omega}{2ic}[\mathbf{r}, H]\mathbf{v} = \frac{i\omega}{2c}[\mathbf{r}, \mathbf{v}]\mathbf{H} = \text{const}.$$

The solution to Eq. (9) is

$$f_1 = C\exp(-\nu t) + A, \tag{11}$$

where $A = -\dfrac{e(\mathbf{v}\cdot\mathbf{E})}{\nu}\dfrac{\partial f_0}{\partial\varepsilon}$.

The parameter t in Eq. (11) has the meaning of the transit time of an electron moving along the trajectory from the reflecting boundary to the point $\mathbf{r}_\perp$ with velocity $\mathbf{v}_\perp$.

Let us solve this equation in the interval (t_{n-1}, t_n) for the case where an electron moves along a trajectory that does not intersect the cylindrical dielectric core of the particle after specular reflection.

At the initial point ($t = 0$), we have

$$f_1(t_{n-1} + 0) = C + A.$$

From this, we can find the constant C:

$$C = f_1(t_{n-1} + 0) - A.$$

Now, we obtain the relation between the initial values of the function f_1 on two neighboring segments of the trajectory. Since $t_n - 0 = t_{n-1} + T$, we have

$$\begin{aligned} f_1(t_n - 0) &= (f_1(t_{n-1} + 0) - A)\exp(-\nu T) + A \\ &= A(1 - \exp(-\nu T)) + f_1(t_{n-1} + 0)\exp(-\nu T). \end{aligned}$$

Using Eq. (10), we obtain

$$\begin{aligned} &f_1(t_n + 0) \\ &= q_2\{A(1 - \exp(-\nu T)) + f_1(t_{n-1} + 0)\exp(-\nu T)\}. \end{aligned} \tag{12}$$

With recurrence relation (12), we express $f_1(t_{n-1} + 0)$ in terms of $f_1(t_{n-2} + 0)$ and so on and arrive at an expression for $f_1(t_n + 0)$ in terms of the sum of the infinite geometrical progression with the denominator $q_2\exp(-\nu T)$. After summing, we obtain

$$f_1(t_n + 0) = \frac{q_2 A(1 - \exp(-\nu T))}{(1 - q_2\exp(-\nu T))}. \tag{13}$$

To find a specific form of the solution to Eq. (9), we use initial condition (13). At $t = 0$, we find

$$\frac{q_2 A(1 - \exp(-\nu T))}{(1 - q_2 \exp(-\nu T))} = C + A.$$

From this, we obtain

$$C = A\left\{\frac{q_2(1 - \exp(-\nu T))}{1 - q_2 \exp(-\nu T)} - 1\right\}$$

$$= A\left\{\frac{q_2 - 1}{1 - q_2 \exp(-\nu T)}\right\}.$$

Therefore,

$$f_{10}(t_2) = A\left\{\frac{q_2 - 1}{1 - q_2 \exp(-\nu T)}\right\}\exp(-\nu t_2) + A$$
$$= A\left\{\frac{(q_2 - 1)\exp(-\nu t_2)}{1 - q_2 \exp(-\nu T_2)} + 1\right\}. \qquad (14)$$

The parameters t_2 and T_2 can be related to the coordinates of the point ($\mathbf{r}_\perp$, $\mathbf{v}_\perp$) in the phase space (at $n = 0$, $\mathbf{v}_{0\perp} = \mathbf{v}_\perp$) by the conditions

$$\mathbf{r}_\perp = \mathbf{r}_{0\perp} + \mathbf{v}_\perp t_2, \quad \mathbf{v}_\perp \mathbf{r}_{0\perp} < 0, \quad r_{0\perp}^2 = R_2^2,$$

$$T_2 = -\frac{2(\mathbf{v}_\perp \cdot \mathbf{r}_{0\perp})}{v_\perp^2},$$

where $\mathbf{r}_{0\perp}$ is the component of the radius vector of an electron in the plane perpendicular to the cylinder axis at the instant of its reflection from the cylindrical boundary of the particle. By eliminating $\mathbf{r}_{0\perp}$ from these expressions, we obtain

$$t_2 = \{\mathbf{r}_\perp \mathbf{v}_\perp + [(\mathbf{r}_\perp \cdot \mathbf{v}_\perp)^2 + (R_2^2 - r_\perp^2)v_\perp^2]^{1/2}\}/v_\perp^2, \qquad (15)$$

$$T_2 = 2[(\mathbf{r}_\perp \cdot \mathbf{v}_\perp)^2 + (R_2^2 - r_\perp^2)v_\perp^2]^{1/2}/v_\perp^2. \qquad (16)$$

Relations (14)–(16) fully determine the function $f_1(\mathbf{r}_\perp, \mathbf{v}_\perp, \mathbf{v}_z)$ in the case where electrons move along a trajectory not intersecting the core of the particle.

Now, we pass to the case of double specular reflection of an electron (from the cylindrical core and from the outer cylindrical boundary of the metal). We solve transport equation (9) in the interval (t_{n-1}, t_n) by assuming that, at some instant, an electron is reflected from the boundary of the metallic layer (previously, the electron was reflected from the core). In this way, we find the deviation $f_{12}(t)$ of the electron distribution function from the equilibrium function:

$$f_{12}(t_2) = A\left\{\frac{q_1(1 - \exp(-\nu T_1) + q_2 \exp(-\nu T_1)) - 1}{1 - q_1 q_2 \exp(-2\nu T_1)}\right.$$
$$\left.\times \exp(-\nu t_2) + 1\right\}. \qquad (17)$$

Likewise, we find the deviation $f_{11}(t)$ of the distribution function for electrons reflected from the cylindrical core of the particle. We directly write out the final result:

$$f_{11}(t_1) = A\left\{\frac{q_2(1 - \exp(-\nu T_1) + q_1 \exp(-\nu T_1)) - 1}{1 - q_1 q_2 \exp(-2\nu T_1)}\right.$$
$$\left.\times \exp(-\nu t_1) + 1\right\}. \qquad (18)$$

The parameter t_1 in Eq. (18) is given by

$$t_1 = \{\mathbf{r}_\perp \mathbf{v}_\perp - [(\mathbf{r}_\perp \cdot \mathbf{v}_\perp)^2 + (R_1^2 - r_\perp^2)v_\perp^2]^{1/2}\}/v_\perp^2. \qquad (19)$$

Indeed, this equation follows from the obvious vector equality $\mathbf{r}_\perp = \mathbf{r}_{0\perp} + \mathbf{v}_\perp t_1$, where $\mathbf{r}_{0\perp}$ is the radius vector of the electron at the moment of reflection from the core of the particle ($r_{0\perp}^2 = R_1^2$). If we square both parts of this equality and then solve it with respect to t_1, we will obtain Eq. (19).

The parameter T_1 (the period of motion of an electron at double reflection, i.e., the time after which the electron is again reflected from the core or from the outer boundary of the metal) can be found using the vector equality $\mathbf{r}_\perp^* = \mathbf{r}_{0\perp} + \mathbf{v}_\perp T_1$, where $\mathbf{r}_{0\perp} = \mathbf{r}_\perp - \mathbf{v}_\perp t_1$, $|\mathbf{r}_{0\perp}| = R_1$, and $|\mathbf{r}_\perp^*| = R_2$ (we assume that the electron moves from the core to the particle boundary). Squaring both sides of this equality, we obtain the quadratic equation

$$v_\perp^2 T_1^2 + 2(\mathbf{r}_\perp - \mathbf{v}_\perp t_1)\mathbf{v}_\perp T_1 + (R_1^2 - R_2^2) = 0, \qquad (20)$$

whose solution (written out below) allows us to find the parameter T_1.

Relations (15) and (17)–(20) fully determine the function $f_1(\mathbf{r}_\perp, \mathbf{v}_\perp, \mathbf{v}_z)$ for the case where electrons are doubly reflected from the cylindrical core and from the outer cylindrical boundary of the particle.

4. ABSORPTION CROSS SECTION

The distribution functions found above allow us to calculate the current (4), the average dissipated power (2), and the cross section (6) for the absorption of the energy of the external electromagnetic field.

When calculating integrals in Eqs. (4) and (2), it is convenient to pass to cylindrical coordinates both in the coordinate space ($r_\perp$, φ, r_z; z is the polar axis coinciding with the cylinder axis and parallel to the vector $\mathbf{H}_0$) and in the velocity space ($v_\perp$, α, v_z; the v_z axis is the polar axis).

In cylindrical coordinates, field (1) has only a φ component,

$$\mathbf{E} = E_\varphi \mathbf{e}_\varphi, \quad E_\varphi = \frac{i\omega}{2c} r_\perp H_0 \exp(-i\omega t). \tag{21}$$

Accordingly, current (4) has only a φ component (current lines are closed circles lying in planes perpendicular to the z axis, with their centers on the z axis).

When integrating expression (4), we should bear in mind that the point of reflection of electrons inside the particle is determined by the angle α in the velocity space. Let us consider different situations.

(i) If the inequality $\alpha_0 \le \alpha \le \pi - \alpha_0$ is satisfied, where the angle α_0 is determined by the expression

$$\alpha_0 = \arccos\left(\frac{\sqrt{r_\perp^2 - R_1^2}}{r_\perp}\right), \tag{22}$$

then the electron trajectory does not intersect the core and the electron is reflected from the outer boundary of the metallic layer of the particle. In this case, the electron scattering from the cylindrical surface is described by the function $f_{10}(\mathbf{r}_\perp, \mathbf{v}_\perp)$ ($t = t_2$, $T = T_2$) [see Eq. (14)].

(ii) If $\pi - \alpha_0 < \alpha \le \pi$, then the electrons move towards the core of the particle and the function $f_1(\mathbf{r}_\perp, \mathbf{v}_\perp)$ becomes $f_{12}(\mathbf{r}_\perp, \mathbf{v}_\perp)$ ($t = t_2$, $T = T_1$) [see Eq. (17)].

(iii) If $0 < \alpha \le \alpha_0$, the electrons move away from the core of the particle and the function $f_1(\mathbf{r}_\perp, \mathbf{v}_\perp)$ becomes $f_{11}(\mathbf{r}_\perp, \mathbf{v}_\perp)$ ($t = t_1$, $T = T_1$) [see Eq. (18)].

The motion of electrons is symmetric with respect to any plane that contains the axis of the particle and in which lies the point of their position on a trajectory; therefore, we can assume that the angle α in the velocity space changes from 0 to π and double the result of integration with respect to this variable.

In terms of symmetry, the integration over the entire range of the velocities v_z can be replaced by integration over the positive range and the result is doubled. Therefore, taking into account that $v_\varphi = v_\perp \sin\alpha$ and substituting the limits of integration, we arrive at the following expression for the components of the vortex current:

$$\begin{aligned} j_\varphi = {} & \frac{3n_0E_\varphi e^2}{\pi v_f^3 m\nu}\int_0^{v_f}\int_{\alpha_0}^{\pi-\alpha_0}\frac{v_\perp^3}{\sqrt{v_f^2 - v_\perp^2}}\left\{\frac{(q_2-1)\exp(-\nu t_2)}{1-q_2\exp(-\nu T_2)} + 1\right\}\sin^2\alpha \, dv_\perp d\alpha \\ & + \frac{3n_0E_\varphi e^2}{\pi v_f^3 m\nu}\int_0^{v_f}\int_{\pi-\alpha_0}^{\pi}\frac{v_\perp^3}{\sqrt{v_f^2 - v_\perp^2}}\left\{\frac{q_1(1-\exp(-\nu T_1) + q_2\exp(-\nu T_1)) - 1}{1-q_1q_2\exp(-2\nu T_1)}\exp(-\nu t_2) + 1\right\}\sin^2\alpha \, dv_\perp d\alpha \\ & + \frac{3n_0E_\varphi e^2}{\pi v_f^3 m\nu}\int_0^{v_f}\int_0^{\alpha_0}\frac{v_\perp^3}{\sqrt{v_f^2 - v_\perp^2}}\left\{\frac{q_2(1-\exp(-\nu T_1) + q_1\exp(-\nu T_1)) - 1}{1-q_1q_2\exp(-2\nu T_1)}\exp(-\nu t_1) + 1\right\}\sin^2\alpha \, dv_\perp d\alpha. \end{aligned} \tag{23}$$

Here, we assumed that the concentration of conduction electrons in metals is determined by Eq. (5).

The absorption cross section of electromagnetic radiation for the inhomogeneous particle is given by

$$\sigma = \frac{1}{2}\frac{8\pi}{cH_0^2}\mathrm{Re}\left\{\int j_\varphi E_\varphi^* d^3r\right\}.$$

With Eqs. (21) and (23), after simple transformations, this expression reduces to the form

$$\sigma = \sigma_1 + \sigma_2 + \sigma_3, \tag{24}$$

where

$$\begin{aligned} \sigma_1 = \mathrm{Re}\Bigg\{ & \frac{3n_0e^2\pi\omega^2 L}{v_f^3 mc^3} 2\int_{R_1}^{R_2} r_\perp^3 dr_\perp \int_0^{v_f}\int_{\alpha_0}^{\pi-\alpha_0}\frac{v_\perp^3}{\sqrt{v_f^2 - v_\perp^2}} \\ & \times\left[\frac{(q_2-1)\exp(-\nu t_2)}{\nu(1-q_2\exp(-\nu T_2))} + \frac{1}{\nu}\right]\sin^2\alpha \, dv_\perp d\alpha\Bigg\}, \end{aligned} \tag{25}$$

$$\sigma_2 = \mathrm{Re}\left\{\frac{3n_0e^2\pi\omega^2L}{v_f^3mc^3}2\int_{R_1}^{R_2}r_\perp^3dr_\perp\int_0^{v_f}\int_{\pi-\alpha_0}^{\pi}\frac{v_\perp^3}{\sqrt{v_f^2-v_\perp^2}}\right.$$
$$\times\left[\frac{q_1(1-\exp(-\nu T_1)+q_2\exp(-\nu T_1))-1}{\nu(1-q_1q_2\exp(-2\nu T_1))}\right. \qquad (26)$$
$$\left.\left.\times\exp(-\nu t_2)+\frac{1}{\nu}\right]\sin^2\alpha dv_\perp d\alpha\right\},$$

$$\sigma_3 = \mathrm{Re}\left\{\frac{3n_0e^2\pi\omega^2L}{v_f^3mc^3}2\int_{R_1}^{R_2}r_\perp^3dr_\perp\int_0^{v_f}\int_0^{\alpha_0}\frac{v_\perp^3}{\sqrt{v_f^2-v_\perp^2}}\right.$$
$$\times\left[\frac{q_2(1-\exp(-\nu T_1)+q_1\exp(-\nu T_1))-1}{\nu(1-q_1q_2\exp(-2\nu T_1))}\right. \qquad (27)$$
$$\left.\left.\times\exp(-\nu t_1)+\frac{1}{\nu}\right]\sin^2\alpha dv_\perp d\alpha\right\}.$$

Let us introduce new variables:

$$\xi = \frac{r_\perp}{R_2}, \quad \rho = \frac{v_\perp}{v_f},$$
$$z = \nu\frac{R_2}{v_f} = \left(\frac{1}{\tau}-i\omega\right)\frac{R_2}{v_f} = x-iy, \qquad (28)$$
$$\kappa = \frac{R_1}{R_2}.$$

Here, $x = R_2/\tau v_f$ is the ratio of the particle radius R_2 to the electron mean free path Λ (τ is the electron relaxation time for the shell, v_f is the Fermi velocity of the electrons in the shell) and $y = R_2\omega/v_f$ is the ratio of the frequency ω of the external field to the frequency v_f/R_2 of electron scattering by the particle surface. For example, for an aluminum particle ($v_f = 2.02 \times 10^6$ m/s) and for $R_2 = 10$ nm, the dimensionless frequency $y = 7$ corresponds to the angular frequency of the external field $\omega = yv_f/R_2 \approx 1.4 \times 10^{15}\ \mathrm{s}^{-1}$ (in this case, the dependence of the absorption cross section on the reflectivities and on the presence of an inner core is most pronounced).

Using Eqs. (28), we transform Eqs. (15), (16), (19), and (22) to the form

$$t_2 = \frac{R_2}{v_\perp}(\xi\cos\alpha+\sqrt{1-\xi^2\sin^2\alpha}) = \frac{R_2}{v_\perp}\eta,$$
$$T_2 = \frac{R_2}{v_\perp}2\sqrt{1-\xi^2\sin^2\alpha} = \frac{R_2}{v_\perp}\eta_0,$$
$$t_1 = \frac{R_2}{v_\perp}(\xi\cos\alpha-\sqrt{\kappa^2-\xi^2\sin^2\alpha}) = \frac{R_2}{v_\perp}\psi,$$
$$\alpha_0 = \arccos\left(\sqrt{1-\frac{\kappa^2}{\xi^2}}\right).$$

Here, we used the relation $\mathbf{r}_\perp\mathbf{v}_\perp = r_\perp v_\perp\cos\alpha$ (all electrons at the Fermi surface inside the cylindrical metal layer move with velocities equal to v_f).

By solving Eq. (20), we determine the parameter T_1:

$$T_1 = \frac{R_2}{v_\perp}(\sqrt{1-\xi^2\sin^2\alpha}-\sqrt{\kappa^2-\xi^2\sin^2\alpha}) = \frac{R_2}{v_\perp}\psi_0.$$

Next, absorption cross section (24) can be rewritten as

$$\sigma = \sigma_0(F_1+F_2+F_3),$$

where

$$\sigma_0 = \frac{3\pi n_0e^2v_fR_2^3L}{mc^3}, \qquad (29)$$

$$F_1 = \mathrm{Re}\left\{2\frac{y^2}{z}\int_\kappa^1\xi^3d\xi\int_0^1\int_{\alpha_0}^{\pi-\alpha_0}\frac{\rho^3}{\sqrt{1-\rho^2}}\right. \qquad (30)$$
$$\left.\times\left[\frac{(q_2-1)\exp(-z\eta/\rho)}{(1-q_2\exp(-z\eta_0/\rho))}+1\right]\sin^2\alpha d\rho d\alpha\right\},$$

$$F_2 = \mathrm{Re}\left\{2\frac{y^2}{z}\int_\kappa^1\xi^3d\xi\int_0^1\int_{\pi-\alpha_0}^{\pi}\frac{\rho^3}{\sqrt{1-\rho^2}}\right.$$
$$\times\left[\frac{q_1(1-\exp(-z\psi_0/\rho)+q_2\exp(-z\psi_0/\rho))-1}{(1-q_1q_2\exp(-2z\psi_0/\rho))}\right. \qquad (31)$$
$$\left.\left.\times\exp(-z\eta/\rho)+1\right]\sin^2\alpha d\rho d\alpha\right\},$$

$$F_3 = \mathrm{Re}\left\{2\frac{y^2}{z}\int_\kappa^1\xi^3d\xi\int_0^1\int_0^{\alpha_0}\frac{\rho^3}{\sqrt{1-\rho^2}}\right.$$
$$\times\left[\frac{q_2(1-\exp(-z\psi_0/\rho)+q_1\exp(-z\psi_0/\rho))-1}{(1-q_1q_2\exp(-2z\psi_0/\rho))}\right. \qquad (32)$$
$$\left.\left.\times\exp(-z\psi/\rho)+1\right]\sin^2\alpha d\rho d\alpha\right\}.$$

Formulas (30)–(32) allow us to calculate the dimensionless absorption cross section for the inhomoge-

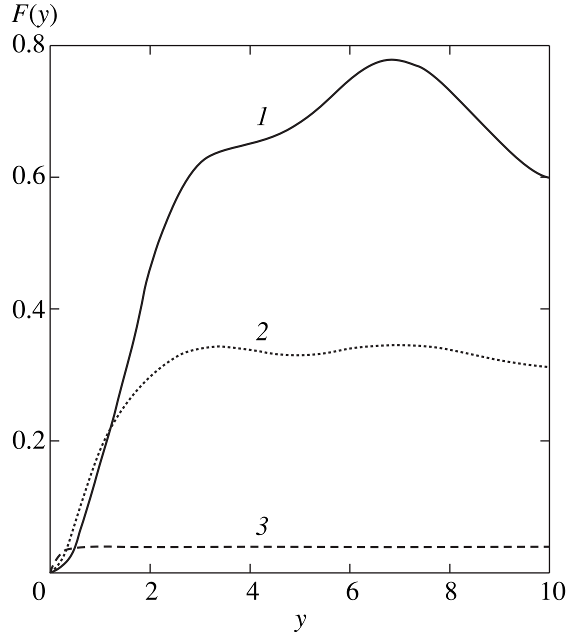

Fig. 1. Dimensionless absorption cross section F as a function of dimensionless frequency $y = R_2\omega/v_f$ at $x = 0.1$; $\kappa = 0.7$; and (*1*) $q_1 = 0$ and $q_2 = 0$, (*2*) $q_1 = 0.5$ and $q_2 = 0.5$, and (*3*) $q_1 = 1$ and $q_2 = 1$.

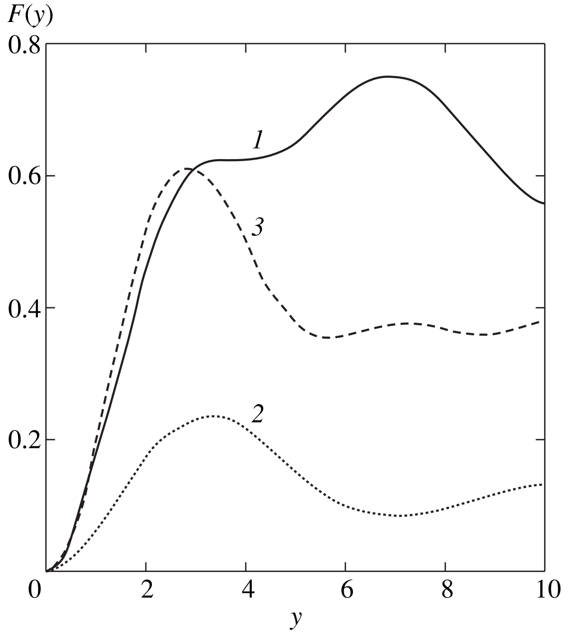

Fig. 2. The same as in Fig. 1, but for $x = 0$; $\kappa = 0.7$; and (*1*) $q_1 = 0$ and $q_2 = 0$, (*2*) $q_1 = 0$ and $q_2 = 1$, and (*3*) $q_1 = 1$ and $q_2 = 0$.

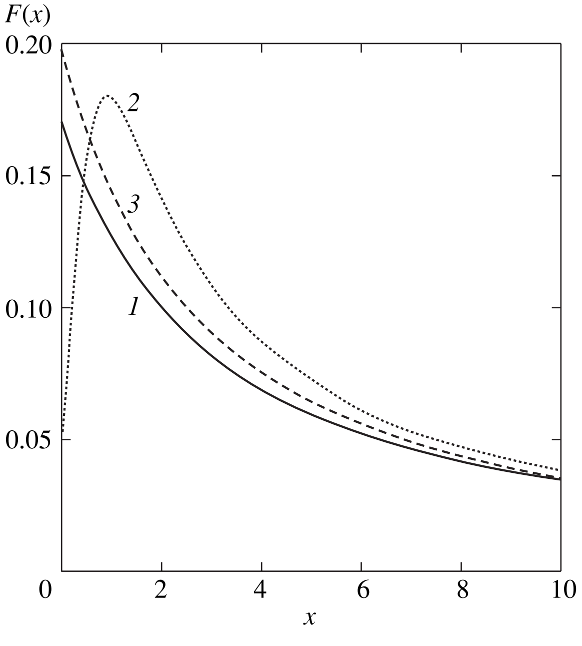

Fig. 3. Dimensionless absorption cross section F as a function of the dimensionless inverse mean free path $x = R_2/\tau v_f$ at $y = 1$; $\kappa = 0.7$; and (*1*) $q_1 = 0$ and $q_2 = 0$, (*2*) $q_1 = 0$ and $q_2 = 1$, and (*3*) $q_1 = 1$ and $q_2 = 0$.

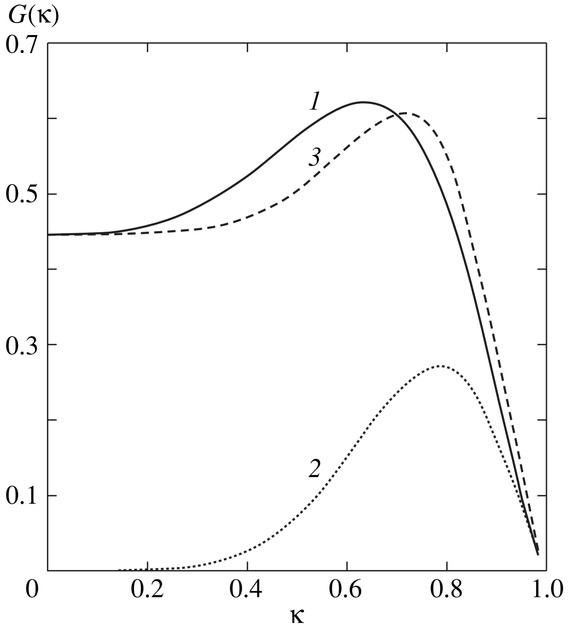

Fig. 4. The quantity G as a function of the ratio (κ) of the core radius to the particle radius at $y = 3$; $x = 0$; and (*1*) $q_1 = 0$ and $q_2 = 0$, (*2*) $q_1 = 0$ and $q_2 = 1$, and (*3*) $q_1 = 1$ and $q_2 = 0$.

neous cylindrical particle,

$$F(x, y, \kappa, q_1, q_2) = F_1(x, y, \kappa, q_1, q_2) + F_2(x, y, \kappa, q_1, q_2) + F_3(x, y, \kappa, q_1, q_2) \quad (33)$$

and the dimensional absorption cross section,

$$\sigma = \sigma_0 F(x, y, \kappa, q_1, q_2). \quad (34)$$

As $\kappa \longrightarrow 0$ ($\alpha_0 \longrightarrow 0$), i.e., in the case where there is

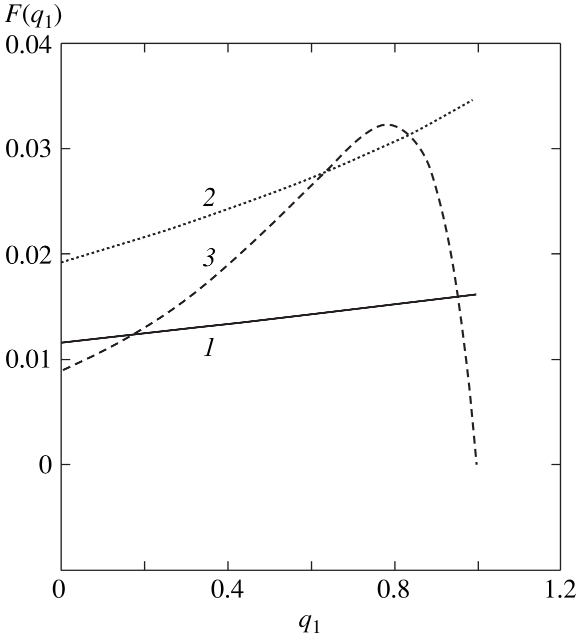

Fig. 5. Dimensionless absorption cross section F as a function of the electron reflectivity q_1 of the inner surface of the metallic layer of the particle at $y = 1$, $x = 0$, $\kappa = 0.95$, and various values of q_2: (*1*) 0, (*2*) 0.5, and (*3*) 1.0.

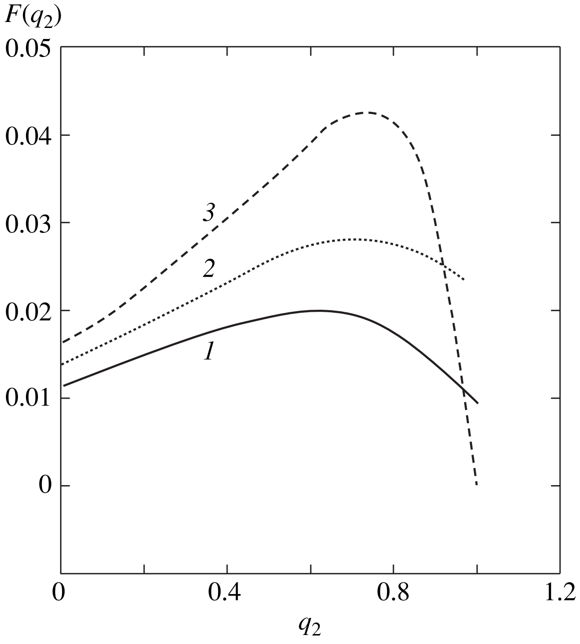

Fig. 6. Dimensionless absorption cross section F as a function of the electron reflectivity q_2 of the outer surface of the metallic layer of the particle at $y = 1$, $x = 0$, $\kappa = 0.95$, and various values of q_1: (*1*) 0, (*2*) 0.5, and (*3*) 1.0.

no core in the particle, it follows from Eq. (33) that

$$F(x, y) = \mathrm{Re}\left\{2\frac{y^2}{z}\int_0^1 \xi^3 d\xi \int_0^1\int_0^\pi \frac{\rho^3}{\sqrt{1-\rho^2}} \times \left[\frac{(q_2-1)\exp(-z\eta/\rho)}{(1-q_2\exp(-z\eta_0/\rho))}+1\right]\sin^2\alpha\, d\rho\, d\alpha\right\}.$$

This expression coincides with the result obtained in [17] for a homogeneous cylindrical metallic particle.

The results of calculations of $F(x, y, \kappa, q_1, q_2)$ are shown in Figs. 1–6.

5. DISCUSSION

In the limit of purely specular reflection of electrons at the boundaries of the metallic layer of the particle ($q_1 = 1$, $q_2 = 1$), using formulas (30)–(32), we obtain the following expression for the dimensionless absorption cross section $F(x, y, \kappa)$:

$$F(z, \kappa) = \mathrm{Re}\left\{\frac{y^2}{z(x, y)}\frac{\pi}{6}(1-\kappa^4)\right\}. \tag{35}$$

Therefore, dimensional absorption cross section (34) becomes

$$\sigma(z, \kappa) = \sigma_0 \mathrm{Re}\left\{\frac{y^2}{z(x, y)}\frac{\pi}{6}(1-\kappa^4)\right\} = \sigma_0\frac{\pi}{6}(1-\kappa^4)\frac{xy^2}{x^2+y^2}. \tag{36}$$

In the case of a metallic particle without a core ($\kappa \longrightarrow 0$), this expression reduces to the classical result for a cylindrical particle (the Drude formula) [15]:

$$\sigma(z) = \sigma_0\frac{\pi}{6}\frac{xy^2}{x^2+y^2}.$$

With Eqs. (28) and (29), absorption cross section (36) coincides exactly with the classical result for a cylindrical metallic layer. The reason for this is that, at $q_1 = 1$ and $q_2 = 1$, the boundaries of the metallic layer of the particle have no effect on the electron distribution function $f(\mathbf{r}_\perp, \mathbf{v}_\perp, \mathbf{v}_z)$. The vortex current inside the specularly reflecting metal layer [see Eq. (23)] satisfies the local Ohm law for any relationship between the layer thickness l and the electron mean free path Λ. Thus, for specular reflection, there are no nonlocal (surface) effects.

Irrespective of the character of reflection of electrons from the boundaries of the metallic layer (i.e., at arbitrary values of q_1 and q_2), macroscopic asymptotic expression (35) also becomes valid as the particle size increases (at $x \gg 1$); in this case, we can disregard the terms with rapidly decaying exponential functions in Eqs. (30)–(32).

Figures 1 and 2 show the dependence of the dimensionless absorption cross section F on the dimensionless frequency of the external field y. Figure 1 corresponds to the case of equal electron reflectivities of the particle surfaces. For each curve, the ratio of the core radius to the particle radius κ is fixed. It is seen in Fig. 1 that, at low dimensionless frequencies y (where $y \ll 1$), F can be greater for particles in which the reflection of conduction electrons is purely specular. At $y > 1$, the dimensionless absorption cross section is greater for particles in which the reflection of conduction electrons from each of the surfaces is purely diffuse. Figure 2 shows the data for very small particles (as compared to the electron mean free path), where $R \ll \Lambda$ ($x = 0$). The curves correspond to different values of the reflectivities q_1 and q_2. The appearance of oscillations in the frequency dependence is due to the fact that the energy dissipation inside the metallic shell of the particle depends on the ratio of the time of flight of an electron between collisions with the surfaces to the period of the external electromagnetic field. This effect is most pronounced for diffuse reflection of electrons from the boundaries of the metallic layer of the particle ($q_1 = 0$ or $q_2 = 0$) and decreases with increasing surface reflectivity. With an increase in the particle radius, the oscillations of the frequency dependence become smoother because of the enhancement of the effect of electron collisions in the bulk. As the reflectivities increase, the absorption cross section decreases, because the surface effects in energy dissipation become less important.

In Fig. 3, the dimensionless absorption cross section F is plotted as a function of the dimensionless inverse mean free path x. The curves correspond to the same dimensionless frequency but various values of the reflectivities q_1 and q_2. Curve *2* starts virtually at the origin and has a maximum. This dependence is close to the classical result (36), since the main contribution to the absorption cross section comes from the electrons specularly reflected from the boundary of the inhomogeneous particle. At intermediate values of the reflectivities ($q \neq 0$, $q \neq 1$), the dimensionless absorption cross section is nonzero even for a highly pure metal, where $x = 0$. As the particle radius increases, all curves merge and we obtain the classical result. As the frequency increases, the absorption cross section also increases, since the intensity of the vortex electric field is directly proportional to the frequency of the external field.

To analyze the dependence of the dimensionless absorption cross section F on the ratio κ of the core radius to the particle radius, we use Fig. 4. This figure shows the dimensionless absorption cross section per unit volume of the metal $G(\kappa)$ (specific absorption cross section),

$$G(\kappa) = \frac{F(\kappa)}{1-\kappa^2},$$

for a metallic cylindrical particle with a dielectric core.

We restrict ourselves to the case of purely metallic particles ($x = 0$) and a fixed value of the dimensionless frequency of the external field y. For such particles (electrons in pure metals have a large mean free path), in a wide range of κ values, the cross section can be greater for specular reflection of electrons from the outer surface of the metallic layer of the particle. At values of κ close to unity, the specific absorption cross section is low at all frequencies and at all values of the reflectivities, since the cylindrical metallic shell of the particle is very thin and, during the flight between the surfaces of the shell, electrons have no time to be appreciably accelerated by the external electromagnetic field (thus, the current density in the shell tends to zero).

Figures 5 and 6 show the effect of the reflectivities q_1 and q_2 on the dimensionless absorption cross section F for a particle with a thin metallic shell (κ is close to unity). In Fig. 5, we see that, in the absence of electron scattering in the bulk of the metal (the size of the metallic layer is extremely small), the dependence of the dimensionless absorption cross section F on the reflectivity q_1 is especially complicated in the case of specular reflection of electrons from the outer boundary of the metallic layer ($q_2 = 1$). In this case, the absorption cross section tends to zero for all values of y when electron scattering by the two reflecting surfaces of the metal becomes purely specular ($q_1 = 1$, $q_2 = 1$). Figure 6 shows how the dimensionless absorption section F depends on the reflectivity q_2. At almost any values of q_2 (except in a narrow region near unity), the absorption cross section increases as the reflection of electrons from the inner boundary of the cylindrical metal layer becomes more specular.

REFERENCES

1. Yu. I. Petrov, *Physics of Small Particles* (Nauka, Moscow, 1984) [in Russian].
2. M. Born and E. Wolf, *Principles of Optics* (Pergamon, Oxford, 1969; Nauka, Moscow 1973).
3. A. G. Lesskis, A. A. Yushkanov, and Yu. I. Yalamov, Zh. Éksp. Teor. Fiz. **83** (1), 310 (1982) [Sov. Phys. JETP **56** (1), 170 (1982)].
4. A. G. Lesskis, A. A. Yushkanov, and Yu. I. Yalamov, Poverkhnost **11**, 115 (1987).
5. H. J. Trodahl, Phys. Rev. B **19**, 1316 (1979).
6. H. J. Trodahl, J. Phys. C: Solid State Phys. **15**, 7245 (1982).
7. E. A. Bondar’, Opt. Spektrosk. **75** (4), 837 (1993) [Opt. Spectrosc. **75** (4), 496 (1993)].
8. E. A. Bondar’, Opt. Spektrosk. **80** (1), 94 (1996) [Opt. Spectrosc. **80** (1), 89 (1996)].

9. R. B. Dingle, Proc. Roy. Soc. A **201**, 545 (1950).
10. A. G. Mal'shukov, Solid State Commun. **44** (8), 1257 (1982).
11. A. G. Mal'shukov, Zh. Éksp. Teor. Fiz. **85** (2), 700 (1983) [Sov. Phys. JETP **58** (2), 409 (1983)].
12. P. M. Tomchuk and B. P. Tomchuk, Zh. Éksp. Teor. Fiz. **112** (2), 661 (1997) [JETP **85** (2), 360 (1997)].
13. R. J. Kubo, Proc. Phys. Soc. Jpn. **17**, 975 (1962).
14. É. A. Manykin, P. P. Poluéktov, and Yu. G. Rubezhnyĭ, Zh. Éksp. Teor. Fiz. **70** (6), 2117 (1976) [Sov. Phys. JETP **43** (6), 1105 (1976)].
15. É. V. Zavitaev, A. A. Yushkanov, and Yu. I. Yalamov, Zh. Tekh. Fiz. **71** (11), 114 (2001) [Tech. Phys. **46** (11), 1460 (2001)].
16. É. V. Zavitaev, A. A. Yushkanov, and Yu. I. Yalamov, Opt. Spektrosk. **92** (5), 851 (2002) [Opt. Spectrosc. **92** (5), 784 (2002)].
17. É. V. Zavitaev, A. A. Yushkanov, and Yu. I. Yalamov, Zh. Tekh. Fiz. **73** (3), 16 (2003) [Tech. Phys. **48** (3), 290 (2003)].
18. É. V. Zavitaev, A. A. Yushkanov, and Yu. I. Yalamov, Zh. Éksp. Teor. Fiz. **124** (5), 1112 (2003) [JETP **97** (5), 996 (2003)].
19. J. M. Ziman, *Electrons and Phonons* (Clarendon, Oxford, 1960; Inostrannaya Literatura, Moscow, 1962).
20. R. D. Averitt, S. L. Westcott, and N. J. J. Halas, J. Opt. Soc. Am. B **16** (10), 1824 (1999).
21. A. Henglein, J. Phys. Chem. B **104** (10), 2201 (2000).
22. A. I. Sidorov, Opt. Zh. **70** (2), 9 (2003).
23. L. D. Landau and E. M. Lifshitz, *Electrodynamics of Continuous Media*, (Nauka, Moscow, 1992; Pergamon, Oxford, 1960).
24. W. A. Harrison, *Solid State Theory* (McGraw-Hill, New York, 1970; Mir, Moscow, 1972).
25. R. Courant, *Partielle Differentialgleichungen* (Unpublished lecture notes, Gottingen, 1932; Mir, Moscow, 1964).

Translated by I. Zvyagin

Physics of the Solid State, Vol. 47, No. 7, 2005, pp. 1201–1204. Translated from Fizika Tverdogo Tela, Vol. 47, No. 7, 2005, pp. 1162–1164.
Original Russian Text Copyright © 2005 by Morozov, Primakov.

METALS AND SUPERCONDUCTORS

Dynamics and Location of Hydrogen in $TaO_{0.03}H_{0.01}$

S. I. Morozov and N. G. Primakov

Leĭpunskiĭ Institute of Physics and Power Engineering, pl. Bondarenko 1, Obninsk, Kaluzhskaya oblast, 249033 Russia
e-mail: morozov@ippe.ru

Received June 15, 2004; in final form, September 13, 2004

Abstract—The dynamics of hydrogen atoms in Ta–H and Ta–O–H interstitial solid solutions is analyzed. The vibrational energies of hydrogen interstitial impurity atoms are determined, and the metal–impurity interaction constants are calculated taking into account the atomic thermal vibrations in the host lattice. It is found that, in the Ta–O–H solid solution, as in the Ta–H solid solution, hydrogen atoms are located in relatively undistorted tetrahedra and the distance between the hydrogen and oxygen atoms is no shorter than that in the third coordination shell of the octahedral interstices. *© 2005 Pleiades Publishing, Inc.*

1. INTRODUCTION

In interstitial ternary alloys, the dynamics and local structure of the nearest hydrogen environment depend on the concentrations of hydrogen atoms and *p* elements, the temperature, and the structure of the host lattice. Oxygen atoms involved in metals can serve as traps for hydrogen atoms. Capture of hydrogen atoms by impurities leads to a number of interesting effects, such as hydrogen stabilization of the α phase at low temperatures, changes in the hydrogen location, etc. For example, in solid solutions of the Ti–O–H system at a particular concentration of oxygen atoms, hydrogen atoms occupy octahedral interstices rather than tetrahedral positions. In this case, hydrogen remains in octahedral interstices of the solid solution down to a temperature of 5 K [1].

It has been found that, in Group Va transition metals, oxygen and nitrogen atoms serve as traps for hydrogen atoms. This finding has been confirmed by various experimental methods. Slow-neutron inelastic scattering has been used primarily for studying solid solutions in the niobium-based system (see, for example, [2]). It has been established that, in solid solutions of the Nb–(O,N)–H system, oxygen and nitrogen atoms act as traps capturing one hydrogen atom per *p* atom and, consequently, suppress the hydride formation down to liquid-helium temperature. Moreover, it has been demonstrated that, in these solid solutions, both untrapped and trapped hydrogen atoms are located in tetrahedral interstices of the host lattice. Heene *et al.* [3] obtained similar results for solid solutions in the Ta–N–H system. Solid solutions in the Ta–O system have not been studied using slow neutron inelastic scattering. However, such investigations are of undeniable interest. In the present work, we studied interstitial solid solutions in the Ta–H and Ta–O–H systems in order to elucidate the mutual influence of interstitial atoms of different types on their location in the crystal structure. Necessary information can be obtained from analyzing the structure of the local modes of oxygen and hydrogen atoms, because the local vibrations of interstitial atoms are very sensitive to variations in the type and size of the interstices, as well as in the local environment of the interstitial atoms themselves. This effect has been reliably established for *Me*–H solid solutions and is especially pronounced in solid solutions in which hydrogen atoms can occupy both tetrahedral and octahedral interstices (V–H [4–6], Ti–O–H [1, 7]).

In the primary Ta–H solid solution, hydrogen atoms occupy tetrahedral interstices (see, for example, [8]). In order to determine the location of hydrogen atoms in interstitial solid solutions of the Ta–O system, we measured the slow-neutron inelastic scattering spectra of the $TaO_{0.03}H_{0.01}$ and $TaH_{0.01}$ compounds.

2. SAMPLE PREPARATION AND EXPERIMENTAL TECHNIQUE

Samples of the $TaH_{0.01}$ compound were prepared through the saturation of tantalum plates with hydrogen from the gas phase. Samples of the $TaO_{0.03}H_{0.01}$ compound were prepared in two stages. At the first stage, tantalum plates were saturated with oxygen from the gas phase at a temperature $T = 1100$°C with subsequent oil quenching after homogenizing annealing for 5 h. According to x-ray diffraction analysis, oxygen atoms are located in an interstitial solid solution with the lattice parameter $a = 3.314 \pm 0.002$ Å corresponding to the composition $TaO_{0.03}$ (3.077 ± 0.002 at. %), which is in good agreement with the amount of the absorbed gas. At the second stage, the $TaO_{0.03}$ sample was divided into two equal parts. Either of these two parts was saturated with oxygen until it reached the composition $TaO_{0.03}H_{0.01}$. For this purpose, gaseous hydrogen was preliminary accumulated in calibrated volumes and was then supplied to the sample placed in a known volume at a temperature of 1000°C. The gas pressure exerted on the sample was increased to a saturation

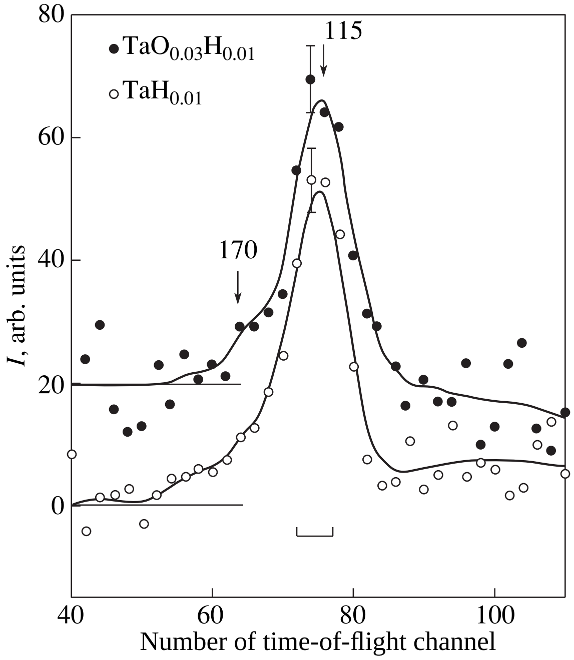

Fig. 1. Slow-neutron inelastic scattering spectra of hydrogen atoms in the $TaH_{0.01}$ and $TaO_{0.03}H_{0.01}$ alloys. Numbers over the arrows are the transferred energies ε given in millielectron-volts. Vertical and horizontal dashes indicate the statistical accuracy and the half-width of the instrumental resolution function, respectively. The solid lines correspond to the smoothening of the experimental spectrum by the fast Fourier transform method.

hydrogen vapor pressure $P \approx 150$ mmHg, which corresponds to the composition $TaH_{0.01}$ at 1000°C. After the homogenizing annealing, the sample was subjected to oil quenching. The composition of the final product was determined from the weight increment and corresponded to the formula $TaO_{0.03}H_{0.01}$. This composition was confirmed by slow-neutron inelastic scattering investigations.

The neutron scattering investigations were carried out on a DIN-2PI time-of-flight direct-geometry spectrometer installed on an IBR-2 reactor [9]. The slow-neutron inelastic scattering spectra were recorded in a neutron energy gain mode. In addition to the $TaH_{0.01}$ and $TaO_{0.03}H_{0.01}$ interstitial solid solutions, the neutron scattering experiments were performed with samples of pure tantalum and the $TaO_{0.03}$ solid solution. All the measurements were carried out in the same geometry. The samples were assembled into flat plates $100 \times 100 \times 1$ mm in size. The mean transmittance of these plates with respect to the neutron scattering cross section was approximately equal to 96%, which excluded noticeable contributions of multiple scattering to the slow-neutron inelastic scattering spectra. The initial energy of neutrons incident on the sample was $E_0 = 8.2$ meV. The scattered neutrons were detected in the angle range 70°–134°. The instrumental resolution was $R \sim 12$ meV in the energy transfer range $\varepsilon = E - E_0 = 0$–$120$ meV, which corresponds to local vibrations of hydrogen atoms.

By subtracting the fast-neutron scattering background (with due regard for the detector efficiency and the attenuation of the primary and singly scattered neutron beams) from the slow-neutron inelastic scattering spectra, we obtained the double-differential scattering cross sections for Ta, $TaH_{0.01}$, $TaO_{0.03}$, and $TaO_{0.03}H_{0.01}$ samples. Then, the spectra of the double-differential scattering cross sections were processed using the subtraction method in the incoherent approximation. As a result, we obtained the partial frequency spectra of oxygen and hydrogen impurity atoms. Practical experience shows that this technique works very well in the case of low (≤2–3 at. %) concentrations of impurity atoms and accounts for the contribution of the multiphonon neutron scattering by the host atoms.

3. RESULTS AND DISCUSSION

The slow-neutron inelastic scattering spectra of the hydrogen-containing solid solutions $TaH_{0.01}$ and $TaO_{0.03}H_{0.01}$ in the energy transfer range $\varepsilon_1 \approx 115$ meV exhibit additional features with respect to the spectra of pure tantalum and the $TaO_{0.03}$ solid solution. Figure 1 shows the angle-averaged differences in the slow-neutron inelastic scattering spectra ($TaO_{0.03}H_{0.01}$–$TaO_{0.03}$) and ($TaH_{0.01}$–Ta).

The difference spectra correspond to scattering by hydrogen atoms. It can be seen from Fig. 1 that, in the spectra of both solid solutions, the location and shape of the peak in the energy transfer range $\varepsilon_1 = 115 \pm 3$ meV coincide with each other. Thus, no noticeable effect of oxygen atoms on the dynamics of hydrogen atoms is observed. However, the dynamics of the interstitial atom is very sensitive to variations in its local environment. Hence, this finding indicates that hydrogen atoms are located in undistorted tetrahedral positions. We can also draw the conclusion that solid solutions in the Ta–O–H system are similar to solid solutions in the Ta–N–H system in terms of both structure and dynamics. The above energy of the low-frequency vibrational mode of hydrogen atoms is close to the value obtained for hydrogen atoms in interstitial solid solutions of the Ta–H and Ta–N–H systems ($\varepsilon_1 = 113 \pm 1$ meV) [3]. As was shown in [3], the energy corresponding to the high-frequency mode of hydrogen [$\varepsilon_{2,3} = (160$–$163) \pm 1$ meV] does not undergo substantial variations either upon addition of nitrogen to the Ta–H solid solution or upon the phase transition of the Ta–H solid solution from the α phase to the hydride phase. The main differences in the spectra of the high-frequency vibrations of hydrogen atoms in tantalum in the presence and in the absence of impurity traps are observed in the linewidth ($\Delta\varepsilon_{2,3} \approx 11.5$ meV for the $TaH_{0.086}$ solid solution, and $\Delta\varepsilon_{2,3} \geq 20$ meV for the $TaN_{0.006}H_{0.003}$ solid solution [3]).

The high-frequency peak, which corresponds to the doubly degenerate vibrations of hydrogen atoms in the tetrahedral positions, is almost entirely absent in the difference spectra presented in Fig. 1. One can see only an insignificant inflection at an energy ε = 170 meV, which corresponds to the predicted energy of high-frequency vibrations of hydrogen atoms in the sample under investigation. This is associated with a small population of the corresponding levels of vibrational energies at room temperature. Based on the above conclusion that the shape of the hydrogen spectrum does not depend on the presence of *p*-element impurities in the alloy, we can summarize both spectra of slow-neutron inelastic scattering in order to increase the statistical accuracy. After this summation, the frequency spectrum of hydrogen atoms was calculated for the averaged spectrum of neutron inelastic scattering by hydrogen atoms. The results of these calculations are presented in Fig. 2. The generalized partial frequency spectrum of hydrogen atoms exhibits a high-energy peak ($\varepsilon \approx 175$ meV). The calculated energy of the high-frequency peak is higher than the energies of the hydrogen doublet reported both for the α phase of the Ta–H solid solution ($\varepsilon_{2,3} \approx 154$–$164$ meV) [3, 8] and for the $TaN_{0.006}H_{0.003}$ solid solution ($\varepsilon_{2,3} \approx 160$–$163$ meV) [3]. However, it is worth noting that the allowance made for the Debye–Waller factor leads to a shift of the maximum toward higher energies. This effect also manifests itself in a shift of the low-frequency singlet (at $\varepsilon_1 = 115 \pm 3$ meV in the slow-neutron inelastic scattering spectrum in Fig. 1 and at $\varepsilon_1 = 118 \pm 3$ meV in the spectrum $g_H(\varepsilon)$ in Fig. 2). The above effect is especially noticeable in the case of broad peaks, which, as a rule, occurs when there are high-frequency modes of hydrogen atoms in Group V transition metals.

Within the limits of experimental error, the ratio between the obtained vibrational frequencies of hydrogen atoms $\varepsilon_{2,3}/\varepsilon_1 \approx \sqrt{2}$ corresponds to a splitting of the vibrational modes in an undistorted tetrahedron of the body-centered cubic structure. The atomic interaction constant for the Ta–H bond was calculated taking into account the vibrations of the host atoms (by analogy with the calculation performed earlier in [10]) in both solid solutions systems: $f_l = (6.9 \pm 0.5) \times 10^4$ dyn/cm. The constant of interaction between the nearest neighbor atoms involved in the Ta–Ta bond was estimated in the Einstein approximation from the mean-square frequency of vibrations of the host atoms $\langle\omega^2\rangle = 257$ meV^2. As a result, we obtained the interaction constant $f_l \approx 6.7 \times 10^4$ dyn/cm. The closeness of the given values of the interaction constants has a stochastic nature. In the similar Nb–H system, the vibrational energies of hydrogen atoms (see, for example, [2]) and, correspondingly, the interaction constant for the Nb–H bond almost coincide with the values obtained for the Ta–H solid solution. However, the interaction constant for the Nb–Nb bond, which was also estimated in the Einstein approximation from the mean-square frequency of vibrations of the host atoms $\langle\omega^2\rangle = 360$ meV^2 [11], gives the value $f_l = 4.8 \times 10^4$ dyn/cm, which is inconsistent with the isotopic approximation.

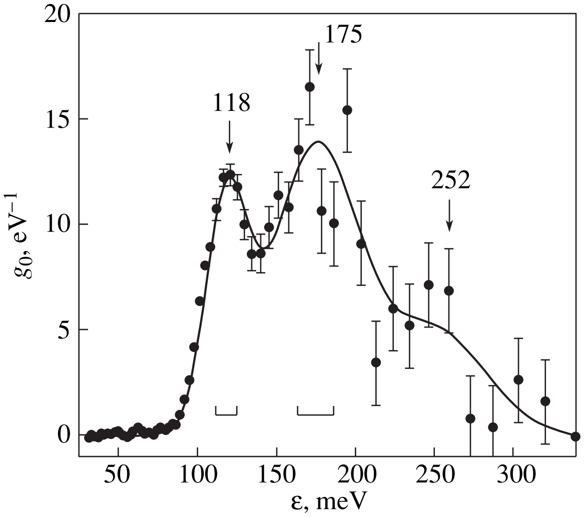

Fig. 2. Generalized partial frequency spectrum of hydrogen atoms in tantalum and in the α-$TaO_{0.03}H_{0.01}$ solid solution. The solid line corresponds to the approximation of the spectrum by three Gaussian functions. The high-frequency wing of the spectrum is attributed to the two-phonon processes. The notation is the same as in Fig. 1.

4. CONCLUSIONS

Thus, the behavior of hydrogen in solid solutions of the Ta–O–H system is similar to that in solid solutions of the Ta–N–H system at least at a temperature $T \approx 300$ K. The results obtained allow us to assert that, both in the α-$TaO_{0.03}H_{0.01}$ alloy and in the α-Ta–H alloy, hydrogen atoms occupy tetrahedral positions. The similarity between the low-frequency spectra of hydrogen atoms in solid solutions of both systems indicates that hydrogen atoms are located in relatively undistorted tetrahedra and that the distance between the hydrogen and oxygen atoms is no shorter than that in the third coordination shell of the octahedral interstices. Otherwise, the $R_{\text{O–H}}$ distance would be either comparable to or less than the $R_{Me\text{–H}}$ distance, which would inevitably lead to a noticeable distortion of the spectrum of local vibrations of hydrogen atoms as compared to the oxygen-free sample.

ACKNOWLEDGMENTS

We would like to thank S.V. Terekhov, V.V. Kazarnikov, and G.P. Nikonorov for their assistance in performing this study.

This work was supported by the Russian Foundation for Basic Research and the Administration of the Kaluga oblast, project nos. 01-02-96002 and 01-03-96009.

REFERENCES

1. A. V. Belushkin, S. I. Morozov, I. Natkanets, and V. V. Sumin, Report No. R14-86-41, OIYaI (Joint Institute for Nuclear Research, Dubna, 1986).
2. A. Magerl, J. J. Rush, J. M. Rowe, D. Richter, and H. Wipf, Phys. Rev. B **27**, 927 (1983).
3. M. Heene, H. Wipf, T. J. Udovic, and J. J. Rush, J. Phys.: Condens. Matter **12**, 6183 (2000).
4. G. Verdan, R. Rubin, and W. Kley, in *Proceedings of the Symposium on Neutron Inelastic Scattering Copenhagen, 1968* (IAEA, Vienna, 1968), Vol. 1, p. 223.
5. D. Klauder, V. Lottner, and H. Scheuer, Solid State Commun. **32** (8), 617 (1979).
6. R. Hempelmann, D. Richter, and D. L. Price, Phys. Rev. Lett. **58** (10), 1016 (1987).
7. K. N. Kréchun, S. I. Morozov, I. Natkaniec, and V. V. Sumin, Fiz. Tverd. Tela (Leningrad) **30** (9), 2585 (1988) [Sov. Phys. Solid State **30** (9), 1487 (1988)].
8. A. Magerl, J. J. Rush, and J. M. Rowe, Phys. Rev. B **33** (4), 2093 (1986).
9. V. A. Parfenov, P. S. Klemyshev, I. G. Morozov, and A. F. Pavlov, in *Proceedings of the Symposium on Neutron Inelastic Scattering, Vienna, 1977* (IAEA, Vienna, 1978), Vol. 1, p. 81.
10. S. I. Morozov and V. V. Kazarnikov, Fiz. Tverd. Tela (St. Petersburg) **35** (11), 3145 (1993) [Phys. Solid State **35** (11), 1549 (1993)].
11. S. I. Morozov, S. A. Danilkin, and V. T. Ém, Zh. Éksp. Teor. Fiz. **109** (6), 2130 (1996) [JETP **82** (6), 1148 (1996)].

Translated by N. Korovin

Physics of the Solid State, Vol. 47, No. 7, 2005, pp. 1205–1210. Translated from Fizika Tverdogo Tela, Vol. 47, No. 7, 2005, pp. 1165–1169.
Original Russian Text Copyright © 2005 by Panova, Chernoplekov, Shikov.

Specific Heat and Electrical Resistivity of an Icosahedral-Structure $Zr_{70}Pd_{30}$ Alloy and of Its Amorphous and Crystalline Analogs

G. Kh. Panova, N. A. Chernoplekov, and A. A. Shikov
Russian Research Center Kurchatov Institute, pl. Kurchatova 1, Moscow, 123182 Russia
e-mail: shikov@isssph.kiae.ru

Received July 16, 2004

Abstract—Binary icosahedral and crystalline phases of the $Zr_{70}Pd_{30}$ alloy were obtained in crystallization from the amorphous state during heat treatment. The specific heat and electrical resistivity of the icosahedral, amorphous, and crystalline phases were measured and compared. An increase in the electronic density of states on the Fermi surface, lattice softening, and an increase in the electron–phonon coupling constant were observed to occur with decreasing structural order. Despite the high valence electron density in the icosahedral phase, where the electronic densities of states are twice those in the crystal, the electrical resistivity of the icosahedral phase is ~50 times as high. Superconductivity was observed for the first time in the icosahedral phase of a binary system of transition metal atoms, $Zr_{70}Pd_{30}$. *© 2005 Pleiades Publishing, Inc.*

1. INTRODUCTION

The icosahedral phase has been observed to form in a number of Zr-based alloys in the course of metallic-glass crystallization occurring under heat treatment. Earlier studies assumed quasicrystalline phases in Zr-based multicomponent alloys to be stabilized by some elements, such as O, Pd, Ag, Au, Pt, and Ti [1–6]. Recent papers have reported the preparation of binary quasicrystalline icosahedral phases in Zr–Pd and Zr–Pt alloys [7–10], thus suggesting that, in order for an icosahedral phase to form, a system need not necessarily be multicomponent.

The structure of the quasicrystalline $Zr_{70}Pd_{30}$ phase obtained in the course of crystallization of a $Zr_{70}Pd_{30}$ amorphous alloy has been studied in considerable detail [7–11]. A structural analysis of quenched and annealed samples of the $Zr_{70}Pd_{30}$ alloy showed that Zr rather than Pd acts as a center of icosahedral clusters in quenched alloys and that the fraction of icosahedral clusters grows under annealing [8]. Note that the binary icosahedral phase in Zr-based alloys is limited to the Zr–Pd and Zr–Pt systems. This may be assigned to the large negative enthalpy of a Zr and Pt mixture, a criterion for the formation of quasicrystalline phases in any system [11]. Earlier studies of $Zr_{75}Rh_{25}$ [12], $Zr_{70}Be_{30}$ [13], $Zr_{70}Co_{30}$, $Zr_{70}Ni_{30}$, and $Zr_{50}Cu_{50}$ [10] alloys revealed that icosahedral phases do not form in these alloys in crystallization from the amorphous state.

The $Zr_{70}Pd_{30}$ alloy arouses interest for a number of reasons. It was established in [9] that this alloy may reside in three phase states, namely, amorphous, icosahedral, and crystalline, which permits one to study the effect of a change in short-range order in the course of transition from the amorphous to the icosahedral or crystalline state without a simultaneous change in the concentration of the components. Moreover, as found in the present work, the alloy is superconducting in all three phases, thus permitting one not only to determine some phonon and electronic characteristics experimentally but also to estimate the electron–phonon coupling. The absence of complex concomitant magnetic effects simplifies separation of the phonon and electronic characteristics of the phases of interest.

To understand the conditions favoring the formation and stabilization of a quasicrystalline structure and to investigate the nature of many of the physical properties of quasicrystals, detailed information is needed concerning the vibrational spectrum and electronic density of states on the Fermi surface. No such information was available on the samples for study.

Thus, this study was aimed at a comparative investigation of the electronic, vibrational, and superconducting characteristics of quasicrystals and of their crystalline and amorphous analogs by measuring the temperature dependence of the heat capacity and electrical resistivity.

2. PREPARATION OF SAMPLES AND THEIR CHARACTERISTICS

A $Zr_{70}Pd_{30}$ alloy was prepared from electrolytically pure zirconium (99.99%) and pure palladium (99.96%). To produce crystalline samples, the starting

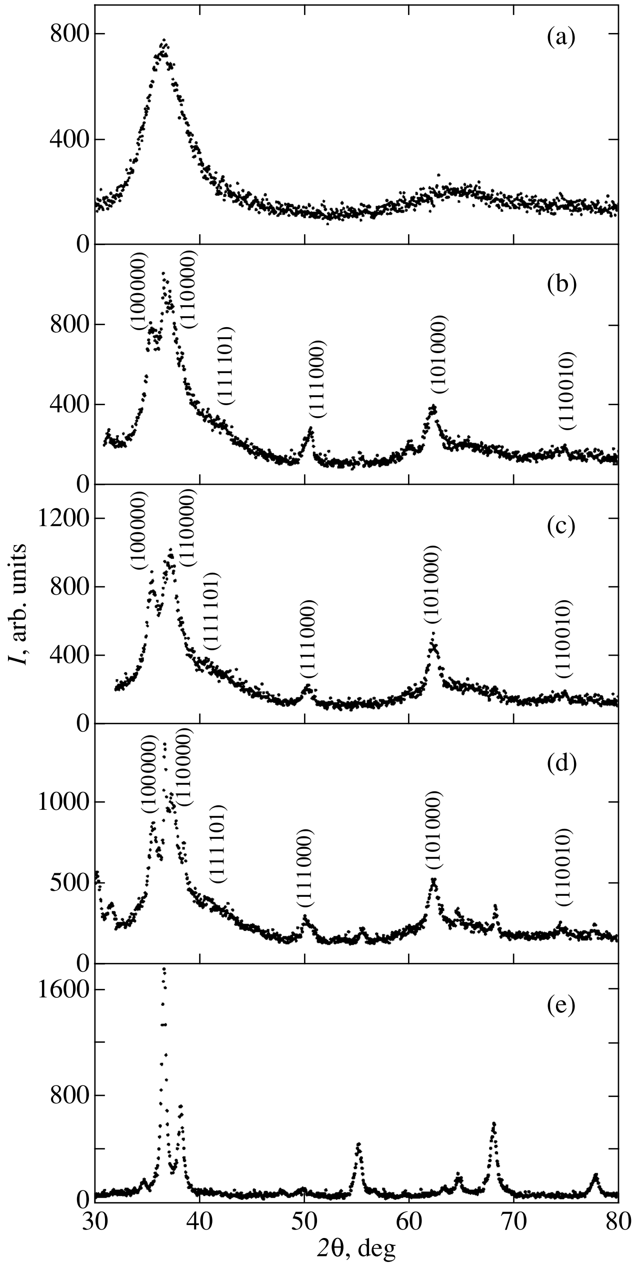

Fig. 1. X-ray diffractograms of (a) the amorphous phase, (b–d) the icosahedral phase for $T_{\rm ann}$ equal to (b) 740 and (c) 760 K and also for (d) $T_{\rm ann}$ = 760 K with the sample held for 2.5 min at this temperature, and (e) the crystalline phase of $Zr_{70}Pd_{30}$. The Bragg peaks corresponding to the icosahedral phase are indexed following the scheme proposed in [14].

elements were melted in an induction furnace in an argon ambient. To obtain amorphous samples, the starting elements were placed in a boron nitride ampoule and melted in an induction furnace at a low argon pressure and then were quenched by spinning in the liquid state on a rotating copper disk. The quenching rate was estimated to be ~10^6 K/s. Amorphous samples prepared in this way were ribbons 1.5- to 2.0-mm wide and ~0.03-mm thick. After measurements, amorphous samples were annealed in a helium gas flow in a quartz tube mounted in a resistance furnace. To find the conditions best suited for preparing a near-perfect icosahedral sample, annealing was conducted at several temperatures, followed by fast quenching.

The crystallization kinetics of a $Zr_{70}Pd_{30}$ alloy was studied with a differential scanning calorimeter. A heating thermogram obtained at a rate of 18 K/min showed that the crystallization passes through two exothermal peaks. The first of them corresponds to a transition to the icosahedral phase at T = 723 K, and the second, at T = 800 K, signals a transition to the crystalline phase, in full agreement with the results reported in [8–11].

The structure of the samples thus prepared and the effect of annealing on their state were determined, using x-ray diffraction, on a DRON-2 diffractometer (CuK_α radiation). The phase assignment and lattice parameter determination were performed from the diffraction patterns. The diffraction pattern of a $Zr_{70}Pd_{30}$ sample quenched from liquid state is displayed in Fig. 1a. The overall shape of the curve is typical of an amorphous metal and reveals that there is no long-range order. The first broad maximum lies at about 2θ = 37°, and the second lies at 2θ = 63°. To find the regime most promising for obtaining as perfect an icosahedral sample as possible, the annealing was carried out at several temperatures, more specifically, at 740 and 760 K and also at 760 K with the sample held at this temperature for 2.5 min followed by fast quenching. The increase in the electrical resistivity of the icosahedral sample observed after annealing up to 760 K and the negative temperature coefficient of the resistivity result from the improved quality of the icosahedral sample. After annealing up to 760 K with the sample held at this temperature for 2.5 min, however, the diffraction pattern characteristic of the icosahedral phase starts to reveal peaks typical of the crystalline phase. The x-ray diffractograms of the icosahedral phase presented in Figs. 1b–1d reveal Bragg peaks that correspond to an icosahedral structure; these peaks are indexed in accordance with the scheme proposed by Bancel *et al.* [14]. The value of the six-dimensional hypercubic lattice parameter as derived from the positions of the [100000] and [110000] peaks is 7.624 Å. Figure 1e displays an x-ray diffraction pattern obtained for the crystalline phase. This phase is tetragonal (space group $J4/mmm$) with the lattice parameters a = 3.306 Å and c = 10.894 Å (according to [15]).

The heat capacity of the samples was measured in an adiabatic calorimeter with pulsed heating [16]. The experimental error in determining the heat capacity was 2% in the temperature interval 2–4 K, 1% at 4–10 K, and 0.2–0.5% in the range 10–40 K. The superconducting transition temperature was derived from the jump in the heat capacity.

The electrical resistivity of the samples was determined using the four-probe method. Measurements were conducted on ribbons about 0.03 × 1.5 × 9 mm in size. The measuring current was small enough (<1 mA) to preclude sample overheating. The temperature was measured to within ±0.01 K with a TSU carbon thermometer. The value of T_c was found from the resistivity at the midpoint of the superconducting transition.

3. EXPERIMENTAL RESULTS AND DISCUSSION

The temperature dependence of electrical resistivity of the $Zr_{70}Pd_{30}$ alloy in the amorphous, icosahedral, and crystalline states was studied within the temperature range 2–300 K in different stages of structural relaxation occurring in the course of thermally induced ordering (Fig. 2).

Heat treatment translates the ρ(T) curves toward an increase in ρ, so they remain nearly parallel to one another. This means that heat treatment has almost no effect on the temperature-dependent components of ρ(T). Therefore, the values of ρ thus found can be used as a measure of the carrier concentration, because ρ in quasicrystals is dominated by the concentrations of free carriers and of structural defects.

The observed increase in ρ with an increase in the annealing temperature and the negative temperature coefficient of electrical resistivity for the icosahedral phase (annealed up to 760 K) argue for the improved quality of the icosahedral sample [17]. The electrical resistivity of the icosahedral phase (T_{ann} = 760 K) is considerably higher than that of the amorphous phase and exceeds the resistivity of the crystalline phase by ~50 times at low temperatures.

The inset to Fig. 2 compares measurements of the low-temperature electrical resistivity and of T_c of the amorphous and crystalline phases, as well as of the icosahedral phase obtained by annealing up to 740 and 760 K and also at 760 K with the sample held at this temperature for 2.5 min. These samples in all three phases are superconducting. The superconducting transition temperatures T_c are 2.97 K for the amorphous phase and 2.54 and 2.05 K for the icosahedral phase annealed up to 740 and 760 K, respectively. No superconducting transition was observed down to 1.5 K during annealing of a sample to 760 K with the sample held at this temperature for 2.5 min, a procedure in which the icosahedral phase starts to convert into the crystalline phase and peaks typical of crystals appear in the diffractogram. The resistivity jumps that are observed to appear after annealing and precede the superconducting transition are apparently due to residues of the amorphous phase in the icosahedral sample. Thus, improvement of the quality of an icosahedral sample gives rise to an increased electrical resistivity, the appearance of a negative temperature coefficient of electrical resistivity, and a decreased value of T_c. The superconducting transition in the crystalline phase is observed at T_c = 1.5 K, which is lower than T_c for the amorphous and icosahedral phases. The above observations reflect the effect of the formation kinetics of the binary $Zr_{70}Pd_{30}$ icosahedral phase in the course of crystallization of the amorphous $Zr_{70}Pd_{30}$ alloy.

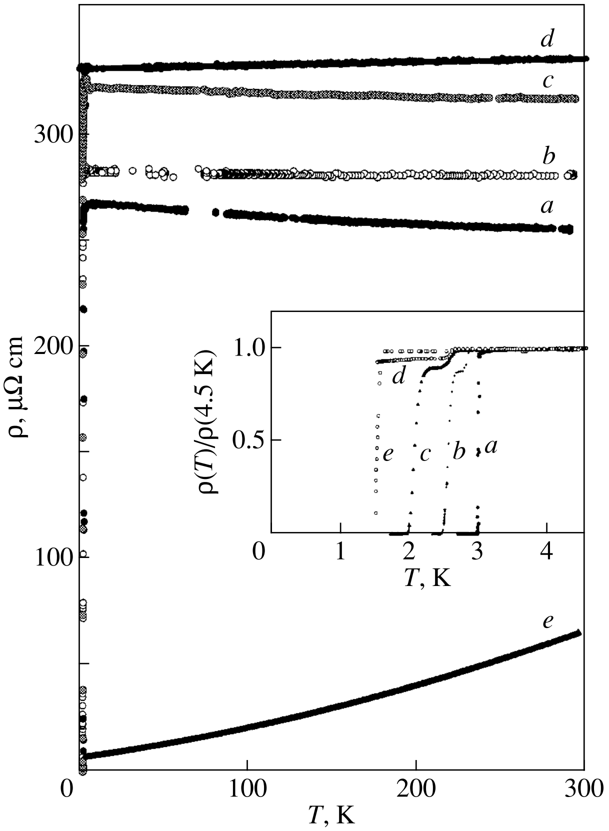

Fig. 2. Temperature dependences of the electrical resistivity of (a) the amorphous phase, (b, c) the icosahedral phase for T_{ann} equal to (b) 740 and (c) 760 K, (d) the icosahedral phase for T_{ann} = 760 K with the sample held for 2.5 min at this temperature, and (e) the crystalline phase of the $Zr_{70}Pd_{30}$ system in the range 2–300 K. The inset shows analogous dependences near the superconducting transition point.

The measured temperature dependence of electrical resistivity of the icosahedral-structure $Zr_{70}Pd_{30}$ alloy differs radically from that for the crystalline and amorphous structures; namely, the resistivity of the icosahedral phase is substantially higher than that of its analogs and increases with increasing structural perfection of the quasicrystal.

Investigation of the evolution of the electronic parameters of the $Zr_{70}Pd_{30}$ icosahedral phase with increasing structural perfection sheds light on what

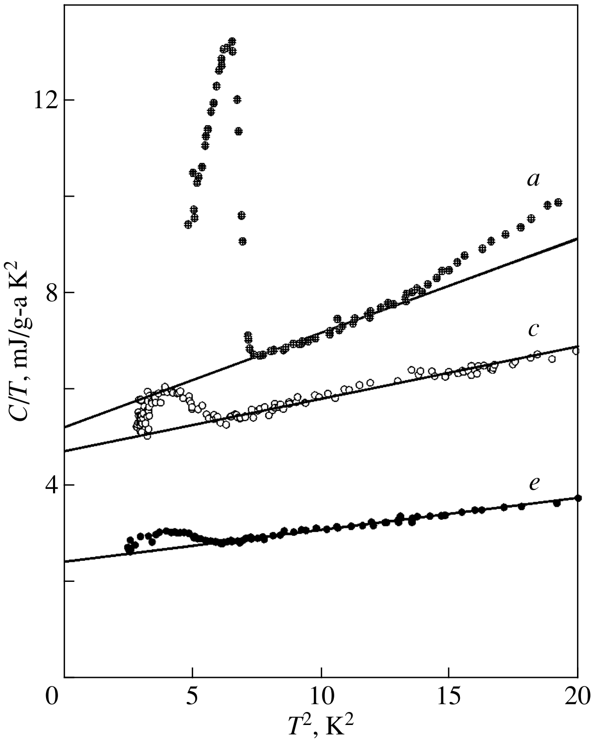

Fig. 3. Temperature dependences of the specific heat of (*a*) the amorphous, (*c*) icosahedral, and (*e*) crystalline phases of $Zr_{70}Pd_{30}$ measured in the range 1.5–4.5 K and plotted in the C/T vs. T^2 coordinates. The curve notation is the same as in Fig. 1.

drives the transformation of a "good" metal to a high-resistivity metal and allows one to draw the fairly general conclusion that electron localization is the driving force (this viewpoint is in qualitative agreement with the cluster model of quasicrystal structure [17]).

The heat capacity of the $Zr_{70}Pd_{30}$ alloy with icosahedral, amorphous, or crystalline structure was measured in the temperature interval 1.5–40 K. Throughout this temperature range, the specific heat of the icosahedral phase is lower than that of the amorphous phase but higher than that of the crystalline phase.

Figure 3 displays the behavior of the low-temperature specific heat of the three phases in the range 1.5–4.5 K plotted as C/T versus T^2 graphs. The amorphous phase exhibits a sharp superconducting transition at a temperature $T_c = 2.6$ K, with a transition width $\Delta T_c = 0.2$ K. The superconducting transitions in the icosahedral and crystalline phases as derived from the heat capacity data are broader and are observed at similar temperatures: $T_c = 2.1$ K ($\Delta T_c = 0.6$ K) for the icosahedral phase and $T_c = 1.9$ K ($\Delta T_c = 0.7$ K) for the crystalline state. Each phase reveals a heat capacity jump at about the same temperature as obtained from resistivity measurements. This suggests a volume character of superconductivity. Note that the absence of a second jump in the heat capacity associated with traces of the amorphous phase (which was observed for the resistivity) indicates that the amount of the amorphous phase present in the icosahedral sample is small (rough estimates yield 1–2%).

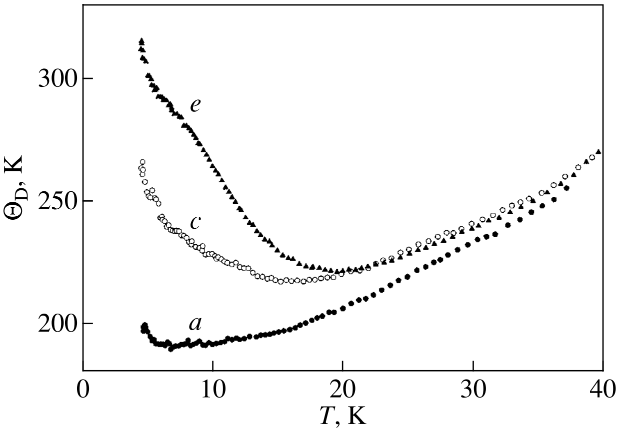

Fig. 4. Temperature dependences of $\Theta_D(T)$ measured in the range 3–40 K for (*a*) the amorphous, (*c*) icosahedral, and (*e*) crystalline $Zr_{70}Pd_{30}$ phases. The curve notation is the same as in Fig. 1.

The data derived from the electrical resistivity and heat capacity measurements are given in the table. As seen from the table, the characteristic parameters of the icosahedral phase lie between those of the amorphous and crystalline phases. A comparison of the electronic heat capacity coefficients for the icosahedral phase with those of the amorphous and crystalline phases reveals that the electronic density of states on the Fermi surface in the icosahedral phase of $Zr_{70}Pd_{30}$ is less than that in the amorphous phase but is twice that of the crystalline phase.

The heat capacity data suggest that the phonon spectrum softens with decreasing structural order, which is observed to occur as one goes over from the crystalline to icosahedral phase and then to the amorphous phase (Fig. 4).

Our results provided an estimate of the electron–phonon coupling constant λ and the electronic density of states $N_F(0)$ within the McMillan theory [18]. Both quantities, λ and $N_F(0)$, increase with decreasing structural order. All three of the phases are weak-coupling superconductors.

Our studies of the kinetic and thermodynamic properties of the amorphous, icosahedral, and crystalline phases of the $Zr_{70}Pd_{30}$ alloy allow us to make a suggestion regarding the mechanism of formation of a pseudogap in the electronic density of states near the Fermi level in the icosahedral phase.

The existence of a pseudogap is certainly insufficient to account for the anomalously high electrical

Parameters characterizing the amorphous, icosahedral, and crystalline phases of the $Zr_{70}Pd_{30}$ system

Parameter	Amorphous phase	Icosahedral phase	Crystalline phase
ρ_{300}, μΩ cm	250	310	70
$\rho_{4.2}$, μΩ cm	270	324	7
T_c (from resistivity), K	2.97	2.05	1.5
ΔT_c (from resistivity), K	0.05	0.15	0.1
γ, mJ/mol K^2	5.25	4.75	2.45
β, mJ/mol K^4	0.195	0.114	0.063
T_c (from heat capacity), K	2.6	2.1	1.9
ΔT_c (from heat capacity), K	0.2	0.6	0.7
$C_{es}/C_{en}(T_c)$	1.98	1.15	1.15
Θ_D, K	215	257	313
λ	0.58	0.54	0.51
$N_F(0)$, states/eV atom	0.70	0.66	0.34

Note: $\rho_{4.2}$ and ρ_{300} are resistivities at 4.2 and 300 K, respectively; coefficients γ and β approximate the specific heat at low temperatures by the relation $C = \gamma T + \beta T^3$; $C_{es}/C_{en}(T_c)$ is the ratio of electronic specific heats in the superconducting and normal states; Θ_D is the low-temperature characteristic Debye parameter; $N_F(0)$ is the electronic density of states on the Fermi surface; and λ is the electron-phonon coupling constant.

resistivity. In actual fact, the reason lies in the anomalously low electron mobility in a perfect quasicrystal, which is associated with the lack of translational symmetry and the lack of universal short-range order in the mutual arrangement of configurations. It is known [19] that quasi-periodicity is capable of appreciably changing the electronic structure and that interaction of the Fermi surface with faces of the Brillouin zone may give rise to the formation of a pseudogap in the electronic density of states.

Electron localization in a quasicrystal differs from the Anderson localization, which occurs due to atomic disorder in a system. In a quasicrystal, an electronic state may become localized by a quasi-periodic potential [20].

Our results provide a positive answer to the question of whether a valence electron system can be localized in a medium that consists only of metal atoms (without metalloid atoms) and is a metal with a standard electron concentration.

An analysis of the experimental data obtained provides support for the conclusion made by Gantmakher [21] that a quasicrystalline system consisting only of metal elements and approaching a metal–insulator transition should support (despite its high valence-electron concentration) the formation of stable atomic configurations that could serve as deep potential wells (traps) for the valence electrons.

4. CONCLUSIONS

For the first time, a comparative study of the electronic, vibrational, and superconducting characteristics of a $Zr_{70}Pd_{30}$ icosahedral quasicrystal and its crystalline and amorphous counterparts has been performed from measurements of the heat capacity and electrical resistivity.

The high electrical resistivity of the $Zr_{70}Pd_{30}$ quasicrystal (~50 times that of the crystalline phase), the negative temperature coefficient of resistivity, and the electronic specific heat being twice that in the crystalline phase should be apparently assigned to electron localization and the existence of a pseudogap in the electronic density of states on the Fermi surface.

Superconductivity has been observed for the first time in the icosahedral phase of $Zr_{70}Pd_{30}$ at the superconducting transition temperature $T_c = 2.1$ K.

ACKNOWLEDGMENTS

The authors are indebted to V.S. Kruglov for his interest in the work, Yu.Kh. Vekilov and A.S. Nigmatulin for helpful discussions, G.F. Syrykh for preparation of the amorphous sample, and G.V. Laskova for x-ray structural measurements.

This study was supported by the Russian Foundation for Basic Research, project no. 04-02-16017-a.

REFERENCES

1. U. Koster, J. Meinhardt, S. Roos, and H. Liebertz, Appl. Phys. Lett. **69** (2), 179 (1996).
2. B. S. Murty, D. H. Ping, K. Mono, and A. Inoue, Appl. Phys. Lett. **76** (1), 55 (2000).
3. B. S. Murty, D. H. Ping, K. Mono, and A. Inoue, Acta Mater. **48** (15), 3985 (2000).
4. J. Saida, M. Matsushita, and A. Inoue, Intermetallics **10** (11–12), 1089 (2002).
5. J. Saida and A. Inoue, J. Non-Cryst. Solids **317** (1–2), 97 (2003).
6. L. Q. Xing, J. Eckert, W. Loser, and L. Schultz, Appl. Phys. Lett. **74** (5), 664 (1999).
7. T. Takagi, T. Ohkudo, Y. Hirotsu, B. S. Murty, K. Hono, and D. Shindo, Appl. Phys. Lett. **79** (3), 485 (2001).
8. M. Kitada, M. Imafuku, J. Saida, and A. Inoue, J. Non-Cryst. Solids **312–314**, 594 (2002).
9. B. S. Murty, D. H. Ping, M. Ohnuma, and K. Hono, Acta Mater. **49** (17), 3453 (2001).

10. J. Saida, M. Matsushita, and A. Inoue, J. Appl. Phys. **90** (9), 4717 (2001).
11. B. S. Murty and K. Hono, Appl. Phys. Lett. **84** (10), 1674 (2004).
12. G. Kh. Panova, N. A. Chernoplekov, A. A. Shikov, and B. I. Savel’ev, Zh. Éksp. Teor. Fiz. **82** (2), 548 (1982) [Sov. Phys. JETP **55** (2), 319 (1982)].
13. G. Kh. Panova, B. I. Savel’ev, M. N. Khlopkin, N. A. Chernoplekov, and A. A. Shikov, Zh. Éksp. Teor. Fiz. **85** (4), 1308 (1983) [Sov. Phys. JETP **58** (4), 759 (1983)].
14. P. A. Bancel, P. A. Heiney, P. W. Stephens, A. I. Goldman, and P. M. Horn, Phys. Rev. Lett. **54** (22), 2422 (1985).
15. M. Nevitt and J. Downey, Trans. Metall. Soc. AIME **224**, 195 (1962).
16. M. N. Khlopkin, N. A. Chernoplekov, and P. A. Cheremnykh, Preprint No. 3549-10, IAÉ (Kurchatov Institute of Atomic Energy, Moscow, 1982).
17. A. F. Prekul, N. Yu. Kuzvin, and N. I. Shchetgolikhina, J. Alloys Compd. **342** (1–2), 405 (2002).
18. W. L. McMillan, Phys. Rev. **167**, 331 (1968).
19. Z. M. Stadnik, Phys. Prop. Quasicryst. **126**, 257 (1999).
20. Y. K. Vekilov, E. I. Isaev, S. F. Arslanov, and P. V. Slobodyanyuk, Mater. Sci. Eng., A **294–296**, 556 (2001).
21. V. F. Gantmakher, Usp. Fiz. Nauk **172** (11), 1283 (2002) [Phys. Usp. **45** (11), 1165 (2002)].

Translated by G. Skrebtsov

Physics of the Solid State, Vol. 47, No. 7, 2005, pp. 1211–1215. Translated from Fizika Tverdogo Tela, Vol. 47, No. 7, 2005, pp. 1170–1174.
Original Russian Text Copyright © 2005 by Kurmaev, Moewes, Wilks, Nechkina, Zatsepin, Kawashima, Takayama-Muromachi.

Local Environment of Fluorine Atoms in $Sr_2Ca_{n-1}Cu_nO_{2n+\delta}F_{2\pm y}$ ($n = 2, 3$) High-Temperature Superconductors Grown under High Pressure

E. Z. Kurmaev*, A. Moewes, R. Wilks**, L. D. Nechkina*,**
D. A. Zatsepin*, T. Kawashima*, and E. Takayama-Muromachi*****
** Institute of Metal Physics, Ural Division, Russian Academy of Sciences,*
ul. S. Kovalevskoĭ 18, Yekaterinburg, 620219 Russia
e-mail: kurmaev@ifmlrs.uran.ru
*** Department of Physics and Engineering Physics, University of Saskatchewan, Saskatoon, S7N 5E2 Canada*
**** National Institute for Materials Science, Tsukuba, 305-0044 Japan*

Received October 22, 2004

Abstract—The local environment of fluorine atoms in $Sr_2Ca_{n-1}Cu_nO_{2n+\delta}F_{2\pm y}$ ($n = 2, 3$) high-temperature superconductors ($T_c = 99$ and 111 K) is studied using soft x-ray emission and absorption spectroscopy. The fluorine spectra of the samples studied are found to be similar to those of SrF_2, which supports the conjecture that fluorine atoms substitute for apex oxygen atoms and form double SrF layers. *© 2005 Pleiades Publishing, Inc.*

1. INTRODUCTION

Methods of high-pressure synthesis of $Sr_2Ca_{n-1}Cu_nO_{2n+\delta}F_{2\pm y}$ ($n = 2$–5) compounds have been developed recently. These superconductors have critical superconducting transition temperatures T_c up to 111 K [1, 2]. The local environments and chemical bond configurations of dopant atoms are crucial for understanding the nature of the superconducting and transport properties of these materials.

According to [3], the tetragonal unit cell parameter c of $Sr_2Ca_{n-1}Cu_nO_{2(n+1)}$ is equal to 20.4 Å for $n = 2$ and 27.2 Å for $n = 3$. These values significantly exceed the parameters $c = 19.88$ Å ($n = 2$) and $c = 26.17$ Å ($n = 3$) obtained for $Sr_2Ca_{n-1}Cu_nO_{2n+\delta}F_{2\pm y}$ ($n = 2$–5) in [1]. This disagreement makes plausible the assumption that fluorine atoms substitute for certain apex oxygen atoms of $Sr_2Ca_{n-1}Cu_nO_{2(n+1)}$, with the formation of $Sr_2Ca_{n-1}Cu_nO_{2n+\delta}F_{2\pm y}$. Models proposed in [1] for the structures of $Sr_2CaCu_2O_{4+\delta}F_{2\pm y}$ (0212–F) and $Sr_2Ca_2Cu_3O_{6+\delta}F_{3\pm y}$ (0223–F) are shown in Fig. 1. In these models, it is supposed that the double “SrF” layers contain interstitial fluorine atoms. It is expected that the interstitial fluorine atoms can be partly substituted for by oxygen (these structures are not shown in Fig. 1).

In the present paper, we report results of studies of the local environment of fluorine atoms in 0212–F and 0223–F performed using soft x-ray emission and absorption spectroscopy, which is sensitive to the local environment of excited atoms in complex compounds.

2. EXPERIMENTAL

X-ray fluorescence spectra of 0212–F and 0223–F superconductors were measured using the fluorescent endstation set on Beamline 8.0.1 of the Advanced Light Source at the Lawrence Berkley National Laboratory (USA). The technical specifications of the endstation are well known (see, e.g., [4]). Fluorescence radiation is directed into a Rowland-circle grating spectrometer equipped with a photon-counting multichannel plate area detector. The instrument resolution for x-ray fluorine K_α spectra is 0.9 eV. X-ray absorption spectra were measured in the total electron yield mode with an energy resolution $E/\Delta E = 5000$. All absorption and emission spectra were normalized to the total number of incoming photons by using a transparent gold mesh installed in front of the sample.

Samples were prepared using only high-purity starting materials: SrF_2 (99.9% pure), CaF_2 (99.9%), $SrCuO_2$, SrO_2, Ca_2CuO_3, and CuO (99.9%). The initial mixture was sealed in a gold capsule and kept at 1250°C under high pressure (5.5 GPa) for 3 h with subsequent annealing at room temperature. The 0212–F and 0223–F phases produced in this way have T_c values of 99 and 111 K, respectively. X-ray diffraction measurements were performed with a Philips PW-1800 diffractometer (Cu K_α radiation), and the crystal lattice parameters were determined by the least square fit. The tetragonal unit cell parameters for our samples are found to be $a = 3.843(1)$ Å and $c = 19.88(1)$ Å for the 0212–F phase and $a = 3.840(1)$ Å and $c = 26.17(1)$ Å for the 0223–F phase.

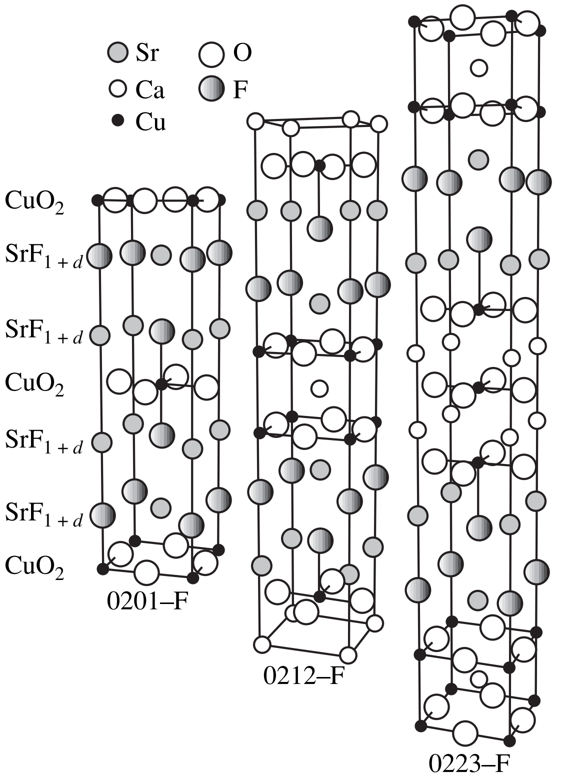

Fig. 1. Model structures of the $Sr_2CaCu_2O_{4+\delta}F_{2\pm y}$ (0212–F) and $Sr_2Ca_2Cu_3O_{6+\delta}F_{3\pm y}$ (0223–F) superconductors.

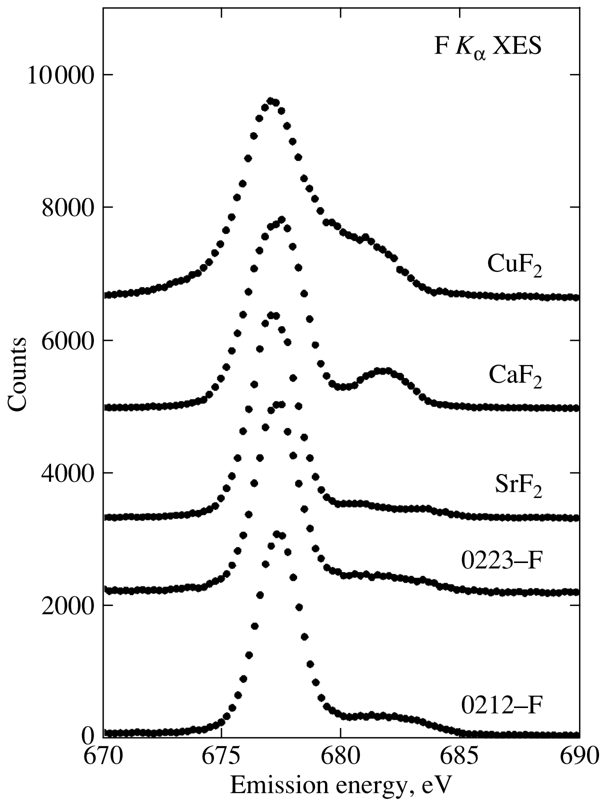

Fig. 2. Nonresonance x-ray F $K\alpha$ emission spectra (XES) of the 0212–F and 0223–F superconductors and reference samples.

3. RESULTS AND DISCUSSION

X-ray emission spectroscopy (XES) and x-ray absorption near-edge spectroscopy (XANES) are mutually supplementing methods and produce full information about electron structure. XES makes it possible to study radiative electron transitions from the valence band to the vacant core levels created by synchrotron radiation. XANES provides data concerning x-ray absorption processes accompanied by excitation of electrons from core levels into the conduction band. Both methods have the advantage of being sensitive mainly to the first coordination shell of the excited atom; so they provide information on the structure of the local electron environment and chemical bonds of that particular atom. Emission and absorption spectra studied using soft x-ray spectroscopy obey the single-electron selection rules $\Delta l = \pm 1$. Therefore, XES F K_α spectra and XANES F 1*s* spectra characterize the distribution of occupied and vacant 2*p* states of fluorine atoms, respectively.

Nonresonance XES F K_α spectra of 0212–F and 0223–F phases are shown in Fig. 2 together with spectra of the reference compounds CuF_2, CaF_2, and SrF_2. The excitation energy of the spectra shown in Fig. 2 is indicated by the letter *d* in the XANES spectra presented in Fig. 3. The emission spectra exhibit a strong

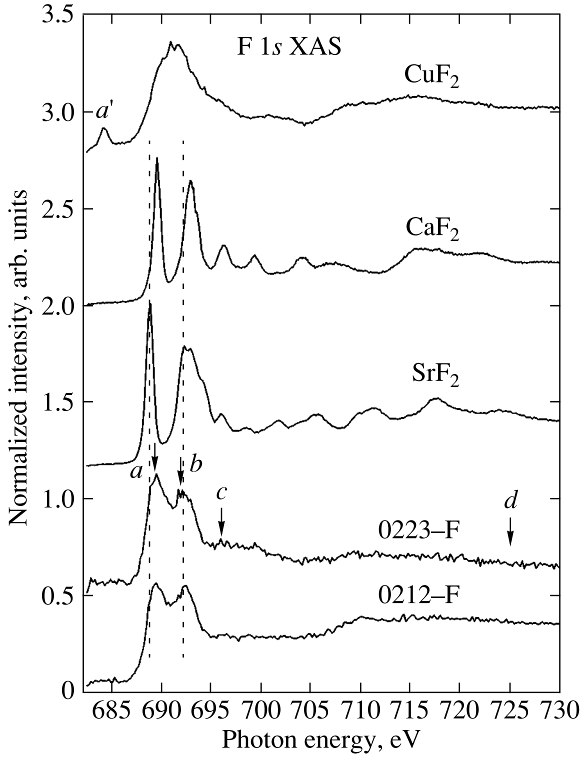

Fig. 3. X-ray F 1*s* absorption spectra (XAS) of the 0212–F and 0223–F superconductors and reference samples.

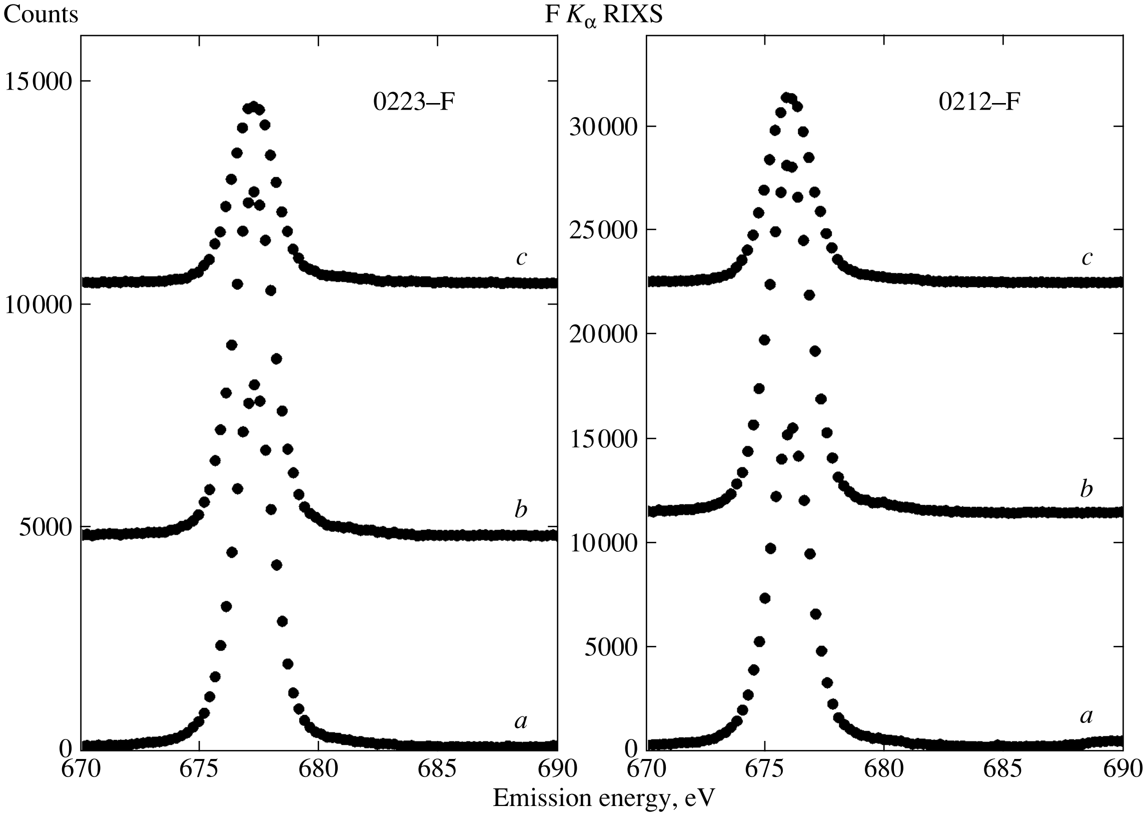

Fig. 4. Resonance x-ray F $K\alpha$ emission spectra (XES) of the 0212–F and 0223–F superconductors.

$K_{\alpha_{1,2}}$ peak (corresponding to the KL electron transition) situated at approximately 677 eV and a satellite $K_{\alpha_{3,4}}$ structure in the higher energy part of the spectra; the intensity of this structure varies significantly as one goes from CuF_2 to CaF_2 and SrF_2. The satellite K^1L^1 structures have been the subject of a number of studies (a review can be found in [5]) and are attributed to the KL transition in the two-hole atomic shell configurations $1s^{-1}2p^{-1}$ [6].

XANES F 1*s* spectra of the two compounds under study and reference samples are shown in Fig. 3. The XANES spectra of the CaF_2 and SrF_2 reference samples have two peaks, *a* and *b*, situated near the absorption edge. According to [7], the interband transition edge in XANES F 1*s* spectra is located at a much higher energy than the peak *a*; so this peak can be attributed to a core exciton forming below the conduction band. The fine structure of the CuF_2 spectrum is quite different; it has a low-intensity peak (*a*') at about 684 eV. It was found that this peak is related to transitions to vacant 3*d* states and that its intensity progressively decreases in the sequence of difluorides of 3*d* metals $Mn_2 \longrightarrow FeF_2 \longrightarrow CoF_2 \longrightarrow NiF_2 \longrightarrow CuF_2$ [8]. So, this peak carries information on the number of holes in the *d* states.

Since the XES F K_α and XANES F 1*s* spectra of the reference samples differ qualitatively, they can be used to identify the features associated with the F–Cu, F–Ca, and F–Sr chemical bonds in the samples under study. The XES F K_α and XANES F 1*s* spectra of the 0212–F and 0223–F samples we measured are very similar to those of SrF_2. The 0212–F and 0223–F spectra differ from the CuF_2 spectra in terms of their fine structure and from the CaF_2 spectra in terms of the energy positions of maxima. It follows that fluorine is surrounded by Sr atoms only; so it has to substitute for oxygen in the apex positions according to the structure models shown in Fig. 1.

It is suggested in [8] that the ratio of the intensities of the satellite F K^1L^1 structure and the main emission band decreases as the covalence of the chemical bonds increases. This trend is well pronounced in the XES F K_α spectra of the reference samples (Fig. 2); indeed, the K^1L^1 satellite in the SrF_2 spectrum is weaker than that in the CaF_2 spectrum and the satellite in the CuF_2 spectrum is the strongest. An increase in the covalence of a bond results either in a decreased probability of radiative relaxation of two-hole states or in a decreased cross section of multiple ionization. Consequently, the low intensity of the K^1L^1 satellite in the spectra of 0212–F and 0223–F suggests that there is a strong covalent Sr–F bond in these compounds, which serves to additionally confirm the models presented in Fig. 1.

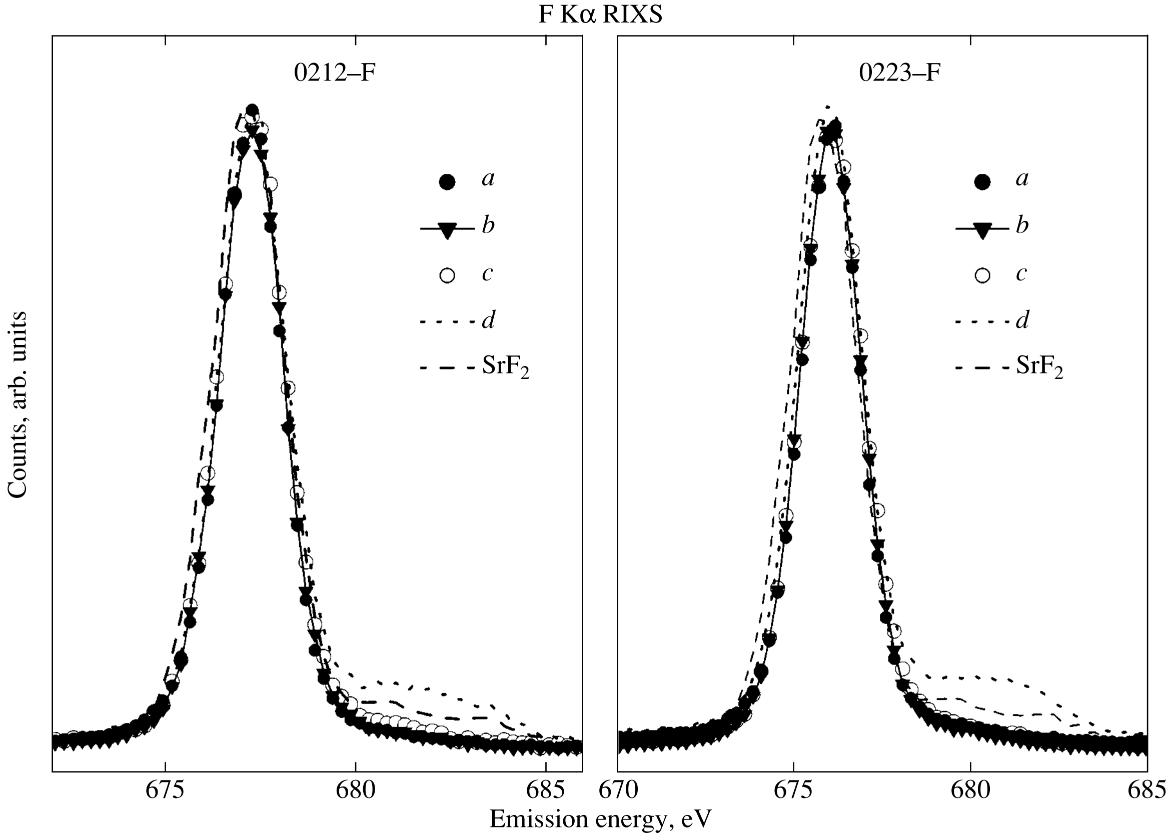

Fig. 5. Comparison of the resonance and nonresonance x-ray F $K\alpha$ emission spectra (XES) of the 0212–F and 0223–F superconductors.

In attempt to verify that fluorine takes the apex oxygen positions in the 0212–F and 0223–F crystal lattices, we studied resonant inelastic x-ray scattering (RIXS) spectra near the F K_α edge. It was shown previously [9, 10] that, for superconducting cuprates and related compounds, it is possible to selectively obtain the x-ray emission spectra of excited oxygen atoms located at nonequivalent lattice sites by carefully choosing the excitation energy. The full widths at half-maximum (FWHM) of the fluorine $K_{\alpha_{1,2}}$ emission lines of reference samples are different (Fig. 2); so the resonance spectra of fluorine atoms in the 0212–F and 0223–F samples can be used to identify the F–Cu, F–Ca, and F–Sr bonds.

The excitation energies for RIXS are chosen to correspond to the energies of the features *a*, *b*, *c*, and *d* in the F 1*s* absorption spectra of the 0212–F and 0223–F samples (Fig. 3). The emission spectra obtained in this way are shown in Figs. 4 and 5.

Notice that the F K^1L^1 satellite does not appear at all in the spectra near the threshold excitation. Therefore, this satellite is indeed due to multiple ionization. The FWHM of the main peak in the 0212–F and 0223–F spectra is independent of the excitation energy (Fig. 5) and virtually coincides with the width of the SrF_2 spectrum, which confirms the assumption that fluorine atoms form double layers in the 0212–F and 0223–F lattices as shown in Fig. 1.

4. CONCLUSIONS

High-temperature superconductors 0212–F and 0223–F produced under high pressure have been studied using resonance and nonresonance x-ray F *K* emission spectroscopy and F 1*s* absorption spectroscopy. It has been shown that fluorine atoms take the apex positions in the crystal lattices of these compounds and form double SrF layers with strong covalent F–Sr bonds. Hence, all our data confirm the structure models of the 0212–F and 0223–F superconductors suggested in [1].

ACKNOWLEDGMENTS

This work was supported by the Research Council of the President of the Russian Federation (grant NSh–1026.2003.2), the Ministry of Science and Education of the Russian Federation (program “Superconductivity of Mesoscopic and Strongly Correlated Systems”), the National Science and Engineering Research Council of Canada, and the Saskatchewan Synchrotron Institute.

The measurements performed using the ALS at the Lawrence Berkeley National Laboratory, USA, were supported by the US Department of Energy (grant DOE-AC03-76SF00098).

REFERENCES

1. T. Kawashima, Y. Matsui, and E. Takayama-Muromachi, Physica C **257**, 313 (1996).
2. T. Kawashima, Y. Matsui, and E. Takayama-Muromachi, Physica C **282–283**, 513 (1997).
3. S. Adachi, H. Yamauchi, S. Tanaka, and N. Mori, Physica C **212**, 164 (1993).
4. J. J. Jia, T. A. Callcott, J. Yurkas, A. W. Ellis, F. J. Himpsel, M. G. Samant, J. Stöhr, D. L. Ederer, J. A. Carlisle, E. A. Hudson, L. J. Terminello, D. K. Shuh, and R. C. C. Perera, Rev. Sci. Instrum. **66**, 1394 (1995).
5. J. Kawai, T. Yamamoto, Y. Harada, and S. Shin, Solid State Commun. **105**, 381 (1998).
6. J.-E. Rubensson, S. Eisebitt, M. Nicodemus, T. Boske, and W. Eberhardt, Phys. Rev. B **50**, 9035 (1994).
7. C. Sugiura, W. Konishi, S. Shoi, and S. Kojima, J. Phys. Soc. Jpn. **59**, 4049 (1990).
8. C. Sugiura, J. Phys. Soc. Jpn. **60**, 2710 (1991).
9. S. M. Butorin, J.-H. Guo, N. Wassdahl, P. Skytt, J. Nordgren, Y. Ma, C. Straem, L.-J. Johansson, and M. Qvarford, Phys. Rev. B **51**, 11915 (1995).
10. E. Z. Kurmaev, S. Stadler, D. L. Ederer, Y. Harada, S. Shin, M. M. Grush, T. A. Callcott, R. C. C. Perera, D. A. Zatsepin, N. A. Ovechkina, M. Kasai, Y. Tokura, T. Takahashi, K. Chandrasekaran, R. Vijayaraghavan, and U. V. Varadaraju, Phys. Rev. B **57**, 1558 (1998).

Translated by G. Tsydynzhapov

Physics of the Solid State, Vol. 47, No. 7, 2005, pp. 1216–1220. Translated from Fizika Tverdogo Tela, Vol. 47, No. 7, 2005, pp. 1175–1179.

Thermal Conductivity of the SiC/Si Biomorphic Composite, a New Cellular Ecoceramic

**L. S. Parfen'eva*, T. S. Orlova*, N. F. Kartenko*, N. V. Sharenkova*,
B. I. Smirnov*, I. A. Smirnov*, H. Misiorek**, A. Jezowski**, F. M. Varela-Feria***,
J. Martinez-Fernandez***, and A. R. de Arellano-Lopez*****

**Ioffe Physicotechnical Institute, Russian Academy of Sciences, Politekhnicheskaya ul. 26, St. Petersburg, 194021 Russia
e-mail: igor.smirnov@pop.ioffe.rssi.ru*

***Institute of Low-Temperature and Structural Research, Polish Academy of Sciences, Wroclaw, 50-950 Poland*

****Universidad de Sevilla, Seville, 41080 Spain*

Received September 2, 2004

Abstract—The thermal conductivity κ and electrical resistivity ρ of a SiC/Si biomorphic composite were measured at temperatures $T = 5$–300 K. The composite is a cellular ecoceramic fabricated by infiltrating molten Si into the channels of a cellular carbon matrix prepared via pyrolysis of wood (white eucalyptus) in an argon ambient. The $\kappa(T)$ and $\rho(T)$ relations were measured on a sample cut along the direction of tree growth. The experimental results obtained are analyzed. © *2005 Pleiades Publishing, Inc.*

1. INTRODUCTION

The SiC/Si biomorphic ceramics, presently also called ecoceramics (environment-conscious ceramics), have recently been attracting considerable attention from technologists, physicists, and engineers on account of their unusual physical properties, as well as because of their remarkable application potential.

Biomorphic composites are fabricated from cellular carbon matrices obtained via pyrolysis (carbonization) of various kinds of wood (pine, eucalyptus, mango, oak, beech, maple, etc.), followed by infiltration of molten Si into the empty through channels (~4 to 100 μm in diameter) of these matrices. Silicon reacts chemically with the carbon matrix to produce a SiC/Si composite [1].[1]

These composites have a cellular (channel-type) structure depending on the actual technology employed for their preparation and on the wood species. Most of a composite sample (85 to 55%) may consist of SiC, while the channels, which are extended along the direction of tree growth and either are filled by Si or remain empty, occupy 15 to 35% and 7 to 30% of the composite volume, respectively.

The SiC/Si ecoceramics feature a variety of unusual properties, which make them promising for applications and more cost-effective than the classical ceramics. They exhibit a high mechanical strength [1–3], are oxidation and corrosion resistant, and have low weight (their density is ~2.3 g/cm^3). Among their technological advantages are a high rate of production at relatively low temperatures and a fairly low production cost.

A unique feature of biomorphic composites is the possibility they offer of fabricating ceramic objects of a desired shape, which can be achieved by a fairly simple woodworking procedure. After the pyrolysis and Si infiltration into such preforms, one obtains high-strength, difficult-to-machine ceramic objects that retain their original shape [1].

SiC/Si biomorphic ceramics can be employed to advantage as a light, superhard material in the aerospace and car industries and in medicine (orthopedics), as well as in the manufacturing of high-temperature heaters, resistance thermometers, etc.

Investigation of the physical properties of this unusual class of materials is of fundamental importance for solid-state physics. Regrettably, physical studies of biomorphic composites have thus far been focused primarily on their structural and mechanical characteristics [1–3]. We have studied (in the range 10–300 K) the behavior of electrical resistivity of the SiC/Si biomorphic composite prepared from carbonized Sapele wood (*African Entandrophragma Cylindricum*) [4].

Note that investigation of a larger number of physical properties of biomorphic composites may, in addition to being of considerable scientific interest, prove to be of advantage (and even necessary) in the search for additional potential applications.

A fundamental physical parameter that can be used to obtain information on the phonon-assisted heat transport and dissipation in composites is the thermal conductivity. It is necessary to know the thermal conductivity when carrying out engineering calculations of

---

[1] Information on the fabrication, study of the structural and mechanical properties, and application potential of the SiC/Si biomorphic composites can be found in review [1], which also gives 60 relevant references.

heat losses and flows in devices and constructions fabricated from this unusual ceramic.

The thermal conductivity of the SiC/Si biomorphic ceramic has not yet been studied. It is this subject that the present communication addresses.

2. PREPARATION OF SAMPLES AND THEIR CHARACTERIZATION

A sample of the SiC/Si biomorphic composite was prepared by infiltrating molten Si in vacuum into a cellular carbon matrix of white-eucalyptus wood obtained by pyrolysis in an argon ambient at 1000°C [1].

Following infiltration, a $2.2 \times 1.5 \times 3.4$ mm parallelepiped-shaped sample was cut from a rod of the SiC/Si biomorphic composite. The long side of the sample was directed along the direction of tree growth. We also prepared a sample of the carbon matrix of white-eucalyptus wood for the study.

For these samples, we performed microstructural and x-ray diffraction studies and measured their density at 300 K.

The photomicrographs obtained with a Philips XL30 scanning electron microscope are similar to those presented in [2]. The microphotograph of the carbon matrix sample reveals a clearly pronounced cellular structure with channels extending along the direction of tree growth. On the end faces of both samples, individual pores with different diameters are observed.[2]

Diffractometric scans of samples of the SiC/Si biomorphic composite and of the corresponding carbon matrix of white-eucalyptus wood obtained on a DRON-2 (CuK_α radiation) are displayed in Fig. 1. The x-ray diffraction pattern of the SiC/Si biomorphic composite shows that this composite consists of a mixture of two phases: cubic 3*C*-SiC (lattice parameter a = 4.358 Å) and Si (a = 5.430 Å). Both phases are well formed. Based on the x-ray diffraction data for the composite and silicon samples, the silicon content in the SiC/Si sample is estimated to be ~15 vol %. The diffraction pattern of the carbon matrix of white-eucalyptus wood contains only diffuse halos typical of amorphous material (see inset to Fig. 1).

The densities of the carbon matrix and SiC/Si composite samples were 0.68 and 2.37 g/cm^3, respectively. Based on these values and on the density of the original white eucalyptus wood (0.84 g/cm^3), the conclusion was drawn in [2] that a SiC/Si sample contains ~6 vol % excess silicon and 15–20% empty channels. Note the appreciable difference between the contents of excess Si estimated from the x-ray diffraction and density measurement data.

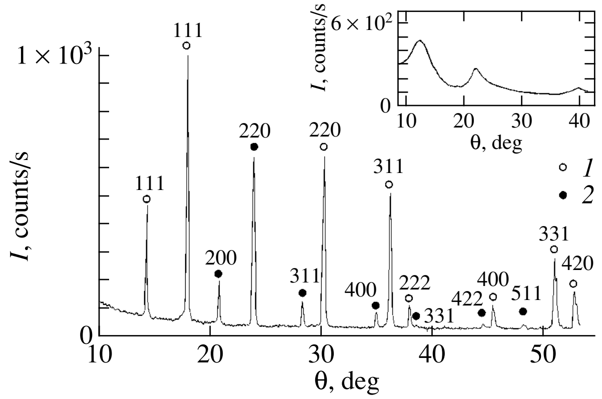

Fig. 1. Diffractometric scan of a SiC/Si biomorphic composite sample with reflections from (*1*) 3*C*-SiC and (*2*) Si. Inset shows the diffraction pattern of the carbon matrix of white eucalyptus.

3. EXPERIMENTAL RESULTS

The thermal conductivity κ_{comp} and electrical resistivity ρ_{comp} of a sample of a SiC/Si biomorphic composite were measured in the temperature interval 5–300 K on a setup similar to that employed in [5] and are displayed in Figs. 2 and 3, respectively. Because the value of ρ_{comp} is fairly large, the quantity κ_{comp} obtained in the experiment is the lattice thermal conductivity (κ_{ph}).

Figure 2 also presents available experimental data on the thermal conductivity of polycrystalline 3*C*-SiC. Unfortunately, we have not succeeded in locating literature data on the thermal conductivity of 3*C*-SiC in the temperature interval 40–300 K. For this reason, Fig. 2 represents a hypothetical curve (dashed curve *11*) connecting the low- and high-temperature parts of the thermal conductivity graph of 3*C*-SiC.

Figure 3 (see also insets to it) shows the $\rho_{comp}(T)$ curve obtained for the sample under study without regard for its porosity. We readily see that, in the low-temperature range (5–20 K), $\rho_{comp}(T)$ = const, but for $T > 20$ K the electrical resistivity increases with temperature to fit the $\rho_{comp} \sim T^{0.3}$ scaling at $T > 150$ K.

4. DISCUSSION OF THE RESULTS

The sample of the biomorphic composite studied here consists of a 3*C*-SiC polycrystalline base, silicon filling the channels, and empty channels (accounting for the sample porosity). Using the Litovskiĭ formula [12]

$$\kappa_{comp} = \kappa^0_{comp}(1-P)\sqrt{1-P} \qquad (1)$$

the porosity P was taken into account and the thermal conductivity κ^0_{comp} relating to 3*C*-SiC and Si only (curve *10* in Fig. 2) was isolated from the experimentally measured κ_{comp}. In these calculations, P was assumed to be 0.2.

---

[2] Electron microscope measurements performed on a large number of carbon matrix samples of white eucalyptus established [1] that small pores (with an average diameter of ~4 Å) and large pores (average diameter of ~62.5 Å) occupy ~29 and ~14% of the total sample volume, respectively.

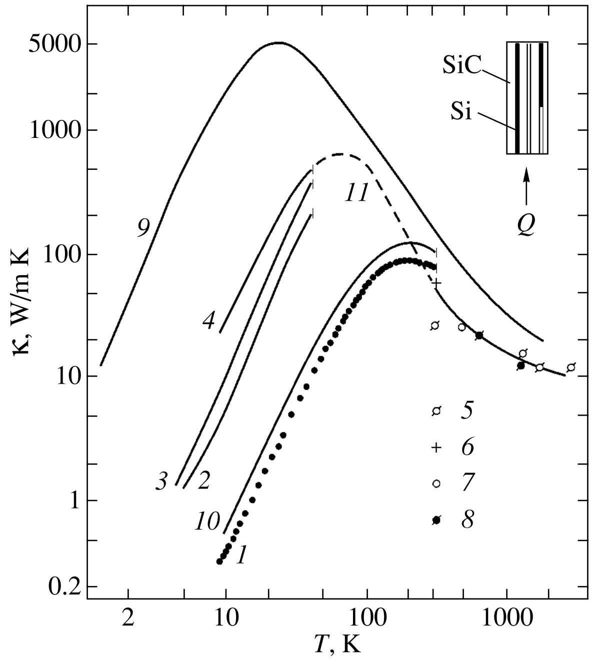

Fig. 2. Temperature dependences of the lattice thermal conductivity (*1*) of a SiC/Si biomorphic composite sample measured in the direction of tree growth; (*2*–*8*) of polycrystalline 3*C*-SiC samples taken from (*2*) [6], (*3*) [7], (*4*, *6*) [8], (*5*, *8*) [9], and (*7*) [10]; and (*9*) of high-purity silicon [11]. (*10*) Thermal conductivity κ^{0}_{comp} of a SiC/Si biomorphic composite sample. (*11*) Hypothetical curve interpolating literature data on the low- and high-temperature thermal conductivity of 3*C*-SiC. Inset shows a SiC/Si biomorphic composite sample (schematic).

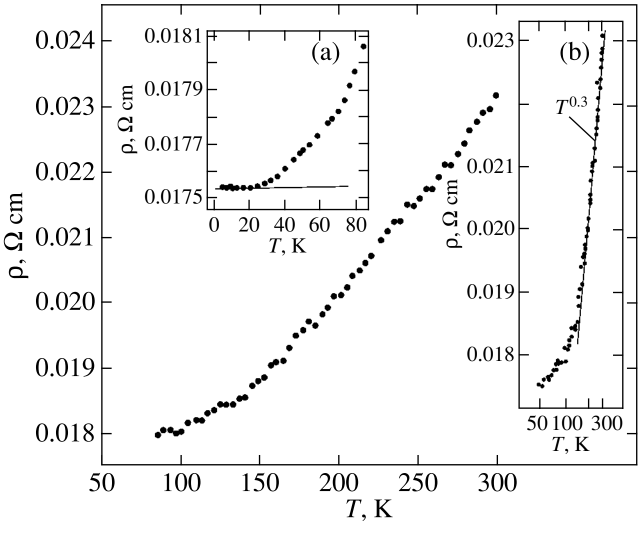

Fig. 3. Temperature dependence of the electrical resistivity ρ_{comp} of the SiC/Si biomorphic composite measured (without inclusion of porosity) on a sample cut along the growth direction of white eucalyptus wood within the range 100–300 K. Insets show the $\rho_{\text{comp}}(T)$ dependence (a) at low-temperatures (5–80 K) and (b) (drawn on a log scale) over the range 50–300 K.

A microstructural analysis of the carbon matrix of white eucalyptus wood and the SiC/Si biomorphic composite fabricated from this matrix shows that the sample has a cellular structure made up of empty and silicon-filled channels. These channels have various diameters and are extended along the longer side of the sample (i.e., along the direction of tree growth). In the subsequent analysis of the experimental data on the thermal conductivity, we assume these channels to be parallel to the heat flow propagating into the sample (see inset to Fig. 2). To calculate the thermal conductivity of a system consisting of alternating parallel layers of different materials, we use the Dul'nev–Zarichnyak formula [13]

$$\kappa^{\text{calc}}_{\text{comp}} = \kappa_1(1-m) + \kappa_2 m, \qquad (2)$$

where κ_1 and κ_2 are the thermal conductivities of 3*C*-SiC and Si, respectively, and m is the percentage of Si in the sample.

In Fig. 4, $\kappa^{\text{calc}}_{\text{comp}}$ as calculated from Eq. (2) is plotted (curve *4*) together with available data on the thermal conductivities of 3*C*-SiC (κ_1, curve *2*) and Si (κ_2, curve *3*). It was found that the values of $\kappa^{\text{calc}}_{\text{comp}}(T)$ in the low-temperature region (curve *4*) lie substantially above the experimental $\kappa^{0}_{\text{comp}}(T)$ values (curve *1*).

Based on the behavior of $\kappa^{0}_{\text{comp}}(T)$ derived experimentally for medium temperatures (200–300 K), one might expect the calculations performed using the above values of the thermal conductivity of 3*C*-SiC and Si to be in better agreement with experiment at higher temperatures, as suggested by Fig. 4.[3]

What could the reason be for the substantial disagreement between the calculated and experimental data for the low-temperature region and, possibly, for there not being such a dramatic discrepancy at high temperatures?

This is most likely due to the fact that the thermal conductivities of the 3*C*-SiC making up the SiC/Si biomorphic composite and of the Si filling its channels differ considerably from (are lower than) the respective literature data for 3*C*-SiC and high-purity Si. The thermal conductivities of these materials should differ strongly from literature data at low temperatures, whereas at high temperatures they can approach the values given in the literature.

To substantiate this assumption, hypothetical curves for the thermal conductivities of the 3*C*-SiC (curve *5*) and Si (curve *6*) making up the SiC/Si composite are constructed in Fig. 4 under the condition

$$\kappa^{\text{calc}}_{\text{comp}} = \kappa^{0}_{\text{comp}}. \qquad (3)$$

---

[3] Unfortunately, we have to restrict ourselves here to the statement "one might expect," because experimental data on $\kappa^{0}_{\text{comp}}(T)$ for temperatures $T > 300$ K are lacking.

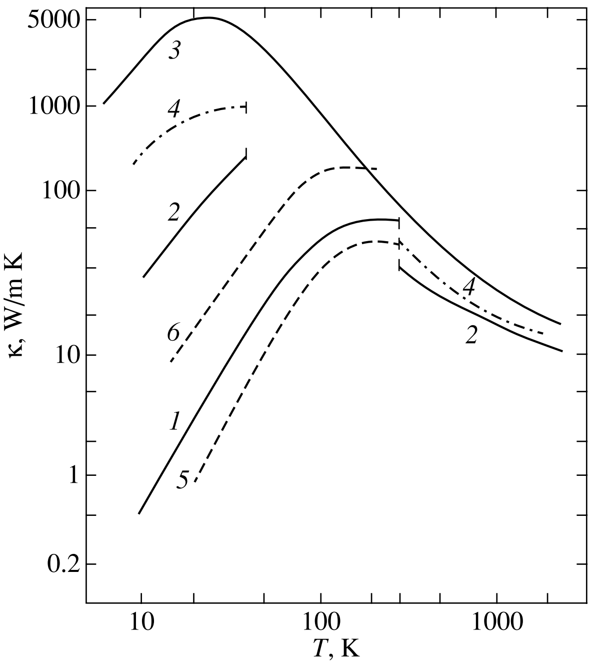

Fig. 4. Temperature dependence of the lattice thermal conductivity (*1*) for the SiC/Si biomorphic composite under study (κ_{comp}^{0}), (*2*) for 3*C*-SiC at low (curve *4* in Fig. 2) and high (curves *5–8* in Fig. 2) temperatures, and (*3*) for high-purity Si [11]; (*4*) $\kappa_{\text{comp}}^{\text{calc}}$ as calculated from Eq. (2); and (*5*, *6*) hypothetical values of the thermal conductivity for the 3*C*-SiC and Si making up the SiC/Si biomorphic composite, respectively.

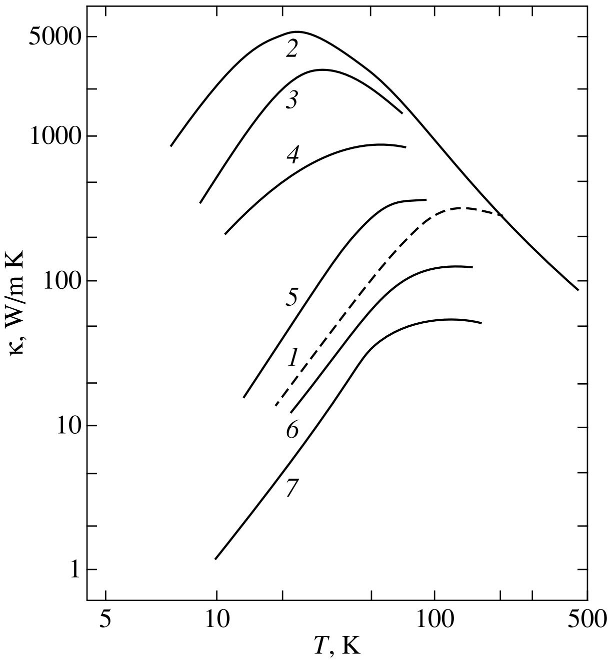

Fig. 5. Temperature dependence of the Si lattice thermal conductivity. (*1*) Hypothetical $\kappa_{\text{ph}}(T)$ curve for Si in channels of the biomorphic composite sample under study (curve *6* in Fig. 4) and (*2–7*) $\kappa_{\text{ph}}(T)$ of Si samples with different carrier concentrations [11] (cm^{-3}): (*2*) $p \sim 10^{12}$, (*3*) $p = 2.2 \times 10^{16}$, (*4*) $p = 2.2 \times 10^{17}$, (*5*) $n = 3 \times 10^{19}$, (*6*) $n = 1.7 \times 10^{20}$, and (*7*) $p = 3 \times 10^{20}$ (*n* and *p* specify the conduction type of the material).

The calculation was performed using Eq. (2) for $m = 0.15$. Condition (3) can also be satisfied at a slightly different ratio of the thermal conductivities of 3*C*-SiC and Si (as compared to that in Fig. 4), but this would not change the overall pattern markedly. The true value of the thermal conductivity of the 3*C*-SiC making up the ecoceramic can be obtained (and compared with the hypothetical curve) only after measuring the thermal conductivity of the SiC/Si biomorphic composite after complete removal of Si from it by chemical means.

A decrease in the thermal conductivity of Si infiltrated into the channels of a white-eucalyptus carbon matrix at a high temperature appears to be a reasonable conjecture, because chemical analysis of such a matrix revealed the presence in it of such impurities as Al, Cu, Fe, S, Tl, and, most of all, Ca and P, which (particularly the latter) may act as a dopant that brings about a decrease in the κ and ρ of Si. The κ of silicon in the composite may also be reduced by specific structural defects forming in the silicon in the course of its infiltration into the carbon matrix channels. Hypothetical curve *6* for the κ(*T*) of Si (Fig. 4) fits well into the family of curves plotting the thermal conductivity of Si with various degrees of purity [11] (Fig. 5).

The impurities mentioned above may also give rise to a decrease in the 3*C*-SiC thermal conductivity as compared to the literature data. The κ of 3*C*-SiC could also be lowered by part of the 3*C*-SiC being present in the biomorphic composite in the nanocrystalline state [1].

The SiC/Si biomorphic composite belongs to nonoxide ceramics featuring a fairly high thermal conductivity for $T \geq 300$ K [14]. In the table, 300-K thermal conductivity data are listed for ceramics based on the 6*H*-SiC polytype, which are used in industry [14]. The thermal conductivity of the SiC/Si ecoceramic sample studied in this work is ~80 W/m K at 300 K, which likewise makes this ecoceramic promising for practical use.

Let us turn to a discussion of the above experimental data on the electrical resistivity of the SiC/Si biomorphic composite sample studied here. This composite is specific in that its ρ_{comp} increases with temperature.[4] This is most probably due to the fact that, for Si and, possibly, for the SiC making up the SiC/Si biomorphic composite, the ρ(*T*) dependence becomes metallic in character, because these materials are doped by the

---

[4] Samples of the SiC/Si biomorphic composite fabricated from the carbon matrix of Sapele wood reveal the same behavior of $\rho_{\text{comp}}(T)$ [4].

Thermal conductivity of 6*H*-SiC-based ceramics at 300 K [14]

χ, W/m K	Additives to the ceramic conducive to its sintering
60	Al
75–90	Al_2O_3–Y_2O_3
120–185	Al_2O_3
170	B
270	BeO

above impurities present in the carbon matrix of white eucalyptus wood.

The $\rho(T)$ dependence acquires a metallic pattern in crystalline carbon [15], but x-ray diffraction did not reveal this carbon in the sample under study (Fig. 1). The possible presence of amorphous carbon in the biomorphic composite sample [1] should have produced the opposite effect, because the ρ of amorphous carbon increases with decreasing temperature [16], as is also the case with the ρ of nanoporous carbon [16]. This leaves us with only one explanation, namely, that the observed behavior of $\rho_{comp}(T)$ of the biomorphic SiC/Si composite is due to Si (and SiC) being doped by the impurities present in the carbon matrix.

5. CONCLUSIONS

We have shown that the calculated lattice thermal conductivity of 3*C*-SiC in the SiC/Si biomorphic composite at temperatures of 5–100 K is much smaller than that of a standard polycrystalline 3*C*-SiC sample, which is apparently associated with the presence of impurities and specific defects in the silicon carbide contained in the biomorphic composite.

It should be pointed out, however, that the SiC/Si non-oxide ecoceramic nevertheless has a sufficiently high thermal conductivity at room temperature, which makes it promising for several applications.

ACKNOWLEDGMENTS

This study was supported by the Russian Foundation for Basic Research (project no. 04-03-33183), the Polish State Committee on Scientific Research KBN (project no. 3 TO8A 05426), and the Ministry of Science and Technology of Spain (project MAT no. 2003-05202-002-01).

REFERENCES

1. A. R. de Arellano-Lopez, J. Martinez-Fernandez, P. Gonzalez, C. Dominguez, V. Fernandez-Quero, and M. Singh, Int. J. Appl. Ser. Tech. **1** (1), 1 (2004).
2. B. I. Smirnov, Yu. A. Burenkov, B. K. Kardashev, F. M. Varela-Feria, J. Martinez-Fernandez, and A. R. de Arellano-Lopez, Fiz. Tverd. Tela (St. Petersburg) **45** (3), 456 (2003) [Phys. Solid State **45** (3), 482 (2003)].
3. B. K. Kardashev, Yu. A. Burenkov, B. I. Smirnov, A. R. de Arellano-Lopez, J. Martinez-Fernandez, and F. M. Varela-Feria, Fiz. Tverd. Tela (St. Petersburg) **46** (10), 1811 (2004) [Phys. Solid State **46** (10), 1873 (2004)].
4. T. S. Orlova, B. I. Smirnov, A. R. de Arellano-Lopez, J. Martinez-Fernandez, and R. Sepulveda, Fiz. Tverd. Tela (St. Petersburg) **47** (2), 220 (2005) [Phys. Solid State **47** (2), 229 (2005)].
5. A. Jezowski, J. Mucha, and G. Pompe, J. Phys. D: Appl. Phys. **20**, 1500 (1987).
6. G. Busch, Philips Res. Rep. **16**, 455 (1961).
7. L. A. Novitskiĭ and I. G. Kozhevnikov, *Handbook of Thermophysical Properties of Materials at Low Temperatures* (Mashinostroenie, Moscow, 1975) [in Russian].
8. G. L. Harris, in *Properties of Silicon Carbide*, Ed. by G. L. Harris, EMIS Ser. Datareviews, (1995), No. 13, p. 5.
9. H. K. Henisch and R. Roy, *Silicon Carbide*, Ed. by H. K. Henisch and R. Roy (Pergamon, Oxford, 1968; Mir, Moscow, 1972).
10. *Handbook of Physicochemical Properties of Semiconductor Matters* (Nauka, Moscow, 1978) [in Russian].
11. *Handbook of Thermal Conductivity of Solid States*, Ed. by A. S. Okhotin (Énergoizdat, Moscow, 1984).
12. E. Ya. Litovskiĭ, Izv. Akad. Nauk SSSR, Neorgan. Mater. **16** (3), 559 (1980).
13. G. N. Dul'nev and Yu. P. Zarichnyak, *Thermal Conductivity of Mixtures and Composite Materials* (Énergiya, Leningrad, 1974) [in Russian].
14. K. Watari, J. Ceram. Soc. Jpn. **109** (1), S7 (2001).
15. N. B. Brandt, S. M. Chudinov, and Ya. G. Ponomarev, *Semimetals Graphite and its Compounds. Problems in Condensed Matter Sciences* (New Holland, 1988), Vol. 20, p. 1.
16. V. V. Popov, S. K. Gordeev, A. V. Grechinskaya, and A. V. Danashevskiĭ, Fiz. Tverd. Tela (St. Petersburg) **44** (4), 758 (2002) [Phys. Solid State **44** (4), 789 (2002)].

Translated by G. Skrebtsov

Physics of the Solid State, Vol. 47, No. 7, 2005, pp. 1221–1224. Translated from Fizika Tverdogo Tela, Vol. 47, No. 7, 2005, pp. 1180–1183.
Original Russian Text Copyright © 2005 by F. Abdullaev, Kerimova, N. Abdullaev.

SEMICONDUCTORS AND DIELECTRICS

Conductivity Anisotropy and Localization of Charge Carriers in $TlInTe_2$ Single Crystals

F. N. Abdullaev, T. G. Kerimova, and N. A. Abdullaev
Institute of Physics, Academy of Sciences of Azerbaijan, pr. Dzhavida 33, Baku, AZ-1143 Azerbaijan
e-mail: farhad@azintex.com

Received October 1, 2004

Abstract—The electrical resistivity of $TlInTe_2$ chain-structure semiconductors in directions parallel and perpendicular to the chains is analyzed as a function of temperature. It is demonstrated that, in both cases, the temperature dependences of the electrical resistivity in the temperature range under investigation are characterized by two portions associated with different mechanisms of electrical conduction. In the high-temperature range, the electrical conduction is predominantly provided by thermally excited impurity charge carriers in the allowed band. In the low-temperature range, the conduction occurs through charge carrier hopping between localized states lying in a narrow energy band near the Fermi level. The activation energy for impurity conduction is determined. The localization lengths and the density of localized states near the Fermi level, the spread in energies of these states, and the average carrier-hopping distances are estimated for different temperatures. © *2005 Pleiades Publishing, Inc.*

1. INTRODUCTION

Single crystals of the $TlInTe_2$ compound belonging to *p*-type semiconductors have been extensively studied as promising materials for a wide range of practical applications. In particular, the $TlInTe_2$ compound and its structural analog $TlInSe_2$ have been used in fabricating high-speed photoresists and x-ray detectors. The theoretical interest expressed in $TlInTe_2$ single crystals is associated with the specific features of their structure. Since $TlInTe_2$ single crystals have a chain structure, their investigation is of importance in revealing the physical phenomena inherent in low-dimensional systems.

The $TlInTe_2$ compound (like its structural analogs $TlInSe_2$ and $TlGaTe_2$) crystallizes in a body-centered lattice of the tetragonal crystal system and belongs to space group D_{4h}^{18}–$I4mcm$, which is characteristic of crystals with an anisotropic lattice of the TlSe type [1]. Indium ions form indium–tellurium chains along the tetragonal *c* axis of the crystal. These chains are linked together through univalent thallium ions. Thallium ions are located in the tetrahedral environment of the tellurium ions. Anisotropy of the crystal structure leads to anisotropy of the bonding forces in the crystal, which, in turn, is responsible for the anisotropy of the physical properties.

The electrical properties of $TlInTe_2$ single crystals have not been adequately investigated. Guseinov *et al.* [2] studied the electrical conductivity and the Hall effect in $TlInTe_2$ single crystals at temperatures above room temperature. The data obtained by those authors are in good agreement with the band structure calculated for $TlInTe_2$ single crystals by Gashimzade and Orudzhev [3]. According to the results of those calculations, the compound under consideration is an indirect-band-gap semiconductor in which the direct transition is forbidden by the selection rules. The numerical values of the minimum direct and indirect band gaps are equal to 1.16 and 0.65 eV, respectively. In the present work, we investigated the charge transfer in $TlInTe_2$ semiconductors with a chain structure at low temperatures.

2. SAMPLE PREPARATION AND EXPERIMENTAL TECHNIQUE

The dc electrical resistivity was measured by a modified four-point probe method [4] in directions parallel ($\rho_{\parallel}$) and perpendicular ($\rho_{\perp}$) to the tetragonal *c* axis (coinciding with the direction of the chains in the crystal) in the temperature range 80–300 K. The samples for measurement were prepared in the form of 0.25- to 0.50-mm-thick rectangular plates, with the chains being aligned with the plate plane. Indium contacts and their sizes and arrangement satisfied the requirements described in [4]. The strength of the applied electric field ($E = 10^2$–10^3 V/cm) corresponded to the ohmic portion of the current–voltage characteristic.

3. SPECIFIC FEATURES OF THE ELECTRICAL CONDUCTIVITY IN $TlInTe_2$ SINGLE CRYSTALS

The temperature dependences of the electrical resistivity of $TlInTe_2$ single crystals in directions parallel (curve *1*) and perpendicular (curve *2*) to the tetragonal *c* axis of the crystal are plotted in the Arrhenius coordi-

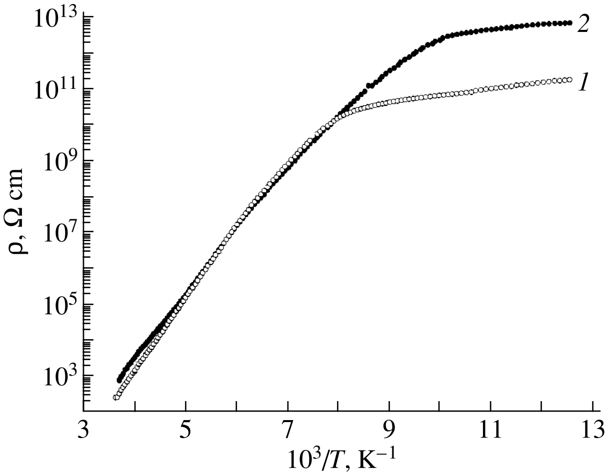

Fig. 1. Temperature dependences of the electrical resistivity in the directions (*1*) parallel and (*2*) perpendicular to the tetragonal *c* axis of $TlInTe_2$ single crystals.

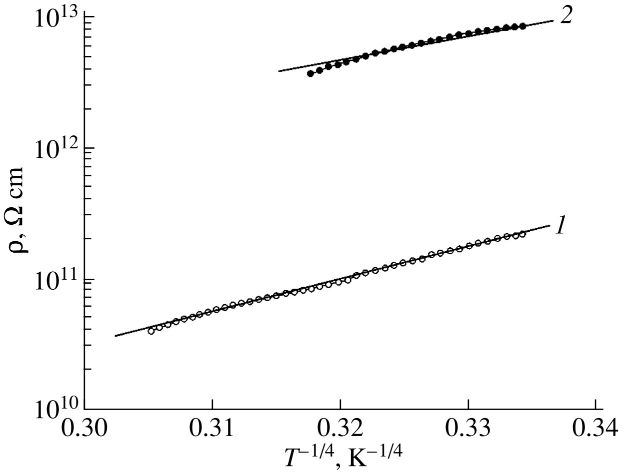

Fig. 2. Temperature dependences of the electrical resistivity of $TlInTe_2$ single crystals in the Mott coordinates (80 K < *T* < 120 K). Designations of the curves are the same as in Fig. 1.

nates in Fig. 1. Both dependences $\rho(T)$ are characterized by two portions with a different behavior upon cooling. In the range of relatively high temperatures (120 K < T < 300 K), the electrical resistivities $\rho_{\|}(T)$ and $\rho_{\perp}(T)$ increase exponentially with a decrease in the temperature. In this temperature range, the electrical conduction is predominantly provided by thermally excited impurity charge carriers in the allowed band. A decrease in the temperature is accompanied by a rapid decrease in the concentration of impurity charge carriers (the so-called range of impurity carrier freeze-out). The activation energies determined for impurity charge carriers from the data on the electrical resistivities $\rho_{\|}(T)$ and $\rho_{\perp}(T)$ are approximately equal to 0.35 and 0.34 eV, respectively. These activation energies are in close agreement with those obtained by Guseinov *et al.* [2]. According to [2], the activation energies determined for acceptors from the data on the electrical conductivity and the Hall effect in the $TlInTe_2$ compound at high temperatures (T > 300 K) are equal to 0.25 and 0.28 eV, respectively. It should also be noted that a decrease in the temperature by a factor of only three (from 300 to 100 K) leads to an increase in the electrical resistivity of the $TlInTe_2$ single crystals in both directions by almost eight orders of magnitude (from 10^3–10^4 to 10^{11}–10^{12} Ω cm). This renders the $TlInTe_2$ single crystals promising for use as sensitive temperature sensors or in systems of high-precision control and stabilization of temperature.

It can be seen from Fig. 1 that, in the temperature range 120 K < T < 300 K, the electrical resistivities satisfy the relationship $\rho_{\|} \simeq \rho_{\perp}$. This is consistent with the inference made from the calculations of the band structure of $TlInTe_2$ single crystals [3] that the effective masses of charge carriers in these crystals are characterized by a weak anisotropy. However, with a further decrease in the temperature (at T < 120 K), the electrical resistivity in the direction perpendicular to the crystal chains becomes considerably higher than that along the chains. The electrical conductivity in the direction of the strong bonding substantially exceeds the conductivity in the direction of the weak bonding. A similar result was obtained earlier for the InSe layered semiconductor [5], the TlSe semiconductor [6] isostructural to the $TlInTe_2$ compound, and many other anisotropic crystals. This anisotropy of conductivity, which does not correspond to the anisotropy of effective masses of charge carriers, was explained in terms of defects and dislocations (typical of crystals characterized by weak bonding) in real crystal structures of the aforementioned compounds.

The electrical conductivity in the low-temperature range (T < 140 K) is of special interest. As can be seen from Fig. 1, the activation energy for electrical conduction gradually decreases in this temperature range. The temperature dependences of the electrical resistivities $\rho_{\|}$ and $\rho_{\perp}$ in the low-temperature range are plotted in the Mott coordinates in Fig. 2. It is clearly seen that the experimental points in these coordinates fit a straight line fairly well. This allows us to assume that, in the temperature range under consideration, charge transfer along and across the chains in the $TlInTe_2$ single crystals occurs through charge carrier hopping between localized states lying in a narrow energy band near the Fermi level. In this case, the electrical conductivity can be adequately described by the Mott relationship [7]

$$\rho = \rho_0 \exp(T_0/T)^{1/4}, \quad T_0 = \beta/kg(\mu)a^3. \tag{1}$$

Here, $g(\mu)$ is the density of localized states at the Fermi level, a is the localization length of localized states near the Fermi level, k is the Boltzmann constant, and β is a number dependent on the dimension of the problem.

Most likely, the rapid freeze-out of impurity charge carriers in the allowed band with a decrease in the tem-

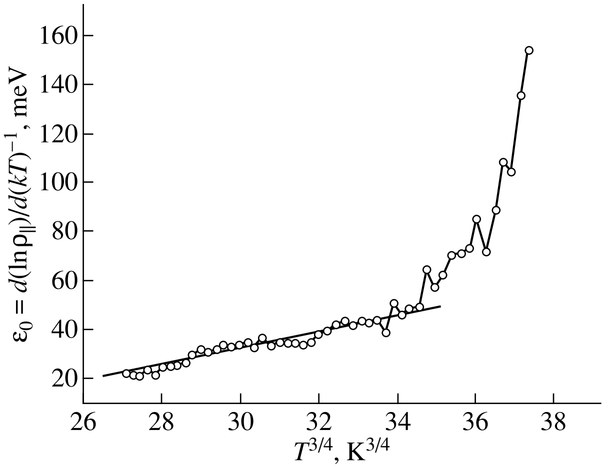

Fig. 3. Temperature dependence of the activation energy $\varepsilon_{\parallel} = d(\ln\rho_{\parallel})/d(kT)^{-1}$ for charge transfer along the tetragonal *c* axis of the crystal at temperatures corresponding to variable-range hopping conduction.

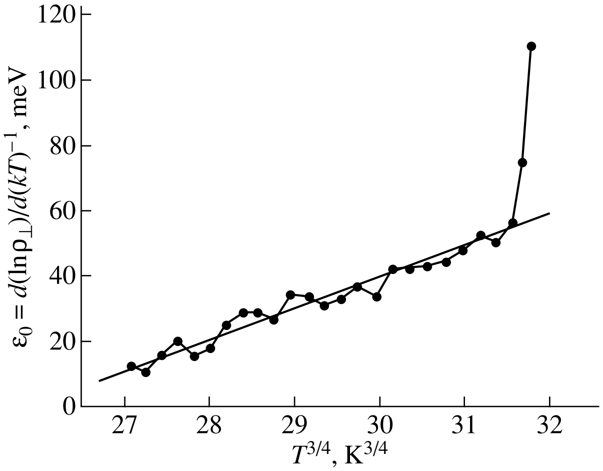

Fig. 4. Temperature dependence of the activation energy $\varepsilon_{\perp} = d(\ln\rho_{\perp})/d(kT)^{-1}$ for charge transfer in the direction perpendicular to the tetragonal *c* axis of the crystal at temperatures corresponding to variable-range hopping conduction.

perature leads to the fact that, at a specific temperature, the dominant contribution to the electrical conduction is made by charge carrier hopping between individual impurity states without activation into the allowed band. Of course, the hopping mechanism of conduction is characterized by a very low mobility of charge carriers, because their hopping occurs through slightly overlapped tails of the wave functions of the nearest neighbor acceptors. However, the contribution of the hopping conduction is larger than the contribution of the band conduction. Actually, all the holes located at acceptors can contribute to the hopping conduction, whereas only an exponentially small number of holes in the valence band can be involved in the band conduction.

The electrical conductivity governed by the Mott law (1) is also referred to as electrical conductivity with a monotonically decreasing activation energy $\varepsilon_0(T)$. According to Shklovskiĭ and Éfros [8], the temperature dependence of the activation energy can be described by the relationship

$$\varepsilon_0(T) = \frac{(kT)^{3/4}}{[g(\mu)a^3]^{1/4}}. \qquad (2)$$

Figures 3 and 4 depict the temperature dependences of the activation energy $\varepsilon_0(T)$, which were experimentally determined as the derivatives $d(\ln\rho)/d(kT)^{-1}$ in the range of hopping conduction at a temperature *T*. It can be seen from these figures that, at temperatures corresponding to variable-range hopping conduction, a decrease in the temperature leads to a monotonic decrease in the activation energy. In this case, the dependences $\varepsilon_0(T^{3/4})$ are approximated well by straight lines.

Let us return to Fig. 2. The temperature $T_0 = 1.06 \times 10^7$ K for the electrical conductivity in the direction parallel to the chains in the $TlInTe_2$ crystals was determined from the slope of the straight line $\log\rho_{\parallel}(T^{-1/4})$. By setting $\beta = 21$ [8] and assuming that the localization length of impurity states is equal to the characteristic length of the Coulomb bound state in $A^{III}B^{III}C_2^{VI}$ crystals ($a_1 = 20$ Å) [9], the density of states localized near the Fermi level in the $TlInTe_2$ single crystals is estimated as $g(\mu) = 3 \times 10^{18}$ eV^{-1} cm^{-3}. Such a high density of localized states in the band gap is characteristic of $A^{III}B^{VI}$ [5] and $A^{III}B^{III}C_2^{VI}$ [9] crystals with layered and chain structures. The anisotropy of bonding forces in layered structures encourages the formation of numerous defects, interstitial impurities, vacancies, and dislocations. This brings about a disturbance of the lattice periodicity and the formation of localized states with energies corresponding to the energies forbidden in an ideal crystal. In our previous study [5] of charge transfer in InSe layered crystals, it was demonstrated that only the real-crystal model accounting for the crystal structure imperfections has offered a satisfactory explanation of the strong conductivity anisotropy, which is inherent not only in $A^{III}B^{VI}$ layered crystals but also in classical layered crystals, such as graphite [10].

At a specified temperature *T*, the relationship [8]

$$\frac{R}{a} = \frac{3}{8}\left(\frac{T_0}{T}\right)^{1/4} \qquad (3)$$

gives an estimate of the average distance *R* of charge carrier hopping between the localized states near the Fermi level. It can be seen that, in the range of applicability of relationship (3), a decrease in the temperature results in an increase in the average carrier-hopping distance. This can be explained by the fact that the decrease in the temperature leads to an increase in the probability of charge carrier hopping between the centers of localization that are more widely spaced but have closer values of the energies. As a rule, the charge carrier executes hopping to a state characterized by the lowest possible activation energy ε. According to Mott and Davis [7], this activation energy, which is equal to the width of the optimum energy band (in the vicinity of the Fermi level) and whose contribution determines the electrical conductivity as a whole at a given temperature, can be estimated from the following expression:

$$\varepsilon = \frac{3}{4\pi R^3 g(\mu)}. \quad (4)$$

From relationships (3) and (4), we obtained the average carrier-hopping distance $R = 135$ Å and the spread in energies of localized states $\varepsilon = 33$ meV at a temperature $T = 100$ K. The same parameters at a temperature $T = 80$ K are found to be $R = 143$ Å and $\varepsilon = 27$ meV. Therefore, as the temperature decreases, the charge carriers execute hoppings to the centers of localization that are more widely spaced but have closer values of the energies. The activation energies calculated from formula (4) are in close agreement with the quantities $d(\ln\rho_{\parallel})/d(kT)^{-1}$ presented in Fig. 3. It should also be noted that, in an electric field, the average distance R is almost seven times larger than the localization length a_1.

Similarly, the temperature $T_0 = 2.6 \times 10^6$ K for the electrical conductivity in the direction perpendicular to the chains in the $TlInTe_2$ crystals was obtained from the slope of the straight line $\log\rho_{\perp}(T^{-1/4})$ in Fig. 2. Taking into account the calculated density of localized states $g(\mu) = 3 \times 10^{18}$ eV^{-1} cm^{-3} and using formula (1), we determine the carrier localization length $a_2 \sim 1.6a_1 = 32$ Å for charge transfer in the direction perpendicular to the chains in the crystals. Thus, the wave function of the localized state is anisotropic and has ellipsoidal symmetry with the semiaxes $a_1 = 20$ Å and $a_2 = 32$ Å. Note that the major semiaxis is aligned parallel to the direction of strong bonding. From expression (3), we obtained the average carrier-hopping distance $R = 152$ Å at $T = 100$ K and $R = 160$ Å at $T = 80$ K. According to formula (4), the spread in energies of localized states is estimated as $\varepsilon = 23$ meV at $T = 100$ K and $\varepsilon = 19.5$ meV at $T = 80$ K. These data are in good agreement with the quantities $d(\ln\rho_{\perp})/d(kT)^{-1}$ presented in Fig. 4. With a decrease in the temperature, charge transfer is provided by charge carrier hopping between the localized states (in the vicinity of the Fermi level), which are widely spaced but energetically more favorable. As was noted above, this is a characteristic feature of variable-range hopping conduction. In the case of conventional hopping conduction, the average carrier-hopping distance is of the order of the average distance between the impurities and remains constant with temperature change.

Strong conductivity anisotropy at low temperatures does not correspond to the anisotropy of the effective masses of charge carriers and can be explained only in terms of the real crystal structure of the compound under investigation. The anisotropic arrangement of defects in the $TlInTe_2$ single crystals (this is possible in an anisotropic crystal structure) and the anisotropy of the wave functions of the localized states can lead to the observed considerable anisotropy of hopping conductivity [11].

4. CONCLUSIONS

Thus, the experimental results have demonstrated that, in $TlInTe_2$ single crystals with a chain structure at temperatures ranging from 300 to 140 K, the electrical conduction in directions parallel and perpendicular to the chains is provided by thermally excited impurity charge carriers in the allowed band. The activation energy for electrical conduction in this temperature range is equal to 0.34 eV. At lower temperatures, the activation energy for electrical conduction decreases monotonically. In the temperature range $80\text{ K} < T < 120$ K, the electrical conduction in $TlInTe_2$ single crystals in both directions is provided by charge carrier hopping between localized states in the vicinity of the Fermi level. At these temperatures, the electrical conduction occurs through the variable-range hopping mechanism.

REFERENCES

1. D. Muller, G. Eulenberger, and H. Hahn, Z. Anorg. Allg. Chem. **398**, 207 (1973).
2. G. D. Guseinov, A. M. Ramazanzade, E. M. Kerimova, and M. Z. Ismailov, Phys. Status Solidi **22**, K117 (1967).
3. F. M. Gashimzade and G. S. Orudzhev, Dokl. Akad. Nauk AzSSR **36** (12), 18 (1980).
4. H. C. Montgomery, J. Appl. Phys. **42** (7), 2971 (1971); B. F. Logan, S. O. Rice, and R. F. Wick, J. Appl. Phys. **42** (7), 2975 (1971).
5. G. L. Belen’kiĭ, N. A. Abdullaev, V. N. Zverev, and V. Ya. Shteĭnshraĭber, Pis’ma Zh. Éksp. Teor. Fiz. **47** (10), 498 (1988) [JETP Lett. **47** (10), 584 (1988)].
6. N. A. Abdullaev, M. A. Nizametdinova, A. D. Sardarly, and R. A. Suleĭmanov, Fiz. Tverd. Tela (St. Petersburg) **35** (1), 77 (1993) [Phys. Solid State **35** (1), 41 (1993)].
7. N. F. Mott and E. A. Davis, *Electronic Processes in Non-Crystalline Materials* (Clarendon, Oxford, 1971; Mir, Moscow, 1974).
8. B. I. Shklovskiĭ and A. L. Éfros, *Electronic Properties of Doped Semiconductors* (Nauka, Moscow, 1979; Springer-Verlag, New York, 1984).
9. S. N. Mustafaeva, V. A. Aliev, and M. M. Asadov, Fiz. Tverd. Tela (St. Petersburg) **40** (4), 612 (1998) [Phys. Solid State **40** (4), 561 (1998)].
10. C. Uher and L. M. Sander, Phys. Rev. B **27** (2), 1326 (1983).
11. B. I. Shklovskiĭ, Fiz. Tekh. Poluprovodn. (Leningrad) **11** (11), 2135 (1977) [Sov. Phys. Semicond. **11** (11), 1253 (1977)].

Translated by O. Borovik-Romanova

Physics of the Solid State, Vol. 47, No. 7, 2005, pp. 1225–1232. Translated from Fizika Tverdogo Tela, Vol. 47, No. 7, 2005, pp. 1184–1191.
Original Russian Text Copyright © 2005 by Argunova, Gutkin, Zabrodskiĭ, Sorokin, Tregubova, Shcheglov, Abrosimov, Je, Yi.

SEMICONDUCTORS AND DIELECTRICS

X-ray Studies of $Si_{1-x}Ge_x$ Single Crystals

T. S. Argunova,* M. Yu. Gutkin, A. G. Zabrodskiĭ,* L. M. Sorokin,***
A. S. Tregubova,* M. P. Shcheglov,* N. V. Abrosimov,* J. H. Je,**** and J. M. Yi******

**Ioffe Physicotechnical Institute, Russian Academy of Sciences, Politekhnicheskaya ul. 26, St. Petersburg, 194021 Russia*

***Institute of Problems of Mechanical Engineering, Russian Academy of Sciences,*
Vasil'evskiĭ Ostrov, Bol'shoĭ pr. 61, St. Petersburg, 199178 Russia

****Institute of Crystal Growth, Berlin, 12489 Germany*

*****Department of Materials Science and Engineering, Pohang University of Science and Technology,*
Pohang, 790-784 Korea

Received October 14, 2004

Abstract—Structural imperfections were studied in $Si_{1-x}Ge_x$ (1–9 at. % Ge) solid-solution single crystals grown using the Czochralski method. The studies were performed using x-ray diffraction topography with laboratory and synchrotron radiation sources, x-ray diffractometry, and synchrotron radiation phase radiography. In all crystals studied, irrespective of the Ge concentration, impurity bands (growth bands) were observed. An increase in the Ge concentration in the range 7–9 at. % was shown to bring about the nucleation and motion of dislocations on a few slip systems and the formation of slip bands. Local block structures were observed in the places where slip bands intersected. The most likely reason for the formation of slip bands is the inhomogeneous distribution of Ge atoms over the ingot diameter and along the growth axis. Therefore, the structure of $Si_{1-x}Ge_x$ solid-solution single crystals can be improved by making them more uniform in composition. *© 2005 Pleiades Publishing, Inc.*

1. INTRODUCTION

Currently, epitaxial $Si_{1-x}Ge_x$ solid-solution layers grown on silicon substrates are used in electronics, but $Si_{1-x}Ge_x$ single crystals also hold promise. To circumvent technological problems associated with the growth of $Si_{1-x}Ge_x$ solid-solution films, thick relaxed $Si_{1-x}Ge_x$ layers are used, on which, in turn, thin elastically strained silicon layers are grown. These additional operations in the fabrication of semiconductor structures increase their cost. For this reason, the idea of growing elastically strained Si layers on $Si_{1-x}Ge_x$ single-crystal substrates is becoming more and more attractive. However, these substrates have to have a high Ge concentration (of up to 20 at. %) and a low density of structural defects.

$Si_{1-x}Ge_x$ solid solutions are also used as an active element in photoelectric converters (solar cells) due to their sensitivity to radiation in the long-wavelength region of the visible spectrum. The quality of solar cells based on epitaxial layers of gallium arsenide and related III–V compounds is low due to structural imperfections caused by the lattice mismatch between the active layer and the silicon substrate. Replacing the Si substrates by $Si_{1-x}Ge_x$ decreases this mismatch and makes it possible to optimize the fabrication technology of GaAs-based solar cells and enhance their reliability.

Large $Si_{1-x}Ge_x$ single crystals are usually grown using the Czochralski method [1, 2]. In this case, the spatial distribution of germanium is inhomogeneous. Due to segregation of germanium in silicon, the germanium concentration in these crystals varies over a cross section and along the length of an ingot. By controlling the growth conditions, ingots with the desired lattice parameter gradient along the growth axis can be obtained [3]. $Si_{1-x}Ge_x$ crystals with lattice parameter profiles hold promise for use in synchrotron radiation optics. For example, a crystal monochromator in which the interplanar distance varies along the surface enables one to decrease the beam divergence and to increase the reflectance of the monochromator, with the reflected beam remaining monochromatic [3].

The growth of $Si_{1-x}Ge_x$ single crystals with a uniform spatial distribution of germanium poses severe problems, which have not yet been overcome. Impurity bands (growth bands) are always present in Czochralski-grown $Si_{1-x}Ge_x$ crystals [4]. These bands arise due to microscopic fluctuations in the growth rate, which, in turn, are caused by nonsteady-state convective flows in a melt [5].

A change in the Ge distribution in silicon leads to a change in the lattice parameter and favors the formation of structural defects. Since defects have an adverse effect on the parameters of devices and the characteristics of x-ray monochromators based on $Si_{1-x}Ge_x$, it is of importance to develop a technology for producing uniform crystals with desired properties. With this aim, the relation between the growth conditions and the structural perfection of crystals should be investigated.

To date, it has been established that (i) the Ge concentration and the growth front curvature have an effect on the distribution of growth bands and their structure [6], (ii) the amount of dislocations in a crystal and their distribution in horizontal and vertical cross sections of an ingot depend on the Ge concentration and the orientation of the growth axis [1, 3], and (iii) the mobility of dislocations is determined by microscopic inhomogeneities of a solid solution [7, 8]. Micro-inhomogeneities in $Si_{1-x}Ge_x$ and $Ge_{1-x}Si_x$ solid solutions also have an effect on the stress–strain curves of these materials [9].

The objective of this work is to comprehensively study the formation of defects in $Si_{1-x}Ge_x$ crystals depending on the Ge content in the range 1–9 at. % for crystals with various orientations of the growth axis. We used different methods based on x-ray diffraction: x-ray topography, diffractometry, and synchrotron radiation phase radiography.

2. SAMPLES AND EXPERIMENTAL TECHNIQUES

2.1. $Si_{1-x}Ge_x$ Single Crystals

$Si_{1-x}Ge_x$ crystals ($0.01 \le x \le 0.09$) were grown using the Czochralski method at the Crystal Growth Institute (Institut für Kristallzüchtung, Berlin, Germany). Ingots up to 42 mm in diameter had a weak Ge concentration gradient along the growth axis. The growth direction was parallel to $\langle 110 \rangle$, $\langle 111 \rangle$, $\langle 001 \rangle$, or $\langle 122 \rangle$ (the last growth direction arose after twinning of a crystal grown along $\langle 001 \rangle$). Crystals (with *n*- or *p*-type conductivity) were lightly doped with phosphorus and boron to a concentration of approximately 10^{15} cm^{-3} and contained oxygen at a concentration of 6×10^{17} cm^{-3}. We studied samples in the form of ~0.4-mm-thick plates cut perpendicular to the growth axis, with both faces polished using chemical and mechanical methods.

2.2. X-ray Images of Crystals

X-ray images of the plates under study provided most of the information on crystal imperfections. The images were obtained in three different ways: (i) x-ray diffraction topography with a laboratory x-ray source, (ii) Bragg diffraction with a synchrotron source, and (iii) Fresnel diffraction with a synchrotron source. Let us describe each of the above means of obtaining images.

(i) Laboratory x-ray topographs were obtained using the Lang projection method in the Bragg or Laue geometry with commercial equipment (Cu and Mo K_{α_1} radiation). The beam divergence was dependent on the radiation wavelength and was of the order of a few minutes of arc. The resolution of the method was a few micrometers. The images were recorded using photographic plates with nuclear emulsion whose resolution corresponded to the highest resolution of the method.

(ii) Synchrotron radiation topographs were obtained using polychromatic radiation with an energy of 10 to 60 keV. The spatial beam divergence was 2 and 5 μrad in the vertical and horizontal planes, respectively. A beam of radiation with small divergence and with a large cross-sectional area on a sample can only be provided by a sufficiently remote source. A source of synchrotron radiation satisfies these requirements and provides high-intensity beams. When radiation with a continuous spectrum is incident on a single crystal, each set of crystallographic planes “selects” the wavelengths for which the angle between the diffracting planes and the beam satisfies the Bragg condition. As a result, there appear many diffracted beams behind the crystal, with each Laue spot being a high-resolution topograph [10]. The contrast of the images in polychromatic radiation is due to variations in the orientation and extinction. In the former case, the intensity varies from point to point depending on the lattice misorientations. The extinction contrast is due to local variations in the crystal imperfection: in the vicinity of a defect, x rays are scattered in much the same way as in a mosaic crystal and the integrated reflection intensity from this region is higher than that from a more perfect region of the crystal [10].

The detecting device consisted of a 200-μm-thick $CdWO_4$ crystal scintillator, a lens to magnify the image, and a CCD camera. The field of vision was 8 × 8 mm in size, and the pixel size was 15 μm. The sample–scintillator distance was 8 cm. Experimentally, there was room for only one Laue topograph on the CCD array.

(iii) The images were also obtained using synchrotron radiation phase radiography. The description of the technique for producing x-ray phase images can be found in [11–13]. We employed this technique to detect inhomogeneities (e.g., Ge inclusions) in which the material density differs from that in the matrix. The images were recorded using a method similar to the white-beam method, but the resolution of the CCD array was significantly higher: the pixel size was 0.14 μm and the sensitivity was 16 bit. The highest resolution of the detecting device was 2 μm. The sample–scintillator distance was 8–10 cm.

Synchrotron radiation experiments were carried out in Pohang (Republic of Korea) at Pohang Light Source, station 7B2 (a third-generation synchrotron radiation source).

2.3. X-ray Diffractometry: Measurement of the Lattice Parameter

The lattice parameter was measured using a triple-crystal spectrometer [14]. The beam diameter in the scattering plane was 0.5 mm. The sample could be displaced within ±20 mm in a horizontal direction. The horizontal displacement and rotation of the sample about the axis perpendicular to the sample surface made it possible to measure the Bragg angle at various points and determine the variation in the lattice param-

Table 1. Parameters of several samples studied

Sample no.	Conductivity type	Resistivity, Ω cm	Orientation	X-ray reflection	Rocking-curve half-width, arc seconds; ±0.1″	Ge content, at. %; ±0.1%
105-3	*p*	10	(110)	220	6	1.5
222-9	*n*	2.2	(110)	220	8–20	3.0–3.2
104-4	*p*	7.2	(110)	220		6.5
33-1	*p*	0.6	(001)	004	7	1.0
33-6	*p*	0.6	(001)	004	7	1.5
60-2	*p*	2.7	(122)	244		4.4
16-14	*n*	2.5	(111)	111	8–12	4.1

eter over the crystal area. The lattice parameter was measured with an accuracy of ±0.00012 Å (including systematic error). The Ge concentration was determined with an accuracy of ±0.1%.

According to Vegard's law, the lattice parameter varies in proportion to the Ge concentration:

$$\Delta d / d_{\mathrm{Si}} = JC, \tag{1}$$

where d is the interplanar distance, C is the Ge concentration (in atomic percent), and J is a coefficient of proportionality. However, it has been found that $Si_{1-x}Ge_x$ single crystals do not follow Vegard's law [3] and that the coefficient J in Eq. (1) for small Ge concentrations can be found from the empirical formula

$$J \approx 3.67 \times 10^{-4} + 1 \times 10^{-4} C. \tag{2}$$

Table 1 lists the values of the Ge concentration for several samples determined using Eqs. (1) and (2). Rocking curves were recorded by scanning near a reflection angle using a double-crystal technique. By comparing the measured and calculated half-widths of the rocking curves, a conclusion was drawn concerning crystal imperfections. For comparison, the calculated half-width of the rocking curve for the (220) reflection from a perfect Si crystal is 5.5 arc seconds.

3. EXPERIMENTAL RESULTS AND DISCUSSION

3.1. $Si_{1-x}Ge_x$ (1–7 at. % Ge)

The main structural imperfections in crystals with 1–7 at. % Ge detected using x-ray topography are impurity bands (due to variations in the Ge concentration) and dislocation slip bands. Figure 1 shows topographs taken of (110)-, (001)- and (122)-oriented plates with various Ge contents. The topograph in Fig. 1a is taken of a sample with 1.5 at. % Ge. It can be seen that there are impurity bands in the form of concentric rings and widely spaced dislocation slip bands corresponding to a single slip system, which look like thin lines in the Bragg geometry. These lines are parallel to the $[11\bar{2}]$ direction, which is the line of intersection of the $(\bar{1}11)$ slip plane and the (110) surface of the sample. The positions of the slip planes and x-ray reflections on the stereogram with respect to the (110) reflection are shown in Fig. 2b. Figure 1b shows a topogram taken of a sample with the same orientation with 3 at. % Ge. It can be seen that there are dislocations on all three slip planes, (111), $(\bar{1}11)$, and $(1\bar{1}1)$. In topograms obtained in the Laue geometry, the slip bands are seen to propagate through the entire thickness of plates and are located, for the most part, at the periphery of the plates. Individual dislocations with the least resolvable separation between them can be seen in the slip bands, which makes it possible to estimate the dislocation density to be ≈10^5 cm^{-2}. At the intersection points of bands

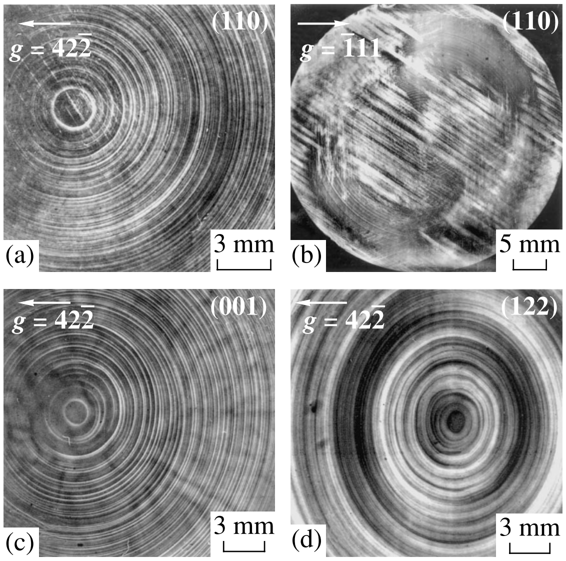

Fig. 1. (a–d) Impurity bands in the form of concentric rings and (a, b) slip bands in $Si_{1-x}Ge_x$ samples. (a) Sample 105-3 with a (110)-oriented surface and a Ge content of 1.5 at. %; (b) sample 222-9 with a (110) surface and 3 at. % Ge; (c) sample 33-6 with a (001) surface and 1.5 at. % Ge; and (d) sample 60-2 with a (122) surface and 4.4 at. % Ge. (a, c, d) Bragg geometry, CuK_{α_1} radiation, and a Bragg angle of 44.8°; and (b) Laue geometry, MoK_{α_1} radiation, and a Bragg angle of 6.6°.

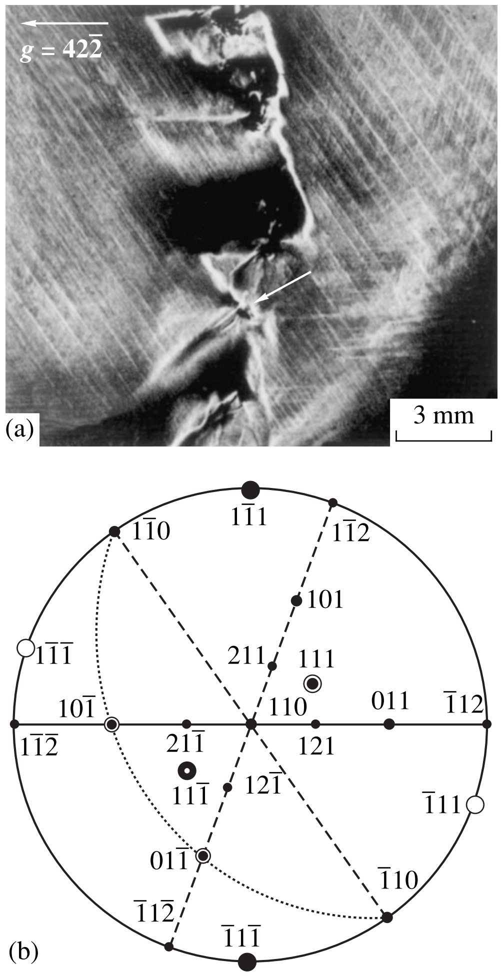

Fig. 2. Structural imperfections (slip bands, a small-angle boundary, sources of long-range stresses) in Si$_{1-x}$Ge$_x$ samples with Ge contents ranging from ~7 to 9 at. %. (a) X-ray topograph taken of sample 104-4 with a (110)-oriented surface and a Ge content of 6.5 at. % (the image of a source of long-range stresses is indicated by an arrow); Bragg geometry, CuK_{α_1} radiation, and a Bragg angle of 44.8°. (b) Stereogram of a cubic crystal (the projection axis is [110]).

belonging to different slip systems, the dislocation density is noticeably higher.

Table 2 lists the products |**g** · **b** × **l**|, where **g** is the diffraction reflection vector, **b** is the Burgers vector, and **l** is a unit vector along the dislocation line. If this product is nonzero, then the edge component of a dislocation with the given Burgers vector will be detected in an x-ray topograph. According to this criterion, all slip systems will be observed with a high contrast in the Laue diffraction spot with **g** = $\bar{1}11$ from a (110)-oriented sample. This is indeed the case and does not contradict the assumption that slip bands consist, for the most part, of 60° dislocations.

Table 2. Product |**g** · **b** × **l**| for 60° dislocations lying in the (111), ($1\bar{1}1$), and ($1\bar{1}\bar{1}$) slip planes and x-ray reflection $\bar{1}11$

Burgers vector, **b**	Dislocation line, **l**	Direction of the vector **b** × **l**	|**g** · **b** × **l**|
[$01\bar{1}$]	[$10\bar{1}$]	[111]	1
[$10\bar{1}$]	[110]	[$1\bar{1}1$]	1
[$01\bar{1}$]	[110]	[$1\bar{1}\bar{1}$]	3

The inhomogeneous intensity distribution in Fig. 1b indicates the presence of unrelaxed elastic strains. Furthermore, the rocking curves obtained using the two-crystal technique are broadened, which indicates that the crystal lattice is bent due to slip bands. The Ge concentration varies over the sample area within ±0.2 at. % (Table 1), which exceeds the measurement error.

In variously oriented samples with a uniform Ge distribution over the sample area and Ge contents ranging from 1 to 7 at. %, slip bands are not observed at all or correspond to a single slip system. Typical topographs for (001)- and (122)-oriented samples are shown in Figs. 1a, 1c, and 1d. The [122] growth direction arose due to twinning of crystals grown along the [001] axis. In plates cut perpendicular to the [122] new growth axis, the main structural imperfections are impurity bands, whereas slip bands are not observed in x-ray topographs at up to 7 at. % Ge. The structure of the growth bands varies with increasing Ge content. By comparing the images shown in Figs. 1a, 1c, and 1d, it can be seen that, as the Ge content increases, the impurity bands in the form of a regular oval ring progressively broaden and become stepped. Analogous patterns were observed in [6], but no explanation was provided for this phenomenon.

Thus, the density of slip bands in Si$_{1-x}$Ge$_x$ crystals increases with Ge content and with increasing degree of inhomogeneity of the Ge distribution over the crystal area (see, e.g., sample 222-9 in Table 1 and Fig. 1b). The reason for the generation and slip of dislocations is most likely the inhomogeneous Ge distribution along both the length and diameter of ingots causing a change in the lattice parameter of the crystal. Moreover, the evaporation of Ge from the melt surface and its deposition on the crystal surface can bring about the formation of misfit dislocations on the lateral surface of the crystal. This effect increases in importance with increasing Ge concentration in the melt. Under these conditions, temperature gradients arising during both the growth and cooling of a crystal produce strong thermoelastic stresses. In the field of these stresses, asperities of the free crystal surface become sources of dislocations. The multiplication of dislocations during their motion increases the dislocation density in slip bands, and when dislocations go into other slip planes, the slip bands broaden.

The dependence of the dislocation density on the orientation of the growth axis in Si$_{1-x}$Ge$_x$ crystals was pointed out in [3]. In that work, the most perfect crystals with a Ge content of approximately 7 at. % were produced in the case where the growth axis was ⟨112⟩ and the most imperfect crystals were grown along the ⟨110⟩ axis. To explain this result, the authors of [3] assumed that the interaction of dislocations in the bulk of crystals grown along the ⟨110⟩ axis occurs in the $(\bar{1}11)$ and $(1\bar{1}1)$ slip planes parallel to the growth axis. In contrast to crystals grown along the ⟨110⟩ axis, a crystal grown along ⟨112⟩ has only one {111} plane parallel to the growth axis. It should also be noted that, under uniaxial loading, there is no shear stress in the planes perpendicular and parallel to the loading axis, because the shear stress τ is equal to $\tau = \sigma\cos\chi\cos\lambda$, where σ is the applied stress and χ and λ are the angles that the normal to the slip plane and the slip direction make with the direction in which the external stress is applied, respectively [15]. Although the stress distribution in the crystals studied is not uniaxial, the existence of a lattice parameter gradient along the growth axis suggests that the stresses in planes parallel (or nearly parallel) to the growth axis are minimum. In crystals grown along ⟨122⟩, none of the {111} slip planes is parallel to the growth axis. Two of them, (111) and $(1\bar{1}1)$, make a large (74.2°) and a small (11.1°) angle with the growth axis, respectively; so the shear stresses in these planes should be less than those in the planes making angles close to 45° with the growth axis. These stresses are likely to be insufficient to produce plastic strains with the formation of dislocations.

3.2. $Si_{1-x}Ge_x$ (7–9 at. % Ge)

In the Ge concentration range 7–9 at. % in samples cut from crystals with all the orientations studied, increased densities of slip bands were observed for all systems of {111} slip planes intersecting the sample surface. Furthermore, x-ray topography revealed structural defects that are sources of long-range stresses. One of these defects is marked in Fig. 2 and is located at a small-angle boundary that crosses the image from the top down. Near this defect, the Bragg reflection intensity is distributed very inhomogeneously, which indicates that the defect causes strong distortions of the lattice: misorientation, deformation, and bending of crystallographic planes. Variations in the reflection intensity near the defect obscure the details of its image. It is noteworthy that the central region of the defect has a zero contrast. This may suggest that the lattice misorientation in this region is higher than the divergence of the incident beam; therefore, the defect has a block structure and a composition close to that of the nearby regions. However, if the defect is an inclusion of another material (e.g., germanium), then the absence of reflection from it can be due to a change in the interplanar distance; in this case, monochromatic radiation satisfying the condition of Bragg reflection for the surrounding matrix will not be reflected from the inclusion. Based on topographs obtained with a weakly divergent monochromatic beam, these two cases cannot be distinguished. For this reason, we used polychromatic synchrotron radiation to analyze the nature of these defects.

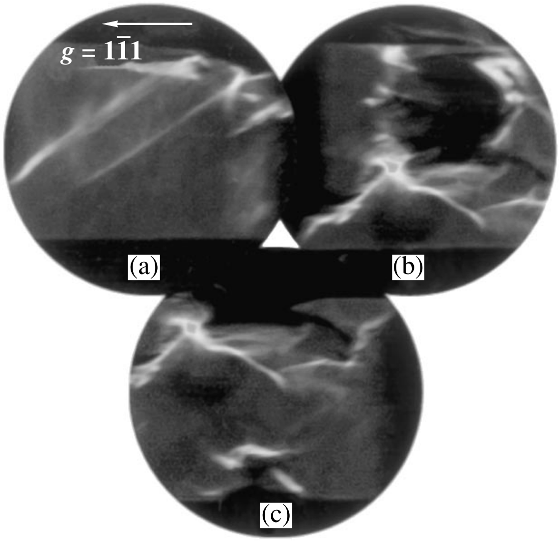

Fig. 3. X-ray topograms taken (in polychromatic synchrotron radiation) of the sample area marked with an arrow in Fig. 2a. Images (a, b, c) differ in terms of the orientation of the sample in the reflection region.

Figure 3 shows synchrotron radiation Laue topograms obtained in the $(1\bar{1}1)$ reflection from the region marked with an arrow in Fig. 2a. It can be seen that the central region of the defect has a zero contrast as before and that there are small-angle boundaries around the zero-contrast region of the defect. In the topogram, these boundaries look like lines of high intensity. This extinction contrast can only be due to a high density of structural defects in these boundaries. Now, the zero contrast can no longer be accounted for as being due to the difference between the interplanar distances of the inclusion and the matrix, because radiation is polychromic and for each set of crystallographic planes there is a wavelength satisfying the Bragg reflection condition. Weak lattice misorientations likewise cannot be the reason why the reflected rays are not detected by the crystal scintillator. A misorientation of blocks of a few degrees can cause a change in the direction of the reflected rays and, hence, in the detected reflection intensity but cannot cause this intensity to vanish.

There is also no reason to believe that these defects are germanium inclusions. Indeed, these defects were not observed in synchrotron radiation phase-radiographic images, although the resolution and sensitivity of this method was sufficient to detect germanium inclusions as small as a few micrometers in size via absorption and refraction of radiation (the Ge density is approximately 2.3 times greater than that of silicon).

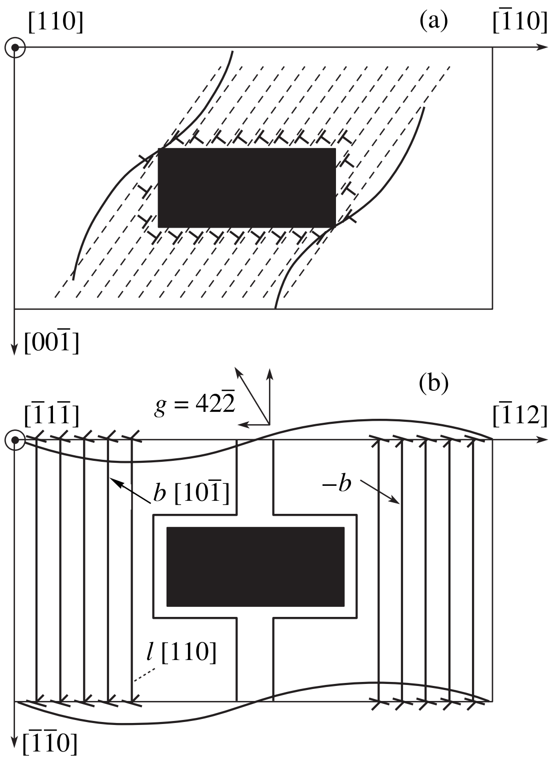

Fig. 4. 60° dislocations (with Burgers vectors opposite in direction) lying in the $(\bar{1}1\bar{1})$ slip plane and piled up before the large-angle boundaries of blocks (schematic). The blocks are positioned within a region shown as a black rectangle in the center of the figure. Bent atomic planes are depicted by curved lines. (a) The plane of the figure is parallel to the sample surface and is perpendicular to [110]; the $(\bar{1}1\bar{1})$ slip planes are depicted by dashed lines, and atomic planes are bent in the direction perpendicular to the sample surface due to the edge components of dislocations. (b) The plane of the figure is parallel to the $(\bar{1}1\bar{1})$ slip plane; dislocation loops are depicted by lines skirting the black rectangle, and atomic planes are bent in the direction perpendicular to the sample surface due to the screw components of dislocations.

Thus, we arrive at the conclusion that the central region of the defect scatters x rays in all directions and, therefore, consists of blocks separated by large-angle boundaries. In this case, the fraction of the scattered radiation falling on the scintillator is small and insufficient to form the image. The region of the crystal not involved in the formation of contrast is several hundreds of micrometers in size.

The noticeable variations in the scattering intensity at a distance from the defect region shown in Fig. 2a can be explained in terms of the following model. Long-range elastic stresses are most likely caused by dislocations that are piled up before large-angle boundaries of the blocks inside the defect core. Since the dislocation density in slip bands is high ($\approx 10^5$ cm^{-2}), the dislocation pileups produce significant stresses. Let us consider the mechanism of dislocation pinning in more detail.

Figure 4 schematically shows dislocations lying in the $(\bar{1}1\bar{1})$ slip plane (only 60° dislocations are depicted). The parallelepiped at the center (its rectangular cross section is shown) has a block structure. In order to explain the contrast observed in the Bragg geometry, we assume that the region with a block structure is located near the free surface of the sample. If a slip plane intersects the large-angle boundaries of blocks, dislocations are stopped at the boundaries and form pileups opposite in sign along opposite sides of the block-structured region [16]. The head dislocations in the pileups can skirt the block-structured region via the Orowan mechanism [17] and form closed slip dislocation loops around it. The dislocation pileups produce strong elastic stress fields, which cause the atomic planes to bend. Since we consider only 60° dislocations, the atomic planes perpendicular to the sample surface will be bent by the edge components of the dislocations, whereas the sample surface will be bent along its normal by the screw components. The bent planes are shown in Fig. 4.

The integrated intensity of a Bragg reflection depends on the mutual orientation of the diffraction vector and the curvature vector of the reflecting planes. The integrated intensity is higher for reflection from concave planes ($\mathbf{g} \cdot \mathbf{N} > 0$) and is lower for reflection from convex planes ($\mathbf{g} \cdot \mathbf{N} < 0$) [18], where $\mathbf{g}$ is the diffraction vector and $\mathbf{N}$ is the curvature vector directed toward the center of curvature. In Fig. 4b, reflection vector $42\bar{2}$ is decomposed into two components, one of which is parallel to the sample surface and the other is perpendicular to it. The higher and lower contrasts near the source of strains shown in Fig. 2a are due to the complicated topography of the bent atomic planes.

Studies into the crystal structure are insufficient to reveal the reason for the formation of regions with a local block structure in $Si_{1-x}Ge_x$ crystals with a high Ge content. However, x-ray images make it possible to draw preliminary conclusions. Figure 5a shows a topograph of a plate cut from a crystal for which the growth axis was along $\langle 111 \rangle$. From this topograph, it follows that segregation bands are not observed in the central part of the crystal but are clearly visible in its periphery. Therefore, the crystallization front was flat in the central region and was concave at the periphery. It is also seen that there are dislocation slip bands along the $(1\bar{1}1)$, $(\bar{1}11)$, and $(11\bar{1})$ planes. Various sources of stresses are seen to be arranged in groups near the central part of the sample. The sources are closely spaced, and their images overlap. As in Fig. 4, the defects are seen to have reflectionless cores around which the reflection intensity varies sharply. It may be assumed that these defects form as follows. It was mentioned previously that slip bands consist of dislocations that are generated by sources located in the periphery of the

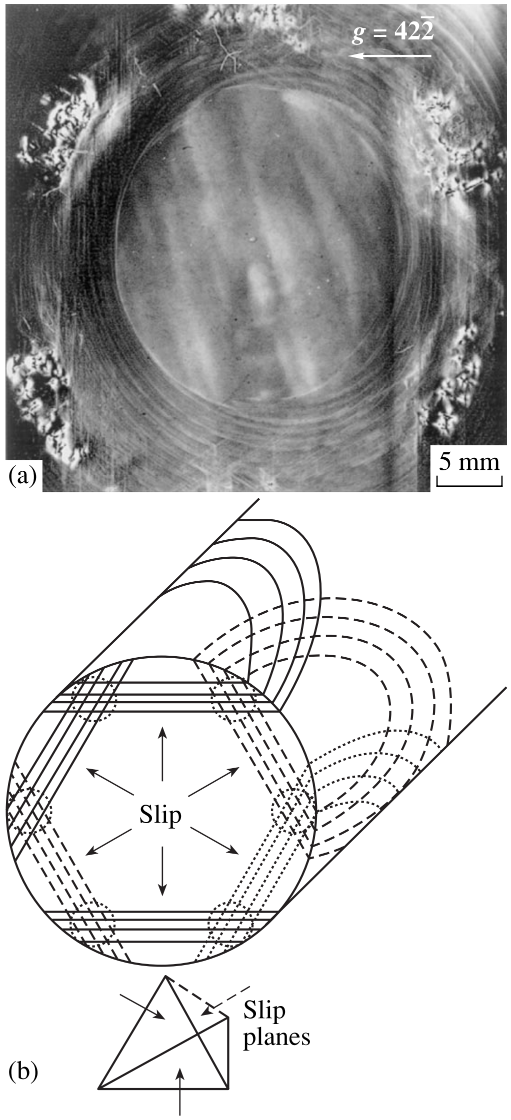

Fig. 5. X-ray topograph taken of a $Si_{1-x}Ge_x$ crystal (sample 16-14) and its interpretation. (a) Bragg geometry, CuK_{α_1} radiation. (b) Dislocation loops moving away from dislocation sources that are located at the crystal surface; the slip planes form a tetrahedron.

crystal and then (driven by thermoelastic stresses) penetrate deep into it. At the intersection points of bands formed by dislocations gliding in the three {111} planes, the dislocation density is high, which favors the formation of regions with a local block structure. The arrangement of groups of these regions exhibits 60° symmetry, as can be seen in Fig. 5a. This symmetry is due to dislocations gliding from opposite sides of an ingot, as shown schematically in Fig. 5b.

The half-width of the rocking curves of x-ray diffraction peaks from various parts of the sample depicted in Fig. 5 varies over a very wide range. For clusters of defects with a local block structure, the half-width of rocking curves is 30 times as large as that for comparatively homogeneous parts of the crystal (Table 1), which supports the conclusion that these defects have a block structure.

4. CONCLUSIONS

Structural imperfections have been studied in $Si_{1-x}Ge_x$ crystals (1–9 at. % Ge) with various orientations of the growth axis and with a weak Ge concentration gradient along the growth axis. Impurity bands have been found to exist in all crystals studied, irrespective of the Ge content and the growth axis orientation, which is consistent with the results of previous studies. As the Ge content increases within the range from 7 to 9 at. %, dislocations move away from dislocation sources located at the free surface of a crystal and single dislocation slip transforms into multiple slip; slip bands arise, and their density increases. In a number of samples, the Ge concentration is distributed nonuniformly over the sample area. In these samples, the slip band density is high even for a small Ge content (3 at. %). The conclusion has been drawn that the most likely reason for the formation of the slip band is the nonuniform Ge distribution along both the diameter and growth axis of an ingot, due to which temperature gradients (which occur during the growth and cooling of crystals) bring about high thermoelastic stresses.

It has been established that, in crystals with Ge contents ranging from 7 to 9 at. %, there appear regions with a local block structure several hundreds of micrometers in size. The formation of these regions is most likely due to the significantly increased dislocation density at the points of intersection of slip bands. These regions can be barriers to the motion of new dislocations and, therefore, can be sources of long-range stresses. Thus, a more uniform Ge distribution in silicon is a necessary condition for producing $Si_{1-x}Ge_x$ crystals with a reduced amount of structural imperfections.

ACKNOWLEDGMENTS

This study was supported by the program “Low-Dimensional Quantum Structures” (no. 6.3) under the Presidium of the Russian Academy of Sciences.

REFERENCES

1. N. V. Abrosimov, S. N. Rossolenko, V. Alex, A. Gerhardt, and W. Schröder, J. Cryst. Growth **166**, 657 (1996).
2. R. H. Deitch, S. H. Jones, and T. G. Digges, Jr., J. Electron. Mater. **29** (9), 1074 (2000).
3. A. Erko, N. V. Abrosimov, and V. Alex, Cryst. Res. Technol. **37** (7), 685 (2002).
4. N. V. Abrosimov, A. Lüdge, H. Riemann, and W. Schröder, J. Cryst. Growth **237–239**, 356 (2002).
5. O. V. Smirnova, V. V. Kalaev, Yu. N. Makarov, N. V. Abrosimov, and H. Riemann, J. Cryst. Growth **266**, 74 (2004).

6. K. Wieteska, W. Wierzchowski, W. Graeff, M. Lefeld-Sosnowska, and M. Regulska, J. Phys. D: Appl. Phys. **36**, A133 (2003).
7. N. V. Abrosimov, V. Alex, D. V. Dyachenko-Dekov, Yu. L. Iunin, V. I. Nikitenko, V. I. Orlov, S. N. Rosselenko, and W. Schröder, Mater. Sci. Eng. A **234–236**, 735 (1997).
8. Yu. L. Iunin, V. I. Nikitenko, V. I. Orlov, D. V. D’yachenko-Dekov, B. V. Petukhov, N. V. Abrosimov, S. N. Rossolenko, and W. Schröder, Zh. Éksp. Teor. Fiz. **121** (1), 129 (2002) [JETP **94** (1), 108 (2002)].
9. I. Yonenaga, Mater. Sci. Eng. A **234–236**, 559 (1997).
10. D. K. Bowen and B. K. Tanner, *High Resolution X-ray Diffractometry and Topography* (Taylor Francis, London, 1998).
11. A. Snigirev, I. Snigireva, V. Kohn, S. Kuznetsov, and I. Schelokov, Rev. Sci. Instrum. **66** (12), 5486 (1995).
12. P. Cloetens, R. Barrett, J. Baruchel, J. P. Guigay, and M. Schlenker, J. Phys. D: Appl. Phys. **29**, 133 (1996).
13. G. Margaritondo and G. Tromba, J. Appl. Phys. **85** (7), 3406 (1999).
14. P. F. Fewster and N. L. Andrew, J. Appl. Cryst. **28**, 451 (1995).
15. R. Berner and H. Kronmüller, *Plastische Verformung von Einkristallen, in Moderne Probleme der Metallphysik*, Ed. by A. Seeger (Springer, Berlin, 1965; Mir, Moscow, 1969).
16. J. P. Hirth and J. Lothe, *Theory of Dislocations* (McGraw-Hill, New York, 1967; Atomizdat, Moscow, 1972).
17. J. Friedel, *Dislocations* (Pergamon, Oxford, 1964; Mir, Moscow, 1967).
18. U. Bonse and W. Graeff, Naturforscher A **28** (5), 558 (1973).

Translated by Yu. Epifanov

Physics of the Solid State, Vol. 47, No. 7, 2005, pp. 1233–1235. Translated from Fizika Tverdogo Tela, Vol. 47, No. 7, 2005, pp. 1192–1194.

Europium Diffusion in SmS

A. V. Golubkov, V. A. Didik, V. V. Kaminskiĭ, E. A. Skoryatina,
V. P. Usacheva, and N. V. Sharenkova

Ioffe Physicotechnical Institute, Russian Academy of Sciences, Politekhnicheskaya ul. 26, St. Petersburg, 194021 Russia
e-mail: didik@mail.ioffe.ru

Received October 19, 2004

Abstract—Europium diffusion in samarium sulfide was studied in the temperature range from 780 to 1100°C. Data on the diffusion coefficient and activation energies for the diffusion of europium in single-crystal and polycrystalline SmS samples were obtained. In single-crystal samarium sulfide, europium was shown to migrate predominantly over lattice sites ($D \simeq 10^{-12}$–10^{-9} cm^2/s). In SmS polycrystals, diffusion was found to exhibit a complex pattern and have both a slow ($D \simeq 10^{-10}$–10^{-9} cm^2/s) and a fast ($D \simeq 10^{-8}$–10^{-7} cm^2/s) component. Europium diffusion in a polycrystal is primarily due to europium migration over the boundaries of single-crystal grains in the polycrystal, whose characteristic size is assumed to be that of x-ray coherent-scattering regions. *© 2005 Pleiades Publishing, Inc.*

The interest in europium diffusion in samarium sulfide (SmS) has arisen in connection with studies of the emf generation in this semiconductor material, because the temperature of the onset of generation and the magnitude of the emf depend on impurity concentration [1]. The most natural impurity to expect in this case is europium, which neighbors samarium in the lanthanide series and, thus, is similar to it in many characteristics. There is a difference, however, in that europium does not change its valence state (Eu^{2+}) under heating, whereas samarium does ($Sm^{2+} \longrightarrow Sm^{3+}$). However, SmS and EuS crystallize in the NaCl structure with extremely close lattice parameters, 5.967 and 5.968 Å, respectively. Note that semiconductors with lattice misfits less than 0.01 Å are believed to be most promising for the development of heterostructures [2]. The substantial difference between the band structures and, in particular, in the depth of the 4*f* levels [3] coupled with the close similarity of the thermal, electrical, and crystallochemical properties accounts for the interest in studies of SmS- and EuS-based heterostructures. Investigation of SmS-based heterostructures is made particularly attractive by the possibility of producing an inverse level population in this semiconductor under a comparatively weak physical action (heating up to $T \sim 400$ K), as is the case with emf generation. In these conditions, one can expect the generation of optical radiation with photon energies of 0.03–0.06 eV [4]. Studying mutual diffusion in heterostructures is also of considerable scientific interest.

SmS polycrystals were synthesized of elemental ingredients (samarium and sulfur) and compacted, with subsequent homogenization annealing performed at different temperatures in sealed molybdenum crucibles. SmS single crystals were prepared by zone melting of polycrystals [5]. Samples of single-crystal SmS were plane-parallel plates cleaved along the (100) planes. The plates measured 8 × 5 × 3 mm. The plane parallelism of the samples (±2 μm) was attained by dry precision grinding with abrasive cloth and checked with an IKV-1 vertical optometer to within 1 μm.

Experiments were performed with the ^{152}Eu radioactive isotope in the temperature interval 780–1100°C. The radioactive europium isotope was introduced into both single-crystal and polycrystalline SmS samples during vacuum annealing. Concentration–depth profiles were obtained by layer-by-layer removal of the material. The gamma activity of the layers removed was determined using a BDZA2-01 NaI(Tl) scintillation detector combined with the corresponding electronics. The measurements yielded profiles of the distribution of the ^{152}Eu radioactive isotope in SmS samples at different temperatures.

The europium penetration profiles in single-crystal SmS samples obtained after annealings of single-crystal SmS samples at temperatures of 950, 1000, and 1050°C (annealing time 1–21 h) are curves that fall off smoothly (Fig. 1a). As should be expected, the profile depth increases with temperature. The europium concentration is 10^{19}–10^{21} cm^{-3} near the sample surface and decays to 10^{15}–10^{16} cm^{-3} deep in the bulk of the sample.

Samples of polycrystalline SmS were annealed at 780–1100°C for 2–10 h. The diffusion profiles of europium in polycrystalline SmS (Fig. 1b) are complex in character; indeed, the europium concentration near the surface is the same as in single crystals, 10^{19}–10^{21} cm^{-3}, and then decreases smoothly to 10^{16}–10^{17} cm^{-3}, after which the profile flattens out at a depth of more than 500 μm. Studies revealed that in polycrystalline sam-

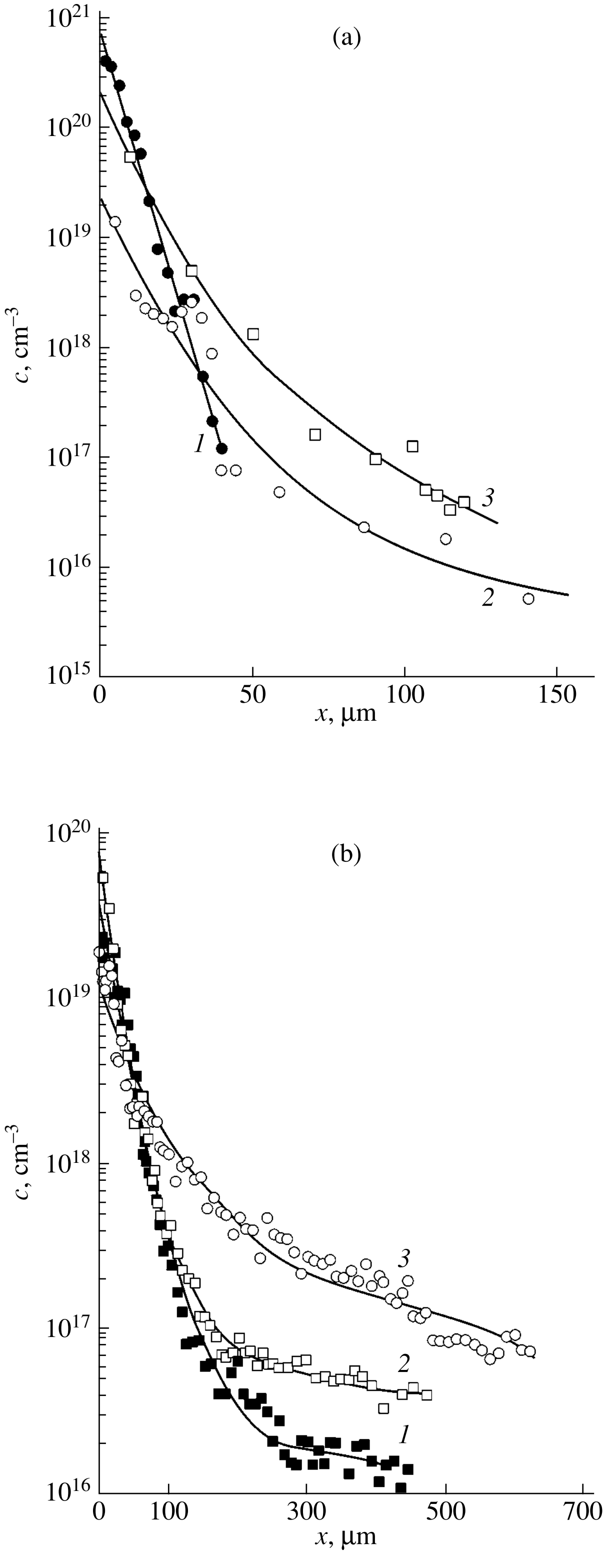

Fig. 1. Europium concentration–depth profiles in samarium sulfide for various temperatures T and annealing times t for (a) single-crystal SmS: (*1*) 950°C and 21 h, (*2*) 1000°C and 10 h, and (*3*) 1050°C and 1 h; and (b) polycrystalline SmS: (*1*) 780°C and 540 min, (*2*) 950°C and 280 min, and (*3*) 1100°C and 140 min.

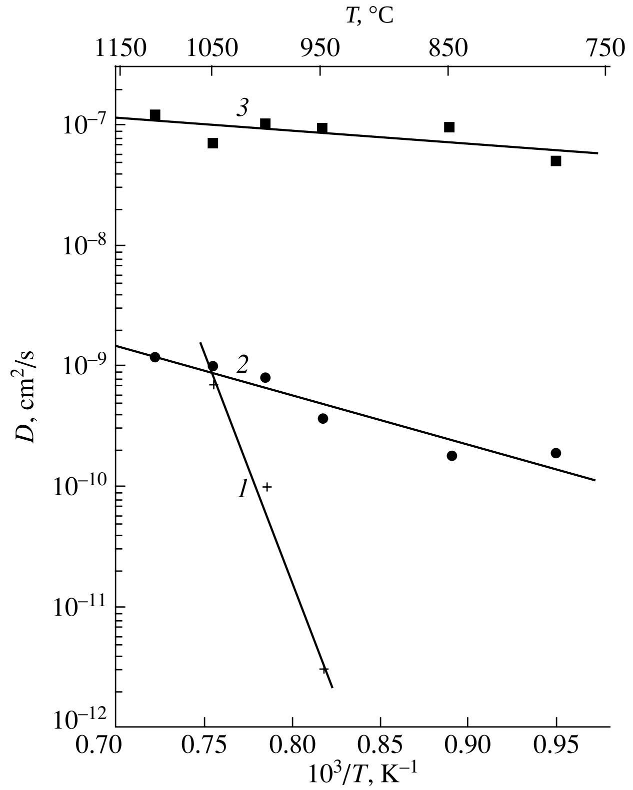

Fig. 2. Diffusion coefficient of europium in samarium sulfide plotted vs. temperature (*1*) for single-crystal SmS and (*2, 3*) for polycrystalline SmS, the slow and fast diffusion components, respectively.

ples europium diffuses considerably faster than in single crystals.

We used the solution to the Fick equation to describe the diffusion processes occurring in SmS samples. The concentration profiles for single-crystal SmS can be satisfactorily fitted by the erfc function. In the temperature region covered, europium diffusion into single-crystal SmS is characterized by a diffusion coefficient $D = 10^{-12}$–10^{-9} cm^2/s. The activation energy is 7.4 eV. The temperature dependence of D (Fig. 2) can be described by the relation $D = 6 \times 10^{19} \exp(-7.4/kT)$ [6].

The concentration–depth profiles of europium in polycrystalline SmS cannot be described by one erfc function. To adequately describe diffusion in these samples, we represented a concentration profile as a sum of two erfc functions corresponding to the fast and slow diffusion components. The diffusion coefficients for the slow component in the temperature region of interest are $D \sim 10^{-10}$–10^{-9} cm^2/s. The activation energy is 0.83 eV, and the temperature dependence of D can be fitted by the expression $D = 1.4 \times 10^{-6} \exp(-0.83/kT)$. We believe that the slow component of diffusion is associated predominantly with impurity diffusion inside the grains.

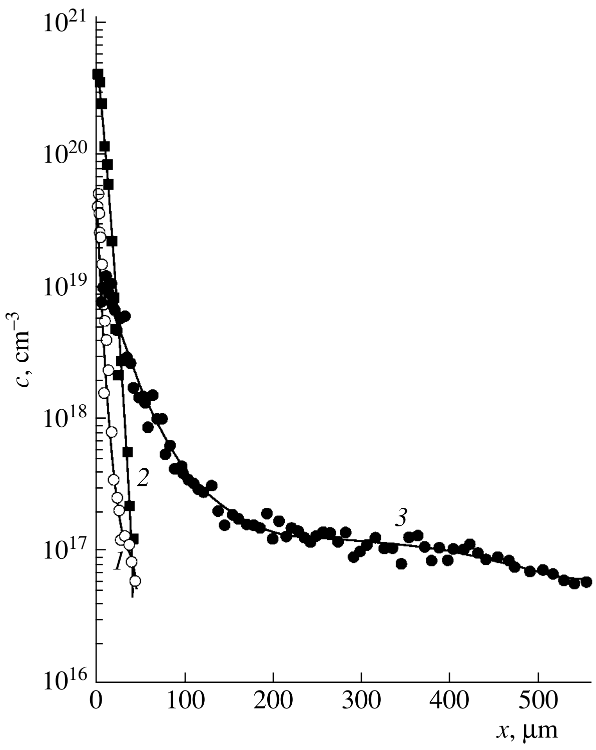

Fig. 3. Europium concentration profile in samarium sulfide plotted against the size of coherent scattering regions for (*1*) single-crystal SmS and (*2*, *3*) polycrystalline SmS. The size of coherent scattering regions is (*2*) 1100 and (*3*) 650 Å.

The values of the diffusion coefficient for the fast component range from $D \simeq 4 \times 10^{-8}$ to 1×10^{-7} cm^2/s. The diffusion coefficient is only weakly dependent on temperature.

The fast diffusion component is most likely associated with impurity migration only over the paths of enhanced diffusion in polycrystals, namely, grain boundaries and pores.

A characteristic feature of polycrystals is the existence of grain boundaries, pores,[1] and other defects, for instance, dislocations, which may be present inside grains (crystallites). In view of this multiplicity of defects, one should have a criterion for characterizing the extent to which a polycrystal is imperfect. We chose for such a criterion the size of the coherent scattering region (CSR) for x-ray radiation. This quantity determines the average size of defect-free single-crystal regions [7]. The dimensions of a CSR range from 10^2 to 10^3 Å, which is one to two orders of magnitude less than the dimensions of pores and crystallites in a polycrystal. Accordingly, the total area of all CSR surfaces exceeds the area of crystallites and pores by several orders of magnitude. Thus, when considering fast diffusion, we may assume that the main contribution to it is from diffusion over CSR surfaces; therefore, its rate should depend primarily on the CSR size.

The validity of this assumption was verified experimentally. Prior to diffusion measurements, the starting polycrystalline SmS samples were annealed at different temperatures and in different regimes (sample 1 at 1700°C and sample 2 at 1200°C). The CSR size as measured using standard x-ray techniques [7] was 1100 Å for sample 1 and 650 Å for sample 2. In both samples, europium diffusion was studied at a temperature of 950°C for 280 min. The concentration profiles obtained are displayed in Fig. 3. Sample 1 shows signs of slow diffusion only, with $D = 5.6 \times 10^{-12}$ cm^2/s. In sample 2, both slow ($D = 5.5 \times 10^{-10}$ cm^2/s) and fast ($D = 4 \times 10^{-8}$ cm^2/s) components of diffusion were observed. We readily see that the smaller the CSR size, the faster the diffusion rate.

This correlation between the values of the CSR size and D suggests that diffusion of europium in polycrystalline SmS is dominated by migration over CSR surfaces. The low diffusion rate and the high activation energy of europium in single-crystal SmS samples lead one to conclude that in this case europium migrates predominantly over crystal lattice sites.

ACKNOWLEDGMENTS

This work was supported by Dial Engineering (St. Petersburg).

REFERENCES

1. V. V. Kaminskiĭ, A. V. Golubkov, and L. N. Vasil'ev, Fiz. Tverd. Tela (St. Petersburg) **44** (8), 1501 (2002) [Phys. Solid State **44** (8), 1574 (2002)].
2. G. Kremer, Usp. Fiz. Nauk **172** (9), 1087 (2002) [Phys. Usp. **45** (9), 965 (2002)].
3. V. P. Zhuze, Ross. Khim. Zh., ZhVKhO Im. D. I. Mendeleeva **XXVI** (6), 695 (1981).
4. V. V. Kaminskiĭ, N. V. Sharenkova, L. N. Vasil'ev, and S. M. Solov'ev, Fiz. Tverd. Tela (St. Petersburg) **47** (2), 217 (2005) [Phys. Solid State **47** (2), 225 (2005)].
5. A. V. Golubkov, E. I. Goncharova, V. P. Zhuze, G. V. Loginov, V. N. Sergeeva, and I. A. Smirnov, *Physical Properties of Rare-Earth Chalcogenides* (Nauka, Leningrad, 1973) [in Russian].
6. V. A. Didik, E. A. Skoryatina, V. P. Usacheva, A. V. Golubkov, and V. V. Kaminskiĭ, Pis'ma Zh. Tekh. Fiz. **30** (9), 18 (2004) [Tech. Phys. Lett. **30** (9), 756 (2004)].
7. S. S. Gorelik, L. N. Rastorguev, and Yu. A. Skakov, *X-ray Radiography and Electron-Optical Analysis* (Metallurgiya, Moscow, 1970) [in Russian].

Translated by G. Skrebtsov

---

[1] The existence of pores in polycrystalline SmS samples is borne out by x-ray diffraction studies of the europium distribution over the sample area. The diffraction patterns reveal a fairly large fraction of impurities built up in pores. The number and area of such clusters decreased with depth.

Physics of the Solid State, Vol. 47, No. 7, 2005, pp. 1236–1244. Translated from Fizika Tverdogo Tela, Vol. 47, No. 7, 2005, pp. 1195–1202.
Original Russian Text Copyright © 2005 by Poklonski, Vyrko, Zabrodskiĭ.

SEMICONDUCTORS AND DIELECTRICS

Fluctuation Model of the High-Frequency Hopping Electrical Conductivity of Moderately Compensated Semiconductors with Hydrogenic Impurities

N. A. Poklonski*, S. A. Vyrko*, and A. G. Zabrodskiĭ**
**Belarussian State University, pr. Skoriny 4, Minsk, 220050 Belarus*
e-mail: poklonski@bsu.by
***Ioffe Physicotechnical Institute, Russian Academy of Sciences, Politekhnicheskaya ul. 26, St. Petersburg, 194021 Russia*

Received October 20, 2004

Abstract—A model is developed according to which a hop of an electron (or hole) between two hydrogenic donors (or acceptors) occurs only when their energy levels become equal due to thermal and/or electrostatic fluctuations in a doped crystal. The main contribution to the real part of the high-frequency hopping electrical conductivity is assumed to come from acceptor pairs in which the time of hole tunneling is equal to the half-period of the external electric field and the phase of tunneling coincides with that of the field. In this case, the imaginary and real parts of the hopping conductivity are approximately equal. The results of calculations based on this model are compared to the experimental data for *p*-Ge : Ga with an intermediate degree of compensation of the main doping impurity. *© 2005 Pleiades Publishing, Inc.*

1. INTRODUCTION

It is experimentally established (see, for example, [1, 2]) that, in the case of electron (hole) hopping between localized states in a doped semiconductor crystal, the frequency dependence of the real part of the high-frequency electrical conductivity follows the law $\mathrm{Re}\,\sigma_h(\omega) \propto \omega^s$ $(0.6 < s < 1)$ in the radio frequency range $(10^2 < \omega/2\pi < 10^7$ Hz).

To date, there is no analytical description of the ac hopping electrical conductivity between the impurity ground states in compensated covalent crystalline semiconductors (see reviews [3–5]). In [6, 7], the parametric frequency and temperature dependences of the hopping electrical conductivity were presented for the case of an extremely low degree of compensation, where electron (hole) hopping occurs only with the absorption or emission of a phonon. The interaction constant of phonons with charge carriers localized on donors (acceptors) acts as a fitting parameter. For example, for an *n*-type semiconductor, it was assumed in [6] that the high-frequency hopping conductivity is due to electron hopping between the ground states of two nearest neighbor donors in charge states (0) and (+1) located in the vicinity of an acceptor in charge state (–1). In [7], the features of the temperature dependence of the high-frequency hopping conductivity of weakly compensated *n*-type crystals were described with regard to the possible electron hopping between two donors via a third (intermediate) donor located in the vicinity of a negatively charged acceptor. It was assumed that one ionized donor is the nearest neighbor of the neutral donor and the energy of the other ionized donor is closest to the energy of the neutral donor. In the models proposed in [3, 6, 7], it was assumed that the impurity band is “classical,” i.e., that the scatter in the energy levels of the main alloying impurity is much greater than the quantum-mechanical broadening of these levels due to the finiteness of the time a charge carrier spends on the impurity. In [8], the temperature dependence of the high-frequency hopping conductivity of amorphous germanium and silicon was described using a model of electron transitions (hops) in pairs of defects with deep levels lying in the band gap. This model takes into account one excited state and the two ground states of the defects of a pair, between which an electron transition occurs through its thermal excitation from one defect to the excited state of the pair and subsequent tunneling to the other defect.

It is important to note that, in the models used in [3–8], the energy of each one-electron state (an impurity level) in doped covalent crystals was assumed to be fixed; i.e., the energy does not change during hopping of an electron (hole) between impurity atoms.

However, when describing small polaron hopping over lattice sites in ionic crystals, Holstein (see reprints of his 1959 article in [9] and also [10–12]) introduced the concept of the “coincidence event” for polaron potential wells. A polaron energy level is a function of the positions of the atoms nearest to it. Due to thermal vibrations of the atoms, their positions vary in time; so the energy of a conduction electron captured by the lattice polarization created by the electron itself also varies in time. At some instant, a situation can arise where the energy of the site with a bound electron becomes equal to the energy of the nearest neighbor free site of the crystalline lattice. This instantaneous coincidence of the energy levels is referred to as the "coincidence event." In the model considered in [9], polaron hopping was assumed to occur when the energies of the initial occupied state and the final free state coincide. In this case, the lattice deformation in the final state is not necessarily the same as that in the initial state. Therefore, in an individual hopping event, the phonon energy is either released or absorbed by the lattice; however, on the average, the polarization energy is not transferred with a moving polaron.

In [13], a model of fluctuation-caused coincidence of the energy levels of localized states (of impurity atoms) was used to describe the dc hopping conductivity of doped semiconductors.[1] It was assumed that temporal fluctuations in the energy of localized states are caused by hopping diffusion of electrons via these states. However, the formulas derived in that study agree only qualitatively with the available experimental data.

In [15, 16], the dc hopping conductivity and thermoelectric power were described in terms of a model in which the majority impurity (acceptors) and a compensating impurity (donors) form a common simple cubic "impurity lattice" in the crystalline matrix. Hopping of holes occurs when the energy levels of acceptors become equal due to thermal fluctuations, whereas donors block the corresponding sites of the lattice of impurity atoms. Let the acceptors be labeled with index α or β. We note that the coincidence of the levels of two closely spaced acceptors can occur due both to the elastic strain of the crystalline lattice near the acceptors created by phonons and to the effect of Coulomb fluctuations arising because of hole hopping between other acceptors. At the instant of coincidence of the levels[2] of a neutral and a negatively charged acceptor, a "resonant" two-site cluster is formed: the hole on an acceptor α becomes bound to a negatively charged acceptor β and belongs simultaneously to these two acceptors. After some time, the resonance conditions are no longer satisfied and the hole can become localized on the acceptor β or again on the acceptor α. After that, the acceptors α and β can again form a resonance cluster or be joined to other resonance clusters (pairs). For the regime of hopping between the nearest neighbor impurity atoms, a quantitative description of the concentration dependence of the activation energy and preexponential factor for the hopping conductivity was given in [15], with application to *p*-Ge : Ga. The results of calculations based on the model developed in [16] agree with available experimental data on the low-temperature hopping thermoelectric power and thermal capacity on the dielectric side of the insulator–metal phase transition.

The aim of this study is to extend the model [15, 16] of fluctuation-caused coincidence of acceptor energy levels in the band gap of a crystal to the high-frequency hopping conductivity in the pair approximation. We analyze the case where the concentrations of acceptors in the (0) and (–1) charge states are approximately equal, i.e., the case of a moderate degree of compensation. We consider relatively low doping levels of *p*-type samples (far from the insulator–metal transition) at temperatures where hole hopping between nearest neighbor acceptors (nearest neighbor hopping, NNH) dominates.

2. HOPPING CURRENT DENSITY AND ELECTRICAL CONDUCTIVITY

Let us consider a *p*-type crystalline semiconductor with a concentration $N = N_0 + N_{-1}$ of hydrogenic acceptors (the indices indicate their charge state) and a concentration $N_{+1} = KN$ of donors in the (+1) charge state, where K is the degree of compensation of acceptors by donors.[3] The electrical neutrality condition is written as $N_{-1} = KN$. We assume that the temperature is sufficiently low for the exchange of holes between acceptors in the (0) and (–1) charge states to occur only by hopping (without involving the states of the valence band and the excited states of the acceptors) and that the doping level is low; so the Bohr radius for a hole localized at an acceptor is much smaller than the average hopping distance.

Let an ac electric field $\mathscr{E} = \mathscr{E}_0\sin(\omega t)$ be applied to a macroscopic three-dimensional semiconductor sample along the x axis ($2\pi/\omega$ is the period of harmonic oscillations, t is time).

The time-dependent probability f_α that an acceptor α is in the (0) charge state satisfies the rate equation [3]

$$\frac{df_\alpha}{dt} = \sum_\beta [f_\beta(1-f_\alpha)\Gamma_{\beta\alpha} - f_\alpha(1-f_\beta)\Gamma_{\alpha\beta}], \qquad (1)$$

where the indices $\alpha, \beta = 1, 2, 3, \ldots$ label all acceptors in the sample and $\Gamma_{\alpha\beta}$ is the probability (per unit time) of hole hopping from acceptor α to acceptor β (hole transition rate).

The ac hopping current density J_h is determined by the time variation of the projection of the electric dipole moment (per unit volume of a crystal with equal num-

---

[1] The model of the fluctuation-induced formation of a barrier through which an atom (or a molecule) can tunnel made it possible to explain the main characteristics of solid-phase cryochemical reactions (see, e.g., [14]).

[2] To within quantum-mechanical broadening of the acceptor levels due to the finite time of hole localization on these levels.

[3] We refer to a compensation degree as moderate if $0.1 < K < 0.9$; these values of K do not belong to the ranges of low ($K \ll 1$) and high ($1 - K \ll 1$) values. At a moderate degree of compensation, the dc hopping conductivity is maximum [17].

bers of ionized acceptors and donors) onto the x axis (cf. [18]):

$$J_h = \frac{e}{2V}\left[\sum_{\alpha} x_{\alpha}\frac{df_{\alpha}}{dt} - \sum_{\beta} x_{\beta}\frac{d(1-f_{\beta})}{dt}\right]. \qquad (2)$$

Here, e is the elementary charge, V is the volume of the sample, and x_{α} is the coordinate of the acceptor α. By substituting Eq. (1) into Eq. (2) and following [3, 19], we obtain

$$\begin{gathered} J_h = \frac{e}{2V}\sum_{\alpha}\sum_{\beta}(x_{\beta}-x_{\alpha}) \\ \times[f_{\alpha}(1-f_{\beta})\Gamma_{\alpha\beta} - f_{\beta}(1-f_{\alpha})\Gamma_{\beta\alpha}], \end{gathered} \qquad (3)$$

where $(x_{\beta}-x_{\alpha}) = r_{\alpha\beta}\cos\theta_{\alpha\beta}$ is the projection of the vector $\mathbf{r}_{\alpha\beta}$ connecting acceptors α and β onto the x axis (parallel to the external electric field) and $\theta_{\alpha\beta}$ is the angle between the vector $\mathbf{r}_{\alpha\beta}$ and the x axis.

We assume that, in an external homogeneous electric field $\mathscr{E} = \mathscr{E}_0\sin(\omega t)$, the frequency of hole hopping between acceptors is

$$\Gamma_{\alpha\beta} = \Gamma_{\alpha\beta}^{(\mathrm{eq})}\exp\left(\frac{e(x_{\beta}-x_{\alpha})\mathscr{E}}{k_{\mathrm{B}}T}\right), \qquad (4)$$

where the superscript (eq) denotes the equilibrium value $\Gamma_{\alpha\beta}^{(\mathrm{eq})}$ (at $\mathscr{E}_0 = 0$) for acceptors α and β separated by a distance $r_{\alpha\beta}$, k_{B} is the Boltzmann constant, and T is temperature.

With regard to Eq. (4), in the case of a weak electric field ($|e(x_{\beta}-x_{\alpha})\mathscr{E}_0| \ll k_{\mathrm{B}}T$), where $f_{\alpha} \approx f_{\alpha}^{(\mathrm{eq})}$, we obtain from Eq. (3) the following expression for the real part of the hopping conductivity (similar to the Titeica relation [20, 21]):[4]

$$\mathrm{Re}\,\sigma_h = \frac{e^2}{Vk_{\mathrm{B}}T}\sum_{\alpha}\sum_{\beta}(x_{\beta}-x_{\alpha})^2 f_{\alpha}^{(\mathrm{eq})}(1-f_{\beta}^{(\mathrm{eq})})\Gamma_{\alpha\beta}^{(\mathrm{eq})}. \quad (5)$$

In what follows, we omit the index (eq) since we consider only equilibrium quantities.

It should be noted that, in Eqs. (1)–(5), we assume that the acceptor coordinates x_{α} and x_{β} are fixed; actually, they are not known and, therefore, formulas of this type cannot be directly applied to quantitative description of the experimental data on hopping electrical transport.

Now, we pass from the discrete description of hopping transport of holes inside pairs of acceptors to a continuous description. To replace summation over α and β in Eq. (5) by integrating with respect to continuous variables r and θ, where $r_{\alpha\beta} \longrightarrow r$ and $\theta_{\alpha\beta} \longrightarrow \theta$, we find the density of the distribution of the distance r between the acceptors in the (0) and (–1) charge states and of the angle θ specifying the orientation of acceptor pairs with respect to the x axis.

In a moderately compensated semiconductor, we can assume that the distribution of charge states of impurity atoms over the sites of the crystalline lattice is random even at rather low temperatures. Then, the probability that there are l acceptors in the (–1) charge state in a volume v does not depend on the shape and location of the volume v and is given by a Poisson distribution [22–25],

$$\mathscr{P}(l, vN_{-1}) = \frac{1}{l!}(vN_{-1})^l\exp(-vN_{-1}), \qquad (6)$$

where $N_{-1} = KN$ is the concentration of ionized acceptors averaged over the crystal.

Let us consider an acceptor in the (0) charge state and choose a spherical system of coordinates with the origin at the acceptor. Between the spheres of radii r and $r + dr$, we choose a ring with radius $r\sin\theta$, width $rd\theta$, and thickness dr. Using Eq. (6) with $l = 1$, we obtain the probability that there is an acceptor in the (–1) charge state in a ring of volume $v = 2\pi\sin\theta r^2 d\theta dr$:

$$P(r, \theta)d\theta dr = 2\pi\sin\theta r^2 KNd\theta dr, \qquad (7)$$

where $0 \le \theta \le \pi$.

We assume that only the pairs of acceptors in the (0) and (–1) charge states contribute to the real part of the high-frequency hopping conductivity. The distance R_{ω} between the acceptors of a pair should be such that the duration of hole tunneling between them is equal to the half-period of harmonic oscillations of the external electric field, since hole transitions with both smaller and greater times do not contribute to $\mathrm{Re}\,\sigma_h(\omega)$. This means that it is necessary to multiply the density $P(r, \theta)$ of the distribution of pair distances by the dimensionless delta function $\delta(1 - r/R_{\omega})$, which satisfies the relation $\int_0^{\infty}\delta(1 - r/R_{\omega})dr = R_{\omega}$. Therefore, the probability that (for an arbitrary pair) the acceptors are in the volume $2\pi\sin\theta r^2 d\theta dr$ and the distance $r = R_{\omega}$ between them lies in the range $(r, r + dr)$ is equal to $P(r, \theta)\delta(1 - r/R_{\omega})drd\theta$, where the density of the distribution of the angle θ between the x axis and a vector of length R_{ω} uniformly distributed over the sphere is $(1/2)\sin\theta$ [22, 25]. Thus, the probability that there is an acceptor at a distance $r = R_{\omega}$ from a given acceptor in the interval $(r, r + dr)$ in the solid angle $2\pi\sin\theta d\theta$ is

$$\frac{1}{2}\sin\theta P(r, \theta)\delta\left(1 - \frac{r}{R_{\omega}}\right)d\theta dr, \qquad (8)$$

where $P(r, \theta)$ is given by formula (7).

According to the above arguments, we make the substitutions $f_{\alpha} \longrightarrow (1 - K)$, $(1 - f_{\beta}) \longrightarrow K$, $(x_{\beta} - x_{\alpha}) \longrightarrow r\cos\theta$, and $\Gamma_{\alpha\beta}(r_{\alpha\beta}) \longrightarrow \Gamma_h(r)$ in Eq. (5) and pass from

---

[4] Harmonic oscillations of the hopping current density J_h shifted in time with respect to the oscillations of the electric field $\mathscr{E}$ are determined by the imaginary part of the electrical conductivity σ_h.

the summation over β to integration over the volume V of the crystal. The remaining sum over α contains $(1 - K)NV$ identical nonzero terms, where $(1 - K)NV$ is the number of acceptors in the (0) charge state. Therefore, from Eqs. (5) and (8) in the pair approximation, the real part of the high-frequency hopping conductivity can be found to be

$$\begin{aligned}\operatorname{Re}\sigma_h(\omega) &= \frac{e^2K(1-K)^2N}{k_\mathrm{B}T}\int_0^\pi \frac{\sin\theta}{2}\int_0^\infty 2\pi\sin\theta r^2 KN \\ &\times \delta\left(1-\frac{r}{R_\omega}\right)(r\cos\theta)^2\Gamma_h(r)drd\theta \qquad (9)\\ &= \frac{\pi^2e^2N_h^2R_\omega^5\Gamma_h(R_\omega)}{4k_\mathrm{B}T},\end{aligned}$$

where $N_h = N_0N_{-1}/N = K(1 - K)N$ is the effective concentration of acceptors involved in hopping conduction and $\Gamma_h(R_\omega)$ is the frequency of hole hopping between the acceptors in the (0) and (–1) charge states, which will be found below.

3. FREQUENCY OF HOLE HOPPING BETWEEN ACCEPTORS

We consider the case of a Gaussian (normal) density $g_a(E_a - \bar{E}_a)$ of the distribution of acceptor energy levels E_a with respect to the average value $\bar{E}_a$. Let $f_0(E_a)$ be the probability that an acceptor with energy level E_a is in the (0) charge state. By averaging over energy,[5] we find the probability that an arbitrary acceptor in the semiconductor is neutral:

$$\begin{aligned}\bar{f}_0 &= \int_{-\infty}^{+\infty} f_0 g_a d(E_a-\bar{E}_a) \\ &= \frac{1}{\sqrt{2\pi}\gamma}\int_{-\infty}^{+\infty}\frac{\exp(-u^2/2\gamma^2)}{1+\exp(-\zeta-u)}du,\end{aligned} \qquad (10)$$

where $g_a = (\sqrt{2\pi}W)^{-1}\exp[-(E_a - \bar{E}_a)^2/2W^2]$ is the density of the distribution of acceptor energy levels in the band gap; W is the effective width of the acceptor band; $(1 - f_0) = f_{-1} = \{1 + \beta_a\exp[(E_a + E_\mathrm{F})/k_\mathrm{B}T]\}^{-1}$ is the probability that the acceptor with an energy level $E_a > 0$ is ionized; β_a is the energy level degeneracy; $E_\mathrm{F} < 0$ is the position of the Fermi level in the band gap measured from the top of the valence band; $\bar{E}_a > 0$ is the center of the acceptor band; and $u = (E_a - \bar{E}_a)/k_\mathrm{B}T$, $\zeta = (E_\mathrm{F} + \bar{E}_a + k_\mathrm{B}T\ln\beta_a)/k_\mathrm{B}T$, and $\gamma = W/k_\mathrm{B}T$ are dimensionless parameters.

The width of the classical acceptor band W is mainly determined by the Coulomb interaction of only the nearest neighbor charges (ionized acceptors and donors) and, according to [26], is equal to[6]

$$W = \left(\int_0^\infty U^2P(r)dr\right)^{1/2} \approx 1.64\frac{e^2}{4\pi\varepsilon}\left(\frac{8\pi}{3}KN\right)^{1/3}, \qquad (11)$$

where $|U| = e^2/4\pi\varepsilon r$ is the modulus of the Coulomb interaction energy of two ions; $\varepsilon = \varepsilon_r\varepsilon_0$ is the static permittivity of the crystalline lattice; ε_0 is the permittivity of free space; $P(r)dr = 4\pi r^2(N_{-1} + N_{+1})\exp[-(4\pi/3)r^3(N_{-1} + N_{+1})]dr$ is, according to Eqs. (6) and (7), the probability that the impurity ion nearest to an acceptor in the (–1) charge state is located at a distance lying in the interval $(r, r + dr)$; and $N_{-1} + N_{+1} = 2KN$ is the total concentration of ionized acceptors and donors.

Thus, according to Eq. (10), the concentrations of neutral and ionized acceptors averaged over the crystal (without regard for the excited states) are

$$N_0 = N\bar{f}_0 = N(1-K), \quad N_{-1} = N(1-\bar{f}_0) = KN.$$

From the electrical neutrality condition $\bar{f}_{-1} = 1 - \bar{f}_0 = K$, with regard to Eq. (11), we can find the dependence of the Fermi level E_F on the temperature T, compensation degree K, and acceptor concentration $N = N_0 + N_{-1}$.

Due to thermal (absorption or emission of phonons) and Coulomb (hole hopping between acceptors) fluctuations, the positions of acceptor energy levels with respect to the top of the valence band of the semiconductor change in time. Following [13, 15], we assume that hopping of a hole between two acceptors in the (0) and (–1) charge states can occur only if the energy levels of these acceptors coincide.[7]

The number of transitions of a hole between acceptors in the (0) and (–1) charge states per event of fluctuation-caused coincidence of their levels $E_{a1} = \bar{E}_a + u_1k_\mathrm{B}T$ and $E_{a2} = \bar{E}_a + u_2k_\mathrm{B}T$ is equal to the integral part of the ratio of the duration $t_i(u)$ of one coincidence event of the two levels $(u_1 = u_2 = u)$ to the tunneling time $\tau(u, r)$. We assume that, during a time interval t, the total duration of all events where the levels of two acceptors coincide is $t_c(u) = \sum_i t_i(u)$. The probability that, during the period of time over which the acceptor levels separated by a distance r remain coincident, $j =$

---

[5] In the case of an intermediate degree of compensation, the correlation between the acceptor positions at the sites of the crystalline lattice and their energies can be disregarded.

[6] We consider samples on the insulator side of the insulator–metal phase transition.

[7] Due to hole hopping, the (–1) charge states of immobile acceptors migrate over the crystal.

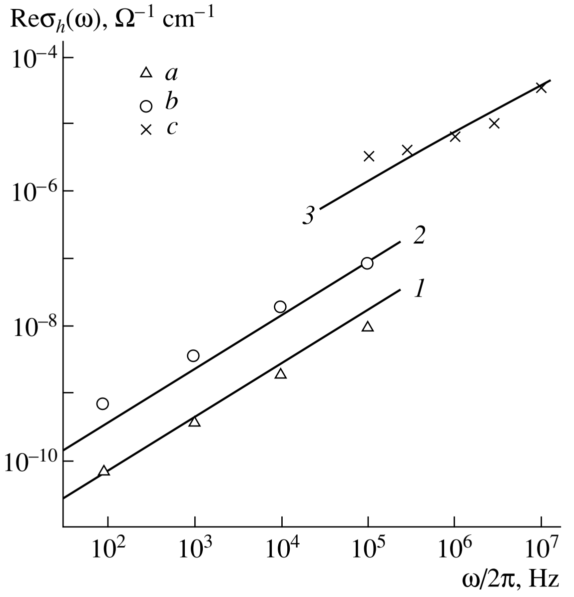

Fig. 1. Frequency dependence of the hopping conductivity. Points are experimental data for *p*-Ge : Ga at K = 0.4: (*a*) T = 4 K, N = 3.2 × 10^{14} cm^{-3} [34]; (*b*) T = 4 K, N = 7.8 × 10^{14} cm^{-3} [34]; and (*c*) T = 2.3 K, N = 3.4 × 10^{15} cm^{-3} [35]. Curves *1*–*3* are calculated using Eq. (21) for data (*a*–*c*), respectively.

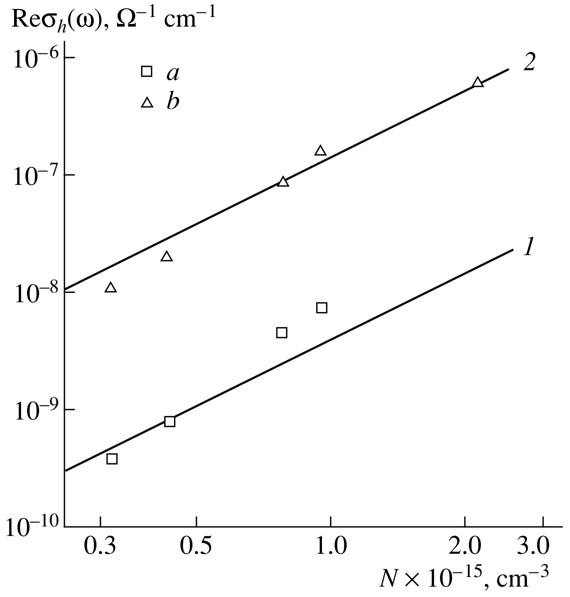

Fig. 2. Gallium concentration dependence of the real part of the hopping conductivity of germanium crystals at K = 0.4 and T = 3.3 K. Points are the experimental data from [34]: (*a*) $\omega/2\pi$ = 10^3 Hz and (*b*) $\omega/2\pi$ = 10^5 Hz. Curves *1* and *2* are calculated using Eq. (21) for data (*a*, *b*), respectively.

0, 1, 2, ... hole transitions occur can be approximated by a Poisson distribution [22–25, 27],

$$\mathcal{P}(j) = \frac{[t_c(u)/\tau(u, r)]^j}{j!}\exp\left[-\frac{t_c(u)}{\tau(u, r)}\right], \qquad (12)$$

where $t_c(u)/\tau(u, r) = \sum_{j=0}^{\infty} j\mathcal{P}(j)$ is the average number of transitions of a hole between the nearest neighbor acceptors. The frequency of hole hopping between two acceptors in the (0) and (–1) charge states in the case where their energy levels remains coincident ($E_{a1} = E_{a2} = E_\tau$) over time t is [15]

$$\Gamma(u, r) = \frac{1}{t}\sum_{j=0}^{\infty} j\mathcal{P}(j) = \frac{t_c(u)}{t\tau(u, r)}. \qquad (13)$$

From the Markov chain theory [22, 27], it follows that, if the hole transitions between two acceptors are observed over a long time interval ($t \gg \tau(u, r)$), then the fraction of time $t_c(u)/t$ spent by the acceptors in one of two possible states (where their energy levels are coincident and noncoincident, respectively) is approximately equal to the stationary probability $\mathcal{P}(u, \zeta)$ of the acceptors being in these states. Therefore, the ratio $t_c(u)/t$ is approximately equal to the probability that the energy levels of the two acceptors in the (0) and (–1) charge states coincide [15]:

$$\frac{t_c(u)}{t} \approx \mathcal{P}(u, \zeta) = \frac{f_0(u, \zeta) f_{-1}(u, \zeta)}{K(1-K)}. \qquad (14)$$

Here, $f_0(u, \zeta) = [1 + \exp(-\zeta - u)]^{-1}$ is the probability that one of the acceptors of a pair with an energy level $E_\tau = \bar{E}_a + uk_BT$ is occupied by a hole; $f_{-1}(u, \zeta) = [1 + \exp(u + \zeta)]^{-1}$ is the probability that the other acceptor of the pair with the same energy level E_τ is in the (–1) charge state, i.e., is ionized; $\bar{f}_0 = (1 - K)$; and $\bar{f}_{-1} = K$ (see formula (10)).

By analogy with the theory of a molecular hydrogen ion (H_2^+), the hole tunneling time between two acceptors in the (0) and (–1) charge states at a distance r from each other in the case where their energy levels are randomly coincident ($u_1 = u_2 = u$) can be estimated as [15, 28, 29]

$$\tau(u, r) = \frac{\pi\hbar}{\delta E_\tau(r)}, \qquad (15)$$

where $\delta E_\tau(r)$ is the energy splitting (broadening) of the hole inter-acceptor tunneling level $E_\tau = \bar{E}_a + uk_BT$ measured from the top of the valence band of the undoped crystal and $a_\tau = e^2/(8\pi\varepsilon E_\tau)$ is the Bohr radius for a hole localized on an acceptor.

Using the quasi-classical approximation and disregarding the acceptor excited states, in the case of $\delta E_\tau(r) \ll E_\tau$, we find [29, 30]

$$\delta E_\tau(r) = 4E_\tau \times \frac{\rho(1+\rho)\exp(-\rho) - [1-(1+\rho)\exp(-2\rho)]S}{\rho(1-S^2)}, \quad (16)$$

where $\rho = r/a_\tau$ and $S = [1 + \rho + (\rho^2/3)]\exp(-\rho)$.

Let us average $\Gamma(u, r)$ over the distribution $g_a = g_a(u, \gamma)$ of tunneling energy levels $u = (E_\tau - \bar{E}_a)/k_BT$ in the acceptor band of width $\gamma = W/k_BT$. Using Eqs. (13)–(15) and (10), the average frequency $\Gamma_h(r)$ of hole hopping between two acceptors separated by a distance r can be written as

$$\Gamma_h(r) = \int_{-\infty}^{+\infty} \Gamma(u, r) g_a(u, \gamma)du = \int_{-\infty}^{+\infty} \frac{\mathcal{P}(u, \zeta) g_a(u, \gamma)}{\tau(u, r)} du, \quad (17)$$

where $g_a(u, \gamma) = (\sqrt{2\pi}\gamma)^{-1}\exp(-u^2/2\gamma^2)$.

It follows from Eqs. (15) and (16) that the tunneling time $\tau(u, r)$ increases monotonically as the tunneling level E_τ is displaced into the band gap of the crystal, i.e., with increasing u. If the temperature is sufficiently low, so that $W \gg k_BT$, then the function $\mathcal{P}(u, \zeta)g_a(u, \gamma)$ has a narrow peak[8] at $u = -\zeta$. Therefore, in Eq. (17), we can take the monotonic function $\tau(u, r)$ (at $u = -\zeta$) out of the integral. In this case, the average equilibrium frequency of hole hopping between the acceptors at a distance r is [15]

$$\Gamma_h(r) \approx \frac{1}{\tau_h(r)\xi_h}, \quad (18)$$

where $\tau_h(r) \equiv \tau_h(u = -\zeta, r)$ is the time of hole tunneling between the acceptors in the (0) and (–1) charge states with equal energy levels $E_\tau = \bar{E}_a - \zeta k_BT$ (coinciding to within $\delta E_\tau \ll E_\tau$). With allowance for Eqs. (10) and (14), the dimensionless parameter ξ_h is defined by the relation [31]

$$\frac{1}{\xi_h} = \frac{1}{K(1-K)}\frac{1}{\sqrt{2\pi}} \times \int_{-\infty}^{+\infty} \frac{\exp(-u^2/2)\exp(\zeta+\gamma u)}{[1+\exp(\zeta+\gamma u)]^2} du. \quad (19)$$

For the case where the acceptor band is narrow as compared to the thermal excitation energy ($\gamma = W/k_BT \ll 1$) or is wide ($\gamma = W/k_BT \gg 1$), formulas (10) and (19) for ζ and ξ_h can be simplified:

(i) for $\gamma \ll 1$, we have $\zeta \approx -\ln[K/(1-K)]$, $\xi_h \approx 1$;

(ii) for $\gamma \gg 1$, we have

$$K = 1 - \bar{f}_0 \approx \frac{1}{2}\left[1 - \operatorname{erf}\left(\frac{\zeta}{\gamma\sqrt{2}}\right)\right], \quad \xi_h \approx \gamma K(1-K)\sqrt{2\pi}\exp\left[\frac{1}{2}\left(\frac{\zeta}{\gamma}\right)^2\right], \quad (20)$$

where ζ/γ is the ratio of the energy corresponding to the Fermi level position to the acceptor band width.

4. REAL PART OF THE AC HOPPING CONDUCTIVITY

We assume that only the pairs of acceptors in which the hole tunneling time $\tau_h(r = R_\omega)$ is equal to the half-period π/ω of the external electric field contribute to the real part of the ac conductivity;[9] i.e., $\tau_h(R_\omega) = \pi/\omega$. In this case, $\Gamma_h(R_\omega) = \omega/(2\pi\xi_h)$ and, from Eqs. (9) and (18), the real part of the high-frequency hopping conductivity $\mathrm{Re}\,\sigma_h(\omega)$ can be found to be

$$\mathrm{Re}\,\sigma_h(\omega) = \frac{\pi e^2 N_h^2 R_\omega^5}{8k_BT\xi_h}\omega, \quad (21)$$

where $R_\omega = \rho_\omega a_\tau$ is the distance of hole hopping between the acceptors of a pair, $a_\tau = e^2/[8\pi\varepsilon(\bar{E}_a - \zeta k_BT)]$ is the Bohr radius, and ρ_ω is the solution to the equation

---

[8] In the case of a narrow impurity band ($W \ll k_BT$), the function $g_a(u, \gamma)\,\mathcal{P}(u, \zeta)$ has a maximum at $u = 0$ and the tunneling energy level for holes is $E_\tau \approx \bar{E}_a$.

[9] In this approximation, the imaginary part of the hopping ac electrical conductivity is equal to its real part.

$$\frac{4(\bar{E}_a - \zeta k_{\mathrm{B}}T)}{\pi\hbar}\,\frac{\rho_\omega(1+\rho_\omega)\exp(-\rho_\omega) - [1-(1+\rho_\omega)\exp(-2\rho_\omega)]S_\omega}{\rho_\omega(1-S_\omega^2)} = \frac{\omega}{\pi} \tag{22}$$

with $S_\omega = [1 + \rho_\omega + (\rho_\omega^2/3)]\exp(-\rho_\omega)$. The quantities $\zeta k_{\mathrm{B}}T = E_F + \bar{E}_a + k_{\mathrm{B}}T\ln\beta_a$ and $\xi_h \geq 1$ are found from Eqs. (10) and (19). The values of ζ and ξ_h for a narrow and wide acceptor band are given by relations (20)[10] and $N_h = K(1 - K)N$.

From Eq. (22), we see that R_ω depends on the angular frequency ω, the energy position of the center of the acceptor band $\bar{E}_a$, the Fermi level position E_{F} (with respect to the top of the valence band), and temperature. The quantity R_ω depends on the acceptor concentration N and compensation degree K via $\bar{E}_a$ and E_{F}. We estimate the effect of R_ω on the $\mathrm{Re}\,\sigma_h(\omega)$ dependence in the frequency range $10^2 < \omega/2\pi < 10^7$ Hz at $K \approx 0.5$ and low temperatures ($\bar{E}_a \gg |\zeta|k_{\mathrm{B}}T$) for gallium-doped germanium crystals ($N = 10^{15}$ cm^{-3}, $\bar{E}_a = 10$ meV, $\varepsilon_r = 15.4$). Under these conditions, from Eq. (22), we obtain the approximation $R_\omega = 155 - 11.3\log(\omega/2\pi)$, where R_ω is measured in nanometers and $\omega/2\pi$ in hertz. Thus, from Eq. (21), we have $\mathrm{Re}\,\sigma_h(\omega) \propto R_\omega^5\omega \propto \omega^s$, where the value $s \approx 0.76$ is close to the experimental values (Fig. 1).

In Eq. (22), the energy $\bar{E}_a$ of thermal ionization of a neutral hydrogenic acceptor (disregarding the shift and fluctuations of the top energy of the valence band) averaged over the crystal can be found to be [26]

$$\bar{E}_a = I_a - \frac{3e^2}{16\pi\varepsilon(\Lambda_s + d)}, \tag{23}$$

where I_a is the ionization energy of an isolated acceptor, $d = 0.554[(1 + K)N]^{-1/3}$ is the average distance between the impurity atoms, and Λ_s is the length (radius) of electrostatic screening of the Coulomb potential by holes migrating over the acceptors. According to [31], the screening (Debye–Hückel) length

$$\Lambda_s = \sqrt{\frac{\varepsilon k_{\mathrm{B}}T\xi_h}{e^2N_h}} \tag{24}$$

is determined by holes with concentration $N_h = K(1 - K)N$ hopping in the acceptor band. We note that the ratio of the diffusion coefficient to the hopping dc drift mobility of holes exceeds the classical value $k_{\mathrm{B}}T/e$ of this ratio by a factor of $\xi_h \geq 1$.

The shift of the center of the acceptor band $\bar{E}_a > 0$ towards the top of the valence band described by Eq. (23) is determined by the decrease in the hole affinity of an ionized acceptor due to static screening of impurity ions by holes hopping over the acceptors [26]. At high temperatures ($k_{\mathrm{B}}T \gg W$), by substituting Eq. (20) into Eq. (24), we find the screening length [32, 33] $\Lambda_s = [\varepsilon k_{\mathrm{B}}T/e^2N_h]^{1/2}$. At low temperatures ($k_{\mathrm{B}}T \ll W$), we find [31] $\Lambda_s = [\varepsilon W\sqrt{2\pi}/(e^2N)]^{1/2}\exp(\zeta^2/4\gamma^2)$, where the ratio ζ/γ is determined from the equation $2K = 1 - \mathrm{erf}(\zeta/\gamma\sqrt{2})$.

Thus, by finding from Eq. (22) the average distance R_ω between the acceptors involved in hopping conduction at a frequency $\omega/2\pi$, we can calculate $\mathrm{Re}\,\sigma_h(\omega)$ from Eq. (21) using Eqs. (10), (11), (19), (23), and (24).

We note that, from Eqs. (21) and (22), it follows that $\mathrm{Re}\,\sigma_h(\omega)|_{\omega \to 0} \longrightarrow 0$; i.e., $\mathrm{Re}\,\sigma_h(\omega)$ is the difference between the real part of the ac hopping conductivity and the dc hopping conductivity.

5. COMPARISON OF THE CALCULATIONS WITH EXPERIMENTAL DATA

In [34, 35], experimental data on the hopping conductivity of gallium-doped *p*-Ge crystals ($K = 0.4$) obtained by neutron irradiation were reported for various temperatures and electric field frequencies.[11] With the results of this study, we try to describe those data quantitatively without any fitting parameters.

Figure 1 compares the results of simulation of the frequency dependence of the ac hopping conductivity $\mathrm{Re}\,\sigma_h(\omega)$, using Eqs. (21) and (22)–(24), with experimental data from [34, 35]. The following parameter values were used in the calculations for *p*-Ge : Ga: $\varepsilon_r = \varepsilon/\varepsilon_0 = 15.4$, $I_a = 11.32$ meV, and $\beta_a = 4$. From Fig. 1, we see that, on the whole, the results of the simulation based on our model of the high-frequency hopping conductivity agree with the experimental data from [34, 35] over a wide range of electric field frequencies.

The experimental [34] and calculated dependences of $\mathrm{Re}\,\sigma_h(\omega)$ on the concentration N of Ga atoms in *p*-Ge : Ga crystals at $K = 0.4$ are shown in Fig. 2 for $\omega/2\pi = 10^3$ and 10^5 Hz; the agreement is seen to be quite satisfactory.

Figure 3 shows the experimental temperature dependences of the ac hopping conductivity of *p*-Ge : Ga at

---

[10] According to Eqs. (20) and (11), the quantity $k_{\mathrm{B}}T\xi_h$ for a wide acceptor band ($W \gg k_{\mathrm{B}}T$) is determined only by the acceptor concentration and the compensation degree.

[11] It has been subsequently shown [36] that the degree of compensation of germanium with natural isotope composition changes in the range from $K = 0.3$ to 0.6, depending on the energy of the reactor neutrons. In particular, the value $K = 0.35$ corresponds to the samples studied in [35].

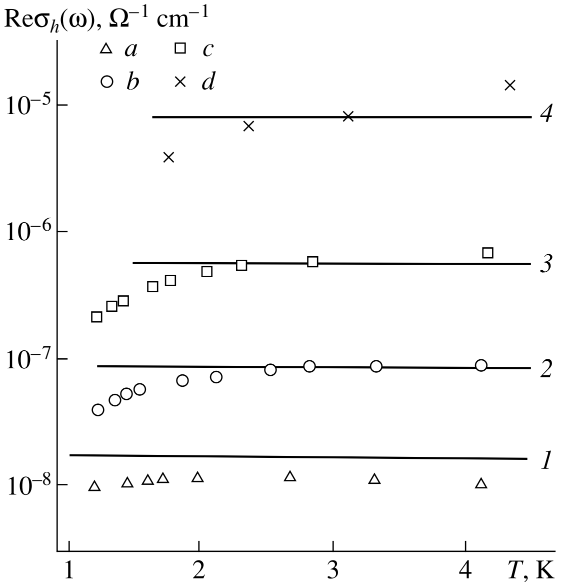

Fig. 3. Temperature dependence of the high-frequency hopping conductivity in neutron transmutation-doped germanium crystals. Points (*a*–*c*) are the experimental data for *p*-Ge : Ga ($K = 0.4$, $\omega/2\pi = 10^5$ Hz) [34]: (*a*) $N = 3.2 \times 10^{14}$, (*b*) 7.8×10^{14}, and (*c*) 2.14×10^{15} cm^{-3}; (*d*) $K = 0.4$, $\omega/2\pi = 10^6$ Hz, $N = 3.4 \times 10^{15}$ cm^{-3} [35]. Curves *1*–*4* are calculated using Eq. (21) for data (*a*–*d*), respectively.

frequencies $\omega/2\pi = 10^5$ and 10^6 Hz [34, 35]. Calculations of the high-frequency hopping conductivity (Figs. 1–3) were performed in the range between the low-temperature (T_l) and high-temperature (T_h) boundaries of the region of the dc NNH conduction regime.[12] The experimental data for T_l and T_h for *p*-Ge : Ga in the range $2 \times 10^{14} < N < 2 \times 10^{16}$ cm^{-3} and $K = 0.3$ [37, 38] can be approximated by the expressions $T_l \approx 2.67 \times 10^{-4} N^{0.244}$ and $T_h \approx 7.6 \times 10^{-4} N^{0.258}$, where T_l and T_h are measured in kelvins and N in cm^{-3}. We see that, according to the calculations based on our model, $\mathrm{Re}\sigma_h(\omega)$ is virtually independent of temperature both at $T \approx T_l$ and at $T \approx T_h$. However, the experiment shows a tendency toward a decrease in the high-frequency hopping conductivity at $T < T_l$.

In the case of a wide acceptor band ($W \gg k_B T$), the decrease in $\mathrm{Re}\sigma_h(\omega)$ at $T < T_l$ even for an intermediate compensation degree ($K \approx 0.5$) is probably caused by the correlation between the spatial distribution of acceptors and their energies (the variable range hopping regime). This correlation implies that the averaging over the distance between acceptors and over the distribution of their energy levels cannot be performed separately [see Eqs. (9), (17)].

For a narrow acceptor band ($W \ll k_B T$), formula (21) predicts that the high-frequency hopping conductivity of a compensated semiconductor should decrease with increasing temperature, since in this case the effect of an ac electric field of constant amplitude on the hole hopping frequency becomes weaker (see the derivation of formula (5)). Although this effect is weak, it can be observed for very lightly doped samples at relatively high temperatures. We note that, when calculating $\mathrm{Re}\sigma_h$ at temperatures $T \approx T_h$ (i.e., in the region of saturation of the dc hopping conductivity [37, 38]), it is probably necessary to take into account the excited states of the acceptors [39]. It is also possible that, even for semiconductors with an intermediate compensation degree, where the doping level approaches the isolator–metal transition, it is necessary to take into account the contribution from the acceptor A^+ band [40, 41] formed by acceptors in the (+1) charge states to the high-frequency conductivity.

6. CONCLUSIONS

To describe the high-frequency hopping conductivity of doped covalent crystalline semiconductors with moderate compensation degree, we have suggested a model of hole (or electron) hopping inside pairs of hydrogenic acceptors (or donors) with a random distribution of charge states. We have described the distribution of acceptor energy levels in the band gap as a Gaussian function and assumed that the width of the acceptor band is entirely determined by the Coulomb interaction of the nearest neighbor ionized acceptors and donors with a random (Poisson) distribution in the crystal. The idea behind the proposed model is that only the pairs of acceptors in the (0) and (–1) charge states with coincident energy levels give the main contribution to the ac hopping conductivity $\mathrm{Re}\sigma_h(\omega)$. Within the framework of equilibrium thermodynamics, we have determined the probability of coincidence of the energy levels of two acceptors under the action of thermal and/or Coulomb fluctuations of hopping nature. An important result for calculations is that the optimum acceptor pairs appear to be located at such a distance that the time of hole tunneling between them is equal to the half-period of oscillations of the external electric field. We have calculated the time of hole tunneling between acceptors using the model of an ionized hydrogen molecule (H_2^+); i.e., we have assumed that hole hopping occurs only if the levels of two hydrogenic acceptors coincide. Analytical expressions have been obtained that describe the relation between the frequency of hole hopping in acceptor pairs, the acceptor concentration, and the compensation degree. The calculations of $\mathrm{Re}\sigma_h(\omega)$ agree with the experimental data for the transmutation-doped *p*-Ge : Ga crystals.

---

[12] As the temperature decreases (at $T < T_l$), the NNH regime is transformed into the hole variable range hopping regime. At $T = T_h$, the hopping conductivity in the NNH regime is equal to the band electrical conductivity of holes in the valence band.

ACKNOWLEDGMENTS

This study was supported by the Belarussian Republican Foundation for Basic Research (grant no. F01-199), the Russian Foundation for Basic Research (project no. 04-02-16587), and a grant from the president of the Russian Federation (project NSh-2223.2003.02).

REFERENCES

1. N. F. Mott and E. A. Davis, *Electronic Processes in Non-Crystalline Materials* (Clarendon, Oxford, 1971; Mir, Moscow, 1982).
2. J. C. Dyre and T. B. Schrøder, Rev. Mod. Phys. **72** (3), 873 (2000).
3. I. P. Zvyagin, *Kinetic Phenomena in Disordered Semiconductors* (Mosk. Gos. Univ., Moscow, 1984) [in Russian].
4. J. C. Dyre and T. B. Schrøder, Phys. Status Solidi B **230** (1), 5 (2002).
5. M. Pollak, Phys. Status Solidi B **230** (1), 295 (2002).
6. S. D. Baranovskiĭ and A. A. Uzakov, Fiz. Tekh. Poluprovodn. (Leningrad) **15** (5), 931 (1981) [Sov. Phys. Semicond. **15** (5), 533 (1981)].
7. B. V. Klimkovich, N. A. Poklonski, and V. F. Stelmakh, Phys. Status Solidi B **134** (2), 763 (1986).
8. B. V. Klimkovich, N. A. Poklonskiĭ, and V. F. Stel'makh, Fiz. Tekh. Poluprovodn. (Leningrad) **19** (5), 848 (1985) [Sov. Phys. Semicond. **19** (5), 522 (1985)].
9. T. Holstein, Ann. Phys. **281** (1-2), 706 (2000).
10. R. R. Heikes, in *Thermoelectricity: Science and Engineering* (Interscience Publishers, New York, 1961), Chap. 4.
11. *Polarons*, Ed. by Yu. A. Firsov (Nauka, Moscow, 1975) [in Russian].
12. P. Nagels, in *Amorphous Semiconductors*, Ed. by M. H. Brodsky (Springer, New York, 1979; Mir, Moscow, 1982), p. 177.
13. A. L. Burin and L. A. Maksimov, Zh. Éksp. Teor. Fiz. **95** (4), 1345 (1989) [Sov. Phys. JETP **68** (4), 776 (1989)].
14. V. I. Gol'danskiĭ, L. I. Trakhtenberg, and V. N. Flerov, *Tunneling Phenomena in Chemical Physics* (Nauka, Moscow, 1986) [in Russian].
15. N. A. Poklonskiĭ, S. Yu. Lopatin, and A. G. Zabrodskiĭ, Fiz. Tverd. Tela (St. Petersburg) **42** (3), 432 (2000) [Phys. Solid State **42** (3), 441 (2000)].
16. N. A. Poklonski and S. Yu. Lopatin, Fiz. Tverd. Tela (St. Petersburg) **43** (12), 2126 (2001) [Phys. Solid State **43** (12), 2219 (2001)].
17. H. Fritzsche and M. Cuevas, in *Proceedings of International Conference on Semicond. Phys. Pub. Czech. Acad. Sci., Prague, 1961*, p. 222.
18. B. Sandow, O. Bleibaum, and W. Schirmacher, Phys. Status Solidi C **1** (1), 92 (2004).
19. A. Miller and E. Abrahams, Phys. Rev. **120** (3), 745 (1960).
20. S. Titeica, Ann. Phys. (Leipzig) **22** (2), 129 (1935).
21. P. S. Zyryanov and M. I. Klinger, *Quantum Theory of Electron Transport Phenomena in Crystalline Semiconductors* (Nauka, Moscow, 1976) [in Russian].
22. P. Whittle, *Probability* (Wiley, New York, 1976; Nauka, Moscow, 1982).
23. D. K. Pickard, J. Appl. Probab. **19** (2), 444 (1982).
24. C. V. Heer, *Statistical Mechanics, Kinetic Theory, and Stochastic Processes* (Academic, New York, 1972; Mir, Moscow, 1976).
25. M. G. Kendall and P. A. Moran, *Geometric Probability* (Hafner, New York, 1963; Nauka, Moscow, 1972).
26. N. A. Poklonski, A. I. Syaglo, and G. Biskupski, Fiz. Tekh. Poluprovodn. (St. Petersburg) **33** (4), 415 (1999) [Semiconductors **33** (4), 402 (1999)].
27. D. R. Cox and W. L. Smith, *Queues* (London, 1961; Mir, Moscow, 1966).
28. E. O. Kane, in *Tunneling Phenomena in Solids*, Ed. by E. Burstein and S. Lundqvist (Plenum, New York, 1967; Mir, Moscow, 1973).
29. L. A. Blumenfel'd and A. K. Kukushkin, *Course of Quantum Chemistry and Structure of Molecules* (Mos. Gos. Univ., Moscow, 1986) [in Russian].
30. A. S. Davydov, *Quantum Mechanics*, 2nd ed. (Nauka, Moscow, 1973; Pergamon, Oxford, 1976).
31. N. A. Poklonski and V. F. Stelmakh, Phys. Status Solidi B **117** (1), 93 (1983).
32. N. A. Poklonski, V. F. Stelmakh, V. D. Tkachev, and S. V. Voitikov, Phys. Status Solidi B **88** (2), K165 (1978).
33. A. A. Uzakov and A. L. Éfros, Zh. Éksp. Teor. Fiz. **81** (5), 1940 (1981) [Sov. Phys. JETP **53** (5), 1008 (1981)].
34. S. Golin, Phys. Rev. **132** (1), 178 (1963).
35. I. V. Klyatskina and I. S. Shlimak, Fiz. Tekh. Poluprovodn. (Leningrad) **12** (1), 134 (1978) [Sov. Phys. Semicond. **12** (1), 76 (1978)].
36. A. G. Zabrodskiĭ and M. V. Alekseenko, Fiz. Tekh. Poluprovodn. (St. Petersburg) **28** (1), 168 (1994) [Semiconductors **28** (1), 101 (1994)].
37. A. G. Zabrodskiĭ, A. G. Andreev, and M. V. Alekseenko, Fiz. Tekh. Poluprovodn. (St. Petersburg) **26** (3), 431 (1992) [Sov. Phys. Semicond. **26** (3), 244 (1992)].
38. A. G. Zabrodskiĭ and A. G. Andreev, Int. J. Mod. Phys. B **8** (7), 883 (1994).
39. N. A. Poklonski, S. A. Vyrko, A. G. Zabrodskiĭ, and S. V. Egorov, Fiz. Tverd. Tela (St. Petersburg) **45** (11), 1954 (2003) [Phys. Solid State **45** (11), 2053 (2003)].
40. N. A. Poklonski and A. I. Syaglo, Fiz. Tekh. Poluprovodn. (St. Petersburg) **33** (4), 402 (1999) [Semiconductors **33** (4), 391 (1999)].
41. V. D. Kagan, Zh. Éksp. Teor. Fiz. **117** (2), 452 (2000) [JETP **90** (2), 400 (2000)].

Translated by I. Zvyagin

Physics of the Solid State, Vol. 47, No. 7, 2005, pp. 1245–1248. Translated from Fizika Tverdogo Tela, Vol. 47, No. 7, 2005, pp. 1203–1206.
Original Russian Text Copyright © 2005 by Krivolapchuk, Kozhanova, Lundin, Mezdrogina, Rodin.

SEMICONDUCTORS AND DIELECTRICS

Parameters of Thulium-Doped Gallium Nitride Crystals with Wurtzite Structure

V. V. Krivolapchuk*, Yu. V. Kozhanova, V. V. Lundin*, M. M. Mezdrogina*, and S. N. Rodin***
**Ioffe Physicotechnical Institute, Russian Academy of Sciences, Politekhnicheskaya ul. 26, St. Petersburg, 194021 Russia*
e-mail: vlad.krivol@mail.ioffe.ru, margaret.m@mail.ioffe.ru
***St. Petersburg State Polytechnic University, Politekhnicheskaya ul. 25, St. Petersburg, 195251 Russia*

Received July 26, 2004; in final form, November 9, 2004

Abstract—A study was made of GaN crystals grown by HVPE and MOCVD. Thulium was introduced by diffusion. It is shown that the Tm rare-earth ion acts as an acceptor in a GaN semiconductor matrix if the undoped crystal contains deep-level defects. Intracenter *f*–*f* transitions characteristic of Tm were observed in the short- and long-wavelength spectral regions. The short-wavelength emission intensity is higher in crystals obtained by MOCVD. *© 2005 Pleiades Publishing, Inc.*

1. INTRODUCTION

Wide-bandgap semiconductors based on nitrides of Group III elements enjoy broad application as a material for fabricating light-emitting devices (lasers, light-emitting diodes) intended for operation in the short-wavelength spectral region. Light-emitting diodes for the visible range have been recently developed using quantum-confined InGaN/GaN structures [1, 2].

Earlier studies revealed that doping GaN crystals with rare-earth metals (Er, Sm, Eu) gives rise to intracenter *f*–*f* transitions with emission lines at wavelengths of 0.54–0.56 (Er, Eu), 0.81 (Sm), and 1.54 μm (Er) (visible, infrared, and far infrared spectral regions, respectively) [3, 4]. It was also shown that a rare-earth (RE) ion in GaN wurtzite-structure crystals can act both as a donor and as an acceptor, depending on the total defect concentration in the starting semiconductor matrix. The intensity of the emission lines characteristic of the *f*–*f* intracenter transitions of RE ions in GaN crystals correlates with the defect concentration in the starting semiconductor matrix; more specifically, the lower the defect concentration, the stronger the intensity of intracenter transition lines.

It has also been established that the mechanisms of RE diffusion and doping in crystals are governed by the defect concentration and the Fermi level position in the GaN semiconductor matrix. If the Fermi level lies in the bandgap at $T = 77$ K (for low defect concentrations of less than $<10^{17}$ cm^{-3}), RE ions most likely enter the original crystal lattice and change its bonding character (from the covalent bond typical of Ga–N to an ionic Er–N bond), because RE ions are substitutional impurities [4]. As the defect concentration in the host matrix increases (up to $n > 10^{18}$ cm^{-3}, where the Fermi level is close to the conduction band bottom at $T = 77$ K), RE ions become apparently embedded in the space between domains of the mosaic structure; in this case, all changes in the crystal parameters are associated with changes in these regions.

Doping GaN crystals with RE ions to obtain structures suitable for developing light-emitting diodes may be considered a more cost-effective alternative to the InGaN/GaN heterostructure technology [5]. Thulium emission lines deriving from intracenter *f*–*f* transitions lie in the visible and near infrared regions of the spectrum. Tm has one charge state (3+), as does Er^{3+}, while the other two ions (Eu, Sm) are characterized by variable charge states (2+, 3+). Defects in the starting semiconductor matrix form both shallow (in the case of doping by Er) and deep (in the case of Sm doping) levels in the bandgap of GaN. The effect of the charge state of impurity RE ions, namely, of Eu and Er (as substitutional impurities), on the change in their position in the host lattice (depending on the method of incorporating these ions into the starting semiconductor matrix and on the defect concentration and type) with respect to the normal position of the Ga ion was studied in [5].

In this paper, we report on a study of the effect of Tm doping on the parameters of near-edge photoluminescence (NEPL) in GaN wurtzite-structure crystals, determination of the nature of impurity centers, and observation of the gettering effect. We also studied the dependence of the intensity of the *f*–*f* intracenter transitions characteristic of Tm that produce spectral lines at 477 nm ($^1G_4$–$^3H_6$), 647 nm ($^1G_4$–$^3H_4$), and 801 nm ($^3F_4$–$^3H_6$) in the presence of defects forming deep levels in the starting semiconductor matrix.

2. EXPERIMENT

As in [3, 4], to explore the possibility of a broader variation in defect concentration in the starting semiconductor matrix, we used crystals prepared using two different methods, namely, MOCVD, or decomposition

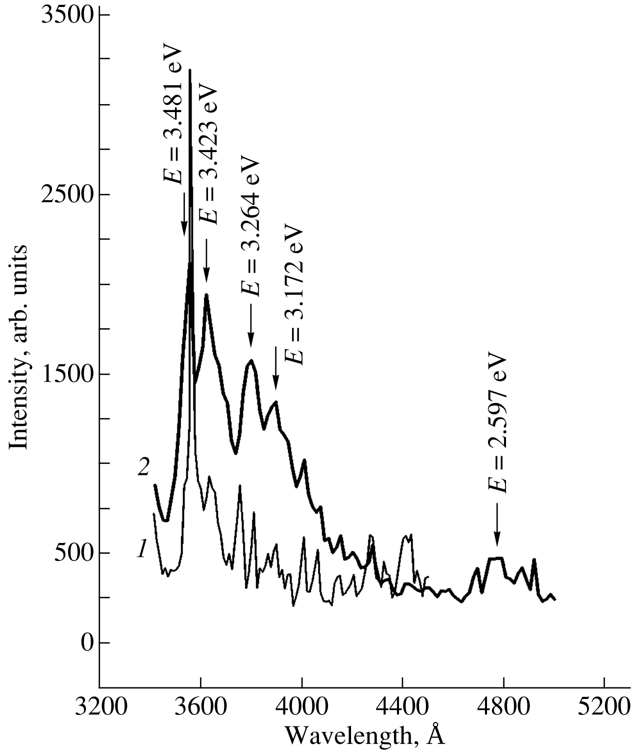

Fig. 1. Photoluminescence spectra of (*1*) undoped and (*2*) Tm-doped MOCVD-grown GaN crystals (type I) taken at $T = 77$ K.

of metalorganic mixtures (type I), and HVPE (type II). Unlike in the previous study [4] of the effect of Er doping on the NEPL spectra of GaN crystals with defects forming shallow levels in the bandgap, the GaN crystals chosen for the present investigation were of different types with defects producing deep levels.

As in [3, 4], RE ions were incorporated by diffusion; the procedure consisted in thermal deposition of a rare-earth metal film on the crystal surface followed by annealing of the sample in ammonia for 1.0–1.5 h at a temperature of 1000–1050°C.

Most of the information on defect concentration in the starting crystals, as in [3, 4], was extracted from photoluminescence (PL) spectra and from the half-width of the diffraction scattering curve (when using x-ray structural analysis).

In the analysis of the PL spectra, attention was primarily focused on the intensity of the NEPL line and its half-width (FWHM). This line is inhomogeneously broadened, because the lines deriving from the radiative recombination of carriers localized at different shallow centers differ slightly in wavelength. The reason for this difference lies in the dispersion of the values of the thermal activation energy of shallow donors E_{LT}. The dispersion of E_{LT}, in turn, stems from different values of the local potential V_{loc} at the sites of shallow impurities. This means that various defects located close to shallow impurities affect the crystal field and, through this, the emission wavelength. Therefore, the noticeable difference in FWHM between the NEPL lines in the starting samples should be assigned to the different concentrations of various defects in these samples. The intensity and FWHM of an NEPL line depend on the density of radiative and nonradiative states and carrier transport to them. The carrier transport parameters are determined by the tails of the density of states function in the bandgap and the position of the percolation level [3]. It follows that samples producing different PL intensities under the same experimental conditions differ primarily in defect concentration. These defects are responsible both for the deep levels (which substantially reduce the free carrier lifetime) and for fluctuations in the density of band states. It was shown in [4] that the FWHM of the NEPL line in *n*-GaN crystals at $T = 77$ K depends on carrier concentration and should be no less than 30 meV for the samples under study ($N_d - N_a > 10^{17}$ cm^{-3}).

Optical measurements were conducted on an SDL-2 grating spectrometer with a reciprocal linear dispersion of 1.3 nm/mm in the edge luminescence region of GaN. Photoluminescence was pumped by an LGI-21 pulsed nitrogen laser operating at a wavelength of 3371 Å with a pulse duration (FWHM) $\tau \approx 10$ ns. To be able to accurately compare emission spectra of different GaN crystals, the controllable parameters, such as the beam incidence angle, pump light intensity, and temperature, were kept constant.

3. RESULTS AND DISCUSSION

Figure 1 presents PL spectra of undoped and Tm-doped GaN crystals (type I).

The undoped GaN crystal exhibits an emission line ($E_{\max} = 3.48$ eV at $T = 77$ K) shifted by 17 meV toward shorter wavelengths relative to the line of the exciton bound to a neutral donor D^0x ($E_{\max} = 3.463$ eV, $T = 77$ K) that is usually observed in MOCVD-grown GaN crystals [3, 4]. It may be assumed that the former emission line derives from free-exciton (FE) emission (*A* at an energy $E = 3.4789$ eV or *B* at an energy $E = 3.48$ eV) [6] of N-face GaN crystals. This shift of the emission line may also originate from strains in the crystal under study. The FWHM of this line is 29 meV, but its intensity is fairly weak.

The NEPL spectrum undergoes substantial changes after crystal doping with Tm. The position of the NEPL peak remains unchanged (at 358 nm, i.e., 3.48 eV) and, as before, it cannot be identified with emission of the bound exciton involving a neutral donor, D^0x (at 3.463 eV). Additional emission lines appear: a line at 3.423 eV (362 nm) and a band deriving from donor–acceptor recombination (DAR) with peaks at 3.264 and 3.170 eV (380 and 390 nm). The spectrum contains emission lines characteristic of the Tm intracenter *f*–*f* transition in the visible range at 477 nm (2.597 eV) and in the near IR range at 798.6, 808, 813, and 820 nm. Studies of RE-doped MOCVD-grown GaN crystals (GaN⟨Eu,Sm,Er⟩) [3, 4] did not reveal any changes in the shape of NEPL spectra; by contrast, crystals grown by HVPE and doped by the same impurities do exhibit changes. The line FWHM measured in the present work on type-I GaN crystals is smaller than that reported in [3, 4]; however, the NEPL spectra of crystals doped by Tm (GaN⟨Tm⟩) changed. The changes in the NEPL spectra caused by Tm doping of type-I crystals having a line (with an FWHM of 29 meV that is weak in intensity) near the free-exciton emission line (FE) are most likely due to doping-induced transformation of the deep states present in the starting semiconductor matrix into shallow levels. Simultaneously, as in earlier studies, a gettering effect is observed (an increase in NEPL intensity, formation of the DAR band). Thus, RE metals exert the same effect on the shape of NEPL spectra of the GaN semiconductor matrix, irrespective of the actual charge state and ionic radius of the dopant.

Figure 2 shows PL spectra of undoped and Tm-doped type-II GaN crystals.

We immediately see that the main emission line in undoped *n*-type crystals (with a high shallow-donor concentration) is the A^0x line associated with the exciton bound to a neutral acceptor (361 nm, 3.454 eV) and that the emission band characteristic of DAR (peaks at 3.25 and 3.17 eV) is weak (curve *1* in Fig. 2). The totality of our experimental data suggests that we witness in this case a shift of the line of the bound exciton involving a neutral donor (D^0x) to longer wavelengths, an effect induced by tensile stresses.

Tm doping of type-II GaN crystals (curve *2* in Fig. 2) brings about a change in the shape of NEPL spectra. The emission line does not change its position (as compared to that of the undoped crystal), but one clearly sees a broadening of this line and an increase in the DAR band intensity, as well as the appearance of emission lines characteristic of the Tm intracenter *f*–*f* transition in the short- (477 nm, 2.597 eV) and long-wavelength (790, 808, 820 nm) regions of the spectrum. The doping-induced increase in the DAR band intensity of GaN⟨Tm⟩ crystals may indicate that the dopant is a shallow acceptor. This is typical of crystals with defects forming deep levels in the bandgap of the starting semiconductor matrix, as is the case with Sm doping [4].

Note also the high intensity of the emission line typical of the Tm intracenter *f*–*f* transition in type-II GaN crystals as compared to the intensity of the same line observed in type-I GaN crystals. Most probably, the concentration of optically active Tm^{3+} centers in type-II GaN is higher than that in type-I crystals because of the difference in the local environment between these centers [7], and this is what accounts for the enhanced intensity of the lines produced in the Tm intracenter *f*–*f* transitions.

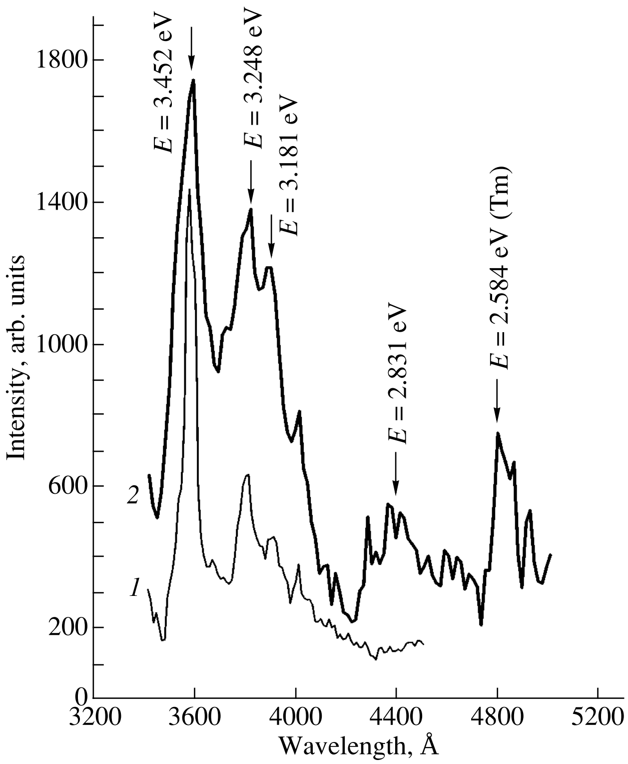

Fig. 2. Photoluminescence spectra of (*1*) undoped and (*2*) Tm-doped HVPE-grown GaN crystals (type II) taken at $T = 77$ K.

Time-resolved spectra obtained by varying the gate delay time in type-II undoped crystals with deep defects exhibit the same pattern as those reported in [4], i.e., for crystals with defects creating shallow levels in the bandgap of the semiconductor matrix. The pattern of time-resolved spectra obtained by varying the time delay for type-I crystals did not differ from that characteristic of crystals having primarily shallow levels in the bandgap [8].

4. CONCLUSIONS

It has been shown that the rare-earth Tm ion incorporated into GaN samples with defects forming deep levels (irrespective of their concentration) acts as an acceptor. We have observed intracenter *f*–*f* transitions characteristic of Tm in the short- and long-wavelength spectral regions. The emission intensity at short wavelengths is stronger in type-II crystals, and that in the long-wavelength region is the same in crystals of types I and II.

ACKNOWLEDGMENTS

This study was supported by the Presidium of the Russian Academy of Sciences (program “Low-Dimensional Quantum Structures”).

REFERENCES

1. X. A. Cao, S. F. Leboeuf, and L. B. Rowland, Appl. Phys. Lett. **82** (21), 3614 (2003).
2. S. Martini, A. A. Quivy, M. J. da Silve, and E. Abramoff, J. Appl. Phys. **99** (11), 7050 (2003).
3. V. V. Krivolapchuk, M. M. Mezdrogina, A. V. Nasonov, and S. N. Rodin, Fiz. Tverd. Tela (St. Petersburg) **45**, 1556 (2003) [Phys. Solid State **45**, 1634 (2003)].
4. V. V. Krivolapchuk, V. V. Lundin, M. M. Mezdrogina, A. V. Nasonov, S. N. Rodin, and N. M. Shmidt, Fiz. Tverd. Tela (St. Petersburg) **46** (5), 814 (2004) [Phys. Solid State **46** (5), 836 (2004)].
5. M. Pan and A. J. Steckl, Appl. Phys. Lett. **83** (1), 9 (2003).
6. V. Kirlyuk, A. R. Zanner, P. C. Christianen, J. R. Wayher, P. R. Hageman, and P. K. Lansen, Appl. Phys. Lett. **84** (17), 2355 (2004).
7. A. N. Georgibiani, A. N. Gruzintsev, M. O. Vorob’ev, U. Kaĭzer, V. Rikhter, and I. I. Khodes, Fiz. Tekh. Poluprovodn. (St. Petersburg) **35**, 725 (2001) [Semiconductors **35**, 695 (2001)].
8. V. V. Krivolapchuk and M. M. Mezdrogina, Fiz. Tverd. Tela (St. Petersburg) **46** (12), 2129 (2004) [Phys. Solid State **46** (12), 2201 (2004)].

Translated by G. Skrebtsov

Physics of the Solid State, Vol. 47, No. 7, 2005, pp. 1249–1253. Translated from Fizika Tverdogo Tela, Vol. 47, No. 7, 2005, pp. 1207–1211.
Original Russian Text Copyright © 2005 by Parfen'eva, Smirnov, Fokin, Misiorek, Mucha, Jezowski.

SEMICONDUCTORS AND DIELECTRICS

Thermal Conductivity of NaCl Embedded in Randomly Distributed Porous-Glass Channels

L. S. Parfen'eva*, I. A. Smirnov*, A. V. Fokin*, H. Misiorek, J. Mucha**, and A. Jezowski****

**Ioffe Physicotechnical Institute, Russian Academy of Sciences, Politekhnicheskaya ul. 26, St. Petersburg, 194021 Russia*
e-mail: igor.smirnov@pop.ioffe.rssi.ru
***Institute of Low-Temperature and Structural Research, Polish Academy of Sciences, Wrocław, 50-950 Poland*

Received October 26, 2004

Abstract—Our earlier experimental data on the thermal conductivity of porous glass and of the porous glass + NaCl composite in the temperature interval 25–300 K are analyzed from a different standpoint. It is shown that the thermal conductivity of sodium chloride filling randomly arranged nanochannels in porous glass behaves exactly like that of a strongly disordered crystalline system and can be described in terms of Einstein's model of the thermal conductivity of solids. *© 2005 Pleiades Publishing, Inc.*

Our earlier study [1] of the thermal conductivity of the porous borosilicate glass + NaCl composite (κ_{comp}) carried out in the temperature interval 5–300 K yielded an interesting result: the thermal conductivities of the composite and of porous glass (κ_{pg}) in the interval 5–25 K turned out to be equal ($\kappa_{comp} = \kappa_{pg}$).

An analysis of the experimental data revealed that, in this temperature region, the thermal conductivity of NaCl embedded in nanochannels of porous glass (κ_{NaCl}) is substantially smaller than that of the matrix ($\kappa_{NaCl} \ll \kappa_{pg}$) and, therefore, introduces only an insignificant contribution to κ_{comp}. In [1], we searched primarily for the physical factors responsible for the small values of κ_{NaCl} at 5–25 K.

In the range 25–300 K, κ_{comp} was found to be larger than κ_{pg}, as should be the case in conventional composite materials. Therefore, the behavior of $\kappa_{comp}(T)$ within this temperature interval was not adequately analyzed in [1].

In [2], we also studied the behavior of the thermal conductivity of NaCl in the opal + NaCl nanocomposite (κ_{NaCl}^{op}) at 5–300 K in the case where sodium chloride filled all first-order voids in the opal; these voids form a close-packed, face-centered cubic lattice.

It is of interest to compare (within the same temperature interval) the behavior of the thermal conductivity of NaCl filling the regular voids in opal with that of NaCl forming clusters in the randomly distributed nanochannels of a porous glass. To do this, we make here a more detailed analysis of the experimental data reported in [1] on the thermal conductivity of porous glass and of the porous glass + NaCl composite relating to the range 25–300 K.

The technique used to prepare the porous glass and the porous glass + NaCl composite was described in [1]. Figure 1 displays the temperature dependences of their thermal conductivities obtained in [1]. We also took from [1] information on the structural features and the values of some physical parameters of this composite, which turned out to be necessary in analyzing experimental data on its thermal conductivity.

Sodium borosilicate glasses consist of SiO_2, B_2O_3, and Na_2O_3, with SiO_2 accounting for 80 to 96% of the

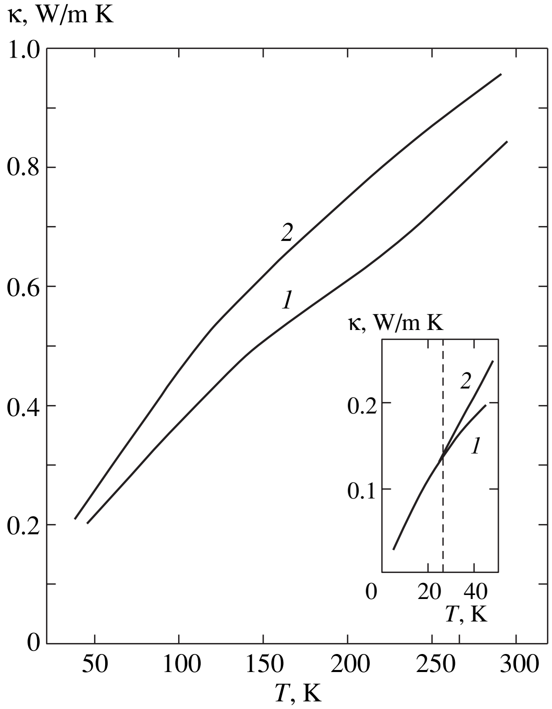

Fig. 1. Temperature dependences of the thermal conductivity of (*1*) porous borosilicate glass and (*2*) the porous glass + NaCl composite [1].

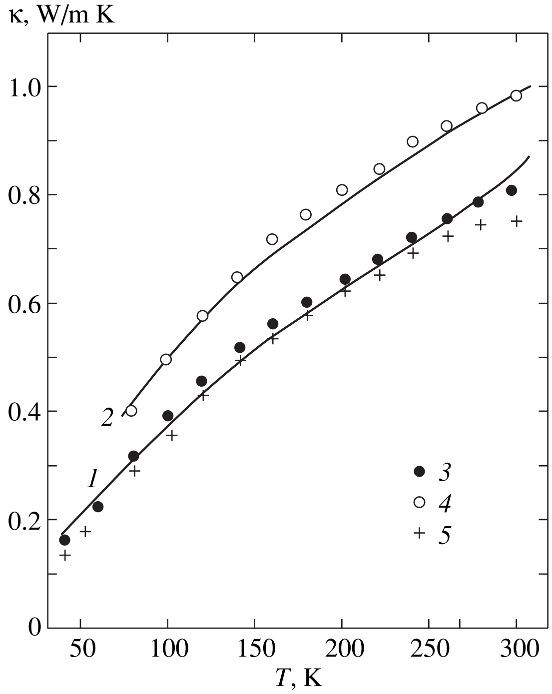

Fig. 2. Temperature dependence of the thermal conductivity of porous borosilicate glass. Solid lines *1* and *2* are data from [1] and [9], respectively; (*3, 4*) thermal conductivity calculated for porous glasses using Eq. (2) [7] for porosities of 30 and 20%, respectively; and (*5*) calculation from Eq. (3) [11, 12] for 30% porosity.

sample volume. Chemical etching removes sodium and boron oxides from the original material, leaving porous glass in the form of an array of close packed spheres of amorphous SiO_2 with various diameters. The space between these spheres (porosity) may add up in glasses to ~20–30% of the sample volume, and the diameters of the randomly distributed pores (channels) may vary from 30 to 150 Å. The channel diameter in the porous glass samples studied in [1] was ~70 Å.

The porous glass + NaCl composite was obtained in [1] by immersing a sample of porous glass in an aqueous solution of NaCl. NaCl occupied 1/4 of the pore volume of the sample.

The crystal structure of an opal is also made up of amorphous SiO_2 spheres [2, 3]. There are, however, two substantial differences from the case of porous glasses.

(i) The amorphous SiO_2 spheres forming the opal are fairly complex in structure. The crystal structure of the opal is made up of close-packed amorphous SiO_2 spheres of the same diameter (most frequently, ~2000–2500 Å), usually called first-order spheres. These spheres contain an array of close-packed amorphous spheres of a smaller size, ~300–400 Å (second-order spheres), which are likewise formed of close-packed amorphous particles ~100 Å in size (third-order spheres).

(ii) First-order amorphous SiO_2 spheres form face-centered cubic structures with giant lattice parameters (~3000–4000 Å).

The dimensions and arrangement of the voids between the SiO_2 spheres in opals and porous glasses are also substantially different. The opal lattice has octahedral and tetrahedral voids interconnected by horn-shaped channels with bottlenecks ~100 Å in diameter. By analogy with amorphous SiO_2 spheres, the voids can also be grouped as belonging to first, second, or third order. The average diameters of octahedral and tetrahedral voids and of channels of the first order are 800, 400, and 300 Å, respectively. First-order voids, just as the amorphous SiO_2 spheres, form a face-centered cubic structure with a lattice parameter of ~3000–4000 Å. First-order opal voids can be filled to 100% of their volume by various fillers using a variety of methods [2, 3] to produce opal-based three-dimensional opal + filler nanocomposites, which can be conceived of as two nested cubic lattices of the matrix and the filler.

In this study, we are interested only in the behavior of the thermal conductivity of NaCl infiltrated into voids of the opal + NaCl nanocomposite [2].

In the studies devoted to analyzing experimental data on the thermal conductivity of opals [4], opal-based nanocomposites, and fillers embedded in first-order opal voids (PbSe [5], HgSe [6], NaCl [1]), the Litovskiĭ formula [7] was used:

$$\kappa_{\mathrm{comp}}/\kappa_{\mathrm{mat}} = (1-p)\sqrt{1-p} + \sqrt[4]{p}\nu, \qquad (1)$$

where $\nu = \kappa_{\mathrm{por}}/\kappa_{\mathrm{mat}}$; κ_{comp}, κ_{por}, and κ_{mat} are the thermal conductivities of the composite, the filler occupying its pores, and the composite matrix, respectively; and p is the filler concentration in the composite.

The value of κ_{comp} of the porous glass + NaCl nanocomposite was estimated in [1] using the fairly crude Odelevskiĭ formula [8], which is not very sensitive to the structural features of a composite. In order to compare the thermal conductivities of NaCl filling regular first-order opal voids [2] and randomly distributed nanochannels in porous glass, we have to estimate the thermal conductivity of the latter also from Eq. (1), as has been done in analyzing data on the thermal conductivity of NaCl in opal [2].

Figure 2 compares the experimental temperature dependences of the thermal conductivities of samples of porous glass studied in [1, 9] with those calculated from the Litovskiĭ formula for porous solids [7][1]

$$\kappa_{\mathrm{pg}} = \kappa_0(1-p')\sqrt{1-p'}, \qquad (2)$$

---

[1] The calculation of the thermal conductivity of the porous glass studied in [9] is presented here to illustrate (and verify) the possibility of using Eq. (2) to describe the behavior of the thermal conductivity of porous solids.

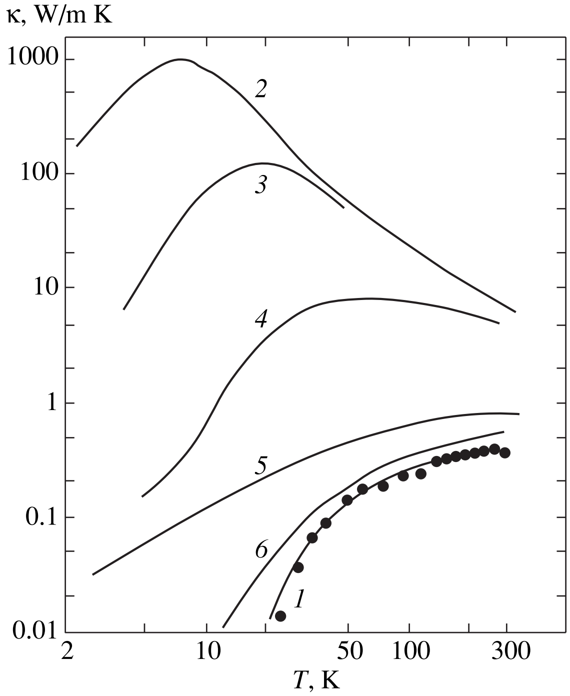

Fig. 3. Temperature dependence of thermal conductivity. (*1*) NaCl in nanochannels of porous glass (κ_{NaCl}); (*2*, *3*) NaCl single crystal, pure and with the addition of 3×10^{-4} at. % Ag, respectively, [10]; (*4*) NaCl in first-order opal voids (the case of 100% filling of the voids by NaCl) (κ_{NaCl}^{op}) [2]; (*5*) $(NaCl)_{0.14}(NaCN)_{0.76}$ [13]; and (*6*) calculated "minimum" thermal conductivity for bulk crystalline NaCl (κ_{min}) [13].

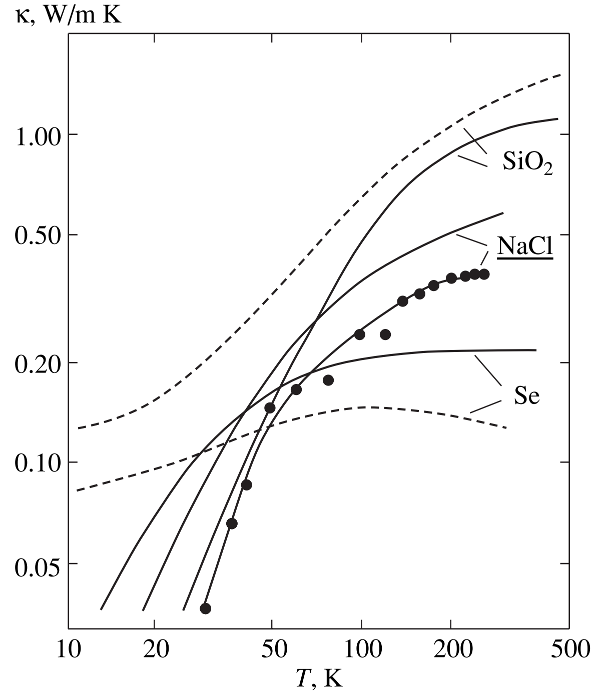

Fig. 4. Comparison of experimental data on the thermal conductivity of amorphous Se and SiO_2 [13] (dashed lines) and crystalline NaCl located in the form of clusters in randomly distributed nanochannels of porous glass (points) with the values of κ_{min} [13] calculated for the corresponding crystalline solids (solid curves).

where p' is the glass porosity and κ_0 is the thermal conductivity of amorphous SiO_2 [10]. The calculated and experimental thermal conductivities of these samples coincide, and the glass porosities derived using the data from [1] and [9] turned out to be 30 and 20%, respectively. The fact that the porosity of the sample studied here is 30% is also supported by calculations of its thermal conductivity based on the widely used Maxwell formula [11, 12] (Fig. 2)

$$\kappa_{pg} = \frac{(1-p')\kappa_0}{1+p'/(d-1)}. \qquad (3)$$

The calculation with Eq. (3) was performed assuming $d = 2$, which corresponds to cylindrical pores.

Figure 3 presents the calculated thermal conductivity of NaCl clusters (κ_{NaCl}) located in randomly distributed nanochannels of porous glass. The calculation was performed with Eq. (1) assuming $\kappa_{mat} = \kappa_0$ and $\kappa_{por} = \kappa_{NaCl}$. The quantity $\kappa_{comp}(T)$ was calculated with due account of the porosity left as a result of partial filling of empty channels in the glass by sodium chloride.

For comparison, Fig. 3 also shows data on the thermal conductivity of NaCl single crystals: pure NaCl, NaCl with an Ag impurity [10], a strongly disordered $(NaCl)_{0.14}(NaCN)_{0.76}$ system [13], and NaCl in first-order opal voids (under 100% filling) [2].[2]

The determination of κ_{NaCl} in porous glass channels yielded an unexpected and interesting result. In the temperature interval 25–300 K, this quantity was found to be close to the thermal conductivity $\kappa_{min}(T)$ for NaCl obtained in [13] using a modified Einstein relation for the thermal conductivity of solids [14] (see [13, Eq. (17)]).[3]

The modified Einstein model of the thermal conductivity of solids divides a sample into randomly distributed regions in which the atomic Einstein oscillators are coherent but there is no coherence among these regions. Einstein's model describes fairly well the temperature dependence of heat capacity [15] but does not fit the temperature dependence of thermal conductivity of crystalline solids. This model is satisfied by amorphous (Figs. 4, 5) and strongly disordered crystalline materials (Figs. 3, 5)[4] [13, 16]. It still remains unclear why Einstein's model of thermal conductivity fits well the behavior of the thermal conductivity of NaCl filling

---

[2] Later on, we will discuss the data in Fig. 3 more comprehensively.

[3] In [13], a brief account is given of Einstein's theoretical study published in 1911 [14].

[4] For instance, the thermal conductivity of the strongly disordered $(NaCl)_{0.14}(NaCN)_{0.76}$ system (curve *5* in Fig. 3) at $T > 100$ K approaches $\kappa_{min}(T)$ for NaCl [13].

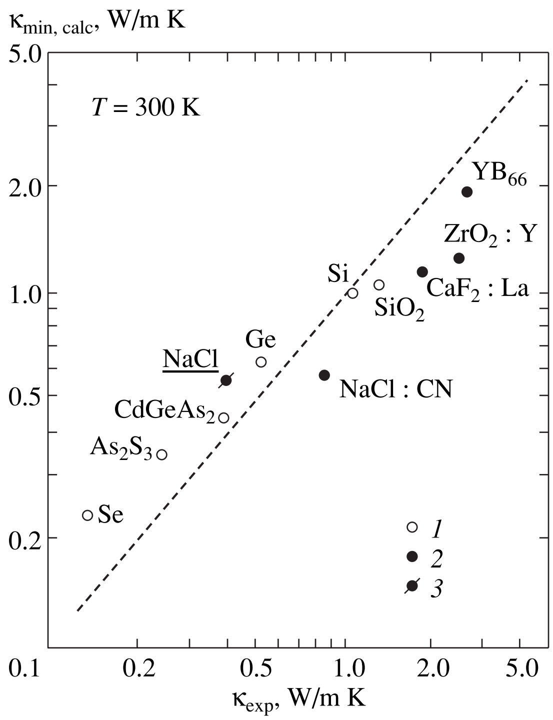

Fig. 5. Comparison of experimental and theoretical (κ_{min}) values of the thermal conductivity at 300 K for some (*1*) amorphous and (*2*) strongly disordered crystalline solids. The data, except point *3* for NaCl (κ_{NaCl}), were taken from [13, 16].

randomly distributed channels in porous glass. X-ray data show NaCl in the porous glass sample under study to be a clearly defined crystalline solid with a lattice constant a = 5.641(1) Å (the tabulated value of a for sodium chloride is 5.6402 Å). There is no information suggesting that the NaCl in channels of porous glass is strongly defective.

It might seem, at first glance, that Einstein’s model fits well the behavior of the thermal conductivity of NaCl filling channels in porous glass. NaCl nanoclusters with a regular lattice are randomly distributed over the matrix channels. Thermal contact among the clusters is established through the glass matrix. A more substantiated conclusion on the reasons behind the unusual behavior of $\kappa_{NaCl}(T)$ can apparently be drawn only after the fine crystal structure of the NaCl clusters located in the porous glass channels has been studied (after their dimensions and geometric arrangement in channels of porous glass have been determined).

Figure 4 compares experimental thermal conductivity data obtained for NaCl in channels of porous glass with those for amorphous Se and SiO$_2$ [13]. The thermal conductivities of these three materials behave in approximately the same way with respect to the corresponding values of $\kappa_{min}(T)$. Note, however, a certain difference in the course of the thermal conductivity of Se and SiO$_2$ from that of $\kappa_{NaCl}(T)$. As the temperature is lowered ($T \le 50$ K), the thermal conductivities of Se and SiO$_2$ deviate from the values for the corresponding $\kappa_{min}(T)$. As pointed out in [13, 16], this behavior is associated with the phonon mean free path l in these materials increasing with decreasing temperature. By contrast, $\kappa_{NaCl}(T)$ in channels of porous glass remains close to $\kappa_{min}(T)$ for NaCl down to the lowest temperatures covered. This behavior of $\kappa_{NaCl}(T)$ can apparently be assigned to the fact that the mean free path l for NaCl in porous glass channels does not grow with decreasing temperature, because phonons are scattered from the walls of the channels filled by sodium chloride (or from NaCl nanocluster boundaries).

In Fig. 5, the experimental thermal conductivities at 300 K for some amorphous and strongly disordered crystalline solids [13, 16] are compared with the values of κ_{min} calculated for the same temperature from Einstein’s relation. The values of the thermal conductivity of NaCl confined to nanochannels of porous glass are seen to group together with the classes of materials mentioned above.

Based on a different theoretical model, Slack [17] obtained values (let us denote them by $\kappa_{min}^{Sl}(T)$) close to $\kappa_{min}(T)$ as calculated with Einstein’s model [13, 16]. The values of $\kappa_{min}^{Sl}(T)$ are reached when the mean free path of phonons becomes comparable to the phonon wavelength, i.e., when the Ioffe–Regel criterion [18, 19] is satisfied. According to the calculations performed by Slack [17], the thermal conductivity of pure alkali halide crystals approaches the corresponding values of κ_{min} only at temperatures close to the melting points of these materials.

One of the aims of the present study was to compare the behavior of the thermal conductivity of NaCl confined to regular opal voids (κ_{NaCl}^{op}) with that of NaCl occupying randomly distributed nanochannels of porous glass (κ_{NaCl}).

Let us return to the plots of thermal conductivity presented in Fig. 3. Curves *1* and *4* represent $\kappa_{NaCl}(T)$ and $\kappa_{NaCl}^{op}(T)$. The thermal conductivities of NaCl in the opal and in porous glass are seen to differ strongly in terms of magnitude and temperature behavior. It is even more significant that their behavior in these two porous media is governed by different physical mechanisms.

Indeed, at low temperatures ($T < 20$ K), $\kappa_{NaCl}^{op}(T)$ is governed by phonon boundary scattering from bottlenecks (~100 Å in diameter) of regularly spaced horn-shaped channels interconnecting first-order octahedral and tetrahedral voids in opal filled by sodium chloride, whereas in the high-temperature range (50–300 K) phonon scattering is due to specific defects that form in sodium chloride because of its being confined to opal voids [2].

Sodium chloride in randomly distributed nanochannels of porous glasses apparently behaves like a strongly disordered crystalline structure whose thermal conductivity can be described in terms of Einstein's model.

In closing, we note that the values of $\kappa_{NaCl}(T)$ calculated in this work are not in conflict with experimental data obtained for the temperature interval 5–25 K and with the conclusion [1] that κ_{pg} is equal to κ_{comp} in this temperature region because $\kappa_{NaCl} \ll \kappa_{pg}$ in the composite. The results of the present study do indeed suggest that $\kappa_{NaCl} \ll \kappa_{pg}$ (Figs. 2, 3).

ACKNOWLEDGMENTS

The authors are indebted to N.F. Kartenko for help with the x-ray structural measurements on the porous glass + NaCl composite.

This study was supported by the Russian Foundation for Basic Research (project no. 02-02-17657) and the Polish State Committee on Scientific Research KBN (project no. 3 T08A 054 26).

REFERENCES

1. L. S. Parfen'eva, I. A. Smirnov, A. V. Fokin, H. Misiorek, J. Mucha, and A. Jezowski, Fiz. Tverd. Tela (St. Petersburg) **45** (2), 359 (2003) [Phys. Solid State **45** (2), 381 (2003)].
2. V. N. Bogomolov, N. F. Kartenko, D. A. Kurdyukov, L. S. Parfen'eva, I. A. Smirnov, N. V. Sharenkova, H. Misiorek, J. Mucha, and A. Jezowski, Fiz. Tverd. Tela (St. Petersburg) **46** (10), 1893 (2004) [Phys. Solid State **46** (10), 1961 (2004)].
3. V. N. Bogomolov and T. M. Pavlova, Fiz. Tekh. Poluprovodn. (St. Petersburg) **29** (5–6), 826 (1995) [Semiconductors **29** (5–6), 428 (1995)].
4. V. N. Bogomolov, D. A. Kurdyukov, A. V. Prokof'ev, L. S. Parfen'eva, S. M. Samoĭlovich, I. A. Smirnov, A. Jezowski, J. Mucha, and H. Misiorek, Fiz. Tverd. Tela (St. Petersburg) **39** (2), 392 (1997) [Phys. Solid State **39** (2), 341 (1997)].
5. L. I. Arutyunyan, V. N. Bogomolov, N. F. Kartenko, D. A. Kurdyukov, V. V. Popov, A. V. Prokof'ev, I. A. Smirnov, and N. V. Sharenkova, Fiz. Tverd. Tela (St. Petersburg) **39** (3), 586 (1997) [Phys. Solid State **39** (3), 510 (1997)].
6. V. N. Bogomolov, N. F. Kartenko, D. A. Kurdyukov, L. S. Parfen'eva, V. V. Popov, L. M. Sorokin, I. A. Smirnov, H. Misiorek, A. Jezowski, and J. Hutchison, Fiz. Tverd. Tela (St. Petersburg) **45** (3), 535 (2003) [Phys. Solid State **45** (3), 566 (2003)].
7. E. Ya. Litovskiĭ, Izv. Akad. Nauk SSSR, Neorg. Mater. **16** (3), 559 (1980).
8. G. N. Dul'nev and Yu. P. Zarichnyak, *Thermal Conductivity of Mixtures and Composite Materials* (Énergiya, Leningrad, 1974) [in Russian].
9. V. N. Bogomolov, N. A. Klushin, M. V. Romanova, I. A. Smirnov, and V. V. Tikhonov, Fiz. Tverd. Tela (Leningrad) **14** (9), 2699 (1972) [Phys. Solid State **14** (9), 2330 (1972)].
10. *Handbook of Thermal Conductivity of Solid States*, Ed. by A. S. Okhotina (Énergoatomizdat, Moscow, 1984).
11. J. C. Maxwell, *A Treatise on Electricity and Magnetism* (Dover, New York, 1954), p. 435.
12. J. D. Albrecht, P. A. Knipp, and T. L. Reinecke, Phys. Rev. B **63**, 134303 (2001).
13. D. G. Cahill, S. K. Watson, and R. O. Pohl, Phys. Rev. B **46** (10), 6131 (1992).
14. A. Einstein, Ann. Phys. **35**, 679 (1911).
15. A. Einstein, Ann. Phys. **35**, 185 (1911).
16. D. G. Cahill and R. O. Pohl, Solid State Commun. **70** (10), 927 (1989).
17. G. A. Slack, *Solid State Physics*, Ed. by F. Seitz and D. Turnbull (Academic, New York, 1979), Vol. 34, p. 57.
18. A. F. Ioffe and A. R. Regel, Prog. Semicond. **4**, 237 (1960).
19. S. N. Taraskin and S. R. Elliot, Phys. Rev. B **61** (18), 12031 (2000).

Translated by G. Skrebtsov

Physics of the Solid State, Vol. 47, No. 7, 2005, pp. 1254–1257. Translated from Fizika Tverdogo Tela, Vol. 47, No. 7, 2005, pp. 1212–1216.
Original Russian Text Copyright © 2005 by Zhiteĭtsev, Ulanov, Zaripov, Zheglov.

DEFECTS, DISLOCATIONS, AND PHYSICS OF STRENGTH

EPR Study of Impurity Iron Ion Clusters in BaF_2 Crystals

E. R. Zhiteĭtsev, V. A. Ulanov, M. M. Zaripov, and E. P. Zheglov
Zavoĭskiĭ Physicotechnical Institute, Kazan Scientific Center, Russian Academy of Sciences,
Sibirskiĭ trakt 10/7, Kazan 29, 420029 Tatarstan, Russia
e-mail: ulanov@dionis.kfti.kcn.ru

Received July 29, 2004

Abstract—Tetragonal paramagnetic centers with spin $S = 7/2$ were detected in x-ray-irradiated BaF_2 : Fe ($c_{Fe} \approx 0.002$ at. %) crystals using the EPR method. Electronic transitions between the $|\pm 1/2\rangle$ states of a Kramers doublet were observed in the X and Q ranges. In the EPR spectra of the tetragonal centers, a ligand hyperfine structure (LHFS) was observed corresponding to the interaction of the electron magnetic moment of the tetragonal center with eight equivalent ligands. The large spin moment, significant anisotropy of the magnetic properties, and the characteristic LHFS indicate that the tetragonal center is a $Fe^{1.5+}$–$Fe^{1.5+}$ dimer in which the two iron ions are bound via superexchange interaction. It is assumed that, before crystal irradiation, this dimer was in the $Fe^{3+}(3d^5)$–$Fe^{+}(3d^7)$ state. *© 2005 Pleiades Publishing, Inc.*

1. INTRODUCTION

The iron impurity centers in fluorite-structure crystals have been studied by several research teams. The authors of [1, 2] studied CdF_2 : Fe and CaF_2 : Fe crystals using the EPR method. At a frequency of 9.3 GHz and $T = 4.2$ K, they observed the EPR spectra of tetragonal paramagnetic centers. These spectra were attributed to electronic transitions $|M_S = +2\rangle \rightleftarrows |M_S = -2\rangle$ in impurity $Fe^{2+}(3d^6, {}^5D)$ ion clusters with an effective electron spin $S = 2$. The authors of [1, 2] assumed that other EPR transitions do not take place due to large initial splittings, which arise in the system of the cluster spin levels due to the static Jahn–Teller effect. CdF_2 : Fe crystals have also been studied using optical [3, 4] and Mössbauer [5, 6] spectroscopy. In those studies, it was shown that the Jahn–Teller effect is much more pronounced in the excited orbital triplet ${}^5T_{2g}$ of the $[FeF_8]^{-6}(O_h)$ cubic cluster, which forms in the CdF_2 : Fe crystal during its doping. In addition to clusters of individual impurity Fe^{2+} ions, the authors of [6] observed clusters of individual Fe^{3+} ions associated with charge compensation defects and Fe^{2+} ion dimers. It was indicated that a large amount of Fe^{2+} dimers are contained in CdF_2 : Fe samples with a high content of impurity iron. It turned out [6] that the concentration of impurity iron dimers significantly deviates from the Poisson distribution. This fact obviously suggests that condensation of individual iron centers into dimers is energetically favorable.

In this paper, we report on the results of an EPR study of BaF_2 : Fe crystals. As shown in our preliminary study [7], the diffusion coefficient of impurity iron ions in BaF_2 crystals at temperatures close to their melting points is so high that impurity clusters with a regular structure can be synthesized. As in CdF_2 : Fe [6], the tendency of complexes of individual iron ions toward condensation into multinuclear clusters was detected in the crystals under study. However, the case considered in this paper differs from that in [6] in the fact that the synthesis of impurity clusters is possible not only in powders but also in single-crystal samples. This offers great opportunities for studying the structure and magnetic properties of synthesized clusters using the very informative method of EPR.

2. EXPERIMENT AND RESULTS

BaF_2 : Fe crystals were grown using the Bridgman method in graphite crucibles in a helium atmosphere with fluorine impurity introduced in the form of a fine-dispersed metal powder. The temperature gradient in the crystallization front region was 10 deg/mm. The grown samples were studied using the EPR method in the X and Q ranges at temperatures of 4.2 and 77–80 K. EPR spectra of at least two types of centers with integer spins and tetragonal symmetry of the magnetic properties were observed in grown (but not irradiated) samples of BaF_2 : Fe crystals with an impurity iron concentration of 0.2 mol % at 4.2 K. The lines of these spectra have no hyperfine structure and are not observed at 77 K and above.

After 30-min room-temperature irradiation with x rays, the spectra of another three types of centers featuring half-integer spins appear in addition to the above-mentioned spectra. The line intensities of centers with integer spins appreciably decrease after sample irradiation. All the new (radiation-induced) centers feature an allowed ligand hyperfine structure (LHFS). It was established in [7] that two types of radiation cen-

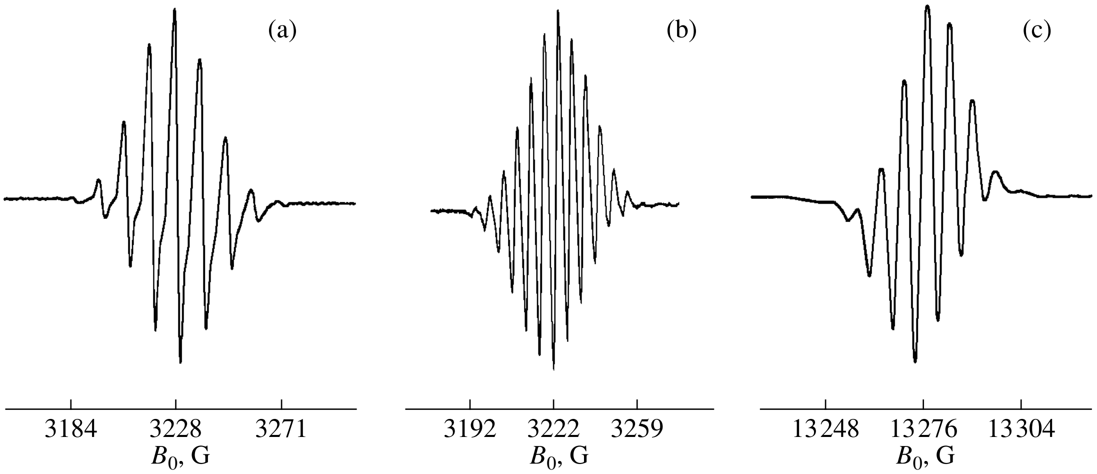

Fig. 1. EPR spectra of type-III paramagnetic centers in a BaF$_2$: Fe crystal for various orientations of an external dc magnetic field: (a) $\langle 001\rangle \parallel \mathbf{B}_0 \parallel z$, (b) $\langle 010\rangle \parallel \mathbf{B}_0 \perp z$, and (c) $\langle 100\rangle \parallel \mathbf{B}_0 \perp z$. $T = 4.2$ K and $\nu_{EPR} = 37.1$ GHz.

ters are formed by individual impurity ions Fe^{3+}($3d^5$, ^6S) associated with a compensator of an excess positive charge (an interstitial fluorine ion). The differences between their magnetic properties are caused by the difference in the relative positions of the Fe^{3+} ion and the charge compensator.

In this study, we expand on the third type of centers (III). In some samples, the concentration of these centers appeared higher than the concentration of centers of individual impurity Fe^{3+} ions. The resonant magnetic field of the central line of the group corresponding to magnetically equivalent type-III centers varies in a very wide range as the vector $\mathbf{B}_0$ rotates in the $\langle 110\rangle$ and $\langle 001\rangle$ crystal planes. The minimum values of the resonant magnetic field in the X and Q ranges at $T = 77$ K correspond to effective g factors of 8.243 and 8.224, respectively. The maximum value of the resonant magnetic field corresponds to an effective g factor of 2.002 (in the X and Q ranges). Three magnetically nonequivalent ensembles of type-III centers are observed simultaneously. Their EPR spectra reveal an LHFS (Fig. 1), which explicitly indicates ligand hyperfine interaction (LHFI) with the magnetic nuclei of eight equivalent fluorine ions ($I_F = 1/2$). The angular dependences of resonant magnetic fields of the central lines of the EPR spectra of the three groups of magnetically nonequivalent type-III centers in the BaF$_2$: Fe crystal are shown in Fig. 2. Curves *1–4* and *5* show the centroid positions of the groups of nondegenerate and doubly degenerate EPR lines, respectively. The angle ϑ_1 defines the orientation of the external dc magnetic field ($\mathbf{B}_0$) during its rotation in one of the $\langle 001\rangle$ crystallographic planes of the sample, and the angle ϑ_2 corresponds to one of the $\langle 110\rangle$ planes. The shape of these curves gives reason to state that these centers are tetragonal.

3. DISCUSSION OF THE EXPERIMENTAL RESULTS

Based on the values of the components of the effective tensor $\mathbf{g}^{\text{eff}}$ ($g_{\parallel}^{\text{eff}} = 2.002$, $g_{\perp}^{\text{eff}} = 8.243$) and the shape of curves *1–5* in Fig. 2, the spin of the type-III center can be determined. Above all, it seems obvious that the spin of this center is half-integer and the observed spectrum corresponds to EPR transitions between the $|M_S = +1/2\rangle$ and $|M_S = -1/2\rangle$ states. It is also clear that the ini-

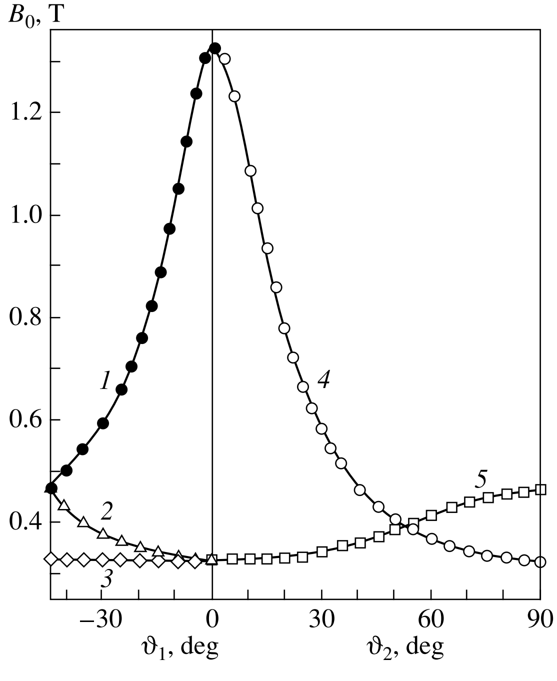

Fig. 2. Angular dependences of resonant magnetic fields of the central lines of the EPR spectra of three groups of magnetically nonequivalent type-III centers in a BaF$_2$: Fe crystal. $T = 4.2$ K and $\nu_{EPR} = 37.1$ GHz.

tial splitting of the spin levels is much larger than the energy quantum corresponding to the Q range of an EPR spectrometer. It can be shown that the spin of the type-III center cannot be smaller than $S = 5/2$. Moreover, it is reasonable to argue that the most probable value is 7/2. Indeed, the effect of states $|M_S = \pm 3/2\rangle$, $|M_S = \pm 5/2\rangle$, etc. on the magnetic properties of the $|\pm 1/2\rangle$ Kramers doublet at a large initial splitting is generally reduced to increasing the actual value of $g_\perp$ by factors of approximately 2, 3, and 4 in the case of S = 3/2, 5/2, and 7/2, respectively. It is clear that the value $g_\perp^{\mathrm{eff}} = 8.243$ is almost improbable at $S = 3/2$, because the actual value of $g_\perp$ would be greater than 4 in this case. If we assume that $S = 5/2$, then it is unclear why the electron Zeeman interaction is highly anisotropic (in this case, the actual value of $g_\perp$ should be approximately equal to 2.7). The reason for this anisotropy is very difficult to explain, at least in the case where a single impurity Fe^{n+} ion is in the neighborhood of eight equivalent fluorine ions (n is an odd integer in this case). Furthermore, experimental statistics associated with the doping of ionic crystals should be taken into account. From the viewpoint of this statistics, it seems unlikely that the effective charge of the Fe^{n+} ion can differ significantly from the charge of the Ba^{2+} ion substituted for it (the Ba^{2+} charge is close to 2+), since the lattice energy should strongly increase in this case.

Let us discuss this situation in more detail. Among the cases possible, we first mention the Fe^{3+} ion, which is in the ground state with electronic configuration $3d^5$. In the free state, its ground term is ^6S and the total spin is $S = 5/2$. Since the orbital angular momentum of the free Fe^{3+} ion is almost zero, there is no reason to expect large deviations of $g_\perp$ from 2.0023. Thus, the case with Fe^{3+} in the $3d^5(^6S)$ state is excluded. Now, let us consider the case where the impurity Fe^{3+} ion in the crystal is in the state with electronic configuration$3d^44s$. We assume that the Hund rule is satisfied. In this case, the ^6D term will most likely be the ground state. In the cubic crystal field, the ground state will be the orbital doublet ^6E_g. Therefore, in the impurity cluster formed, the static Jahn–Teller effect is possible, which is associated with the interaction of the impurity ion with tetragonal-symmetry nuclear vibration. However, the spin–orbit coupling in the $\mathrm{Fe}^{3+}(3d^44s)$ ion is unlikely to be much larger than 100 cm^{-1}. Therefore, the effect of this coupling on the ^6E_g ground-state doublet is only a second-order correction of the perturbation theory. For this reason, the value $g_\perp = 2.7$ seems unlikely. Moreover, the static Jahn–Teller effect should be considered in this case. Due to this effect the eight ligands of the iron ion become nonequivalent, which contradicts observations.

Let us consider the possibility that $S = 7/2$. Here, it should be emphasized that this value of the total spin seems impossible for iron-group ions. However, there is a low probability that the electronic configuration $3d^54s4p$ with parallel electron spins can be the ground state of the Fe^+ ion under the crystal field. The monovalent state itself is not unexpected for the impurity iron ion in crystals. However, the probability that this configuration is the ground state in the crystal field seems low. Although it was shown in [8, 9] that the ground state of the Mn^+ ion in CaF_2 and SrF_2 crystals is the $3d^54s$ configuration with spin $S = 3$, it seems more probable that the type-III center is the exchange-coupled pair $\mathrm{Fe}^{2+}(3d^6)$–$\mathrm{Fe}^+(3d^7)$. Let us consider this assumption. It is known that the ground state of the free Fe^{2+} ion is the ^5D term. In a cubic field, the ground state is the orbital doublet ^5E_g; hence, the static Jahn–Teller effect is possible. Since the matrix elements of the spin–orbit coupling operator for the ^5E_g representation are zero, the static Jahn–Teller effect can bring about the formation of a system of five ground levels separated from the other states of the Fe^{2+} ion by a wide energy interval. As is known, the magnetic properties of this system of levels can be described in terms of the effective spin $S_{\mathrm{eff}} = 2$ and the spin Hamiltonian of tetragonal symmetry.

The ground state of the free $\mathrm{Fe}^+(3d^7)$ ion is the ^4F term. In a cubic field, this term is split and the ground state becomes the orbital singlet $^4A_2$. In this case, the vibronic interactions cannot be efficient. Therefore, the four ground states corresponding to the different projections of the total spin $S = 3/2$ form a spin quadruplet. Under the influence of the axial component of the crystal field induced by a neighboring Fe^{2+} ion, this quadruplet is split into two Kramers doublets, $|M_S = \pm 1/2\rangle$ and $|M_S = \pm 3/2\rangle$. Thus, under steady-state conditions, the low-temperature magnetic properties of the $\mathrm{Fe}^{2+}(3d^6)$–$\mathrm{Fe}^+(3d^7)$ pair can be approximately described by the spin Hamiltonian

$$\begin{aligned}\mathbf{H}_S = {} & \mathbf{S}_1 \cdot \mathbf{J} \cdot \mathbf{S}_2 + \beta_e \mathbf{S}_1 \cdot \mathbf{g}_1 \cdot \mathbf{B}_0 + B_2^0 \mathbf{O}_2^0(\mathbf{S}_1) \\ & + \beta_e \mathbf{S}_2 \cdot \mathbf{g}_2 \cdot \mathbf{B}_0 + B_2^0 \mathbf{O}_2^0(\mathbf{S}_2),\end{aligned} \tag{1}$$

where $\mathbf{S}_1$ and $\mathbf{S}_2$ are the electron spin operators of the fragments of the impurity dimer formed by individual $\mathrm{Fe}^{2+}(3d^6)$ and $\mathrm{Fe}^+(3d^7)$ ions with $S_1 = 2$ and $S_2 = 3/2$, respectively; $\mathbf{J}$ is the tensor of the exchange interaction between the fragments of this pair; g_1 and g_2 are the tensors of the electron Zeeman interaction of the pair fragments with an external magnetic field; β_e is the Bohr magneton; $\mathbf{B}_0$ is the external magnetic field; and $\mathbf{O}_2^0(\mathbf{S}_1)$ and $\mathbf{O}_2^0(\mathbf{S}_2)$ are the Stevens spin operators.

The experimental facts we obtained suggest that the exchange interaction in the dimer is ferromagnetic and much stronger that the interaction with the external magnetic field. The ground states in the dimer are eight states whose transformation properties can be approximately described by the total spin $S = 7/2$. The EPR spectra shown in Fig. 1 also suggest that the electronic state of the $Fe^{2+}(3d^6)$–$Fe^{+}(3d^7)$ dimer is not stationary. Indeed, in the cubic BaF_2 crystal, an electron jump from the Fe^+ to the Fe^{2+} ion can result in the formation of the energetically equivalent $Fe^{+}(3d^7)$–$Fe^{2+}(3d^6)$ state of the dimer. It seems that the barrier to electron transfer from one dimer fragment to the other is insufficiently high; therefore, the frequency of electron jumps is higher than the EPR frequency. This resulted in the EPR spectra representing an averaged pattern in which both impurity ions (dimer fragments) are in the (1.5+) valence states (with a mixed valence) and the dimer molecular structure features D_{4h} symmetry. In this case, the sixteen fluorine ions belonging to the first coordination shells of the two iron ions are separated into two groups (with eight equivalent F^- ions in each group). It is clear that the bond between the iron ions in the dimer caused their displacement towards each other. The LHFI with one group of ligands became stronger than the interaction with the other group. As a result, the LHFS corresponding to the LHFI with the group or more distant ligands is not resolved and only the resolved LHFS caused by the interaction with the other eight ligands is observed.

Thus, in the case of the half-integer spin, the equivalence of the eight fluorine ions in orientations $\langle 001 \rangle \parallel \mathbf{B}_0 \parallel z$ and $\langle 010 \rangle \parallel \mathbf{B}_0 \perp z$ clearly indicates that the ions of the impurity pair rapidly exchange electrons and that each event of such exchange (superexchange) corresponds to a tunneling transition of this pair from one well of the adiabatic double-well potential [corresponding to the $Fe^{2+}(3d^6)$–$Fe^{+}(3d^7)$ state] to the other well [corresponding to the $Fe^{+}(3d^7)$–$Fe^{2+}(3d^6)$ state]. Hence, the averaged molecular structure of the radiation-induced $Fe^{1.5+}$–$Fe^{1.5+}$ dimer has the form shown in Fig. 3 (bold lines represent the bonds of iron ions with the ligands for which the LHFI is detected in the EPR spectra).

As mentioned above, the crystal contains tetragonal centers with an integer spin that transform into type-III centers under irradiation. If our interpretation of the type-III centers is correct, one of the ensembles of centers with an integer spin corresponds to the Fe^{3+}–Fe^{+} impurity pair. The high concentration of these pairs in the crystal is explained by the fact that the Coulomb interaction of uncompensated charges of two individual centers (Fe^{3+}, Fe^{+}) favors the formation of these impurity pairs. An example demonstrating that the formation of pairs from impurity centers with unlike uncompensated charges can be favorable is the formation of titanium ion dimers in SrF_2 : Ti crystals [10]. In some SrF_2 : Ti crystal samples, the titanium dimer concentration was tens times higher than that of centers of single titanium ions.

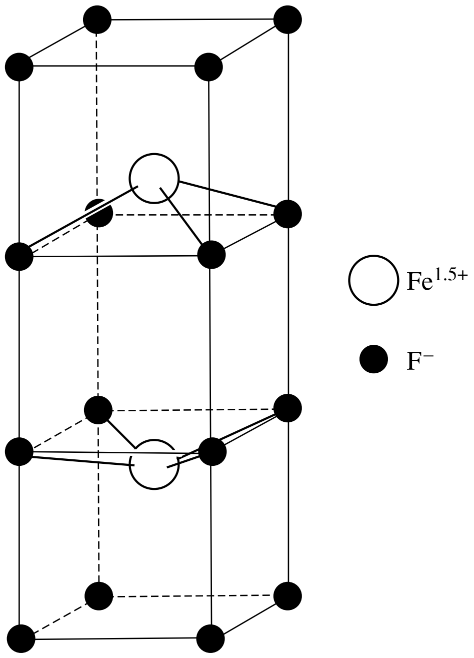

Fig. 3. Molecular structure of the $Fe^{1.5+}$–$Fe^{1.5+}$ dimer in a BaF_2 : Fe crystal.

ACKNOWLEDGMENTS

This study was supported by the Russian Foundation for Basic Research, project no. 04-02-16616.

REFERENCES

1. M. M. Zaripov, V. S. Kropotov, L. D. Livanova, and V. G. Stepanov, Fiz. Tverd. Tela (Leningrad) **9** (10), 2983 (1967) [Sov. Phys. Solid State **9** (10), 2344 (1967)].
2. M. M. Zaripov, V. S. Kropotov, L. D. Livanova, and V. G. Stepanov, *Paramagnetic Resonance (1944–1969)* (Nauka, Moscow, 1971), pp. 95–103 [in Russian].
3. W. Ulrici, Phys. Status Solidi B **44**, K29 (1971).
4. W. Ulrici, Phys. Status Solidi B **62**, 431 (1974).
5. Y. Sato, Phys. Status Solidi B **82**, 611 (1977).
6. J. Steger and E. Kostiner, J. Chem. Phys. **58** (8), 3389 (1973).
7. E. P. Zheglov, V. A. Ulanov, M. M. Zaripov, E. R. Zhiteĭtsev, G. S. Shakurov, and V. F. Tarasov, in *Proceedings of XXXIII Meeting on Low Temperature Physics, Yekaterinburg, 2003*, p. 252.
8. P. G. Baranov, Fiz. Tverd. Tela (Leningrad) **22**, 229 (1980) [Sov. Phys. Solid State **22**, 133 (1980)].
9. P. J. Alonso and R. Alcala, Phys. Status Solidi B **127**, K77 (1985).
10. I. I. Fazlizhanov, V. A. Ulanov, M. M. Zaripov, and R. M. Eremina, Fiz. Tverd. Tela (St. Petersburg) **44** (8), 1483 (2002) [Phys. Solid State **44** (8), 1553 (2002)].

Translated by A. Kazantsev

Physics of the Solid State, Vol. 47, No. 7, 2005, pp. 1258–1266. Translated from Fizika Tverdogo Tela, Vol. 47, No. 7, 2005, pp. 1217–1225.
Original Russian Text Copyright © 2005 by Mironov, Danilenko, Myshlyaev, Korneva.

DEFECTS, DISLOCATIONS, AND PHYSICS OF STRENGTH

Analysis of the Spatial Orientation Distribution of Building Blocks in Polycrystals as Determined Using Transmission Electron Microscopy and a Backscattered Electron Beam in a Scanning Electron Microscope

S. Yu. Mironov*, V. N. Danilenko*, M. M. Myshlyaev, and A. V. Korneva***

** Institute for Metals Superplasticity Problems, Russian Academy of Sciences,*
ul. Khalturina 39, Ufa, 450001 Bashkortostan, Russia
*** Institute of Solid State Physics, Russian Academy of Sciences, Chernogolovka, Moscow oblast, 142432 Russia*

Received August 31, 2004

Abstract—The advantages and disadvantages of the method of automatic analysis of electron backscattering diffraction (EBSD) patterns for studying spatial orientation distributions are considered as compared to transmission electron microscopy (TEM). A misorientation spectrum in a test alloy (Kh20N80 alloy) having a high content of annealing twins is experimentally studied using both TEM and EBSD, and the results obtained are compared. *© 2005 Pleiades Publishing, Inc.*

1. INTRODUCTION

Until recently, two radically different materials science approaches to the description of polycrystalline microstructures had been conventionally distinguished. In one of them, the morphology of crystallites is described, their characteristic sizes are measured, and so on; such methods can conventionally be called “metallographic” [1]. As a rule, such experiments are performed with optical and scanning (or, less often, transmission) electron microscopy. The aim of the other approach is to study a crystal lattice, namely, its preferred orientation (texture), internal stresses, etc.; such studies, as a rule, are conducted using x-ray diffraction. The methods used in this approach can conventionally be called “x-ray diffraction” methods [2]. For a long time, these two approaches to the integrated description of a microstructure were employed independently and they helped make it possible to achieve significant progress in studying structural evolution during heat or mechanical treatment.

However, to refine the knowledge of certain processes occurring in solids (e.g., martensitic transformations, twinning, fragmentation), it is necessary to obtain qualitatively novel information that could not be obtained by using these two approaches separately. A technique is needed that combines these two approaches and allows the determination of local crystallite orientations. Until recently, this problem had been solved using only one method, namely, transmission electron microscopy (TEM). A fundamentally new method for microstructural studies in which the spatial orientation distributions are examined makes it possible to measure a radically new microstructural characteristic, the misorientation of neighboring crystallites. This method, alongside other factors, has given impetus to the rapid development of the concepts of plastic flow of metals at the stage of large (developed) deformation [3].

The recently developed method of automatic analysis of electron backscattering diffraction patterns (EBSD analysis) likewise enables one to study spatial orientation distributions. In this respect, this method competes with TEM. Currently, EBSD is being more and more extensively applied to investigate the microstructure of crystalline materials. However, we believe there is a lack of publications in Russia dealing with the analysis of the specific features, advantages, and disadvantages of this new method as compared to the traditional TEM method. This circumstance makes it difficult to interpret EBSD data and compare them with TEM results.

The goal of this work is to compare the EBSD-scanning method and TEM as applied to investigate spatial orientation distributions. We hope this information will prove useful in studies with an EBSD attachment and in interpreting experimental data obtained with this attachment.

2. EXPERIMENTAL

We studied a germanium single crystal, nichrome alloy Kh20N80 (20% chromium, 80% nickel), and commercial-purity Grade 2 titanium.

With the germanium single crystal, we determined the EBSD-measurement error for the misorientation angle. The nichrome and titanium were used to experimentally determine the limiting permissible error in determining the orientation by using EBSD. We chose

1063-7834/05/4707-1258$26.00 © 2005 Pleiades Publishing, Inc.

Table 1. EBSD-scanning conditions

EBSD-scanning parameters	Material		
	Kh20N80	germanium single crystal	grade 2 titanium
Microscope type	Philips XL-30 JSM-840A	JSM-840A	JSM-840A
Software for EBSD scanning	TexSEM Lab.(TSL) INCA Crystal 300	INCA Crystal 300	INCA Crystal 300
Accelerating voltage, kV	20 20	20	20
Scanning grid	Hexagonal Square	Square	Square
Number of scanned regions	1 1	4	1
Scanning area, μm^2	100×100 131×61.5	72×47	260×80
Scanning step, μm	0.2 1	1	2
Total number of scanned points	288 711 7620	3220	4953

titanium and nichrome as the objects of investigation for this purpose, since they differ significantly in terms of their lattice symmetry. The choice of the Kh20N80 alloy was dictated by the fact that it contains a high density of annealing twins (and special Σ3 60°⟨111⟩ boundaries) after a certain thermomechanical treatment. This feature makes this alloy very convenient for performing comparative experimental determination of a misorientation spectrum by using TEM and EBSD.

The Kh20N80 alloy was hot-rolled at room temperature to a 70% reduction and then annealed at 993 K for 2 h in a salt bath. As a result, the alloy underwent primary recrystallization with the formation of a uniform structure with an average grain size of 6 μm and a low dislocation density, which is characteristic of primary recrystallization. The commercial-purity titanium was in the form of a hot-rolled rod, and its structure consisted of equiaxed grains with an average size of 20 μm.

TEM measurements of spatial orientation distributions in the Kh20N80 alloy were performed on a Tesla BS-540 microscope at an accelerating voltage of 120 kV. A detailed description of the experimental procedure can be found in [4]. To determine misorientations, we used a single-reflection technique. A detailed description of this technique and its adaptation to a Tesla BS-540 can be found in [3] and [4], respectively. The essence of the single-reflection technique consists in measuring the laboratory coordinates of several (at least two) reciprocal lattice vectors and calculating the orientation matrix for each crystallite using the information obtained. We determined the orientations of 54 grains and then used them to calculate the misorientations of 134 grain boundaries.

The procedure of EBSD analysis is described in detail in [5]. In general, it consists in the following. A sample (inclined at an angle of 70°) is placed in a scanning electron microscope. An electron beam in the microscope is contracted to its minimum size, and the surface under study is subjected to automatic step-by-step scanning from point to point. Backscattered diffracted electrons at each scanned point form a Kikuchi pattern on a fluorescent screen located inside the microscope chamber; the image from this screen is transferred to a digital video camera. Diffraction patterns taken at each scanned point are averaged, digitized, and automatically identified. Then, the following data are calculated and saved to computer: three Euler angles characterizing the crystallite orientation, the (x, y) coordinates determining the position of a point on the sample surface, a coefficient characterizing the sharpness of Kikuchi lines, a coefficient specifying the probability of correct orientation determination, and the phase of the material. This process is repeated until the given surface area of a sample is scanned. In this way, we find the spatial distribution of crystallite orientations on the polished-section surface to be studied. The conditions of EBSD scanning of the materials under study are given in Table 1.

In all cases, we described misorientations using a description with the minimum misorientation angle of all crystallographically equivalent descriptions. To attribute a misorientation to a special boundary, we used the Brandon angle criterion.

3. RESULTS AND DISCUSSION

3.1. Analysis of the Advantages and Disadvantages of EBSD Scanning as Compared to TEM

When studying spatial orientation distributions, EBSD analysis has a number of advantages, which make it not only competitive with TEM but even preferable in some cases. The most substantial advantages and our comments are given below.

3.1.1. Advantages of the EBSD Analysis

3.1.1.1. Less labor-intensive preparation of samples. In many cases, the requirements imposed on samples for EBSD analysis are not much more stringent than those for ordinary metallographic examination. Emphasis is usually placed on three factors. First, there must not be any oxide film on the sample surface, since this film can substantially hinder or even falsify scanning results. Second, surface-roughness requirements are more stringent, since a sample is inclined at a significant angle during EBSD recording and even a small relief can significantly hinder examination. Third, a surface to be studied must not be damaged during the preparation of the sample for the experiment. This requirement is especially important for materials that can easily generate twins, e.g., for titanium; a high content of twins forming upon polishing can substantially change the misorientation spectrum. However, even under these restrictions, a sample for EBSD analysis is much easier to prepare than a thin foil in many cases. Another advantage of the EBSD analysis is the possibility of studying bulk samples, since a significantly larger surface area to be examined provides more representative results from a statistical standpoint. Moreover, a wider range of samples, from thin foils to bulk samples, can be investigated.

3.1.1.2. Simplicity and accessibility. Complete automation of both the process of obtaining information and its processing facilitates investigations. Decreasing the amount of human labor substantially decreases the qualifications required for an operator. Even recently, misorientation studies have been rather rare and have been considered an art because of the strict skills required by the researcher for the obtainment and processing of data. The increased number of recent publications dealing with misorientation measurements (mainly performed using EBSD) suggests that such investigations are gradually becoming a regular occurrence and will eventually become routine.

3.1.1.3. High objectivity upon obtaining primary information (by analyzing electron diffraction patterns). This advantage stems, first, from the exclusion of the human factor (error) and, second, from the more comprehensive analysis of the electron diffraction patterns. For example, in many cases, a large number of Kikuchi lines and poles are present in the electron diffraction patterns. Although it suffices to identify two Kikuchi poles in order to determine the orientation of a crystallite, a software program can analyze all of their possible combinations (by extrapolating the Kikuchi lines that intersect beyond the electron diffraction pattern). Therefore, as a rule, a few solutions are obtained and arranged according to their probabilities. The solution with the maximum probability is chosen. This circumstance also ensures relatively high objectivity for subsequent data processing, e.g., for the rejection of low-probability results. In [5], orientations were determined both by several independent operators and using a software program. The computer determination of the orientations was found to be more accurate.

3.1.1.4. High productivity. Complete automation of the process, the use of high-speed processors, and modern methods of image processing (subtraction of the background of an electron diffraction pattern, the Hough transforms of Kikuchi patterns [6], etc.) ensure a data-processing rate of 1 to 25 points (electron diffraction patterns) per second. Moreover, it is possible to operate for a long time without a break. In principle, the scanning time is only limited by the life of a cathode (this is especially important for thermionic cathodes) and by the extent of contamination of a sample surface during an experiment. As shown in [7], the use of microscopes with field-emission cathodes allows scanning for a few days without a break.

3.1.1.5. Significantly larger statistical sample of experimental results. This advantage is a consequence of the advantages described in Subsections 3.1.1.1 and 3.1.1.4 and is one of the key advantages, since many structural characteristics are statistical in nature; a large sample means a better approximation to reality. This statement refers to comprehensive study of the distribution of structural characteristics rather than to calculating their average values. For the description of such a distribution to be most accurate, the relation between the number of intervals n in a histogram and the size of the experimental sample (the number of measurements) N should be $n \sim N^{1/3}$ [8]. In other words, for a sample of 1000 measurements, the most correct histogram should contain 10 intervals. Thus, an increase in the sample size leads to decreased intervals in a histogram (and to an increased number of intervals) and, as a consequence, to the possibility of describing a distribution more accurately. For example, the maximum misorientation angle in α titanium is about 93.8° for the description with a minimum angle. A sample of 30000–40000 grain boundaries (which is impossible for TEM studies) allows a distribution to be constructed in steps of 3°, which makes the description fairly accurate. It should be noted that EBSD scanning describes misorientation distributions using the boundary length rather than the number of boundaries, which is better grounded from a physical standpoint in some cases.

3.1.1.6. Large amount of diverse information obtained in one scanning. This advantage is a result of the statistical sample being relatively large and the standard software used with an EBSD attachment; in the case of TEM, this information is either used in single instances or is not used at all. Above all, we note the possibility of not only obtaining microtexture data but also comparing the orientations measured using EBSD and x-ray diffraction (XRD). We also note a number of advantages of the EBSD analysis as compared to standard XRD analysis. First, since EBSD scanning provides complete information on a crystallite orientation in a scanned area, full pole figures can be constructed for any plane of interest. We recall that pole figures constructed using XRD (the tilt method), as a rule, are incomplete (up to 65°–75°) and that constructing a pole figure for each plane would requires a separate experiment. Second, the possibility of constructing inverse pole figures (IPFs) for a few external directions is an advantage. As a rule, the software makes it possible to construct them for at least three directions: the normal to a sample surface and two preferred directions in this plane. However, since there is complete information on the orientation, one can process this information for any external direction. Note that constructing an IPF for a new direction using standard XRD analysis would require an additional experiment and is not always possible. For example, it is impossible to construct an IPF for a foil sample in the rolling direction. Third, the orientation at each scanned point is determined experimentally during EBSD analysis. Therefore, the orientation distribution function plotted from these data is more correct than in the case of XRD (where the orientation distribution function is calculated rather than measured directly) [5].

Given the spatial orientation distribution, one can derive information on the size of building blocks; that is, one can determine the average grain size and construct the size and specific-area distributions of grains for a scanned surface. As a rule, the concept of a “grain” can vary; that is, one can vary the minimum misorientation angle of a boundary that completely borders a crystallite. The grain size is frequently taken to be the diameter of a circle whose area is equal to the grain cross-sectional area [the so-called equal circle diameter (ECD)] rather than the length of a random secant, which is usually applied in metallography. The use of the ECD is especially convenient in cases where a change occurs both in the grain shape (e.g., its elongation) and in the grain size during structural evolution; the use of ECD instead of the length of a random secant allows one to detect the instant of grain refinement more reliably.

3.1.1.7. Less labor-intensive separation of phases. EBSD analysis offers this advantage when studying multiphase materials (e.g., simultaneously analyzing up to six different phases with INCA Crystal 300). Owing to its large statistical sampling, EBSD analysis can also be used to determine the percentage ratios of phases.

It should be noted that these studies can also be performed using TEM and, as shown in [9], even unknown phases can be identified in certain cases.

3.1.2. Disadvantages of EBSD analysis

Apart from its obvious advantages, EBSD analysis also has disadvantages, which are discussed below.

Table 2. Determination of the measurement error for the misorientation angle measured by EBSD scanning

Maximum permissible error in orientation determination, deg	Number of misorientations above 0°	Maximum misorientation, deg
1	5954	0.79
2	3049	1.41
3	3789	1.06
4	1529	1.65

3.1.2.1. Lower accuracy of orientation determination. As has been indicated in the literature, this accuracy is 1°. Thus, the error in determining the misorientation angle is about 2° (for comparison, the error in determining the misorientation angle by using the single-reflection technique (TEM) is about 0.5° [4]). The main problem resulting from this large error is that one cannot reliably detect grain boundaries with a misorientation angle of less than 2°; as a rule, misorientation angle distributions of boundaries are constructed starting from 2° or above. Therefore, the EBSD examination of low-angle boundaries and the EBSD determination of the relation between low-angle and high-angle boundaries are rather conventional. For this reason, we believe that it is more helpful to use EBSD analysis to study variations in these structural parameters (rather than their absolute values) when a material is subjected to an external action (e.g., deformation).

In certain EBSD attachments (e.g., INCA Crystal 300), this problem can be solved by decreasing the permissible error for determining the orientation (or by increasing the level of confidence for determining the orientation) upon scanning. The points at which the orientation is determined with an insufficient confidence probability (so-called black points) are rejected (excluded from further consideration). To reveal the error in determining the misorientation angle, we carried out EBSD scanning of a germanium single crystal at different tolerances for orientation determination. The results are given in Table 2.

The results of scanning are shown in Fig. 1. It is seen that, at the minimum error of orientation determination, the most probable error for the misorientation angle is 0.05° and the maximum error does not exceed 0.75°.[1] An increase in the tolerance does not change the most probable error of orientation determination, and the maximum error shifts gradually to reach approximately 1.5°. Thus, our experiment shows that, with EBSD scanning, a misorientation can be determined with an accuracy comparable to that of TEM. However, decreasing the tolerance for orientation determination

---

[1] When the maximum permissible error of orientation determination was less than 1°, the software program could not determine a misorientation; at a permissible error above 4°, high-angle misorientations appeared.

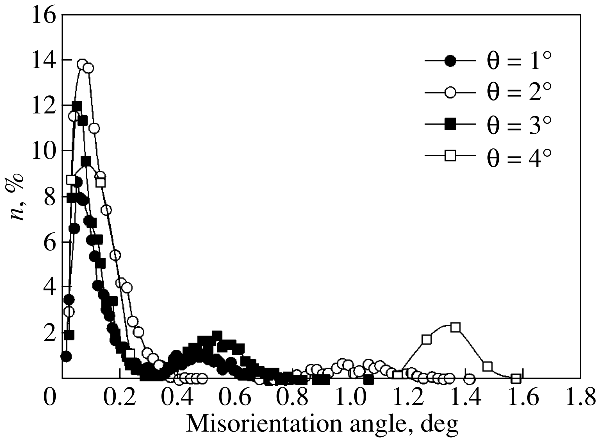

Fig. 1. Effect of the maximum permissible error in orientation determination θ on the misorientation angle distribution in a germanium single crystal (EBSD scanning).

is fraught with the rejection of a large number of points and, thus, with the loss of a significant body of potentially important information. Hence, in each specific case, a researcher should either find a compromise between the measurement accuracy and the body of information obtained or perform several scannings with different tolerances.

3.1.2.2. Lower spatial resolution. Upon TEM examination, a crystal lattice can be resolved directly and orientations can be determined for crystallites (as small as several nanometers in size) that are capable of generating single reflections [4, 9]. The resolution of EBSD analysis is specified by the volume of a material that backscatters electrons having an energy sufficient for them to reach a detector. In turn, this volume depends on both the microscope parameters (the accelerating voltage, the cathode heater current, the current through a sample) and the material (the larger the atomic number of an element, the smaller the volume). The spatial resolution can be roughly estimated as follows. If a structure revealed during EBSD scanning is similar (in morphology and size) to the structure revealed by other methods (e.g., TEM), the spatial resolution is satisfactory. Otherwise, the resolution is most likely unsatisfactory. An analysis of the data from [7, 10] indicates that, for thermionic cathodes, the spatial resolution varies from 0.5 to 0.1 μm while, in the case of field microscopy, this resolution is several tens of nanometers. Thus, in most cases, EBSD scanning can be used to study a structure with a characteristic size of down to a fraction of a micron. For example, submicrocrystalline materials were successfully investigated in [7, 10].

3.1.2.3. Discreteness in orientation determination. During EBSD scanning, as noted above, the crystallite orientation is measured at certain points on a surface to be studied, which are specified by the scanning grid and the scanning step. As a rule, the surface is thoroughly polished and structural features (especially fine features) are invisible; therefore, choosing the correct scanning step is a problem. If the scanning step is large, certain boundaries can be omitted; this is especially true of low-angle boundaries, which are not spaced far apart. At a relatively small scanning step (e.g., 0.05–0.1 μm), it is highly probable that all boundaries (with a misorientation angle of higher than 2°!) would be recorded in a selected area. However, as the scanning step decreases, the area to be studied also decreases (at the same recording time). When a relatively coarse-grained structure is examined, the entire area of scanning can fall inside either one grain or one grain boundary. Therefore, the fraction of high-angle grain boundaries can be overestimated (or underestimated, respectively). Moreover, scanning results are unlikely to be statistically representative in this case, since they are substantially determined by the orientations of this grain and the neighboring grains. Examination of an area at a minimum scanning step requires a long time and, hence, cannot always be accomplished (e.g., because of a limited cathode life).

In these cases, it seems reasonable to perform a few scannings at different steps for the same structure and to use the totality of information to analyze the structure. In particular, to study the relation between the fractions of low-angle and high-angle boundaries and to examine an array of low-angle boundaries, it is recommended that data obtained at a minimum scanning step be used. When an array of high-angle grain boundaries or of special and near-special boundaries (which are usually high-angle) is analyzed, it is better to use the results of scanning at a step at which the number of high-angle grain boundaries becomes statistically representative.

3.1.2.4. Significant deterioration of the scanning quality with increasing lattice microstrain. This deterioration occurs due to the smearing of Kikuchi lines and results in a decreased probability of correct orientation determination (or even in incorrect determination) and, correspondingly, in a significant increase in the fraction of the so-called wrong points and black points. Because of this, accurate interpretation of the experimental data becomes difficult.

However, this fact does not mean that such materials cannot be studied using EBSD. Our experience and the data from [7, 10] indicate that these materials can be analyzed in many cases. The methods for obtaining information can conventionally be divided into three groups.

First, experience suggests that there is a substantial potential for increasing the quality of EBSD information at the stage of recording. This potential consists in the following:

(a) scanning an as-prepared surface that has been thoroughly polished immediately before scanning;

(b) choosing a compromise combination of the accelerating voltage, the cathode heater current, and the sample current to reach the minimum beam size that provides for a still sufficient intensity of backscattered electrons (field-emission microscopy is highly desirable in this case);

(c) averaging images of several Kikuchi patterns taken from the same scanned point;

(d) increasing the time it takes for an orientation to be determined at each scanned point; and

(e) using modern achievements in image processing (subtraction of the background of an electron diffraction pattern, the Hough transform, etc.), which allow a computer to detect even rather weak and smeared Kikuchi patterns that cannot be detected by the human eye.

Second, the efficiency of scanning results can be enhanced even at a relatively high content of black points and wrong points.

Vorhauer *et al.* [10] proposed a method for extracting information on the average grain size under conditions with a relatively high content of black points. They proposed constructing a misorientation angle distribution as a function of the distance between scanned points. In other words, they proposed measuring misorientations not only between neighboring points but also between second, third, and more distant neighbor points. It was found that, as the distance between scanned points increases, the content of low-angle boundaries gradually decreases and virtually disappears at a certain distance between the points. This distance was considered in [10] to be the equivalent of the average grain size. It was emphasized in [10] that, with this method of data processing, the information obtained can be used more completely. We would like to add that, in this case, it is also useful to consider the misorientation spectrum obtained for the misorientations of all possible permutations of scanned points (so-called uncorrelated distribution). Its comparison with a real spectrum (involving misorientations only between neighboring points) will enable one to determine the relation of the uncorrelated distribution to texture.

Unlike black points, which carry no information on the structure, wrong points carry distorted information. Therefore, wrong points are much more dangerous from the standpoint of interpreting results; hence, it is desirable to eliminate these points. However, this is not easy, since, in contrast to black points (which are clearly visible in EBSD-scanning maps), wrong points can only be identified from indirect signs. The criterion for their determination could be a certain error in orientation determination during the interpretation of a Kikuchi pattern. To estimate this error, we carried out the following experiment: the software was adjusted to titanium (hcp lattice) but was applied to scans of nichrome (fcc lattice). In addition, we performed an inverse experiment in which titanium was scanned using software adjusted for nichrome. In this way, we modeled a situation where the computer solution was wrong in advance. Orientations were determined by the software program with a relatively large error. The error distribution is shown in Fig. 2. It is seen that, beginning from an error of 3.5°–4°, the EBSD-scanning results are extremely questionable. Note that this finding correlates with the data given in Fig. 1; specifically, if the tolerance is higher than 4°, high-angle misorientations are detected during scanning of the single crystal (i.e., the result is obviously wrong). Thus, the scanned points with this error were qualified as wrong points in orientation determination and were rejected (eliminated from consideration).

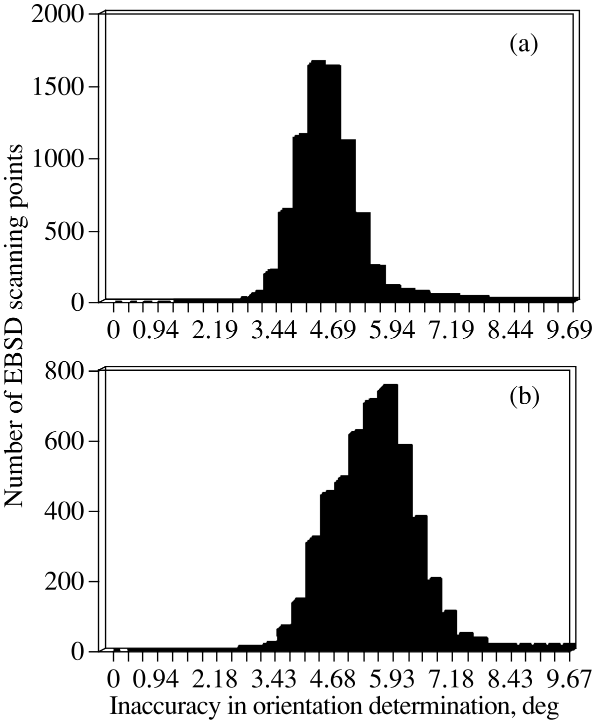

Fig. 2. Frequency distribution of the inaccuracy in orientation determination: (a) nichrome EBSD scanned as “titanium” and (b) titanium EBSD scanned as “nichrome.”

Apart from rejecting points, the software program can also automatically change the orientations of questionable points. During this operation, to each questionable point is assigned the orientation of one of the adjacent points whose orientation is determined with a minimum error. A similar procedure can also be used to eliminate black points. However, it should be remembered that this procedure actually entails falsification of the experimental data. Therefore, wherever possible, this procedure should be avoided, and questionable points should simply be rejected.

Third, in extreme cases (when information cannot be obtained using other methods), it is recommended to subject a material to a low-temperature annealing to relieve internal stresses. In some cases, this approach gives excellent results [7]. However, it is necessary to carefully choose the heat-treatment conditions in order to exclude changes in the spatial orientation distribution (e.g., due to recrystallization).

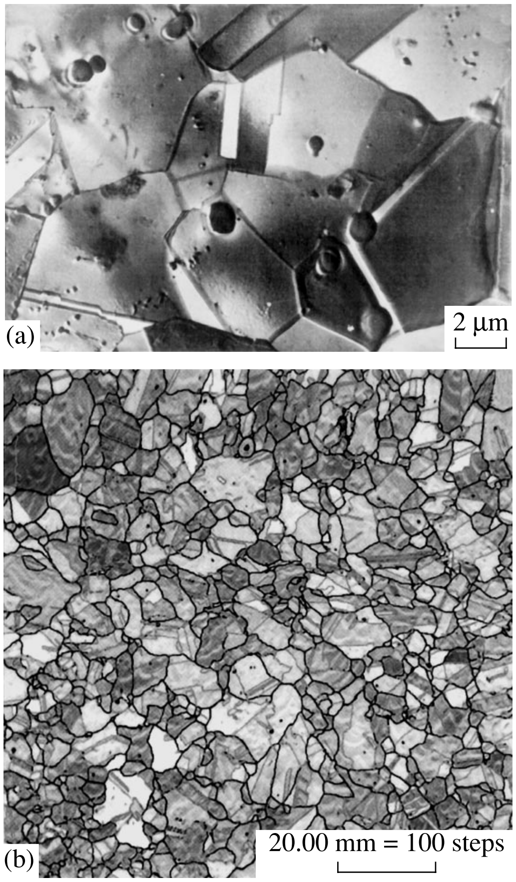

Fig. 3. Microstructure of a Kh20N80 alloy: (a) TEM and (b) EBSD map.

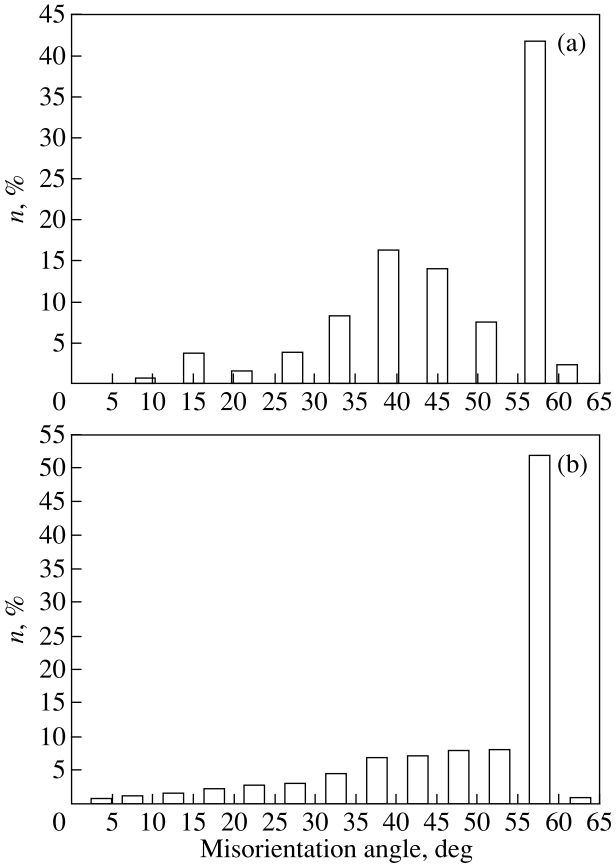

Fig. 4. Misorientation angle distribution of boundaries in nichrome: (a) TEM and (b) EBSD. The distribution is over the number of boundaries for TEM and over the boundary lengths for EBSD.

3.1.2.5. Conventionality of the computer representation of a real structure. (i) Depending on the scanning grid, a certain shape (e.g., a square or a hexagon) is assigned to each scanning point; thus, a real structure is "reconstructed" from these geometrical figures. If the scanning step is small as compared to the crystallite size, this reconstruction is virtually invisible; however, if they are comparable, the representation of a real crystallite shape is distorted.

(ii) The misorientation spectrum obtained can depend on the scanning grid chosen (quadratic, hexagonal, etc.), i.e., on the number of neighbors near each point. In order to obtain as much information as possible, it is recommended that a scanning grid be used that provides the maximum number of neighbors for each point.

Table 3. Relation between low-angle and high-angle grain boundaries in nichrome examined by TEM and EBSD

Boundary type	TEM	EBSD
Low-angle boundaries (misorientation angles up to 15° inclusive)	0.50	3.55
High-angle boundaries (misorientation angles above 15°)	99.5	96.45
Total boundary length, μm	240	23813.8

EBSD scanning is still an unusual method for structural studies. Its specific features and disadvantages necessitate experimental verification on a real polycrystalline structure. In the next subsection, we compare the misorientation spectra of the Kh20N80 alloy constructed using TEM and EBSD. Unless otherwise specified, the misorientations are reduced to the total boundary length.

3.2. Experimental Study of the Misorientation Spectrum of a Test Material by Using EBSD Scanning and TEM

The microstructure of the Kh20N80 alloy, observed in a transmission electron microscope, and its EBSD-scanning map are shown in Fig. 3. It is seen that these images are very similar. In both cases, the microstructure consists of approximately equiaxed grains (metallographic texture is absent) with clear, relatively straight-line boundaries. The microstructure also features a significant number of crystallites approximately rectangular in shape (annealing twins) located inside coarser equiaxed grains. As is seen from Table 3, the misorientation spectra in both cases are characterized by predominant high-angle grain boundaries, whose content exceeds 95%. It should be noted that the total length of low-angle boundaries revealed with TEM is slightly lower than that revealed with EBSD (approximately 1 and 5%, respectively).

As follows from Fig. 4, the misorientation angle distributions of boundaries measured using these two different methods are qualitatively very similar. The two histograms are characterized by a sharp peak near a misorientation angle of 60° and a weaker maximum near 40°, which is revealed more clearly by TEM. Small quantitative differences should be noted: the peak at about 60° is more pronounced in the EBSD spectrum, and the peak at about 40° is better defined in the TEM spectrum.

The contents and ranges of special and near-special boundaries revealed by both methods are given in Table 4. The results obtained using these two experimental methods are seen to be very similar both qualitatively and quantitatively. Indeed, the total contents of special boundaries virtually coincide, misorientation $\Sigma3$ dominates in all cases, and the content of misorientations $\Sigma9$ and $\Sigma27$ is elevated. However, there are small quantitative discrepancies: the contents of $\Sigma3$, $\Sigma9$, and $\Sigma27$ as revealed by TEM are slightly higher, and, on the contrary, the contents of the other misorientations are lower (most of them are altogether absent).

Table 4. Percentage of special boundaries in nichrome measured by TEM and EBSD

Special boundary	TEM	EBSD
$\Sigma3$	**50.7**	**49.55**
$\Sigma5$	0.30	0.36
$\Sigma7$	0.00	0.39
$\Sigma9$	**4.9**	**2.85**
$\Sigma11$	0.00	1.00
$\Sigma13$	0.00	0.75
$\Sigma15$	0.00	0.21
$\Sigma17$	0.00	0.32
$\Sigma19$	0.00	0.46
$\Sigma21$	0.00	0.35
$\Sigma23$	0.00	0.11
$\Sigma25$	0.00	0.29
$\Sigma27$	**3.2**	**1.38**
$\Sigma29$	0.00	0.56
Total content of boundaries	59.6	62.56

Note: The boundaries whose content exceeds 1% are in boldface.

Thus, the misorientation spectra obtained with TEM and EBSD are qualitatively similar and are characterized by the following common features: a predominance of high-angle grain boundaries; similar shapes of the misorientation angle distributions of boundaries; and high contents of special boundaries, in particular, $\Sigma3$ boundaries. Moreover, the quantitative characteristics of the spectra determined using both methods are also quite similar. The slight discrepancies (in the relations between low-angle and high-angle boundaries and the contents of special boundaries) are likely due to the much larger statistical sampling in EBSD or to the procedures used for constructing misorientation angle distributions (distributions over the number of boundaries for the case of TEM and distributions over the boundary length in the case of EBSD).[2] However, these differences are unlikely to be fundamental; therefore, we can conclude that both methods for examining microstructures give reproducible results. On the one hand, this finding suggests that our experimental results reflect the real state of things, and, on the other, these results imply that EBSD analysis can be used to study real polycrystalline structures.

4. CONCLUSIONS

We have compared the advantages and disadvantages of EBSD scanning as compared to TEM when studying spatial orientation distributions. The advantages of EBSD analysis are the following: the possibility of examining bulk samples, less labor involved in the sample preparation, a wider range of samples, simplicity and accessibility for users, high objectivity of the analysis of electron diffraction patterns, high productivity, the possibility of operating for a long time without a break, a significantly larger statistical sample of experimental results, the possibility of studying orientation distributions over grain boundary lengths, the possibility of obtaining a large amount of diverse information in one scanning, and less labor required to separate phases when studying multiphase materials. The disadvantages of EBSD analysis are the following: a lower accuracy of orientation determination, a lower spatial resolution, discreteness in orientation determination, significant deterioration of the scanning quality with an increase in lattice microstrain, and the conventionality of the computer representation of a real structure. The misorientation spectrum of a test Kh20N80 alloy has been studied using TEM and EBSD. The reproducibility of the results obtained by both techniques implies that EBSD analysis can be used to study real polycrystalline structures.

---

[2] When morphologically anisotropic (e.g., fibrous) structures are studied, the results obtained using these two procedures will be likely to differ much more strongly.

ACKNOWLEDGMENTS

This work was supported by the Russian Foundation for Basic Research, project nos. 04-02-16129, 04-02-97261, and 04-02-17627.

REFERENCES

1. S. A. Saltykov, *Stereometric Metallography* (Metallurgiya, Moscow, 1976) [in Russian].
2. S. S. Gorelik, Yu. A. Skakov, and L. N. Rastorguev, *X-ray and Electron-Optical Analysis* (Mosk. Inst. Stali Splavov, Moscow, 1994) [in Russian].
3. V. V. Rybin, *Large Plastic Deformations and Fracture of Metals* (Metallurgiya, Moscow, 1986) [in Russian].
4. V. Yu. Gertsman, V. N. Danilenko, and R. Z. Valiev, Fiz. Met. Metalloved. **68** (2), 348 (1989).
5. B. L. Adams, S. I. Wright, and K. Kunze, Met. Trans. A **24**, 819 (1993).
6. N. C. K. Lassen, K. Conradsen, and D. Juul-Jensen, Scanning Microsc. **6**, 115 (1992).
7. A. Gholinia, P. B. Prangnell, and M. V. Markushev, Acta Mater. **48**, 1115 (2000).
8. M. A. Stremel', *Strength of Alloys* (Mosk. Inst. Stali Splavov, Moscow, 1999), Part 1, p. 326 [in Russian].
9. I. I. Kryukov, E. V. Nesterova, V. V. Rybin, and A. I. Rybnikov, Fiz. Met. Metalloved. **52** (4), 880 (1981).
10. A. Vorhauer, T. Hebesberger, and R. Pippan, Acta Mater. **51**, 677 (2003).

Translated by K. Shakhlevich

Physics of the Solid State, Vol. 47, No. 7, 2005, pp. 1267–1272. Translated from Fizika Tverdogo Tela, Vol. 47, No. 7, 2005, pp. 1226–1231.
Original Russian Text Copyright © 2005 by Dubinin, Loshkareva, Teploukhov, Sukhorukov, Balbashov, Arkhipov, Parkhomenko.

DEFECTS, DISLOCATIONS,
AND PHYSICS OF STRENGTH

Ordering of Oxygen Vacancies in a $CaMnO_{3-\delta}$ Perovskite Single Crystal

S. F. Dubinin*, N. N. Loshkareva*, S. G. Teploukhov*, Yu. P. Sukhorukov*, A. M. Balbashov, V. E. Arkhipov*, and V. D. Parkhomenko***

** Institute of Metal Physics, Ural Division, Russian Academy of Sciences, ul. S. Kovalevskoĭ 18,*
Yekaterinburg, 620219 Russia
e-mail: dubinin@uraltc.tu
*** Energy Research Institute, Russian Academy of Sciences, ul. Vavilova 44/2, Moscow, 117935 Russia*

Received October 22, 2004

Abstract—The structure of a $CaMnO_{3-\delta}$ perovskite single crystal was studied for the first time using thermal neutron diffraction in the temperature range 300–840 K. It was detected that oxygen vacancies in the crystal are ordered into two types of superstructure. A phase with a relative number of vacancies $\delta = 1/4$ occupies the largest volume fraction of oxide (~75%); the other volume is occupied by a superstructure with a lower vacancy content ($\delta = 1/5$). The oxygen deficiency in the crystal lattice was determined to be $\delta = 0.238$. The mechanism of oxygen vacancy ordering in the oxide is discussed taking into account its charge state. *© 2005 Pleiades Publishing, Inc.*

The compounds $CaMnO_{3-\delta}$ belong to a wide class of nonstoichiometric $ABO_{3-\delta}$ oxides with a perovskite structure. In these compounds, excess electrons are donated by oxygen vacancies rather than by an isovalent impurity. Relatively long ago [1], it was indicated that oxygen vacancy ordering can occur in oxygen-deficient perovskites (with respect to the stoichiometric composition). At small values of the parameter δ, oxygen vacancies are randomly arranged in the lattice of these oxides. However, as δ increases, an interaction between vacancies arises and an ordered arrangement of these defects in the lattice becomes energetically favorable. In this case, the electrical neutrality of an oxide with defects is provided by an adequate decrease in the valence of transition-metal ions. Currently, the values of δ in the $CaMnO_{3-\delta}$ compound near which superstructures of oxygen vacancies can exist are known. By using electron powder diffraction, these values were determined in [2] to be

$$\delta_1 = 0.2, \quad \delta_2 = 0.25, \quad \delta_3 = 0.333, \quad \delta_4 = 0.5. \qquad (1)$$

The main objective of this work is to study order parameters of oxygen vacancies in a $CaMnO_{3-\delta}$ single crystal with a relatively low oxygen deficiency ($0.2 < \delta < 0.25$). In this case, the required experimental sensitivity, namely, a sharp contrast of oxygen vacancies in the lattice, was achieved by using thermal-neutron diffraction. Indeed, the amplitude of nuclear scattering of neutrons for oxygen ions is largest among the chemical elements in the oxide: $b_O = 0.58 \times 10^{-12}$ cm, $b_{Mn} = -0.37 \times 10^{-12}$ cm, and $b_{Ca} = 0.47 \times 10^{-12}$ cm [3].

The $CaMnO_{3-\delta}$ single crystal for neutron diffraction studies was grown in the Energy Research Institute by using float-zone melting in a URN-2-ZM furnace in an argon atmosphere, which is reducing, in contrast to air and oxygen. Polycrystalline samples needed to grow the crystal were prepared using a solid-phase reaction from $CaCO_3$ and Mn_3O_4 in stoichiometric ratio. The initial synthesis was carried out at a temperature of 1100°C for 10 h. The ceramics obtained was ground, sifted, and pressed into a cylindrical rod. Final annealing was performed at 1250°C for 10 h. The single crystal growth rate was 9.5 mm/h at 1000°C in an annealing furnace placed immediately below the crystallization front. The grown crystal was annealed again at 1000°C for 3 h and then was cooled slowly (for 5 h) to room temperature. The crystallization chamber atmosphere during the growth and annealing was maintained by high-purity argon flowing at a rate of 10 l/h. The crystalline samples used for measurements were cylinders with linear sizes $d = 3$ mm and $l = 6$ mm. The cylinder axis was approximately parallel to the [001] crystallographic direction.

Experiments with elastic scattering of thermal neutrons were carried out using a special multichannel diffractometer for studying single crystals [4]. The incident neutrons were formed by a double-crystal monochromator made of pyrolytic graphite and deformed germanium, and their wavelength λ was 1.567 Å. Highly monochromatized primary beams and an optimum selection of the wavelength of monochromatic neutrons made it possible to almost completely suppress the effects of multiple diffraction harmonics in the neutron diffraction pattern of the single crystal, which significantly improved the sensitivity of the technique. For example, the relative intensity of Bragg

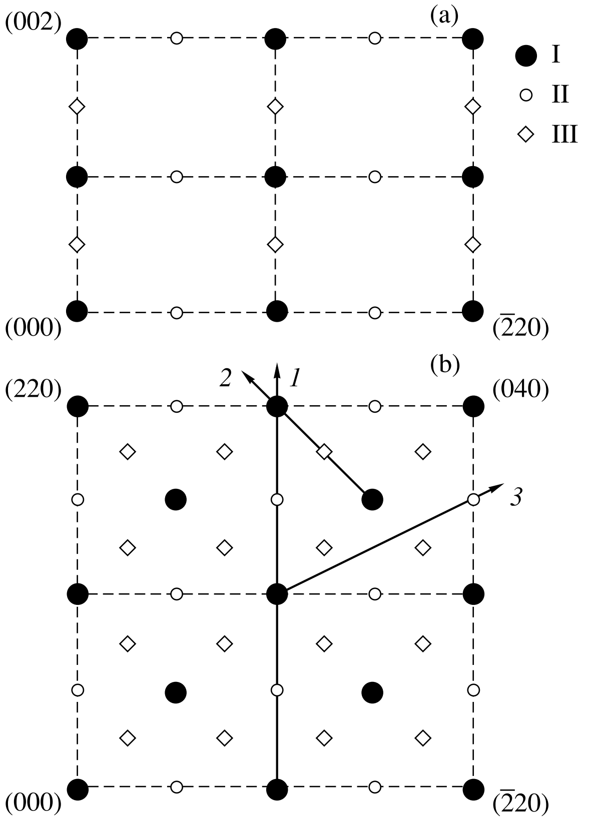

Fig. 1. Positions of (I) structural and (II, III) superstructural reflections in (a) the (110) and (b) (001) planes of the reciprocal lattice of the $CaMnO_{3-\delta}$ perovskite crystal at 300 K.

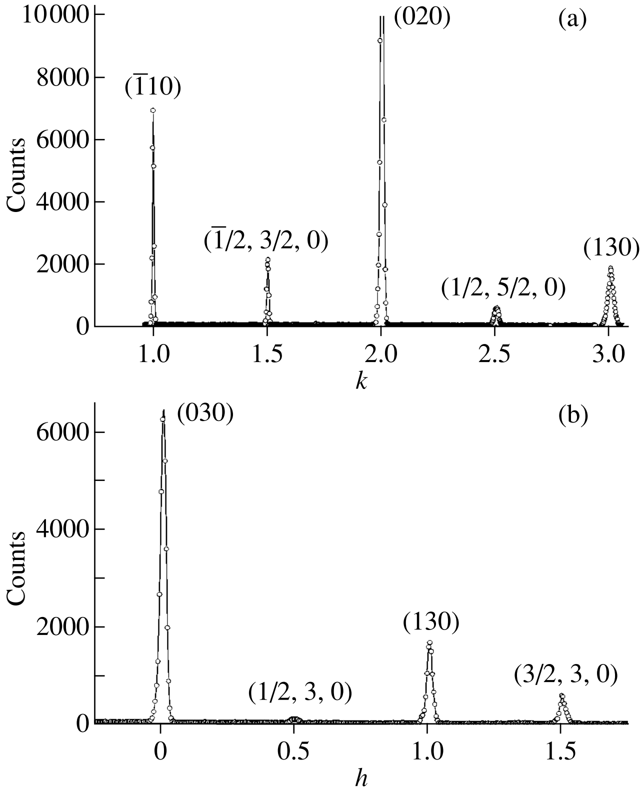

Fig. 2. Neutron scattering pattern of the $CaMnO_{3-\delta}$ crystal measured at 300 K (a) in the [110] direction with respect to the $(\bar{1}10)$ reciprocal lattice point and (b) in the [100] direction with respect to the (030) reciprocal lattice point.

reflections in the x-ray diffraction pattern of a reference oxide crystal, which correspond to the wavelength λ/2, was only 0.02% of the intensity of the main Bragg reflections.

We note once again that appropriate choice of the technique and the use of a single-crystal sample in experiments significantly increase the reliability and accuracy of determination of the periods of possible oxygen vacancy ordering.

Neutron scattering patterns of the $CaMnO_{3-\delta}$ crystal were taken at $T \geq 300$ K. It is known [5] that the compound to be studied is in the paramagnetic state in this temperature range. This circumstance significantly simplifies the interpretation of experimental results, since the diffraction patterns of the crystal do not contain any magnetic Bragg reflections in the paramagnetic region.

Figures 1a and 1b schematically show the neutron diffraction pattern of the crystal in planes of two symmetric sections of its reciprocal lattice, i.e., (110) and (001), respectively. Solid circles (I) correspond to the positions of main structural reflections. The other symbols (II, III) correspond to positions of additional reflections. As an example, Figs. 2a and 2b show two actual diffraction patterns measured at 300 K along the crystallographic directions indicated by straight lines *1* and *2* in Fig. 1b, respectively (the scanning direction is indicated by arrows). As can be seen in Figs. 2a and 2b, all additional maxima are positioned strictly halfway between the main Bragg reflections corresponding to the perovskite cubic structure. In other words, the positions of additional peaks in the scattering pattern coincide with the positions of reflections corresponding to half the wavelength, $\lambda/2 = 0.7835$ Å. As mentioned above, the relative intensity of multiple reflections is $I_{hkl}(\lambda/2)/I_{hkl}(\lambda) = 0.0002$; i.e., it is very small. Under actual conditions of exposure, the strongest multiple-reflection signal does not exceed two counts and cannot be detected in the diffraction pattern. Thus, all additional reflections in Figs. 1a and 1b are not multiple diffraction harmonics and should be considered to be superstructural. This superstructure is characterized by the system of wave vectors

$$\mathbf{q}_1 = (1/2, 1/2, 0)2\pi/a_c, \quad \mathbf{q}_2 = (0, 0, 1/2)2\pi/a_c, \\ a_c = 3.73\ \text{Å}. \tag{2}$$

The superstructural reflections, such as $\mathbf{q}_2$ in the (001) reciprocal lattice plane (Fig. 1b), indicate the existence of structural domains in the $CaMnO_{3-\delta}$ crystal. Vector relations (2) uniquely define the unit cell size of the observed superstructure. Figure 3a (solid lines) shows the cell size in the (x, y) plane. As can be seen in Fig. 3b, the unit cell parameter c is $2a_c$ in the z direction. Figures 3a and 3b show the positions of manganese ions (I) and oxygen anions (II); calcium ions are not shown, since they are not involved in the superstructure formation. Physically, the superstructure unit cell in the crystal can be indicated only by oxygen vacancies (III in Fig. 3). There is only one vacancy per twelve oxygen ions in this cell. Since the unit cell includes four oxide formula units, the number of vacancies per formula unit is obviously $\delta_2 = 0.25$.

Thus, the fact that the ordered arrangement of vacancies with density $\delta_2 = 1/4$ can exist in the bulk $CaMnO_{3-\delta}$ crystal follows even from symmetry considerations. Below, we will substantiate this prediction by directly analyzing the intensities of superstructural and structural reflections.

To substantiate the formation of superstructure (2), it is instructive to consider its temperature dependence in the bulk $CaMnO_{3-\delta}$ crystal. Two mechanisms of thermal destruction of the oxygen vacancy superstructure are possible. One of them is associated with reduction of the sample stoichiometric composition in oxygen (i.e., with a decrease in the parameter δ caused by an increase in temperature). For example, according to the data from [5], the parameter δ becomes zero after annealing of a polycrystalline $CaMnO_{2.84}$ sample in the presence of oxygen at a temperature of 1000 K. This effect is irreversible. The other mechanism is associated with oxygen vacancy mobility at high temperatures. There is an empirical relation between the starting temperature T_S of vacancy motion and the melting temperature of a material T_m [6]:

$$T_S \cong 0.3 T_m. \tag{3}$$

In our opinion, the second mechanism is dominant in a bulk $CaMnO_{3-\delta}$ single crystal. This is confirmed by the temperature dependence of the peak intensity of the $(\overline{1/2}, 3/2, 0)$ superstructural reflection in the range 300–840 K (Fig. 4). We can see from Fig. 4 that the superstructural reflection intensity in the diffraction pattern decreases when the crystal is heated above 530 K. This temperature is close to T_S determined from Eq. (3), where $T_m = 1770$ K is the temperature at which the liquid phase appears in the phase diagram of $CaMnO_3$ [7]. Figure 5 shows rocking curves of the $CaMnO_{3-\delta}$ crystal measured in the vicinity of the $(\overline{1/2}, 3/2, 0)$ reflection at 300 (curve *1*) and 780 K (curve *2*). We can see from Fig. 5 that only the peak intensity depends on temperature, while the reflection width remains unchanged over the temperature range 300–780 K. Moreover, the superstructure reflection intensity recovers its initial value (to within experimental error) after slow cooling of the sample from $T = 840$ K. Thus, the facts presented above count in favor of the conclu-

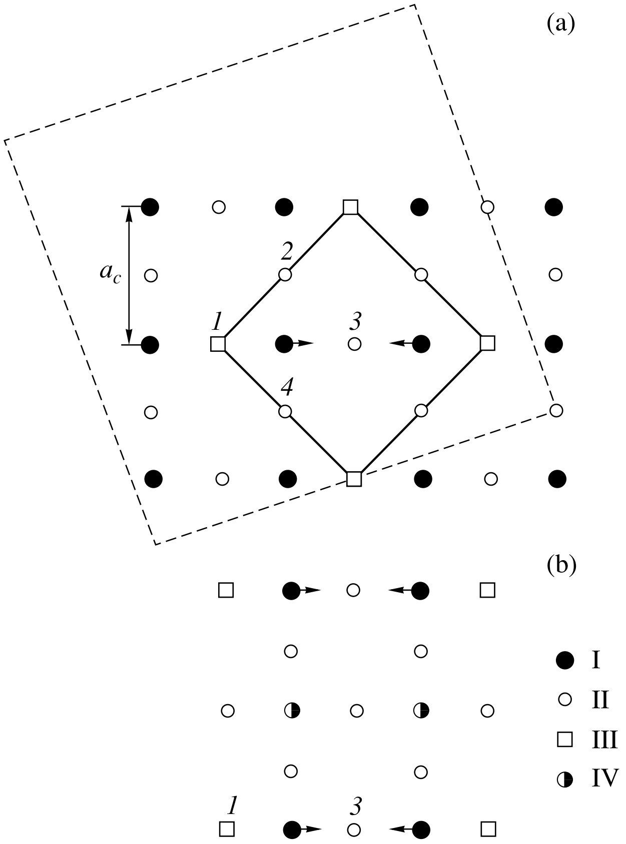

Fig. 3. Oxygen vacancy ordering in the $CaMnO_{2.75}$ perovskite crystal (a) in the (110) plane (the unit cell dimensions are indicated by solid lines) and (b) in the [001] direction (with respect to the *1*–*3* line in panel (a)). I–IV are Mn^{3+}, O^{2-}, oxygen vacancy, and Mn^{4+}, respectively.

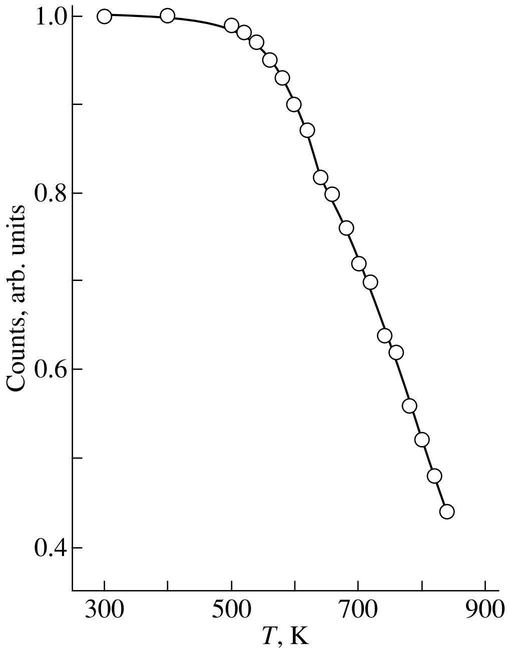

Fig. 4. Temperature dependence of the peak intensity of the $(201)_0$ superstructural reflection in the neutron scattering pattern of the $CaMnO_{3-\delta}$ crystal.

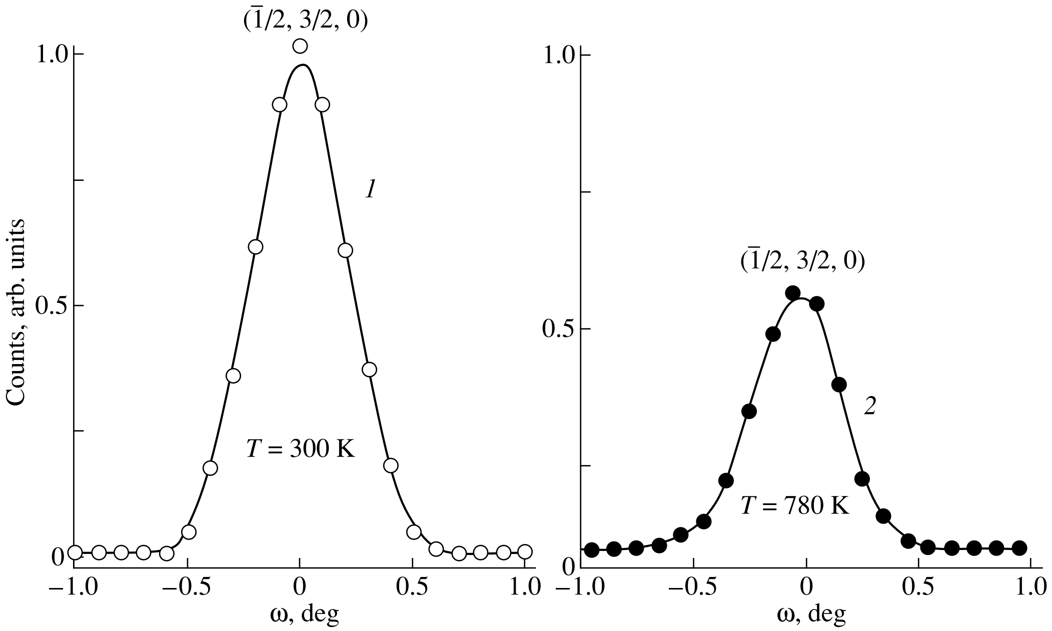

Fig. 5. Rocking curves of the $CaMnO_{3-\delta}$ crystal measured in the vicinity of the ($\bar{1}/2$, 3/2, 0) superstructural reflection at (*1*) 300 and (*2*) 780 K.

sion that the superstructure in the bulk $CaMnO_{3-\delta}$ single crystal is destroyed at not very high temperatures due to oxygen vacancy diffusion.

It should be noted that the oxygen vacancy superstructure described above is the main superstructure but is not the only one in the $CaMnO_{3-\delta}$ crystal. We intentionally did not complicate Fig. 1 and did not indicate the reflections from another superstructure, whose intensities are much lower than those from the main superstructure. Let us determine the unit cell and the volume fraction of the weaker superstructure in the crystal under study. This seems to be instructive, since the result could identify the mechanism of the concentration-induced transition in $CaMnO_{3-\delta}$ between the ordered states specified in Eq. (1).

Figure 6 shows the neutron scattering pattern of the crystal obtained at 300 K in the $[\bar{1}30]$ direction with respect to the (020) reciprocal lattice point. In Fig. 1b, this direction is indicated by line *3*. As can be seen in Fig. 6, the pattern contains the ($\overline{0.3}$, 2.9, 0) superstructure peak in addition to already known structural and superstructural peaks. The wave vector of the second phase is

$$\mathbf{q}_3 = (030) - (\overline{0.3}, 2.9, 0) = (0.3, 0.1, 0)2\pi/a_c. \quad (4)$$

We note that it is practically impossible to determine a wave vector like that in Eq. (4) from neutron powder diffraction data because its orientation in the crystal reciprocal lattice is asymmetric. Using Eq. (4), we can construct the unit cell of the second superstructure. Its dimensions in the $(110)_c$ plane are indicated by dashed lines in Fig. 3a. The cell parameter of the second superstructure in the (xy) plane is $a = [(3a_c)^2 + (a_c)^2]^{0.5} = 3.162a_c$; i.e., it is incommensurate with the perovskite cube parameter. This cell is tetragonal, since its parameter c in the $[001]_c$ direction is identical to the perovskite cube parameter. It can be easily concluded from Fig. 3a that the cell includes 30 oxygen sites (ten formula units), two of which are vacant: one is at a corner of the cell and the other is at the center of a basal face. Thus, the vacancy density per formula unit is $\delta_1 = 0.2$. Two conclusions follow from this fact. First, the existence of two superstructures in one sample suggests that phase separation occurs in the oxide in the case where the parameter δ is not equal to one of the values in Eq. (1). Therefore, the transition from the structure with $\delta_1 = 0.2$ to the superstructure with $\delta_2 = 0.25$ occurs via the formation of nuclei of the new phase and their further growth as the oxygen vacancy concentration increases in the crystal. Second, it is reasonable to assume the existence of a vacancy superstructure with the minimum parameter $\delta_0 = 0.1$. For this ordering, the basic periods are the same as those in Eq. (4). The difference is that oxygen vacancies are arranged only at the corners of the cell bounded by the dashed lines in Fig. 3a.

The volume fraction of the ordered phases in the crystal can be estimated using the simple relation $I(\overline{1/2}, 7/2, 0)/I(\overline{0.3}, 2.9, 0) = 4.5 \cong \nu\delta_2^2/(1-\nu)\delta_1^2$, where ν is the fraction of the main superstructure. Thus, the value of ν in the sample is ≅75% and the average density of oxygen vacancies in the crystal under study is given by

$\delta = 0.75\delta_2 + 0.25\delta_1 = 0.238$. Now, we can calculate the intensities in the neutron diffraction pattern of the $CaMnO_{3-\delta}$ crystal in order to describe in more detail the unit cells of superstructures (2) and (4). As an example, let us carry out this procedure for the superstructure corresponding to an oxygen vacancy content δ_2 in the oxide.

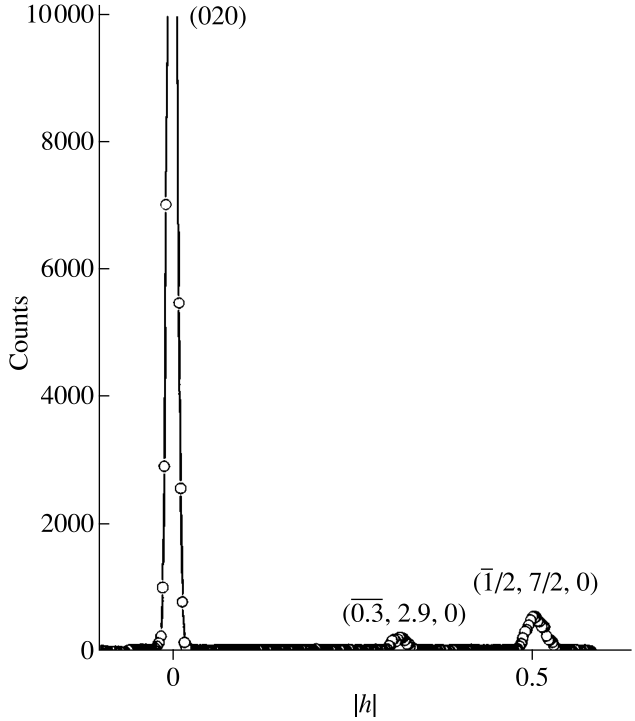

Fig. 6. Neutron scattering pattern of the $CaMnO_{3-\delta}$ crystal taken at 300 K in the $[\bar{1}30]$ direction with respect to the (020) reciprocal lattice point.

The unit cell dimensions for superstructure (2) are shown in Fig. 3, and the atomic coordinates for the unit cell are listed in the table. It is convenient to compare the intensities of the $(\bar{1}10)_c$ structural peak and the $(\overline{1/2}, 3/2, 0)_c$ superstructural reflection. These reflections are closely spaced in the scattering plane and have slightly different intensities in the scattering pattern (Fig. 2a). The experimental ratio of their intensities is $I(\bar{1}10)_c/I(\overline{1/2}, 3/2, 0)_c = 3.3$. Let us compare this value with calculations. In the basis of the superstructure cell, the indices of these reflections will be (200) and (210), respectively. The structure amplitudes for the (200) and (210) reflections can be calculated using the well-known relation

$$F_{hkl} = \Sigma b_j \Sigma_{xyz} \cos 2\pi(hx + ky + lz), \qquad (5)$$

where b_j are the nuclear scattering amplitudes of oxygen, manganese, and calcium. For the (200) structural reflection, the quantity in Eq. (5) is $F_{(200)} = (3 \times 0.58 + 4 \times 0.37 - 4 \times 0.47) \times 10^{-12}$ cm $= 1.34 \times 10^{-12}$ cm. From the expanded form of $F_{(200)}$, it is evident that we took into account the existence of an oxygen vacancy in the cell and that the small structure amplitude is caused, in particular, by the fact that the nuclear scattering amplitudes of manganese and calcium are close in magnitude and correspond to neutron scattering in antiphase. The structure amplitude $F_{(210)}$ is equal to $-1 \times 0.58 \times 10^{-12}$ cm if only the oxygen vacancy is taken into account in Eq. (5). In this approximation, we have $I(\bar{1}10)_c/I(\overline{1/2}, 3/2, 0)_c = F^2_{(200)}/\nu F^2_{(210)} = 7.1$, which substantially exceeds the experimental value. To attain better agreement with experiment, we complicated the unit cell model. The modification is associated with a partial change in the electronic structure of manganese ions in the $CaMnO_{2.762}$ crystal with oxygen vacancies. Indeed, beginning from the stoichiometric $Ca^{2+}Mn^{4+}O_3^{2-}$ perovskite, the generation of one anionic vacancy results in the reduction of $2Mn^{4+}$ to $2Mn^{3+}$. Simultaneously, two $Mn^{4+}O_6$ octahedra are transformed into two $Mn^{3+}O_5$ pyramids in which the Mn^{3+} ion is obviously not a Jahn–Teller ion. Thus, the fraction of Mn^{3+} ions is two times greater than the fraction of oxygen vacancies in $CaMnO_{2.75}$ (Fig. 3). In order to fit the calculated intensities to the experimental data, we assumed that Mn^{3+} ions are displaced into the pyramid by $0.02\sqrt{2}$. The displacement directions are indicated in Fig. 3 by arrows. In our opinion, these displacements reduce the

Atomic coordinates in the basis of the unit cell of the superstructure described by Eqs. (2)

Oxygen ions								Manganese ions				Calcium ions			
nos.	*x*	*y*	*z*	nos.	*x*	*y*	*z*	nos.	*x*	*y*	*z*	nos.	*x*	*y*	*z*
1	0	0	0	7	0	0	1/2	1	1/4	1/4	0	1	3/4	1/4	1/4
2	0	1/2	0	8	0	1/2	1/2	2	3/4	3/4	0	2	1/4	3/4	1/4
3	1/2	1/2	0	9	1/2	1/2	1/2	3	1/4	1/4	1/2	3	3/4	1/4	3/4
4	1/2	0	0	10	1/2	0	1/2	4	3/4	3/4	1/2	4	1/4	3/4	3/4
5	1/4	1/4	1/4	11	1/4	1/4	3/4								
6	3/4	3/4	1/4	12	3/4	3/4	3/4								

local stresses caused by oxygen vacancies in $CaMnO_{2.75}$. Thus, the structure amplitudes and structure factors calculated within our model are $F_{(210)} = -1 \times 0.58 - \cos 292° \times 0.37 - \cos 292° \times 0.37 = 0.85$ and $F^2_{(210)} = 0.72$; so $F^2_{(200)}/\nu F^2_{(210)} = 3.3$, which is in good agreement with the experimental data.

The established fact of Mn^{3+} ion displacements is fundamental, since it indicates that, in the $CaMnO_{3-\delta}$ paramagnetic crystal, there occurs charge ordering, which is closely related to oxygen vacancies. Indeed, on the one hand, Mn^{3+} ions arise in the oxide only in the presence of oxygen vacancies and, on the other hand, cause their long-range Coulomb interaction, via which superstructures (2) and (4) form. Under these conditions, it seems quite natural that separation into two superstructures occurs in an imperfect crystal with an arbitrary value of δ. These superstructures strictly correspond to the δ_1 and δ_2 levels, and even partial disorder in the arrangement of vacancies, which necessarily exists in a single phase, is energetically unfavorable.

ACKNOWLEDGMENTS

The authors are grateful to L.N. Rybin for his assistance in the preparation of single crystals.

This study was supported by the Russian Foundation for Basic Research (projects no. 02-02-16425, 02-02-16429), the federal program for support of leading scientific schools (no. NSh-639.2003.2), the program of the Department of Physical Sciences of the Russian Academy of Sciences “Neutron Studies of Materials Structure and Fundamental Properties of Matter”, and the Ministry of Industry, Science, and Technology of the Russian Federation (contract no. 40.012.1.1.1150).

REFERENCES

1. K. R. Poeppelmeier, M. E. Leonowicz, and J. M. Longo, Solid State Chem. **44**, 89 (1982).
2. A. Reller, J. M. Thomas, and D. A. Jefferson, Proc. R. Soc. London, Ser. A **394**, 223 (1984).
3. I. I. Gurevich and L. V. Tarasov, *Low-Energy Neutron Physics* (Nauka, Moscow, 1965; North-Holland, Amsterdam, 1968).
4. S. G. Teploukhov, V. V. Chernobrovkin, L. A. Vysotskaya, B. N. Goshchitskiĭ, M. B. Dorofeeva, S. F. Dubinin, A. I. Kozlov, and S. K. Sidorov, Instrum. Exp. Tech., No. 3, 37 (1983).
5. J. Briatico, B. Alascio, R. Allub, A. Butera, A. Caneiro, M. T. Causa, and M. Tovar, Phys. Rev. B **53** (21), 14020 (1996).
6. G. J. Dienes and G. H. Vineyard, *Radiation Effects in Solids* (Interscience, New York, 1957; Inostrannaya Literatura, Moscow, 1960).
7. P. V. Muan and A. Riboud, J. Am. Ceram. Soc. **46**, 33 (1963).

Translated by A. Kazantsev

Physics of the Solid State, Vol. 47, No. 7, 2005, pp. 1273–1277. Translated from Fizika Tverdogo Tela, Vol. 47, No. 7, 2005, pp. 1232–1236.

Instability of Plastic Flow in the Microstructure of Alkali Halide Crystals

E. B. Borisenko and A. G. Melent'ev

Institute of Solid State Physics, Russian Academy of Sciences, Chernogolovka, Moscow oblast, 142432 Russia

e-mail: borisenk@issp.ac.ru

Received July 15, 2004; in final form, October 8, 2004

Abstract—Spatial localization of deformation bands in LiF and KCl single crystals caused by instability of plastic flow in the strain rate range from 5×10^{-6} to 2×10^{-4} s^{-1} was studied experimentally. The geometrical parameters of localized shift bands (LSB) were studied as a function of strain rate and temperature. To study the LSB relief, a surface profilometry technique was used for the first time, which made it possible to determine the LSB parameters at the early stages of plastic flow (for strains in the range from 0.5 to 2%). The formation and branching of LSB steps on the surface of a deformed crystal due to the generation and motion of dislocations were found to be scaled. It was shown experimentally that the LSB formation is a thermally activated process that occurs through dislocation glide and is limited by dislocation creep. *© 2005 Pleiades Publishing, Inc.*

1. INTRODUCTION

It is well known that a growing nonuniformity of strain can cause instability of plastic flow followed by localization of deformation [1]. The beginning of the localized flow is usually accompanied by a yield drop in the stress–strain curve. A yield drop can appear due to "geometrical softening" caused by rotation of a glide plane; "physical" softening caused by intense dislocation multiplication, which occurs when a certain stress is reached; and dynamic strain-induced aging [1, 2]. Under these conditions, localized slip bands (LSBs) associated with slight strengthening were observed in metals and alloys.

In alkali halide crystals, strain localization has been studied in compression tests at a constant strain rate in the range 10^{-4}–10^{-2} s^{-1} [3–5] or under a constant load [6, 7] at temperatures above $0.5T_m$ (where T_m is the melting point) and for strains in the range 5–15%. Rough traces forming in this case are commonly referred to as localized shift bands (LSBs) [3–8]. The LSB parameters for deformation at a constant rate are listed in Table 1. In this work, we study the regularities of LSB formation in pure KCl and LiF crystals as a function of strain rate (unlike in previous studies [3–8], where the LSB parameters were studied as a function of strain and stress). To investigate these objects, we used surface profilometry for the first time, which made it possible to study localization of plastic flow at strains from 0.5 to 2% and to establish the range of strain rates at which the LSB formation occurs for these small total strains.

2. EXPERIMENTAL

Pure LiF and KCl single crystals were chosen for the studies. The content of metal impurities in both crystals was measured using the inductively coupled plasma (ICP–MS) technique and was found to be lower than the detection threshold. Therefore, the concentration of the tested impurities (Ca, Mg, Mn, Cu, Sr, Cd, Ba, Cs) was lower than 10^{-4} wt %.

Specimens were cleaved along the {100} cleavage planes in the form of rectangular prisms $3 \times 3 \times 15$ mm in size, compressed in an Instron test machine at constant rates ranging from 5×10^{-6} to 2×10^{-4} s^{-1} up to a strain $\varepsilon = 0.5$–2% in the temperature range 20–750°C (0.26–$0.91T_m$) for LiF and 20–650°C (0.28–$0.88T_m$) for KCl, and then cooled in the furnace in steps of 50°C.

Table 1. LSB parameters in LiF under various deformation conditions

T_d, K	Deformation type	Strain rate, s^{-1}	Strain, %	Step height, μm	LSB width, μm	LSB spacing, μm	Reference
>600	Compression	10^{-4}	14–15	>100	10–50	100–500	[3]
573–1123	Compression, tension	10^{-3}, 10^{-2}	12–30		10		[4]
673–1073	Compression	10^{-4}	15	10–160	5–20	50–100	[5]

Table 2. Step heights H_{LSB} left by LSBs on a face where screw dislocations end

Material	T_d, K (fraction of T_m)	v, s^{-1}	ε, %	H_{LSB}, μm
KCl	723 (0.70)	5×10^{-6}	1	1.2
	923 (0.88)	5×10^{-6}	1	1.8
LiF	573 (0.50)	10^{-5}	0.5	1.1
	993 (0.88)	10^{-5}	1	8
	993 (0.88)	5×10^{-6}	1	20

In order to study the microstructure and to analyze the LSB relief, we used surface profilometry and light microscopy.

The surface microstructure was studied using Docuval and Neophot optical microscopes. The surface topography of the deformed specimens was studied at room temperature using a Talystep profilometer (Taylor–Hobson) in accordance with a technique developed in [9]. To analyze the surface relief quantitatively, the {100} faces of the deformed specimens were scanned using a standard conical diamond stylus designed for measurements of step heights. A stylus with a radius of curvature of 12.5 μm moved automatically at a rate of 25 μm/s normally to a defect line and covered a distance of 100–250 μm. A step profile was simultaneously recorded by a plotter pen on a paper sheet and also displayed on a monitor. The measurement accuracy depended on the chosen magnification scale of vertical movement of the stylus and was either ±0.1 μm (for a magnification of 5×10^3) or ±0.01 μm (for a magnification of 5×10^4). The choice of the scale was conditioned by the mean step height, which was different for LiF and KCl.

The accuracy of step height measurements was no worse than 5%.

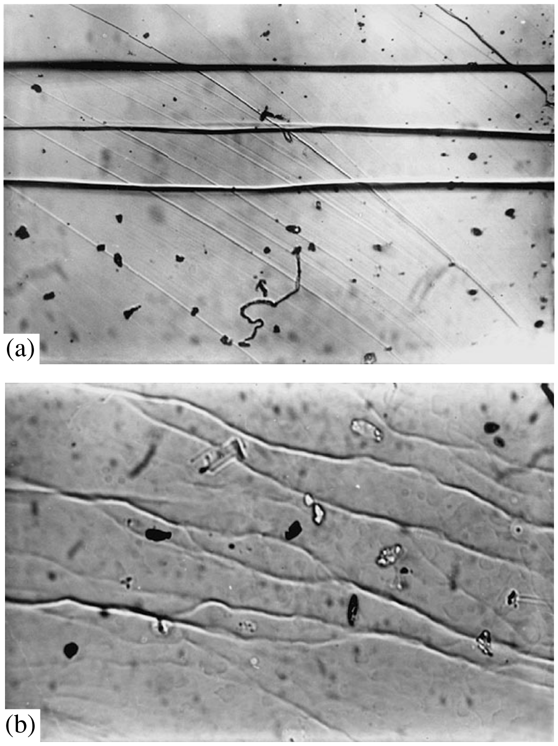

Fig. 1. Microphotographs of LSBs on faces where screw dislocations end in (a) LiF and (b) KCl compressed at $T_d = 0.88T_m$ and $v = 10^{-5}$ s^{-1}.

3. EXPERIMENTAL RESULTS

It was found experimentally that localization of plastic deformation begins both in LiF and KCl crystals at the same homologous temperature $0.51T_m$, which is 300 and 260°C, respectively. Strain rates at which this phenomenon was observed lie within the range 5×10^{-6}–10^{-4} s^{-1}. At higher compression strain rates beyond these limits, the deformation was observed to develop in the conventional way, with slip bands propagating throughout the specimen volume.

In what follows, we will consider the specific character of LSB formation on the faces where screw dislocations end (in generally accepted terms [7]) within the temperature and strain rate ranges indicated above.

Experimentally, it was shown that the regularities of LSB formation with variations in the temperature (T_d), strain rate (v), and strain (ε) in LiF and KCl are similar. Thus, the height of the LSB steps on a face where screw dislocations end increases with deformation. For example, if $T_d = 0.88T_m$ and $v = 10^{-5}$ s^{-1}, then the mean LSB height in LiF is 3 μm at ε = 0.5% and 10 μm at ε = 1.5%, which agrees well with the observed changes in LSB height in LiF at larger strains [5]. It follows from Table 2 that, for a fixed strain, the step height increases with temperature and with a decrease in the strain rate. It also follows from Table 2 that LSB heights in KCl are several times lower than in LiF, with all other deformation parameters being equal.

The number of dislocations involved in the formation of an LSB could be estimated using the measured height of steps left on the surface after passage of the LSB. In [1], the following formula was derived:

$$\gamma = n^3 b \rho_0^{1/2}/z, \tag{1}$$

where $\gamma = h/d$ = 5–10 is the localized-shift deformation (the height-to-width ratio of a step); n is the number of dislocations involved in the step formation; $b = 2.85 \times 10^{-8}$ cm is the Burgers vector; ρ_0 is the initial dislocation density; and z is the number of possible slip systems, which is equal to 12 in an fcc lattice. For LiF compressed at 720°C to a strain of 0.5% at a strain rate of 10^{-5} s^{-1} (10 μm/min), we find that n = 100–150 if the initial dislocation density is 10^6 cm^{-2}.

Figure 1 shows microphotographs of LSBs on faces where screw dislocations end taken for LiF and KCl

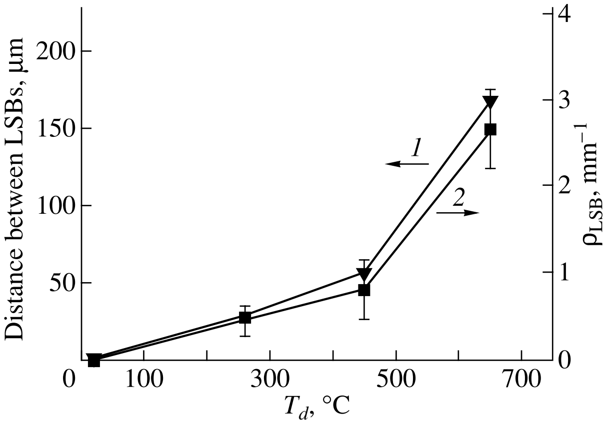

Fig. 2. Dependence of (*1*) the distance between LSBs and (*2*) the LSB linear dislocation density on temperature T_d for KCl crystals deformed at $v = 5 \times 10^{-6}$ s^{-1} up to $\varepsilon = 1$ %.

crystals. It can be seen from Fig. 1 that the LSBs in KCl are far wavier than those in LiF. It is likely that the LSB waviness on crystal faces is caused by cross slip in the bulk of a specimen. This difference is probably due to the fact that, under the same external conditions, cross slip is more intense in a softer KCl crystal than in a harder LiF crystal. It should be noted that LSBs become wavier with an increase in T_d in both types of crystals. The volume fraction of the material deformed due to LSB generation and propagation increases with T_d (curve *2* of Fig. 2). The strain rate also affects the LSB shape significantly. As is seen from Fig. 3a, an increase in v causes LSBs to branch. Figure 3b shows the profile of a branched step in LiF. It was found that the sum of the branch heights is equal to the step height before branching. This result is consistent with the results reported in [7]. This behavior is observed both in LiF and in KCl crystals.

As the strain rate increases, the number of branches in a group increases (as seen in Fig. 4), while the distances between LSBs in a group decrease (Fig. 5). It follows from Fig. 2 (curve *1*), Fig. 5, and Table 2 that an increase in temperature and a decrease in strain rate have a similar effect on LSBs. Indeed, the distances between LSBs and the heights of surface steps caused by the passage of an LSB increase with a decrease in v or an increase in T_d. The LSB density varies nonmonotonically with the strain rate: it first increases and then decreases (curve *2* of Fig. 4). The increase in LSB density is associated with LSB branching within a separate group, while the decrease in LSB density is due to the fact that not only LSB expansion contributes to the deformation. Indeed, as the strain rate v increases, the deformation becomes more homogeneous over the bulk and develops in the conventional way through the expansion of glide lines and slip bands.

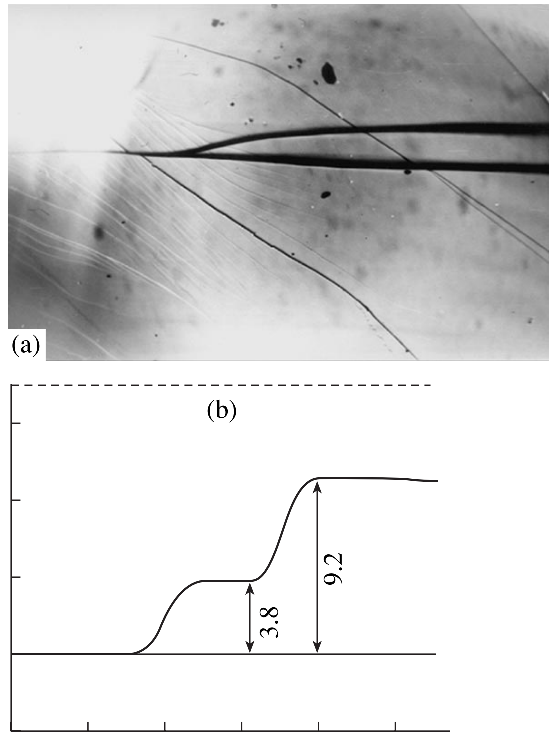

Fig. 3. Branched LSB in LiF at $T_d = 0.88T_m$, $v = 5 \times 10^{-5}$ s^{-1}, and ε = 1%. (a) Microphotograph and (b) profilogram (numerals indicate the LSB step heights in micrometers measured with a profilometer).

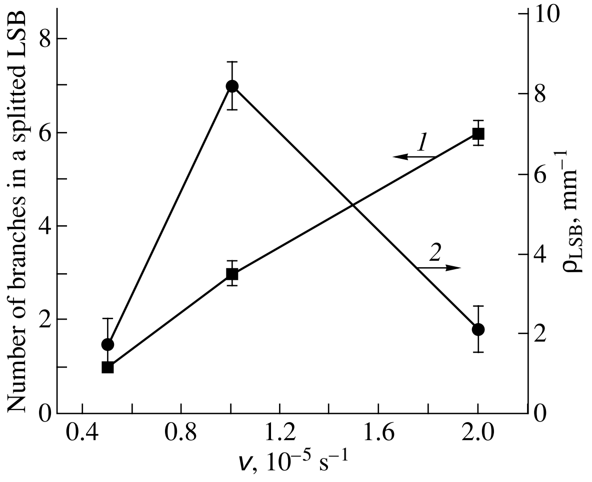

Fig. 4. Dependence of (*1*) the number of LSB branches and (*2*) LSB density in LiF on strain rate at $T_d = 0.88T_m$ and ε = 1%.

4. DISCUSSION

The observed effects of the deformation temperature and strain rate on the formation of LSBs (an increase in the LSB step heights, variations in the LSB density with an increase in T_d or a decrease in v) indicate that inhomogeneous deformation caused by LSB

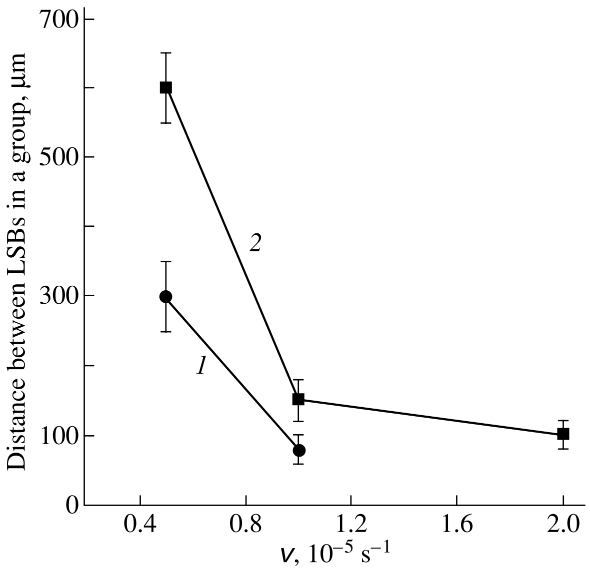

Fig. 5. Dependence of the distance between LSBs in a group on strain rate for a LiF crystal deformed at $T_d = 0.88T_m$ up to ε equal to (*1*) 0.5 and (*2*) 1%.

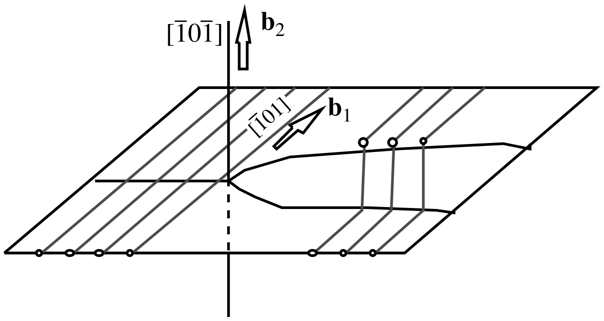

Fig. 6. Dislocation configuration associated with LSB branching (schematic).

development in alkali halide crystals is a thermally activated process. This conclusion is consistent with the data [4] on the temperature dependence of the strain rate, which indicate that localized deformation in LiF is a diffusion-controlled process and is limited by dislocation creep. The experimental data obtained in the present study enable us to estimate the strain rate in LiF crystals at the stage of deformation localization in the absence of strengthening. According to [1], the strain rate in this case is given by

$$\varepsilon^* = \rho_\infty b \langle v_{\mathrm{LSB}} \rangle, \qquad (2)$$

where, in our case, $\rho_\infty = 10^5$ cm^{-2} is the dislocation density far from LSBs, $b = 2.85 \times 10^{-8}$ cm is the Burgers vector in LiF, and $\langle v_{\mathrm{LSB}} \rangle = h/t$ is the cross-slip rate of LSBs (h is the LSB width, t is the LSB expansion time). Taking into account the linear dependence of the LSB-generated surface step height on the total deformation [5], we assume, as in [10], that an LSB propagates during the entire time of loading. In this case, at $\varepsilon = 0.5\%$ and $v = 10$ μm/min, the time of LSB expansion is 400 s; the measured mean value of h is 10 μm. Consequently, we have $\langle v_{\mathrm{LSB}} \rangle = 2.5 \times 10^{-2}$ μm/s and $\varepsilon^* = 7 \times 10^{-9}$ s^{-1}. According to [1], this strain rate corresponds to deformation through creep-limited dislocation glide.

Special attention should be paid to the observed branching of LSBs in which the sum of branch heights is equal to the step height before splitting. A possible mechanism of this LSB branching (Fig. 3) is illustrated in Fig. 6. It should be noted that single dislocations with kinks resulting from dislocations cutting through one another have a similar configuration [11]. This result agrees with the conclusions drawn from examining a surface relief with a tunneling microscope [12]. According to the data from [12], the formation of surface steps caused by dislocation generation and motion in deformed crystals is scaled. It is clearly seen in Fig. 6 that, after intersecting, the branches move at different levels, which means that the intersection of dislocations belonging to different slip systems leads to step generation. The motion of steps is not conservative and is limited by the diffusion of vacancies [1].

5. CONCLUSIONS

(1) It has been shown experimentally that, in alkali halide crystals at temperatures exceeding $0.5T_m$, plastic flow instability leads to localization of plastic deformation if the total strain is small (0.5–2%) and the strain rate lies in the range from 2×10^{-6} to 10^{-4} s^{-1}. It has been found that localization of plastic deformation is observed in LiF and KCl crystals under the same externally imposed deformation conditions.

(2) It has been shown that an increase in strain rate causes LSB branching and the generation of steps, whose number increases with strain rate. From our experiments, it follows that the surface step formation in deformed crystals that is related to dislocation generation and motion is scaled.

(3) The experimental results indicate that LSB formation is thermally activated and is controlled by dislocation creep.

ACKNOWLEDGMENTS

This study was supported by the Russian Foundation for Basic Research, project no. 04-02-17140.

REFERENCES

1. M. A. Shtremel', *Strength of Alloys* (Mosk. Inst. Stali Splavov, Moscow, 1997), Part 2, p. 55.
2. E. Rizzi and P. Hähner, Int. J. Plast. **20**, 121 (2004).
3. G. V. Berezhkova, N. P. Skvortsova, P. P. Perstnev, and V. R. Regel', Fiz. Tverd. Tela (Leningrad) **26** (4), 1074 (1984) [Sov. Phys. Solid State **26** (4), 654 (1984)].

4. N. P. Skvortsova, Fiz. Tverd. Tela (St. Petersburg) **37** (11), 3347 (1995) [Phys. Solid State **37** (11), 1839 (1995)].
5. B. I. Smirnov, R. S. Chudnova, and V. V. Shpeĭzman, Fiz. Tverd. Tela (St. Petersburg) **34** (6), 1759 (1992) [Phys. Solid State **34** (6), 936 (1992)].
6. G. V. Berezhkova and N. P. Skvortsova, Fiz. Tverd. Tela (St. Petersburg) **36** (6), 1724 (1994) [Phys. Solid State **36** (6), 943 (1994)].
7. B. I. Smirnov, Fiz. Tverd. Tela (St. Petersburg) **36** (7), 2037 (1994) [Phys. Solid State **36** (7), 1112 (1994)].
8. G. V. Berezhkova and N. P. Skvortsova, Kristallografiya **39** (3), 567 (1994) [Crystallogr. Rep. **39** (3), 507 (1994)].
9. A. G. Melent'ev, Kristallografiya **40** (4), 736 (1995) [Crystallogr. Rep. **40** (4), 681 (1995)].
10. G. V. Berezhkova and N. P. Skvortsova, Fiz. Tverd. Tela (Leningrad) **33** (2), 400 (1991) [Sov. Phys. Solid State **33** (2), 230 (1991)].
11. M. A. Shtremel', *Strength of Alloys* (Mosk. Inst. Stali Splavov, Moscow, 1999) [in Russian].
12. V. I. Vettegren', S. Sh. Rakhimov, and V. N. Svetolov, Fiz. Tverd. Tela (St. Petersburg) **37** (4), 913 (1995) [Phys. Solid State **37** (4), 495 (1995)].

Translated by E. Borisenko

Physics of the Solid State, Vol. 47, No. 7, 2005, pp. 1278–1281. Translated from Fizika Tverdogo Tela, Vol. 47, No. 7, 2005, pp. 1237–1240.
Original Russian Text Copyright © 2005 by Golovin, Dmitrievskiĭ, Suchkova, Badylevich.

DEFECTS, DISLOCATIONS, AND PHYSICS OF STRENGTH

Multistage Radiation-Stimulated Changes in the Microhardness of Silicon Single Crystals Exposed to Low-Intensity β Irradiation

Yu. I. Golovin*, A. A. Dmitrievskiĭ*, N. Yu. Suchkova*, and M. V. Badylevich**
** Tambov State University, Internatsional'naya ul. 33, Tambov, 392622 Russia*
e-mail: dmitr2002@tsu.tmb.ru
*** Institute of Solid State Physics, Russian Academy of Sciences, Chernogolovka, Moscow oblast, 142432 Russia*

Received August 6, 2004

Abstract—Radiation-stimulated and postradiation changes in the microhardness of silicon single crystals exposed to irradiation with a low-intensity flux of β particles ($I = 9 \times 10^5$ cm^{-2} s^{-1}, $W = 0.20 + 0.93$ MeV) are studied. It is established that the inversion of the radiation-induced plastic effect occurs at a characteristic irradiation time $\tau_c = 75$ min; i.e., irradiation of silicon single crystals for a time $\tau < \tau_c$ leads to nonmonotonic reversible hardening, whereas nonmonotonic reversible softening is observed under irradiation for a time $\tau > \tau_c$. It is demonstrated that there exists a correlation between the nonmonotonic dependences of the microhardness and the concentration of electrically active defects at acceptor levels with energies $E_c - 0.11$ eV, $E_c - 0.13$ eV, and $E_c - 0.18$ eV on the irradiation time. *© 2005 Pleiades Publishing, Inc.*

1. INTRODUCTION

Irradiation of single-crystal silicon by electrons with an energy higher than the defect-producing threshold ($W > 170$ keV) provides a means for selectively modifying the electrical properties of this material [1, 2]. At present, the majority of electrically active radiation-induced defects have been reliably identified. Irradiation at temperatures $T \geq 300$ K is of most interest. This is associated with the thermal stability of electron-generated defects at temperatures close to room temperature [3]. It is known [4, 5] that, at $T \approx 300$ K, the microhardness of silicon single crystals is primarily governed by the mobility of nonequilibrium point defects and, quite possibly, by phase transitions occurring under an indenter. Therefore, the microhardness can serve as an indication of the states of intrinsic and radiation-induced structural defects. Actually, in our previous work [6], we revealed nonmonotonic reversible changes in the microhardness of silicon single crystals under β irradiation with low doses (at fluences $F < 1.2 \times 10^{12}$ cm^{-2}) at room temperature. It was found that, in the range of fluences F from 3×10^{11} to 1.2×10^{12} cm^{-2}, the microhardness regains its initial value H_0. Relaxation of the microhardness H to the initial value H_0 was also observed when the irradiation was terminated after the fluence reached a value $F = 3 \times 10^{11}$ cm^{-2}. It is interesting to note that, in both cases, the rates of recovery of the microhardness coincide with each other (within the limits of experimental error). On this basis, it was assumed [6] that there can exist a critical fluence (at an earlier stage of irradiation) responsible for the subsequent evolution of the subsystem of structural defects in silicon crystals.

It should be noted that, in contrast to spectroscopic methods, microhardness testing does not allow one to identify the particular type of point defects involved; hence, it is expedient to record, for example, the deep-level transient spectra simultaneously with the microhardness measurements. In this respect, the purpose of the present work was to determine the particular stages of irradiation initiating further changes in the microhardness and to reveal a correlation between the radiation-stimulated changes in the microhardness and the concentration of electrically active defects.

2. SAMPLE PREPARATION AND EXPERIMENTAL TECHNIQUE

Experiments were performed with dislocation-free single-crystal silicon samples of two types: *Fz*-Si (BIGE-600) crystals grown using crucibleless zone melting and *Cz*-Si (KÉF-10) crystals grown by the Czochralski method. The concentration of oxygen in these samples differs by two orders of magnitude. However, it was demonstrated earlier in [6] that, under β irradiation, the changes in the microhardness of both types of samples occur in much the same manner.

The samples were irradiated with the use of a radioactive source ^{90}Sr + ^{90}Y with an activity $A = 14.5$ MBq. The mean energy of emitted electrons was equal to 0.20 MeV for ^{90}Sr and 0.93 MeV for ^{90}Y, and the irradiation intensity was $I = 9 \times 10^5$ cm^{-2} s^{-1}. Irradiation was performed in air at room temperature in the range of fluences F from 10^9 to 1.2×10^{12} cm^{-2}. The Vickers microhardness H of the (111) surfaces was measured on a PMT-3 microhardness tester. The state of deep-lying levels generated by radiation-induced defects was controlled by recording the deep-level transient spectra [7]. For this purpose, a Schottky-barrier diode was produced on the (111) surface of the studied sample (this series of experiments was performed with *Cz*-Si single crystals in which the contents of oxygen and carbon were usually of the same order of magnitude) through the deposition of a 2- to 3-μm-thick gold layer under vacuum at a residual pressure of no higher than 10^{-3} Pa. The deep-level transient spectra were obtained according to the standard technique. In order to test the microhardness and to measure the deep-level transient spectra, the samples were periodically withdrawn from the irradiation chamber. Subsequently, the time spent to measure the microhardness (~30 min) was taken into account (i.e., it was subtracted from the total time of the experiment) when constructing the dose dependence of the microhardness.

3. RESULTS AND DISCUSSION

It is found that the behavior and kinetics of the radiation-stimulated variations in the microhardness H of *Fz*-Si single crystals depend on the dose of β irradiation (Fig. 1). Exposure of the silicon single crystals to β irradiation for a time τ = 20 min leads to nonmonotonic reversible hardening of the samples (Fig. 1a). The results of microhardness testing of two different samples irradiated under the same conditions are represented by squares and rhombuses in Fig. 1a. As can be seen from this figure, the time dependences of the microhardness $H(t)$ measured for two samples coincide with each other. This indicates that the manifestation of the postradiation hardening effect at such low doses is quite reliable, even if unexpected at first glance. Exposure of the samples to irradiation with β particles for a time τ_c = 75 min results in suppression of the postradiation hardening effect, and further variations in the microhardness of the samples are not revealed (within the limits of experimental error) (Fig. 1b). Irradiation of the samples for 2 h leads to reversible softening (Fig. 1c). It follows from these findings that, in the vicinity of the characteristic irradiation time τ_c, there exists a point of inversion of the radiation-induced plastic effect. In the case of continuous irradiation for 413 h, the microhardness H nonmonotonically decreases with subsequent recovery of the initial value H_0 (Fig. 1d). The time dependence of the microhardness $H(t)$ in the case of continuous irradiation for 400 h was also examined for two samples. The results obtained indicate that, even at the early stages of irradiation ($F \sim 10^9$ cm^{-2}), long-term processes affecting the microhardness H are initiated in the subsystem of structural defects. Most probably, the nonmonotonic character of the postradiation changes in the microhardness is due to variations in the concentrations of different complexes of radiation-induced defects with time.

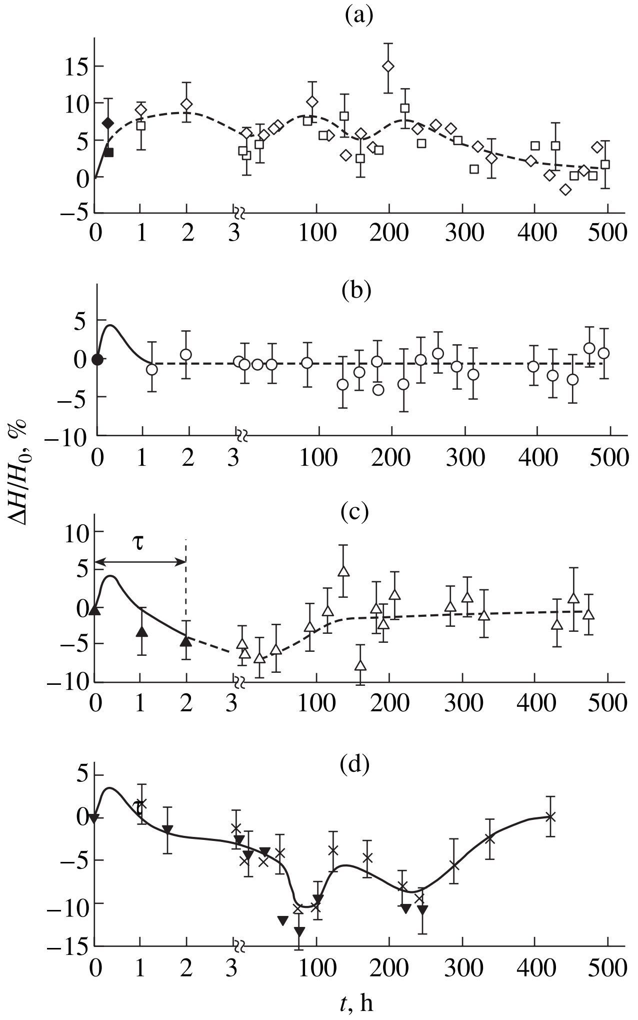

Fig. 1. Dependences of the relative change in the microhardness $\Delta H/H_0$ ($\Delta H = H_t - H_0$, where H_0 and H_t are the initial microhardness and the microhardness measured at the instant t, respectively) on the time (including the irradiation time τ) for *Fz*-Si samples irradiated for times τ = (a) 0.3, (b) 1.25, (c) 2, and (d) 413 h.

Since the radiation-stimulated changes in the microhardness could also be caused by electrically active complexes of radiation-induced defects, we carried out the second series of experiments in which the microhardness was tested simultaneously with the recording of the deep-level transient spectra characterizing the concentration of acceptor complexes N as a function of the irradiation time τ.

It is known [8, 9] that, as a rule, irradiation with a fluence $F > 10^{14}$ cm^{-2} and an intensity $I = 10^{12}$ cm^{-2} s^{-1} at room temperature brings about the generation of donor and acceptor complexes, which are identified as divacancies, *A* centers, *E* centers, *K* centers, etc.

Figure 2 shows a typical deep-level transient spectrum obtained under the conditions of our experiment ($I = 9 \times 10^5$ cm^{-2} s^{-1}, $F = 4 \times 10^{11}$ cm^{-2}). It can be seen from this figure that the spectrum exhibits only three peaks (as opposed to the case of high-intensity irradi-

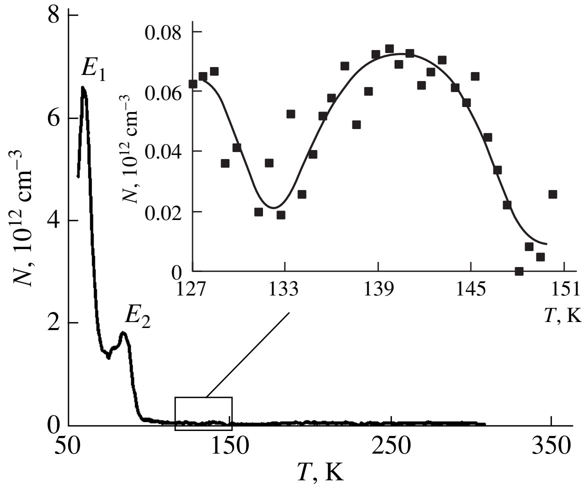

Fig. 2. Typical deep-level transient spectrum obtained under the following conditions: frequency $\nu = 164$ Hz, pulse width $\tau_p = 0.1$ μs, blocking voltage $U_b = 4.0$ V, inverted-pulse voltage $U_p = 3.5$ V, and irradiation time $\tau = 137$ h.

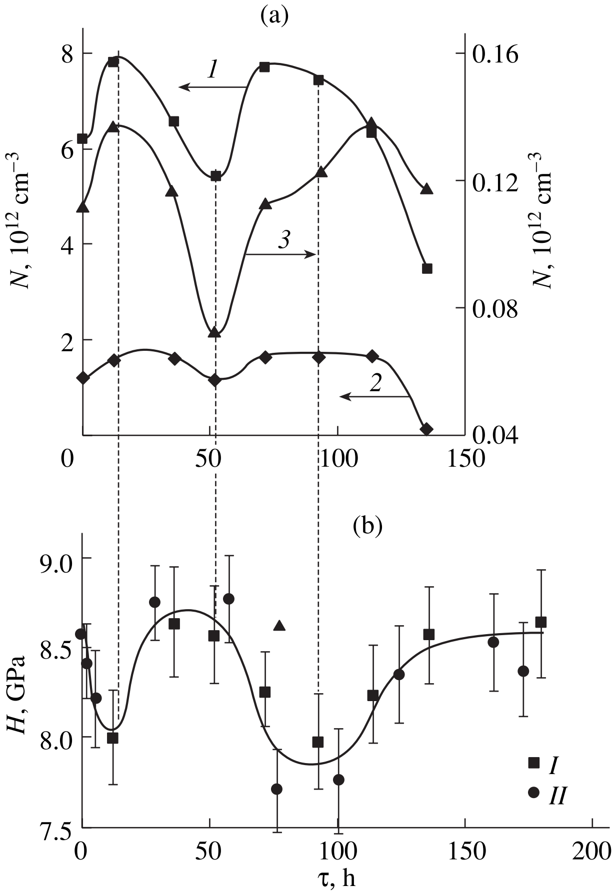

Fig. 3. Dependences of the change in (a) the concentration N of acceptor complexes with energies (*1*) $E_1 = E_c - 0.11$ eV, (*2*) $E_2 = E_c - 0.13$ eV, and (*3*) $E_3 = E_c - 0.18$ eV and (b) the microhardness H of *Cz*-Si single crystals on the irradiation time τ. Roman numerals *I* and *II* indicate the dependences $H(\tau)$ measured with two samples of different types.

ation up to fluences F in the range from ~10^{14} to 10^{15} cm^{-2}, in which there appear additional peaks associated with divacancies and vacancy–impurity complexes). The results presented in Fig. 3 demonstrate a correlation between radiation-stimulated variations in the concentration N of acceptor complexes with energies $E_1 = E_c - 0.11$ eV, $E_2 = E_c - 0.13$ eV, and $E_3 = E_c - 0.18$ eV (Fig. 3a, curves *1*–*3*, respectively) and the microhardness H of *Cz*-Si single crystals exposed to irradiation with β particles (Fig. 3b).

Interstitial silicon atoms can displace carbon atoms (located at lattice sites) into interstitial sites according to the Watkins reaction $\mathrm{Si}_i + \mathrm{C}_s \longrightarrow \mathrm{Si}_s + \mathrm{C}_i$. Interstitial carbon atoms correspond to an acceptor level at an energy $E_c - 0.11$ eV [8]. The carbon atoms displaced into interstitial sites can form bonds with carbon atoms located at lattice sites [10]. The acceptor level corresponding to the C_i–C_s complex is characterized by an energy $E_c - 0.17$ eV [8, 10]. It is known [11] that free vacancies generated in a silicon single crystal under irradiation diffuse over the crystal and are most actively captured by isolated oxygen atoms to form complexes of the acceptor type $V + \mathrm{O} \longrightarrow V$–O (the depth of their location corresponds to an energy $E_c - 0.17$ eV). Therefore, the peaks observed at energies $E_c - 0.11$ eV and $E_c - 0.18$ eV in our experiment can be assigned to interstitial carbon C_i and an *A* center or a C_i–C_s complex, respectively. The acceptor level at an energy $E_c - 0.13$ eV is usually attributed either to interstitial boron [8] or an FeAl pair [12], or, in proton-irradiated silicon, to a hydrogen-containing complex [13]. The samples and the type of irradiation used in the present work rule out the possibility that the last three radiation-induced defects can be formed in amounts sufficient for identification. For this reason, we cannot determine the nature of the observed defect at an acceptor level with an energy $E_c - 0.13$ eV.

The concentrations of two identified defects can vary as a result of many reactions proceeding with the formation of electrically inactive products:

$$V + \mathrm{O}_i \longrightarrow V\mathrm{O}, \quad \mathrm{Si}_i + V\mathrm{O} \longrightarrow \mathrm{O}_i,$$

$$V + \mathrm{C}_i \longrightarrow \mathrm{C}_s, \quad \mathrm{Si}_i + \mathrm{C}_s \longrightarrow \mathrm{Si}_s + \mathrm{C}_i,$$

$$\mathrm{C}_i + \mathrm{C}_s \longrightarrow \mathrm{C}_i\mathrm{C}_s, \quad \mathrm{Si}_i + V \longrightarrow \mathrm{Si}_s, \text{ etc.}$$

It seems likely that the high mobility at room temperature and relatively low concentrations (at an irradiation intensity $I = 9 \times 10^5$ cm^{-2} s^{-1}) of generated vacancies and interstitial atoms lead to a nonmonotonic change in the concentrations of the aforementioned complexes, as well as to the generation of more complicated aggregates. In our opinion, the nonmonotonic dependences of the concentration $N(\tau)$ and the microhardness $H(\tau)$ are associated with the multistage competing reactions with the participation of radiation-induced defects.

4. CONCLUSIONS

Thus, in the present work, we studied the kinetics of radiation-stimulated variations in the microhardness of *Fz*-Si single crystals exposed to β irradiation. The transformation of the subsystem of structural (intrinsic and radiation-induced) defects was found to occur through multistage competing reactions. It was revealed that the inversion of the radiation-induced plastic effect is observed at a critical irradiation time τ_c (irradiation intensity $I = 9 \times 10^5$ cm^{-2} s^{-1}). It was demonstrated that, upon exposure of *Cz*-Si single crystals to low-intensity irradiation, the concentration of interstitial carbon atoms, as well as the concentration of oxygen–vacancy complexes or complexes consisting of interstitial carbon atoms and carbon atoms located at lattice sites, change in a nonmonotonic manner. As the fluence increases, the nonmonotonic changes in the concentration of the aforementioned defects and in the microhardness H of the silicon single crystals under investigation occur in the antiphase.

ACKNOWLEDGMENTS

We would like to thank Yu.I. Iunin for his assistance in performing the experiments.

This work was supported by the Russian Foundation for Basic Research (project nos. 02-02-17571, 02-02-17024) and performed within the framework of the program “Universities of Russia” (project no. UR.01.01.013).

REFERENCES

1. V. S. Vavilov, Usp. Fiz. Nauk **84** (3), 431 (1964) [Sov. Phys. Usp. **7** (3), 797 (1964)].
2. V. A. Kozlov and V. V. Kozlovskiĭ, Fiz. Tekh. Poluprovodn. (St. Petersburg) **35** (7), 769 (2001) [Semiconductors **35** (7), 735 (2001)].
3. *Radiation Effects in Semiconductors*, Ed. by L. S. Smirnov (Nauka, Novosibirsk, 1979) [in Russian].
4. B. Ya. Farber, V. I. Orlov, V. I. Nikitenko, and A. H. Heuer, Philos. Mag. A **78**, 671 (1998).
5. Yu. I. Golovin, A. I. Tyurin, and B. Ya. Farber, Philos. Mag. A **82** (10), 1857 (2002).
6. Yu. I. Golovin, A. A. Dmitrievskiĭ, I. A. Pushnin, and N. Yu. Suchkova, Fiz. Tverd. Tela (St. Petersburg) **46** (10), 1790 (2004) [Phys. Solid State **46** (10), 1851 (2004)].
7. D. V. Lang, J. Appl. Phys. **45** (7), 3023 (1974).
8. B. G. Svensson, in *EMIS Datareviews*, Ser. 20 (1998), p. 763.
9. V. S. Vavilov, N. P. Kekelidze, and L. S. Smirnov, *Effect of Radiations on Semiconductors* (Nauka, Moscow, 1998) [in Russian].
10. L. W. Song, X. D. Zhan, B. W. Benson, and G. D. Watkins, Phys. Rev. Lett. **60**, 460 (1988).
11. G. D. Watkins and J. W. Corbett, Phys. Rev. **121**, 1001 (1961).
12. A. A. Istratov, H. Hieslmair, and E. R. Weber, Appl. Phys. A **69** (44), 13 (1999).
13. K. Irmscher, H. Klose, and L. Maass, J. Phys. C **17**, 6317 (1984).

Translated by O. Moskalev

Physics of the Solid State, Vol. 47, No. 7, 2005, pp. 1282–1288. Translated from Fizika Tverdogo Tela, Vol. 47, No. 7, 2005, pp. 1241–1246.
Original Russian Text Copyright © 2005 by Dunin-Barkovskiĭ, Morgunov, Tanimoto.

The Influence of a Static Magnetic Field up to 15 T on the Manifestation of the Portevin–Le Chatelier Effect in NaCl : Eu Crystals

L. R. Dunin-Barkovskiĭ*, R. B. Morgunov*, and Y. Tanimoto**
** Institute of Solid-State Physics, Russian Academy of Sciences, Chernogolovka, Moscow oblast, 142432 Russia*
*** Hiroshima University, Higashi Hiroshima, 739-8526, Japan*

Received August 11, 2004

Abstract—The influence of a static magnetic field on the instability of plastic flow (the Portevin–Le Chatelier effect) is revealed in NaCl : Eu quenched crystals. It is found that, in an external magnetic field, the yield stress of the crystals is reduced, the probability of plastic strain jumps and their amplitude decrease, and the amplitude distribution of the plastic strain jumps becomes random. The number of shear bands formed on the surface of crystals strained in the magnetic field is halved as compared to that observed without a magnetic field. *© 2005 Pleiades Publishing, Inc.*

1. INTRODUCTION

The first reliable experimental evidence supporting the existence of the magnetoplastic effect in ionic crystals was obtained by Alshits *et al.* [1], who revealed that a static magnetic field with an induction of ~1 T initiates displacements of individual dislocations under internal stresses. More recently, it was established that the magnetoplastic effect in ionic crystals can manifest itself as a decrease in the microhardness [2], the internal friction [3], the yield stress [4], and the strain hardening coefficient [5] (comprehensive reviews of the existing literature on the magnetoplastic effects in ionic crystals are given in [6–8]). All these macroscopic characteristics of plasticity are related in an intricate ambiguous fashion to the mobility of individual dislocations and the elementary processes occurring in a magnetic field. Hence, it is important to investigate the magnetoplastic effect on the mesoscopic level under conditions where plastic deformation manifests itself as jumps in the stress–strain curves, steps on the crystal surface, shear bands, dislocation slip bands, etc. As is known, jerky plastic flow, i.e., the Portevin–Le Chatelier effect, has been observed in NaCl : Eu crystals at a specific impurity concentration [9]. This effect is associated with the dynamic aging of dislocations; in other words, it is caused by the formation of Cottrell or Snoek impurity clouds around the dislocation cores. This process is accompanied by the clustering of individual impurity–vacancy dipoles. Earlier [10–13], it was shown that an external magnetic field affects the structure of Eu^{2+} small-sized clusters formed in NaCl : Eu crystals in the course of impurity aggregation or dislocation motion. Therefore, we can assume that the Portevin–Le Chatelier effect should be sensitive to variations in a magnetic field. In this respect, it is of interest to examine the Portevin–Le Chatelier effect in magnetic fields with the aim of revealing a correlation between the structure of europium impurity clusters and the dislocation motion.

The purpose of this work was to create the appropriate experimental conditions for studying the Portevin–Le Chatelier effect in a static magnetic field and to elucidate the influence of the magnetic field on the mesoscopic characteristics of plastic flow and on the motion of large-sized ensembles of dislocations in NaCl : Eu crystals.

2. SPECIMEN PREPARATION AND EXPERIMENTAL TECHNIQUE

The influence of a magnetic field on plasticity was studied with NaCl : Eu crystals (600 ppm) $2 \times 2 \times 5$ mm in size. The crystals were quenched using isothermal treatment at a temperature of 770 K for 2 h and subsequent rapid cooling on a metal plate to 293 K. Then, the crystals were subjected to uniaxial compression in two regimes: (1) on an Instron hard compression testing machine, which made it possible to specify the strain linearly increasing with time ($\varepsilon \sim t$) and to measure the mechanical stress σ; and (2) on a soft compression testing machine, which made it possible to specify the mechanical stress linearly increasing with time ($\sigma \sim t$) and to measure the strain ε. It is known that the soft machine has significant advantages over the hard machine for studying the Portevin–Le Chatelier effect, because the experimental data obtained in the former case can be analyzed without regard for the characteristics of the machine itself and the noise level of the machine is considerably lower [14]. We specially checked that the eigenfrequency of vibrations of the soft compression machine is two orders of magnitude higher than the mean frequency of plastic strain jumps characteristic of the Portevin–Le Chatelier effect in the crystals under testing. The time constant of the strain gauge is approximately equal to 1 ms, which is three orders of magnitude shorter than the expectation time (~1 s) for the appearance of strain jumps. The gauge resolution with respect to the displacement magnitude was 0.1 μm. This corresponds to the strain $\varepsilon = 2 \times 10^{-5}$ for crystals 5 mm in height.

The Instron hard compression machine was equipped with an electromagnet producing a magnetic field with a maximum induction of 0.9 T. During compression of the crystals, the magnetic field was switched on for short times ranging from 10 to 100 s. The soft compression machine was mounted on a JMTD-LH15T40 superconducting magnet, which produced a magnetic field with a maximum induction of 15 T at room temperature. Since the time required to create a magnetic field in the superconducting magnet was as long as a few hours [this time considerably exceeded the time (~30 min) spent to strain the studied crystals], the check experiments without a magnetic field were carried out on the compression machine remounted from the superconducting magnet to an isolated frame. In the measurements performed at different inductions $B < 15$ T, the rod length was varied so that the specimen appeared to be in a vertical bore of the superconducting magnet at a point with the known magnetic induction.

Moreover, particular care was taken to exclude artefacts associated with the influence of the magnetic field on the operation of the compression machine. The compression machines of both types were equipped with quartz rods in order to keep movable parts of the machine from pulling in the magnetic field and to insure against an uncontrollable change in the effective load on the crystal. It was verified that, in the experiments with the soft machine, the displacement of the upper quartz rod, which was freely suspended by soft springs and was loaded with a linearly increasing weight, did not depend on the magnetic field (Fig. 1). During loading the upper rod mounted on the fixed lower brass rod, the magnetic field also did not affect the dependence $\varepsilon(\sigma)$, which, in this case, characterized the elastic properties of the machine (Fig. 1). These findings and the absence of differences between the stress–strain curves obtained for unquenched as-grown crystals in the magnetic field and without it (see below) indicate that any changes revealed in the stress–strain curves of the specimens in the magnetic field cannot be explained in terms of the influence exerted by the field on the operation of the compression machine and displacement gauges. Furthermore, as is seen from Fig. 1, the elastic characteristics of the soft compression machine cannot lead to substantial changes in the stress–strain curve whose mean slope differs significantly from the slopes of the reference stress–strain curves obtained in the check experiments without specimens. The spatial inhomogeneity of the plastic deformation on the surface of the strained crystals was examined with a Neophot-32 optical microscope.

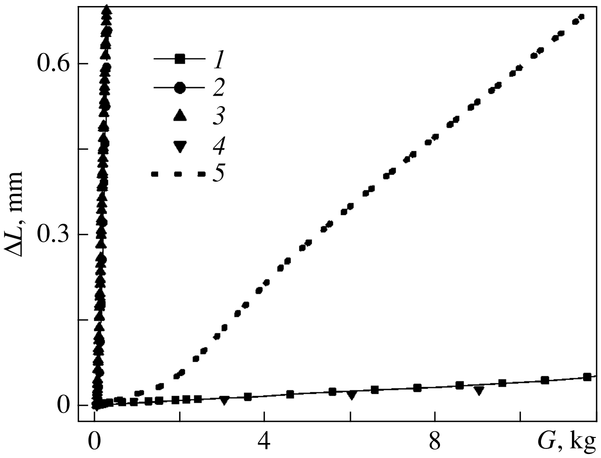

Fig. 1. Dependences of the displacement Δ*L* of the upper rod on the load *G* in the soft compression machine: (*1*, *4*) the loading upper rod in the absence of a specimen rests firmly against the fixed lower rod, and (*2*, *3*) the loading upper rod in the absence of a specimen is freely suspended by soft springs. The measurements are performed in (*1*, *2*) the magnetic field with an induction of 15 T and (*3*, *4*) zero magnetic field. (*5*) Stress–strain curve for the NaCl : Eu specimen.

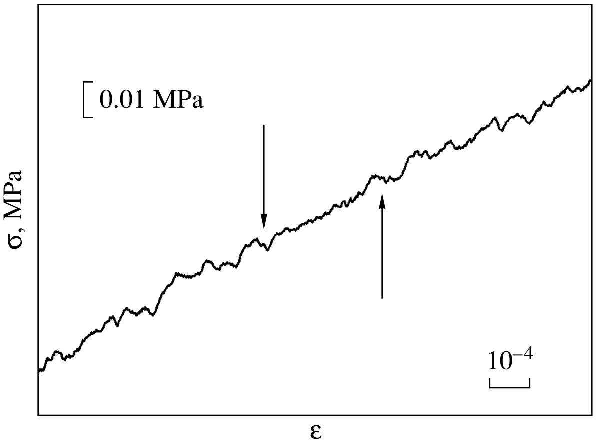

Fig. 2. A typical fragment of the stress–strain curve measured for the NaCl : Eu as-quenched crystal in the Instron hard compression testing machine. Arrows indicate the instants of time when the magnetic field with an induction of 0.9 T is switched on and switched off.

3. RESULTS AND DISCUSSION

The experiments with the hard compression machine were performed using NaCl : Eu as-quenched crystals at a strain rate of 5×10^{-5} s^{-1}. It can be seen from Fig. 2 that, above the yield point, the stress–strain curve is characterized by jumps in the compressive stress, i.e., the Portevin–Le Chatelier effect. Upon application of a static magnetic field with an induction of 0.9 T, the amplitude of stress jumps decreases and the stress–strain curve becomes smoother (Fig. 2). This manifestation of the magnetoplastic effect can be repeated several times under compression of the same crystal. The magnetoplastic effect was revealed in other specimens.

The experiments with the soft compression machine were also carried out using NaCl : Eu as-quenched crystals. The mean strain rate was approximately equal to $\sim 10^{-5}$ s^{-1}. The yield point was determined taking into account the specimen shape; i.e., the yield stress was normalized to the length-to-width ratio of the specimen base. A comparison of the stress–strain curve obtained by averaging over ten curves measured in the magnetic field with an induction of 15 T and the stress–strain curve obtained by averaging over ten curves measured without a magnetic field showed that the yield stress is halved in the magnetic field (Fig. 3a). This is comparable to the change in the yield stress of NaCl : Eu crystals in magnetic fields with an induction $B < 1$ T [4]. For NaCl : Eu unquenched crystals, the averaged stress–strain curves obtained in zero magnetic field are identical to those measured in the magnetic field with an induction of 15 T (Fig. 3b).

The manifestation of the Portevin–Le Chatelier effect revealed in the experiments performed with the soft compression machine differs from that revealed with the hard compression machine [14]. In the former case, the Portevin–Le Chatelier effect manifests itself in the form of a serrated deformation (Fig. 4). It should be noted that, in an external magnetic field, the parameters of the serrated deformation change significantly. Figure 4 shows typical stress–strain curves measured in a magnetic field and without it. The application of the magnetic field leads to a substantial decrease in the

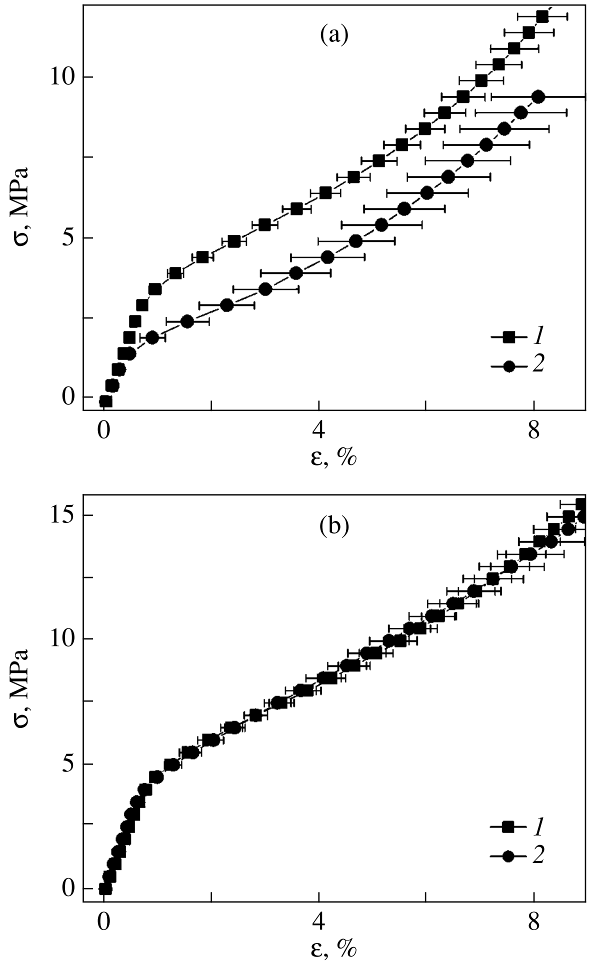

Fig. 3. Averaged stress–strain curves for (a) NaCl : Eu as-quenched specimens and (b) NaCl : Eu aged specimens (not subjected to special heat treatment) in (*1*) zero magnetic field and (*2*) the magnetic field with an induction of 15 T.

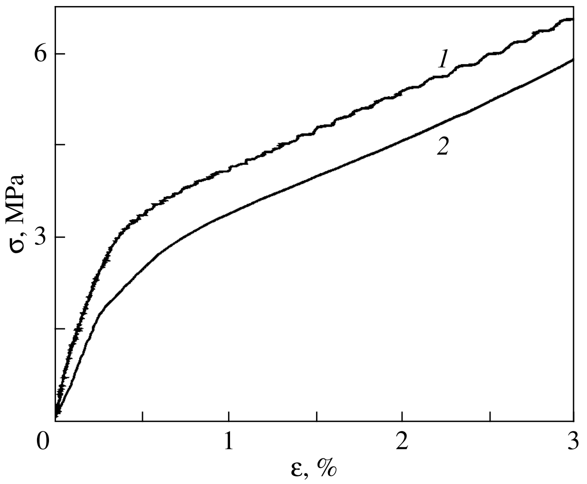

Fig. 4. Typical stress–strain curves for NaCl : Eu specimens in (*1*) zero magnetic field and (*2*) the magnetic field with an induction of 15 T.

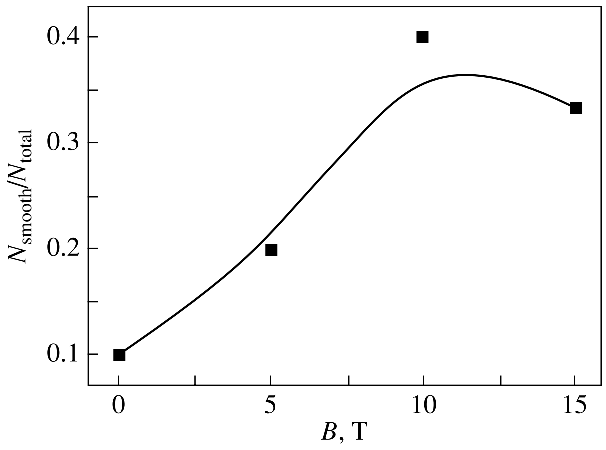

Fig. 5. Dependence of the fraction of the specimens free of Portevin–Le Chatelier instabilities on the magnetic induction *B*.

probability of plastic strain jumps. Figure 5 presents the ratio between the number of crystals characterized by a smooth stress–strain curve ($N_{\rm smooth}$) and the total number of specimens ($N_{\rm total} = 10$) as a function of the magnetic induction. It can be seen from this figure that, in the magnetic field, the ratio $N_{\rm smooth}/N_{\rm total}$ increases by a factor of four.

However, for a number of specimens strained in the magnetic field, the stress–strain curves exhibit jumps. A comparison between the portions of the serrated stress–strain curves for the specimens strained in the magnetic field and those for the specimens strained without a magnetic field (Fig. 6) shows that, in the magnetic field, the size distribution of the steps in the stress–strain curve depicted in Fig. 6b becomes random; i.e., the distribution of the expectation time for the appearance of a strain jump (which is proportional to the increment of the mechanical stress $\Delta\sigma$) and the distribution of the strain amplitude $\Delta\varepsilon$ become less regular. The dependence of the average strain amplitude $\langle\Delta\varepsilon\rangle$ (obtained by averaging of individual jumps over ten specimens) on the magnetic induction B is shown in Fig. 7. As can be seen from this figure, the average strain amplitude decreases by a factor of approximately two with an increase in the magnetic induction and reaches saturation in magnetic fields with an induction $B > 10$ T.

As a rule, an increase in the inhomogeneity of the plastic deformation with time is accompanied by the spatial inhomogeneity of the deformation of the specimen, which frequently manifests itself in the form of deformation steps or shear bands on the surface of the strained crystal [15]. Since the amplitude of strain jumps in the stress–strain curves obtained in our experiments falls in the range 1–10 μm, these jumps should correspond to spatial inhomogeneities with the sizes lying in approximately the same range. Examination of the surfaces of the strained crystals under the optical microscope revealed alternating regions (bands) of plastic deformation with a mean width of ~20 μm (Fig. 8a). These bands are aligned parallel to the (001) plane to which the mechanical load is applied. The crystals strained in the magnetic field with an induction of 15 T are characterized by a decrease in the number of deformation bands (cf. Figs. 8a and 8b). Taking into account that the number of bands reflected the deformation prehistory of the crystal, the total number of inhomogeneous deformation bands was determined for six pairs of specimens (in each pair, one specimen was strained in the magnetic field, whereas the other specimen was strained without a magnetic field). It was found that the number of deformation bands on the surface of the crystals strained in the magnetic field, on average, is halved as compared to that of the crystals strained without a magnetic field.

The results obtained in the experiments with the soft compression machine were analyzed using the following procedure. First, for the specimens characterized by Portevin–Le Chatelier instabilities, we determined the

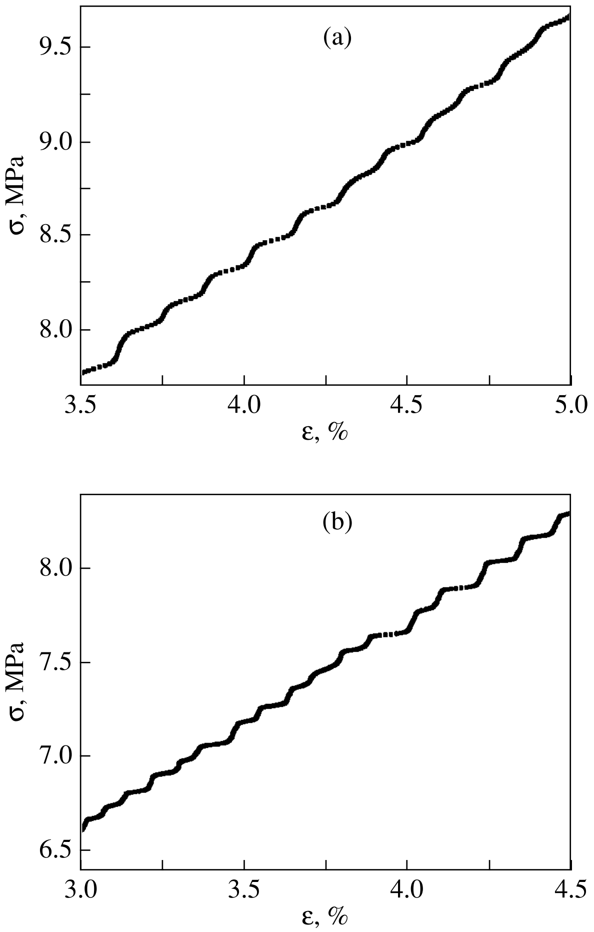

Fig. 6. Fragments of the stress–strain curves for the NaCl : Eu specimens characterized by instability of the plastic flow in (a) zero magnetic field and (b) the magnetic field with an induction of 15 T.

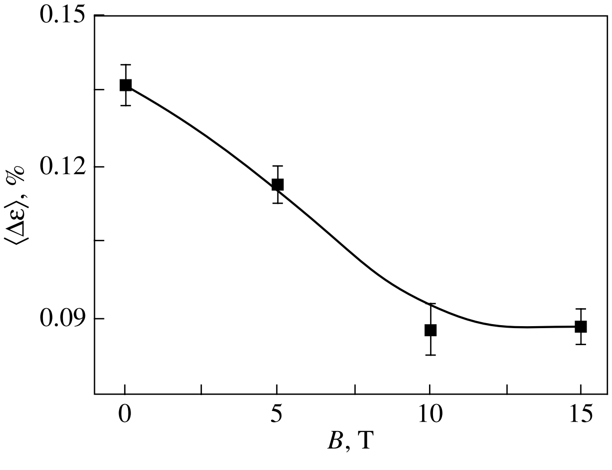

Fig. 7. Dependence of the average strain amplitude (or the average step width in Fig. 6) $\langle\Delta\varepsilon\rangle$ on the magnetic induction B.

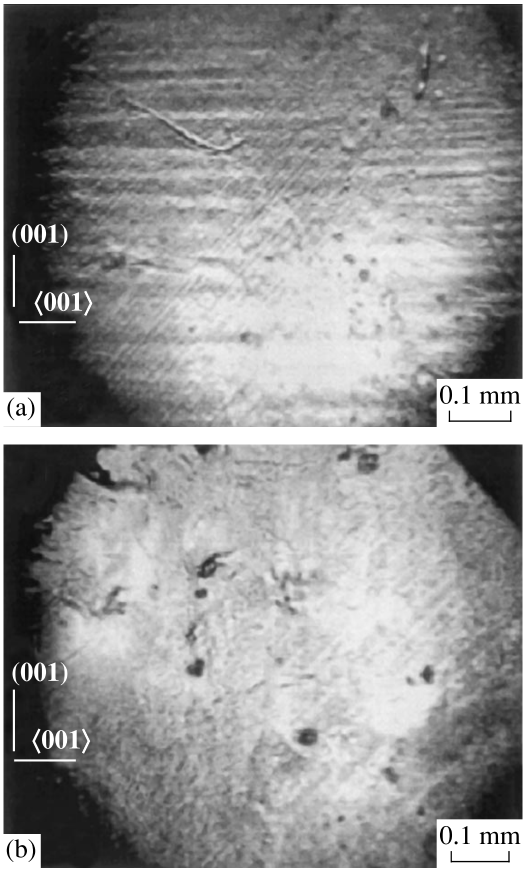

Fig. 8. Micrographs of the surface of the NaCl : Eu crystals strained in (a) zero magnetic field and (b) the magnetic field with an induction of 15 T. Fragments of the stress–strain curves for these specimens are shown in Fig. 6.

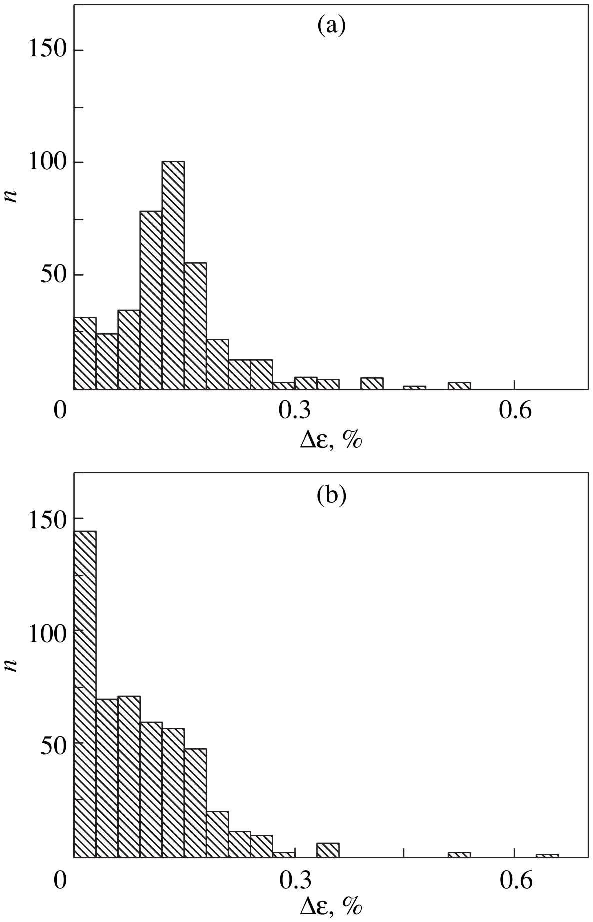

Fig. 9. Averaged histograms of the distribution of strain jumps over their amplitude Δε in (a) zero magnetic field and (b) the magnetic field with an induction of 15 T.

derivative of the stress–strain curve. As a result, we obtained the curve $d\sigma/d\varepsilon$ with maxima (instead of the monotonic stress–strain curve), which is more convenient for counting and analyzing the strain jumps. Then, the coordinates of all peaks in the curve $d\sigma/d\varepsilon$ were determined and the histograms of the distribution of separations between the peaks, i.e., the histograms of the distribution of the strain amplitudes Δε, were constructed with the use of a computer. The obtained histograms of the distributions of strain jumps over their amplitude were averaged for all the crystals strained under identical conditions. It can be seen from Fig. 9a that, in the check experiments at $B = 0$, the averaged histogram exhibits a maximum at $\Delta\varepsilon = 0.15\%$. However, for crystals strained in the magnetic field, the maximum in the histograms is either altogether absent or shifted toward the range of very small strain amplitudes (Fig. 9b).

The probability densities p of amplitude distributions of strain jumps in the crystals strained in the magnetic field and without a magnetic field also differ from each other (Fig. 10). The probability density of the amplitude distribution of strain jumps was calculated from the formula $p = N_i(\Delta\varepsilon)/(\varepsilon_i - \varepsilon_{i-1})N_{\text{total}}$, where $N_i(\Delta\varepsilon)$ is the number of strain jumps in the range $\varepsilon_i - \varepsilon_{i-1}$. The curves depicted in Fig. 10 allow us to assume that the probability density of the amplitude distribution of strain jumps can be represented as the sum of two components, namely, the Gaussian distribution with amplitude A_1 and a noiselike distribution described by the function $A_2/\Delta\varepsilon$ with amplitude A_2. To put it differently, plastic deformation in the crystals can occur through two additive flows of events: (i) motion of correlated ensembles of dislocations and (ii) independent noiselike motion of dislocation groups. Under this assumption, the probability densities of amplitude distributions obtained were approximated by the sum of the two aforementioned functions. As can be seen from Fig. 10, the calculated curves adequately describe the experimental data obtained both from the measurements in the magnetic field and from the check experiments without a magnetic field. This made it possible to construct the dependences of the amplitudes A_1 and A_2 on the magnetic induction B (Fig. 11). It can be seen from Fig. 11

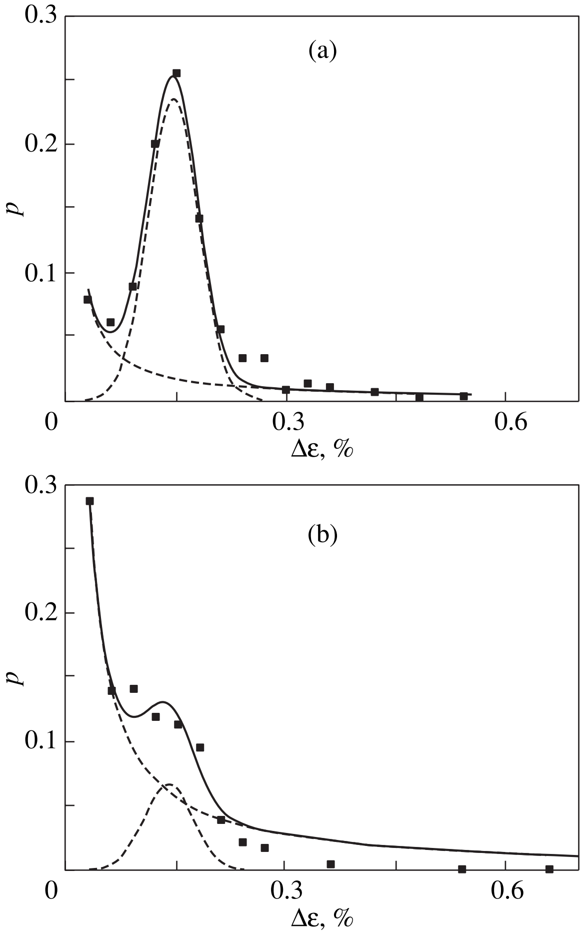

Fig. 10. Probability density p of the distribution of strain jumps over their amplitude $\Delta\varepsilon$ (symbols) and the approximation of the probability density (solid line) by the sum of the Gaussian function with amplitude A_1 (dashed line) and of the function $A_2/\Delta\varepsilon$ with amplitude A_2 (dashed line) in (a) zero magnetic field and (b) the magnetic field with an induction of 15 T.

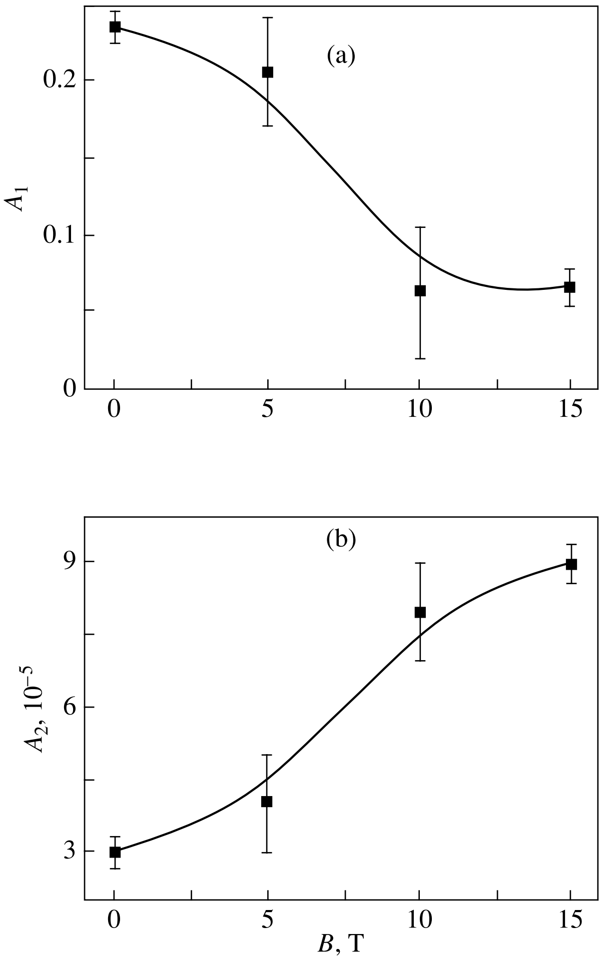

Fig. 11. Dependences of the amplitudes in the decomposition of the probability density of the strain amplitude distribution into (a) the Gaussian function (A_1) and (b) the function $A_2/\Delta\varepsilon$ (A_2) on the magnetic induction B.

that the magnetic field decreases the contribution from the correlated component of the dislocation motion and increases the contribution from the noiselike component. This implies that, in the magnetic field, the amplitude distribution of strain jumps becomes noiselike in character. The dislocation slip bands revealed on the surface of the NaCl : Eu crystals (Fig. 8) are located at an angle of 45° with respect to the [001] direction of the deformation. It is quite probable that these bands correspond to the contribution from the noiselike component of the amplitude distribution of strain jumps. The bands aligned with the (001) plane, whose number decreases in the magnetic field, are most likely associated with the contribution of the Gaussian component to the amplitude distribution of strain jumps.

In [10–13], it was shown that the influence of a magnetic field on the plasticity of NaCl : Eu crystals can manifest itself, among other factors, through changes both in the spin state and in the atomic structure of obstacles to dislocation motion, namely, small-sized europium nonequilibrium clusters, which can be formed either upon aggregating individual impurity–vacancy dipoles into complexes or upon cutting large-sized precipitates by dislocations. The magnetic field favors the formation of precipitates from nonequilibrium clusters arising in the course of plastic deformation. Moreover, it was found [9] that the presence of precipitates in NaCl : Eu crystals leads to suppression of the Portevin–Le Chatelier effect. Taking into account the fast formation of precipitates in a magnetic field in our experiments, the suppression of the Portevin–Le Chatelier effect can be explained by the fact that the time required for depinning of dislocations from obstacles (large-sized clusters) changes and that the plastic strain of the crystals no longer exhibits instabilities. However, it is not ruled out that, in strong magnetic fields, the plasticity of crystals can be affected by the magnetic field through other factors, such as aggregates of paramagnetic ions moving along the dislocation cores due to a magnetic-field gradient, the effect of the Lorentz force on mobile charged dislocations, etc.

4. CONCLUSIONS

Thus, it was established that a static magnetic field with an induction of up to 15 T partially suppresses the Portevin–Le Chatelier effect in NaCl : Eu quenched crystals. This manifests itself in the fact that the probability of plastic strain jumps and their amplitude decrease, the amplitude distribution of the plastic strain jumps becomes random, and the number of shear bands on the surface of the strained crystals decreases. The Portevin–Le Chatelier effect is observed in many metals and alloys important for practical applications. As a rule, this effect plays a negative role: it leads to a heterogeneous plastic flow and a premature fracture of the material. In this respect, one of the applied problems associated with the Portevin–Le Chatelier effect is to devise efficient methods for suppressing serrated plastic deformation. In the present work, it was demonstrated that serrated plastic deformation can be suppressed by applying a static magnetic field.

ACKNOWLEDGMENTS

This work was supported by the Council on Grants from the President of the Russian Federation for the Support of Young Doctors of Sciences (project no. 02-15-99302), the Russian Foundation for Basic Research (project no. 04-02-17577), and the State Program of the Russian Academy of Sciences “Spintronics.”

REFERENCES

1. V. I. Alshits, E. V. Darinskaya, T. M. Perekalina, and A. A. Urusovskaya, Fiz. Tverd. Tela (Leningrad) **29** (2), 467 (1987) [Sov. Phys. Solid State **29** (2), 265 (1987)].
2. Yu. I. Golovin, R. B. Morgunov, A. A. Baskakov, and D. V. Lopatin, Phys. Status Solidi A **160**, R58 (1997).
3. N. A. Tyapunina, V. L. Krasnikov, É. P. Belozerova, and V. N. Vinogradov, Fiz. Tverd. Tela (St. Petersburg) **45** (1), 95 (2003) [Phys. Solid State **45** (1), 98 (2003)].
4. V. I. Alshits, E. V. Darinskaya, T. M. Perekalina, and A. A. Urusovskaya, Zh. Éksp. Teor. Fiz. **115** (3), 951 (1999) [JETP **88** (3), 523 (1999)].
5. Yu. I. Golovin and R. B. Morgunov, Pis’ma Zh. Éksp. Teor. Fiz. **61** (7), 583 (1995) [JETP Lett. **61** (7), 596 (1995)].
6. V. I. Alshits, E. V. Darinskaya, M. V. Koldaeva, and E. A. Petrzhik, Kristallografiya **48** (5), 768 (2003) [Crystallogr. Rep. **48** (5), 768 (2003)].
7. Yu. I. Golovin, Fiz. Tverd. Tela (St. Petersburg) **46** (5), 769 (2004) [Phys. Solid State **46** (5), 789 (2004)].
8. R. B. Morgunov, Usp. Fiz. Nauk **174** (2), 131 (2004) [Phys. Usp. **47** (2), 125 (2004)].
9. E. Orozco and F. Agullo-Lopez, Acta Metall. **34** (9), 1701 (1986).
10. R. B. Morgunov, S. Z. Shmurak, A. A. Baskakov, and Y. Tanimoto, Zh. Éksp. Teor. Fiz. **124** (4), 840 (2003) [JETP **97** (4), 754 (2003)].
11. R. B. Morgunov, S. Z. Shmurak, B. K. Ponomarev, A. A. Baskakov, and V. I. Kulakov, Pis’ma Zh. Éksp. Teor. Fiz. **76** (5), 366 (2002) [JETP Lett. **76** (5), 307 (2002)].
12. R. B. Morgunov and A. A. Baskakov, Fiz. Tverd. Tela (St. Petersburg) **45** (1), 91 (2003) [Phys. Solid State **45** (1), 94 (2003)].
13. A. A. Baskakov, L. R. Dunin-Barkovskiĭ, R. B. Morgunov, Y. Tanimoto, and S. Z. Shmurak, Zh. Éksp. Teor. Fiz. **125** (12), 1632 (2004) [JETP **100** (1), 66 (2005)].
14. L. P. Kubin and Y. Estrin, Acta Metall. **33** (3), 397 (1985).
15. P. Penning, Acta Metall. **20**, 1169 (1972).

Translated by O. Borovik-Romanova

Physics of the Solid State, Vol. 47, No. 7, 2005, pp. 1289–1295. Translated from Fizika Tverdogo Tela, Vol. 47, No. 7, 2005, pp. 1247–1252.
Original Russian Text Copyright © 2005 by Malygin.

DEFECTS, DISLOCATIONS, AND PHYSICS OF STRENGTH

Effect of Disperse Particles on the Formation of Defectless Channels and the Deformation Stability of Neutron-Irradiated Metals

G. A. Malygin
Ioffe Physicotechnical Institute, Russian Academy of Sciences,
Politekhnicheskaya ul. 26, St. Petersburg, 194021 Russia
e-mail: malygin.ga@mail.ioffe.ru

Received October 5, 2004

Abstract—Dislocation-kinetics equations are used to consider the effect of precipitates and disperse particles on the conditions of formation of defectless channels and the appearance of a yield drop and a yield plateau in the stress–strain curves of neutron-irradiated metals and alloys. It is found that, at a volume particle concentration higher than a certain critical value depending on the radiation dose, channels do not form and the yield drop and yield plateau in the stress–strain curves disappear. A high concentration of disperse particles in a metal strongly decreases the uniform strain above which plastic instability in the form of a neck appears in a tensile specimen. The theoretical results are illustrated by available experimental data for copper and copper alloys. *© 2005 Pleiades Publishing, Inc.*

1. INTRODUCTION

The effect of radiation hardening on the stress–strain curves and the plastic-deformation stability of pure fcc metals was theoretically considered in [1]. Using a kinetic equation for a dislocation density, it was shown that deformation instability and the appearance of a yield drop and a yield plateau in the initial stage of the stress–strain curves of irradiated metals are related to strong deformation localization at a microscopic level due to the transformation of radiation defects (vacancy and interstitial loops) into mobile dislocations. Because of their high density, dislocations annihilate partly to form defectless channels (along dislocation-slip planes) with a width $\Delta\Lambda = 0.1$–0.5 μm and a spacing $\Lambda = 1$–5 μm between them, and these channels deteriorate the strength properties of an irradiated material.

Experiments have shown that, if a material has a sufficiently high volume fraction of precipitates or other disperse particles before irradiation, then its plastic deformation after irradiation does not cause the formation of defectless channels and its stress–strain curves have no yield drop or yield plateau. For example, this situation was reported in [2, 3] to be observed in a copper CuNiBe alloy if the volume fraction of Be particles in it was rather high and comparable to the radiation-defect density. A similar situation was also detected in an irradiated Cu–Al_2O_3 alloy containing a few percent of aluminum dioxide particles [2]. It is obvious that disperse particles in these alloys are obstacles to dislocation motion and violate the conditions of formation of defectless channels in irradiated materials.

The authors of [4] found that defectless channels form in a CuCrZr alloy containing Zr precipitates whose volume density is an order of magnitude lower than the radiation-defect density and that the stress–strain diagram of the irradiated alloy contains a yield drop. It should be noted that, near rather coarse zirconium particles, defectless channels are formed; this formation is likely related to a relaxation of local stresses due to the difference in the elastic constants or the thermal expansion coefficients of the zirconium particles and the copper matrix.

In the copper alloys studied in [2–4], precipitates and oxides in channels remained unbroken (no cutting or decrease in their size was detected) despite intense dislocation motion along them. This phenomenon, however, takes place in neutron-irradiated austenitic steel [5]. When deformation is localized in 0.05- to 0.10-μm-wide channels, precipitates and vacancy voids are obstacles to dislocation motion and fail as a result of deformation localization in the channels.

The short review of experimental data given above indicates that precipitates and other disperse particles substantially affect the strength and deformation properties of irradiated materials. Their most important action is the effect on deformation localization and stability in both the initial and final deformation stages; in the latter case, a neck that forms in a tensile specimen upon tension is a deformation localization zone. The strain at which a neck forms decreases as the radiation dose and volume fraction of precipitates increase. The purpose of this work is to theoretically study these phenomena.

1063-7834/05/4707-1289$26.00 © 2005 Pleiades Publishing, Inc.

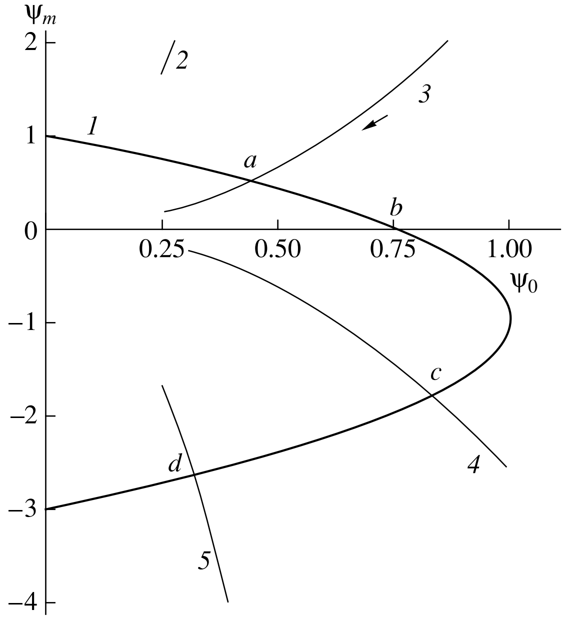

Fig. 1. Regions of values of the parameters ψ_0 and ψ_m in which defectless channels form according to Eqs. (3) and (6) at volume concentrations of disperse particles of (*2*, *5*) 10^{-3} and (*3*, *4*) 10^{-5} and dislocation immobilization coefficients of (*2*, *3*) 1.5 and (*4*, *5*) 0.5.

As in [1], we use a kinetic equation to describe the dislocation density. In Section 2, we apply this equation to consider the effect of the volume concentration of disperse particles on the formation criterion for defectless channels. In Section 3, we analyze the effect of these particles on the appearance of a yield drop and a yield plateau in the stress–strain curves of irradiated and precipitation-hardened metals. Finally, Section 4 deals with an analysis of the effect of disperse particles on the uniform strain before the beginning of formation of a neck-type plastic instability during tension of such materials.

2. DISPERSE PARTICLES AND A CRITERION FOR CHANNEL FORMATION

With allowance for kinetic interaction between dislocations and disperse particles, the kinetic equation for the density of radiation-induced dislocations $\rho_i = \pi d_i N_i$ (where d_i is the diameter of radiation vacancy or interstitial dislocation loops and N_i is their current volume density) has the form [1, 6]

$$\rho_i \frac{d\rho_i}{d\gamma_i} + (\xi - 1)\frac{\lambda_y}{b}\frac{\partial^2 \rho_i}{\partial y^2} = \frac{n}{b} + (1 - \beta_{im})k_m\rho_i - k_a\rho_i^2. \quad (1)$$

Here, $n = n(\rho_{i0})$ is the volume density of dislocation sources; $\rho_{i0} = \pi d_i N_{i0}$ and N_{i0} are the initial densities of radiation dislocations and radiation defects, respectively; $k_m = 1/bl_m$; $l_m = (d_p N_p)^{-1/2}$ is the mean path of dislocations between incoherent and uncuttable disperse particles with a volume density N_p and an average size d_p; b is the Burgers vector; β_{im} is the coefficient of dislocation immobilization due to particles; k_a is the dislocation annihilation coefficient; λ_y is the characteristic dislocation diffusion distance in the direction normal to the plane of dislocation motion; $\xi > 1$ is the coefficient of sign inversion of the dislocation diffusion flux due to strain hardening [6]; and γ_i is the local shear strain in the channels.

For further analysis, it is convenient to put Eq. (1) in dimensionless form,

$$3\psi\frac{\partial\psi}{\partial\Gamma_i} + 2\frac{\partial^2\psi}{\partial Y^2} = \psi_0 + 2\psi_m\psi - 3\psi^2, \quad (2a)$$

where the following dimensionless variables and parameters are introduced:

$$\psi = \frac{\rho}{\rho_{i0}}, \quad \Gamma_i = k_a\gamma_i, \quad Y = \frac{y}{\Lambda_0}, \quad \psi_0 = \frac{3n}{bk_a\rho_{i0}^2},$$
$$\psi_m = \frac{3(1-\beta_{im})}{2bk_a l_m \rho_{0i}}, \quad \Lambda_0 = \left[\frac{3(\xi-1)\lambda_y}{2bk_a\rho_{i0}}\right]^{1/2}. \quad (2b)$$

As is seen from the structure of Eq. (2a), its solutions depend on two parameters, namely, ψ_m and ψ_0. Defectless channels appear when the following relation between these parameters is satisfied [6, 7]:

$$\psi_0 < 1 - \frac{1}{4}(1 + \psi_m)^2. \quad (3)$$

When this condition is met, Eq. (2) describes the motion of the Lüders front in the direction normal to a dislocation slip plane; this motion is accompanied by the formation of a system of defectless channels with a width $\Delta\Lambda$ and an average spacing Λbetween them [6, 7]. In the case of polycrystals, the direction of motion of the Lüders front coincides with the tensile axis of an irradiated sample and channels in grains arise along slip planes with the maximum Schmid factor.

Criterion (3) of channel formation can also be rewritten in the form $\psi_m < \pm 2(1 - \psi_0)^{1/2} - 1$. According to this criterion, curve *1* in Fig. 1 confines the region of values of the parameters ψ_m and ψ_0 where defectless channels can form. Negative values of the parameter ψ_m mean that the coefficient of dislocation immobilization due to disperse particles β_{im} is larger than unity; that is, the particles mainly act as dislocation stoppers rather than dislocation obstacles at which dislocations can multiply (in the latter case, $\beta_{im} < 1$).

It follows from condition (3) that, in the absence of disperse particles ($\psi_m = 0$), channels appear if $\psi_0 < 3/4$. Since the volume density of dislocation sources in Eq. (2b) is $n = \delta_0 l_i^{-3}$ (where $l_i = \rho_{i0}^{-1/2}$ is the average length of dislocation segments forming Frank–Read dislocation sources and $\delta_0 < 1$ is the relative fraction of effective sources), we arrive at the conclusion that channels will appear if the initial density of radiation dislocations ρ_{i0} and, hence, the initial density of radiation defects N_{i0} exceeds the critical values $\rho_{ic} = (4\delta_0/bk_a)^2$ and $N_{ic} = \rho_{ic}/\pi d_i$, respectively. These critical values are specified by the balance of the processes of dislocation generation and annihilation during plastic deformation of an irradiated material. The initial density of radiation defects depends on the radiation dose ϕ according to the expression [1]

$$N_{i0} = N_{im}\left[1-\exp\left(-\left(\frac{\phi}{\phi_0}\right)^{\frac{2}{3}}\right)\right]. \qquad (4)$$

Therefore, in the absence of disperse particles, channels will form when the dose exceeds the critical value

$$\phi_c = \phi_0\left[\ln\left(\frac{1}{1-\frac{N_{ic}}{N_{im}}}\right)\right]^{3/2}. \qquad (5)$$

For copper [1, 8], $N_{im} = 7\times10^{17}$ cm^{-3}, $\phi_0 = 3\times10^{20}$ cm^{-2}, $d_i = 2$ nm, $\delta_0 = 5\times10^{-2}$, $k_a = 3.5$, and $b = 0.256$ nm. Using the equations given above, we obtain $\rho_{ic} = 5\times10^{10}$ cm^{-2}, $N_{ic} = 8\times10^{16}$ cm^{-3}, and $\phi_c = 1.2\times10^{19}$ cm^{-2}; these values are close to the experimental values from [1].

According to the notation introduced in Eq. (2b), the parameter ψ_m depends not only on the radiation-defect density but also on the volume density of disperse particles. Since the volume concentration of particles is $f = \pi d_p^3 N_p/6$, the average interparticle distance can be written as $l_m = d_p(\pi/6f)^{1/2}$. Therefore, the parameters ψ_0 and ψ_m depend on the radiation dose ϕ and the particle concentration f as

$$\psi_0 = \frac{3\delta_0}{bk_a\rho_{i0}^{1/2}(\phi)},$$
$$\psi_m = \frac{3(1-\beta_m)}{2bk_ad_p\rho_{i0}(\phi)}\left(\frac{6}{\pi}\right)^{1/2}f^{1/2}. \qquad (6)$$

According to Eq. (6), we have $\psi_m = \delta_m f^{1/2}\psi_0^2$. This relation between the parameters ψ_m and ψ_0 is plotted in Fig. 1 (curves *2*, *3*) at two values of the particle concentration f (10^{-3} and 10^{-5}, respectively), particle size $d_p = 5$ nm [2, 3], $\delta_m = 8\times10^3$, and dislocation immobilization coefficient $\beta_{im} = 0.5$, with the radiation dose varying from 10^{18} to 10^{22} cm^{-2}. The values of the other parameters are given above. Curves *4* and *5* illustrate the relationship between the parameters ψ_m and ψ_0 in the case of predominant dislocation immobilization due to disperse particles ($\beta_{im} = 1.5$). The arrow near curve *3* shows the direction in which the radiation dose increases for curves *2–5*.

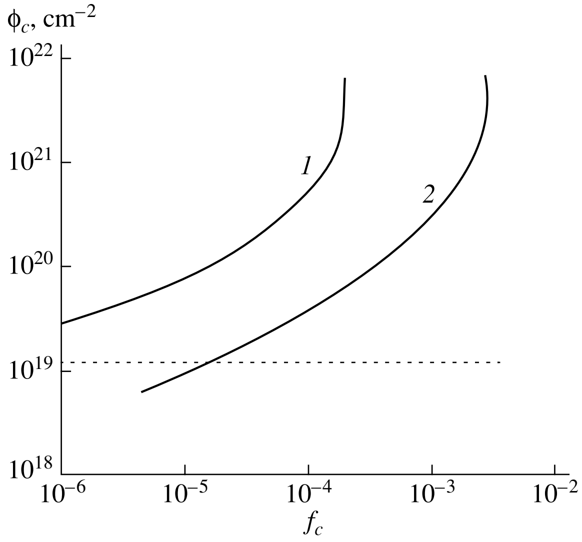

Fig. 2. Dependence of the critical radiation dose for the formation of defectless channels ϕ_c on the volume concentration of disperse particles f_c at dislocation immobilization coefficients of (*1*) 1.5 and (*2*) 0.5. The dashed line demonstrates the critical dose in the absence of particles.

The points of intersection of curves *3–5* with curve *1* in Fig. 1 (points *a–d*) specify the critical values of the parameters ψ_m and ψ_0 and, hence, the critical dose ϕ_c and the critical particle concentration f_c for the formation of defectless channels and the appearance of a yield drop and a yield plateau in the stress–strain curves of radiation- and precipitation-hardened copper alloys. Point *b* corresponds to the absence of disperse particles in a material. As is seen from Fig. 1, curve *2* does not intersect curve *1*; therefore, at the volume particle concentration $f = 10^{-3}$ (where particles mainly act as centers of dislocation multiplication), channels do not form. This behavior results from the fact that, according to Eq. (4), the density of radiation defects reaches the saturation value N_{im} at high doses; hence, there exists a limiting value of the parameter ψ_0 (which is $\psi_0 \approx 0.25$ in the case considered) at which the curves do not intersect and, hence, condition (3) is not satisfied.

Using Eq. (6) and criterion (3), we can represent the relationship between the critical values of f and ϕ in implicit form as

$$f_c = \frac{2\pi}{27}\left[\frac{\pm2(-\psi_0(\phi_c))^{1/2}-1}{1-\beta_{im}}\right]^2 k_a^2 d_p^2 \rho_{i0}(\phi_c). \qquad (7)$$

Figure 2 shows this dependence for the parameter values given above and with the dislocation immobilization coefficient equal to 0.5 (curve *2*) and 1.5 (curve *1*). The plus and minus signs in Eq. (7) correspond to the former and latter curves, respectively. It is seen that the

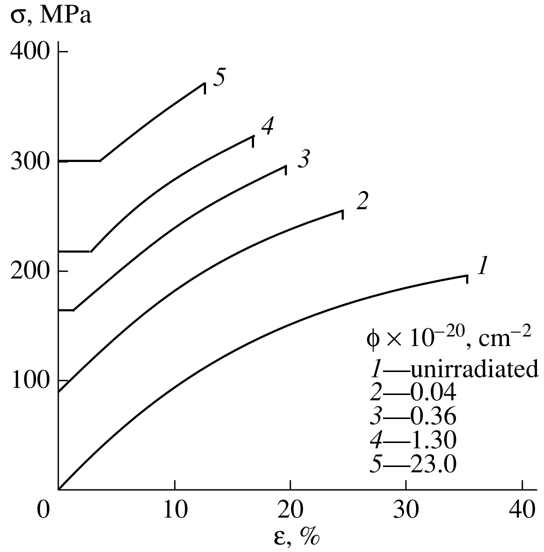

Fig. 3. Stress–strain curves calculated from Eqs. (8) and (9) for pure copper irradiated to various doses ϕ [1].

higher the concentration of disperse particles, the higher the radiation dose required for the channel formation. The volume concentration of precipitates in the CuNiBe alloy was 3.3×10^{-2} [2, 3]. As follows from Fig. 2, this concentration is significantly higher than the critical particle concentration for the formation of defectless channels in this alloy. In the case of the CuCrZr alloy, the concentration of Zr particles was an order of magnitude lower (2×10^{-3}) and, in agreement with theory, the formation of channels was observed in this alloy [2, 4]. The radiation dose for both alloys was the same (0.3 dpa), which corresponds to the limiting concentration of radiation defects in copper N_{im} (see Eq. (4)) and to the dose $\phi \approx 3 \times 10^{22}$ cm^{-2} [8].

3. YIELD DROP AND YIELD PLATEAU

In [1], we used Eq. (1) to analyze the mechanism of formation of a yield drop and a yield plateau in neutron-irradiated copper in the absence of disperse particles, i.e., for $k_m = 0$ in Eq. (1). Figure 3 shows the calculated stress–strain (σ–ε) curves for copper irradiated to various doses ϕ. The calculation is based on a linear summation of stresses:

$$\sigma(\varepsilon, \phi) = \sigma_i(\varepsilon, \phi) + \sigma_d(\varepsilon), \qquad (8)$$

where $\sigma_i = m\alpha_i' b\mu\rho_i^{1/2}$ and $\sigma_d = m\alpha b\mu\rho_d^{1/2}$ are the stresses induced by radiation and strain hardening, respectively; α_i' [1] and α are the corresponding interaction constants; μ is the shear modulus; and m is the Taylor factor. Curve *1* in Fig. 3 illustrates the stress–strain curve of unirradiated copper according to the law [1]

$$\sigma_d(\varepsilon) = \sigma_3\left[1 - \exp\left(-\frac{1}{2}mk_a\varepsilon\right)\right], \qquad (9)$$

where $\sigma_3 = m\alpha b\mu\rho_3^{1/2}$ is the flow stress at the end of the third stage of the stress–strain curve (the stage of dynamic recovery), $\rho_3 = (k_f/k_a)^2$ is the dislocation density at the end of this stage, and k_f is a coefficient that determines the intensity of dislocation multiplication at forest dislocations during multiple slip ($bk_f \approx 10^{-2}$). In our calculations, we used the following relation between the local shear strain in channels γ_i and the tensile strain ε: $\varepsilon = (\Delta\Lambda/\Lambda)\gamma_i/m$, where $\Delta\Lambda/\Lambda = 0.1$ is the volume fraction of channels in the material [6, 7]. As can be seen from Fig. 3, a yield plateau in the stress–strain curves for copper appears at doses above 10^{19} cm^{-2}.

To analyze the effect of disperse particles on the character of the stress–strain diagrams of an irradiated metal, we need to know the dependence of the stress σ_i not only on the radiation dose ϕ but also on the volume particle concentration f. To this end, it is necessary to solve Eq. (1) with the coefficient $k_m \neq 0$. As follows from Eq. (2), the dimensionless form of this equation in a uniform approximation is

$$\psi\frac{\partial\psi}{\partial\Gamma_i} = \bar{\psi}_0 + \bar{\psi}_m\psi - \psi^2. \qquad (10)$$

The parameters $\bar{\psi}_0 = \psi_0/3$ and $\bar{\psi}_m = 2\psi_m/3$ are given by Eqs. (6). By solving Eq. (10), we obtain the dependence of the dislocation density in channels $\psi = \rho_i/\rho_{i0}$ on the local strain γ_i in the implicit form

$$\gamma_i = \frac{-1}{2k_a}\left[\left(1 + \frac{\bar{\psi}_m}{\Delta}\right)\ln\frac{\psi - \frac{1}{2}(\bar{\psi}_m + \Delta)}{1 - \frac{1}{2}(\bar{\psi}_m + \Delta)}\right.$$
$$\left. + \left(1 - \frac{\bar{\psi}_m}{\Delta}\right)\ln\frac{\psi - \frac{1}{2}(\bar{\psi}_m - \Delta)}{1 - \frac{1}{2}(\bar{\psi}_m - \Delta)}\right], \qquad (11)$$
$$\Delta(\phi, f) = [\bar{\psi}_m^2(\phi, f) + 4\bar{\psi}_0(\phi)]^{1/2}.$$

The dependence of the dislocation density in channels on the strain in them is illustrated in Fig. 4 in the absence of disperse particles (curve *1*) and for the case where their concentration increases (curves *2*–*4*) in a copper alloy irradiated to a dose of 10^{20} cm^{-2} (the dislocation immobilization coefficient is $\beta_{im} = 0.5$). The dashed line demonstrates the initial density of radiation dislocations. It is seen that, at the given radiation dose

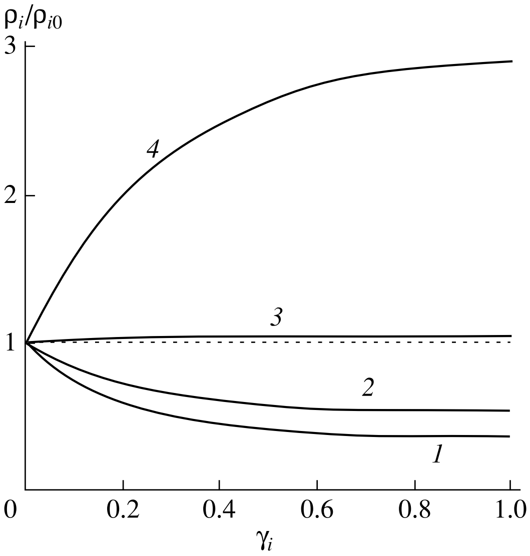

Fig. 4. Dependence of the radiation-dislocation density ρ_i on the shear strain in channels γ_i (*1*) in the absence of disperse particles and (*2–4*) at a volume concentration f equal to (*2*) 10^{-5}, (*3*) 10^{-4}, and (*4*) 10^{-3}. The dashed line demonstrates the initial dislocation density.

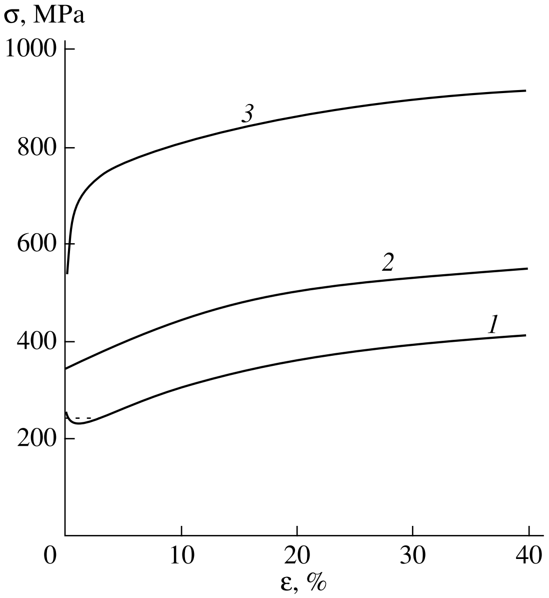

Fig. 5. Stress–strain curves calculated from Eq. (13) for copper irradiated to a dose of 10^{20} cm^{-2} at various values of the concentration of disperse particles f: (*1*) 10^{-5}, (*2*) 10^{-4}, and (*3*) 10^{-3}.

and a particle volume concentration below 10^{-4}, the dominating process in the alloy (as in the pure metal) is dislocation annihilation, which brings about the formation of defectless channels and softening of the irradiated material. At higher particle concentrations, dislocation multiplication is dominant, channels do not form, and the material is additionally strain-hardened.

Apart from the fact that disperse particles contribute to the strain hardening, they are also obstacles that limit dislocation mobility. Dislocations can bypass particles during their motion in a slip plane if the shear stress is equal to [9]

$$\tau_{\mathrm{or}} = \beta_{\mathrm{or}}\frac{\mu b}{l_m - d_p}, \quad \beta_{\mathrm{or}} = \frac{1}{2\pi}\ln\frac{l_m}{b}. \tag{12}$$

Here, $l_m = d_p(\pi/6f)^{1/2}$ is the interparticle distance introduced in Section 3. With inclusion of the Orowan stress $\sigma_{\mathrm{or}} = m\tau_{\mathrm{or}}$, the flow stress of a precipitation-hardened and irradiated alloy is equal to

$$\sigma(\varepsilon, \phi, f) = \sigma_i(\varepsilon, \phi, f) + \sigma_{\mathrm{or}}(f) + \sigma_d(\varepsilon). \tag{13}$$

Formula (13) implies a linear law of summation of the stresses σ_{or} and σ_d. Figure 5 shows the flow stresses calculated from Eq. (13) for copper irradiated to a dose of 10^{20} cm^{-2} at various concentrations of disperse particles. It is seen that, at a particle concentration below 10^{-4}, the stress–strain curves have a yield drop, which indicates softening of the irradiated alloy. The dashed line in Fig. 5 demonstrates the level of a yield plateau plotted using the equal-area rule [1]. The length of the yield plateau (Lüders strain ε_L) is 3%. For a particle concentration equal to or higher than 10^{-4}, the results of calculations shown in Figs. 2 and 4 indicate that the yield drop and yield plateau disappear and that the flow stresses increase substantially due to precipitation hardening.

4. UNIFORM STRAIN AND ULTIMATE STRENGTH

When calculating the stress–strain curves in Fig. 5, we did not take into account that, as the radiation and precipitation hardening increase, the uniform strain to necking ε_u (to the beginning of plastic instability and deformation localization in the form of a neck) decreases significantly. As a result, segments with a decreasing stress appear in the stress–strain curves. Their appearance and the value of the strain ε_u are dictated by the well-known Considère criterion $d\sigma/d\varepsilon \le \sigma$. By substituting stress (13) into this criterion, we find the dependence of the strain ε_u and the ultimate tensile strength $\sigma_u = \sigma(\varepsilon_u)$ on the particle concentration and radiation dose:

$$\varepsilon_u(\phi, f) = \frac{2}{mk_a}\ln\frac{1 + \frac{1}{2}mk_a}{1 + \frac{\sigma_{im}(\phi, f) + \sigma_{\mathrm{or}}(f)}{\sigma_3}}, \tag{14}$$

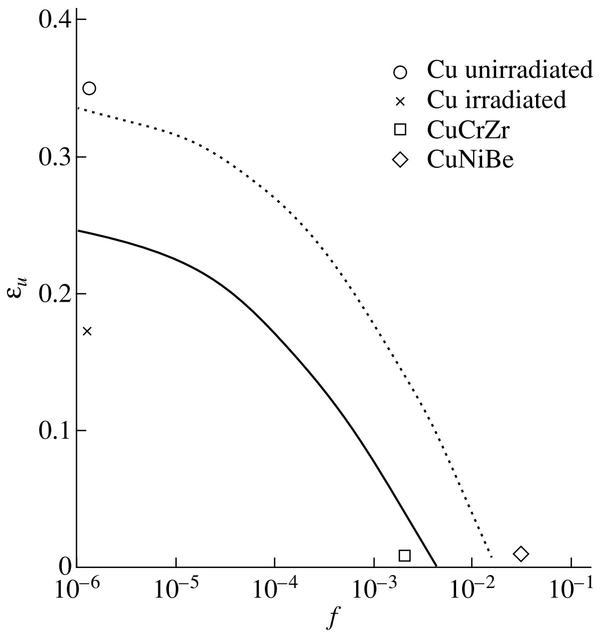

Fig. 6. Dependence of the uniform strain ε_u on the concentration of disperse particles f in copper irradiated to a dose of 10^{20} cm^{-2} (solid line) and in the absence of irradiation (dashed line). Experimental points correspond to Cu [10], CuCrZr, and CuNiBe [2, 3].

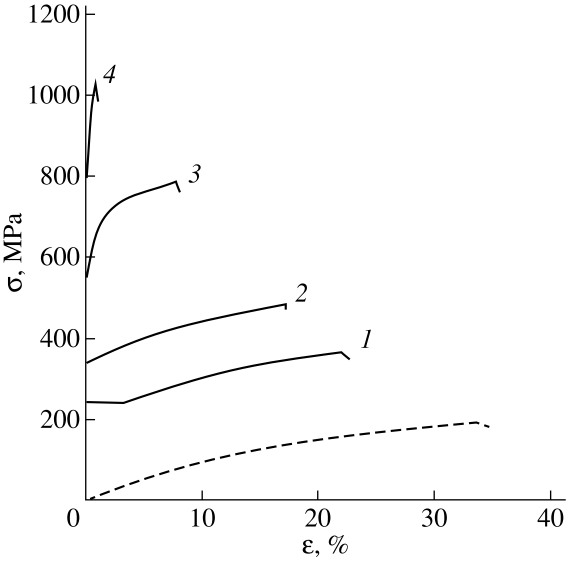

Fig. 7. Stress–strain curves for copper irradiated to a dose of 10^{20} cm^{-2} calculated with allowance for deformation localization in a neck at various values of the concentration of disperse particles f: (*1*) 10^{-5}, (*2*) 10^{-4}, (*3*) 10^{-3}, and (*4*) 4×10^{-3}. The dashed line is the stress–strain curve of copper in the absence of irradiation and particles.

$$\sigma_u(\phi, f) = \frac{\frac{1}{2}mk_a}{1+\frac{1}{2}mk_a}[\sigma_3 + \sigma_{im}(\phi, f) + \sigma_{\rm or}(f)], \tag{15}$$

$$\sigma_{im}(\phi, f) = \sigma_{i0}(\phi)\left[\frac{\bar{\psi}_m(\phi, f) + \Delta(\phi, f)}{2}\right]^{1/2}.$$

The stresses σ_{i0} and σ_{im} entering into Eqs. (14) and (15) correspond to the initial (ρ_{i0}) and the limiting (at $\gamma_i > 0.5$, $\varepsilon > 1.7\%$) densities of radiation dislocations (Fig. 4).

In Fig. 6, the solid curve illustrates the strain ε_u calculated from Eq. (14) for copper irradiated to a dose of 10^{20} cm^{-2} as a function of the volume concentration of disperse particles in it. The dashed line demonstrates an analogous dependence in the absence of irradiation. It is seen that, at particle concentrations above 1%, the uniform strain in the irradiated copper does not exceed 1%. Irradiation additionally decreases this strain, and the drop increases with radiation dose (Fig. 3). The results of calculations agree with the experimental data obtained for pure copper and the copper alloys indicated in Fig. 6. Figure 7 shows the stress–strain curves calculated with allowance for deformation localization (necking) for copper irradiated and hardened by disperse particles. At a particle concentration of 4×10^{-3}, deformation localization begins at a uniform strain of 0.7% (curve *4* in Fig. 7).

From Eq. (15) and the results shown in Fig. 7, it follows that, as the radiation dose and the particle concentration increase, the stress σ_u at which a tensile specimen loses its plastic stability and begins to fragment plastically (i.e., begins to fail) increases. According to Eq. (15), this is mainly caused by the increased yield strength $\sigma_y(\phi, f) = \sigma_{0r}(f) + \sigma_{i0}(\phi)$. In this case, the ratio σ_u/σ_y decreases and tends to a value close to unity, which indicates a loss of the plasticity margin and the embrittlement of a radiation- and precipitation-hardened material under tension conditions. This situation should lead, for example, to unstable propagation of plastic microcracks in structural materials irradiated at high radiation doses, which makes these materials (ductile in their structure and nature) brittle and unreliable in operation.

In conclusion, we note that calculations of the deformation and strength properties of crystalline (in particular, metallic) materials using physical microscopic (involving dislocation) rather than phenomenological relations between stresses and strains allow one to naturally take into account the effect of structural factors (in our case, radiation defects and disperse particles) on the strength and deformation properties of these materials.

REFERENCES

1. G. A. Malygin, Fiz. Tverd. Tela (St. Petersburg) **47** (4), 632 (2005) [Phys. Solid State **47** (4), 656 (2005)].

2. D. J. Edwards, B. N. Singh, P. Toft, and M. Eldrup, J. Nucl. Mater. **258–263**, 978 (1998).
3. B. N. Singh, N. M. Ghoniem, and H. Trinkaus, J. Nucl. Mater. **307–311**, 159 (2002).
4. B. N. Singh, J. F. Stubbins, and P. Toft, Ris. Report, No. R-1128 (EN), March 2000.
5. V. I. Shcherbak and V. D. Dmitriev, Fiz. Met. Metalloved. **64** (3), 591 (1987).
6. G. A. Malygin, Usp. Fiz. Nauk **169** (9), 979 (1999) [Phys. Usp. **42** (9), 887 (1999)].
7. G. A. Malygin, Fiz. Tverd. Tela (Leningrad) **33** (4), 1069 (1991) [Sov. Phys. Solid State **33** (4), 606 (1991)].
8. M. Victoria, N. Baluc, C. Bailat, Y. Dai, M. I. Luppo, R. Schaublin, and B. N. Singh, J. Nucl. Mater. **276**, 114 (2000).
9. M. F. Ashby, *Physics of Strength and Plasticity* (Metallurgiya, Moscow, 1972), p. 88 [in Russian].
10. M. J. Makin, *Radiation Effects*, Ed. by W. F. Sheely (Gordon and Breach, New York, 1967), p. 627.

Translated by K. Shakhlevich

Physics of the Solid State, Vol. 47, No. 7, 2005, pp. 1296–1298. Translated from Fizika Tverdogo Tela, Vol. 47, No. 7, 2005, pp. 1253–1254.
Original Russian Text Copyright © 2005 by Smirnov, Bekkauer, Voloshin.

DEFECTS, DISLOCATIONS, AND PHYSICS OF STRENGTH

The Influence of Preliminary Magnetic and Thermomagnetic Treatment on the Microhardness of KDP Crystals

A. E. Smirnov*, N. N. Bekkauer, and A. É. Voloshin***

** Shubnikov Institute of Crystallography, Russian Academy of Sciences,*
Leninskiĭ pr. 59, Moscow, 119333 Russia
e-mail: asmirnov46@mail.ru
*** Peoples Friendship University, ul. Miklukho-Maklaya 6, Moscow, 117198 Russia*

Received July 16, 2004; in final form, November 17, 2004

Abstract—The influence of preliminary treatment of KH_2PO_4 (KDP) crystals in a static magnetic field of 0.5 T for 1 h on the microhardness is revealed. It is found that, for a sample subjected to magnetization, the microhardness as a function of time t exhibits a nonmonotonic behavior with a sharp maximum at $t = 4$ days. The time required to reach the maximum microhardness decreases to three days when the sample is quenched before magnetization. *© 2005 Pleiades Publishing, Inc.*

1. INTRODUCTION

The first paper [1] concerned with the influence of preliminary magnetic treatment on the microhardness of LiF crystals was published in 1987. The scheme of the experiment was as follows: (i) preliminary magnetic treatment, (ii) storage for a certain period of time, and (iii) measurement. These experiments demonstrated that the microhardness of as-magnetized LiF samples was no different from that of the initial (unmagnetized) crystal. Then, the microhardness increased, passed through a maximum within approximately two days of the magnetic treatment, and gradually vanished. Unfortunately, in [1], similar experiments were not performed with a reference sample that had not been subjected to magnetic treatment. Nonetheless, it was apparently first shown in the aforementioned work that the microhardness is responsive to magnetic treatment; i.e., the microhardness increases with an increase in the magnetic field strength and the magnetic treatment time. In [1], it was assumed that paramagnetic centers transform in response to a magnetic field. This assumption was experimentally confirmed by Golovin and Morgunov [2] and Tyapunina *et al.* [3], who managed to separate the magnetic and mechanical effects.

Earlier [4], we studied the influence of preliminary magnetization on the yield strength of NaCl crystals containing nickel paramagnetic impurities. Analysis of the dependences of the yield strength on the duration of preliminary magnetic treatment and on the time elapsed from this treatment demonstrated that, in both cases, the impurity subsystem undergoes a magnetic transformation with time.

More recently, the influence of preliminary thermomagnetic treatment on the yield strength of NaCl : Eu [5] and NaCl : Ni [6] crystals was studied using the following scheme: (i) thermal treatment, (ii) storage for a certain period of time, (iii) magnetic treatment, and (iv) measurement. For example, in our previous work [6], samples were annealed at 1000 K for 3 h, quenched in liquid nitrogen, and allowed to stand at room temperature over different periods from 0 to 240 h, with the yield strength being measured at regular intervals. It was found that the yield strength varies nonmonotonically: as the storage time increases, the yield strength first remains constant, then decreases significantly after storage for ~40 h, and again increases.

Obviously, the above phenomena are determined by the magnetic memory of the materials: magnetic or thermomagnetic treatment results in the formation of an impurity structure that evolves with time and whose response to a magnetic field can be revealed from a change in the microhardness or the yield strength of the crystal. The effects observed exhibit a relaxation nature due to the redistribution of the internal energy in the crystal.

The purpose of the present work was to elucidate how the preliminary magnetic and thermomagnetic treatment affects the microhardness of KH_2PO_4 (KDP) crystals grown from a solution at the Shubnikov Institute of Crystallography of the Russian Academy of Sciences.

2. SAMPLE PREPARATION AND EXPERIMENTAL TECHNIQUE

The initial microhardness of aged, sawed out, mechanically ground, and polished samples (5 × 5 × 1 mm in size) was determined with a PMT-3 microhardness meter at a load of 5 g. The samples were divided into two groups.

In the first series of experiments, one of two samples with a known initial microhardness was magnetized in a magnetic field of 0.5 T for 1 h. Then, the microhardnesses of this sample and the reference (unmagnetized) crystal were measured again. These samples were allowed to stand for 14 days, during which their microhardnesses were measured at regular intervals. The spread of microhardnesses about a mean value was ±4 kg/mm^2.

In the second series of experiments (thermomagnetic treatment), the magnetic treatment of one of two samples with a known initial microhardness was preceded by annealing (437 K, 1 h) and subsequent quenching to room temperature. The conditions of thermal treatment are determined by the brittleness of the KDP crystals, specifically by their instability against heating and thermal shock.

3. RESULTS AND DISCUSSION

Figure 1 shows the time dependences of the microhardness of a magnetized KDP crystal (curve *1*) and a reference (unmagnetized) sample (curve *2*). It can be seen that the microhardness of the reference sample slightly increases with time. The microhardness of the preliminarily magnetized sample remains nearly constant and close to the initial value for the first two days, then increases considerably, and reaches a maximum within four days of the magnetic treatment. With a further increase in the storage time, the microhardness decreases to the background values obtained for the reference sample.

A similar dependence is observed in the second series of experiments (Fig. 2), with the only difference that, after the thermal treatment, the maximum of the hardening effect is shifted to the left by one day; i.e., the maximum microhardness is reached within three days of the treatment but its magnitude remains the same as in the first series of experiments (cf. curves *1* in Figs. 1 and 2). Moreover, the microhardness of the reference sample (heat treated but not exposed to a magnetic field) does not change with time (curve *2*). This can be explained by the fact that mechanical treatment (cutting with a water jet saw, grinding, polishing) of the samples leads to the formation of a surface crystalline layer saturated with water. During thermal treatment, the water evaporates and thus ensures a constant microhardness of the crystal. The evaporation of water from the sample not subjected to thermal treatment (curve *2* in Fig. 1) proceeds over an extended period; as a result, the microhardness of the sample increases gradually.

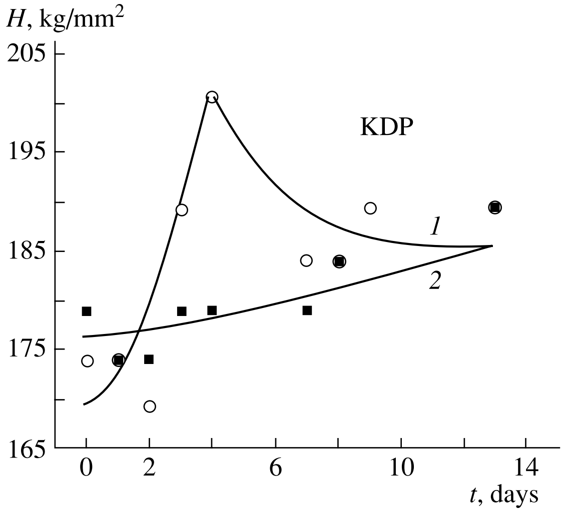

Fig. 1. Comparison of the time dependences of the microhardness H for (*1*) the sample subjected to magnetic treatment and (*2*) the reference (unmagnetized) sample.

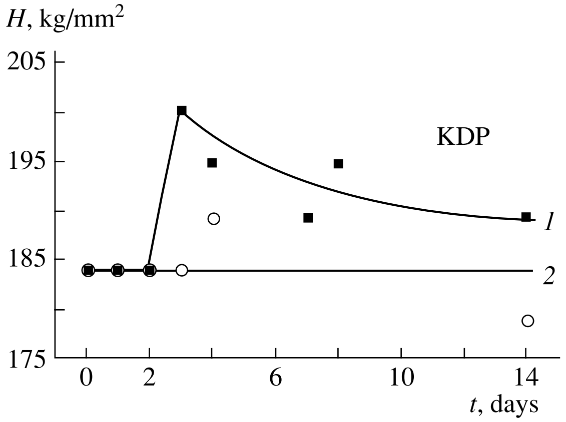

Fig. 2. Comparison of the time dependences of the microhardness H for (*1*) the sample subjected to thermomagnetic treatment and (*2*) the reference (unmagnetized) sample.

It is assumed that the conditions responsible for the sensitivity of nonmagnetic crystals to a magnetic field and those favorable for a spin transition removing the forbiddenness of an electron transition can arise only when the initial impurity structure is nonequilibrium. This can be achieved through preliminary thermal treatment of the crystals. As a consequence, the impurity subsystem probably evolves with an earlier formation of magnetically sensitive states, i.e., point defect complexes that respond to subsequent magnetic action. Annealing causes the decay of impurity complexes, whereas quenching “freezes” centers formed after the decay. The newly formed impurity structure evolves through diffusion in such a way that small paramagnetic centers increase in size. This manifests itself in the fact that the microhardness as a function of time exhibits a nonmonotonic behavior, with a maximum being reached in three days (Fig. 2). A similar dependence is observed without thermal treatment; however, in this case, the maximum of the hardening effect is reached in a longer time, t = 4 days (Fig. 1).

ACKNOWLEDGMENTS

The authors are grateful to V.I. Al'shits for his participation in discussions of the results and helpful remarks. A.E. Smirnov and A.É. Voloshin acknowledge the support of the Russian Foundation for Basic Research, project no. 03-02-16423.

REFERENCES

1. A. E. Smirnov and A. A. Urusovskaya, Fiz. Tverd. Tela (Leningrad) **29** (3), 852 (1987) [Sov. Phys. Solid State **29** (3), 485 (1987)].
2. Yu. I. Golovin and R. B. Morgunov, Pis'ma Zh. Éksp. Teor. Fiz. **58** (3), 189 (1993) [JETP Lett. **58** (3), 191 (1993)].
3. N. A. Tyapunina, V. L. Krasnikov, and É. P. Belozerova, Kristallografiya **45** (1), 156 (2000) [Crystallogr. Rep. **45** (1), 150 (2000)].
4. A. A. Urusovskaya, A. E. Smirnov, and N. N. Bekkauer, *Proceedings of XXXVI International Workshop on Basic Problems of Strength, Vitebsk, Belarus, 2000*, Part 1, p. 294.
5. R. B. Morgunov and A. A. Baskakov, Fiz. Tverd. Tela (St. Petersburg) **43** (9), 1632 (2001) [Phys. Solid State **43** (9), 1700 (2001)].
6. A. E. Smirnov, N. N. Bekkauer, and V. V. Sadchikov, Kristallografiya **48** (6), 1040 (2003) [Crystallogr. Rep. **48** (6), 972 (2003)].

Translated by V. Artyukhov

Physics of the Solid State, Vol. 47, No. 7, 2005, pp. 1299–1305. Translated from Fizika Tverdogo Tela, Vol. 47, No. 7, 2005, pp. 1255–1260.
Original Russian Text Copyright © 2005 by Gaviko, Korolev, Arkhipov, Bebenin, Mukovskiĭ.

MAGNETISM
AND FERROELECTRICITY

X-ray Studies of the (La,Sr)MnO_3 Perovskite Manganite Structure

V. S. Gaviko*, A. V. Korolev*, V. E. Arkhipov*, N. G. Bebenin*, and Ya. M. Mukovskiĭ**

** Institute of Metal Physics, Ural Division, Russian Academy of Sciences,*
ul. S. Kovalevskoĭ 18, Yekaterinburg, 620219 Russia
e-mail: gaviko@imp.uran.ru
*** Moscow State Institute of Steel and Alloys, Leninskiĭ pr. 4, Moscow, 119049 Russia*

Received August 2, 2004

Abstract—X-ray studies of perovskite manganites $(La_{0.9}Sr_{0.1})_{0.9}MnO_3$ and $La_{1-x}Sr_xMnO_3$ ($x = 0.1, 0.15, 0.2, 0.25$) are reported. The atom positions and interatomic distances and angles are calculated as a function of Sr doping at room temperature using the FullProf software. The temperature dependences of the crystal lattice parameters and unit cell volume are investigated. The effects of structural and magnetic phase transitions on the crystal lattice parameters are studied in detail. The bulk magnetoelastic contribution to thermal expansion is studied experimentally and calculated. © *2005 Pleiades Publishing, Inc.*

1. INTRODUCTION

Rare-earth manganites $La_{1-x}Sr_xMnO_3$ have three different lattice structures at room temperature depending on the Sr or oxygen content: monoclinic ($P2_1/c$), orthorhombic ($Pnma$), and rhombohedral ($R\bar{3}c$) [1–6]. All these lattices are derived from the perovskite cubic lattice. The orthorhombic unit cell is constructed as follows: two of its three primitive vectors point in the [110] and $[1\bar{1}0]$ directions of the cubic cell, and the third is directed along the [001] cubic axis. In the *Pnma* settings, the [001] cubic axis coincides with the orthorhombic axis **b**. The monoclinic cell differs from the orthorhombic cell in that one of the angles between its faces is not equal to 90°. The basic axes of the rhombohedral cell coincide with the [110], [101], and [011] directions of the cubic cell. The angles between these directions are equal to 60° in a perfect cubic lattice, but they deviate from this value in the rhombohedral setting (space group $R\bar{3}c$). When a rhombohedral lattice is described in the hexagonal setting, the hexagonal axis **c** is chosen to be along the [111] cube body diagonal. In a first approximation, all these lattice types of perovskite manganites can be considered a distorted cubic lattice. Usually, the following two types of distortion are discussed: rotations of MnO_6 octahedra relative to one another and Jahn–Teller deformations, for which octahedra themselves are distorted. In the latter case, there are six different values for the Mn–O bond lengths (the bond lengths are stretched or shortened depending on their direction). Depending on the type of deformation, Q_2 or Q_3 Jahn–Teller modes are considered (see, e.g., [1, 2, 5, 6] for details).

Two modifications are distinguished in the orthorhombic structure: the pseudocubic (O^*) phase, where the lattice parameters are close to each other, $a \approx c \approx b/\sqrt{2}$, and the O' phase, where a, c, and $b/\sqrt{2}$ differ considerably. The Jahn–Teller mode Q_2 is usually present in the O' phase [1, 2]. This mode shifts oxygen ions in the MnO_6 octahedron in such a way that all three kinds of Mn–O distances become different. The O^* phase is affected by the Q_2 mode to a much lesser degree. In several papers, another rhombohedral phase (O'') has been reported. This phase is distinguished by complete suppression of Jahn–Teller deformations [7, 8].

Apart from the reasons discussed above, the lattice can be significantly affected by various kinds of ordering, such as charge ordering of Mn^{+4} and Mn^{+3} ions, dopant alignment, and magnetic ordering. In order to understand the properties of perovskite manganites, it is important to study how orderings affect the lattice parameters. This influence can be detected by studying the temperature dependences of the parameters. The most complete data on the variation in structure with temperature were obtained by using neutron diffraction on powder samples and can be found in [4]. In the present work, a detailed study on the crystal structure of single crystals and powders of $(La_{0.9}Sr_{0.1})_{0.9}MnO_3$ and $La_{1-x}Sr_xMnO_3$ ($x = 0.1, 0.15, 0.2, 0.25$) was performed using x-ray analysis in the temperature range 80–600 K; the influence of magnetic ordering on the lattice parameters is found. Currently, there are very little data concerning the magnetoelastic contribution.

1063-7834/05/4707-1299$26.00 © 2005 Pleiades Publishing, Inc.

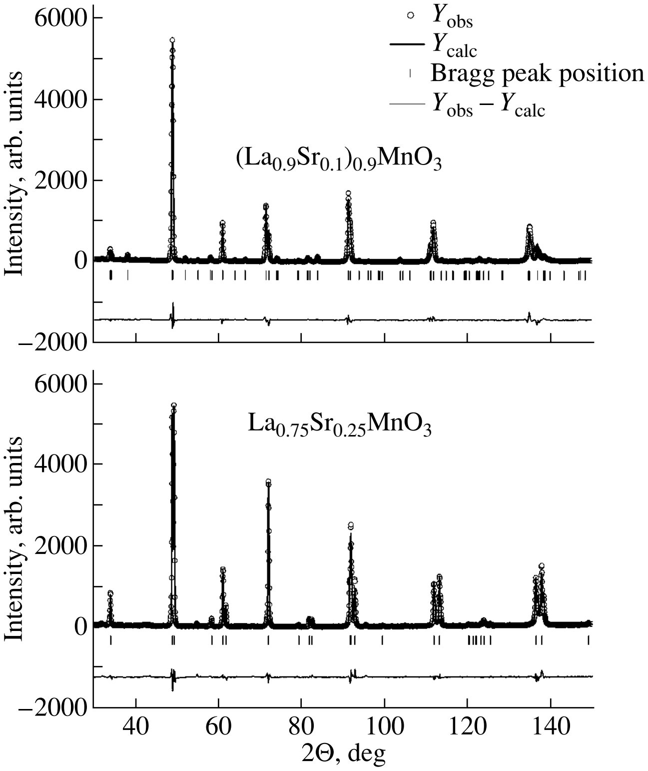

Fig. 1. Portions of measured (Y_{obs}) and calculated (Y_{calc}) x-ray diffraction patterns, the difference ($Y_{obs} - Y_{calc}$) between them, and the Bragg peak positions for manganite polycrystals.

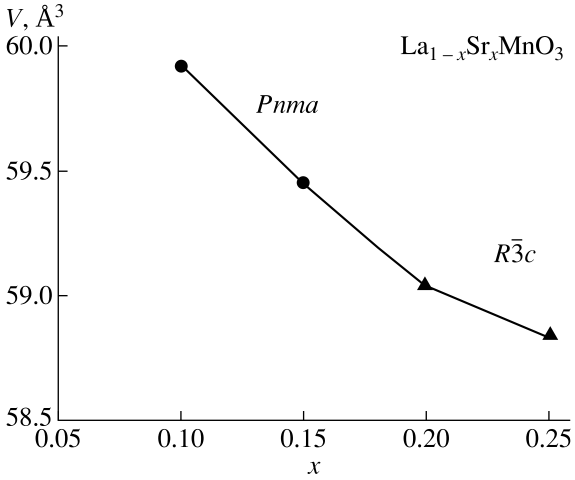

Fig. 2. Molar unit cell volume of manganites $La_{1-3}Sr_xMnO_3$ as a function of Sr content for orthorhombic (circles) and rhombohedral (triangles) lattices.

2. SAMPLE PREPARATION AND EXPERIMENTAL SETUP

Polycrystalline samples were obtained by sintering La, Sr, and Mn oxides in a standard procedure. Next, single crystals were grown from ceramic preforms by the floating zone method using a xenon lamp for sample heating [9]. The orientation and composition of single crystals were controlled using x-ray methods. Needle-shaped single crystals about 0.3-mm thick were studied in RKU and RKV x-ray diffraction cameras using a photographic method for recording diffraction patterns.

The crystal lattice parameters were determined from the diffraction patterns of powders made from the single crystals. Powders with grains 32–64 μm in size were prepared by milling some of the crystals and bolting through the appropriate sieves. The diffraction patterns were taken at room temperature by means of automatic DRON x-ray diffractometers (CrK_α radiation). Temperature-dependent x-ray studies were performed in a special vacuum chamber using filtered FeK_α radiation. The atom positions and the angles and distances between them were calculated using the FullProf 2001 software package [10].

3. RESULTS AND DISCUSSION

3.1. Crystal Structure of Manganites at Room Temperature

According to the phase diagram [1, 2, 6, 11], manganites $(La_{0.9}Sr_{0.1})_{0.9}MnO_3$ and $La_{1-x}Sr_xMnO_3$ ($x = 0.1$, 0.15) have an orthorhombic *Pnma* structure or (for x = 0.2, 0.25) a rhombohedral $R\bar{3}c$ structure at room temperature. All of our single crystal samples proved to be twinned; that is, they contained structural domains oriented relative to each other in a certain way. The twinning structures typical of orthorhombic manganite single crystals were described in [12]. We observed twinning structures in the smallest single crystals, which were rods ~0.3 mm in diameter; all three types of domains were simultaneously present in these orthorhombic samples. Therefore, we can conclude that the size of the structural domains does not exceed 100 μm. A similar value of the structural domain size was obtained for $LaMnO_3$ samples from magnetic measurements of textured and nontextured samples. More specifically, we failed to produce textured samples of $LaMnO_3$ for powders with grains smaller than 100 μm, whereas powders with large grains were easily textured [13].

An example of calculated and measured diffraction curves for orthorhombic $(La_{0.9}Sr_{0.1})_{0.9}MnO_3$ and rhombohedral $La_{0.75}Sr_{0.25}MnO_3$ powders is shown in Fig. 1. Solid lines below the diffraction patterns show the difference between the measured and calculated intensities, and bars indicate calculated positions of the Bragg peaks. Diffraction patterns of all other compositions are similar to one of the two patterns shown in Fig. 1. It is clearly seen from Fig. 1 that the samples under study are single-phase. The calculated atomic positions in the lattice and the total and isotropic temperature factors for all compositions are given in Tables 1 and 2 together

Table 1. Crystal lattice parameters, atomic coordinates, total (O) and isotropic atomic (B) temperature factors, and convergence parameters (R_P, R_{wP}) as calculated for the orthorhombic ($Pnma$) lattice, where the atomic positions for manganites (La,Sr)MnO_3 are the following: the La/Sr positions are 4c (x, 1/4, z), the Mn positions are 4a (0, 0, 0), the O1 positions are 4c (x, 1/4, z), and the O2 positions are 8d (x, y, z)

		$(La_{0.9}Sr_{0.1})_{0.9}MnO_3$	$(La_{1-x}Sr_x)MnO_3$	
			$x = 0.1$	$x = 0.15$
La/Sr	x	0.9761	0.9822	0.9998
	z	0.5025	0.5038	0.4934
	B (Å^2)	0.0236	0.6220	0.0429
Mn	B (Å^2)	0.0218	0.1725	0.0019
O1	x	0.5060	0.5062	0.5666
	z	0.4130	0.4684	0.4970
	B (Å^2)	0.0161	0.8014	0.0018
O2	x	0.2722	0.2462	0.2193
	y	0.9778	0.9649	0.9656
	z	0.2473	0.2830	0.2668
	B (Å^2)	0.0391	0.0690	0.0500
a, Å		5.550	5.548	5.545
b, Å		7.780	7.748	7.790
($b/\sqrt{2}$, Å)		(5.501)	(5.479)	(5.508)
c, Å		5.542	5.576	5.506
V, Å^3		239.30	239.69	237.84
O, Å^2		0.1313	0.1168	0.01416
R_P (%)		7.25	5.35	4.81
R_{wP} (%)		8.4	7.35	6.35

with the crystal lattice parameters. The unit cell volume per formula unit (Fig. 2) decreases with growing x, since the Sr ionic radius is smaller than that of La. Mitchell *et al.* [3] constructed the P–x structure phase diagram and presented data on the crystal lattice parameters of all the phases that occur in the system depending on the oxygen pressure P during the synthesis of polycrystals. From those data on the lattice parameters, it follows that the lower the oxygen pressure (that is, the lower the oxygen concentration in the sample), the larger the unit cell volume. Unfortunately, the authors of [3] did not discuss this fact and did not even give the values of the unit cell volumes.

In our case, the unit cell volume of $(La_{0.9}Sr_{0.1})_{0.9}MnO_3$ is smaller than that of $La_{0.9}Sr_{0.1}MnO_3$. From comparing the crystal lattice parameters (Tables 1, 2) to the data from [3], we conclude that our samples are similar in composition to those obtained in [3] at an oxygen pressure of 1 mbar.

Table 2. Crystal lattice parameters, atomic coordinates, total (O) and isotropic atomic (B) temperature factors, and convergence parameters (R_P, R_{wP}) as calculated for the rhombohedral ($R\bar{3}c$) lattice, where the atomic positions for manganites (La,Sr)MnO_3 are the following: the La/Sr positions are 6a (0, 0, 1/4), the Mn positions are 6b (0, 0, 0), and the O positions are 18e (x, 0, 1/4)

		$(La_{1-x}Sr_x)MnO_3$	
		$x = 0.2$	$x = 0.25$
La/Sr	B (Å^2)	0.11315	0.02501
Mn	B (Å^2)	0.10096	0.03228
O	x	0.44898	0.44520
	B (Å^2)	0.18854	0.33117
a, Å		5.532	5.522
c, Å		13.368	13.370
c/A		0.414	0.413
V, Å^3		351.83	350.61
O, Å^2		0.00763	0.0696
R_P (%)		4.54	5.4
R_{wP} (%)		5.5	7.35

As follows from Table 1, the crystal lattice parameters a, $b/\sqrt{2}$, and c of orthorhombic $La_{0.9}Sr_{0.1}MnO_3$ samples at room temperature are very different due to the Jahn–Teller effect, which is typical of the O' phase. In $(La_{0.9}Sr_{0.1})_{0.9}MnO_3$ samples, the parameters a and c are close to each other, and in $La_{0.85}Sr_{0.15}MnO_3$ samples the parameters $b/\sqrt{2}$ and c are similar. These compositions can also be attributed to the O' phase [14, 15]. The lattice parameters we obtained are in good agreement with the previously published data (see, e.g., [4, 7]).

Calculated values of the interatomic Mn–O distances and the Mn–O–Mn and O–Mn–O angles in the MnO_6 octahedron for all compositions are shown in Fig. 3. It can be seen that, as the Sr concentration increases at room temperature, the differences in the interatomic distances decrease and finally vanish in the rhombohedral phase. In the rhombohedral lattice, the oxygen and manganese atoms each occupy only one crystallographic position, (18e) and (6b), at the (x, 0, 1/4) and (0, 0, 0) points, respectively; so there is only one interatomic Mn–O distance (Tables 2, 3). The MnO_6 octahedra in the rhombohedral lattice are slightly distorted, and, according to our calculations, the O–Mn–O angle is about 91°. Furthermore, the octahedra in the rhombohedral phase are rotated relative to each other through 164° (the Mn–O–Mn angles; see Fig. 3).

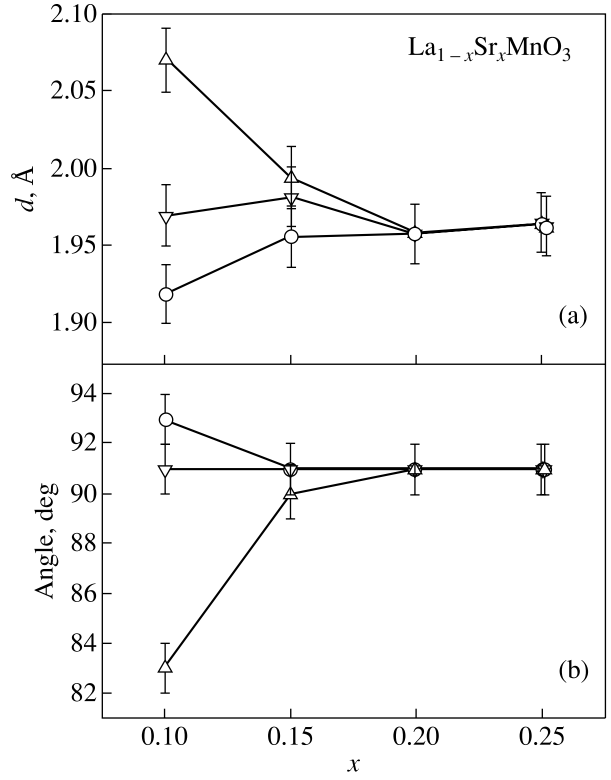

Fig. 3. Interatomic Mn–O distances and O–Mn–O angles in the MnO_6 octahedron of $La_{1-x}Sr_xMnO_3$ as a function of Sr content.

3.2. Temperature Dependence of the Lattice Parameters

All samples studied undergo structural phase transitions in the temperature range 80–600 K. For $La_{0.9}Sr_{0.1}MnO_3$ manganites, the orthorhombic O' phase exists in the temperature range $100 \text{ K} \le T \le 330$ K and transforms into the pseudocubic O^* phase both below and above this interval (Fig. 4a). It was established in [5] that the O'–O^* phase transitions are induced by the Jahn–Teller deformation mode Q_2, which arises in the temperature range where the O' phase exists. For the $La_{0.9}Sr_{0.1}MnO_3$ composition, the low-temperature O^*–O' transition occurs in a narrow (3°- to 5°-wide) temperature range and is first-order. The high-temperature O'–O^* transition occurs gradually over a temperature interval 40°- to 50°-wide (Fig. 4a). Both transitions entail a change in the unit cell volume (Fig. 5). The Jahn–Teller phase O' has a significantly larger unit cell volume than the O^* phase. A similar transition from the O' to the O^* phase was observed in manganites $La_{0.89}Sr_{0.11}MnO_3$ in [4] as a first-order phase transition occurring via a mixture of phases. We did not observe coexisting phases in our samples.

Another type of structural phase transition is observed in samples with $x = 0.15$ and 0.2, namely, the transition from the low-temperature orthorhombic *Pnma* phase to the high-temperature rhombohedral $R\bar{3}c$ phase. This transition takes place at $T \sim 360$ and 115 K for $x = 0.15$ and 0.2, respectively (Figs. 4b, 4c). In both cases, this transition is first-order and there is a temperature range where the orthorhombic and rhombohedral phases coexist. For $x = 0.2$ manganites, this range (about 5-K wide) is considerably narrower than that for $x = 0.15$ (about 20-K wide). There is a clear tendency of the transition region to be wider where the structural phase transition takes place at a higher temperature irrespective of the transition type. The transition from the orthorhombic to the rhombohedral phase is accompanied by a decrease in the unit cell volume (Fig. 5). Published data concerning the $Pnma$–$R\bar{3}c$ transition in manganites $La_{1-x}Sr_xMnO_3$ are scarce, and there are no data on the phase coexistence during this transition or data on variations in the unit cell volume.

Table 3. Interatomic distances Mn–O (in angstrom) and Mn–O–Mn and O–Mn–O angles for manganites (La,Sr)MnO_3

	$(La_{0.9}Sr_x)_{0.9}MnO_3$	$La_{1-x}Sr_xMnO_3$			
	$x = 0.1$	$x = 0.1$	$x = 0.15$	$x = 0.20$	$x = 0.25$
		Distance, Å			
Mn–O	2.014	1.970	1.982	1.966	1.964
	2.022	2.070	1.995		
	1.930	1.919	1.957		
		Angle, deg			
Mn–O–Mn	150	160	159	164	164
	165	161	163		
O–Mn–O	98	93	91	91	91
	92	83	91		
	91	91	90		

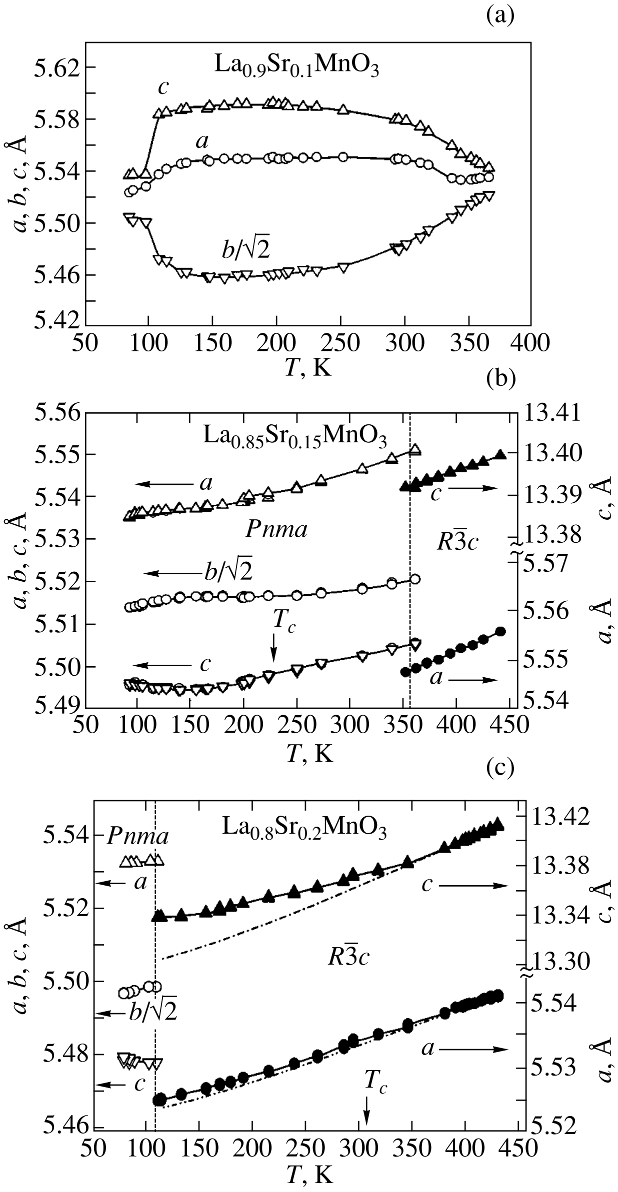

Fig. 4. Temperature dependence of the lattice parameters of manganite polycrystals for the orthorhombic (open symbols) and rhombohedral phases (close symbols). Dot-and-dash lines show the phonon contribution to the lattice thermal expansion.

The temperature dependences of the lattice parameters exhibit clear features (kinks) related to magnetic ordering. The Curie temperatures T_c are shown in Fig. 4 by arrows. It is clearly seen that these features start at temperatures somewhat higher than the Curie temperatures. This is due to the fact that magnetically ordered clusters are formed in the paramagnetic matrix at temperatures much higher than T_c. Thus, the crystal lattice parameters are sensitive not only to long-range order, which appears at $T = T_c$, but also to short-range order,

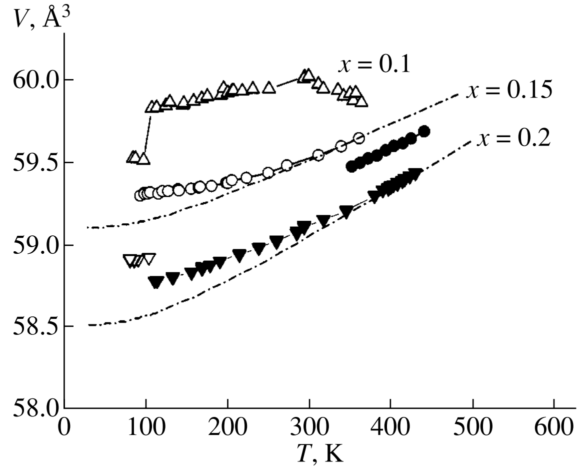

Fig. 5. Temperature dependence of the molar unit cell volume of manganite polycrystals. Dot-and-dash lines show the phonon contribution to the volume thermal expansion.

which appears at a temperature much higher than the Curie temperature.

The magnetoelastic contribution can be found by comparing the measured temperature dependence of the unit cell volume to the calculated phonon contribution. We calculated the phonon contribution from an equation derived using the Debye theory and the Grüneisen law [16]:

$$z(T) = z_0 + A_z T F(T_\Theta/T),$$

where z is a lattice parameter or the unit cell volume, $F(T_\Theta/T) = \frac{1}{T}\int_0^T C_V dT$, C_V is the specific heat at constant volume, A_z is a constant, z_0 is the value of z at $T = 0$ (we found this value by extrapolation), and T_Θ is the Debye temperature. In our calculations, we assumed that the temperature dependence of the lattice parameters coincides with that of the phonon contribution at temperatures much higher than the magnetic ordering temperature. The values of the Debye temperatures are taken from [17]: $T_\Theta = 390$ K for $x = 0.15$ and $T_\Theta = 400$ K for $x = 0.2$. In Fig. 4c, the phonon contribution for the case of $x = 0.2$ is shown by a dot-and-dash line. It is clearly seen that the magnetoelastic contribution is anisotropic for La$_{0.8}$Sr$_{0.2}$MnO$_3$; i.e., the deviations of the lattice parameter temperature dependence from the calculated Debye–Grüneisen curve for the parameters a and c are different. The magnetoelastic contribution measured along the **c** axis is significantly larger than that along the **a** axis.

The temperature dependencies of the unit cell volume V for $x = 0.1$, 0.15, and 0.2 are shown in Fig. 5. The $V(T)$ curves for $x = 0.15$ and 0.2 clearly indicate a jump in the unit cell volume due to the first-order phase transition from the high-temperature rhombohedral $R\bar{3}c$ phase to the low-temperature orthorhombic *Pnma*

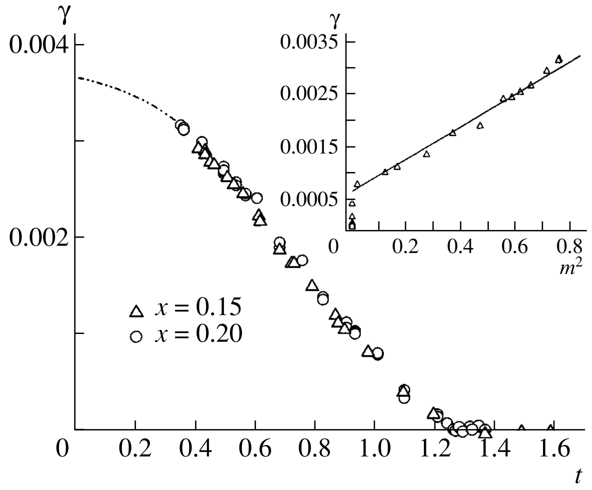

Fig. 6. Temperature dependence of the magnetoelastic contribution $\gamma = \Delta V/V(t)$ ($t = T/T_c$) of $La_{1-x}Sr_xMnO_3$ for x = 0.15 and 0.2 (triangles and circles, respectively). The dot-and-dash line is extrapolation of γ to $t = 0$. The inset shows γ as a function of m^2 ($m = M/M_s(t)$) for $x = 0.15$.

phase. The calculated phonon contribution for these compositions is shown in Fig. 5 by a dot-and-dash line. The difference ΔV between the measured unit cell volume V and the phonon contribution normalized to the experimentally measured volume (i.e., $\gamma = \Delta V/V$) is shown in Fig. 6 as function of $t = T/T_c$. The dot-and-dash line in Fig. 6 is extrapolation to $t = 0$. The inset to Fig. 6 shows the $\gamma(m^2)$ dependence (here, $m = M(H = 10\ \text{kOe})/M_s$, M is the magnetization, M_s is the saturation magnetization). It is clearly seen that the $\gamma(m^2)$ dependence is approximately linear for $m^2 > 0.015$, which is typical of the magnetoelastic contribution.

The deviation of the $\gamma(m^2)$ curve from a straight line at low m^2 is due to a nonuniform state forming in the vicinity of the magnetic phase transition, because the magnetic short-range order has a significant effect on the magnetoelastic contribution to the thermal expansion of the crystal lattice. This contribution is noticeable up to $t \sim 1.25$; therefore, clusters possessing short-range magnetic order are preserved up to these values of t in the paramagnetic matrix of manganites (Figs. 4–6).

By extrapolating $\gamma(t)$ to $t = 0$ for samples with x = 0.15 and 0.2, we estimated the maximum magnetoelastic contribution to thermal expansion to be $\sim 3.7 \times 10^{-3}$. It is important to stress that the manganites with x = 0.15 and 0.2 have different crystal structures near T_c: their structure is orthorhombic for $x = 0.15$ and rhombohedral for $x = 0.2$; nevertheless, the $\gamma(t)$ dependences are identical.

It is well known (see, e.g., [6]) that a charge-ordered state appears in manganites with $x = 0.15$ at $T < 200$ K. Our measurements show that the charge ordering does not have a significant influence on the volume temperature dependence.

4. CONCLUSIONS

The crystal structure of rare-earth manganites $(La_{0.9}Sr_{0.1})_{0.9}MnO_3$ and $La_{1-x}Sr_xMnO_3$ (x = 0.1, 0.15, 0.2, 0.25) has been studied. The crystal lattice parameters, atomic coordinates, and interatomic distances at room temperature have been found. The degree of distortion of the MnO_6 octahedron was shown to be different for $(La_{0.9}Sr_{0.1})_{0.9}MnO_3$ and $La_{1-x}Sr_xMnO_3$ samples with x = 0.1 and 0.15, which have an orthorhombic structure at room temperature (space group *Pnma*). The distortion is the strongest in $(La_{0.9}Sr_{0.1})_{0.9}MnO_3$ samples and is the weakest in $La_{0.85}Sr_{0.15}MnO_3$ samples. The orthorhombic phase of $La_{0.85}Sr_{0.15}MnO_3$ is closer (in distortion magnitude and degree of rotation of the octahedra relative to each other) to the rhombohedral phase (space group $R\bar{3}c$), which exists in manganites with x = 0.2 and 0.25 at room temperature.

X-ray studies at low temperatures have been performed to determine the temperature dependences of the crystal lattice parameters and the volume changes caused by structural phase transitions. The magnetoelastic contribution to thermal expansion has been calculated. It has been shown that the bulk magnetoelastic contribution γ is independent of the crystal structure and is approximately 3.7×10^{-3} at $T \sim 0$ K.

5. ACKNOWLEDGMENTS

The authors are grateful to G.V. Ivanova and T.P. Lapina, employees of the Institute of Metal Physics (Ural Division, Russian Academy of Sciences), for their help with the x-ray measurements of single crystals and to R.I. Zaĭnulina for the magnetic data.

This work was supported by the Russian Foundation for Basic Research (project nos. 02-02-16425, 00-02-17544, 03-02-16065) and the Ministry of Education and Science of the Russian Federation (program “Integration”).

REFERENCES

1. Y. Yamada, O. Hino, S. Nohdo, R. Ranao, T. Inami, and S. Katano, Phys. Rev. Lett. **77**, 904 (1996).
2. H. Kawano, R. Kajimoto, M. Kubota, and H. Yoshizawa, Phys. Rev. B **53**, R14709 (1996).
3. J. F. Mitchell, D. N. Argyriou, C. D. Potter, D. G. Hinks, J. D. Jorgensen, and S. D. Bader, Phys. Rev. B **54**, 6172 (1996).
4. B. Dabrowski, X. Xiong, Z. Bukowski, R. Dybzinski, P. W. Klamut, J. E. Siewenie, O. Chmaissem, J. Shaffer, C. W. Kimball, J. D. Jorgensen, and S. Short, Phys. Rev. B **60**, 7006 (1999).
5. S. V. Gaviko, E. V. Arkhipov, A. V. Korolev, V. E. Naĭsh, and Ya. E. Mukovskiĭ, Fiz. Tverd. Tela **41** (6), 1064 (1999) [Phys. Solid State **41** (6), 969 (1999)].
6. V. E. Naĭsh, Fiz. Met. Metalloved. **92** (5), 16 (2001).
7. L. Pinsard, J. Rodrigues-Carvajal, and A. Revcolevsci, J. Alloys Compd. **262–263**, 152 (1997).

8. Q. Huang, A. Santoro, J. W. Lynn, R. W. Erwin, J. A. Borchers, J. L. Peng, and R. L. Greene, Phys. Rev. B **55**, 14987 (1997).
9. A. M. Balbashov, S. G. Karabashev, Y. M. Mukovskii, and S. A. Zver'kov, J. Cryst. Growth **167**, 365 (1996).
10. J. Rodrigues-Carvajal, Physica B **192**, 55 (1993).
11. A. Urushibara, Y. Moritomo, T. Arima, A. Asamitsu, G. Kido, and Y. Tokura, Phys. Rev. B **51**, 14103 (1995).
12. F. Moussa, M. Hennion, J. Rodriguez-Carvajal, H. Moudden, L. Pinsard, and A. Revcolevschi, Phys. Rev. B **54**, 15149 (1996).
13. A. V. Korolev, V. E. Arkhipov, V. S. Gaviko, M. I. Kurkin, T. P. Lapina, and Ya. M. Mukovskii, J. Magn. Magn. Mater. (in press).
14. R. I. Zainullina, N. G. Bebenin, V. V. Mashkautsan, A. M. Burkhanov, V. S. Gaviko, V. V. Ustinov, Y. M. Mukovskii, D. A. Shulyatev, and V. G. Vassil'ev, Zh. Éksp. Teor. Fiz. **120**, 139 (2001) [JETP **93**, 121 (2001)].
15. R. I. Zainullina, N. G. Bebenin, A. M. Burkhanov, V. V. Ustinov, and Ya. M. Mukovskii, Phys. Rev. B **66**, 064421 (2002).
16. N. W. Ashcroft and N. D. Mermin, *Solid State Physics* (Holt, Rinehart and Winston, New York, 1976; Mir, Moscow, 1979).
17. T. Okuda, A. Asamitsu, Y. Tomioka, T. Kimura, Y. Taguchi, and Y. Tokura, Phys. Rev. Lett. **81**, 3203 (1998).

Translated by G. Tsydynzhapov

Physics of the Solid State, Vol. 47, No. 7, 2005, pp. 1306–1309. Translated from Fizika Tverdogo Tela, Vol. 47, No. 7, 2005, pp. 1261–1264.
Original Russian Text Copyright © 2005 by Ol'khovik, Sizova, Shurinova, Kamzin.

MAGNETISM AND FERROELECTRICITY

Determination of the Surface Anisotropy Contribution to the Magnetic Anisotropy Field of a Nanocrystalline Barium Ferrite Powder at Various Temperatures

L. P. Ol'khovik*, Z. I. Sizova*, E. V. Shurinova*, and A. S. Kamzin**

**Kharkov National University, Svobody sq. 4, Kharkov, 61077 Ukraine*
e-mail: Larisa.P.Olkhovik@univer.kharkov.ua
***Ioffe Physicotechnical Institute, Russian Academy of Sciences,*
Politekhnicheskaya ul. 26, St. Petersburg, 194021 Russia

Received August 31, 2004

Abstract—The temperature dependence of the average anisotropy field of a nanocrystalline barium hexaferrite powder was studied by treating remanent-magnetization curves with inclusion of thermal fluctuations. The contribution of surface anisotropy was isolated; its nonstandard temperature dependence is intimately related to the specific features of formation of near-surface regions in ultrathin particles. *© 2005 Pleiades Publishing, Inc.*

1. INTRODUCTION

The recent rise in research interest in nanocrystalline magnetic materials has been spurred, on the one hand, by the specific features of their magnetic properties and, on the other hand, by their obvious application potential in nano- and microelectronics. A fundamental parameter of a magnetic material is its anisotropy field H_a. Because particles of any real highly dispersed system, irrespective of the method by which it was prepared, are distributed in size, these systems are characterized not by one value of H_a but rather by a distribution in anisotropy fields. It follows that investigation of the magnetic anisotropy and, in particular, of the anisotropy field should be performed separately for systems in different states of dispersion.

The goal pursued by this study was to establish the temperature dependence of the parameters characterizing the magnetic anisotropy of highly anisotropic barium hexaferrite with the particle size reduced to the nanometer scale.

2. OBJECT OF STUDY

The object of study was a highly anisotropic magnetically uniaxial ferrimagnet, hexagonal barium ferrite, with an unsubstituted magnetic matrix ($BaFe_{12}O_{19}$) featuring the following main room-temperature magnetic parameters: the magnetocrystalline anisotropy field H_{ak} = 17.8 kOe, anisotropy constant $K_1 = 3.3 \times 10^6$ erg cm^{-3}, saturation magnetization I_S = 358 emu cm^{-3} (300 K), and Curie temperature T_C = 733 K [1].

The sample to be studied was a nanocrystalline powder with cryochemical prehistory synthesized at T = 800°C. A detailed description of the technology of its preparation can be found in [2].

The powder particles were platelets ranging from $d \approx 10$ to 100 nm in diameter (Fig. 1). An important morphological parameter governing the anisotropy-field distribution is the particle thickness. As seen from Fig. 1, the powder sample under study is dominated by 5- to 10-nm-thick particles (2–4 unit cell parameters c).

The decisive role in the creation of the magnetic anisotropy in such particles is played by the open surface, which accounts for the formation of a structurally imperfect near-surface region in a crystal.

Layer-by-layer diagnostics of the elemental composition of a $BaFe_{12}O_{19}$ single crystal along the hexagonal axis c performed by us earlier [3] revealed the presence of a near-surface region of finite thickness in which the deviation of elemental composition from stoichiometry decreases exponentially with distance from the surface into the bulk of the crystal. We succeeded in estimating the thickness of this near-surface region with a magnetically perturbed structure by using depth-selective conversion Mössbauer spectroscopy [4]. It was shown that this thickness is only 2–5 nm for a highly anisotropic $BaFe_{12}O_{19}$ crystal, at 300 K [5]. For platelet-shaped particles (with both faces parallel to the (001) basal plane), the total thickness of the near-surface region turns out to be comparable to the thickness of the nanocrystals under study.

Another essential factor to bear in mind in analyzing experimental data is that the particles of the powder sample under study are small Stoner–Wohlfarth parti-

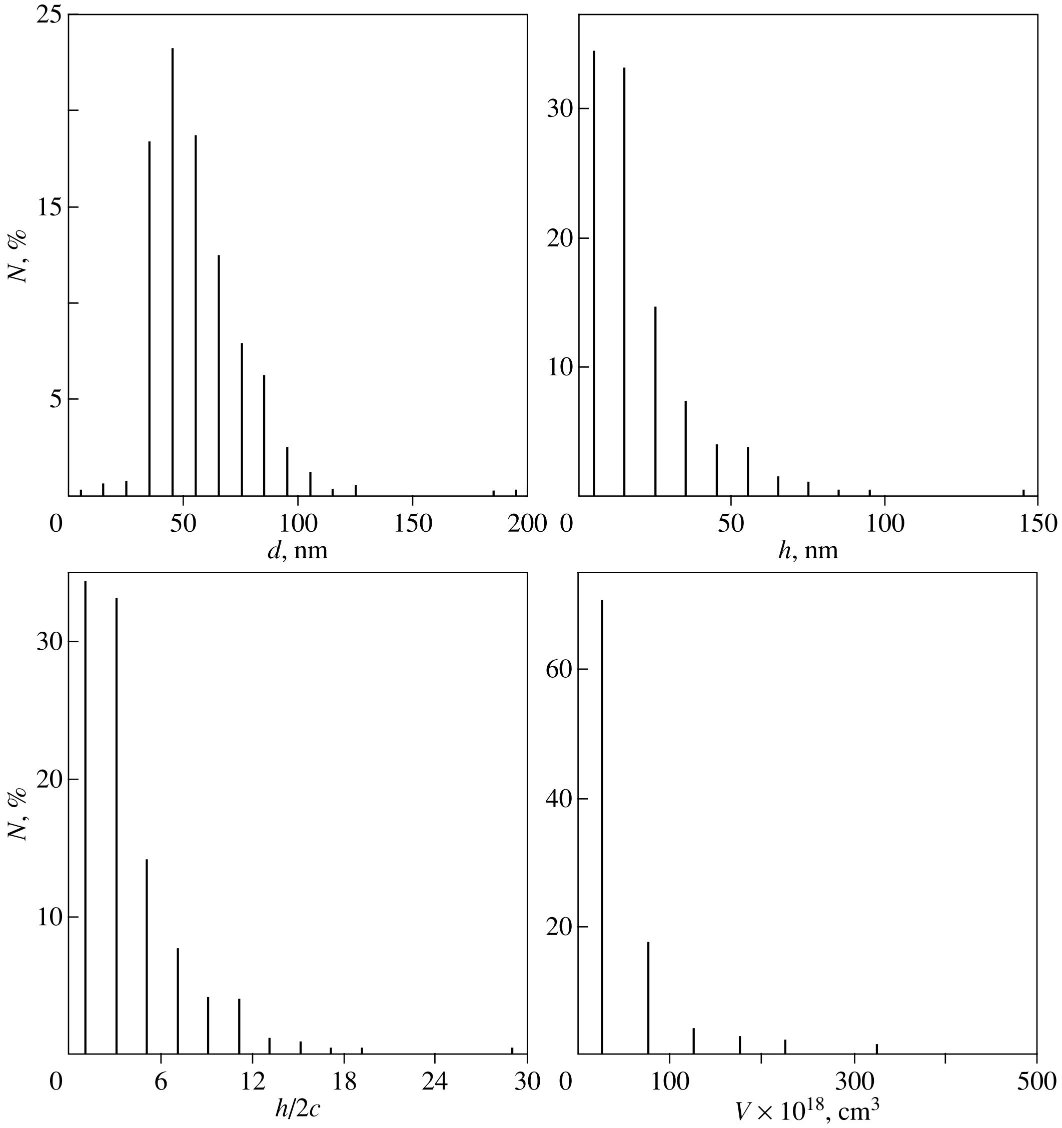

Fig. 1. Particle-size distribution in a nanocrystalline powder: d, h, and V are the diameter, thickness, and volume of particles, respectively, and c is the lattice parameter. Sampling contains $N = 520$ particles.

cles; i.e., they meet the criterion $V \leq 100V_{so}$ [6]. This substantiates the particle-volume distribution displayed in Fig. 1 ($\langle V \rangle \cong 30 \times 10^{-18}$ cm^3) for a critical (superparamagnetic) value of the volume V_{so} (300 K) = 0.5 × 10^{-18} cm^3.

Thus, an analysis of anisotropic properties of the nanodisperse powder under study should take into account both surface effects and the influence of thermal fluctuations [6].

3. EXPERIMENTAL TECHNIQUE

Finding the distribution in anisotropy fields in a system of small particles is a challenging task. The distribution function $f(H_a)$ for an ensemble of randomly oriented particles was first derived analytically in [6] by solving the integral equation

$$\frac{dm_r(H)}{dH} = \int_{0.5}^{1} \frac{1}{h} f\left(\frac{H}{h}\right) \frac{d}{dh}\mu_r(h)\,dh. \qquad (1)$$

Here, m_r is the averaged isothermal specific remanent magnetization reduced to the magnetization value for an infinitely high magnetic field, h is the external magnetic field reduced to the anisotropy field H_a, and $\mu_r(h) = m_r(H)$.

Because the experiment reported in this paper was aimed at determining the average anisotropy field as an integral characteristic of a nanodisperse powder, we restricted ourselves to the zero approximation to the

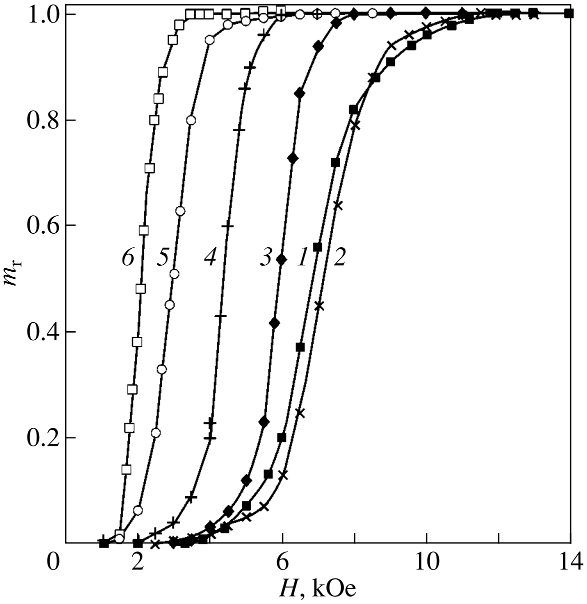

Fig. 2. Field dependence of the isothermal remanent magnetization at various temperatures: (*1*) 300, (*2*) 360, (*3*) 550, (*4*) 590, (*5*) 610, and (*6*) 620 K.

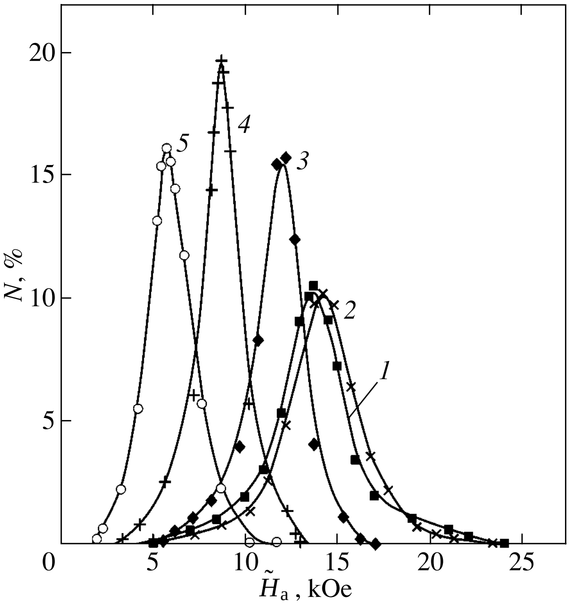

Fig. 3. Anisotropy field distribution of particles in a nanocrystalline powder at various temperatures: (*1*) 300, (*2*) 360, (*3*) 550, (*4*) 590, and (*5*) 610 K.

solution of Eq. (1), which yields a simple expression for the particle anisotropy-field distribution function [7]:

$$f(H_a) = \left(\frac{dm_r}{dH}\right)_{H = H_a/2}. \qquad (2)$$

The $m_r(H)$ relation for a close-packed (packing factor $p = 0.4$), thermally demagnetized powder sample with randomly oriented particles was found by measuring hysteresis loops as the maximum field was increased gradually up to $H = 20$ kOe. The measurements were run in the temperature range 300–630 K.

4. EXPERIMENTAL RESULTS AND DISCUSSION

Figure 2 plots $m_r(H)$ graphs whose differentiation yielded the particle anisotropy-field distribution (Fig. 3). We readily see that the distribution is symmetric with respect to the maximum and fairly broad at all temperatures. Also, the anisotropy field range tends to narrow with increasing temperature. Indeed, at 300 K, the half-width of the distribution function is 3.5 kOe, while at 621 K it drops to one-half this value. The average anisotropy fields $\langle \tilde{H}_a \rangle$ were identified with the fields corresponding to the maximum in the distribution function $N = f(\tilde{H}_a)$.

Figure 4 presents an experimental temperature dependence of the average anisotropy field. This dependence was obtained with inclusion of the effect of thermal fluctuations, for which purpose we made use of the expression from [6] relating the true anisotropy field $\langle H_a \rangle$ with the experimentally found value $\langle \tilde{H}_a \rangle$:

$$\langle H_a \rangle(T) = Z(T)\langle \tilde{H}_a \rangle(T), \qquad (3)$$

$$(Z-1)Z^{-0.3} = (50kT/I_S\langle \tilde{H}_a \rangle)^{0.7}\langle V \rangle^{-0.7}. \qquad (4)$$

Here, Z is the thermal fluctuation coefficient, $\langle V \rangle$ is the average volume of particles in the powder sample, and k is the Boltzmann constant.

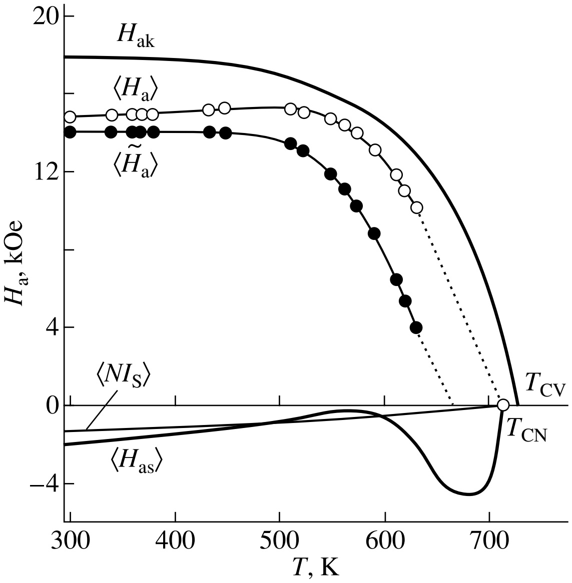

Fig. 4. Temperature dependence of the average anisotropy field and of its components for a nanocrystalline powder.

Note that the experimental data were treated disregarding the fact that, starting from $T \cong 400$ K, the smallest particles undergo a transition (induced by the external magnetic field) from the magnetically stable to a superparamagnetic state; in other words, the average volume was calculated taking into account all particles of the system.

The temperature dependences of $\langle \tilde{H}_{\mathrm{a}} \rangle$ and $\langle H_{\mathrm{a}} \rangle$ in Fig. 4 are compared with that of the magnetocrystalline anisotropy field H_{ak} of a bulk crystal. We readily see that the $\langle \tilde{H}_{\mathrm{a}} \rangle = f(T)$ graph follows the same behavior as $H_{\mathrm{ak}}(T)$. Note, however, that $\langle \tilde{H}_{\mathrm{a}} \rangle$ vanishes at T = 670 K, which is about 60 K below the Curie temperature of the bulk crystal. Taking thermal fluctuations into account changes both the pattern of the relation (in the range 300–450 K, $\langle H_{\mathrm{a}} \rangle$ rises slightly) and the value of the temperature at which the anisotropy field vanishes. As should be expected, $\langle H_{\mathrm{a}} \rangle(T)$ extrapolates to the Curie point of the nanocrystalline powder under study, $T_{\mathrm{CN}} = 710$ K.

The values of $\langle H_{\mathrm{a}} \rangle$ obtained in the temperature interval covered lie approximately 10–20% lower than those for the bulk crystal. Indeed, at 300 K, we have $\langle H_{\mathrm{a}} \rangle$ = 14.8 kOe, whereas H_{ak} = 17.8 kOe. This discrepancy cannot be accounted for by only the negative contribution provided by the shape anisotropy field, which is $\langle NI_{\mathrm{S}} \rangle$ = 1.4 kOe for particles of the system under study at the given temperature. Therefore, in contrast to the approach employed in [6, 8], where the magnetocrystalline and particle shape anisotropies were taken into account, we also included the surface anisotropy, which is characteristic of ultrasmall particles.

The contribution of surface anisotropy (H_{as}) to the average anisotropy field was estimated from the relation

$$\langle H_{\mathrm{a}} \rangle = H_{\mathrm{ak}} - \langle HI_{\mathrm{S}} \rangle \pm H_{\mathrm{as}}. \tag{5}$$

The $H_{\mathrm{as}}(T)$ relation thus obtained is plotted in Fig. 4. Note the anomalous behavior of the temperature dependence of H_{as} as compared to that of H_{ak}, which becomes particularly evident if we recall that surface anisotropy is also magnetocrystalline in origin. The only difference consists in the fact that the surface anisotropy is due to single-ion contributions of Fe^{3+} ions localized in positions with lower symmetry relative to the analogous positions in the bulk of the crystal. As shown in [9], lowering of the local symmetry of crystallographic positions may give rise to a nonstandard temperature dependence of the parameters characterizing the anisotropic properties of crystals.

ACKNOWLEDGMENTS

This study was carried out within a bilateral agreement on scientific cooperation between Kharkov National University (Kharkov, Ukraine) and the Ioffe Physicotechnical Institute, Russian Academy of Sciences (St. Petersburg, Russia), and was supported by the Ministry of Education and Science of Ukraine (Basic Research Program, project no. 0304U004181) and the Russian Foundation for Basic Research (project nos. 02-02-39006, 05-02-17791).

REFERENCES

1. J. Smit and H. P. J. Wijn, *Ferrites* (Wiley, New York, 1959; Inostrannaya Literatura, Moscow, 1962).
2. L. P. Ol'khovik, N. M. Borisova, T. G. Kuz'micheva, and V. P. Shabatin, Funct. Mater. **3** (1), 84 (1996).
3. A. S. Kamzin, V. L. Rozenbaum, L. P. Ol'khovik, and E. D. Kovtun, J. Magn. Magn. Mater. **161**, 139 (1996).
4. E. Moll and E. Kankeleit, Nukleonik **7**, 180 (1965).
5. A. S. Kamzin, B. Shtal', R. Gellert, G. Klingel'khover, É. Kankeleit, L. P. Ol'khovik, and D. Vcherashniĭ, Fiz. Tverd. Tela (St. Petersburg) **42** (5), 873 (2000) [Phys. Solid State **42** (5), 897 (2000)].
6. H. Pfeiffer, Phys. Status Solidi A **118**, 295 (1990).
7. H. Pfeiffer and W. Schüppel, Phys. Status Solidi A **119**, 259 (1990).
8. E. C. Stoner and E. P. Wohlfarth, IEEE Trans. Magn. **24** (4), 3469 (1991).
9. Yu. A. Mamaluĭ and L. P. Ol'khovik, Ukr. Fiz. Zh. **33** (2), 287 (1988).

Translated by G. Skrebtsov

Physics of the Solid State, Vol. 47, No. 7, 2005, pp. 1310–1315. Translated from Fizika Tverdogo Tela, Vol. 47, No. 7, 2005, pp. 1265–1269.
Original Russian Text Copyright © 2005 by Gatalskaya, Shiryaev, Barilo, Szymczak, Baran.

MAGNETISM AND FERROELECTRICITY

Low-Temperature Magnetic Properties of $HoMn_{0.5}Co_{0.5}O_3$ Single Crystals

V. I. Gatalskaya[1, 2], S. V. Shiryaev[1, 2], S. N. Barilo[1], R. Szymczak[2], and M. Baran[2]
[1] *Institute of Solid State and Semiconductor Physics, National Academy of Sciences of Belarus,*
ul. Brovki 17, Minsk, 220072 Belarus
e-mail: v_gatal@ifttp.bas-net.by
[2] *Institute of Physics, Polish Academy of Sciences, Warsaw, 02-668 Poland*

Received September 21, 2004

Abstract—The magnetic behavior of a $HoMn_{0.5}Co_{0.5}O_3$ single crystal grown by electrochemical deposition was studied by measuring magnetization in the temperature range 5–300 K in magnetic fields of up to 50 kOe. The results obtained are treated within a model of the two-phase magnetic state of a crystal. A comparative analysis of the magnetic properties of $HoMn_{0.5}Co_{0.5}O_3$ and $LaMn_{0.5}Co_{0.5}O_3$ single crystals was carried out. © *2005 Pleiades Publishing, Inc.*

1. INTRODUCTION

Substitution of magnetic or nonmagnetic ions for manganese in pure $LaMnO_3$, which is an antiferromagnetic (AFM) insulator, is one of the reasons for the appearance of the metallic ferromagnetic (FM) state. Pure $LaMnO_3$ has been studied in considerable detail (see review [1] and references therein). A number of publications dealing with investigation of the structural and magnetic properties of $LaMn_{1-x}Co_xO_3$ were aimed at establishing the source of ferromagnetism in this system [2–8]. Studies of the La–Mn–Co–O (LMCO) system have been performed, with the exception of [7, 8], on polycrystalline samples and have yielded contradictory results. The FM state in LMCO was assumed to be associated with, for instance, monovalent Mn^{3+}–O–Mn^{3+} [2] or positive superexchange Mn^{4+}–Co^{2+} [3–9] interaction. However, $RMnO_3$ compounds, where R stands for a rare-earth ion, have been studied comparatively poorly. There are a few studies of $PrMnO_3$ and $NdMnO_3$ [10] and $HoMnO_3$ [11]. As far as we know, the $HoMnO_3$ system with partial substitution of cobalt for manganese has not yet been studied at all. There is a publication dealing with the structural and magnetic characteristics of polycrystalline $RMn_{0.5}Co_{0.5}O_3$ and $RMn_{0.5}Ni_{0.5}O_3$ for a number of rare-earth elements [12]. Preparation of high-quality $HoMn_{0.5}Co_{0.5}O_3$ (HMCO) single crystals and measurement of their magnetic characteristics will provide a firm basis for our understanding of the competing interactions in the Mn(Co) and Ho sublattices. A comparative analysis of the magnetic properties of HMCO and LMCO single crystals (the results of our measurements of the latter have been published recently [7, 8]) will permit interpretation of the specific features of these two magnetic semiconductor systems within a model of the two-phase magnetic state of a crystal (an AFM matrix with embedded FM clusters) at low temperatures.

2. SAMPLES AND EXPERIMENTAL TECHNIQUE

HMCO single crystals with a cobalt content close to 0.5 were obtained by electrochemical deposition in 100-cm^3 platinum crucibles from a melt solution of the Cs_2MnO_4–MoO_3 binary system in a 2.2 : 1 molar ratio. The crystal-forming compounds were introduced into the melt in the molar ratio $Ho_2O_3 : Mn_2O_5 : Co_3O_4 = 1 : 0.14 : 0.31$. Crystals were grown at a current density of 5–10 mA cm^{-2} for 80–100 h at a temperature of 1000°C. The cation composition of a single crystal was determined using x-ray fluorescence on an x-ray spectrometer, which was equipped with a Si(Li) semiconductor detector with a resolution of 200 eV at the 5.9 keV line. The x-ray fluorescence analysis established the crystal composition as $HoMn_{0.57}Co_{0.43}O_3$. The phase composition, lattice parameters, and single-crystal orientation were determined using x-ray diffractometry. The Laue diffraction patterns confirmed that the samples obtained were single crystals with a small content of twins. X-ray measurements performed on crystalline powders showed the HMCO single crystals to be single phase and to have orthorhombic structure with $a = 5.26$ Å, $b = 5.57$ Å, and $c = 7.45$ Å (space group *Pbnm*). Table 1 lists the crystallographic characteristics of the HMCO single crystal, including the distances m(Mn–O_1) between Mn(Co) ions and an apical oxygen ion and the short (s) and long (l) distances between Mn(Co) and O_{11} ions in the MnO_4 plane. The values of *m*, *s*, and *l* were calculated from the expressions [13]

$$m^2 = (a^2+b^2+c^2)/32; \quad s^2 = c^2/8 - m^2; \quad l^2 = b^2s^2/(16s^2-b^2). \tag{1}$$

To illustrate Jahn–Teller distortions of the structure, we chose $R_t = l/s$, as was done in [14].

The magnetization of single crystals was measured with a SQUID magnetometer (Quantum Design, MPMS-5) in magnetic fields *H* of up to 50 kOe and at temperatures from 5 to 300 K.

3. EXPERIMENTAL RESULTS

Figure 1 plots the temperature dependence of reciprocal susceptibility $\chi^{-1} = H/M$ for an HMCO single crystal. At high temperatures, $\chi^{-1}(T)$ obeys the Curie–Weiss law and deviates from it at temperatures below ~80 K. The Curie constant *C* in the temperature region 80–300 K is 16.48 emu K Oe^{-1} mol^{-1}, and the paramagnetic (PM) Curie temperature is $\Theta_p = 10.94$ K for fields above 50 Oe. The effective PM moment of the Ho^{3+} ion, p_{eff}(Ho), was calculated from the Curie constant by subtracting the contributions from the Mn^{4+} and Co^{2+} ions:

$$p_{\mathrm{eff}}^2 = 0.57g^2S_{\mathrm{Mn}(+4)}(S_{\mathrm{Mn}(+4)}+1) + 0.43g^2S_{\mathrm{Co}(+2)}(S_{\mathrm{Co}(+2)}+1) + p_{\mathrm{eff(Ho)}}^2, \tag{2}$$

where $p_{\mathrm{eff}}^2 = 3Ck_{\mathrm{B}}/(N\mu_{\mathrm{B}}^2)$; $g = 2$; k_{B} is the Boltzmann constant; *N* is the Avogadro number; μ_{B} is the Bohr magneton; and $S_{\mathrm{Mn}(+4)}$ and $S_{\mathrm{Co}(+2)}$ are the spin quantum numbers for the Mn^{4+} and Co^{2+} ions, respectively. The experimental value of $p_{\mathrm{eff(Ho)}}$ is $10.7\mu_{\mathrm{B}}$, which is very close to the theoretical value of $10.6\mu_{\mathrm{B}}$ for the free Ho^{3+} ion.

Figure 2 presents temperature dependences of the susceptibility $\chi = M/H$ for an HMCO single crystal measured at various values of the magnetic field in the FC and ZFC modes. For $H = 0.1$ kOe, the PM–FM transition occurs at $T_c = 74$ K. The value of T_c grows weakly with magnetic field; indeed, for 1 kOe, we have $T_c = 76$ K and, for 10 kOe, $T_c = 78$ K. Thus, T_c increases by 4 K as the field increases from 0.1 to 10 kOe, but the PM–FM transition becomes diffuse (Fig. 2a). At low temperatures ($T \le 30$ K), $\chi(T)$ is seen to deviate from the typical FM behavior (saturation at low temperatures); more specifically, the susceptibility (magnetization) of the single crystal increases, which is due to the contribution from the PM holmium ions. The deviation from the typical FM behavior increases with magnetic field; indeed, the deviations of the magnetization *M*(*T*) are ~1, ~2.7, and 25 emu/g in fields of 0.1, 1, and 10 kOe, respectively. This appears only natural, because the ratio of the magnetization of the FM manganese and cobalt ions to that of the PM ion of holmium decreases with increasing magnetic field.

Table 1. Structural data for $R\mathrm{Mn}_{1-x}\mathrm{Co}_x\mathrm{O}_3$ single crystals (R = Ho, La; $x \approx 0.5$)

Single crystal		HMCO	LMCO
	Space group	*Pbnm*	*Pbnm*
300 K	*a*, Å	5.26	5.451
	b, Å	5.57	5.509
	c, Å	7.45	7.742
	V/*z*, Å^3	54.57	58.23
	Structure	*O*	*O*
300 K	*m*(Mn(Co)–O$_1$), Å	1.89	1.937
	s(Mn(Co)–O$_{11}$), Å	1.834	1.934
	l(Mn(Co)–O$_{11}$), Å	2.14	1.962
	$R_t = l/s$	1.17	1.014
	r_A, Å	1.072	1.216
	t	0.86	0.91

A comparison of Figs. 2a and 2b suggests the existence of a clearly pronounced temperature irreversibility (particularly in weak fields) between $\chi_{\mathrm{ZFC}}(T)$ and $\chi_{\mathrm{FC}}(T)$. The susceptibility $\chi_{\mathrm{ZFC}}(T)$ starts to deviate from $\chi_{\mathrm{FC}}(T)$ near T_c; as the temperature decreases, a maximum forms in the $\chi_{\mathrm{ZFC}}(T)$ curves, with its position dependent on the applied magnetic field. As the field increases, the maximum in $\chi_{\mathrm{ZFC}}(T)$ shifts toward lower temperatures: from 69 K at 0.1 kOe to 60 K at 1 kOe. In a field of 10 kOe, this maximum becomes very diffuse (Fig. 2b). Below ~30 K, the susceptibility rises steeply, with the major contribution to $\chi(T)$ being due to the holmium PM ions. Note that, in fields $H \ge 10$ kOe, there is practically no thermomagnetic irreversibility between $\chi_{\mathrm{ZFC}}(T)$ and $\chi_{\mathrm{FC}}(T)$ of HMCO.

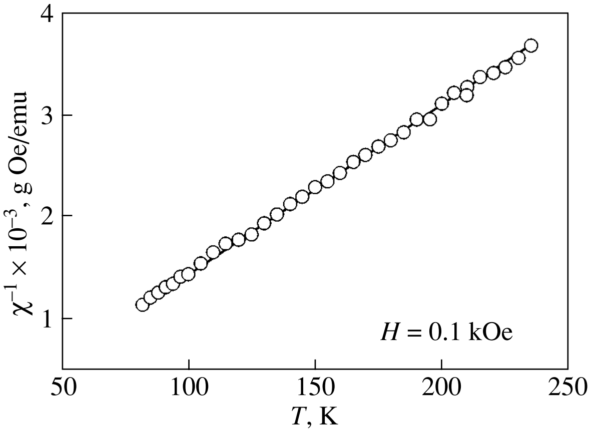

Fig. 1. Temperature dependence of the reciprocal susceptibility of an HMCO single crystal.

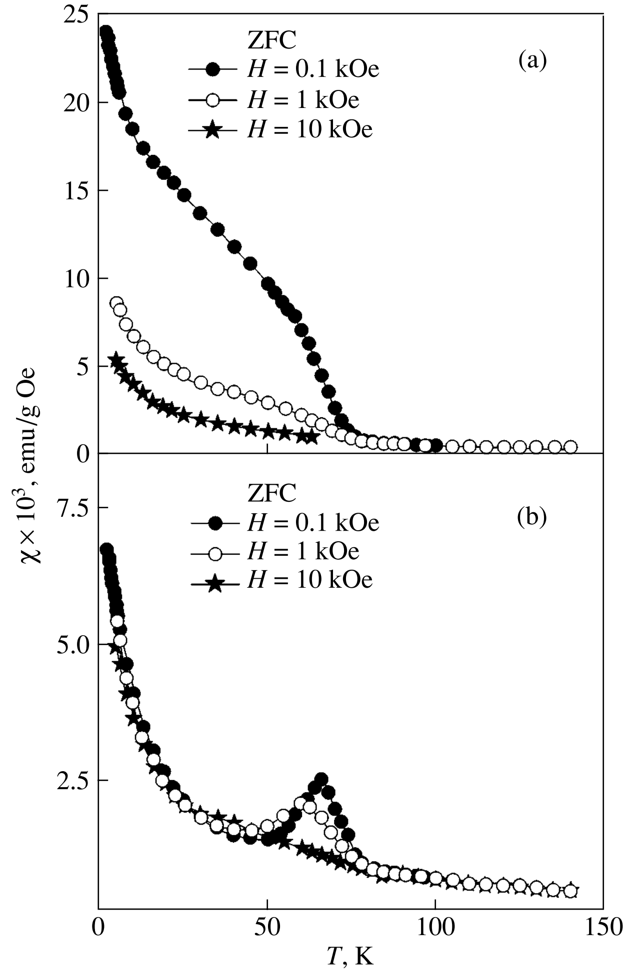

Fig. 2. Temperature dependence of the susceptibility of an HMCO single crystal measured in different magnetic fields in (a) the FC and (b) ZFC modes.

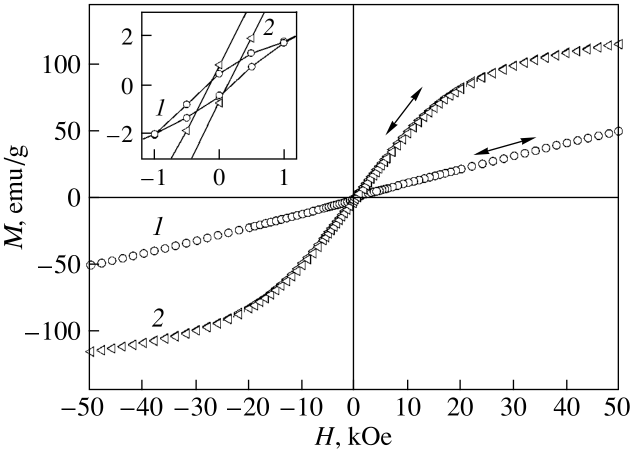

Fig. 3. Field dependences of the magnetization $M(H)$ of an HMCO single crystal measured at temperatures of (*1*) 65 and (*2*) 5 K. Inset: $M(H)$ dependence in the range of weak fields.

The field dependences of magnetization $M(H)$ of an HMCO single crystal were measured in the temperature interval 5–100 K; for illustration, Fig. 3 plots $M(H)$ isotherms for 5 and 65 K in the field interval $-50 \le H \le 50$ kOe. At 65 K, the magnetization varies with field practically linearly, except in the low-field region $|\mu_0 H| \le 1.5$ kOe (inset to Fig. 3), where there is a small hysteresis in the $M(H)$ graph, with a loop width of ~290 Oe along the H axis. Thus, the FM component in HMCO is observed in the low-field region for $T \le 65$ K. At lower temperatures ($T = 5$ K), the hysteretic behavior of $M(H)$ persists up to fields $|\mu_0 H| \le 15$ kOe, but the magnetization does not saturate up to 50 kOe. The high-field susceptibility at 5 K as derived from the $M(H)$ curve for the HMCO single crystal is $\chi_{hf} \approx 2.4 \times 10^{-3}$ emu/(g Oe).

It should be pointed out that the hysteresis loops measured in the FC mode shift along the H axis by ΔH. For instance, at 5 K, the value of ΔH is 10 Oe, with the loop width being ~290 Oe (inset to Fig. 3). The results obtained are listed in Table 2, which also contains, for comparison, the magnetic characteristics of the LMCO single crystal (with similar manganese and cobalt contents: $Mn_{0.46}$, $Co_{0.54}$) taken from our earlier publications [7, 8]. Note that $LaMn_{0.5}Co_{0.5}O_3$ features two FM phases with different structures and different T_c, more specifically, a rhombohedral structure with a high T_c (220–240 K) and an orthorhombic structure with a low T_c (150–170 K) [4, 5, 9]. The LMCO single crystals studied in [7, 8] had an orthorhombic structure with $T_c = 170$ K (Table 1).

4. DISCUSSION OF THE RESULTS: COMPARATIVE ANALYSIS OF THE MAGNETIC PROPERTIES OF HMCO AND LMCO SINGLE CRYSTALS

We used the values of the cation radii r_A and r_B and of the anion radius r_0 to calculate the tolerance factor $t = (r_A + r_0)/\sqrt{2}\,(r_B + r_0)$ for perovskites with the general formula ABO_3, which is a measure of the deviation of a given structure from an ideal cubic perovskite with $t = 1$. The values assumed for the calculation were $r_A = 1.072$ (for Ho^{3+}) and 1.216 Å (for La^{3+}) and $r_B = 0.530$ (for Mn^{4+}) and 0.745 Å (for Co^{2+}) [15]. For HMCO, we have $t = 0.86$, and for LMCO, $t = 0.91$ (Table 2). The values of T_c at which the PM–FM transition occurs differ markedly for the two crystals, which is in good agreement with the data from [12, 16]. This difference between the two systems under study should be assigned to the fact that, as the largest trivalent lanthanide ion, La^{3+}, is replaced by the holmium ion (having a substantially smaller radius), the value of t decreases. The B–O–B bond angle depends on the size of the ion in the A position (and, hence, on the tolerance factor t); namely, as t decreases, the distortion of the structure increases and the bond angle decreases by

Table 2. Magnetic characteristics of HMCO and LMCO single crystals

Single crystal	T_c, K	Θ_p, K	exp. p_{eff}, μ_{B}	calc. p_{eff}, μ_{B}	calc. μ_s (Mn–Co), μ_{B}	exp. μ_s, μ_{B}	$2H_c$ (5 K) kOe	ΔH (5 K) Oe	χ_{hf} emu/(g Oe)	J_F/k_{B}	J_A/k_{B}
HMCO	74	10.94	10.64	10.7	3.00	2.41	0.29	10	2.4×10^{-3}	4.25	–6.3
LMCO	170	173	0	0	3.00	1.84	~20	250	8×10^{-4}	17.15	–0.3

deviating by a progressively greater amount from the ideal value of 180° (for $t = 1$). The distortion gives rise to increased stresses caused by the replacement of La^{3+} by the Ho^{3+} ion, which reduces T_c noticeably (Table 2). Note that, while the PM Curie temperature Θ_p for HMCO is positive (like that for LMCO [7, 8]), it is lower by ~162 K. Interestingly, for $HoMnO_3$ and $HoCoO_3$, the values of Θ_p are negative and equal to –17 [11] and –15.8 K [17], respectively, which indicates the AFM character of these compounds, in contrast to HMCO and LMCO. Note that there are common features in the behavior of the $M(T)$ relations for these systems: (i) thermomagnetic irreversibility between $M_{\mathrm{FC}}(T)$ and $M_{\mathrm{ZFC}}(T)$ which is particularly pronounced in weak fields; (ii) the presence of a maximum in the $M_{\mathrm{ZFC}}(T)$ curves, whose position depends on the field; (iii) the absence of this maximum in strong fields; and (iv) the persistence of thermomagnetic irreversibility up to high fields. The observed effects suggest that these crystals reside in a two-phase magnetic state. The difference between these systems consists in the fact that the irreversibility between $M_{\mathrm{ZFC}}(T)$ and $M_{\mathrm{FC}}(T)$of LMCO persists even in fields as high as 50 kOe at temperatures below 50 K [7, Fig. 2], whereas for HMCO this difference is observed in substantially weaker fields (H ~ 10 kOe). For both crystals, the temperature dependences $M(T)$ in high fields are described by the Langevin function with an effective cluster magnetic moment of $10\mu_{\mathrm{B}}$ (HMCO) and $15\mu_{\mathrm{B}}$ (LMCO) [7, 8]. These values refer to the effective magnetic moment of clusters containing several formula units.

Extrapolating $1/H$ to zero in the M versus $1/H$ graph yields the saturated magnetic moment in the strong field limit to be $\mu_{s,\,\mathrm{exp}} = 2.41\mu_{\mathrm{B}}$ per formula unit for HMCO and $\mu_{s,\,\mathrm{exp}} = 1.84\ \mu_{\mathrm{B}}$ for LMCO (Table 2). In the case of LMCO (where the La^{3+} ion has zero magnetic moment), we associate the value of μ_s with the total contribution of the Mn^{4+} and Co^{2+} ions [7, 8]. However, the expected value of $\mu_{s,\,\mathrm{calc}}$ associated with FM ordering of the Mn^{4+} and Co^{2+} ions (the pure spin value $\mu_{s,\,\mathrm{calc}} = gS\mu_B$, where $g = 2$ and $S = 3/2$ for both ions) is $3\mu_{\mathrm{B}}$/f.u., which is substantially larger than $\mu_{s,\,\mathrm{exp}}$. This fact also argues for the two-phase magnetic state of the crystals. Note that the difference between $\mu_{s,\,\mathrm{exp}}$ and $\mu_{s,\,\mathrm{calc}}$ for LMCO was attributed in [18] to a decrease in the Mn/Co ratio (for the cobalt concentration $x_{\mathrm{Co}} \geq 0.5$) and to enhanced Mn(Co)d–Op hybridization causing a decrease in the magnetic moment of the manganese and cobalt ions. The value of μ_s calculated in [18] for LMCO practically coincides with the observed value of $1.84\mu_{\mathrm{B}}$. Another situation is encountered in the HMCO system, where the Ho^{3+} ions possess a magnetic moment. Assuming the average moment of the Mn–Co sublattice to be the same in both systems (i.e., FM ordering of the Mn^{4+} and Co^{2+} ions at $T < T_c$), we considered the following two possible versions for HMCO: the (Mn^{4+}–Co^{2+}) and Ho^{3+} spins are ordered (i) ferromagnetically or (ii) antiferromagnetically. The pure spin value of the Ho^{3+} magnetic moment is $4\mu_B$. Thus, the total magnetic moment is 7 and 1 μ_B/f.u. for the first and second versions, respectively, which is inconsistent with the observed value of $2.41\mu_B$ (Table 2).

The field dependences of $M(H)$ of the HMCO and LMCO crystals follow noticeably different patterns. The hysteresis loop measured on LMCO at 5 K has $H_c \approx 10$ kOe, and the isotherms remain nonlinear up to 200 K ($T_c = 170$ K) [8, Fig. 4]. The high values of H_c at low temperatures suggest a heavy contribution of domain effects in this material. A similar pattern was observed in $LaMn_{0.5}Co_{0.5}O_3$ [9]. In the case of HMCO, the magnetization of Ho^{3+} ions becomes appreciable only at low temperatures (below ~30 K) and is superimposed on the magnetization of Mn^{4+} and Co^{2+}. Far from T_c, for instance, at 5 K, the magnetization of 3d ions saturates in relatively low fields, whereas the magnetization of Ho^{3+} is induced by the applied magnetic field; as a result, the high-field susceptibility χ_{hf} in HMCO is considerably higher than that in LMCO (Table 2).

The shift ΔH of the hysteresis loop along the H axis in HMCO at 5 K is of the order of 10 Oe, which is about ~5% of the loop width, and for LMCO, $\Delta H \approx 250$ Oe, i.e., ~1%. A shift of hysteresis loops was first observed in partially oxidized cobalt [19], CuMn, and AgMn [20]. Hysteresis shift in CoO was observed only at temperatures below the Néel point T_N, where the material was in the AFM state. For CoO, T_N ~ 300 K and the loop shift increases with decreasing temperature. The shift ΔH was attributed in [19] to exchange interaction of FM cobalt particles with their AFM CoO shells. This new type of anisotropy is termed exchange anisotropy. The shift ΔH was also observed in single-crystal $La_{0.9}Sr_{0.1}MnO_3$ and thin $R_{0.6}Ba_{0.4}MnO_3$ epitaxial films (R = La, Pr, Nd, Gd) [21, 22]. Knowing ΔH, one can derive the exchange anisotropy constant $K_u = \Delta HM_s$, where M_s is the saturated magnetization in a crystal

[19]. For HMCO and LMCO crystals, $K_u \sim 10^4$ erg/cm^3, which is consistent with the data quoted in [21, 22].

The shift of the hysteresis loop supports the validity of the model of the two-phase magnetic state in crystals. As in [19], the exchange anisotropy constant for our single crystals is a measure of the exchange integral J describing the Mn(Co)–O–Mn(Co) coupling through the interface separating the FM and AFM phases. The estimate $|J| \sim 10^{-6}$ eV obtained in [21, 22] is two orders of magnitude smaller than the magnitude of the negative exchange integral between FM layers in LaMnO$_3$, which was derived from neutron diffraction measurements [23]. In our study [24] of magnetic ordering in LaMnO$_{3+\delta}$ single crystals with various oxygen contents, we estimated the exchange constants associated with positive interaction in the *ab* plane (J_F) and negative interaction along the **c** axis (J_A) [23]. For this purpose, we used the measured values of T_c and Θ_p and the following relations [25]:

$$\begin{aligned} T_c &= 2/3S(S+1)(4|J_F| + 2|J_A|)/k_B, \\ \Theta_p &= 2/3S(S+1)(4J_F + 2J_A)/k_B. \end{aligned} \quad (3)$$

The values of J_F/k_B and J_A/k_B calculated for HMCO and LMCO are presented in Table 2. The observed difference between the exchange coupling constants for these two systems can be assigned to the differences between the LaMnO$_3$ and HoMnO$_3$ magnetic structures studied in [11]. As suggested by neutron diffraction measurements, in the case of a large-radius cation (i.e., La^{3+}), magnetic interaction between neighboring manganese ions in the Mn–O layers perpendicular to the **c** axis (space group *Pbnm*) is ferromagnetic, while adjacent layers are coupled antiferromagnetically. This means that there are four FM and two AFM bonds for each manganese ion. In the case of a cation with a smaller radius (Ho^{3+}), magnetic interaction in the Mn–O layers can be identified as AFM with two manganese ions and FM with the other two manganese ions. Adjacent layers along the **c** axis are coupled antiferromagnetically, which implies, according to [11], two FM and four AFM bonds for each manganese ion. The magnetic structure of both LaMnO$_3$ and HoMnO$_3$ is treated in terms of orbital ordering of ε_g orbitals in each Mn–O plane. The deviation of the Mn–O–Mn bond angle from 180° in HoMnO$_3$ is large compared to that in LaMnO$_3$, as already mentioned, and equals 141.1, and the tilt of the MnO$_6$ octahedra $\omega = (180 - \langle\text{Mn–O–Mn}\rangle)/2$ increases from 24.8° for La^{3+} to 36.5° for Ho^{3+} [11].

5. CONCLUSIONS

An analysis of the totality of magnetic measurements of HMCO and LMCO single crystals with cobalt contents close to 0.5 allows one to conclude that, at low temperatures, both systems reside in a two-phase magnetic state. In other words, at low enough temperatures, these crystals can be described as an AFM matrix with embedded FM clusters (drops) [26, 27]. This conclusion is substantiated by the following experimental evidence characteristic of HMCO and LMCO single crystals: (i) thermomagnetic irreversibility is observed between the $M_{FC}(T)$ and $M_{ZFC}(T)$ curves; (ii) the magnetic moment per formula unit is noticeably below the theoretical value for complete FM ordering; (iii) the temperature dependences of $M(T)$ in strong magnetic fields are described by Langevin functions with a cluster moment of $10\mu_B$ and $15\mu_B$ for HMCO and LMCO, respectively; and (iv) the hysteresis loops are shifted along the magnetic field axis. The observed differences between the magnetic properties of the two systems should be assigned to the specific features of the HMCO and LMCO magnetic structures.

ACKNOWLEDGMENTS

This work was supported in part by the Committee for Scientific Research, KBN (Warsaw) (project no. PO3B 038 27), and NATO linkage grant PST CLG no. 979369.

REFERENCES

1. J. M. D. Coey, M. Viret, and S. von Molnár, Adv. Phys. **48** (2), 167 (1999).
2. J. B. Goodenough, A. Wold, R. J. Arnott, and N. Menyuk, Phys. Rev. **124** (2), 373 (1961).
3. J. H. Jonker, J. Appl. Phys. **37** (3), 1424 (1966).
4. P. A. Joy, Y. B. Khollam, and S. K. Date, Phys. Rev. B **62** (13), 8608 (2000).
5. V. L. J. Joly, P. A. Joy, and S. K. Date, J. Phys.: Condens. Matter **13** (10), L841 (2001).
6. J.-H. Park, S.-W. Cheong, and T. C. Chen, Phys. Rev. B **55** (17), 11072 (1997).
7. S. N. Barilo, V. I. Gatalskaya, S. V. Shiryaev, L. A. Kurochkin, R. Szymczak, and M. Baran, Low Temp. Phys. **28** (11), 853 (2002).
8. S. N. Barilo, V. I. Gatalskaya, S. V. Shiryaev, L. A. Kurochkin, S. N. Ustinovich, H. Szymczak, R. Szymczak, and M. Baran, Phys. Status Solidi A **199** (3), 484 (2003).
9. R. Machendiran, Y. Bread, M. Hervieu, B. Raveau, and P. Schiffer, Phys. Rev. B **68**, 104402 (2003).
10. V. A. Cherepanov, L. Yu. Barkhatova, A. N. Petrov, and V. I. Voronin, J. Solid State Chem. **118** (1), 53 (1995).
11. A. Muñoz, M. T. Casáls, J. A. Alonso, M. J. Martinez-Pope, J. L. Martinez, and M. T. Fernandez-Diaz, Inorg. Chem. **40** (5), 1020 (2001).
12. K. Asai, K. Fujiyoshi, N. Nishimori, Y. Sator, Y. Kobayashi, and M. Mizoguchi, J. Phys. Soc. Jpn. **67** (12), 4218 (1998).
13. A. K. Bogushi, V. I. Pavlov, and L. V. Balyko, Cryst. Res. Technol. **18** (3), 589 (1983).
14. C. Ritter, M. R. Ibarra, J. M. De Teresa, P. A. Algasaba, C. Marquina, J. Blanco, J. Garcia, S. B. Ozeroff, and S. W. Cheong, Phys. Rev. B **56** (14), 8902 (1997).
15. R. D. Shannon, Acta Crystallogr., Sect. A **32** (5), 751 (1976).

16. V. L. J. Joly, P. A. Joy, and S. K. Date, Solid State Commun. **121** (4), 219 (2002).
17. Y. S. Im, K. H. Ryu, K. H. Kim, and Ch. H. Yo, J. Phys. Chem. Solids **58** (12), 2079 (1997).
18. Zh. Yang, L. Ye, and X. Xie, Phys. Rev. B **59** (10), 7051 (1999).
19. W. H. Meiklejohn and C. P. Bean, Phys. Rev. **102** (5), 1413 (1956); Phys. Rev. **105** (3), 904 (1957).
20. J. S. Kouvel, J. Phys. Chem. Solids **21** (1), 57 (1961).
21. R. V. Dremin, L. I. Koroleva, R. Szymczak, and H. Szymczak, Pis'ma Zh. Éksp. Teor. Fiz. **75** (7), 402 (2002).
22. O. Yu. Gorbenko, R. V. Demin, A. R. Kaul', L. I. Koroleva, R. Szymczak, H. Szymczak, and M. Baran, Zh. Éksp. Teor. Fiz. **125** (3), 693 (2004) [JETP **98** (3), 612 (2004)].
23. F. Moussa, M. Hennion, J. Rodriguez-Carvajal, H. Moudden, L. Pinsard, and A. Revcolevschi, Phys. Rev. B **54** (21), 15149 (1996).
24. S. N. Barilo, V. I. Gatalskaya, S. V. Shiryaev, G. L. Bychkov, L. A. Kurochkin, S. N. Ustinovich, R. Szymczak, M. Baran, and B. Krzymańska, Fiz. Tverd. Tela (St. Petersburg) **45** (1), 139 (2003) [Phys. Solid State **45** (1), 146 (2003)].
25. V. Skumryev, F. Ott, J. M. D. Coey, A. Anane, J.-P. Renard, L. Pinsard-Gaudar, and A. Revcoevschi, Eur. Phys. J. B **11** (3), 401 (1999).
26. É. L. Nagaev, Usp. Fiz. Nauk **166** (8), 833 (1996) [Phys. Usp. **39** (8), 781 (1996)].
27. E. Dagotto, J. Burgy, and A. Moreo, Solid State Commun. **126** (1), 9 (2003).

Translated by G. Skrebtsov

Physics of the Solid State, Vol. 47, No. 7, 2005, pp. 1316–1325. Translated from Fizika Tverdogo Tela, Vol. 47, No. 7, 2005, pp. 1270–1279.
Original Russian Text Copyright © 2005 by Krynetskiĭ, V. M. Matveev, V. V. Matveev.

MAGNETISM AND FERROELECTRICITY

Low-Temperature Quasi-Adiabatic Magnetization Reversal of Rare-Earth Ising Metamagnets

I. B. Krynetskiĭ*, V. M. Matveev, and V. V. Matveev****
**Moscow State University, Vorob'evy gory, Moscow, 119899 Russia*
***Federal State Unitary Enterprise Lukin Scientific Research Institute of Physical Problems, Zelenograd, Moscow, 124460 Russia*

Received November 26, 2004

Abstract—The magnetization and magnetically induced elastic strains of rare-earth Ising antiferromagnets $DyAlO_3$ and $TbAlO_3$ are shown to exhibit an unusual behavior associated with low-temperature metamagnetic phase transitions. As an external magnetic field is applied and then removed slowly, the state of the magnetic system in these compounds follows quite different paths on the H–T diagram. Small alternating-sign variations in the field magnitude cause the magnetic system to switch reversibly from one path to another, which is accompanied by sharp changes in the magnetization and elastic strains. The observed anomalies are shown to be due to the magnetization process being quasi-adiabatic in character in the compounds under study. This fact should be taken into account in interpreting the data on the magnetization and magnetostriction in Ising antiferromagnets undergoing metamagnetic transitions at low temperatures. Experimentally, quasi-adiabatic magnetization makes it possible to determine the critical fields for metamagnetic transitions very exactly and to investigate the H–T phase diagram at temperatures that are far below the minimum temperature of a helium bath and are unattainable under strictly isothermal conditions. *© 2005 Pleiades Publishing, Inc.*

1. INTRODUCTION

Rare-earth oxides $DyAlO_3$ and $TbAlO_3$ are four-sublattice antiferromagnets with a distorted perovskite structure [1]. Below the Néel temperature (3.52 K for $DyAlO_3$ and 3.8 K for $TbAlO_3$), the rare-earth ions in these compounds become ordered in the *ab* plane and form the Γ_5 antiferromagnetic (AFM) structure (AFM cross) shown in Fig. 1a [2, 3]. In this case, the Dy and Tb ions can be treated as Ising ions, with their anisotropy axis lying in the *ab* plane and making angles of 57° (Dy) and 35° (Tb) with the *a* axis and with their magnetic moments being close in magnitude to the maximum possible values for these ions, $10\mu_B$ and $9\mu_B$, respectively.

Our studies have shown that these compounds behave in a qualitatively similar way under a magnetic field to within a 90° rotation of the field. In particular, the observed patterns of anomalies are the same for $TbAlO_3$ in the case of $\mathbf{H} \parallel a$ and for $DyAlO_3$ in the case of $\mathbf{H} \parallel b$. For this reason, we consider only dysprosium orthoaluminate (except in Fig. 3), to which all experimental and theoretical results presented here are related and for which most measurements were made. Dysprosium orthoaluminate is a pure dipole model metamagnet, for which all parameters can be calculated exactly and varied by changing the form of the crystal [4]. This allows us to avoid uncertainties when elucidating the nature of the observed anomalies and interpreting them theoretically, which is the main objective of this study.

In dysprosium orthoaluminate, the total internal magnetic field H_m acting on the magnetic moments of Dy ions in the Γ_5 structure at zero temperature is 5.6 T, which agrees well with the Néel temperature observed experimentally in [4], $T_N = 3.5$ K. This field is calcu-

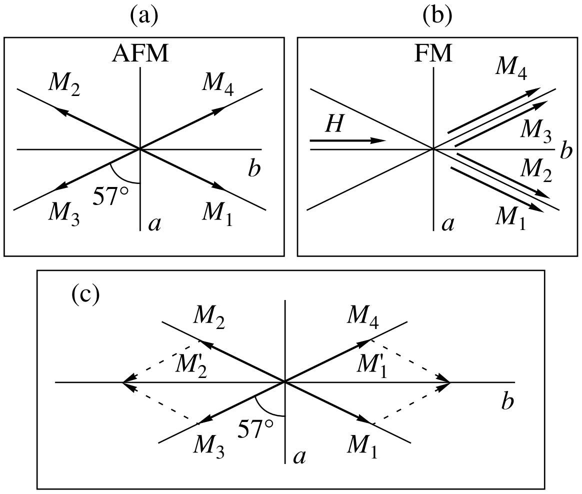

Fig. 1. Magnetic structures of Dy^{3+} ions in dysprosium orthoaluminate. (a) Γ_5 antiferromagnetic structure in a zero magnetic field, (b) high-field ferromagnetic structure in a field $H > H_m/\cos 33°$ applied along the *b* axis of the crystal, and (c) model two-sublattice structure with $M'_1 = (M_1 + M_4)\cos 33°$ and $M'_2 = (M_2 + M_3)\cos 33°$.

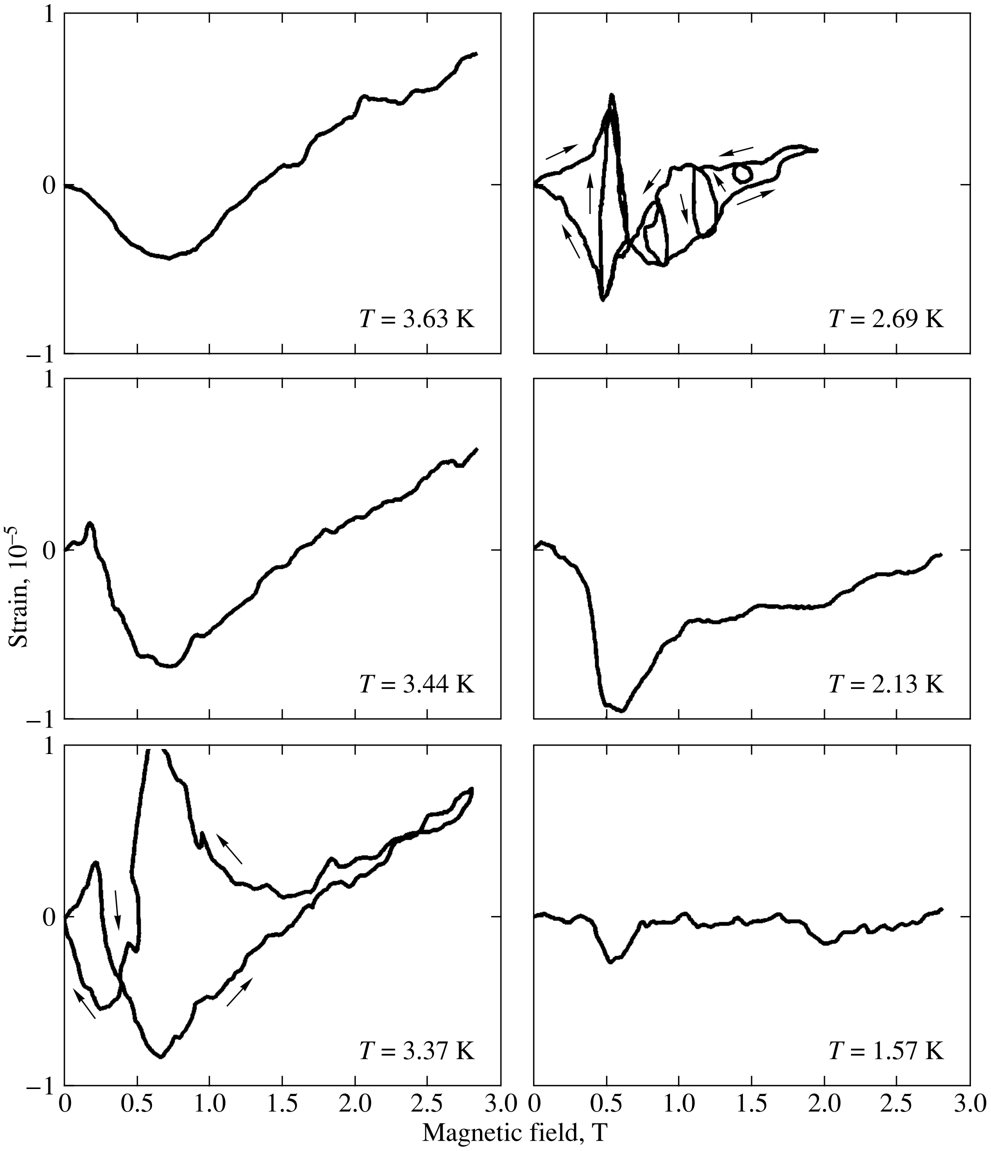

Fig. 2. Field dependences of magnetically induced strains in $DyAlO_3$ at various temperatures. Arrows indicate the direction of the magnetization process (increase or decrease in the external magnetic field).

lated by directly summing the dipole fields exerted on an ion by all magnetic ions of the crystal. The intra- and intersublattice fields H_{ij} (where i, j are the sublattice indices) are calculated by summing only the dipole fields exerted on a magnetic moment of sublattice j by all magnetic moments of sublattice i; these fields depend on the shape of a sample and can vary over wide limits and even change sign for a pair of sublattices (under the condition that the total field $H_m = H_{11} + H_{12} + H_{13} + H_{14}$ remain unchanged). For this reason, the H–T phase diagram of a metamagnet can vary widely. An external magnetic field applied in the *ab* plane of a crystal induces metamagnetic (single-or two-step) transitions from the initial AFM configuration to a high-field ferromagnetic (FM) configuration [1]. For example, a magnetic field $H > H_m/\cos 33°$, when applied along the *b* axis of a crystal, causes a single-step magnetization reversal of sublattices 2 and 3 along the respective Ising axes. As a result, a metamagnetic transition occurs to an FM configuration in which the magnetic moments of sublattices 1 and 2 have the same magnitude and direction, as do the magnetic moments of sublattices 3 and 4 (Fig. 1b).

Metamagnetic transitions in rare-earth Ising antiferromagnets have been studied using various methods [4–6], and in almost all cases the changes in the magnetic characteristics (magnetization, torques, etc.) caused by these transitions have been explained in terms of the conventional models of the isothermal magnetization reversal of two- or four-sublattice meta-

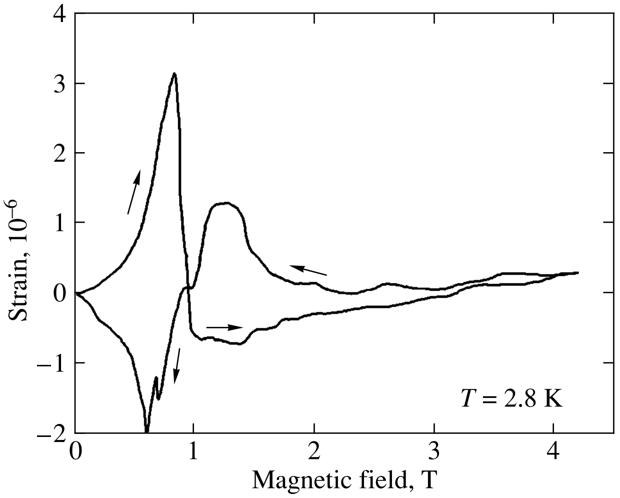

Fig. 3. Field dependence of magnetically induced strains in $TbAlO_3$.

magnets. For the first time, we measured the field dependences of elastic strains in $DyAlO_3$ and $TbAlO_3$ that cannot be described in terms of the existing models of the changes in the magnetostriction of rare-earth ions associated with the transition from the AFM to the FM structure.

2. EXPERIMENTAL

The unusual behavior of magnetically induced strains caused by metamagnetic transitions was first observed in the field dependence of the magnetostriction of dysprosium orthoaluminate measured for various orientations of the external magnetic field in the *ab* plane of a crystal. Measurements were performed over the temperature range 1.5–4.2 K in magnetic fields of up to 4 T in order to determine the magnetoelastic constants of rare-earth ions. Since the anomalous behavior of strains was observed to be most pronounced for a crystal magnetized along the *b* axis, we used this symmetrical orientation of the field, which simplifies the interpretation of the experimental data and makes it possible to use the two-sublattice model of the Ising antiferromagnet. The crystal for measurements had a special form for which the intra- and intersublattice interactions in the two-sublattice approximation were approximately equal in magnitude. In this case, the mathematical description of the magnetic system and of the effect of a magnetic field on this system is significantly simplified (see Section 3).

Magnetically induced elastic strains were measured using a strain-gage dilatometer with a bridge circuit and wire strain sensors fabricated from an alloy exhibiting a low galvanomagnetic effect. An *X*–*Y* recorder was used to record the strains induced by an external magnetic field, which was first increased from zero and then decreased. A magnetic field was produced by a superconducting system and was varied at rates ranging from 0.05 to 0.5 kOe/s. The maximum magnitude of the field was 4.3 T. The strain sensitivity of the experimental setup was better than 5×10^{-7}.

Figure 2 shows field dependences of magnetically induced strains along the *b* axis of a $DyAlO_3$ crystal measured at various temperatures in the range 1.5–4.2 K. The following anomalies can be seen:

(i) According to theory (see Section 3), the derivative of the magnetostriction with respect to the field can change sign only once during a metamagnetic transition driven by isothermal magnetization of a two-sublattice Ising antiferromagnet. Our measurements show that this derivative changes sign twice during a phase transition that occurs as the external field increases from zero or decreases to zero.

(ii) The graphs of the magnetically induced elastic strain versus field obtained for a field increasing from zero and for a field decreasing to zero differ radically from each other and are, to a certain extent, mirror images of each other in the abscissa axis. The mirror symmetry is more pronounced for $TbAlO_3$ (Fig. 3).

(iii) A reversal in the sign of the change in the field magnitude at any moment during an increase or a decrease in field causes the magnetic system to switch rapidly from one branch of the graph of the magnetically induced strain versus field to the other. In this case, very small dynamic variations in the field magnitude produced by repeated reversals of the sign of the change in the current passing through the solenoid bring about a reversible switching of strains.

(iv) As the temperature decreases from $T = T_N$ in the range where Dy ions are ordered, the observed anomalies first increase rapidly and then, below $T \simeq 2.2$ K, decrease sharply to vanish almost completely at the lowest temperature attained in our experiments (about 1.5 K).

Additional experiments were carried out in which the amplitude of cyclic magnetic-field sweeping was varied (Fig. 4). It was shown that the difference between the elastic strains measured in the case where the magnetic field increases from zero and in the case where the field decreases to zero is not due to the existence of metastable states of the magnetic system. At any (even very small) value of the maximum to which the field increases from zero, the change in the sign of the field variation (i.e., a decrease in the field value) causes the system to switch to the decreasing-field branch of the entire field-sweeping curve (i.e., the curve that is obtained for the maximum field value attained in our experiments, 4.3 T).

Analogous changes in the magnetic state have been observed in hard type-II superconductors with strong pinning [7]. For this reason, our preliminary interpretation of the observed anomalies was based on the assumption that they are associated with the mesoscopic structure of the AFM compound under study over

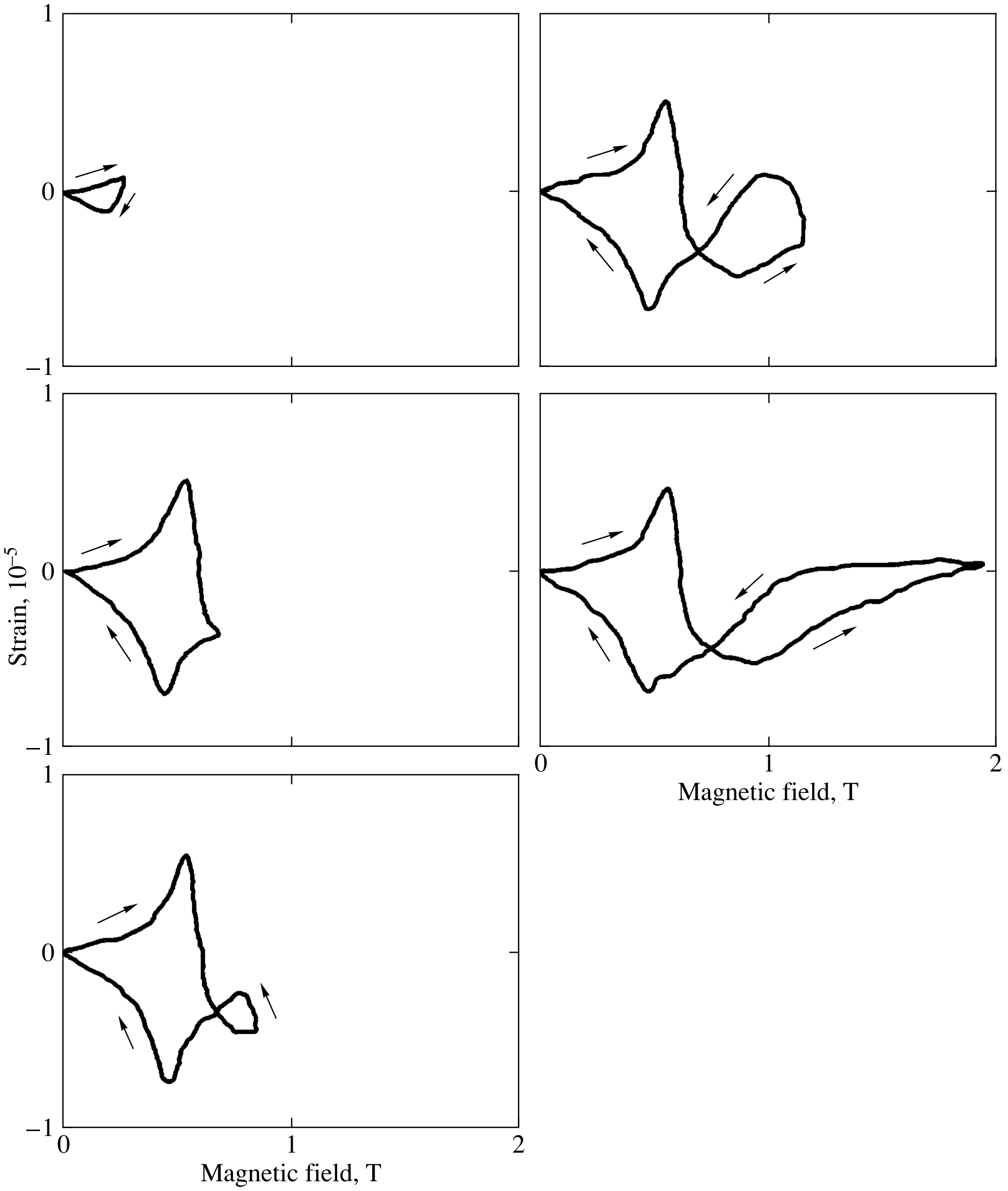

Fig. 4. Variations in magnetically induced strains in $DyAlO_3$ in a magnetic field increasing from zero and then decreasing to zero for various values of the amplitude of the field. The temperature of the liquid-helium bath is $T = 2.69$ K.

the entire range where Ising Dy ions are ordered. The magnetocaloric effect was taken into account at the outset, but the quasi-adiabatic magnetization seemed at first to be impossible, because the rates of the increase and decrease in the external magnetic field were far less than those in pulsed-field experiments, where the magnetocaloric effect is indeed of fundamental importance.

An adequate interpretation of the observed anomalies was made on the basis of the magnetization curves (Fig. 5) and of the field dependences of the magnetically induced strains measured for various rates of an increase in the field (Fig. 6). It can be seen from Fig. 5 that the magnetization curves are also anomalous in character; these curves are radically different in the case where the field increases from zero and in the case where the field decreases to zero. In both cases, there is an elbow near which the magnetization variation changes in character. For example, as the field increases from zero, the magnetization values before the elbow are similar to those measured at temperatures significantly lower than the temperature of the liquid-helium bath, whereas above the elbow the values of magnetization are similar to those measured at significantly higher temperatures (and, as a consequence, the saturation occurs in fields much higher than the saturation field calculated for isothermal magnetization of the

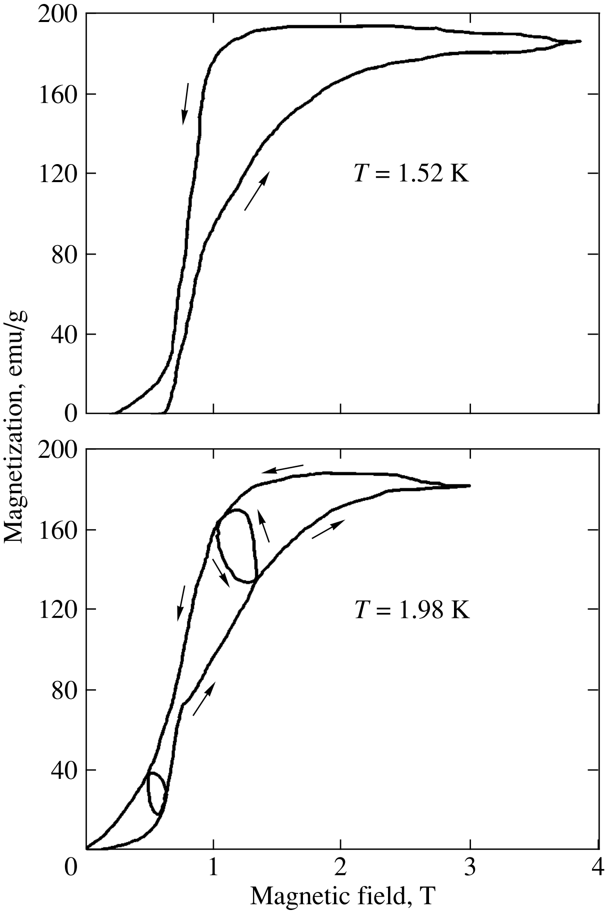

Fig. 5. Variations in the magnetization of $DyAlO_3$ in a magnetic field increasing from zero and then decreasing to zero.

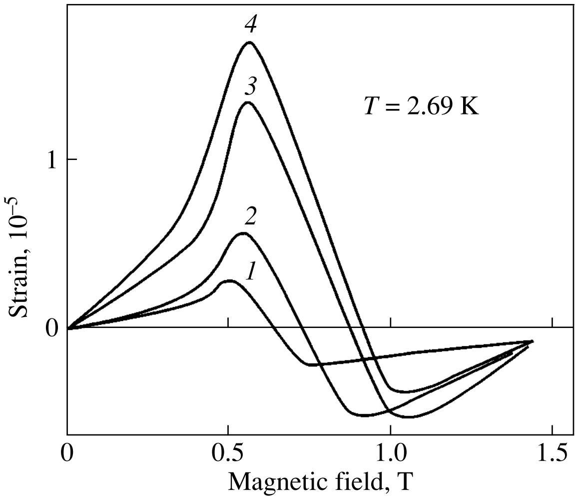

Fig. 6. Field dependences of magnetically induced strains for various values of the rate of field increase dH/dt: (*1*) 0.84, (*2*) 1.5, (*3*) 4.2, and (*4*) 9.1 kOe/min.

crystal). In the case where the field decreases to zero, the situation is reversed; a decrease in field in the saturation range at first even causes a small increase in magnetization. What is more important, small field variations bring about switching between the increasing- and decreasing-field branches (as is the case for strain–field curves); namely, a small decrease in field on the increasing-field branch causes a jumplike increase in magnetization, whereas an increase in field on the decreasing-field branch causes a jumplike decrease in magnetization. Therefore, these processes are quasi-adiabatic rather than isothermal.

Another argument for the magnetization process being quasi-adiabatic is the effect of the rate of the increase or decrease in field on the field dependence of the magnetically induced elastic strains. It can be seen from Fig. 6 that, for a higher rate of field increase from zero (i.e., for a higher degree of adiabaticity of the magnetization process), the anomalies in the field dependences become noticeably more pronounced (and the same is true for a higher rate of decrease in the field to zero).

3. THEORY

Our interpretation of the observed magnetization anomalies associated with the AFM–FM metamagnetic transition occurring in the $DyAlO_3$ Ising antiferromagnet takes into account the geometry of the experiment and the results obtained and is based on the following assumptions:

(i) The Ising two-sublattice model of an antiferromagnet can be used in which one sublattice replaces sublattices 1 and 4 and the other replaces sublattices 2 and 3 (Fig. 1c). In fact, this approximation is equivalent to the assumption that an external magnetic field is directed exactly along the *b* axis of the crystal, because in this case the four-sublattice model of dysprosium orthoaluminate reduces to the two-sublattice model (for the actual values of the intersublattice interactions dictated by the sample geometry chosen). Obviously, in the two-sublattice model, the Ising axis of the antiferromagnet is the *b* axis of the crystal.

(ii) At low temperatures, the magnetic Dy^{3+} ions in dysprosium orthoaluminate can be considered two-level quantum-mechanical systems, because the energy separation between the ground-state Kramers doublet and the excited levels is large (of the order of 50 cm^{-1}).

(iii) Due to the still unclear slowing of the heat transfer from the spin system of the crystal to the liquid-helium bath (thermostat), the magnetization of the Ising antiferromagnet is quasi-adiabatic even in very slowly varying magnetic fields.

(iv) The temperature of the spin system has a tendency to approach the temperature of the liquid-helium bath, which is characterized by a single parameter, the heat-transfer coefficient between the spin system and the thermostat.

(v) The conventional quantum-mechanical (phenomenological) model of magnetostriction of rare-earth ions can be used (see, e.g., [1, Chap. 12]).

Based on assumptions (i, ii), the nonequilibrium thermodynamic potential (per ion) of dysprosium orthoaluminate in an external magnetic field **H** || b can be written as [1]

$$\begin{aligned}\Phi(m_1, m_2) = \Phi_0 + \frac{1}{3}\Big\{&-\frac{1}{2}\lambda_{11}M_0'^2(m_1^2 + m_2^2)\\ &+ \lambda_{12}M_0'^2 m_1 m_2 - HM_0'(m_1 + m_2)\\ &- T[S(m_1) + S(m_2)]\Big\},\end{aligned} \tag{1}$$

where Φ_0 is the nonmagnetic part of the potential; $m_{1,2} = M'_{1,2}/M'_0$ are the reduced magnetic moments of the sublattices of the model two-sublattice system; $M'_{1,2}$ are defined in the capture to Fig. 1; M'_0 = $M'_{1,2}(T = 0)$; λ_{11} and λ_{12} are the intra- and intersublattice interaction parameters, respectively, which can be calculated exactly and are considered positive (the FM character of interactions within sublattices 1 and 2 and the AFM character of the intersublattice interaction are taken into account in the thermodynamic potential itself); and $S(m)$ is the entropy of the two-level system, which is given by the well-known formula

$$\begin{aligned}S(m) &= \ln 2 - \int_0^m \operatorname{arctanh} m\, dm\\ &= \ln 2 - \frac{1}{2}(1 + m)\ln(1 + m) - \frac{1}{2}(1 - m)\ln(1 - m).\end{aligned} \tag{2}$$

We introduce the following dimensionless quantities: the FM moment $m = (m_1 + m_2)/2$, the AFM moment $l = (m_1 - m_2)/2$, the magnetic field $h = H/H_m$, the temperature $t = T/T_N$, and the parameter $\tau_c = \lambda_{11}/(\lambda_{11} + \lambda_{12})$, which characterizes the relationship between the intra- and intersublattice interactions. In our case, as mentioned above, $H_m = 5.6$ T and $T_N = 3.5$ K. Since $T_N = M'_0 H_m = M_0'^2(\lambda_{11} + \lambda_{12})$, the magnetic part of the potential in Eq. (1) can be rewritten as

$$\begin{aligned}\frac{\Phi_m(m_1, m_2)}{T_N} = &-mh - \frac{1}{2}(2\tau_c - 1)m^2 - \frac{1}{2}l^2\\ &- \frac{1}{2}t[S(m + l) + S(m - l)].\end{aligned} \tag{3}$$

For the samples used in our experiments, we have τ_c = 0.5–0.7. Over this range of τ_c values, the H–T phase diagram does not change qualitatively. Therefore, for the sake of simplicity, we present analytical expressions only for the simpler case of $\tau_c = 0.5$ in what follows. In this case, the second term in Eq. (3) for the thermodynamic potential is equal to zero. Computations for specific samples are performed using numerical methods.

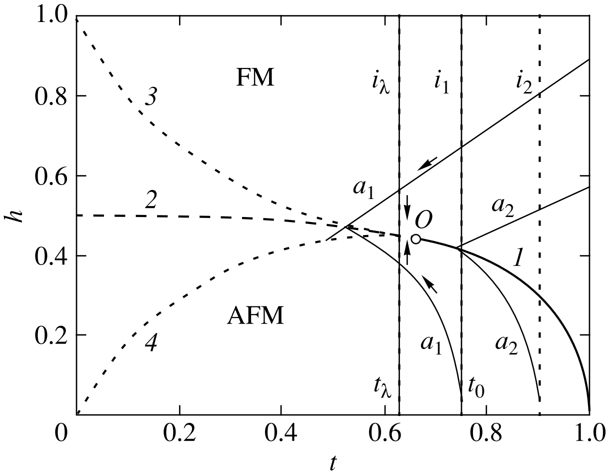

Fig. 7. H–T phase diagram of the $DyAlO_3$ sample under study drawn for reduced magnetic field and temperature. (*1*) Line of a second-order phase transition; (*2*) line of a first-order phase transition; (*3*, *4*) lines of the loss of stability of the AFM and FM phases, respectively; i_λ and $i_{1,2}$ are isotherms; $a_{1,2}$ are isentropic curves (adiabats); O is the tricritical point; t_0 is the temperature of the liquid-helium bath; and t_λ is the λ point of helium.

Minimizing thermodynamic potential (3) with respect to m and l at $\tau_c = 0.5$ gives the following equations for the equilibrium values of these parameters:

$$\begin{aligned}\operatorname{arctanh}(m + l) + \operatorname{arctanh}(m - l) &= 2h/t,\\ \operatorname{arctanh}(m + l) - \operatorname{arctanh}(m - l) &= 2l/t.\end{aligned} \tag{4}$$

These equations can be rewritten in a simpler form,

$$m_1 = \tanh(h_1/t), \quad m_2 = \tanh(h_2/t),$$

where h_1 and h_2 are the effective internal magnetic fields acting on sublattices 1 and 2, respectively:

$$h_1 = 0.5(m_1 - m_2) + h, \quad h_2 = 0.5(m_2 - m_1) + h.$$

In addition, the following condition of stability should be satisfied:

$$(m + l)^2 + (m - l)^2 < 2(l - t). \tag{5}$$

The corresponding H–T phase diagram of the Ising antiferromagnet is shown in Fig. 7. From Eqs. (4) and (5), the equilibrium value of m and the $h_{FM} = H_{FM}(t)$ line along which stability of the FM phase is lost can be found in explicit form to be

$$m = \tanh(h/t), \quad h_{FM} = t\operatorname{arctanh}(1 - t)^{1/2}. \tag{6}$$

Above the curve corresponding to the loss of stability (curve *1* in Fig. 7), the system is in a paramagnetic state, which is the consequence of the condition $\tau_c = 0.5$.

Under this condition, the intra- and intersublattice interactions are equal in magnitude in the FM phase and, therefore, the total internal dipole field acting on the magnetic moments is equal to zero.

For the AFM phase ($l \neq 0$), Eqs. (4) can be written in the form

$$h = t\,\mathrm{arctanh}\left(\frac{\tanh(l/t) - l}{\tanh(l/t) - l\tanh^2(l/t)}\right)^{1/2}, \qquad (7)$$
$$m = \tanh(h/t)[1 - l\tanh(l/t)].$$

In this case, the equilibrium values of m and l can be found in a "semiexplicit" form as follows: at given values of l and t, the value of h is determined from the first of equations (7) and then the value of m can be found from the second equation.

The phase diagram has a tricritical point with coordinates $t_c = 2/3$ and $h_c = (2/3)\,\mathrm{arctanh}(1/\sqrt{3}) = 0.44$. At $t > t_c$, the AFM–FM metamagnetic transition driven by an external field is a second-order phase transition. The line of these phase transitions is described by the second of equations (6). At $t < t_c$, the AFM–FM metamagnetic transition is first-order. The line of first-order phase transitions (curve *2* in Fig. 7) is almost parallel to the temperature axis. Note that, as the parameter τ_c increases, the tricritical point shifts to higher temperatures and to lower fields and the line corresponding to the loss of stability of the FM phase crosses the temperature axis; so, at very low temperatures, the FM phase becomes stable (metastable) even in a zero field.

In systems similar to that considered here, in the region of the *H*–*T* phase diagram bounded by the lines corresponding to the loss of stability of the AFM and FM phases at $t < t_c$ (curves *3*, *4* in Fig. 7, respectively), an intermediate state generally occurs in which the crystal is broken into domains of the coexisting AFM and FM phases. This state corresponds to a minimum of the magnetostatic energy, which is usually not included in the initial thermodynamic potential. In the case of a pure dipole antiferromagnet considered here, this energy is included automatically; the shape of the *H*–*T* phase diagram is determined only by the dipole–dipole interaction, which depends on the specific form of samples. Clearly, the dipole fields acting on the Dy ions include the demagnetizing field. Nonetheless, there is good reason to believe that, in the intermediate region mentioned above, the transition from the low-field AFM configuration to the high-field FM configuration can occur via an intermediate state consisting of layered many-sublattice (in fact, micromagnetic) structures, which are mesoscopic in the direction perpendicular to the layers (i.e., along the *c* axis of the crystal). This inhomogeneous state proves to be energetically favorable. However, in order to analyze this state theoretically, we have to go beyond the Ising two-sublattice model of a ferromagnet and even beyond the model of a ferromagnet with a finite number of sublattices. This is a separate, very complicated problem. Since it is planned for the near future to compare our theoretical results with experimental magnetic neutron scattering data, we will use the statement made above as a hypothesis, which does not contradict the observed anomalies in magnetically induced strains but, of course, is not necessary for explaining these anomalies (see below).

Based on assumption (iii) concerning the quasi-adiabatic magnetization of the system under study, we constructed $S(h, t)$ = const isentropic curves calculated from the equations presented above and isotherms t = const on the *H*–*T* diagram in Fig. 7. As might be expected for the Ising antiferromagnet magnetized adiabatically at a fixed liquid-helium bath temperature, the isentropic curve in the *H*–*T* plane first deviates sharply to very low temperatures (far less than the liquid-helium temperature) and then, at fields above the critical field for the phase transition, goes to higher temperatures (above the liquid-helium temperature). This behavior can be explained as follows. Isothermal magnetization of the AFM phase is accompanied by a decrease in the magnetization of one of the sublattices (m_2) and an increase in entropy. Therefore, for the entropy to remain unchanged during adiabatic magnetization, the temperature of the spin system has to decrease (adiabatic demagnetization). Isothermal magnetization of the FM phase is accompanied by a decrease in entropy; therefore, during adiabatic magnetization, the temperature of the spin system has to increase. The change in the sign of entropy variations for an isotherm or in the sign of variations in the temperature of the spin system for an isentropic curve occurs at the AFM–FM phase transition point. In the latter case, the phase transition temperature is significantly lower than the temperature of the liquid-helium bath.

Note also the following important fact. From Eq. (2), it follows that, if the total entropy $S(m, l) = [S(m + l) + S(m - l)]/2$ is constant, then the quantity $m^2 + l^2$ is approximately constant. For isentropic curves in the FM phase, we have the exact equality m = const; hence, it follows from Eqs. (6) that these curves are straight lines, $h = \mathrm{const}\,t$ (Fig. 7). For isentropic curves in the AFM phase, the condition

$$m^2(h, t) + l^2(h, t) = l_0^2 \qquad (8)$$

[which replaces the exact condition $S(m, l) = S(0, l_0)$ is satisfied to within approximately 5%. In Eq. (8), $l_0 = l(0, t_0)$, where t_0 is the temperature of the liquid-helium bath.

According to assumption (iv) made above, the temperature of the spin system always has a tendency to approach the temperature of the liquid-helium bath. As a consequence, the actual paths followed by the magnetization process differ from ideal isentropic curves. This tendency is formally taken into account by introducing a single empirical parameter, the heat-transfer coefficient α between the spin system and the liquid-helium bath. With this parameter, the dependence of the temperature on the magnetic field during a quasi-adiabatic process is described by the equation

$$\frac{dt}{dh} = \left(\frac{dt}{dh}\right)_S \mp \frac{\alpha}{v_H}(t-t_0) = \frac{(\partial S/\partial h)_t}{(\partial S/\partial t)_h} \mp \alpha'(t-t_0), \quad (9)$$

where v_H is the rate of change of the magnetic field, $\alpha' = (\alpha/v_H)$, and t_0 is the temperature of the liquid-helium bath. The minus and plus signs of the second term in Eq. (9) correspond to an increase and a decrease in the magnetic field, respectively.

For the FM phase, the magnetization does not change along isentropic curves and Eq. (9) reduces to the simple linear equation

$$\frac{dt}{dh} = t/h \mp \alpha'(t-t_0). \quad (10)$$

For the AFM phase, an approximate differential equation for quasi-adiabats can be derived in explicit form only for temperatures close to the Néel temperature (where the quantities m, l, h, $1-t$ are small). In this case, as follows from Eqs. (7), isentropic curves can be approximated by the equation $t = t_0 - (2/3)h^2$ and Eq. (9) reduces to

$$\frac{dt}{dh} = \frac{4}{3}h \mp \alpha'(t-t_0). \quad (11)$$

Figure 8 shows typical phase trajectories in the *H–T* plane, which are calculated using Eq. (10) and more accurate analogs of Eq. (11) and along which the magnetic state of the system varies as the magnetic field is varied in different regimes.

The first feature to note is that the theoretically calculated changes in the temperature of the spin system relative to the liquid-helium bath temperature reproduce (to within the sign) almost all experimentally observed anomalies in the field dependences of magnetically induced strains. These anomalous features are as follows: (i) a radical difference between the increasing- and decreasing-field dependences of strains and their approximate mirror symmetry; (ii) the existence of sharp peaks in these dependences and an abrupt switching of strains between the increasing- and decreasing-field branches caused by a change in the sign of field variation [this switching is a consequence of the jumplike transition from the situation where the changes in temperature in the processes of adiabatic heat generation and heat transfer (described by the first and second terms in Eq. (9), respectively) differ in sign to the situation where these changes are of the same sign]; (iii) an increase of the anomalies in magnitude with an increase in the rate of field variation; and (iv) a decrease of anomalies at very low temperatures due to the "cutoff" of quasi-adiabats.

The last statement requires clarification. The fact is that a manyfold increase in the helium heat conductivity at temperatures below the λ point of helium (2.18 K) causes a sharp increase in the heat-transfer coefficient α and the transition from a quasi-adiabat to a quasi-isotherm at this point, as indicated by arrows in Fig. 7 for adiabat a_1 and isotherm i_λ (see also Fig. 8). Figuratively speaking, as the magnetic field increases (or decreases), a quasi-adiabatic path followed by the magnetic state of the system turns along an almost impenetrable wall (behind which helium becomes a superfluid) and then moves along this wall. As a result, as the initial temperature of the liquid-helium bath decreases below the Néel temperature, the quasi-adiabatic changes in the temperature of the spin system (and the magnetoelastic-strain anomalies associated with this change) first decrease and then (after the onset of the cutoff of quasi-adiabats at the helium λ point) decrease to vanish almost completely at very low temperatures. The cutoff effect also accounts for the noticeable separation between the strain peaks in the increasing- and decreasing-field dependences of magnetically induced strains (see, e.g., curves in Fig. 2 for $T = 3.37$ K) corresponding to the breakpoint of the phase path at $t = t_\lambda$.

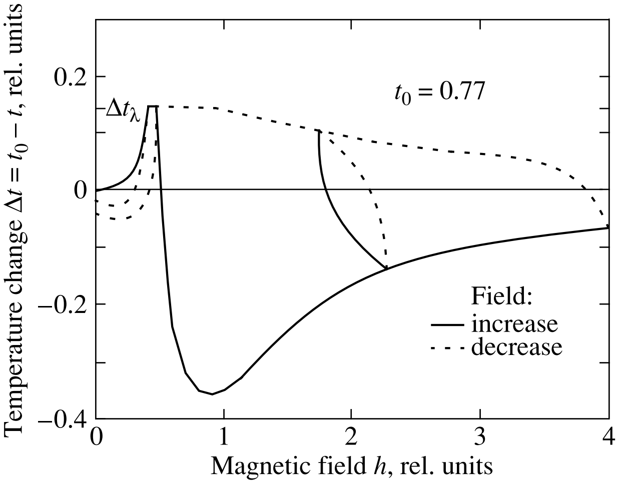

Fig. 8. Typical paths of adiabatic magnetization on the *H–T* diagram of $DyAlO_3$ calculated for $\alpha' = 2$.

Note that the cutoff of quasi-adiabats at low (different) temperatures could also occur at the boundary of the region of intermediate states mentioned above (this boundary is similar to the lines corresponding to the loss of stability of the AFM and FM phases on the *H–T* diagram in Fig. 7). However, first, this assumption needs direct experimental verification and, second, the simple and obvious assumption of a sharp change in the heat-transfer coefficient α at the λ point makes it possible to adequately describe the observed anomalies.

Since the coefficient of thermal expansion of dysprosium orthoaluminate is negative at low temperatures, it is natural to assume (taking into account the calculated phase paths) that the observed strains are due to thermal expansion of the crystal during quasi-adiabatic or quasi-isothermal magnetization, whereas the contribution from magnetostriction is small. The small-

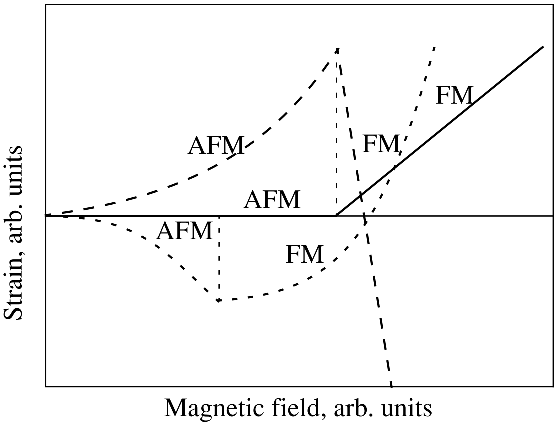

Fig. 9. Thermal expansion and magnetostriction during adiabatic and isothermal magnetization of a crystal in the AFM and FM phases. The solid and dashed lines are magnetostriction during adiabatic and isothermal magnetization, respectively, and the dotted line is thermal expansion.

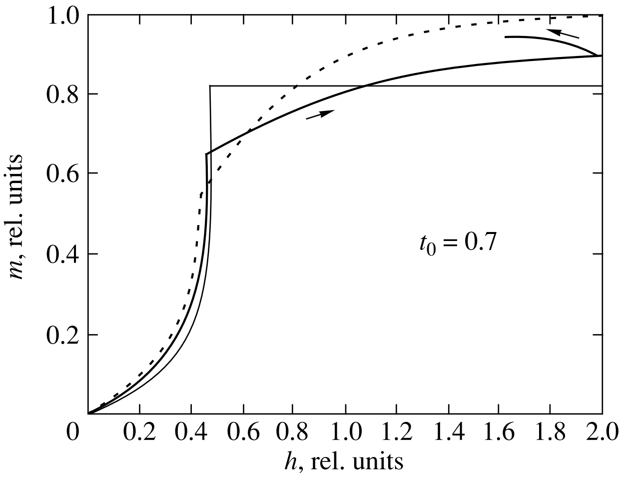

Fig. 10. Variations in magnetization along an ideal adiabat (thin solid line), an isotherm (dotted line), and a real quasi-adiabat (thick solid line).

ness of this contribution is clearly demonstrated by the strain–field curve at the lowest temperature in Fig. 2. In this case, temperature variations are suppressed due to the cutoff effect and the strains are very small, although the system certainly undergoes a transition from the AFM to the FM phase. The smallness of magnetostriction along the b axis for **H** || b is a confirmed experimental fact. For example, at **H** || a, the four-sublattice magnetic system of Dy ions undergoes a radically different metamagnetic transition and the strains are at least one order of magnitude greater.

However, it is more important that, in this case, an additional, adiabatic mechanism of suppression of magnetostriction is operative and, as a result, nonmagnetic thermal expansion manifests itself to the maximum possible degree and is accompanied by anomalies. This statement can be illustrated by the following simple calculations.

According to [1], the field dependence of the magnetostriction strain due to rare-earth ions in the Ising antiferromagnet under study (for the geometry of magnetization used) is given by

$$\Delta l/l = A(m_2h_1 + m_2h_2), \tag{12}$$

where A is the corresponding magnetostriction constant; $h_{1,2}$ are the effective magnetic fields acting on sublattices 1 and 2, respectively; and $m_{1,2}$ are the magnetic moments of these sublattices.

From Eqs. (4) for the low-field AFM phase, we obtain

$$h_1 = l + h, \quad h_2 = -l + h, \tag{13}$$

and, therefore,

$$\Delta l/l = 2A(l^2 + mh). \tag{14}$$

From the first of equations (7), it is easy to find the $l = l(h)$ and $m = m(h)$ dependences for isothermic ($t = t_0$) and isentropic ($m^2 + l^2 = l_0^2$) processes near the Néel temperature. The result is

$$l = \sqrt{l_0^2 - 3h^2}, \quad m = h, \tag{15}$$

for an isotherm and

$$l = \sqrt{l_0^2 - h^2}, \quad m = h, \tag{16}$$

for an isentropic curve. Substituting these expressions into Eq. (14) gives the strains (measured from the initial strain $2Al_0^2$ in a zero field) to be

$$\Delta l/l = -4h^2 \tag{17}$$

for an isotherm and

$$\Delta l/l = 0 \tag{18}$$

for an isentropic curve. Thus, in the AFM phase, magnetostriction is completely suppressed during an isentropic process and only magnetically induced thermal expansion of the crystal is observed.

In the FM phase (at $l = 0$), the suppression of magnetostriction during an adiabatic magnetization process manifests itself in the fact that the magnetostriction varies in proportion to the field (because the magnetization is constant along an isentropic curve), whereas during an isothermal magnetization the magnetostriction increases as the square of the field (until saturation). These features are illustrated in Fig. 9.

Note also that the character of the field dependence of magnetization is adequately described in terms of the model of quasi-adiabatic magnetization of the Ising antiferromagnet, as can be seen from Fig. 10, which shows the variations in the magnetization along calculated paths in the *H*–*T* phase plane. In particular, the experimentally observed (and, at first glance, unexplained) increase in the saturated magnetization with a decrease in field is explained by the fact that, in actuality, the magnetization is not saturated (Fig. 10). It is also important that, along a purely isentropic curve, "saturation" of magnetization (m = const) occurs in very low fields immediately after the transition to the FM phase, which should be taken into account when interpreting experimentally observed effects and the results of measurements.

4. CONCLUSIONS

Based on an adequate model and the intersublattice interaction constants (which can be calculated exactly), we have described almost all anomalies in the elastic strains and magnetization observed in the model Ising antiferromagnet $DyAlO_3$. It has been shown that the anomalies are mainly due to the fact that the magnetization process occurring in the magnetic system under study is quasi-adiabatic. The results obtained indicate that the magnetocaloric effect in such magnetic systems has to be taken into account exactly even if the external field varies slowly and that the observed effects and the results of measurements should be interpreted with due regard for the adiabaticity of the magnetization process. The high degree of adiabaticity of this process makes it possible, in principle, to study the *H*–*T* phase diagram at very low temperatures that are experimentally unattainable under isothermal conditions.

ACKNOWLEDGMENTS

This study was supported by the Russian Foundation for Basic Research, project no. 02-02-16704.

REFERENCES

1. A. K. Zvezdin, V. M. Matveev, A. A. Mukhin, and A. I. Popov, *Rare-Earth Ions in Magnetically Ordered Crystals* (Nauka, Moscow, 1985).
2. H. Shuchert, S. Hufner, and R. Faulhaber, Z. Phys. **222**, 105 (1969).
3. L. M. Holmes, R. Sherwood, and L. G. van Uitert, J. Appl. Phys. **39**, 1373 (1968).
4. I. B. Krynetskii, V. M. Matveev, and V. V. Matveev, J. Magn. Magn. Mater. **140–144**, 1579 (1995).
5. L. M. Holmes, L. G. van Uitert, R. R. Hecker, and G. W. Hull, Phys. Rev. B **5**, 138 (1972).
6. N. P. Kolmakova, I. B. Krynetskii, M. Lukina, and A. A. Mukhin, Phys. Status Solidi B **159**, 845 (1990).
7. A. S. Borukhovich, Usp. Fiz. Nauk **169** (7), 737 (1999) [Phys. Usp. **42** (7), 653 (1999)].

Translated by Yu. Epifanov

Physics of the Solid State, Vol. 47, No. 7, 2005, pp. 1326–1330. Translated from Fizika Tverdogo Tela, Vol. 47, No. 7, 2005, pp. 1280–1284.
Original Russian Text Copyright © 2005 by Ponomarev, Popov, Steep, Wiegelmann, Jansen, Wyder, Red'kin.

MAGNETISM AND FERROELECTRICITY

Anisotropy of the Magnetoelectric Effect in Terbium Molybdate

B. K. Ponomarev*, A. I. Popov, E. Steep***, H. Wiegelmann***, A. G. M. Jansen***, P. Wyder***, and B. S. Red'kin***

**Institute of Solid State Physics, Russian Academy of Sciences,*
Chernogolovka, Moscow oblast, 142432 Russia
e-mail: ponom@issp.ac.ru
***Moscow State Institute of Electronic Engineering (Technological University),*
Zelenograd, Moscow oblast, 103498 Russia
****Grenoble High Magnetic Field Laboratory,*
B.P. 166, Grenoble Cedex 9, F-38042 France

Received September 6, 2004

Abstract—Anisotropy of the nonlinear magnetoelectric effect in a single-crystal, single-domain sample of the β' metastable ferroelectric paramagnetic phase of terbium molybdate $Tb_2(MoO_4)_3$ was studied experimentally in dc magnetic fields of up to 6 T at temperatures of 4.2 and 1.8 K. It was shown that the existing models of the magnetoelectric effect cannot explain the experimental dependences of magnetic field–induced electric polarization on the direction of the applied magnetic field. A model of the magnetoelectric effect is proposed that qualitatively describes the observed angular dependence of the magnetic field–induced electric polarization.

1. INTRODUCTION

The metastable orthorhombic ferroelectric–ferroelastic paramagnetic phase of terbium molybdate β'-$Tb_2(MoO_4)_3$ (TMO) exists at temperatures below 160°C [1]. The first measurements of the nonlinear magnetoelectric effect (MEE) in paramagnetic TMO were reported in [2]. It was shown in [3] that the MEE in TMO can be accounted for in terms of a magnetostriction model proposed in [3]. In [4], the first observation of the MEE in gadolinium molybdate $Gd_2(MoO_4)_3$ (GMO) was described and it was found that the MEE in GMO is about two orders of magnitude smaller than that in TMO.

The anisotropy of the MEE in GMO was measured in [5] at 4.2 and 0.4 K. It was shown that the angular dependences of MEE in GMO are described well by the model of the paramagnetoelectric effect proposed in [6]. It was also found that, at magnetization values not very close to the saturation level, the field dependences of the MEE in GMO are satisfactorily described by a single-ion magnetostriction model put forward in [7].

In this paper, we report on a study of the dependence of the MEE in TMO on the direction of a magnetic field applied in the basal plane of the crystal for magnetic fields of up to 6 T at temperatures of 4.2 and 1.8 K. It is demonstrated that, unlike GMO, the behavior of the MEE in TMO defies description within the present theories. A theory is advanced capable of accounting qualitatively for the specific features of the MEE in TMO.

2. SAMPLES AND EXPERIMENT

A TMO single crystal was Czochralski-grown [8]. The sample was a rectangular parallelepiped measuring 7 × 7 × 1 mm. The major face was parallel to the (001) plane. Prior to measurements, the sample was made single-domain. The methods involved and the MEE measurements made in a dc magnetic field at the above temperatures are described in [9–12]. The measurement error was 5%. The random scatter of points for one isotherm did not exceed 2%. The magnetic field–induced electric polarization (MEP) $P(H)$ was measured along the [001] axis. A magnetic field was applied in the (001) plane. The angle φ between the [010] axis and the field could be varied from 0 to 90°.

3. RESULTS

Figure 1 displays some of the experimental $P(H)$ isotherms measured by us in TMO at temperatures T = 4.2 K (curves *1*–*6*) and 1.8 K (curves *7*, *8*) and for various values of the angle φ between the [010] axis and the magnetic field, with the latter varied up to 6 T. The $P(H)$ dependences are nonlinear. The magnetic field directed along the [010] axis induces positive changes in the electric polarization along the [001] axis (a positive paraelectric process in the ferroelectric subsystem). A field directed along the [100] axis induces negative changes in the electric polarization along the [001] axis, i.e., a negative paraelectric process. The sign of $P(H)$ was determined by comparing it with the sign of

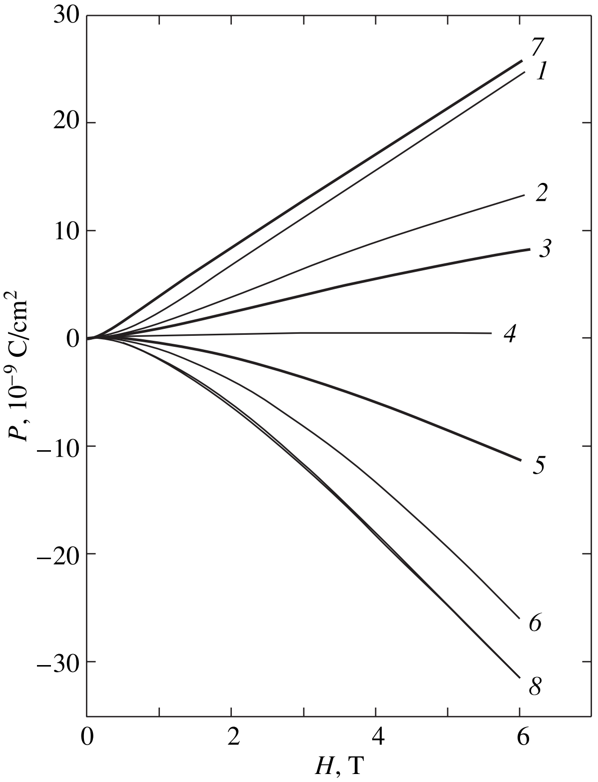

Fig. 1. Electric polarization in TMO induced along the [001] axis by a magnetic field in the (001) plane for various values of the angle φ between the field and the [010] axis at $T = 4.2$ K (curves *1*–*6*) and $T = 1.8$ K (curves *7*, *8*): (*1*) φ = 0°, (*2*) 35.5°, (*3*) 45°, (*4*) 55.3°, (*5*) 66.6°, (*6*) 90°, (*7*) 0°, and (*8*) 90°.

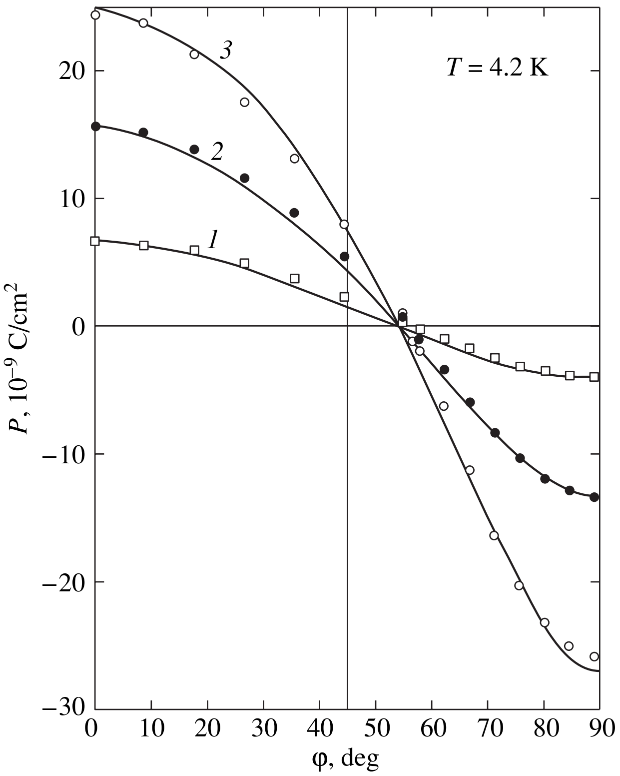

Fig. 2. Experimental (points) and calculated (solid lines) dependences of MEP in TMO on magnetic field orientation in the (001) plane at $T = 4.2$ K for various values of the magnetic field: (*1*) 2, (*2*) 4, and (*3*) 6 T. The angle φ is reckoned from the [010] axis.

the jump in electric polarization occurring when the spontaneous polarization switches in a critical magnetic field directed along the [100] axis [13]. We readily see that the $P(H)$ dependences follow essentially different patterns for magnetic fields directed along [010] (curves *1*, *7*) and [100] (curves *6*, *8*). In a field parallel to the [010] axis, the $P(H)$ graphs obtained for $H > 1$ T are close to linear. In a field parallel to [100], the $P(H)$ relations are noticeably nonlinear up to $H = 6$ T. An essential feature of the magnetoelectric effect in TMO is the difference between the absolute values of MEP in fields directed along the [010] and [100] crystallographic axes. At $T = 4.2$ K, a field $H = 6$ T directed along the [010] axis ($\varphi = 0$) induces a change in electric polarization $P(\varphi = 0) = 24.3 \times 10^{-9}$ C/cm^2. In a field $H = 6$ T along the [100] axis ($\varphi = 90°$), $P(\varphi = 90°) = -26 \times 10^{-9}$ C/cm^2. The difference between the absolute values of $P(\varphi = 0)$ and $P(\varphi = 90°)$ exceeds the experimental error. This difference is even larger at $T = 1.8$ K: $P(\varphi = 0) = 25.7 \times 10^{-9}$ C/cm^2 (curve *7*) and $P(\varphi = 90°) = -31.3 \times 10^{-9}$ C/cm^2 (curve *8*). In a field parallel to the bisectrix of the angle between the [010] and [100] axes (curve *3* in Fig. 1, $\varphi = 45°$), the MEP is nonzero throughout the field range covered. The MEP constitutes a sizable part of the spontaneous electric polarization ($P_S(T = 20°\text{C}) = 180 \times 10^{-9}$ C/cm^2 [1]).

Figure 2 presents $P(\varphi)$ graphs obtained at $T = 4.2$ K for various values of the applied magnetic field. The points refer to experimental values of $P(\varphi)$. Their arrangement is not symmetric relative to $\varphi = 45°$. The absolute values of $P(\varphi = 0)$ and $P(\varphi = 90°)$ are different throughout the magnetic field range covered. The value of $P(\varphi = 45°)$ is nonzero. $P(\varphi)$ reverses sign at $\varphi \approx 56°$. The solid curves are calculated using the model advanced by us here and will be discussed in a subsequent section.

Figure 3 plots $P(\varphi)$ relations obtained at $T = 1.8$ K for various values of the magnetic field. Points refer to experimental values. Qualitatively, these graphs are similar to the $P(\varphi)$ relations in Fig. 2, but their asymmetry with respect to the $\varphi = 45°$ and $P = 0$ axes is more pronounced than in Fig. 2. $P(\varphi)$ reverses sign at $\varphi \approx 60°$. The solid curves are calculated with our model. Thus, the experimental $P(\varphi)$ relations obtained for TMO at $T = 4.2$ and 1.8 K in fields of up to 6 T are not harmonic functions.

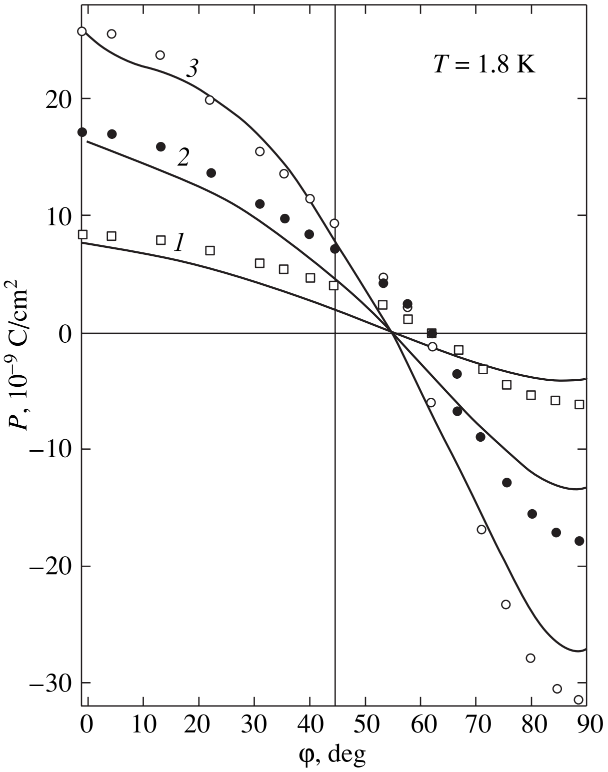

Fig. 3. Same as in Fig. 2 but for $T = 1.8$ K.

4. DISCUSSION

The theory of the MEE in paramagnets [6] yields for the $P(\varphi)$ angular dependence an expression which can be written (for an appropriately chosen reference direction for measuring the angle φ) in the form

$$P(\varphi) = P(0)\cos 2\varphi. \qquad (1)$$

The experimental results obtained are inconsistent with the predictions from the theory developed in [6].

(i) Following this theory, the absolute values of $p_{\text{red}}(\varphi) = P(\varphi)/P(0)$ should be the same for $\varphi = 0$ and $\pi/2$ and should be field-independent. This prediction from the theory fails in the case of TMO.

(ii) As seen from Eq. (1), the effect has to reverse sign at $\varphi = 45°$. In TMO, the angle of sign reversal differs from 45° and depends on temperature (cf. Figs. 2, 3).

(iii) The pattern of the experimental $p_{\text{red}}(\varphi)$ relation differs noticeably from a sine curve. Obviously enough, a new approach is needed for description of the MEE in TMO. Such an approach was developed in [14, 15].

The magnetic field–induced electric polarization in crystals is, like the magnetostriction and magnetic linear birefringence, an even-parity magnetic effect. The classical theory of even effects was treated in [16, 17]. This theory describes well the properties of weakly anisotropic compounds, in particular, of those having *d* ions. The situation with *f* ions is, however, more complex. According to [14, 15], even magnetic effects in rare-earth compounds are governed by magnetic susceptibilities of the mean multipole moments of the rare-earth ion *f* shell. Their calculation requires knowledge of the energy level and wave functions of these ions. The energy spectrum of a rare-earth ion in crystals is dominated by the interaction with the crystal field and by the Zeeman interaction with the external magnetic field. The exchange coupling among Tb^{3+} ions in TMO is fairly weak. The antiferromagnetic ordering temperature is $T_N = 0.45$ K [18]. Therefore, in fields $H \geq 1$ T and at temperatures $T \gg T_N$, the exchange can be disregarded altogether. It was established in [19] that the ground state of Tb^{3+} ions in TMO is apparently a combination of three close-lying singlets, which belong to different irreducible representations of the symmetry group of the ion environment and are separated by 2.7 cm^{-1} in energy. In this case, as in the case of a quasi-doublet, the terms dominating the dependence of even magnetic effects on the strength and orientation of the field and on temperature are

$$P_\alpha = a_{\alpha\beta\gamma}H_\beta M_\gamma + b_{\alpha\beta\gamma}H_\beta H_\gamma. \qquad (2)$$

Here, α, β, and γ are each *x*, *y*, or *z*; $a_{\alpha\beta\gamma}$ and $b_{\alpha\beta\gamma}$ are constants of the theory; M_γ is the magnetization of the rare-earth ions originating from the field-induced splitting of their ground state (quasi-triplet); and H_β and H_γ are the magnetic field vector components.

At low temperatures, the first term provides the main contribution. In the case where the magnetic field is in the *xy* plane, Eq. (2) can be recast in the form

$$\begin{aligned} P_z(T, H, \varphi) = {} & AH_xM_x(T) + BH_yM_y(T) \\ & + CH_xM_y(T) + DH_yM_x(T) \\ & + EH_x^2 + FH_xH_y + GH_y^2. \end{aligned} \qquad (3)$$

Here, *T* is the temperature; *A*, *B*, *C*, *D*, *E*, *F*, and *G* are constants of the theory, which do not depend on temperature;

$$H_x = H_{[010]} \qquad (4)$$

is the magnetic field component along the [010] axis;

$$M_x = M_{[010]} - \chi_{VV[010]}H_{[010]}, \qquad (5)$$

where $M_{[010]}$ is the experimental value of magnetization along the [010] axis;

$$H_y = H_{[100]} \qquad (6)$$

is the magnetic field component along the [100] axis;

$$M_y = M_{[100]} - \chi_{VV[100]}H_{[100]}; \qquad (7)$$

$M_{[100]}$ is the experimental value of magnetization along the [100] axis; $\chi_{VV[010]}$ and $\chi_{VV[100]}$ are the van Fleck susceptibilities along the [010] and [100] axes, respectively; and M_x and M_y are the magnetization components of the Tb^{3+} ion quasi-triplet in the basal plane. The values of the constants *A*, *B*, *E*, and *G* are derived from experimental $P_z(H_i)$ isotherms and $M_i(H_i)$ magnetizations measured in fields parallel to [010] (for $i = x$) and [100] (for $i = y$).

Experimental data on $P_z(H_i)$ and $M_i(H_i)$ can be used to construct the relations

$$\frac{P_z(H_i)}{M_i(H_i)} = f\left(\frac{H_i}{M_i}\right). \tag{8}$$

As follows from Eq. (3), the function on the right-hand side of Eq. (8) is a linear relation of the form

$$f\left(\frac{H_x}{M_x}\right) = A + E\frac{H_x}{M_x} \tag{9}$$

for a field parallel to the [010] axis and

$$f\left(\frac{H_y}{M_y}\right) = B + G\frac{H_y}{M_y} \tag{10}$$

for a field parallel to the [100] axis. A linear approximation of experimental relation (8) performed for the [010] axis yields the values of constants *A* and *E*. Constants *B* and *G* are derived from measurements made along the [100] axis in a similar manner.

Figure 4 plots experimental relations (8) obtained on TMO at $T = 4.2$ K along the [010] (straight line *1*) and [100] (straight line *2*) axes. These relations are constructed using the measurements of MEP (curves *1*, *6* in Fig. 1) and the magnetization from [19]. We readily see that the plots in Fig. 4 are indeed linear with satisfactory accuracy, in full agreement with Eqs. (8)–(10). The intercepts of straight lines (*1*) and (*2*) on the vertical axis are constants $A = 1.13$ and $B = -0.33$, and the slopes of these lines are constants $E = 0.06$ and $G = -0.57$. The values of the constants are given in units of measure corresponding to the scales in Fig. 4.

The constants *C*, *D*, and *F* are derived from the relations

$$\left(\frac{\partial P_z}{\partial \varphi}\right)_{\varphi = 0} = 0, \tag{11}$$

$$\left(\frac{\partial P_z}{\partial \varphi}\right)_{\varphi = \frac{\pi}{2}} = 0. \tag{12}$$

By differentiating Eq. (3) with respect to φ and substituting the values of *A*, *B*, *E*, and *G* already found and the values $\varphi = 0$ and $\pi/2$, we obtain two equations in the unknowns *C*, *D*, and *F*. A third equation is obtained by substituting the value $\varphi = 45°$ and the corresponding experimental value of P_z ($\varphi = 45°$) into Eq. (3). Solving this system of three equations for the unknown *C*, *D*, and *F* yields $C = -0.29$, $D = -0.25$, and $F = 0.71$. The solid lines in Fig. 2 plot theoretical $P(\varphi)$ curves for TMO calculated from Eq. (3) with the use of the above constants. We readily see that the calculated $P(\varphi)$ curves reproduce all the specific features of the experimental relations and agree with the latter quantitatively. Analogous theoretical $P(\varphi)$ curves for $T = 1.8$ K are presented in Fig. 3. The calculation made use of the same values of constants *A*, *B*, *C*, *D*, *E*, *F*, and *G* as in the case of $T = 4.2$ K. We do not have at our disposal any experimental dependences of the magnetization on field for $T = 1.8$ K. The $M_x(H_x)$ and $M_y(H_y)$ relations for $T = 1.8$ K are calculated using the theory of singlet magnetism and the parameters quoted in [19]. The $P(\varphi)$ curves calculated for $T = 1.8$ K are seen to agree qualitatively with the experimental data. Thus, the singlet magnetism theory explains satisfactorily the MEE anisotropy in TMO at $T = 4.2$ and 1.8 K.

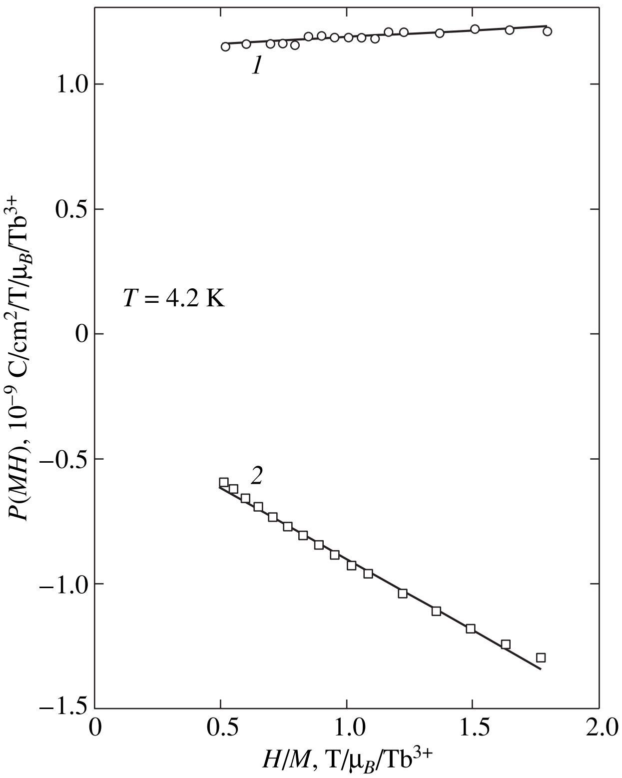

Fig. 4. Determination of the constants *A*, *B*, *E*, and *G* in Eq. (3) from experimental data using Eqs. (8)–(10).

5. CONCLUSIONS

Low-temperature measurements of the angular dependence of the magnetoelectric effect in TMO have revealed the existence of an anisotropy different from that observed in weakly anisotropic magnets (GMO), where the behavior of the electric polarization with field orientation in a crystal fits a straightforward harmonic function of the angle setting the field direction. The MEE anisotropy in TMO exhibits essentially different angular dependences. The behavior of MEE in TMO has been theoretically analyzed. This analysis is based on the relation of the electric polarization of TMO with magnetic field–induced variations in the quadrupole electric moments of terbium ions. A necessary condition for the observed features in the MEE behavior to exist is the presence of ions with a nonzero orbital moment, with the ground state of these ions in the crystal being a doublet, quasi-doublet, or quasi-triplet well-separated from higher lying levels. It has been demonstrated that the theoretical dependences of the MEE on the magnitude and orientation of the applied magnetic field fit the experimental results satisfactorily.

ACKNOWLEDGMENTS

This study was supported by the Russian Foundation for Basic Research, project nos. 02-02-16679 and 03-02-17166.

REFERENCES

1. L. H. Brixner and J. R. Barkley, *Handbook on the Physics and Chemistry of Rare Earths* (North-Holland Publishing Company, 1979), p. 610.
2. S. A. Ivanov, V. N. Kurlov, B. K. Ponomarev, and B. S. Red'kin, Pis'ma Zh. Éksp. Teor. Fiz. **52** (7), 1003 (1990) [JETP Lett. **52** (7), 394 (1990)].
3. B. K. Ponomarev, S. A. Ivanov, B. S. Red'kin, and V. N. Kurlov, Physica B **177**, 327 (1992).
4. B. K. Ponomarev, B. S. Red'kin, H. Wiegelmann, A. G. M. Jansen, P. Wyder, and J. van Tol, Ferroelectrics Lett. **18** (3–4), 394 (1994).
5. B. K. Ponomarev, E. Stiep, H. Wiegelmann, A. G. M. Jansen, P. Wyder, and B. S. Red'kin, Fiz. Tverd. Tela (St. Petersburg) **42** (4), 716 (2000) [Phys. Solid State **42** (4), 734 (2000)].
6. S. L. Hou and N. Bloembergen, Phys. Rev. **138** (4A), A1218 (1965).
7. H. B. Callen and E. Callen, J. Phys. Chem. Solids **27** (8), 1271 (1966).
8. B. S. Red'kin, V. N. Kurlov, I. S. Pet'kov, and S. N. Rossolenko, J. Cryst. Growth **104** (1), 77 (1990).
9. B. K. Ponomarev, S. A. Ivanov, B. S. Red'kin, and V. N. Kurlov, Pis'ma Zh. Éksp. Teor. Fiz. **55** (6), 353 (1992) [JETP Lett. **55** (6), 356 (1992)].
10. B. K. Ponomarev, V. D. Negrii, B. S. Red'kin, and Yu. F. Popov, J. Phys. D **27**, 1995 (1994).
11. B. K. Ponomarev, S. A. Ivanov, Yu. F. Popov, V. D. Negrii, and B. S. Red'kin, Ferroelectrics **161**, 43 (1994).
12. H. Wiegelmann, B. K. Ponomarev, J. van Tol, A. G. M. Jansen, P. Wyder, and B. S. Red'kin, Ferroelectrics **183**, 195 (1997).
13. B. K. Ponomarev, Ferroelectrics **280**, 95 (2002).
14. A. K. Zvezdin, V. M. Matveev, A. A. Mukhin, and A. I. Popov, *Rare-Erth Ions in Magneto-Ordered Crystalls* (Nauka, Moscow, 1985) [in Russian].
15. N. F. Vedernikov, A. K. Zvezdin, R. Z. Levitin, and A. I. Popov, Zh. Éksp. Teor. Fiz. **93**, 2161 (1987) [Sov. Phys. JETP **66** (6), 1233 (1987)].
16. N. S. Akulov, *Ferromagnetics* (Gostekhizdat, Moscow, 1939) [in Russian].
17. E. R. Callen and H. B. Callen, Phys. Rev. **139**, A455 (1965).
18. R. A. Fisher, E. W. Hornung, G. E. Brodale, and W. F. Giauque, J. Chem. Phys. **63**, 1295 (1975).
19. B. K. Ponomarev, A. I. Popov, J. van Tol, H. Wiegelmann, A. G. M. Jansen, P. Wyder, and B. S. Red'kin, J. Magn. Magn. Mater. **258–259**, 510 (2003).

Translated by G. Skrebtsov

Physics of the Solid State, Vol. 47, No. 7, 2005, pp. 1331–1339. Translated from Fizika Tverdogo Tela, Vol. 47, No. 7, 2005, pp. 1285–1292.
Original Russian Text Copyright © 2005 by Glinchuk, Zaulychny, Stephanovich.

MAGNETISM AND FERROELECTRICITY

Depolarization Field and Properties of Thin Ferroelectric Films with Inclusion of the Electrode Effect

M. D. Glinchuk*, B. Y. Zaulychny*, and V. A. Stephanovich**
** Frantsevich Institute of Materials Science Problems, National Academy of Sciences of Ukraine,*
ul. Krzhizhanovskogo 3, Kiev, 03142 Ukraine
e-mail: zaulychny@ukr.net
e-mail: glin@materials.kiev.ua
*** Institute of Mathematics and Informatics, Opole University, Opole, 45-052 Poland*

Received August 16, 2004

Abstract—The influence of metallic electrodes on the properties of thin ferroelectric films is considered in the framework of the Ginzburg–Landau phenomenological theory. The contribution of the electrodes with different screening lengths l_s of carriers in the electrode material is included in the free-energy functional. The critical temperature T_{cl}, the critical thickness of the film, and the critical screening length of the electrode at which the ferroelectric phase transforms into the paraelectric phase are calculated. The Euler–Lagrange equation for the polarization P is solved by the direct variational method. The results demonstrate that the film properties can be calculated by minimizing the free energy, which has a standard form but involves the coefficient of the term P^2. This coefficient depends not only on the temperature but also on the film thickness, the surface and correlation effects, and the electrode characteristics. The calculations of the polarization, the dielectric susceptibility, the pyroelectric coefficient, and the depolarization field show that the ferroelectric state of the film can be destroyed using electrodes from a material whose screening length exceeds a critical value. This means that the electrodes being in operation can induce a transition from the ferroelectric phase to the paraelectric phase. The quantitative criteria obtained indicate that the phase state and properties of thin ferroelectric films can be controlled by choosing the appropriate electrode material. *© 2005 Pleiades Publishing, Inc.*

1. INTRODUCTION

The influence of electrodes on the properties of thin ferroelectric films has attracted the unwavering attention of researchers and engineers. This is associated both with the profound effect of the electrodes on the depolarization field and with the necessity of choosing the optimum (superconducting, metallic, or semiconducting) electrodes for practical applications. The depolarization field substantially affects the physical properties of ferroelectrics, because this field tends to suppress spontaneous electric polarization and, thus, to destroy the ferroelectric state. It is known that internal factors, such as the domain structure and free charge carriers, are responsible for partial weakening of the depolarization field. Moreover, external factors, including the electrode effect, can also considerably decrease the depolarization field. For example, superconducting electrodes in bulk ferroelectrics leads to complete compensation for the depolarization field. In thin ferroelectric films, the polarization inhomogeneity due to the contribution of the surface effects brings about only a partial compensation for the depolarization field even in the case of superconducting electrodes [1]. The allowance made for the effect exerted by the metallic electrodes requires inclusion of the electrode contribution in the free energy. However, the contribution of nonsuperconducting electrodes appeared to be considerably more complex (see [2] and references therein). For this reason, no calculations of the effect of nonsuperconducting electrodes on the properties of thin ferroelectric films have been performed to date.

In the present work, these calculations were carried out within the model of a single-domain ferroelectric material—an ideal insulator. This model is quite realistic because a decrease in the film thickness results in the formation of a single-domain film [3] and the conductivity of the majority of ferroelectrics is very low (see, for example, [4]). The polarization, the dielectric susceptibility, and the pyroelectric coefficient were calculated in the framework of the Ginzburg–Landau phenomenological theory with allowance made for the contribution of the metallic electrodes. A comparison with the results of calculations performed earlier for superconducting electrodes [5, 6] showed that an increase in the screening length of carriers in electrodes results in a decrease in the critical temperature and an increase in the critical thickness corresponding to a size-driven transition from the ferroelectric phase to the paraelectric phase.

2. BASIC EQUATIONS

Let us consider a thin ferroelectric film located between two metallic electrodes (Fig. 1). Taking into

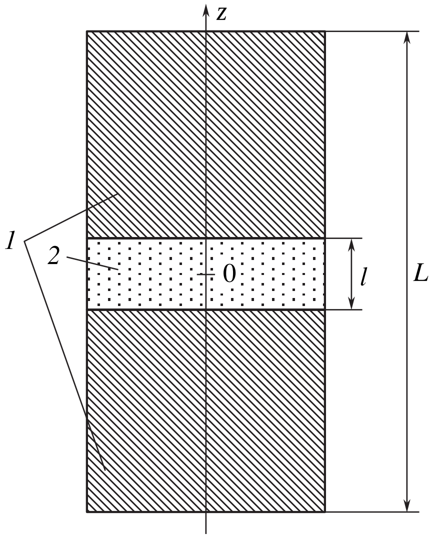

Fig. 1. Schematic diagram illustrating the geometry of the problem: (*1*) electrodes and (*2*) film.

account that, technologically, it is possible to fabricate single-domain films self-polarized along the normal to the surface [7, 8], we will analyze a film polarized along the z axis (i.e., $P = P_z \neq 0$, $P_x = P_y = 0$).

Equilibrium polarizations can be determined in the framework of the phenomenological theory from the condition of free-energy functional minimum [9]. The free energy can be represented as the sum of the free energies of the film (with allowance made for the depolarization field) and the electrodes. It is known that the depolarization field is opposite to the direction of the spontaneous polarization and, hence, tends to destroy it. Within the model of a single-domain film without charge carriers, only electrons in the electrodes can contribute to a decrease in the depolarization field. This effect is maximum for superconducting electrodes. For nonsuperconducting metallic electrodes, the field screening at the electrodes can be described by the expression [10]

$$\frac{d^2E}{dz^2} = \frac{1}{l_s^2}E, \tag{1a}$$

where the screening length l_s has the form

$$l_s^2 = \frac{\varepsilon_e}{4e^2}\left(\frac{\pi}{3}\right)^{1/3}\frac{\hbar^2}{m^*}\frac{1}{n_0^{1/3}}. \tag{1b}$$

Here, e is the carrier charge, m^* is the effective mass of carriers, n_0 is the charge density, and ε_e is the permittivity of the electrode material.

It can be seen that, since the parameters ε_e, m^*, and n_0 vary over wide ranges, the screening length l_s can change from $l_s = 0$ (for superconductors) to several angströms or even several tens of angströms. We can expect that, with an increase in the screening length l_s, the contribution of the electrodes to the decrease in the depolarization field should decrease. It is not ruled out that the ferroelectric state can be destroyed even in films that are not very thin, provided the electrodes used are characterized by a sufficiently large screening length.

In order to analyze quantitatively the effect of the electrodes on the properties of the film and on the critical parameters of the size-driven phase transition from the ferroelectric phase to the paraelectric phase, the free-energy density for second-order phase transitions can be written in the following form [2]:

$$\begin{aligned}\frac{F}{S} = {} & \frac{1}{l}\int_{-l/2}^{l/2} dz\left\{\frac{1}{2}AP^2 + \frac{1}{4}BP^4 + \frac{1}{2}C\left(\frac{dP}{dz}\right)^2\right. \\ & \left. + \frac{V_0}{(2\alpha l_s + l)}P\right\} + 2\pi\left(1 - \frac{l}{(2\alpha l_s + l)}\right)\bar{P}^2 \\ & + \frac{l_s\beta}{2\varepsilon_e(2\alpha l_s + l)^2 l}\{2\pi l^2\bar{P}^2 - V_0 l\bar{P} + V_0^2\} \\ & + \frac{1}{2}C\delta^{-1}\left[P^2\left(-\frac{1}{2}\right) + P^2\left(\frac{l}{2}\right)\right];\end{aligned} \tag{2}$$

$$\alpha = \frac{\cosh\left(\frac{L-l}{2l_s}\right) - 1}{\sinh\left(\frac{L-l}{2l_s}\right)}, \quad \beta = \frac{\sinh\left(\frac{L-l}{2l_s}\right) - \frac{L-l}{l_s}}{\sinh^2\left(\frac{L-l}{l_s}\right)},$$

$$\bar{P} = \frac{1}{l}\int_{-\frac{l}{2}}^{\frac{l}{2}} P dz, \quad A = A_0(T - T_c).$$

Here, $\alpha \approx \beta \approx 1$ (since $L - l \gg l_s$) are parameters; V_0 is the electric voltage applied across the electrodes; T_c and A_0 are the ferroelectric transition temperature and the inverse Curie–Weiss constant for the bulk sample, respectively; and δ is the extrapolation length.

The variation in functional (2) leads to the Euler–Lagrange equation for the polarization P with the boundary conditions

$$AP + BP^3 - C\frac{d^2P}{dz^2} = E_{\text{ext}} + E_d, \tag{3a}$$

$$\left.\frac{dP}{dz}\right|_{z = \pm\frac{l}{2}} = \mp\frac{P\left(\pm\frac{l}{2}\right)}{\delta}, \tag{3b}$$

$$E_{\text{ext}} = -\frac{V_0 a}{l}, \quad E_d = -4\pi(P - a\bar{P}), \tag{3c}$$

$$a = l\left(\frac{1}{2\alpha l_s + l} - \frac{l_s\beta}{2\varepsilon_e(2\alpha l_s + l)^2}\right). \tag{3d}$$

It can be seen that, in the limit, we have the depolarization field $E_d \longrightarrow -4\pi(P - \bar{P})$, because $a \longrightarrow 1$ at $l_s \longrightarrow 0$ (this corresponds to the limit of superconducting electrodes, which was considered in [1]). In the general case, the quantity a satisfies the inequality $a < 1$ and decreases with an increase in the screening length l_s, so that the depolarization field E_d increases as compared to the depolarization field in the case of superconducting electrodes. Making allowance for the inequality $l_s \ll l$, the quantity a can be written with a high accuracy in the following form:

$$a \approx 1 - \frac{l_s}{l}\left(2\alpha + \frac{\beta}{2\varepsilon_e}\right). \tag{3e}$$

3. EFFECT OF ELECTRODES ON THE CRITICAL PARAMETERS OF THE SIZE-DRIVEN PHASE TRANSITION

Equation (3a) for the polarization $P(z)$ is an inhomogeneous nonlinear integro-differential equation, for which the exact analytical solution in the general case has not been obtained to date. However, in the paraelectric phase, the spontaneous polarization is absent and the polarization induced by an external field, as a rule, is insignificant; hence, the nonlinear term BP^3 in Eq. (3a) can be ignored. It should be noted that this approximation is valid only at $T \neq T_c$, because $A = A_0(T - T_c) = 0$ at $T = T_c$. The solution to the linear equation with boundary conditions (3b) can be written in the form

$$P^{\mathrm{PE}}(\xi) = \frac{(1 - \varphi(\xi))}{A_0(T - T_c) + 4\pi(1 - a + a\Phi)}E_{\mathrm{ext}}, \tag{4a}$$

$$\varphi(\xi) = \left(\frac{(w + 1 + e^{-h}(w - 1))}{(w + 1)^2 - e^{-2h}(w - 1)^2}\right)(e^{\xi - h} + e^{-\xi}), \tag{4b}$$

$$\begin{aligned}\Phi &= \langle\varphi\rangle = \frac{1}{l}\int_{-l/2}^{l/2}\varphi(z)dz \\ &= 2\frac{(1 + w - (1 - w)e^{-h})}{((1 + w)^2 - (1 - w)^2 e^{-2h})}\frac{(1 - e^{-h})}{h}.\end{aligned} \tag{4c}$$

Here, we introduced the dimensionless parameters

$$\begin{aligned}&w = \frac{\delta}{l_d}, \quad \xi = \left(z + \frac{l}{2}\right)\frac{1}{l_d}, \quad \text{where} \quad l_d = \sqrt{\frac{C}{4\pi}}, \\ &h = \frac{l}{l_d}, \quad z \in \left[-\frac{l}{2}; \frac{l}{2}\right], \quad \xi \in [0; h].\end{aligned} \tag{4d}$$

According to relationships (4a)–(4c), the average polarization can be represented by the expression

$$\bar{P}^{\mathrm{PE}}(\xi) = \frac{(1 - \Phi)}{A_0(T - T_c) + 4\pi(1 - a + a\Phi)}E_{\mathrm{ext}}. \tag{5}$$

The derivative $\chi = \left.\frac{dP}{dE}\right|_{E = 0}$, which is the linear dielectric susceptibility of the film, is given by expression (5) with the quantity E_{ext} omitted.

Since the numerator and the second term in the denominator are always positive, we have $\chi > 0$ at $T > T_c$ or $T < T_c$. In the latter case, the second term in the denominator should be larger than the first term. The dielectric susceptibility tends to infinity when the denominator in formula (5) tends to zero. This situation occurs at $T \longrightarrow T_{cl}$ (l = const) or at $l \longrightarrow l_c$ (T = const). The quantities T_{cl} and l_c are the critical temperature and the critical thickness that correspond to a size-driven transition from the ferroelectric phase to the paraelectric phase. In order to obtain the dependences $T_{cl}(h, w, l_s)$ and $l_c(T, w, l_s)$ in an explicit form, the denominator in relationship (5) can be simplified taking into account that $h = \frac{l}{l_d} \gg 1$ (because the quantity l_d, as a rule, does not exceed a few nanometers). By transforming expression (4c) into the form $\Phi \simeq \frac{2}{1 + w}\frac{1}{h}$ and writing relationship (3e) through the dimensionless parameters (screening length $h_s = \frac{l_s}{l_d}$, critical thickness $h_c = \frac{l_c}{l_d}$, critical temperature $\tau_c = \frac{T_{cl}}{T_c}$), we obtain

$$\begin{aligned}\tau_c = 1 - \frac{4\pi}{A_0 T_c}&\left[\frac{2}{h(1 + w)}\right. \\ &\left. + \frac{h_s}{h}\left(2\alpha + \frac{\beta}{2\varepsilon_e}\right)\left(1 - \frac{2}{h(1 + w)}\right)\right]\end{aligned} \tag{6}$$

for the parameters

$$\begin{aligned}&h_s \ll h_c, \quad h_c = \frac{K}{A_0(T_c - T)}, \\ &K = 4\pi\left[\frac{2}{1 + w} + \left(2\alpha + \frac{\beta}{2\varepsilon_e}\right)\right].\end{aligned} \tag{7}$$

As can be seen, the critical temperature satisfies the inequality $\tau_c < 1$ and decreases linearly with an increase in the screening length h_s, whereas the critical thickness increases linearly with an increase in the screening length h_s.

Figures 2 and 3 show the dependences of the critical temperature on the film thickness and the screening length. For convenience, we introduced the parameter $l_0 = l_d\sqrt{\frac{4\pi}{A_0 T_c}}$; hence, for standard values $A_0 \sim 4 \times 10^{-5}$

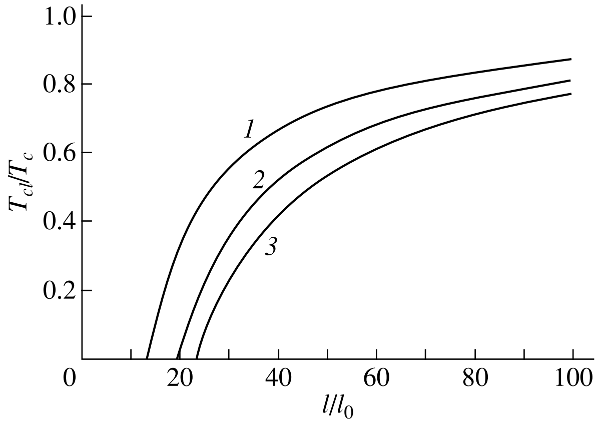

Fig. 2. Dependences of the critical temperature on the film thickness for screening lengths l_s/l_0 = (*1*) 0, (*2*) 0.03, and (*3*) 0.05.

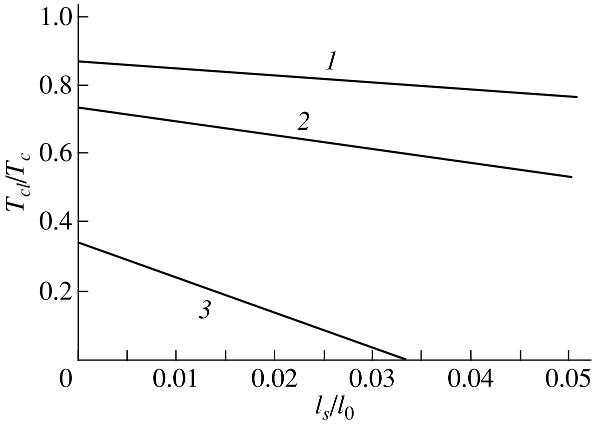

Fig. 3. Dependences of the critical temperature on the screening length for film thicknesses l/l_0 = (*1*) 100, (*2*) 50, and (*3*) 40.

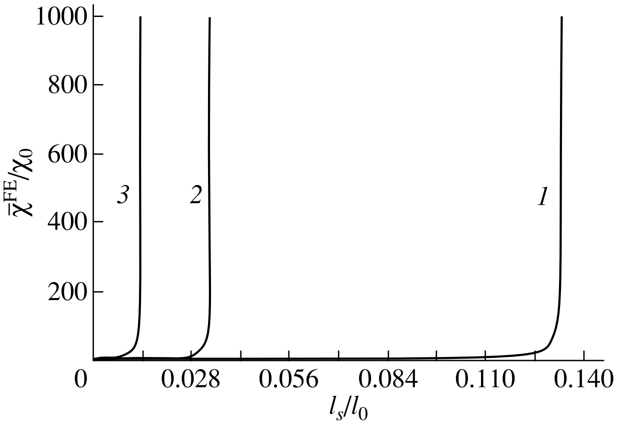

Fig. 4. Dependences of the average dielectric susceptibility on the screening length for film thicknesses l/l_0 = (*1*) 100, (*2*) 50, and (*3*) 40.

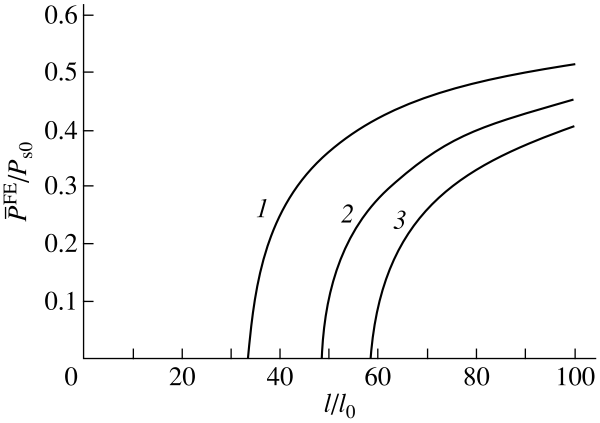

Fig. 5. Dependences of the average polarization on the film thickness for screening lengths l_s/l_0 = (*1*) 0, (*2*) 0.03, and (*3*) 0.05.

and $T_c \sim 10^2$–10^3, we have $\frac{l_0}{l_d} \sim \sqrt{\pi(10^3-10^2)}$, i.e., $l_0 \gg l_d$. (Hereinafter, for illustration, the dependences depicted in the figures are calculated using the parameters of the BaTiO$_3$ compound $w = \frac{d}{l_d} = 0.5$ and $\frac{4\pi}{A_0 T_c} = 100$ [6]). Therefore, the parameter $l_0 = 10l_d$ can be of the order of several tens of nanometers. In the figures, we use dimensionless variables, including the quantity $P_{s0} = \sqrt{\frac{A_0 T_c}{B}} = \sqrt{\frac{K}{Bh_c}}$ (corresponding to the polarization in the bulk sample at $T = 0$) and the temperature $\tau = \frac{T}{T_c} = 0.6$ in Figs. 4–8. It can be seen from Fig. 2 that the critical thickness, which corresponds to the temperature $T_{cl} = 0$, increases with an increase in the screening length. As is seen from Fig. 3, the critical temperature T_{cl} decreases linearly with an increase in the screening length. This temperature decreases more rapidly with a decrease in the film thickness (cf. curves *1*, *3* in Fig. 3). Since curve *1* in Fig. 2 corresponds to the film with superconducting electrodes, the use of nonsuperconducting electrodes leads to a decrease in the transition temperature and to a considerable increase in the critical thickness. Note also that Fig. 2 can be considered a phase diagram accounting for the influence of different metallic electrodes: the paraelectric phase (PE) exists at $T > T_{cl}$ and $l < l_c$, and the ferroelectric (FE) phase is observed at $T < T_{cl}$ and $l > l_c$; in this case, the quantities T_{cl} and l_c depend on the electrode type.

4. THE FREE ENERGY OF FILMS WITH DIFFERENT ELECTRODES

In the ferroelectric phase ($T < T_{cl}$, $l > l_c$), the nonlinear terms in Eq. (3a) cannot be disregarded. In order to account for these terms, we use the direct variational method. The solution to Eq. (3a) is sought in the form

$$P^{\mathrm{FE}}(\xi) = P(1-\varphi(\xi)), \tag{8a}$$

$$\varphi(\xi) = \begin{cases} \dfrac{1}{w+q}e^{-\xi}, & 0 \le \xi \ll \dfrac{h}{2} \\ 0, & \xi \sim \dfrac{h}{2} \\ \dfrac{1}{w+q}e^{\xi-h}, & 0 \le h-\xi \ll \dfrac{h}{2}. \end{cases} \tag{8b}$$

Here, P is the variational parameter and relationships (8b) representing the function $\varphi(\xi)$ are obtained from expression (4b) with allowance made for the inequality $h \gg 1$. Substitution of relationships (8a) and (8b) into the free-energy functional (2) and subsequent integration give the following formula for the free energy:

$$\begin{aligned} F &= \frac{A}{2}(1-A_1)\left(1+\frac{4\pi}{A}(1-a(1-A_1))\right)P^2 \\ &\quad + \frac{1}{4}B(1-B_1)P^4 - PE_{\mathrm{ext}}(1-A_1), \\ A_1 &= \frac{1}{l}\int_{-l/2}^{l/2}\varphi(z)dz = \frac{2}{(1+w)h}, \\ B_1 &= \frac{1}{6h}\left[\frac{48}{1+w} - \frac{36}{(1+w)^2} + \frac{16}{(1+w)^3} - \frac{3}{(1+w)^4}\right]. \end{aligned} \tag{9a}$$

Since the average polarization is represented in the form $\bar{P}^{\mathrm{FE}} = P(1-A_1)$, the free energy (9a) can be rewritten as follows:

$$\begin{aligned} F &= \frac{A}{2(1-A_1)}\left(1+\frac{4\pi}{A}(1-a(1-A_1))\right)\bar{P}^2 \\ &\quad + \frac{B(1-B_1)}{4(1-A_1)^4}\bar{P}^4 - \bar{P}E_{\mathrm{ext}}. \end{aligned} \tag{10a}$$

It is easy to see that relationships (9a) and (10a) are polynomials, which can be conveniently represented in the form universally accepted for ferroelectric materials:

$$\begin{aligned} F &= \frac{a_0}{2}P^2 + \frac{b_0}{4}P^4 - E'P, \\ E' &= E_{\mathrm{ext}}(1-A_1), \\ a_0 &= A(1-A_1)\left(1+\frac{4\pi}{A}(1-a(1-A_1))\right), \\ b_0 &= B(1-B_1); \end{aligned} \tag{9b}$$

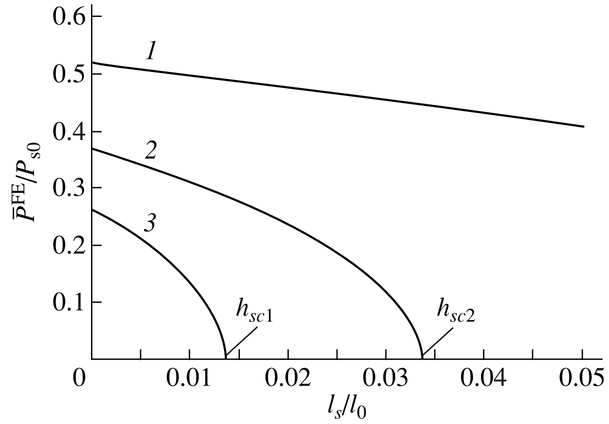

Fig. 6. Dependences of the average polarization on the screening length for film thicknesses l/l_0 = (*1*) 100, (*2*) 50, and (*3*) 40.

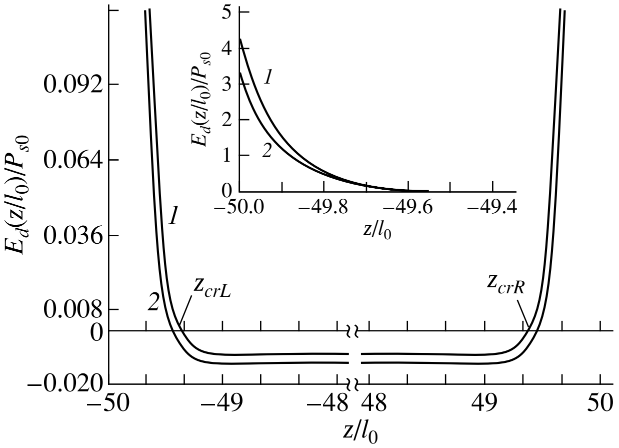

Fig. 7. Depolarization field profiles for the film thickness l/l_0 = 100 and screening lengths l_s/l_0 = (*1*) 0 and (*2*) 0.05. The inset illustrates the behavior of the depolarization field near the left surface of the film.

$$\begin{aligned} F &= \frac{a_1}{2}\bar{P}^2 + \frac{b_1}{4}\bar{P}^4 - E_{\mathrm{ext}}\bar{P}, \\ a_1 &= \frac{A}{(1-A_1)}\left(1+\frac{4\pi}{A}(1-a(1-A_1))\right), \\ b_1 &= \frac{B(1-B_1)}{(1-A_1)^4}. \end{aligned} \tag{10b}$$

It should be noted that, since the analytical form of the trial function for the polarization in the ferroelectric phase was chosen in the form of the solution for the paraelectric phase, the free energies (9) and (10) describe both the ferroelectric and paraelectric phases.

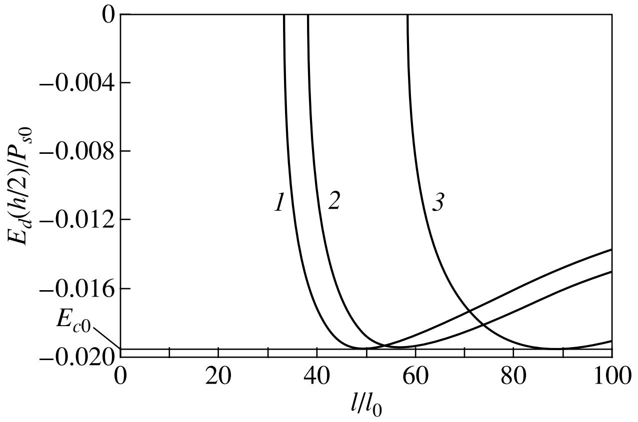

Fig. 8. Dependences of the depolarization field on the film thickness for screening lengths l_s/l_0 = (*1*) 0, (*2*) 0.03, and (*3*) 0.05.

The coefficient a_0 in relationships (9b) and the coefficient a_1 in formulas (10b) can be expressed through the critical temperature or the critical thickness; that is

$$a_0 = A_0(T - T_{cl})(1 - A_1),\quad a_1 = \frac{A_0(T - T_{cl})}{(1 - A_1)} \tag{11a}$$

or

$$a_0 = K(1 - A_1)\frac{1}{h}\left[1 - \frac{h}{h_c}\right],\quad a_1 = \frac{K}{(1 - A_1)}\frac{1}{h}\left[1 - \frac{h}{h_c}\right]. \tag{11b}$$

Taking into account that, at $h \gg 1$, the inequalities $A_1 \ll 1$ and $B_1 \ll 1$ are satisfied, we obtain

$$a_0 = a_1 = A_0(T - T_{cl}),\quad b_0 = b_1 = B,\quad E' = E_{\text{ext}} \tag{12a}$$

or

$$a_0 = a_1 = K\frac{1}{h}\left(1 - \frac{h}{h_c}\right),\quad b_0 = b_1 = B,\quad E' = E_{\text{ext}}. \tag{12b}$$

Note that coefficients (12a) and (12b) should be used for analyzing the dependences of the film properties on the temperature with a fixed thickness and on the size (thickness) with a fixed temperature, respectively. It is seen that polynomials (12a) and (12b) coincide with the standard polynomials of the free energy for bulk samples but with a renormalized coefficient of the quadratic term, whereas the coefficient of the quartic terms coincides with the corresponding coefficient for bulk samples. Since the critical temperature T_{cl} in formula (12a) depends on the film thickness, the extrapolation and correlation lengths, and the electrode characteristics [see expression (6)], the coefficient a_0 also depends on these parameters. In turn, this implies that all the physical properties of the films, which can be determined by minimizing the free energies (9b) or (10b), should depend on the electrode characteristics and on the material of the film. By minimizing the free energy (9b) with due regard for relationships (8), we can find the distributions of physical properties across the film of constant thickness (profiles of physical properties), whereas the minimization of the free energy (10b) gives the averages of these properties. Now, we turn to analysis of the physical properties of the films.

5. SPECIFIC FEATURES OF THE PHYSICAL PROPERTIES OF FILMS

First and foremost, we consider the temperature and thickness dependences of the average spontaneous polarization, the average dielectric susceptibility, and the average pyroelectric coefficient $\bar{\Pi} = \frac{d\bar{P}}{dT}$. From expressions (10b), (12a), and (12b), we obtain the following formulas for the above quantities in the ferroelectric phase ($T < T_{cl}$, $h > h_c$):

$$\bar{P} = \sqrt{\frac{A_0(T_{cl} - T)}{B}},\quad \bar{\chi} = \frac{1}{2A_0(T_{cl} - T)},\quad \bar{\Pi} = \frac{\sqrt{A_0}}{2\sqrt{B(T_{cl} - T)}}; \tag{13a}$$

$$\bar{P} = \sqrt{\frac{K\left(1 - \frac{h_c}{h}\right)}{Bh_c}},\quad \bar{\chi} = \frac{1}{\frac{2K}{h_c}\left(1 - \frac{h_c}{h}\right)},\quad \bar{\Pi} = \frac{1}{2}\frac{A_0}{\sqrt{\frac{KB}{h_c}\left(1 - \frac{h_c}{h}\right)}}. \tag{13b}$$

For the paraelectric phase ($T > T_{cl}$, $h < h_c$), we have $\bar{P} = 0$ and $\bar{\Pi} = 0$ and the dielectric susceptibility has the form

$$\bar{\chi} = \frac{1}{A_0(T - T_{cl})}, \tag{14a}$$

$$\bar{\chi} = \frac{1}{\frac{K}{h_c}\left(\frac{h_c}{h} - 1\right)}. \tag{14b}$$

Formulas (13a) and (14a) describe the temperature dependences of the average spontaneous polarization, the average dielectric susceptibility, and the average pyroelectric coefficient for thin ferroelectric films, whereas relationships (13b) and (14b) describe the thickness dependences of these characteristics. From relationships (9b), (12a), (10b), (12b), and (8a), it follows that the magnitudes of the above properties are described by formulas (13) and (14), which, after the multiplication into the function $[1 - \varphi(\xi)]$, gives the profiles of these properties. Figure 4 depicts the dependences of the dielectric susceptibility on the screening length l_s of carriers in the electrode material for films with different thicknesses. It can be seen from Fig. 4 that, for each thickness there is a critical screening length l_s at which the dielectric susceptibility diverges. This means that the film undergoes a transition from the ferroelectric phase to the paraelectric phase. A comparison of curves *1–3* in Fig. 4 shows that the critical screening length increases with an increase in the film thickness. This is associated with the fact that an increase in the film thickness results in an increase in the polarization (Fig. 5). The polarization can be suppressed by a sufficiently strong depolarization field that is enhanced as the screening length l_s increases. Therefore, we can make the inference that the phase transition is induced by the electrodes at a constant film thickness and a constant temperature (Fig. 6). The critical screening length h_{sc} can be determined from the condition $\overline{P}^{\mathrm{FE}} = 0$, which leads to $T = T_{cl}$ [see relationships (13a)], where T is a constant temperature. Taking into account expression (6), we obtain

$$h_{sc} = \frac{1}{\left(2\alpha + \dfrac{\beta}{2\varepsilon_e}\right)}\left[\frac{(T_c - T)}{4\pi}A_0 h - \frac{2}{1 + w}\right]. \tag{15a}$$

It follows from expression (15a) that the critical screening length satisfies the relationship $h_{sc} \sim h$ in accordance with the numerical results presented in Fig. 4. Moreover, since the critical screening length must be positive, it exists only for films whose thicknesses obey the inequality

$$h > h_0 = \frac{8\pi}{(1 + w)(T_c - T)A_0}. \tag{15b}$$

The thickness h_0 tends to infinity ($h_0 \longrightarrow \infty$) at $T \longrightarrow T_c$, and the minimum thickness $h_{0\min}$ corresponds to zero temperature ($T = 0$). According to the estimates, the minimum thickness $h_{0\min}$ can be equal to several tens or several hundreds of nanometers.

By comparing the thickness h_0 at an arbitrary temperature T with the critical thickness h_c defined by expression (7), we find that $h_0 < h_c$. Consequently, the film with thickness $h = h_0$ is in the paraelectric phase. Therefore, in order to retain the ferroelectric state of the film, it is necessary to choose film thicknesses $h > h_0$ in the thickness range $h > h_c$ and to use electrodes with screening lengths $h_s < h_{sc}$, which cannot induce transition from the ferroelectric phase to the paraelectric phase. It is seen from Figs. 5 and 6 that the polarization is maximum for superconducting electrodes ($h_s = 0$). As a consequence, the stability of the ferroelectric phase in films with superconducting electrodes is higher than that in films with other electrodes.

6. EFFECT OF ELECTRODES ON THE DEPOLARIZATION FIELD

After substitution of $P^{\mathrm{FE}} = P[1 - \varphi(\xi)]$ and $\overline{P}^{\mathrm{FE}} = P[1 - A_1]$, expression (3c) for the depolarization field takes the form

$$E_d = -4\pi P[1 - \varphi(\xi) - a + aA_1]. \tag{16}$$

Taking into account the inequality $h \gg 1$, we obtain $A_1 = \dfrac{2}{(1 + w)h} \ll 1$. Furthermore, since $a \approx 1$ [see expression (3e)], we have $E_d(\xi) \approx 4\pi P\varphi(\xi)$ in the vicinity of the surface. From this relationship, it follows that $E_d(\xi) > 0$ near the surface. However, the exact formula (16) indicates that the depolarization field changes sign away from the surface. Hence, there are points at which the depolarization field becomes zero ($E_d = 0$). The coordinates of these points can be easily derived from formula (16); that is,

$$\begin{aligned}
\xi_{crL} &= \ln\left(\frac{h}{h(1 - a)(1 + w) + 2a}\right) \\
&\simeq \ln\left(\frac{h}{h_s\left(2\alpha + \dfrac{\beta}{2\varepsilon_e}\right)(1 + w) + 2}\right), \\
\xi_{crR} &= h - \ln\left(\frac{h}{h(1 - a)(1 + w) + 2a}\right) \\
&\simeq h - \ln\left(\frac{h}{h_s\left(2\alpha + \dfrac{\beta}{2\varepsilon_e}\right)(1 + w) + 2}\right).
\end{aligned} \tag{17}$$

Therefore, the behavior of the depolarization field across the film of thickness h is characterized by the following relationships:

$$\begin{gathered}
0 < \xi < \xi_{crL}, \quad E_d(\xi) > 0, \\
\xi = \xi_{crL}, \quad E_{d(\xi)} = 0, \\
\xi_{crL} < \xi < \xi_{crR}, \quad E_d(\xi) < 0, \\
\xi = \xi_{crR}, \quad E_d(\xi) = 0, \\
\xi_{crR} < \xi < h, \quad E_d(\xi) > 0.
\end{gathered} \tag{18}$$

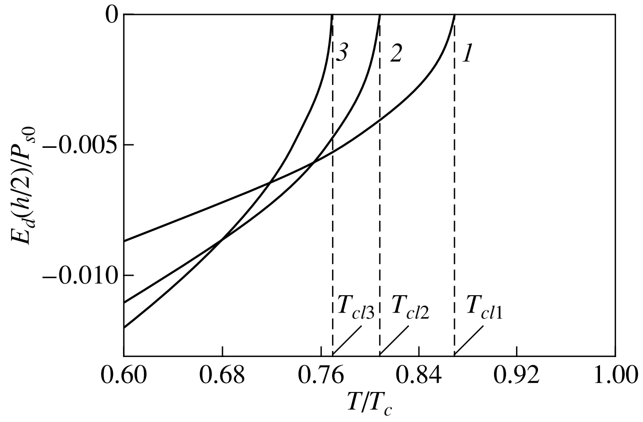

Fig. 9. Temperature dependences of the depolarization field for the film thickness $l/l_0 = 100$ and screening lengths $l_S/l_0 =$ (*1*) 0, (*2*) 0.03, and (*3*) 0.05.

Figure 7 clearly illustrates this behavior of the depolarization field profile. As follows from a comparison of curves *1* and *2* in Fig. 7, the superconducting electrodes provide a larger increase in the polarization in the vicinity of the surface as compared to the nonsuperconducting electrodes, whereas the decrease in the polarization in the range $z_{crL} < z < z_{crR}$ for the superconducting electrodes is smaller than that for the nonsuperconducting electrodes. In both cases, the polarization profile in the film becomes more flattened, so that the polarization in the film is more uniform and the average value of the polarization turns out to be smaller than the average value of the polarization for the nonsuperconducting electrodes (Figs. 5, 6). Let us examine in more detail the behavior of the depolarization field $E_d < 0$ over a wide range in which it tends to destroy the ferroelectric state, as is usually the case in bulk materials. Making allowance for the wide plateau in this range, we consider the behavior of the depolarization field at the center of the film, because the approximate equality $E_d(z_{crL} < z < z_{crR}) \approx E_d\left(\frac{h}{2}\right)$ holds true.

Although the quantity A_1 is small, it makes a significant contribution (because $a \approx 1$), especially in the vicinity of the center of the film, where the relationship $\varphi\left(\xi = \frac{h}{2}\right) \simeq 0$ is satisfied. Consequently, according to relationship (16), the depolarization field can be written in the form

$$E_d\left(\frac{h}{2}\right) = -\frac{K}{h}\sqrt{\frac{K}{B}\left(\frac{1}{h_c} - \frac{1}{h}\right)} \qquad (19a)$$

or

$$E_d\left(\frac{h}{2}\right) = -A_0(T_c - T_{cl})\sqrt{\frac{A_0}{B}(T_{cl} - T)}. \qquad (19b)$$

Expressions (19a) and (19b) describe the dependences of the depolarization field on the thickness and temperature, respectively. As can be seen from formulas (6) and (7), the quantities $(T_c - T_{cl})$ and K increase with an increase in the screening length h_s, so that the depolarization field at the center of the film increases in proportion to the screening length.

From expressions (19a) and (19b), it follows that the depolarization field $E_d\left(\frac{h}{2}\right)$ tends to zero at $T \longrightarrow T_{cl}$ and $h \longrightarrow h_c$ (this corresponds to the phase transitions) or at $h \longrightarrow \infty$, as is the case with the bulk sample. The magnitude of the depolarization field at the center of the film reaches a maximum value $E_{d\max} = E_{c0} = -\frac{2}{3\sqrt{3}}\frac{K}{h_c}\sqrt{\frac{K}{h_c B}}$ at thickness $h = h_{\max} = \frac{3}{2}h_c$. The depolarization field at this thickness is equal in magnitude to the coercive field of the bulk sample. Actually, making allowance for expression (7) relating the quantities K and h_c, it is easy to obtain the standard formula for the temperature dependence of this field $E_{d\max} = E_{c0} = -\frac{2}{3\sqrt{3}}A_0(T_c - T)\sqrt{\frac{A_0(T_c - T)}{B}}$. The dependences of the depolarization field $E_d\left(\frac{h}{2}\right)$ on the film thickness are depicted in Fig. 8. It can be seen from this figure that, as the screening length h_s increases, the magnitude of the depolarization field $E_d\left(\frac{h}{2}\right)$ at the maximum shifts toward larger thicknesses h [see formula (7)]. As is easily seen, the electrodes with larger screening lengths h_s suppress the depolarization field more weakly (cf. curves *1* and *2*, *3* in Fig. 8).

Figure 9 shows the temperature dependences of the depolarization field at the center of the film for different screening lengths h_s It is seen from Fig. 9 that, as the screening length h_s increases, the rate of change in the depolarization field $E_d\left(\frac{h}{2}\right)$ also increases and $E_d\left(\frac{h}{2}\right) \longrightarrow 0$ at $T \longrightarrow T_{cl}$ [see relationships (17)]. Different rates of change in the depolarization field and an increase in the temperature of the induced phase transition with a decrease in the screening length h_s ($T_{cl1} > T_{cl2} > T_{cl3}$) [see formula (6)] result in the intersection of the dependences in the low-temperature range (Fig. 9). It is worth noting that, only far from all the critical temperatures T_{cli} ($i = 1$–3) does the depolarization field satisfy the inequalities $|E_d(h_s = 0)| < |E_d(h_s = 0.03)| < |E_d(h_s = 0.05)|$. At the same time, there are temperature ranges in the vicinity of the critical temperatures T_{cli} ($i = 1$–3) in which the depolarization field for the superconducting electrodes is stronger than that for the nonsuperconducting electrodes. Such an unusual behavior is observed in the vicinity of the critical thicknesses at which the depolarization field $E_d(h_s = 0)$ can be stronger than the depolarization field $E_d(h_s \neq 0)$ (Fig. 8). These features are most likely associated with the fact that the depolarization field tends to zero ($E_d \longrightarrow 0$) at $T \longrightarrow T_{cl}$ or $h \longrightarrow h_c$ irrespective of the electrode type. Therefore, there exist temperature ranges (at a fixed thickness) or thickness ranges (at a fixed temperature) in which the superconducting electrodes are not preferable. It can be seen from Fig. 9 that these ranges can be of the order of $(0.1–0.2)T_c$ below the critical temperature T_{cl} for the nonsuperconducting electrode.

7. CONCLUSIONS

Unlike the bulk ferroelectrics, in which the depolarization field considerably decreases because of the presence of the domain structure, thin ferroelectric films do not have a domain structure, so that only the fields induced by carriers at electrodes can reduce the depolarization field and, thus, retain the ferroelectric state. The above analysis demonstrated that, although the superconducting electrodes are characterized by a maximum deleterious effect of the depolarization field on the spontaneous polarization of the ferroelectric material, the difference between the polarizations in the case of superconducting and metallic electrodes decreases with an increase in the film thickness (Fig. 5). In particular, for the $BaTiO_3$ film with $l_0 = 2$ nm [6], the polarization of the sample with superconducting electrodes at film thicknesses $l > 70l_0$ is only ~20% higher than that with nonsuperconducting metallic electrodes.

Apart from the metallic electrodes considered above, semiconducting electrodes are also used in practice. For a quantitative analysis of these electrodes, it is necessary to take into account the band bending and effects associated with the space charge [11]. Qualitatively, it can be assumed that, since the screening length in semiconductors, as a rule, is larger than the screening length in normal metals, the depolarization field in a ferroelectric film with semiconducting electrodes should be stronger. This brings about a decrease in the spontaneous polarization and an increase in the critical thickness corresponding to a phase transition from the ferroelectric phase to the paraelectric phase. In general, the phase state and properties of thin ferroelectric films can be controlled by choosing the appropriate electrode material.

REFERENCES

1. R. Kretchmer and K. Binder, Phys. Rev. B **20**, 1065 (1979).
2. D. R. Tilley, in *Ferroelectric Thin Films*, Ed. by C. Paz de Araujo, J. F. Scott, and G. W. Taylor (Gordon and Breach, Amsterdam, 1996), p. 11.
3. A. M. Bratkovsky and A. P. Levanyuk, Phys. Rev. Lett. **84**, 3177 (2000).
4. G. Suchaneck, T. H. Sander, R. Kohler, and G. Gerlach, Integr. Ferroelectr. **27**, 127 (1999).
5. M. D. Glinchuk, E. A. Eliseev, and V. A. Stephanovich, Physica B (Amsterdam) **322**, 356 (2002).
6. M. D. Glinchuk, E. A. Eliseev, V. A. Stephanovich, and R. Farhi, J. Appl. Phys. **93**, 1150 (2003).
7. G. E. Pike, W. L. Warren, D. Dimos, B. A. Tuttle, R. Rames, J. Lee, V. G. Keramidas, and J. T. Evans, Appl. Phys. Lett. **66**, 484 (1995).
8. R. Bruchaus, D. Pitzer, R. Primig, M. Schreiter, and W. Wersing, Integr. Ferroelectr. **25**, 1 (1999).
9. V. M. Fridkin, *Photoferroelectrics* (Nauka, Moscow, 1976; Springer-Verlag, Berlin, 1979).
10. C. Kittel, *Introduction to Solid State Physics*, 5th ed. (Wiley, New York, 1976; Nauka, Moscow, 1978).
11. I. P. Batra, P. Wurfel, and B. D. Silverman, Phys. Rev. Lett. **30**, 384 (1973).

Translated by O. Borovik-Romanova

Physics of the Solid State, Vol. 47, No. 7, 2005, pp. 1340–1345. Translated from Fizika Tverdogo Tela, Vol. 47, No. 7, 2005, pp. 1293–1297.
Original Russian Text Copyright © 2005 by Shur, Lomakin, Rumyantsev, Yakutova, Pelegov, Sternberg, Kosec.

MAGNETISM
AND FERROELECTRICITY

Polarization Switching in Heterophase Nanostructures: PLZT Relaxor Ceramics

V. Ya. Shur*, G. G. Lomakin*, E. L. Rumyantsev*, O. V. Yakutova*, D. V. Pelegov*, A. Sternberg, and M. Kosec*****

** Research Institute of Physics and Applied Mathematics, Ural State University,*
pr. Lenina 51, Yekaterinburg, 620083 Russia
e-mail: vladimir.shur@usu.ru
*** Institute of Solid State Physics, University of Latvia, Riga, LV-1063 Latvia*
**** Jozef Stefan Institute, Ljubljana, 1000 Slovenia*

Received August 17, 2004

Abstract—The polarization switching is experimentally investigated in hot-pressed PLZT-*x*/65/35 ceramics with a lanthanum content from 5 to 12 at. %. The specific features in the temperature dependence of the polarization switching in a heterophase state are interpreted by analyzing the change in the switched charge measured over wide ranges of fields and temperatures. Particular emphasis is placed on the role of depolarization fields induced by interphase boundaries. A model of the evolution of polydomain nanostructures with a change in the temperature and in the response to an external field is considered. It is assumed that the low-temperature dielectric anomaly and the temperature hysteresis are associated with the loss of stability of a large-scale domain structure and its transformation into a nanodomain state. *© 2005 Pleiades Publishing, Inc.*

1. INTRODUCTION

Relaxor ferroelectrics (with smeared phase transitions) are highly inhomogeneous systems [1, 2]. These materials are characterized by anomalies of the susceptibilities over an extremely wide range of temperatures. The unique properties of relaxor ferroelectrics offer strong possibilities for their practical application [2].

In this work, the heterophase structure that arises in a relaxor ferroelectric upon cooling in the temperature range of the smeared phase transition is considered to be a set of isolated ferroelectric (polar) nanoregions embedded in a paraelectric (nonpolar) matrix. As the temperature decreases, the heterophase structure undergoes a qualitative transformation, because an increase in the fraction of the polar phase results in the formation of finite-sized polar clusters composed of nanodomains [3–5]. A further decrease in the temperature leads to the formation of an "infinite" polar cluster. In this case, isolated regions of the nonpolar phase are located in "windows" of the infinite polar cluster [5]. As the temperature T_f (hereafter, T_f is the freezing temperature) of the transition from the heterophase state to the ferroelectric state is approached, the sizes and the total volume of isolated nonpolar regions decrease [6].

The domain structure formed in the ferroelectric phase upon cooling without an external electric field (zero-field cooling) consists of nanodomains. The domain sizes are determined by the spatial scale of compositional inhomogeneities (chemical domains) [6, 7]. Spontaneous polarizations P_S in different polar nanoregions and nanodomains are oriented in a random manner. As a result, the spontaneous polarization P_S averaged over the macrovolume is equal to zero. Note that the spontaneous polarizations P_S can be ordered only under the action of an external electric field.

Since nanoregions and nanodomains have ultrasmall sizes [6, 8, 9], it is impossible to use direct methods for studying the kinetics of domains under the action of external electric fields, for example, visualization of instantaneous domain configurations with an optical microscope. For this reason, the polarization switching in relaxor ferroelectrics has been studied using indirect integrated methods based on recording (directly in the course of switching) hysteresis loops [10], switching currents [11], and elastic light scattering [4, 5, 12, 13]. It is obvious that, in order to obtain reliable information on the switching kinetics in polar regions with a nanodomain structure, it is necessary to develop a consistent approach to the interpretation of measured integrated characteristics.

2. SAMPLE PREPARATION AND EXPERIMENTAL TECHNIQUE

The samples used in measurements had the form of thin plates prepared from transparent coarse-grained lead zirconate titanate ceramics $(Pb_{1-x}La_x)(Zr_{0.65}Ti_{0.35})O_3$ doped with lanthanum at contents from 5 to 12 at. % (PLZT-*x*/65/35, where *x* is the percentage of lanthanum). The ceramics was fabricated by hot pressing. The grain size varied from 4 to 7 μm, and the plate thickness ranged from 90 to 300 μm. The polarization switching was performed either with continuous gold electrodes applied by thermal evaporation or with transparent indium–tin oxide electrodes produced by magnetron reactive sputtering.

The dielectric measurements were carried out at temperatures from –150 to 200°C in the frequency range from 20 Hz to 200 kHz. Prior to measurements, the sample was polarized in a dc electric field at temperatures corresponding to the ferroelectric state under cyclic changes in the temperature (heating and subsequent cooling).

The hysteresis loops were measured in a sinusoidal electric field at a frequency of 0.04 Hz and at amplitudes of up to 8 kV/cm. The switched charges were determined by integrating the measured switching current. It was assumed that the rate of the field rise is sufficiently low and switching can be considered to be quasi-static. The measurements were carried out in the temperature range from 25 to 200°C.

3. EVOLUTION OF THE POLYDOMAIN STRUCTURE IN AN ELECTRIC FIELD

Figure 1 shows typical hysteresis loops of the PLZT-8/65/35 sample in the temperature range from 25 to 50°C. It can be seen from Fig. 1 that a change in the temperature leads to a qualitative change in the loop shape. Below a particular temperature, the dependence $Q(E)$ corresponds to a classical dielectric hysteresis loop observed in ferroelectrics. Above this temperature, there arises a constriction in the central part and a double hysteresis loop appears (Fig. 2a).

In order to determine the temperature of the crossover from the classical "ferroelectric" hysteresis loop to the double hysteresis loop, we analyzed the field dependence of the derivative of the switched charge with respect to the field applied to the sample ($dQ(E)/dE$), because this quantity is most sensitive to a change in the shape of the hysteresis loop. It should be noted that, upon switching in a linearly increasing field, this dependence agrees in shape with the current hysteresis loop. In the ferroelectric phase, the dependence $dQ(E)/dE$ exhibits two pronounced peaks corresponding to conventional processes of macroscopic polarization switching in ferroelectrics. For the classical hysteresis loop, the maxima of the peaks, as a rule, are located at fields close to the coercive fields E_C determined by the standard method [14]. For the real experimental hysteresis loop of inhomogeneous ferroelectrics, the fields corresponding to the maxima in the dependence $dQ(E)/dE$ are equal to the effective threshold fields E_{th} at which the switching rate is maximum. These fields are more adequate characteristics of polarization switching (as compared to the classical coercive fields).

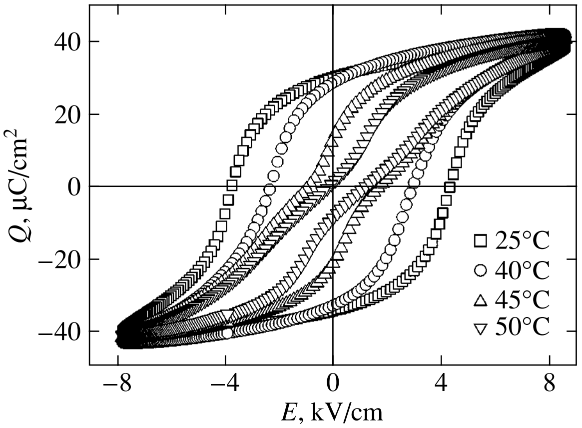

Fig. 1. Hysteresis loops for the PLZT-8/65/35 sample measured upon heating at different temperatures.

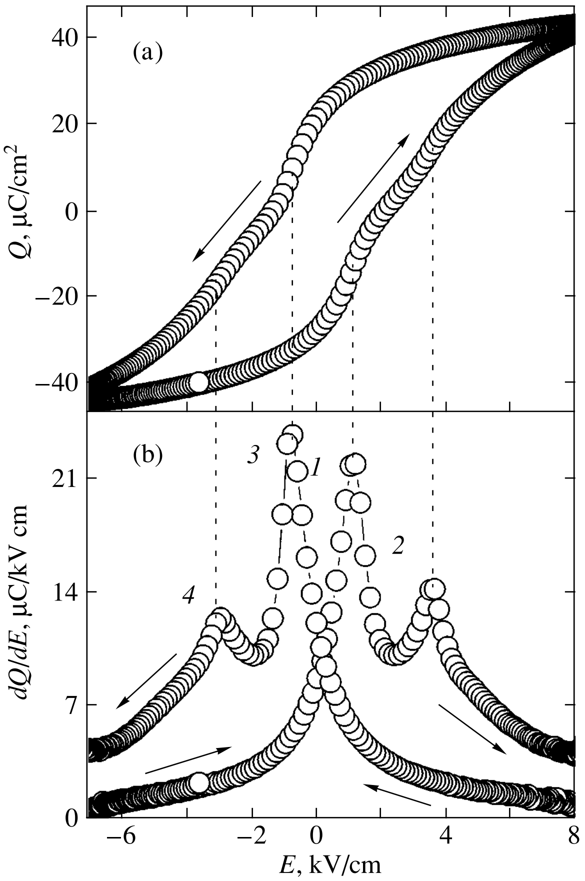

Fig. 2. Specific features of the polarization switching in the relaxor phase of the PLZT-8/65/35 sample: (a) the hysteresis loop $Q(E)$ and (b) the field dependence of the derivative dQ/dE. Arrows indicate the direction of changes in the electric field. $T = 44$°C.

As the temperature increases, the hysteresis loop changes in shape and the dependence $dQ(E)/dE$ exhibits four maxima (Fig. 2b). Taking into account that the dependences $dQ(E)/dE$ in increasing and decreasing fields almost coincide, we restricted our consideration to the case of the dependence $dQ(E)/dE$ in the increasing field. The evolution of the dependence $dQ(E)/dE$

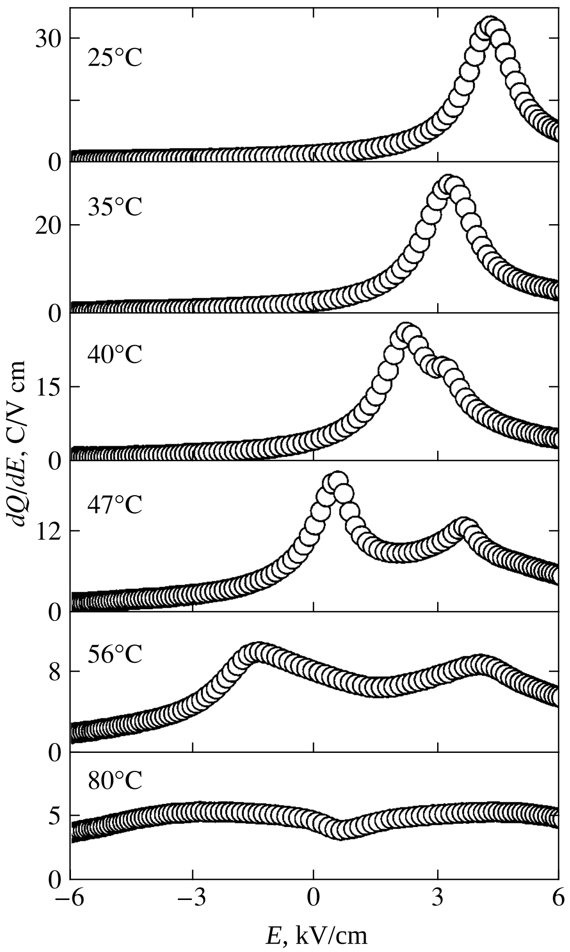

Fig. 3. Evolution of the dependence $dQ(E)/dE$ for the PLZT-8/65/35 sample measured upon heating in an increasing field.

with an increase in the temperature is illustrated in Fig. 3. The data on the positions of the maxima were used to construct the temperature dependence of the effective threshold field E_{th} (Fig. 4), from which we determined the temperature corresponding to the crossover of the switching mechanism (i.e., to the change in the number of maxima). This temperature (designated as T_f) was identified with the point of the transition from the purely ferroelectric state to the relaxor state. According to the experimental data presented in Fig. 4 for the PLZT-8/65/35 sample, this temperature is found to be 38°C.

4. TEMPERATURES OF DIELECTRIC ANOMALIES

The typical temperature dependences of the permittivity for PLZT-x/65/35 ceramic materials upon heating and subsequent cooling of the PLZT-8/65/35 sample are plotted in Fig. 5. It can be seen from this figure that the dependence of the permittivity measured at a frequency of 1 kHz upon heating of the polarized ceramic sample exhibits a smeared frequency-dependent maximum at T_m = 106°C and a low-temperature dielectric anomaly (a narrow maximum) at T_1 = 46°C. When the sample was cooled after heating to temperatures above T_m, the low-temperature anomaly $\varepsilon(T)$ was not observed (Fig. 5), as was the case with heating of the thermally depolarized sample.

It was demonstrated that, in all the samples, the Curie–Weiss law holds at temperatures below T_1 and the quadratic temperature dependence typical of smeared phase transitions (Fig. 6) [15, 16] is observed in the vicinity of the temperature T_m corresponding to the maximum of the permittivity:

$$1/\varepsilon = (T - T_m)^2/\varepsilon_m\sigma^2,$$

where σ is the parameter of smearing of the phase transition.

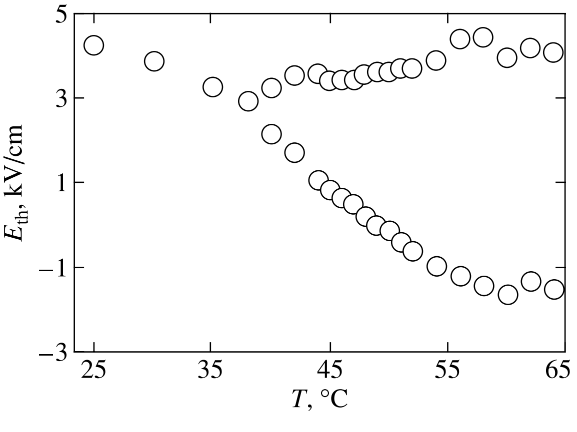

Fig. 4. Temperature dependence of the position of the maxima in the dependence $dQ(E)/dE$ for the PLZT-8/65/35 sample measured upon heating in an increasing field.

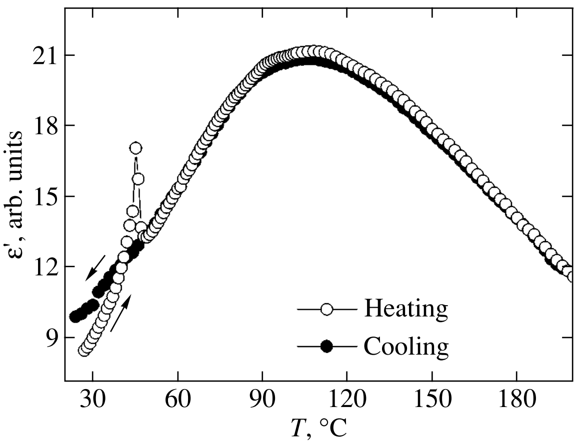

Fig. 5. Temperature dependences of the permittivity measured at a frequency of 1 kHz for the polarized PLZT-8/65/35 sample upon heating and cooling.

Figure 7 presents the obtained temperatures T_m and T_1 of the dielectric anomalies as functions of the lanthanum content and the data (taken from [17]) on the temperature T_m at $x = 0$, 2, 4, and 15 at. %. According to the aforementioned concepts, the difference between the temperatures of the dielectric anomalies $\Delta T = T_m - T_1$ characterizes the temperature range of existence of the relaxor phase. It can be seen from Fig. 7 that the relaxor phase ($\Delta T \neq 0$) is formed only at a lanthanum content of higher than 5 at. % and the difference $\Delta T(x)$ is saturated at high contents ($x > 10$ at. %). It should be noted that the experimentally obtained concentration dependences change qualitatively with an increase in the lanthanum content. The dependences exhibit a linear behavior at $x < 4$ at. % and an exponential behavior at $x > 5$ at. % (Fig. 7).

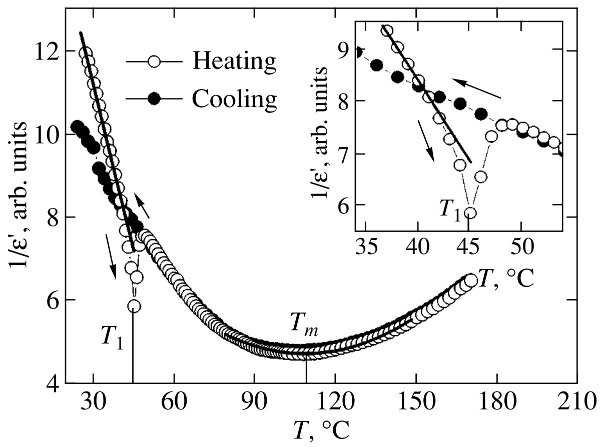

Fig. 6. Temperature dependences of the reciprocal of the permittivity measured at a frequency of 1 kHz for the polarized PLZT-8/65/35 sample upon heating and cooling. The inset shows the portion of the dependence with a temperature hysteresis. Experimental points are approximated by the linear and quadratic functions.

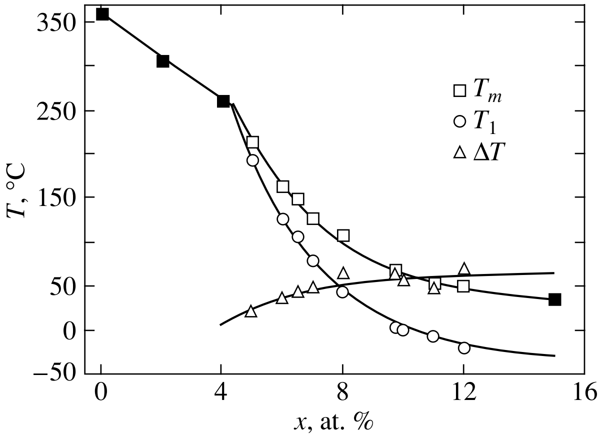

Fig. 7. Dependences of the temperatures of dielectric anomalies on the lanthanum content. Closed squares indicate the experimental data taken from [17]. Experimental points are approximated by the exponential functions.

5. DISCUSSION OF THE EXPERIMENTAL RESULTS

According to the classical concepts of relaxor ferroelectrics [2, 18–20], an increase in the temperature leads to a transition from the homogeneous ferroelectric state to the heterogeneous (heterophase) state. When analyzing the experimental data obtained in this work, one should take into account that the "low-temperature" heterophase structure formed in the vicinity of the critical point is a ferroelectric polydomain matrix with isolated inclusions of the nonpolar phase (nanoregions).

The bound charges induced as a result of polarization jumps at nanoregion boundaries (interphase boundaries) generate depolarization fields, which stimulate the decay of large-sized domains and the formation of a nanodomain structure. Unlike the depolarization fields produced by surface bound charges, whose effect is predominantly compensated for by fast processes of external screening (the redistribution of charges at the electrodes), the fields under consideration can only be compensated for by slow processes of bulk screening [3, 21, 22].

The depolarization fields induced by space bound charges bring about a partial backswitching (the formation of domains with polarization opposite in sign) in the bulk near the nonpolar inclusions. As a consequence, in the bulk, there arises a structure with charged domain walls, which contribute substantially to the dielectric response [23–25], because the domain walls are characterized by an anomalously high concentration of steps. These steps are mobile even in the weak fields used to measure the dielectric characteristics.

In the framework of the concepts under consideration, the temperature hysteresis of the permittivity (see inset to Fig. 6) can be explained by the spontaneous transformation of the large-scale domain structure in the response to an inhomogeneous bias field induced by nonpolar regions [3]. The preliminary polarization in a strong dc field in the ferroelectric state at low temperatures ($T < T_f$) leads to an irreversible increase in the domain sizes. Heating at temperatures above T_f results in the formation of nanoregions composed of the nonpolar phase. Further heating leads to an increase in the volume of nonpolar inclusions and in the surface area of charged domains walls. This is accompanied by a rapid increase in the dielectric response. However, such a polydomain heterophase state is unstable and the large-scale domain structure at the temperature T_1 begins to transform under the action of depolarization fields. This results in the formation of a small-scale domain structure that consists of submicrodomains and nanodomains separated by neutral and charged domain walls. Such a transformation leads to a considerable decrease in the concentration of charged walls and, hence, to a decrease in the dielectric response. A similar polydomain heterophase structure is formed upon thermal depolarization.

The change in the shape of the hysteresis loop and the appearance of additional peaks in the field dependence of the derivative dQ/dE (Fig. 2b) can also be interpreted within the proposed model. The first peak corresponds to the spontaneous backswitching (the return to the polydomain state) under the action of the depolarization field. The second peak is associated with the switching from the polydomain state to the single-domain state in the response to the external field, which is weakened by the depolarization field. Therefore, the depolarization field plays the role of a spatially inhomogeneous bias field distorting the shape of the hysteresis loop. Upon reversal switching, a similar effect is observed for domains in which the spontaneous polarization without field is of opposite sign. This leads to the formation of the double hysteresis loop. An increase in the temperature results in an increase in the mean depolarization fields due to an increase in the volume of nonpolar inclusions and, correspondingly, leads to an increase in the mean bias fields.

Naturally, the double hysteresis loop and additional peaks in the curve $dQ(E)/dE$ arise only upon transition to the heterophase state, in which the depolarization fields are induced by bound charges located at the interphase boundaries. Within the proposed approach, the temperature corresponding to the appearance of the two peaks in the dependence $dQ(E)/dE$ is the temperature of the transition from the purely ferroelectric state to the relaxor (heterophase) state. This approach to analyzing the experimental data enables us to determine the freezing temperature T_f.

It should be noted that the obtained temperature T_f is significantly lower than the temperature T_1 determined from the dielectric measurements. This situation seems to be quite reasonable because the temperature T_1 in the framework of the proposed model corresponds to the temperature of the loss of stability of the large-scale domain structure and its transformation into a nanodomain state. In the range between the temperatures T_f and T_1, the depolarization fields have already induced in the bulk and, hence, lead to the formation of charged domain walls in the vicinity of nonpolar inclusions; however, the strength of these fields is insufficient for a radical transformation of the domain structure.

6. CONCLUSIONS

Thus, the specific features of the polarization switching and dielectric anomalies in hot-pressed PLZT-*x*/65/35 ceramics with a lanthanum content from 5 to 12 at. % were experimentally investigated in the temperature range of existence of the smeared phase transition. The features revealed in the hysteresis loop and the temperature hysteresis of the permittivity were explained within the proposed model, which is based on the concept of the decisive role played by depolarization fields induced by bound charges at boundaries of nonpolar inclusions. A method was devised for determining the temperature of the transition from a ferroelectric state to a heterophase state. The evolution of polydomain nanostructures with a change in the temperature and in the response to an external field was analyzed.

ACKNOWLEDGMENTS

This work was supported by the Russian Foundation for Basic Research (project no. 04-02-16770), the Ministry of Education of the Russian Federation (project nos. E 02-3.4-395, UR.06.01.028), the scientific program “Russian Universities: Basic Research,” and the US Civilian Research and Development Foundation for the New Independent States of the Former Soviet Union (grant no. EK-005-X1).

REFERENCES

1. G. A. Smolenskiĭ and A. I. Agranovskaya, Fiz. Tverd. Tela (Leningrad) **1** (10), 1563 (1959).
2. L. E. Cross, Ferroelectrics **151**, 305 (1994).
3. V. Ya. Shur, Phase Transit. **65**, 49 (1999).
4. V. Ya. Shur, G. G. Lomakin, V. P. Kuminov, D. V. Pelegov, S. S. Beloglazov, S. V. Slovikovskiĭ, and I. L. Sorkin, Fiz. Tverd. Tela (St. Petersburg) **41** (3), 505 (1999) [Phys. Solid State **41** (3), 453 (1999)].
5. V. Ya. Shur, G. G. Lomakin, E. L. Rumyantsev, S. S. Beloglazov, D. V. Pelegov, A. Sternberg, and A. Krumins, Ferroelectrics **299**, 75 (2004).
6. X. Dai, Z. Xu, and D. Viehland, Philos. Mag. B **70**, 33 (1994).
7. T. Egami, S. Teslic, W. Dmowski, D. Viehland, and S. Vakhrushev, Ferroelectrics **199**, 103 (1997).
8. P. Lehnen, W. Kleemann, Th. Wöike, and R. Pankrath, Phys. Rev. B **64**, 224109 (2001).
9. K. Terabe, S. Takekawa, M. Nakamura, K. Kitamura, S. Higuchi, Y. Gotoh, and A. Gruverman, Appl. Phys. Lett. **81** (11), 2044 (2002).
10. V. V. Gladkiĭ, V. A. Kirikov, and T. R. Volk, Fiz. Tverd. Tela (St. Petersburg) **44** (2), 351 (2002) [Phys. Solid State **44** (2), 365 (2002)].
11. T. R. Volk, D. V. Isakov, and L. I. Ivleva, Fiz. Tverd. Tela (St. Petersburg) **45** (8), 1463 (2003) [Phys. Solid State **45** (8), 1537 (2003)].
12. M. D. Ivey and V. W. Bolie, IEEE Trans. Ultrason. Ferroelectr. Freq. Control **38**, 379 (1991).
13. A. Krumins, T. Shiosaki, and S. Koizumi, Jpn. J. Appl. Phys. **33**, 4946 (1994).
14. C. B. Sawyer and C. H. Tower, Phys. Rev. **35** (1), 269 (1930).
15. B. N. Rolov, Fiz. Tverd. Tela (Leningrad) **6** (7), 2128 (1964) [Sov. Phys. Solid State **6** (8), 1676 (1964)].
16. V. A. Isupov, Izv. Akad. Nauk SSSR, Ser. Fiz. **54** (6), 1131 (1990).

17. Qi Tan and D. Viehland, J. Am. Phys. Soc. **53** (21), 14103 (1996).
18. V. A. Isupov, Izv. Akad. Nauk SSSR, Ser. Fiz. **47** (3), 559 (1983).
19. W. Kleemann and R. Lindner, Ferroelectrics **199**, 1 (1997).
20. M. El Marssi, R. Farhi, J.-L. Dellis, M. D. Glinchuk, L. Seguin, and D. Viehland, J. Appl. Phys. **83** (10), 5371 (1998).
21. V. Ya. Shur, Yu. A. Popov, and N. V. Korovina, Fiz. Tverd. Tela (Leningrad) **26** (3), 781 (1984) [Sov. Phys. Solid State **26** (3), 471 (1984)].
22. V. Ya. Shur and E. L. Rumyantsev, Ferroelectrics **191**, 319 (1997).
23. V. Ya. Shur, Yu. A. Popov, and A. L. Subbotin, Fiz. Tverd. Tela (Leningrad) **25** (2), 564 (1983) [Sov. Phys. Solid State **25** (2), 318 (1983)].
24. V. Ya. Shur, A. L. Gruverman, V. V. Letuchev, E. L. Rumyantsev, and A. L. Subbotin, Ferroelectrics **98**, 29 (1989).
25. V. Ya. Shur, E. L. Rumyantsev, E. V. Nikolaeva, and E. I. Shishkin, Appl. Phys. Lett. **77** (22), 3636 (2000).

Translated by O. Borovik-Romanova

Physics of the Solid State, Vol. 47, No. 7, 2005, pp. 1346–1352. Translated from Fizika Tverdogo Tela, Vol. 47, No. 7, 2005, pp. 1298–1303.
Original Russian Text Copyright © 2005 by Topolov.

MAGNETISM AND FERROELECTRICITY

Dual Structures and Transition Regions in xPbTiO$_3$–(1 – x)Pb(Zn$_{1/3}$Nb$_{2/3}$)O$_3$ Crystals

V. Yu. Topolov
Rostov State University, ul. Zorge 5, Rostov-on-Don, 344090 Russia
e-mail: topolov@phys.rsu.ru

Received September 7, 2004

Abstract—Model concepts of dual structures are developed as applied to crystals of xPbTiO$_3$–(1 – x)Pb(Zn$_{1/3}$Nb$_{2/3}$)O$_3$ solid solutions in the range $0 \le x \le 0.08$. The conditions of the formation of dual structures upon partial and complete relaxation of internal mechanical stresses are considered. A new model of transition regions is proposed for analyzing several variants of changing the unit cell parameters that satisfy the condition of complete stress relaxation inside the transition regions in crystals at concentrations $x = 0.045$ and 0.08. The influence of the intermediate phase $P4mm$ and stability of its 90° domain structure on the formation of dual structures at $x \ge 0.045$ is discussed. © *2005 Pleiades Publishing, Inc.*

1. INTRODUCTION

Crystals of xPbTiO$_3$–(1 – x)Pb(Zn$_{1/3}$Nb$_{2/3}$)O$_3$ (xPT–PZN) solid-solution ferroelectric relaxors with a perovskite-type structure in the composition region corresponding to the morphotropic phase boundary ($x \approx$ 0.08–0.09) are characterized by a combination of unique electromechanical properties [1–4], a variety of heterophase states [5–10], and different (frequently, rather complex) domain and twin structures [6, 11] of the coexisting phases. The dual structures recently revealed in crystals of the xPT–PZN solid solutions in the range $0 \le x \le 0.08$ at room temperature [12, 13] are of particular interest. According to x-ray diffraction data [12], the rhombohedral (Rh) distortions of the perovskite cells in outer layers (1–5) × 10^{-5} m thick are greater than those observed in the bulk of the crystal at the same concentration x. The corresponding unit-cell parameters inside the sample (a_{in}) and near the sample surface (a_{out}) obey the inequalities

$$a_{\text{in}} > a_{\text{out}}, \quad \alpha_{\text{in}} > \alpha_{\text{out}}. \tag{1}$$

The differences between the unit cell parameters a_{in} and a_{out}, for example, at $x = 0.045$, can be as large as 6%. Rhombohedral distortions inside the sample at $x = 0$ are not found. The unit cell parameters of the new phase (X phase) satisfy the equalities $a_{\text{in}} = b_{\text{in}} = c_{\text{in}}$ and $\alpha_{\text{in}} = \beta_{\text{in}} = \gamma_{\text{in}} = 90°$ [12] for the paraelectric cubic (C) phase $Pm3m$ and the relationships $a_{\text{in}} = b_{\text{in}} \ne c_{\text{in}}$ and $\alpha_{\text{in}} = \beta_{\text{in}} = \gamma_{\text{in}} = 90°$ [13] for the ferroelectric tetragonal (T) phase $P4mm$ [1, 14] in the xPT–PZN system. Xu *et al.* [15] also revealed that the unit cell parameters measured in the surface layers and in the bulk of crystals in the related system yPbTiO$_3$–(1 – y)Pb(Mg$_{1/3}$Nb$_{2/3}$)O$_3$ ($0.10 \le y \le 0.27$) obey relationships similar to inequalities (1) and that the rhombohedral distortions of the perovskite cell tend to increase with an increase in the concentration y. However, the aforementioned data and other experimental results do not clarify the problem of the formation of dual structures and the elastic matching of the single-domain or polydomain regions of the crystals with particular unit-cell parameters. The aim of this work was to analyze the specific features in the formation of dual structures and the conditions of their existence and to develop physical concepts of heterophase states in xPT–PZN rhombohedral crystals.

2. TWO-PHASE STATES AND INTERNAL MECHANICAL STRESSES

In our consideration, we use the algorithm proposed in [16] and specify the distortion matrices $\|M_{af}\|$ and $\|N_{af}\|$ [4, 8, 10] for the rhombohedral phases inside the crystal (Rh_{in}) and in the surface layer (Rh_{out}) at $x > 0$ (or for the phases X_{in} and Rh_{out} at $x = 0$). In this case, the shape of the interphase boundary can be approximated by a second-degree surface:

$$\sum_{a,\,b\,=\,1}^{3} D_{ab} x_a x_b = 0. \tag{2}$$

Here,

$$D_{ab} = \sum_{f\,=\,1}^{3} (N_{af} N_{bf} - M_{af} M_{bf}) \tag{3}$$

and the OX_a axes of the rectangular coordinate system ($X_1X_2X_3$) are directed parallel to the translational vectors of the perovskite cell. It is assumed that the spontaneous polarization vectors of 71° (109°) domains in the rhombohedral phases Rh_{in} and Rh_{out} are parallel to each other ($\mathbf{P}_{Rj,\,\text{in}} \uparrow\uparrow \mathbf{P}_{Rj,\,\text{out}}$, $j = 1$–4) and that the planar walls separating the domains are aligned with the faces of the perovskite cell. The interphase boundaries (second-degree surfaces) are classified according to the signs of invariants of Eq. (2) [17]; that is,

$$I = D_{11} + D_{22} + D_{33}, \quad D = \det\|D_{ab}\|,$$

$$J = \begin{vmatrix} D_{11} & D_{12} \\ D_{21} & D_{22} \end{vmatrix} + \begin{vmatrix} D_{22} & D_{23} \\ D_{32} & D_{33} \end{vmatrix} + \begin{vmatrix} D_{33} & D_{31} \\ D_{13} & D_{11} \end{vmatrix}. \tag{4}$$

The analysis of invariants (4) calculated for the heterophase structures under consideration demonstrates that, in crystals of the xPT–PZN solid solutions in the range $0 \le x \le 0.08$, the condition of the existence of zero mean strain planes [16] is not satisfied. In other words, the elastic matching of the phases with the structural parameters determined in [12] does not provide complete relaxation of mechanical stresses at the X_{in}–Rh_{out} or Rh_{in}–Rh_{out} phase boundaries. The interaction of the phase X_{in} with the polydomain phase Rh_{out} at particular volume concentrations of 71° (109°) domains in the crystals at $x = 0$ favors both the formation of conical interfaces (due to the inequalities $DI < 0$ and $J > 0$) and a partial relaxation of mechanical stresses. According to [18], the criterion for this relaxation is a decrease in the quantity $|D|$. The inclusion of the weak tetragonal distortion of the perovskite cell in the phase X_{in} ($c_{\text{in}}/a_{\text{in}} \approx 1.001$ [13]) leads to the inequalities $DI > 0$ and $J > 0$. This means that, at any volume concentrations of 71° (109°) domains in the phase Rh_{out}, the surfaces defined by expression (2) degenerate into a point corresponding to a vertex of an imaginary cone. The elastic interaction of the rhombohedral phases Rh_{in} and Rh_{out} in the crystals at $x = 0.045$ and 0.08 favors the degeneration of surfaces (2) either into a pair of imaginary planes ($D = 0$, $J > 0$) or into a point corresponding to a vertex of an imaginary cone ($DI > 0$, $J > 0$). This behavior of the xPT–PZN crystals is primarily governed by the three equal (or, in the case of the tetragonal distortion of the phase X_{in} [13], almost equal) linear unit-cell parameters for each of the coexisting phases and also by the relatively small differences between the angles of shear $\omega_{\text{in}} = 90° - \alpha_{\text{in}}$ and $\omega_{\text{out}} = 90° - \alpha_{\text{out}}$ of their cells [12]. The balance of distortions of the coexisting phases with given symmetries changes upon formation of a 71° (109°) domain structure [16]. However, this change turns out to be insufficient for zero mean strain planes to appear at the X_{in}–Rh_{out} or Rh_{in}–Rh_{out} phase boundaries in the xPT–PZN ($0 \le x \le 0.08$) crystals.

3. TRANSITION REGIONS AND THE CONDITION OF COMPLETE STRESS RELAXATION

The aforementioned limited possibilities for relaxing stresses and the experimentally revealed relation between the unit cell parameters and the depth of x-ray penetration [13] have given impetus to investigating the specific features in the elastic matching of several polydomain crystal layers that form the so-called transition regions with varying unit cell parameters. Transition regions were previously observed in polydomain (twinned) crystals of $BaTiO_3$ [19] and KH_2PO_4 [20] ferroelectrics and in the coexisting phases of $CH_3NH_3Al(SO_4)_2 \cdot 12H_2O$ [21], $BaTiO_3$ [22], Pb_2CoWO_6 [18], and other compounds. These regions are characterized by a continuous change from the crystallographic parameters of one domain (twinned component, phase) to the corresponding crystallographic parameters of another domain (adjacent twinned component of the coexisting phase). The formation of transition regions in a number of heterogeneous crystals leads to a partial relaxation of internal stresses. This can be associated, for example, with the strong spontaneous strains of the unit cell in the $CH_3NH_3Al(SO_4)_2 \cdot 12H_2O$ compound [21] or with the jumps in the unit cell parameters that do not satisfy the condition of the existence of zero mean strain planes [8, 16] at interphase boundaries in the Pb_2CoWO_6 compound [18].

Within the framework of the proposed model, the transition region is represented by a set of polydomain layers adjacent to each other along the {100} planes of the perovskite cell. It is assumed that the linear unit-cell parameters $a_i = b_i = c_i$ and the angles of shear $\omega_i = 90° - \alpha_i$ vary from layer to layer. The spontaneous polarization vectors of 71° (109°) domains in the rhombohedral phases are oriented in the adjacent layers in the manner shown in the Fig. 1. The distortion matrices of the ith and $(i + 1)$st layers depicted in Fig. 1a can be written respectively as

---

$$\|M_{ab}^{(i)}\| = \left(\frac{1}{a_0}\right)\begin{pmatrix} a_i\cos\omega_i & a_i\sin\omega_i(2m_i - 1) & a_i\sin\omega_i(2m_i - 1) \\ a_i\sin\omega_i(2m_i - 1) & a_i\cos\omega_i & a_i\sin\omega_i \\ a_i\sin\omega_i(2m_i - 1) & a_i\sin\omega_i & a_i\cos\omega_i \end{pmatrix},$$

$$\|M_{ab}^{(i+1)}\| = \left(\frac{1}{a_0}\right)\begin{pmatrix} a_{i+1}\cos\omega_{i+1} & a_{i+1}\sin\omega_{i+1}(2m_{i+1} - 1) & -a_{i+1}\sin\omega_{i+1}(2m_{i+1} - 1) \\ a_{i+1}\sin\omega_{i+1}(2m_{i+1} - 1) & a_{i+1}\cos\omega_{i+1} & -a_{i+1}\sin\omega_{i+1} \\ -a_{i+1}\sin\omega_{i+1}(2m_{i+1} - 1) & -a_{i+1}\sin\omega_{i+1} & a_{i+1}\cos\omega_{i+1} \end{pmatrix}.$$

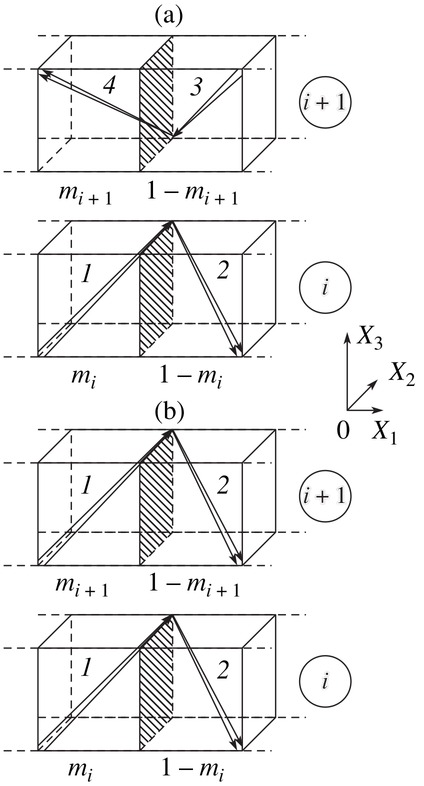

Fig. 1. Schematic drawing of the polydomain layers in rhombohedral transition regions of the *x*PT–PZN crystals. Designations: m_i is the volume concentration of domains of type *1* in the *i*th layer, and m_{i+1} is the volume concentration of domains of (a) type *4* or (b) type *1* in the $(i + 1)$st layer. Arrows indicate the spontaneous polarization vectors $\mathbf{P}_{Rj}$ of domains with $j = 1$–4. Hatched planes correspond to 71° (109°) domain walls aligned parallel to the (100) plane of the perovskite cell.

Here, a_0 is the unit cell parameter extrapolated to room temperature for the cubic phase, and a_i and ω_i are the unit cell parameters of the rhombohedral phase in the *i*th layer. Taking into account the alternation of the layers, the distortion matrices of the $(i + 2)$nd, $(i + 4)$th, …, and $(i + 2p)$th layers can be obtained from the distortion matrix $\|M_{ab}^{(i)}\|$ by replacing the index i with the indices $i + 2$, $i + 4$, …, and $i + 2p$, respectively. Similarly, the distortion matrices of the $(i + 3)$rd, …, and $(i + 2p + 1)$st layers can be obtained from the distortion matrix $\|M_{ab}^{(i+1)}\|$ by replacing the index $i + 1$ with the indices $i + 3$, …, and $i + 2p + 1$, respectively. The distortion matrix $\|M_{X,ab}\|$ of the phase X has nonzero matrix elements $M_{X,gg} = a_X/a_0$, where a_X is the unit cell parameter of the phase X; and $g = 1$, 2, and 3. For the structure drawn in Fig. 1b, the distortion matrices of the *i*th, $(i + 1)$st, …, and $(i + p)$th layers are equal to the matrices $\|M_{ab}^{(i)}\|$, $\|M_{ab}^{*(i+1)}\|$, …, $\|M_{ab}^{*(i+p)}\|$, respectively. Here, the matrix $\|M_{ab}^{*(i+p)}\|$ is derived from the matrix $\|M_{ab}^{(i)}\|$ by simply substituting the index $i + p$ for the index i (where $p = 1, 2, \ldots$).

By analogy with matrix elements (3), the elements of the matrix $\|D_{ab}^{(i,i+1)}\|$ for the polydomain layers depicted in Figs. 1a and 1b are defined respectively as

$$D_{ab}^{(i,i+1)} = \sum_{f=1}^{3}(M_{af}^{(i+1)}M_{bf}^{(i+1)} - M_{af}^{(i)}M_{bf}^{(i)}),$$
$$D_{ab}^{(i,i+1)} = \sum_{f=1}^{3}(M_{af}^{*(i+1)}M_{bf}^{*(i+1)} - M_{af}^{(i)}M_{bf}^{(i)}). \tag{5}$$

These layers are matched along the zero mean strain plane [16] under the conditions

$$\det\|D_{ab}^{(i,i+1)}\| = 0, \quad J^{(i,i+1)} \le 0, \tag{6}$$

and the orientation of the interphase boundaries $\mathbf{n}_i(h_i\, k_i\, l_i)$ is calculated from the formulas obtained by Metrat [23]. The invariant $J^{(i,i+1)}$ in conditions (6) is determined from relationships (4) by replacing the matrix elements D_{ab} with the matrix elements $D_{ab}^{(i,i+1)}$ given by formulas (5). The analysis of the conditions providing the existence of zero mean strain planes is substantially simplified under the assumption that the volume concentrations of domains in all the layers under consideration are equal to each other; i.e., $m_i = 1/2$, where $i = 1, 2, \ldots, N$ for the coexistence of the rhombohedral phases Rh_{in} and Rh_{out} and $i = 2, 3, \ldots, N$ or $i = 1, 2, \ldots, N - 1$ for the coexistence of the phase X_{in} and the rhombohedral phase Rh_{out}.[1] This implies that, when changing over from layer to layer, the position of the domain walls parallel to the (100) plane remains virtually unchanged and adjacent domains *1–4* or *2–3* (Fig. 1a) and *1–1* or *2–2* (Fig. 1b) form structures with varying unit-cell parameters. In this case, for both systems of layers (Fig. 1), we have

$$\det\|D_{ab}^{(i,i+1)}\| = \begin{vmatrix} D_{11}^{(i,i+1)} & 0 & 0 \\ 0 & D_{22}^{(i,i+1)} & D_{23}^{(i,i+1)} \\ 0 & D_{23}^{(i,i+1)} & D_{22}^{(i,i+1)} \end{vmatrix}$$

and only the matrix elements $D_{23}^{(i,i+1)}$ differ from each other due to the nonequality $M_{af}^{(i+1)} \ne M_{af}^{*(i+1)}$ [see formulas (5)].

---

[1] Note that, in the study of dual structures [12], the *x*PT–PZN crystals were heated to temperatures considerably higher than the temperature of the phase transition to the paraelectric cubic phase and were then cooled in order to remove residual effects. These effects were induced by the preceding action of the poling field, without which the volume concentrations of 71° (109°) domains of different types in the rhombohedral phases could become almost equal.

The polydomain layers under consideration are separated by boundaries, i.e., zero mean strain planes, when the following relationships for the unit cell parameters satisfy conditions (6):

$$a_{i+1}\cos\omega_{i+1} = a_i\cos\omega_i \tag{7a}$$

or

$$a_{a+1}(\cos\omega_{i+1} + \sin\omega_{i+1}) = a_i(\cos\omega_i - \sin\omega_i) \tag{7b}$$

or

$$a_{a+1}(\cos\omega_{i+1} - \sin\omega_{i+1}) = a_i(\cos\omega_i + \sin\omega_i) \tag{7c}$$

for four types of domains in Fig. 1a and relationship (7a) or

$$a_{a+1}(\cos\omega_{i+1} + \sin\omega_{i+1}) = a_i(\cos\omega_i + \sin\omega_i) \tag{7d}$$

or

$$\begin{aligned} &a_{i+1}^2\cos\omega_{i+1}(\cos\omega_{i+1} + 2\sin\omega_{i+1}) \\ &\quad = a_i^2\cos\omega_i(\cos\omega_i + 2\sin\omega_i) \end{aligned} \tag{7e}$$

for two types of domains in Fig. 1b.

For the elastic matching of the phase X_{in} and the polydomain rhombohedral phase Rh_{out}, it is assumed that, in relationships (7), $a_i = a_X$ and $\omega_i = 0$, where $i = 1$ or $i = N$. The corresponding interfaces between the layers in the transition regions of the *x*PT–PZN ($0 \le x \le 0.08$) crystals are nearly parallel to the {100} planes of the perovskite cell and, hence, to the 71° (109°) domain walls in the rhombohedral phases.

4. RESULTS OF CALCULATIONS AND DISCUSSION

The numerical estimates given in Table 1 indicate that complete relaxation of internal stresses upon formation of transition regions can occur in different ways. This follows from relationships (7) for regular and irregular changes in the angle of shear ω_i of the unit cell. The results obtained suggest that the elastic matching involving four types of 71° (109°) domains (Fig. 1a) in the *x*PT–PZN rhombohedral crystals is more probable. However, the elastic matching with the participation of two types of 71° (109°) domains (Fig. 1b) is also of interest because the two conditions (7d) and (7e) for the existence of zero mean strain planes are simultaneously satisfied over the entire transition region of the crystal at $x = 0$ (see Note 3 to Table 1). In this case, the elastic matching is achieved in layers in which the angles of shear of the perovskite cells are related by the expression

$$\omega_{i+1} - \omega_i = \omega_{i+2} - \omega_{i+1} = \ldots = \omega_N - \omega_{N-1} = \text{const}, \tag{8}$$

irrespective of $\operatorname{sgn}(\omega_{i+1} - \omega_i)$. For comparison, we note that relationship (8) for the crystal at $x = 0.045$ is valid on limited intervals $[\omega_i; \omega_{i+p}]$. For the crystal at $x = 0.08$, such intervals are entirely absent when the angle of shear ω_i is decreased from the value corresponding to the rhombohedral phase Rh_{out}. The parameters of the perovskite cell a_i and ω_i for the crystals at concentrations $x \ge 0.045$ [12] satisfy the condition of the existence of zero mean strain planes only when the elastic matching involves four types of 71° (109°) domains (Table 1).

It is interesting to note that, among the five conditions given by formulas (7) for the existence of zero mean strain planes, the four, three, and two conditions are satisfied at $x = 0$, 0.045, and 0.08, respectively. This circumstance, together with the validity of relationship (8) on limited intervals and the applicability of only one scheme for the elastic matching (Fig. 1a), allow us to assume that the formation of Rh_{in}–Rh_{out} dual structures and transition regions in the crystals at concentrations $x \ge 0.045$ is affected by the tetragonal phase. It is known [14] that, at a molar concentration $x_{\text{tr}} \approx 0.045$, the *x*–*T* phase diagram of the *x*PT–PZN system is characterized by a triple point. In the vicinity of this point, the phase diagram involves regions of thermodynamic stability of the cubic phase *Pm*3*m*, the rhombohedral phase *R*3*m*, and the tetragonal phase *P*4*mm*. The studied crystals upon cooling without an electric field undergo the first-order phase transitions *C*–*Rh* ($0 < x < x_{\text{tr}}$) or *C*–*T*–*Rh* ($x_{\text{tr}} < x \lesssim 0.09$) [1, 14]. As follows from the recent results obtained by Ohwada *et al.* [24], the *C*–*T*–*X* phase transitions are observed at a concentration $x = 0.08$.

According to our estimates from the formulas derived in [4, 8, 23], the optimum volume concentrations of 90° domains in the intermediate tetragonal phase (Table 2), which correspond to zero mean strain planes at interphase boundaries, change only slightly with a decrease in the temperature *T* in the vicinity of the morphotropic boundary. As a consequence, the low-temperature rhombohedral phase ($x = 0.09$) or the new phase *X* ($x = 0.08$) is formed without noticeable changes in the 90° domain structure that arises upon the *C*–*T* first-order phase transition. For comparison, we note that the constancy of the volume concentrations of 90° domains was also revealed in limited temperature ranges in the vicinity of the *Pm*3*m*–*R*3*m*–*P*4*mm* triple point of the $\text{Pb}(\text{Zr}_{1-z}\text{Ti}_z)\text{O}_3$ system with a perovskite-type structure [25].

As regards the *x*PT–PZN crystals, one of the factors responsible for the aforementioned stability of the 90° domain structure is associated with the temperature dependences of the linear unit-cell parameters $a_C(T)$, $a_{Rh}(T)$, and $a_X(T)$ in the cubic, rhombohedral, and *X* phases, respectively [1, 24]. At $x = \text{const}$, the relationships $da_C/dT \approx da_{Rh}/dT$ and $da_C/dT \approx da_X/dT$ hold true. Extrapolating the dependence $a_C(T)$ to the stability region of the rhombohedral and *X* phases leads to the approximate equalities $a_C \approx a_{Rh}$ ($x = 0.09$) and $a_C \approx a_X$ ($x = 0.08$), respectively. Another factor responsible for

Table 1. Calculated parameters of the perovskite cell in transition regions of the *x*PT–PZN crystals at room temperature

$x = 0$, polydomain layers in Fig. 1a										
ω_i, deg	0	0.005	0.010	0.015	0.020	0.080				
a_i, 10^{-10} m	4.067 (4.067(1))	4.067	4.066	4.064	4.061	(4.061(1))	According to conditions (7b) and (7a)			
ω_i, deg	0	0.01	0.02	0.03	0.08					
a_i, 10^{-10} m	4.067 (4.067(1))	4.066	4.064	4.061	(4.061(1))		According to conditions (7b) and (7a)			
$x = 0$, polydomain layers in Fig. 1b										
ω_i, deg	0	0.01	0.02	0.03	0.04	0.05	0.06	0.07	0.08	
a_i, 10^{-10} m	4.067 (4.067(1))	4.066	4.066	4.065	4.064	4.064	4.063	4.062	4.061	According to condition (7d) and (7e)
ω_i, deg	0.08	0.07	0.06	0.05	0.04	0.03	0.02	0.01	0	
a_i, 10^{-10} m	4.061 (4.061(1))	4.062	4.062	4.063	4.064	4.065	4.065	4.066	4.067	According to condition (7d) and (7e)
$x = 0.045$, polydomain layers in Fig. 1a										
ω_i, deg	0.070	0.075	0.080	0.100						
a_i, 10^{-10} m	4.070 (4.070(1))	4.060	4.049	(4.045(1))	According to conditions (7b) and (7a)					
ω_i, deg	0.07	0.08	0.09	0.10						
a_i, 10^{-10} m	4.070 (4.070(1))	4.059	4.047	(4.045(1))	According to conditions (7b) and (7a)					
ω_i, deg	0.070	0.085	0.095	0.100						
a_i, 10^{-10} m	4.070 (4.070(1))	4.059	4.046	(4.045(1))	According to conditions (7b) and (7a)					
ω_i, deg	0.100	0.095	0.090	0.070						
a_i, 10^{-10} m	4.045	4.059	4.072	(4.070(1))	According to conditions (7c) and (7a)					
ω_i, deg	0.100	0.09	0.08	0.07						
a_i, 10^{-10} m	4.045	4.058	4.071	(4.070(1))	According to conditions (7c) and (7a)					
$x = 0.08$, polydomain layers in Fig. 1a										
ω_i, deg	0.070	0.075	0.080	0.110						
a_i, 10^{-10} m	4.066 (4.066(1))	4.056	4.045	(4.046(1))	According to conditions (7b) and (7a)					
ω_i, deg	0.07	0.08	0.09	0.11						
a_i, 10^{-10} m	4.066 (4.066(1))	4.055	4.043	(4.046(1))	According to conditions (7b) and (7a)					

Notes: 1. The experimental values of the linear unit-cell parameters a_i [12] for the rhombohedral phase Rh_{in} or the phase X_{in} (at the minimum angle of shear ω_i) and the rhombohedral phase Rh_{out} (at the maximum angle of shear ω_i) are given in parentheses.

2. Condition (7a) is satisfied for the unit cell parameters of the last two layers (see the data in the right part of the table), except for the elastic matching of domains shown in Fig. 1b at $x = 0$.

3. The differences between the linear unit-cell parameters a_i calculated from formulas (7d) and (7e) at $x = 0$ and fixed angles ω_i do not exceed 0.5% due to the inequality $\sin\omega_i \ll \cos\omega_i$.

Table 2. Optimum volume concentrations of 90° domains in the tetragonal phase according to the calculations for the first-order phase transitions in the *x*PT–PZN crystals

x	Experimental temperature dependence of the unit cell parameters	Phase transition	Optimum volume concentration of 90° domains
0.08	Data taken from [24]	$C \longrightarrow T$ $T \longrightarrow X$	0.642; 0.358 0.619; 0.381
0.09	Data taken from [1]	$C \longrightarrow T$ $T \longrightarrow Rh$	0.636; 0.364 0.616; 0.384

Notes: 1. The tetragonal phase is assumed to be separated into 90° domains with the spontaneous polarization vectors $\mathbf{P}_{T1}(0; 0; P)$ and $\mathbf{P}_{T2}(P; 0; 0)$. The rhombohedral phase is assumed to be separated into 71° (109°) domains with the spontaneous polarization vectors $\mathbf{P}_{Rj}$ (j = 1–4, see Section 3), and the crystal has cubic symmetry, because the volume concentrations of these domains are equal to one another. According to the experimental data obtained by Ohwada *et al.* [24], the phase *X* also has macroscopic cubic symmetry.

2. Any deviations from the equality of the volume concentrations of 71° (109°) domains in the rhombohedral phase lead to an insignificant change (by less than 1%) in the optimum concentration of 90° domains in the tetragonal phase upon transition from the tetragonal phase to the rhombohedral phase. In particular, upon formation of the single-domain rhombohedral phase with the spontaneous polarization vectors $\mathbf{P}_{R1}$ and $\mathbf{P}_{R4}$, the optimum volume concentrations of 90° domains in the tetragonal phase are equal to 0.620 and 0.380, respectively [4, 8].

the stability of the 90° domain structure stems from the specific features of the jumps in the unit cell parameters a_T and c_T of the tetragonal phase upon *C*–*T* and *T*–*Rh* (or *T*–*X*) phase transitions. According to the experimental data obtained by Kuwata *et al.* [1], the relationship $(a_T - a_C)/(c_T - a_C) \approx (a_{Rh} - a_T)/(a_{Rh} - c_T)$ is valid at x = 0.09. Furthermore, the results reported by Ohwada *et al.* [24] indicate that a similar relationship, i.e., $(a_T - a_C)/(c_T - a_C) \approx (a_X - a_T)/(a_X - c_T)$, is satisfied at $x = 0.08$. Hence, we can assume that the *x*PT–PZN ($x_{\mathrm{tr}} < x < 0.08$) crystals are characterized by similar temperature dependences of the unit cell parameters. Consequently, the formation of dual structures can be assisted by the *T*–*X*–*Rh* three-phase states in which 90° domains of the tetragonal phase provide efficient relaxation of internal mechanical stresses at the *T*–*X* and *T*–*Rh* phase boundaries. Upon cooling of the crystal, the domains of the tetragonal phase disappear and the fields of internal mechanical stresses change significantly. This favors the formation of transition regions [18]. The coexistence of the tetragonal, *X*, and rhombohedral phases is confirmed by the fact that three-phase states are inherent in the *x*PT–PZN system at room temperature. Recently, Bertram *et al.* [26] revealed the coexistence of the tetragonal, monoclinic (symmetry *Pm*), and rhombohedral phases in the vicinity of the morphotropic boundary with complete relaxation of internal mechanical stresses [10]. An increase or a decrease in the molar concentration *x* results in the formation of two-phase states, namely, the monoclinic–tetragonal or rhombohedral–monoclinic states, respectively [26]. These two states are characterized by complete stress relaxation [8, 10].

5. CONCLUSIONS

Thus, the results obtained in this work can be summarized as follows.

(1) The concept of transition regions in ferroelectric and related crystals was applied for the first time to the description of the dual structures in crystals of *x*PN–PZN solid solutions in the range $0 \le x \le 0.08$. The fundamental difference between the new model of transition regions and the models proposed earlier in [18–20] lies in the assumption regarding the elastic matching of polydomain layers in which the balance of longitudinal and shear distortions is provided by 71° (109°) domains. The proposed schemes of the elastic matching of 71° (109°) domains in the rhombohedral phases (Fig. 1) along the {100} boundaries (zero mean strain planes) and the corresponding relationships (7) for the change in the unit cell parameters (Table 1) suggest that the relaxation of mechanical stresses upon the formation of dual structures can occur in different ways.

(2) The formation of dual structures in crystals of the *x*PN–PZN solid solutions at $x \ge 0.045$ is favored by the following circumstances: (i) the temperature dependences of the unit cell parameters $a_C(T)$, $a_{Rh}(T)$, and $a_X(T)$ are similar to each other; and (ii) the optimum concentrations of 90° domains in the intermediate tetragonal phase remain almost unchanged (Table 2). This leads to complete relaxation of internal mechanical stresses in the *T*–*X*, *T*–*Rh*, and *T*–*X*–*Rh* heterophase states.

ACKNOWLEDGMENTS

The author would like to thank A.V. Turik (Russia), Z.-G. Ye (Canada), M. Kamlah (Germany), and G. Xu (United States) for their ongoing interest in the investigation of polydomain and heterophase ferroelectric crystals.

REFERENCES

1. J. Kuwata, K. Uchino, and S. Nomura, Ferroelectrics **37** (1–4), 579 (1981).
2. S.-E. Park and W. Hackenberger, Curr. Opin. Solid State Mater. Sci. **6** (1), 11 (2002).
3. W. Ren, S.-F. Liu, and B. K. Mukherjee, Appl. Phys. Lett. **80** (17), 3174 (2002).
4. V. Yu. Topolov and A. V. Turik, Fiz. Tverd. Tela (St. Petersburg) **44** (7), 1295 (2002) [Phys. Solid State **44** (7), 1355 (2002)].
5. S.-E. Park and T. R. Shrout, J. Appl. Phys. **82** (4), 1804 (1997).

6. K. Fujishiro, R. Vlokh, Y. Uesu, Y. Yamada, J.-M. Kiat, B. Dkhil, and Y. Yamashita, Jpn. J. Appl. Phys., Part 1 **37** (9B), 5246 (1998).
7. V. Yu. Topolov and Z.-G. Ye, Ferroelectrics **253** (1–4), 71 (2001).
8. V. Yu. Topolov, Phys. Rev. B **65** (9), 094207 (2002).
9. V. Yu. Topolov, Fiz. Tverd. Tela (St. Petersburg) **45** (7), 1235 (2003) [Phys. Solid State **45** (7), 1295 (2003)].
10. V. Yu. Topolov, J. Phys.: Condens. Matter **16** (13), 2455 (2004).
11. Z.-G. Ye, M. Dong, and L. Zhang, Ferroelectrics **229** (1–4), 223 (1999).
12. G. Xu, H. Hiraka, G. Shirane, and K. Ohwada, Appl. Phys. Lett. **84** (20), 3975 (2004).
13. G. Xu, Z. Zhong, Y. Bing, Z.-G. Ye, C. Stock, and G. Shirane, Phys. Rev. B **67** (10), 104 102 (2003).
14. D. La-Orauttapong, B. Noheda, Z.-G. Ye, P. M. Gehring, J. Toulouse, D. E. Cox, and G. Shirane, Phys. Rev. B **65** (14), 144 101 (2002).
15. G. Xu, D. Viehland, J. F. Li, P. M. Gehring, and G. Shirane, Phys. Rev. B **68** (21), 212 410 (2003).
16. V. Yu. Topolov, L. E. Balyunis, A. V. Turik, I. S. Ba, and O. E. Fesenko, Izv. Akad. Nauk, Ser. Fiz. **56** (10), 127 (1992).
17. G. A. Korn and T. M. Korn, *Mathematical Handbook for Scientists and Engineers* (McGraw-Hill, New York, 1968; Nauka, Moscow, 1978), p. 90.
18. V. Yu. Topolov, H. Rabe, and H. Schmid, Ferroelectrics **146** (1–4), 113 (1993).
19. N. S. Afonikova, V. Sh. Shekhtman, and I. M. Shmyt'ko, Fiz. Tverd. Tela (Leningrad) **27** (11), 3201 (1985) [Sov. Phys. Solid State **27** (11), 1929 (1985)].
20. N. S. Afonikova, V. V. Borovikov, and I. M. Shmyt'ko, Fiz. Tverd. Tela (Leningrad) **29** (3), 813 (1987) [Sov. Phys. Solid State **29** (3), 462 (1987)].
21. B. Sh. Bagautdinov, V. F. Glushkov, V. K. Magataev, and I. M. Shmyt'ko, Fiz. Tverd. Tela (Leningrad) **33** (11), 3128 (1991) [Sov. Phys. Solid State **33** (11), 1767 (1991)].
22. T. Malis and H. Gleiter, J. Appl. Phys. **50** (7), 4920 (1979).
23. G. Metrat, Ferroelectrics **26** (1–4), 801 (1980).
24. K. Ohwada, K. Hirota, P. W. Rehrig, Y. Fujii, and G. Shirane, Phys. Rev. B **67** (9), 094111 (2003).
25. V. Yu. Topolov and A. V. Turik, Fiz. Tverd. Tela (St. Petersburg) **43** (8), 1525 (2001) [Phys. Solid State **43** (8), 1585 (2001)].
26. R. Bertram, G. Reck, and R. Uecker, J. Cryst. Growth **253** (1–4), 212 (2003).

Translated by O. Borovik-Romanova

Physics of the Solid State, Vol. 47, No. 7, 2005, pp. 1353–1357. Translated from Fizika Tverdogo Tela, Vol. 47, No. 7, 2005, pp. 1304–1308.

LOW-DIMENSIONAL SYSTEMS AND SURFACE PHYSICS

Effect of Temperature on Structural Transformations of Nickel Nanoclusters

Yu. Ya. Gafner*, S. L. Gafner*, R. Meyer, L. V. Redel*, and P. Entel*****
** Khakas State University, Abakan, 655017 Russia*
e-mail: ygafner@khsu.ru
*** Département de Physique, Université de Montréal (Québec), Montréal, H3C 3J7 Canada*
**** Universität Duisburg-Essen, Duisburg, 47048 Germany*
Received July 16, 2004

Abstract—The gas-phase condensation of nickel nanoclusters is simulated by the molecular dynamics method with the use of tight-binding potentials. It is revealed that subsequent heating of the synthesized clusters to temperatures of 400–500 K leads to a substantial improvement of their internal structure with a hexagonal close-packed phase predominating. Upon heating of the nanoparticles above the melting point and subsequent gradual cooling, the formation of a cluster structure depends strongly on the cooling rate. The inference is made that heating of the nanoclusters synthesized from a gas phase can be used for the controlled formation of nickel nanoparticles with a predicted structure. *© 2005 Pleiades Publishing, Inc.*

1. INTRODUCTION

Nanoparticles possess a great variety of interesting physical properties that differ from those exhibited by bulk materials due to an extremely large surface-to-volume ratio. Since these properties of nanoparticles can be used in various technical devices, investigations into the processes controlling the formation of nanoparticles are of considerable interest. The general introduction to the physics of nanoparticles and nanomaterials can be found, for example, in [1–3].

At present, there exist numerous techniques for synthesizing nanoparticles of different chemical elements. Among these methods, gas-phase synthesis is of crucial importance in preparing very small, chemically pure particles with approximately equal sizes [4]. In the gas-phase synthesis, nanoparticles are condensed from a supersaturated metal vapor in a noble-gas atmosphere [5–7].

Over the course of more than 30 years, the structure of metallic clusters has been intensively investigated using theoretical and experimental methods. Computer simulations have demonstrated that, unlike conventional bulk materials, nanoclusters are characterized by several structural modifications. For example, nanoclusters of metals with a face-centered cubic lattice can exist in face-centered cubic, hexagonal close-packed, icosahedral, and decahedral modifications [8–10]. However, it should be noted that currently available experimental methods for determining the structure of metallic nanoclusters have a number of disadvantages. In particular, diffraction scattering techniques are appropriate only in the case of cluster ensembles and, hence, their use leads to the averaging of the properties exhibited by individual clusters.

Furthermore, considerable difficulties are encountered in interpreting diffraction data [11, 12]. For this reason, direct examination of the structure of individual clusters located on a substrate has often been performed with a high-resolution electron microscope [13, 14].

However, a high-resolution electron microscope forms only a projection image of the structure and correct interpretation of the results requires further computer simulation. Moreover, the high-energy electron beam necessary for high-resolution electron microscopy can heat particles and, as a consequence, they can undergo structural transformations. This is especially true in regard to small-sized clusters [15].

Computer simulation is the most suitable method for studying the internal structure of nanoparticles. The use of modern computers and realistic interatomic potentials makes it possible to simulate nanoparticles accurately at times of the order of several nanoseconds. However, the majority of previously performed calculations were aimed at searching for a structure with the lowest energy at $T = 0$ K and at revealing a correlation between this energy and the cluster size.

In this work, we carried out a molecular dynamics simulation of the influence of temperature on the transformation of an internal structure of nickel nanoclusters prepared through gas-phase condensation.

2. SIMULATION TECHNIQUE

The interatomic interactions were calculated using the tight-binding potentials [16] with a fixed cutoff radius. Although complex models (for example, those based on *ab initio* methods) seem more realistic, we used a simpler, more efficient computer program for simulating a system involving several thousands of atoms in the time interval up to several nanoseconds. It should be noted that, even in the current state of the art in the development of high-performance computers, an *ab initio* simulation of this system remains impossible. On the other hand, the potentials proposed by Cleri and Rosato [16] have already worked well in cluster studies [17–20].

In our model, the potential energy of the system was calculated from the relationship

$$E = \sum_{i}\left[-\left(\sum_{i \neq j}\xi_{\alpha\beta}^{2}e^{-2q_{\alpha\beta}(r_{ij}/r_{\alpha\beta}^{0}-1)}\right)^{1/2} + \frac{1}{2}\sum_{i \neq j}A_{\alpha\beta}e^{-p_{\alpha\beta}(r_{ij}/r_{\alpha\beta}^{0}-1)}\right],$$

where r_{ij} is the distance between the ith and jth atoms, and α and β stand for atoms of different types. In our calculation, the parameters of the components of the simulated system ($\xi_{\alpha\beta}$, $p_{\alpha\beta}$, $A_{\alpha\beta}$, $q_{\alpha\beta}$, $r_{\alpha\beta}^{0}$) were taken directly from [16]. The velocities of atomic motion in the simulation were determined using the Verlet algorithm with a time step $h = 2$ fs.

The computer simulation was performed with the standard methods described in [21]. In the computer experiment simulating the gas-phase condensation of nanoparticles, a nickel cluster consisting of 8000 atoms arranged in a simple cubic lattice with a lattice parameter equal to $15a_B$ (where a_B is the Bohr radius) was used as the initial configuration with periodic boundary conditions. The choice of the simple cubic lattice for the simulation may seem somewhat unexpected. However, the distance between the atoms in this lattice appears out to be larger than the cutoff radius r_c (for the interaction potential used in our case, $r_c = 11.1a_B$). Moreover, the initial velocities of atomic motion are randomly specified in accordance with the Maxwell distribution at the initial temperature $T_i = 1000$ K. This gives grounds to believe that the simulated system very rapidly loses its memory regarding the initial distribution.

An important factor in the simulation of the condensation process is the interaction of the system with a thermal reservoir. Since the formation of clusters is accompanied by the release of a large amount of energy, this interaction is required to eliminate a physically incorrect considerable increase in the temperature. In the simulation experiment, we used an Anderson thermostat [21, 22] to cool nickel atoms to the final condensation temperature $T_f = 77$ K.

Within this stochastic model, the simulated atoms experience random collisions with virtual particles. The effect of collisions manifests itself in the fact that the velocity of real particles at the $(n + 1)$st step in the molecular dynamics simulation experiment decreases in a random manner as compared to the velocity corresponding to the Maxwell distribution at the nth step. In our case, these collisions simulate the interaction with a noble gas used in real experiments on the gas-phase synthesis of nanoclusters. During the simulation experiment, the temperature was determined from the mean kinetic energy of atoms.

3. RESULTS AND DISCUSSION

In the framework of the problem under consideration, our primary interest is in investigating the temperature dependence of the structural properties of the nickel nanoclusters prepared through the gas-phase condensation. During the investigation, we first simulated direct experiments on the condensation [3, 23] and then analyzed the following situations.

(1) The nanoparticles condensed from the gas phase are gradually heated from $T = 77$ K for the purpose of forming a more perfect structure. In this simulation, we revealed two typical tendencies.

(i) For nickel clusters with a close-packed core and a small number of stacking faults, the long-range order is slightly disturbed already at $T = 600$ K and completely destroyed at $T = 1100$ K.

(ii) For nickel clusters in which there is no well-defined close-packed core, intensive kinetic processes result in the formation of a similar core in the temperature range from 300 to 600 K (Fig. 1). A further increase in the temperature is accompanied by the destruction of the long-range order, and this process is completed at $T = 1100$ K. Therefore, the heating of condensed nickel nanoparticles for several nanoseconds to temperatures $T = 400$–500 K leads to a substantial improvement of their internal structure with a hexagonal close-packed phase predominating.

(2) The nickel nanoclusters synthesized from the gas phase are heated to the temperature $T = 1800$ K, which is considerably higher than the melting point; then, the nanoclusters are gradually cooled to liquid-nitrogen temperature at different rates. For the majority of nickel nanoclusters, this procedure results in an increase in the size of the close-packed cluster core. When the cluster has already had a regular structure prior to melting, the number of atoms involved in the close packing increases by only a few percent. If this type of structure is absent before melting, the heating and subsequent gradual cooling lead to the formation of a regular structure and, in a number of cases, the percentage of atoms involved in local close packing increases by a factor of two.

A comparison of the structures obtained by two methods shows that gradual cooling of the clusters from the molten state leads to a better improvement of the cluster structure; however, the final result depends substantially on the cooling rate. The best results are obtained at a cooling rate $U = 0.025$ ps^{-1}. For other cooling rates ($U = 0.035, 0.015, 0.005$ ps^{-1}), the fraction

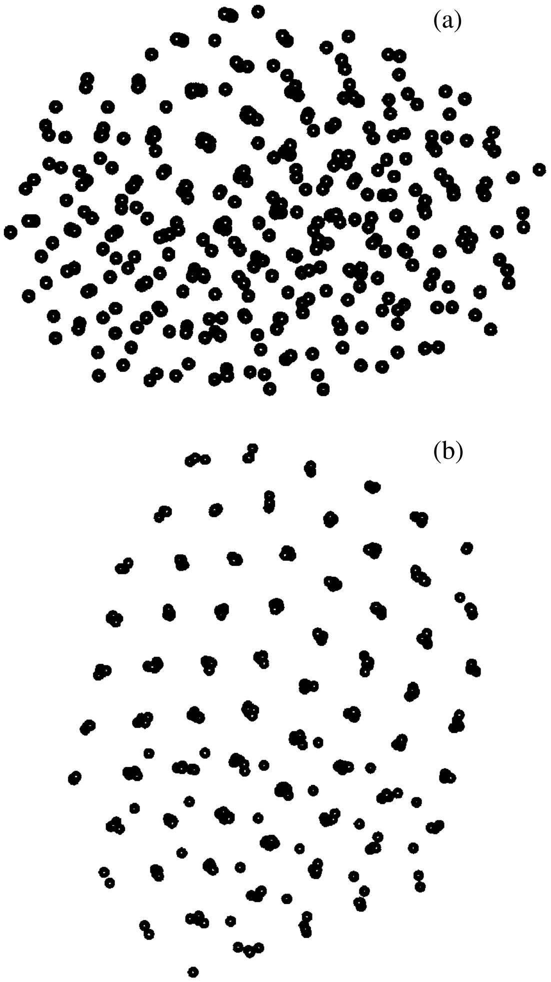

Fig. 1. Nickel clusters ($N = 340$ atoms) synthesized from the gas phase at T = (a) 200 and (b) 400 K.

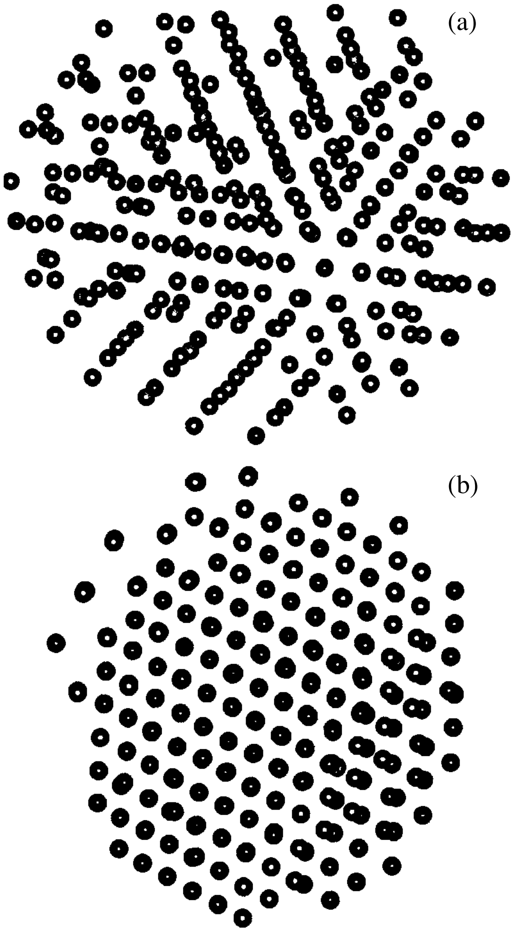

Fig. 2. Nickel cluster configurations (N = 527 atoms) obtained upon cooling in the temperature range from 1800 to 77 K. Cooling rates, ps^{-1}: (a) 0.015 (icosahedral phase) and (b) 0.025 (face-centered cubic phase).

of atoms involved in local close packing in the cluster decreases.

Moreover, the cluster structures before and after melting differ qualitatively. In particular, upon free condensation of nickel atoms from the gas phase, the majority of clusters have a hexagonal close-packed structure. When the nanoparticles are heated to temperatures above the melting point and then are gradually cooled, the final structure also depends very strongly on the cooling rate. For example, upon cooling at the rate U = 0.025 ps^{-1}, the cluster structure can transform either into the face-centered cubic modification or into the hexagonal close-packed modification in approximately equal proportions. However, cooling at other rates (U = 0.035, 0.015, 0.005 ps^{-1}) leads to the formation of either a hexagonal close-packed phase in most cases or an icosahedral phase in rare cases (Fig. 2).

In order to illustrate the transformation of the cluster structure and the change in the cluster shape with increasing temperature, we consider two large-sized clusters (N = 1816, 2082 atoms) synthesized from the gas phase. The first cluster is formed through the agglomeration of two nearly spherical nanoparticles, with the symmetry corresponding to a mixture of face-centered cubic and hexagonal close-packed structures (Fig. 3a) and a disordered region at their boundary. Then, the simulated cluster is heated from 77 to 600 K and, then, to 900 K.

During heating, the cluster components aggregate very rapidly (for 2 ns) into a single cluster with the initial structure (a mixture of face-centered cubic and hexagonal close-packed structures) (Figs. 3b, 3c). Despite the similarity of their internal structures, the clusters formed upon heating to T = 600 K and T = 900 K differ significantly in appearance. Specifically, the shape of the cluster heated to T = 600 K is similar to that of the initial cluster (T = 77 K), whereas the cluster heated to T = 900 K “forgets” its initial shape and takes the form of an almost regular ellipsis (Fig. 3c). This phenomenon can be explained by the enhancement of surface diffusion during heating and, consequently, by the

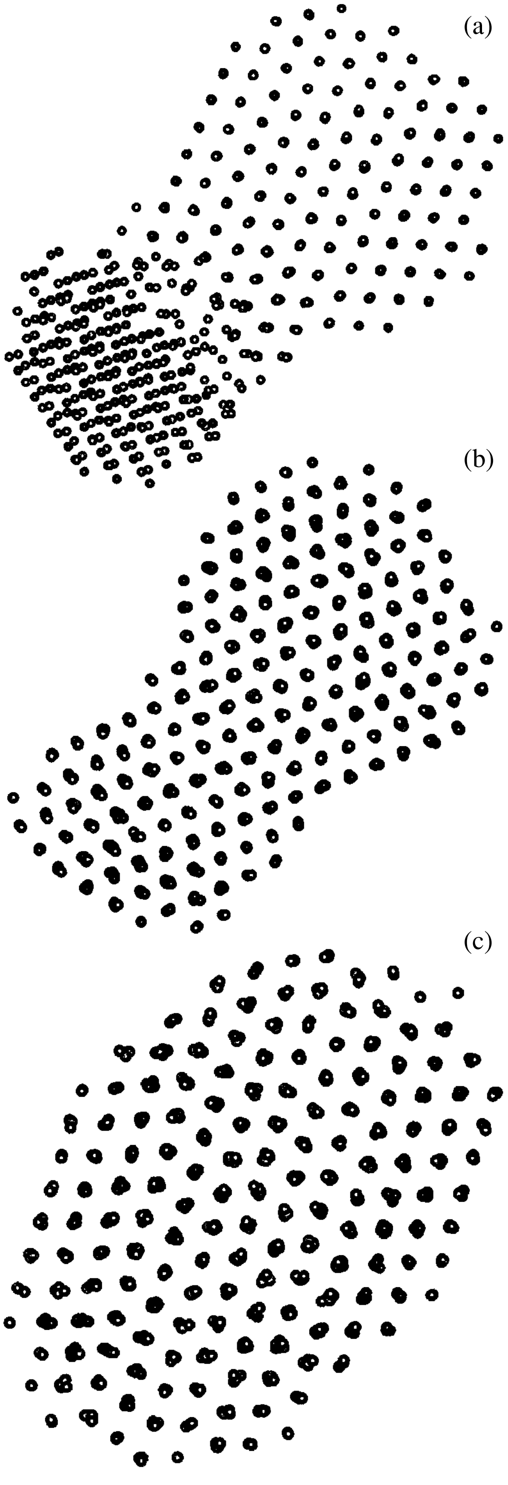

Fig. 3. Nickel cluster configurations (N = 1816 atoms) at T = (a) 77, (b) 600, and (c) 900 K.

increase in the rate of mass transfer required for a change in the cluster shape. At both temperatures, the transformation of the internal structure leads to complete disappearance of the disordered region at the boundary of the initial clusters.

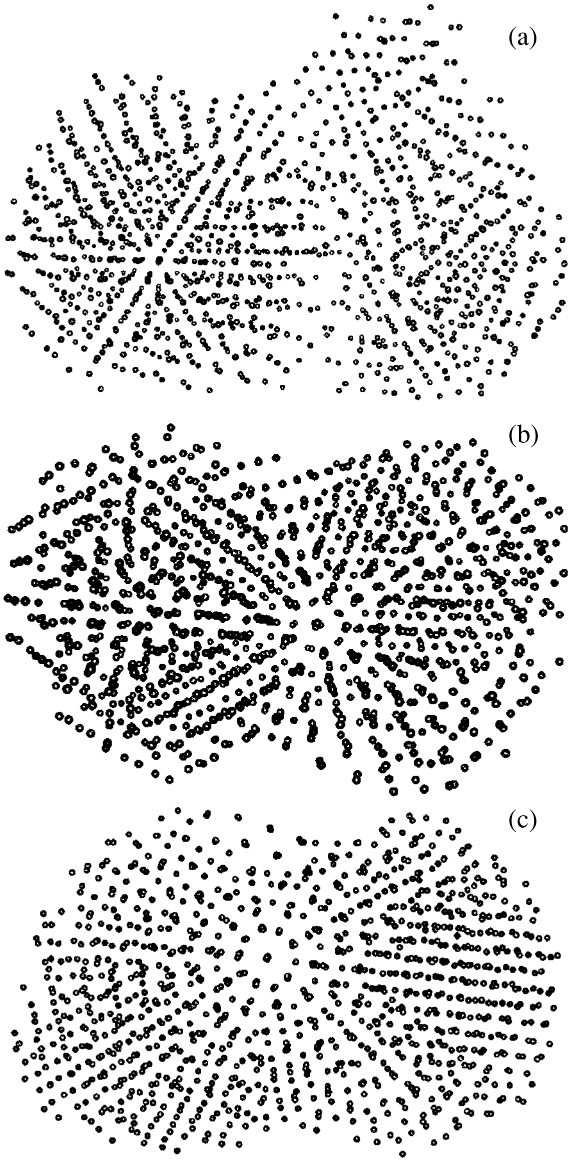

Fig. 4. Nickel cluster configurations (N = 2082 atoms): (a) T = 77; (b) T = 600 K, t = 1 ns; and (c) T = 600 K, t = 4 ns.

The second example is provided by a nickel nanocluster (N = 2082 atoms) that is formed through the agglomeration of three components, of which the component with the largest size involves a nucleus of the icosahedral phase (Fig. 4a). At T = 600 K, the icosahedral structure is formed in the cluster within only 1 ns after heating (Fig. 4b). The structural transformation of the cluster is completed within 4 ns after heating (Fig. 4c), and neither structure nor shape of the cluster change with time (to 20 ns). As in the first case, the cluster heated to T = 900 K becomes nearly elliptical in shape. These two examples also demonstrate that thermally induced processes substantially affect the formation of a cluster structure. For nickel nanoclusters, the icosahedral structure is more energetically favorable at

$T = 0$ K [24]. However, the formation of a similar structure in nickel nanoclusters at higher temperatures occurs only in the case when there is a large-sized nucleus of the icosahedral phase. This can be judged from comparing Figs. 1 and 4.

4. CONCLUSIONS

Thus, the gas-phase condensation of nickel clusters was simulated by the molecular dynamics method. The results of this simulation should be treated as tentative because the number of clusters formed is too small to make any valid inferences. However, the above investigations revealed a number of tendencies specific to gas-phase synthesis of nickel nanoclusters.

It was established that subsequent heating of the synthesized nanoclusters to temperatures of 400–500 K for even a few nanoseconds leads to substantial improvement of their internal structure with a hexagonal close-packed phase predominating. Upon heating of the nanoclusters above the melting point and subsequent gradual cooling, the formation of a cluster structure depends strongly on the cooling rate. Therefore, heat treatment of nickel nanoclusters synthesized from a gas phase can be used for the controlled formation of nickel nanoparticles with a predicted structure and, hence, with specified physical properties. This could prove indispensable for manufacturing modern technical devices, in particular, new forms of memory storage for computers.

ACKNOWLEDGMENTS

This work was supported by the German Physical Society within the framework of the SFB 445 program “Nano-Partikel aus der Gasphase: Entstehung, Struktur, Eigenschaften.” S.L. Gafner acknowledges the support of the Deutscher Akademischer Austausch Dienst (DAAD) for providing an opportunity to perform investigations at the Universität Duisburg-Essen (Germany).

REFERENCES

1. H. G. Rubahn, *Nanophysik und Nanotechnologie* (Teubner, Stuttgart, 2002).
2. W. Fahrner, *Nanotechnologie und Nanoprozesse* (Springer-Verlag, Berlin, 2003).
3. *Nanomaterials: Synthesis, Properties, and Applications*, Ed. by A. S. Edelstein and R. C. Cammarata (Inst. Phys., Bristol, 1996).
4. A. Giesen, A. Kowalik, and P. Roth, Phase Transit. **77**, 115 (2004).
5. H. J. Freund and S. H. Bauer, J. Phys. Chem. **81**, 994 (1977).
6. R. W. Siegel, S. Ramasamy, H. Hahn, Li Zongquan, Lu Ting, and R. Gransky, J. Mater. Res. **3**, 1367 (1988).
7. S. Stappert, B. Rellinghaus, M. Acet, and E. F. Wassermann, J. Cryst. Growth **252**, 440 (2003).
8. J. A. Ascencio, M. Perez, and M. Jose-Yacaman, Surf. Sci. **447**, 73 (2000).
9. J. M. Soler, Phys. Rev. B **61**, 5771 (2000).
10. F. Balleto, R. Ferrando, A. Fortunelli, F. Montalenti, and C. Mottet, J. Chem. Phys. **116**, 3865 (2002).
11. D. Reinhard, B. D. Hall, P. Berthoud, S. Valkealahti, and R. Monot, Phys. Rev. B **58**, 4917 (1998).
12. B. D. Hall, J. Appl. Phys. **87**, 1666 (2000).
13. P.-A. Buffat, M. Flueli, R. Spycher, P. Stadelmann, and J. P. Borel, Faraday Discuss. Chem. Soc. **92**, 173 (1991).
14. J. A. Ascencio, C. Gutierrez-Wing, M. E. Espinosa, M. Marin, S. Tehuacanero, C. Zorilla, and M. Jose-Yacaman, Surf. Sci. **396**, 349 (1998).
15. Y. Chushak and L.S. Bartell, Eur. Phys. J. D **16**, 43 (2001).
16. F. Cleri and V. Rosato, Phys. Rev. B **48**, 22 (1993).
17. E. F. Rexer, J. Jellinek, E. B. Krissinel, and E. K. Parks, J. Chem. Phys. **117**, 82 (2002).
18. S. Darby, T. V. Mortimer-Jones, R. L. Johnston, and C. Roberts, J. Chem. Phys. **116**, 1536 (2002).
19. K. Michaelian, M. R. Beltran, and I. L. Garzon, Phys. Rev. B **65**, 041403(R) (2002).
20. R. Meyer, L. J. Lewis, S. Prakash, and P. Entel, Phys. Rev. B **68**, 104303 (2003).
21. M. P. Allen and D. J. Tildesley, *Computer Simulation of Liquids* (Clarendon, Oxford, 1987).
22. H. S. Anderson, J. Phys. Chem. **72**, 2384 (1980).
23. S. Stappert, B. Rellinghaus, M. Acet, and E. F. Wassermann, Proc. Math. Phys. Soc. **704**, 73 (2002).
24. K. Mannien and M. Mannien, Eur. Phys. J. D **20**, 243 (2002).

Translated by O. Borovik-Romanova

Physics of the Solid State, Vol. 47, No. 7, 2005, pp. 1358–1364. Translated from Fizika Tverdogo Tela, Vol. 47, No. 7, 2005, pp. 1309–1315.
Original Russian Text Copyright © 2005 by Arbuzova, Naumov, Kozlov.

LOW-DIMENSIONAL SYSTEMS AND SURFACE PHYSICS

Elastic-Stress Relaxation in Compacted Nanocrystalline CuO

T. I. Arbuzova*, S. V. Naumov*, and E. A. Kozlov**
** Institute of Metal Physics, Ural Division, Russian Academy of Sciences,*
ul. S. Kovalevskoĭ 18, Yekaterinburg, 620219 Russia
e-mail: naumov@imp.uran.ru
*** Zababakhin All-Russia Research Institute of Applied Physics, Russian Federal Nuclear Center,*
Snezhinsk, Chelyabinsk oblast, 456770 Russia

Received August 11, 2004

Abstract—The magnetic properties of two types of nanocrystalline antiferromagnetic CuO samples, namely, dense nanoceramics and loose powders, were studied. For nanomaterials with smaller particles, the magnetic susceptibility χ was shown to increase with a decrease in temperature $T < T_N$. The increase in χ in both series of samples is related to the disordering of Cu^{2+} spins at the surfaces of nanoparticles. The magnetic properties of nanopowders characterize the properties of isolated nanoparticles. In a dense nanoceramic, the size effect is compensated for by the interaction between nanoparticles. The magnetic properties of nanoceramics are determined by elastic stresses induced by an external action. Elastic-stress relaxation results in the recovery of magnetic order and decreases the magnetic susceptibility. © *2005 Pleiades Publishing, Inc.*

1. INTRODUCTION

There has been increased interest in nanocrystalline materials over recent years. This interest is related to fundamental problems in the study of surface phenomena and to applied aspects of the use of nanoparticles [1–3]. A decrease in the crystallite size below a threshold value $d < 100$ nm is known to change the physical properties of crystallites as compared to ordinary polycrystals. Nanocrystalline materials are in a nonequilibrium metastable state. Knowledge of the processes occurring in the nanocrystalline state of solids opens up new opportunities for nanotechnology in designing structural and functional materials, since a decrease in particle size is an effective method for changing properties. Nanomaterials are used as catalysts for chemical reactions and are applied in the production of microelectronic devices, photosensitive elements, gas sensors, and gas and soot absorbents.

Nanocrystalline materials have small particle sizes and long interfaces. In magnetic nanoparticles, the total energy consists of the exchange, anisotropy, magnetoelastic, and magnetostatic energies. A loss of three-dimensional structural periodicity, a lower ionic coordination, and the presence of various types of defects in the surface and interface layers of nanoparticles can affect exchange interaction and, hence, can change the relations between the components of the total energy. A decrease in the particle size results in an increased contribution from surface anisotropy to the total anisotropy constant of an ensemble of nanoparticles $K = K^V + 2K^s/d$, where K^V and K^s are the volume and surface anisotropy constants, respectively, and d is the particle size. Stress-induced lattice distortions affect the contribution from volume anisotropy. The coupling between the volume and surface of nanoparticles is very sensitive to the surface morphology. Core–surface stresses increase the magnetoelastic coupling, which also contributes to the anisotropy. A change in the relations between the exchange energy and other contributions can change the ground state of nanoparticles and significantly modify their magnetic properties.

The main consequence of a decrease in the particle size in magnetic materials is spin disordering in the surface layer because of exchange-coupling frustrations, which manifests itself in superparamagnetism and superantiferromagnetism. In ferromagnetic and ferrimagnetic nanoparticles at low temperatures (below the blocking temperature T_B), disordered surface spins become "frozen," and their state is similar to the spin-glass phase. This leads to an increased coercive force, irreversible magnetization reversal in the ZFC and FC modes, and a shift in the hysteresis loops [1]. As the temperature increases, the spin-glass phase transforms into a canted spin structure. In antiferromagnetic nanoparticles, the ground state is a multisublattice state. The decompensation of the magnetic sublattices results in superantiferromagnetism, which is characterized by a nonlinear field dependence of the magnetization and by an increase in the susceptibility with decreasing temperature ($\chi \sim 1/T$) [4]. In ionic compounds, valence electrons are spatially localized. In semiconducting 3*d* oxides, the magnetic order is determined by superexchange interaction and depends on the overlapping of the 3*d* and 2*p* orbitals of metal and oxygen ions; therefore, the magnetic coupling is very sensitive to the atomic environment. A lowered atomic density and changes in the interatomic distances and in the exchange interaction in the surface layers of nanoparticles can cause a stronger size effect in ionic compounds, as compared to metals, over a wide temperature range up to T_C or T_N. The properties of antiferromagnetic and ferrimagnetic nanocrystalline oxides are less well understood than the properties of ferromagnetic 3*d*-metal nanoparticles.

An informative method for studying the magnetic properties of nanomaterials is measurement of the magnetic susceptibility. In this work, we investigate the effect of nanoparticle size on the magnetic properties of CuO and the stability of the nanocrystalline state. To this end, in the temperature range $77 < T < 600$ K, we measure the magnetic susceptibility of nanocrystalline CuO samples fabricated by different methods, because the magnetic properties of nanocrystalline materials can depend on the fabrication technique. We chose CuO, since it is unique in the series of 3*d* monoxides. CuO has a monoclinic lattice and is a low-dimensional antiferromagnet with a high Néel temperature (T_N = 230 K) [5, 6]; these features allow us to study the effect of a decreased particle size over a wide temperature range. CuO is the basis for cuprate high-temperature superconductor (HTSC) compounds and exhibits properties similar to the properties of their semiconductor phases. Therefore, CuO has been extensively studied since the discovery of HTSCs [7]. It is also important that, when the copper-to-oxygen concentration ratio changes, the Cu–O system can contain diamagnetic phases (Cu_2O, Cu), which have no effect on the magnetism of bulk CuO. Other magnetically ordered phases do not form under these conditions.

2. EXPERIMENTAL

The magnetic properties of nanopowders and nanolayers are mainly specified by the effects related to the nanoparticle size and the state of the surface layers. In compacted nanomaterials, the interaction between nanoparticles and the surface effects induced by the microstructure of grain boundaries (e.g., the presence of nanovoids and other free volumes, the nonequilibrium stressed state of interfaces) can be significant. Two series of nanocrystalline CuO samples with nanoparticle size d = 5–110 nm were prepared using different methods to separate the size effect from other factors. One series of samples was fabricated with polycrystalline CuO subjected to spherically converging isentropic shock waves [8]. After subjection to shock waves, the CuO ceramic was in the form of a ball of radius R = 22 cm. The density of the loaded CuO was 99%. Samples having a certain nanoparticle size (d = 5, 15, 30, 70, 110 nm) were cut from different zones of the loaded ball. The other series of nanocrystalline CuO samples (with average particle size d = 15, 45, 60 nm) was produced via condensation of copper vapors. A drop of molten metal was levitated in an argon flow and heated to 2000°C by a high-frequency magnetic field. The evaporated metal was cooled with the inert gas and condensed to form a nanopowder. The nanoparticle sizes were controlled by the argon pressure and the argon flow rate. The design of the device prevents the molten metal from being contaminated by uncontrolled impurities. The Cu and CuO nanopowders were then oxidized in air at 90–240°C for 0.5–2 h. The samples of this series consisted of a loose nanopowder.

Phase and structural analyses were performed with a DRON-2.0 x-ray diffractometer. X-ray diffraction data showed that the nanocrystalline CuO samples were single-phase and that the broadening of the diffraction lines was mainly caused by the small particle size. In the dense nanoceramics, an additional contribution to the line broadening was induced by elastic stresses due to shock-wave loading. The nanoparticle size was controlled with an STM-U1 scanning tunneling microscope. For each sample, we took ten or more images at different points and then used them to determine the average nanoparticle size [9, 10]. The magnetic susceptibility was measured on a magnetic balance. As a rule, nanomaterials subjected to severe plastic deformation have a high level of microstrains and a large amount of defects. Grain boundaries in such materials are in a nonequilibrium state and are sources of high elastic stresses. The nanoceramic and nanopowder samples were stored at room temperature for three years, and then the magnetic measurements were repeated to analyze the state of nanocrystalline CuO and of the interfaces in it.

3. MAGNETIC SUSCEPTIBILITY OF CuO NANOPARTICLES

The magnetic properties of CuO are specified by the competition between the strong antiferromagnetic superexchange interaction of Cu^{2+} ions through O^{2-} ions in the $[10\bar{1}]$ direction and a weaker ferromagnetic superexchange interaction in all other directions. The magnetic structure consists of zigzag antiferromagnetic Cu–O–Cu chains along the $[10\bar{1}]$ axis. Below T = 212 K, CuO exhibits 3D collinear antiferromagnetism, and in the range $212 < T < T_N = 230$ K the structure becomes noncollinear. Above T_N, the interaction between the chains become negligible and the system transforms into a low-dimensional antiferromagnetic state [5, 6, 10]. Near T_N, the slope of the $\chi(T)$ curve changes, but the susceptibility maximum (typical of 3D collinear antiferromagnets) is absent. The susceptibility of CuO continues to increase with T up to 550 K [11]. The shape of the temperature dependence of the susceptibility is characteristic of low-dimensional (1D, 2D) antiferromagnets, which transform into a 3D state with long-range magnetic order as the temperature decreases [12].

Figure 1 shows the temperature dependences of the magnetic susceptibility in a constant magnetic field H = 8.9 kOe for a Cu polycrystal with grain size d = 5–15 μm and for dense nanoceramics with a grain size in

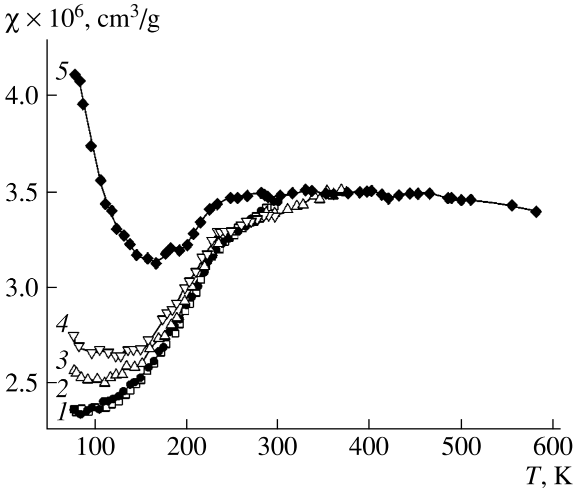

Fig. 1. Temperature dependences of the magnetic susceptibility in a constant magnetic field H = 8.9 kOe for (*1*) a CuO polycrystal with grain size d = 5–15 μm and (*2*–*5*) dense nanoceramics with various values of the grain size d: (*2*) 70, (*3*) 30, (*4*) 15, and (*5*) 5 nm.

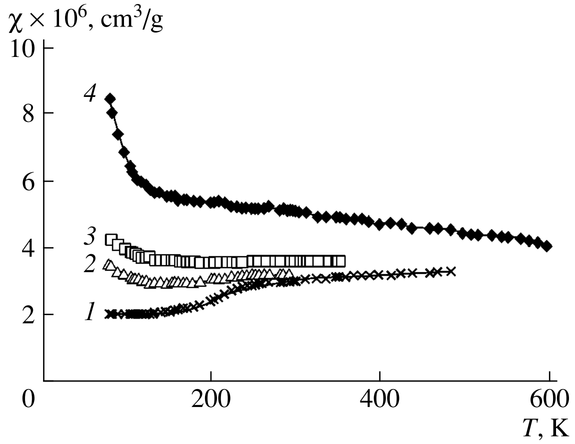

Fig. 2. Temperature dependences of the magnetic susceptibility of CuO in a magnetic field H = 8.9 kOe for (*1*) a polycrystal and (*2*–*4*) nanopowders with various values of the average grain size d: (*2*) 60, (*3*) 45, and (*4*) 15 nm.

the range $5 \leq d \leq 110$ nm. The $\chi(T)$ dependence for the nanocrystalline samples with a large grain size ($d >$ 70 nm) coincides with that for CuO polycrystals fabricated using a standard method. A decrease in the grain size leads to increased values of χ at low temperatures. There is a correlation between the grain size and the magnetic susceptibility: the smaller the value of d, the higher the value of χ. For the nanoceramics with d = 5 nm at T < 140 K, the susceptibility obeys the law $\chi \sim 1/T$. The general shape of the temperature dependence of the magnetic susceptibility for nanoceramic CuO samples with a small grain size is characteristic of alternated chains [12], strongly frustrated antiferromagnets, and antiferromagnetic nanoparticles [4]. Since long-range magnetic order is unlikely to be destroyed in the bulk of nanoparticles at temperatures well below 230 K, the most probable cause of the $\chi \sim 1/T$ dependence and, accordingly, the appearance of an uncompensated magnetic moment is the breakage of the antiferromagnetic bonds of Cu^{2+} ions located in the surface layer because of a loss of 3D periodicity. As the grain size decreases, the number of disordered surface spins increases; as a result, the total susceptibility of nanocrystalline CuO increases. In the high-temperature range (T > 300 K), the $\chi(T)$ dependences are identical for all samples. This fact indicates that the decrease in the grain size has no effect on the short-range magnetic order, which remains unchanged up to 550 K.

The surface effects characteristic of CuO are most pronounced in the magnetic properties of nanopowders. Figure 2 shows the temperature dependences of the susceptibility in a field H = 8.9 kOe for single-phase CuO nanopowders with average grain sizes d = 15, 45, and 60 nm. The susceptibility decreases with increasing temperature in the range T < 140 K for samples with d = 45 and 60 nm and decreases over the entire temperature range covered, 77 < T < 600 K, for samples with d = 15 nm. As in the case of nanoceramics, there is a correlation between χ and d. However, at the same nanoparticle size, the susceptibility of nanopowders is significantly higher. Qualitatively similar $\chi \sim 1/T$ dependences were observed for nanopowders produced using the sol-gel method [13] or ball mills [14] and for multilayers of CuO films of thickness d = 2–200 nm [15].

In nanomaterials, not only the particle size but also the particle microstructure and the state of interfaces in particles play important roles. The effect of interfaces on the properties is most pronounced in compacted nanomaterials [3]. As a result of strong external actions, the grain boundaries are in a thermodynamically nonequilibrium stressed state with an excess energy, and this state can be unstable even at room temperature. High-temperature annealing or storage of samples at room temperature for a long time leads to elastic-stress relaxation. Grain boundaries transform into a stable state with a relatively high degree of short-range order in the atomic arrangement in nanoparticle boundaries; therefore, the magnetic properties of as-produced and aged samples are different. Figure 3 shows the temperature dependences of the magnetic susceptibility for the same nanoceramic CuO samples as in Fig. 1 but after three-year storage at room temperature. It is seen that the “paramagnetic” contribution $\chi \sim 1/T$ disappears for all samples. The $\chi(T)$ dependences became similar to those typical of ordinary CuO polycrystals, which indicates a low degree of disordering of Cu^{2+} ion spins in the surface layer. The recovery of the long-range antiferromagnetic order in the aged nanoceramic samples is not due to an increase in the grain size or grain-boundary migration. Indeed, Fig. 4 shows the micro-

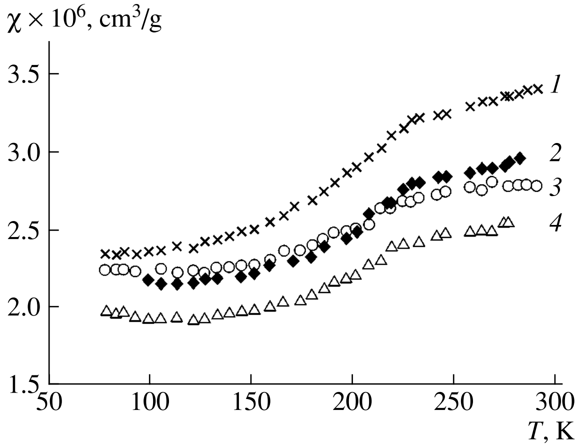

Fig. 3. Temperature dependences of the magnetic susceptibility for high-density CuO ceramics (see Fig. 1) after three-year storage at room temperature. The grain size *d* is (*1*) >1000, (*2*) 30, (*3*) 15, and (*4*) 5 nm.

structures of nanoceramics with a grain size $d = 15$ nm observed with a scanning tunneling microscope immediately after shock-wave treatment and after three years. According to the scanning tunneling microscopy data, the grain size does not change with time. It should be noted that, in the aged nanoceramic samples, all $\chi(T)$ dependences are below the analogous curve for polycrystals. The susceptibility decreases in absolute value with decreasing grain size both above and below T_N. This behavior of the magnetic susceptibility can be related to a change in the oxygen concentration in the surface layers of CuO. Indeed, the degree of nonstoichiometry with respect to oxygen increases with decreasing *d* because of the increased length of grain boundaries. Using positron annihilation, it was found that local regions of oxygen vacancies are formed in grain boundaries in our samples [16]. A deviation of the composition toward oxygen deficiency, a decreased nanoparticle size, and an increased bond ionicity [17] stimulate the formation of nonmagnetic Cu^{3+} ($3d^{10}$) ions at interfaces. The lower values of the susceptibility can be caused by a lower concentration of magnetic Cu^{2+} ions. The nanoceramics can also exhibit explosion-induced anisotropy. Since the parallel susceptibility is minimal ($\chi_{\parallel} = 1.0 \times 10^{-6}$ cm³/g [18]), the low values of χ in the annealed nanoceramics can be related to the increased $\chi_{\parallel}$ contribution to the total susceptibility.

The behavior of the magnetic properties of CuO nanopowders with time is different. After storage for three years, the temperature dependence of the susceptibility remains virtually unchanged, which indicates the stability of the nanoceramic composition and the absence of any relaxation processes.

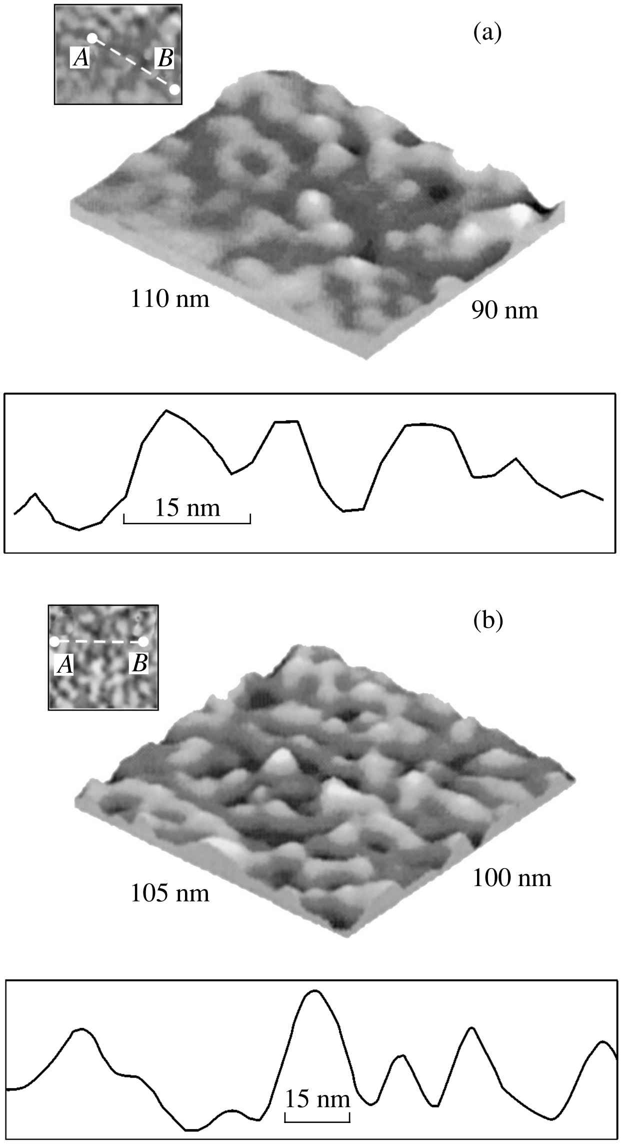

Fig. 4. Microstructure of CuO nanoceramics with grain size $d = 15$ nm (a) immediately after shock-wave treatment and (b) after three years. The insets show *A*–*B* scanning lines.

4. FACTORS AFFECTING THE MAGNETIC PROPERTIES OF THE NANOMATERIALS

The magnetic properties of antiferromagnetic nanocrystalline materials depend on the nanoparticle size, the interparticle interaction, and the grain-boundary microstructure. The question of whether the transition from the polycrystalline to nanocrystalline state is first-order remains open; that is, it is unknown whether there exists a critical particle size below which the only properties that are exhibited by nanomaterials are those characteristic of nanoparticles. To answer this question, we need data on the magnetic properties of a system of isolated nanoparticles in order to prevent other factors, such as interparticle interaction, from having an effect. Among our samples, the nanoparticle isolation condition is best satisfied by the loose CuO nanopowders, whose susceptibility increases with decreasing d and decreases smoothly with increasing temperature ($\chi \sim 1/T$) in the range $T < 300$ K. A similar behavior of the susceptibility is observed in antiferromagnetic hematite α-Fe_3O_4 [19], NiO [20], and CuO multilayers [15]. In hematite particles with $d > 100$ nm, the susceptibility remains equal to its value for bulk hematite. When the particle size decreases within the range $100 > d > 20$ nm, χ increases rapidly. The magnetic susceptibility of nanocrystalline NiO varies in inverse proportion to the nanoparticle size in the range $200 > d > 7$ nm at $T = 298$ K. For CuO multilayer films of different thicknesses ($d = 2$–200 nm) sputtered on substrates of nonmagnetic phases (MgO or Al_2O_3), the susceptibility varies in inverse proportion to temperature in the range $4.2 < T < 300$ K. At 4.2 K, the susceptibility increases linearly with the number of interfaces. Since the effect of grain boundaries depends on the method of nanomaterial production, nanocrystalline samples having identical values of d can differ in terms of their magnetic properties. For example, in CuO nanoparticles fabricated using the sol-gel method in combination with high-temperature annealing, an uncompensated magnetic moment appears at $d < 9$ nm [13], whereas in nanoparticles produced in a ball mill this moment appears at $d < 21.2$ nm [14]. The temperature dependence of the susceptibility of compacted nanoceramics differs from the $\chi(T)$ dependence for a CuO polycrystal at $d \le 60$ nm (Fig. 1). The absolute values of χ of materials with identical values of d are also different. Based on the results of an analysis of the magnetic properties performed for the two types of nanocrystalline CuO and on the available data, we can assume that the size dependence of the susceptibility of copper monoxide is smooth and that the transition from the polycrystalline to nanocrystalline state is not first-order.

Exchange interaction in oxides is specified by both the distance between magnetic ions and the superexchange coupling angle between them. The violation of 3D periodicity at the surface of nanoparticles can cause disordering of surface spins. Simulation of a spin configuration in nanoparticles of antiferromagnetic oxides has shown that a multisublattice state is preferred to a two-sublattice state [1]. Due to disordering of the surface spins and decompensation of the magnetic moments of the sublattices, the temperature dependence of the susceptibility of an ensemble of nanoparticles is described by the expression [4, 20]

$$\chi = \chi_{AF} + \frac{1}{\langle V \rangle}\frac{[\mu_{nc}(T)]^2}{3k_B T}, \qquad (1)$$

where χ_{AF} is the susceptibility of the antiferromagnetic nanoparticle core, μ_{nc} is the average uncompensated magnetic moment, $\langle V \rangle$ is the average nanoparticles volume, and k_B is the Boltzmann constant.

As follows from Eq. (1), a decrease in the nanoparticle volume and, hence, in the nanoparticle size should increase the total susceptibility. The experimental data on the magnetic susceptibility of antiferromagnetic oxide nanoparticles support this conclusion. The difference in the $\chi(T)$ dependence between the CuO nanoceramics and nanopowders is caused by the difference in the relationship between the first and second terms in Eq. (1) for them. Since the susceptibility of bulk CuO is small ($\chi = 2 \times 10^{-6}$ cm^3/g), the second term in Eq. (1) determines the $\chi(T)$ dependence of an ensemble of nanoparticles as the particle size decreases.

In nanoparticles, the fraction of surface spins can reach 30–50%. However, not all of the surface spins are disordered, because nanoparticles interact with one another. Based on magnetic and Mössbauer measurements, the authors of [15] concluded that, apart from the basic antiferromagnetic phase CuO, 2-nm-thick multilayer films also contain 7–10% paramagnetic Cu^{2+} ions localized in the interface layers. Our estimation shows that the concentration of disordered Cu^{2+} ions in dense nanoceramics with $d = 5$ nm is 3%. The concentration of paramagnetic Cu^{2+} ions in nanopowders is slightly higher: 2% at $d = 60$ nm and 8% at $d = 15$ nm. In the nanoceramics produced with shock waves, the interparticle distance is small; therefore, the exchange interaction between the nearest neighbor nanoparticles results in partial ordering of the surface Cu^{2+} spins. Upon strong interparticle exchange interaction, all surface spins can be ordered; as a result, the magnetic properties of nanomaterials and coarse-grained polycrystals are identical [21].

Apart from the nanoparticle size and interparticle interaction, an important factor that influences the properties of nanomaterials is the long-range stress field induced by severe plastic deformation. This field causes lattice strains both in the cores of nanoparticles and near their surfaces. The strains are maximum in grain boundaries. Annealing decreases the lattice strains. As-produced nanoceramics have a large number of high-energy nonequilibrium grain boundaries. One of the challenges with nanomaterials is to investigate the microstructure of compacted materials, the relaxation of grain boundaries, and the recovery of properties upon annealing. Computer simulation was used in [22, 23] to study different mechanisms of relaxation of a nonequilibrium grain-boundary structure in metallic nanocrystals. For example, the relaxation time of rigid translation in nonequilibrium grain boundaries for nanocrystalline palladium with grain size $d = 8$ nm was estimated to be $t_{rel} = 0.3$ s at an annealing temperature $T = 600$ K. At room temperature, the time of relaxation to the equilibrium state is $t_{rel} = 8 \times 10^6$ days; that is, the grain boundaries retain a nonequilibrium atomic structure for an infinitely long time [22]. In [24], compacted nanocrystalline palladium was studied using x-ray diffraction and EXAFS methods and it was found that, at room temperature, grain boundaries transform from a nonequilibrium state with weak short-range order into a more ordered state. Simultaneously, the crystallite size increases from 12 to 25–80 nm in 120–150 days, which indicates that the nonequilibrium state differs in nature from a rigid translation.

The study of the magnetic properties of nanocrystalline magnetic semiconductors began only recently. At present, there are no theoretical or experimental studies on the elastic-stress relaxation in compacted nanocrystalline oxides of transition metals. After shock-wave treatment, our nanoceramic CuO samples contain a large amount of high-energy nonequilibrium grain boundaries. In time, high internal stresses relax and grain boundaries acquire a quasi-equilibrium state with a lower energy. The occurrence of elastic-stress relaxation is confirmed by the time dependences of the magnetic properties of nanoceramics. The increase in the susceptibility with decreasing temperature in the range $T < T_N$ in the as-produced ceramics characterizes the degree of spin disordering and depends mainly on elastic stresses. After annealing of strains without a change in grain size (Fig. 4), the temperature dependence of the susceptibility acquires the shape characteristic of coarse-grained CuO polycrystals. In the nanoceramics, the contributions of the size effect and interparticle interaction to the disordering of Cu^{2+} spins are likely to balance each other. Because of the production procedure, the CuO nanopowders have a low level of stresses; therefore, even after long-term storage, the temperature dependence of their susceptibility remains virtually unchanged.

Nonequilibrium interfaces are an effective channel for diffusion relaxation of elastic stresses. Interfaces can contain three types of defects: single vacancies, vacancy nanovoids, and large voids at the site of absent crystallites [3]. Dislocations located directly in interfaces and uncompensated disclinations in triple junctions stimulate grain-boundary diffusion. The splitting of disclinations is accompanied by a change in the grain-boundary structure, namely, by a decrease in the lattice strains in the grain-boundary phase. Using positron annihilation, it has been found that small agglomerates of oxygen vacancies are present in local regions of interfaces in annealed CuO nanoceramics [16]. Conceivably, the grain boundaries might still be in a nonequilibrium state after three-year storage. A certain structural disorder can be retained due to residual internal stress fields and the weakening of the Cu–O covalent bond, which is responsible for the overlapping of the 3*d* and 2*p* orbitals.

5. CONCLUSIONS

Thus, the anomalous behavior of the magnetic susceptibility below T_N in CuO nanoceramics is specified by three factors: the nanoparticle size, the interaction between magnetic nanoparticles, and long-range internal stress fields. The size factor and elastic stresses lead to breakage of the exchange couplings and disordering of the surface spins. The interaction between magnetic nanoparticles favors the conservation of long- and short-range magnetic order in an ensemble of nanoparticles. In CuO nanopowders, a large number of uncompensated Cu^{2+} ion spins in the surface layers contribute significantly to the magnetic susceptibility and characterize the size effect in isolated nanoparticles. In compacted nanoceramics, the magnetic susceptibility depends mainly on induced elastic stresses due to the compensation of the size effect and interparticle interaction. As a result of elastic-stress relaxation, the magnetic order and magnetic properties are recovered and the magnetic susceptibility of the ensemble of nanoparticles becomes identical to the $\chi(T)$ dependence of bulk CuO.

ACKNOWLEDGMENTS

We thank B.A. Gizhevskiĭ, A.E. Ermakov, and K.V. Shal'nov for their assistance in this study.

This work was supported by the OFN-19 and FTsNTP-40.012.1.1.1153 programs.

REFERENCES

1. R. H. Kodama and A. E. Berkowitz, Phys. Rev. B **59** (9), 6321 (1999).
2. A. Hernando, J. Phys.: Condens. Matter **11** (48), 9455 (1999).
3. A. I. Gusev, *Nanocrystalline Materials: Methods of Production and Properties* (URO Ross. Akad. Nauk, Yekaterinburg, 1998) [in Russian].
4. C. Gilles, P. Bonville, H. Rakoto, J. M. Broto, K. K. W. Wong, and S. Mann, J. Magn. Magn. Mater. **241**, 430 (2002).
5. J. B. Forsyth, P. J. Brown, and B. M. Wahklyn, J. Phys. C **21**, 2917 (1988).
6. T. I. Arbuzova, A. A. Samokhvalov, I. B. Smolyak, B. V. Karpenko, N. M. Chebotaev, and S. V. Naumov, J. Magn. Magn. Mater. **95**, 168 (1991).
7. E. Gmelin, Indian J. Pure Appl. Phys. **30**, 596 (1992).
8. B. A. Gizhevskiĭ, E. A. Kozlov, M. V. Degtyarev, L. M. Voronova, S. V. Naumov, and G. N. Tatarinova, Fiz. Khim. Obr. Mater. **3**, 52 (1999).
9. T. I. Arbuzova, S. V. Naumov, A. A. Samokhvalov, B. A. Gizhevskiĭ, V. A. Arbuzov, and K. V. Shal'nov, Fiz. Tverd. Tela (St. Petersburg) **43** (5), 846 (2001) [Phys. Solid State **43** (5), 878 (2001)].
10. T. I. Arbuzova, S. V. Naumov, V. A. Arbuzov, K. V. Shal'nov, A. E. Ermakov, and A. A. Mysik, Fiz. Tverd. Tela (St. Petersburg) **45** (2), 290 (2003) [Phys. Solid State **45** (2), 304 (2003)].
11. M. O. Keefe and F. S. Stone, J. Phys. Chem. Solids **23**, 261 (1962).
12. R. Karling, *Magnetochemistry* (Mir, Moscow, 1989) [in Russian].
13. A. Punnoose, H. Magnone, and M. S. Seehra, Phys. Rev. B **64**, 174420 (2001).

14. R. A. Borzi, S. J. Stewart, R. C. Mercader, G. Punte, and F. Garcia, J. Magn. Magn. Mater. **226–230**, 1513 (2001).
15. M. Sohma, K. Kawaguchi, and Y. Fujii, J. Appl. Phys. **77** (3), 1189 (1995).
16. A. P. Druzhkov, B. A. Gizhevskii, V. L. Arbuzov, E. A. Kozlov, K. V. Shalnov, S. V. Naumov, and D. A. Perminov, J. Phys.: Cond. Matter **14**, 7981 (2002).
17. V. R. Palker, P. Ayyub, S. Chattopadhyay, and M. Multani, Phys. Rev. B **53**, 2167 (1996).
18. T. I. Arbuzova, I. B. Smolyak, A. A. Samokhvalov, and S. V. Naumov, Zh. Éksp. Teor. Fiz. **113** (3), 1026 (1998) [JETP **86** (3), 559 (1998)].
19. G. J. Muench, S. Arais, and E. Matijevic, J. Appl. Phys. **52** (3), 2493 (1981).
20. J. T. Richardson, D. I. Yiagas, B. Turk, K. Forster, and M. V. Twigg, J. Appl. Phys. **70** (11), 6977 (1991).
21. M. F. Hansen and S. Morup, J.Magn. Magn. Mater. **184**, 262 (1998).
22. D. B. Bachurin and A. A. Nazarov, Fiz. Met. Metalloved. **97** (2), 17 (2004).
23. V. N. Chuvil'deev, O. É. Pirozhnikova, and A. V. Petryaev, Fiz. Met. Metalloved. **92** (6), 14 (2001).
24. J. Lofflet, J. Weismuller, and J. Gleiter, Nanostruct. Mater. **6** (1–4), 105 (1995).

Translated by K. Shakhlevich

Physics of the Solid State, Vol. 47, No. 7, 2005, pp. 1365–1371. Translated from Fizika Tverdogo Tela, Vol. 47, No. 7, 2005, pp. 1316–1322.
Original Russian Text Copyright © 2005 by Sorokin, Grigor'ev, Kalmykov, Sokolov.

LOW-DIMENSIONAL SYSTEMS AND SURFACE PHYSICS

Structural Properties and Current Transport in a Nanocomposite Formed on a Silicon Surface by Oxidation of the Porous Layer

L. M. Sorokin*, L. V. Grigor'ev, A. E. Kalmykov*, and V. I. Sokolov***

**Ioffe Physicotechnical Institute, Russian Academy of Sciences,*
Politekhnicheskaya ul. 26, St. Petersburg, 194021 Russia
e-mail: aekalm@mail.ioffe.ru
***Fock Institute of Physics, St. Petersburg State University,*
ul. Ul'yanovskaya 1, Petrodvorets, St. Petersburg, 198504 Russia

Received August 26, 2004

Abstract—The possibility of obtaining a Si–SiO$_2$ nanocomposite layer by oxidation of porous silicon is demonstrated. The nanocomposite thus prepared consists of silicon oxide with inclusions of crystalline silicon in the form of rounded particles 5 to 30 nm in diameter and a filamentary cellular structure with filaments a few nanometers thick. The *I–V* characteristics of these structures were measured under different sample excitation conditions (photo- and thermal stimulation). The trap concentration and effective carrier mobility are estimated. Carriers are found to be captured intensely by traps created in the large-area interface in the composite structure. *© 2005 Pleiades Publishing, Inc.*

1. INTRODUCTION

Featuring a richer variety of physical properties than their constituent components, nanocomposite materials enjoy broad application in various fields of technology [1]. Oscillations in current observed in a layer of thermally oxidized porous silicon [2] suggest that this material is a nanocomposite. Porous silicon is a nanostructural material and is already employed to advantage in the development of optoelectronic devices [3–5].

The electrophysical and optical properties of a material change appreciably as one goes from a bulk semiconductor to a system of isolated nanocrystallites. A substantial qualitative transformation occurs, in particular, with the factors governing the processes of generation and recombination of carriers. First, the role played by the surface and by the associated electronic states of defects increases. Second, charge carriers turn out to be confined to a limited region of space and cannot interact freely with one another. For this reason, for instance, the dependence of the photoluminescence intensity of a nanocrystalline semiconductor on the pumping level should differ from that observed in a bulk material. Indeed, linear and sublinear dependences are observed in nanocrystalline silicon [6], whereas in single-crystal silicon the interband photoluminescence intensity versus pumping level relation is a power-law function [7].

In recent years, widespread interest has evolved in silicon nanocomposites (silicon nanocrystals embedded in a SiO$_2$ dielectric matrix), which exhibit noticeable room-temperature photo- and electroluminescence in the visible region as a result of quantum confinement [3, 7–12]. The luminescence quantum yield, however, is at present below one percent. However, the above publications did not present any structural data that could serve as convincing evidence that these measurements were in fact carried out on nanocomposites. In order to find ways to improve the quantum yield of the luminescence, one needs to know the processes dominating the generation and recombination of nonequilibrium carriers and the current-transport mechanisms operative in a silicon nanocomposite, with due account of its structure. In the present work, we performed an electron-microscope study of the Si : SiO$_2$ nanocomposite prepared by the oxidation of porous silicon and an investigation into the mechanisms of current transport in it.

2. PREPARATION OF THE NANOCOMPOSITE

To prepare porous layers, 350-μm-thick, [100]-oriented plates of KDB-10 single-crystal silicon were electrochemically etched in an aqueous solution of 30 vol % HF in a horizontal reactor (shown schematically in Fig. 1). The reactor was a Teflon cup with a hole in the bottom. The hole is covered by pressing the sample to the cup bottom using a Teflon nut. The cup assembled in this way is mounted in a cell filled with electrolyte, which provides rear contact with the sample. The cup is filled with an aqueous solution of hydrofluoric acid, an electrode is put in place, and a dc voltage is applied. The bubbles forming during etching are removed from time to time from the silicon surface

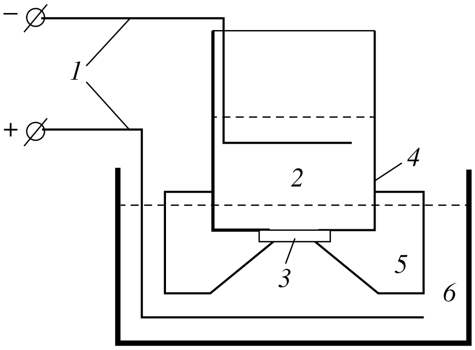

Fig. 1. Reactor for preparation of a porous layer (schematic). (*1*) Platinum electrodes, (*2*) solution of hydrofluoric acid, (*3*) sample, (*4*) cup, (*5*) clamping nut, and (*6*) water solution of NaCl.

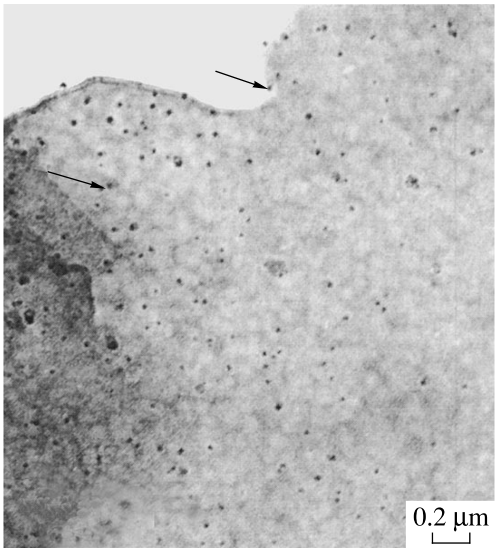

Fig. 2. Electron photomicrograph of the nanocomposite before etching.

with a Teflon stirrer. In this paper, we report on a study of a sample etched for 5 min at a current density of 300 mA/cm^2. On termination of the electrochemical etching, the sample was rinsed in flowing deionized water and subsequently oxidized in water vapor at 1223 K. The oxidation time was chosen such as to provide the formation of inclusions of silicon nanoparticles in the grown SiO_2 film. The thickness of the oxide thus grown was about 0.15 µm. To study the electrophysical properties of the silicon nanocomposite, the oxide was removed from the idle side of the sample and an In–Ga eutectic layer was deposited on it. Circular semitransparent Al electrodes were evaporated on the nanocomposite surface. Prior to measurement of the *I*–*V* curves, deep marks were cut into the sample by scribing down to the single-crystal substrate.

3. STRUCTURE OF THE NANOCOMPOSITE

The structure of a nanocomposite layer was studied with an ÉM-200 electron microscope at an accelerating voltage of 100 kV. Samples for the studies were prepared in the standard way; namely, wafers 3 mm in diameter cut to match the holder were attached with a wax, porous-layer front to a 1-mm-thick circular Teflon substrate 10 mm in diameter. The sample was thinned down to a thickness transparent for 100-keV electrons by wet etching with a CP-8 solution on the side opposite to the porous layer to produce a central window in silicon down to the oxide layer. Next, the sample was peeled off the substrate and rinsed. If the oxide layer was so thick that the sample became charged when viewed with an electron microscope, the layer was additionally thinned with an ion beam (I = 4–6 µA, U = 5 kV).

Figure 2 shows a typical sample structure after oxidation. In order to preserve the structure responsible for the electrophysical properties described in the next section, no ion beam etching was performed on this sample. The electron diffraction pattern of this sample was a diffuse halo against which weak pointlike reflections relating to the residual silicon layer could be barely discerned. Hence, this region of the sample consists predominantly of the oxide. The image exhibits isolated dark rounded particles 5–30 nm in size (indicated by arrows). Some of them are surrounded by a bright halo. Tilting the sample in the microscope through up to 30° did not reveal elongation of these particles in any direction, a feature to be expected if the porous layer had a columnar structure. Dark-contrast particles stood out clearly against the background of a slightly washed-out cellular structure. Their surface concentration was in excess of 10^9 cm^{-2}.

After ion beam etching, silicon reflections became visible in addition to the diffuse halo in the electron diffraction pattern (Fig. 3a). The pattern suggests that the surface layer retains, on the whole, the single-crystal structure after the electrochemical etching. Single arc-shaped reflections (indicated by arrows) indicate a certain misorientation between adjacent nanoparticle regions. Figures 3b and 3c are images of the region of which the electron diffraction pattern was obtained, with Fig. 3c being a dark-field image in the (111) reflection from Si. Dark particles similar to those in Fig. 2 are also present in Fig. 3b. Viewed in the dark-field mode in Fig. 3c, they are seen as bright spots. This implies that they are silicon particles in the reflecting position. The bright halo surrounding them in the bright-field image is possibly associated with their oxidation.

Viewed under high magnification, the cellular structure looks like a network formed by thin (~5-nm-thick) dark-contrast filaments (Fig. 4). The filaments are sur-

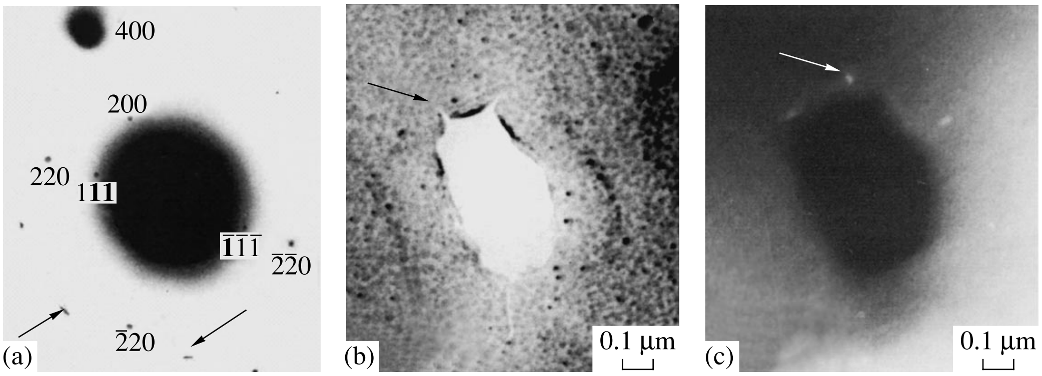

Fig. 3. (a) Electron micrograph of a sample after ion beam thinning and (b) bright-field and (c) dark-field microscope images of the same region. Arrows indicate silicon particles.

rounded by a coat. Because the photomicrograph was taken in the diffraction contrast mode, one may conclude that the dark filaments are actually silicon nanoinclusions encapsulated in an oxide coat. The filaments are nonuniform in thickness. In some places, they make up a sequence of single, closely located, small particles.

Figure 5 schematically shows a model of formation of the nanocomposite. Etching produces pores whose walls are thinned by oxidation to form a thin network structure of silicon filaments. The walls between the pores left after electrochemical etching are of different thicknesses. As a result, the silicon filaments forming after oxidation of the porous layer (Fig. 2) are likewise of different thicknesses. The single large particles (~5 to 30 nm in size) are apparently remnants of the thickest regions between the pores that were left incompletely oxidized.

4. TRANSPORT PROPERTIES OF THE SILICON NANOCOMPOSITE

The transport properties of the nanocomposite were studied by measuring *I–V* curves at different pumping levels, with subsequent estimation of the carrier mobility and trap concentration. We used a V7-30 electrometer in the current measurement mode. The rate of variation in the voltage applied to the sample did not exceed 0.01 V/s.

The characteristic measured was the current flowing through the sample. The maximum current was 40 nA. The nonequilibrium carriers present in the layer of thermally oxidized porous silicon were either injected from the electrodes or photoexcited from traps. To determine the possible current-transport mechanisms, let us estimate the electric fields produced in the bulk of the nanocomposite. Because the thickness of the nanocomposite layer is about 0.15 µm, the maximum average electric field strength $\langle E \rangle$ in a SiO_2 layer at a sweep voltage amplitude of 3 V does not exceed 200 kV/cm. Next, let us estimate the maximum electric field strength E_m at the surface of a silicon nanocluster. As follows from our electron-microscope studies, the average size of silicon nanoscopic inclusions, nanoclusters, is ~10 nm. According to [13], the value of E_m in a nonuniform dielectric with conductive spherical inclusions of this size is

$$E_m = \langle E \rangle / 0.63. \qquad (1)$$

Substituting the average $\langle E \rangle$ into Eq. (1), we find that the electric field at the surface of a silicon nanocluster embedded in a dielectric matrix does not exceed 320 kV/cm. Photoemission measurements and *I–V* injection curves [14, 15] suggest that the Si–SiO_2 barrier height for electrons is more than 2.7 eV. These estimates exclude the Fowler–Nordheim (because of the small E_m) and the Schottky emission (because of the

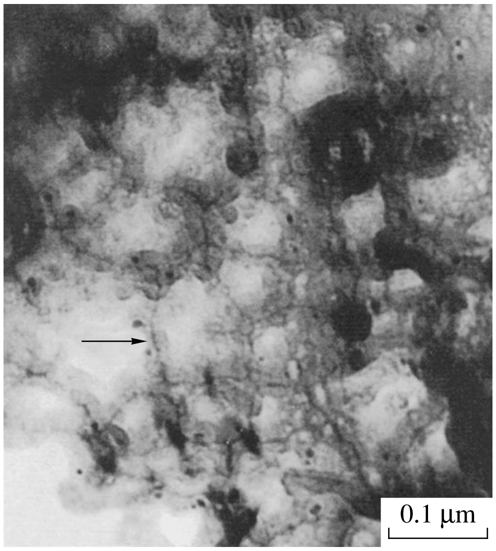

Fig. 4. Filamentary cellular structure of the nanocomposite.

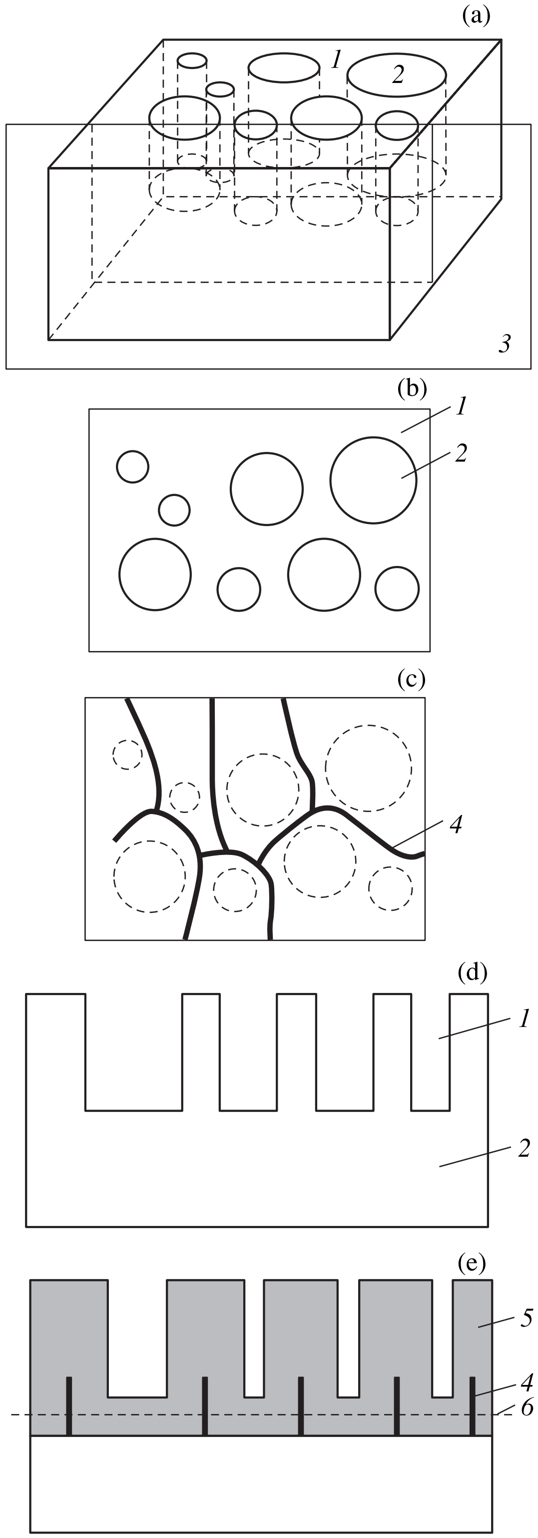

Fig. 5. Illustration of the nanocomposite formation (schematic). (a) Silicon plate after etching in the reactor, (b) top view of the plate, (c) same after oxidation, (d) cross section of the plate after etching, and (e) cross section of the plate after etching and oxidation. (*1*) Silicon plate, (*2*) pores, (*3*) cross-sectional plane involved in panels (d) and (e), (*4*) silicon filament, (*5*) oxide, and (*6*) lower boundary of the sample part studied with an electron microscope.

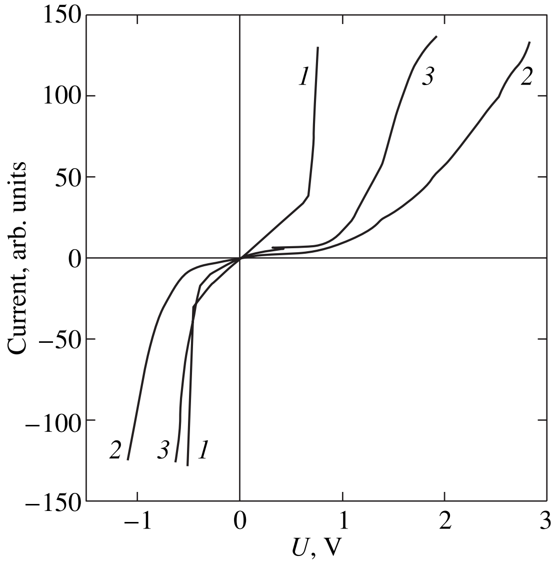

Fig. 6. *I–V* curve of the layer of thermally oxidized porous silicon.

high barrier at the Si–SiO$_2$ interface and the absence of short-wavelength radiation in the sample illumination) from consideration as possible candidates for the current-transport mechanisms operative in a dielectric nanocomposite layer. Because the silicon dioxide is an amorphous dielectric (as follows from the structural studies mentioned above), it contains a large number of electrically active defects (traps) localized close to the midgap of the dielectric. According to [16], carrier transport in weak electric fields can occur not over the allowed bands of the dielectric but rather over a system of localized states lying in the dielectric bandgap. Therefore, the carrier transport in a nanocomposite layer can be assumed to occur primarily via the hopping mechanism [17, 18].

Figure 6 presents a family of *I–V* curves measured in different nanocomposite excitation modes. To estimate the concentration of thermally activated shallow traps and photostimulated traps, let us consider first the *I–V* curve (curve *1* in Fig. 6) for the case where the sample under study is maintained at room temperature and is illuminated by light with a maximum photon energy not exceeding 1.8 eV. In this case, the *I–V* curve consists of two branches. If the bias applied to the nanocomposite layer is positive and varies from 0 to 0.68 V, the current follows a linear relation. In this case, Ohm's law holds at low enough fields inside the nanocomposite layer (~45 kV/cm). The nanocomposite contains thermally activated carriers with a concentration n_0 and nonequilibrium carriers with a concentration n_t. The carriers with concentration n_0 may originate from groups of fairly shallow traps located in the near-surface region of silicon nanoclusters, which are thermally depleted at room temperature. Deep traps are filled and are not directly involved in carrier transport at room temperature. We assume that traps are actually singly charged centers, i.e., that a trap is capable of capturing or releasing one electron. No noticeable deviations from Ohm's law occur as long as the nonequilibrium carrier concentration n_t does not exceed the concentration n_0. After the voltage has reached $U_0 = 0.68$ V, the current rises very steeply. This behavior of the current can be attributed to traps being filled by nonequilibrium carriers, as a result of which the injected charge starts to exceed the charge at the traps. Let us estimate the concentration n_t of thermally activated shallow traps using the relation [18, 19]

$$n_t = n_0 = 2.21 \times 10^{20} U_0, \tag{2}$$

where U_0 is the voltage at which the *I–V* curve switches from Ohm's law to a steep current rise.

Substituting the values of U_0 into Eq. (2), we obtain 1.5×10^{20} cm^{-3} for the trap concentration. The effective carrier mobility in the nanocomposite layer biased by a voltage U_0 can be estimated using the following relation from [18, 19]:

$$\mu_{\text{eff}} = 8IL^3/9\varepsilon\varepsilon_0 U_0, \tag{3}$$

where ε is the relative permittivity of the dielectric (SiO_2), L is the thickness of the dielectric (in meters), and I is the current at voltage $U = U_0$.

In this case, the effective mobility was found to be 0.45×10^{-15} cm^2/(V s). Let us estimate the concentration of thermally activated shallow traps for the case where a negative bias is applied to the structure under study. At low bias voltages, this branch of the *I–V* curve also has a section with a linear rise in current. The voltage U_0 at which the current starts to rise steeply is –0.44 V. In this particular case, the trap concentration calculated from Eq. (2) is 0.97×10^{20} cm^{-3}. The effective carrier mobility μ_{eff} derived from Eq. (3) is 0.47×10^{-15} cm^2/(V s). An analysis of the behavior of the *I–V* curves obtained under a bias with opposite signs suggests that the trap concentrations and effective mobilities at the U_0 point in these two cases coincide in order of magnitude. This gives us grounds to believe that the mechanisms involved in the current transport are the same in both cases. According to [16], the trap concentration in the layer of thermally oxidized silicon lies in the range 10^{19} to 10^{21} cm^{-3} and the effective mobility of electrons does not exceed 10^{-11} cm^2/(V s). Such a high concentration of traps indicates that they may originate from defects that form in silicon dioxide due to rupture of the Si–O bonds [16]. The trap concentration in the dielectric layer of the composite is of the same order of magnitude as that for the thermally oxidized silicon. This suggests that the nature of the traps can possibly be identified with rupture of the same bonds. The fact that the effective mobility is substantially lower (by several orders of magnitude) may be attributed to a more intense capture of carriers (in comparison with the case of thermally produced silicon dioxide) due to the presence of traps localized near silicon nanoparticles in the surface layer of the dielectric.

Curve *2* in Fig. 6 is a *I–V* characteristic measured at room temperature in the dark. This curve consists of several portions described by different functional relations. In the absence of illumination, trap depletion by light can be neglected. As before, the nanocomposite layer contains thermally depleted shallow traps that create a carrier concentration n_0 and nonequilibrium carriers with a concentration n_t. The nonequilibrium carriers are injected from the electrode only. For a positive bias applied to the nanocomposite, the dependence of current on voltage is seen to be linear in the voltage interval 0–0.52 V.

As the voltage at the positive electrode is increased from 0.52 to 2.8 V, the current scales as $I \sim U^k$, where $k \approx 2.5$. The fact that the current graph differs from curve *1* suggests that the traps are distributed in activation energy. One has therefore to modify the approach to evaluate the carrier concentration. As follows from our electron-microscope studies, current transport takes place in a disordered dielectric (silicon nanocrystallites are embedded in the amorphous layer of silicon dioxide). The current transport in an amorphous dielectric is described using a normal (Gaussian) distribution of electrically active defects in activation energy near the dielectric midgap [16, 18]. In the case of a normal distribution of electrically active defects in activation energy, the energy width ΔE of the distribution can be estimated as 1.2 eV. The choice of this value is substantiated by the fact that the maximum pump photon energy does not exceed ~1.8 eV. Therefore, photons should deplete predominantly traps ranging within ΔE in activation energy. According to [19], the shallow trap concentration can be calculated from the formula

$$n_t = 1.84 \times 10^{20} U_1, \tag{4}$$

where U_1 is the voltage at which the *I–V* curve switches from a linear relation to a power-law relation.

From Eq. (4), the trap concentration is calculated to be 0.94×10^{20} cm^{-3}. The effective mobility calculated from Eq. (3) at the point of crossover from a linear relation to a power-law relation in the *I–V* curves is 0.45×10^{-16} cm^2/(V s). A comparative analysis of curves *1* and *2* suggests that, for approximately equal trap concentrations, the effective carrier mobility in the dark decreases by almost one order of magnitude. We will consider this point later.

When negative voltages ranging from 0 to –0.48 V are applied to the nanocomposite layer, Ohm's law also holds and the mechanism of current transport through the nanocomposite layer remains similar to the one discussed earlier. For reverse biases above 0.48 V, the *I–V* branches can be approximated by a power-law relation $I \sim U^k$ with $k = 3.2$. In this case, the dependence of the current on voltage can be described in terms of the same model of distribution of electrically active defects. The trap concentration as estimated from Eq. (4) is not less than 0.86×10^{20} cm^{-3}. The effective mobility in these conditions is 0.8×10^{-16} cm^2/(V s). We readily see that both the trap concentration and the effective carrier mobility for the negative branch are close to their respective values obtained for a positive bias.

Carrier transport within the dielectric nanocomposite layer can occur only over localized states within its bandgap [15–17]. Assuming the traps to obey a quasi-continuous (Gaussian) distribution in activation energy near the dielectric midgap, the carrier transport can be described in terms of the constant-range hopping conductivity model in strong fields [17]. The hopping conductivity model [16, 18] offers the following explanation for the mechanism of charge buildup and transport in a nanocomposite. Localized states are located at different distances from one another and have different activation energies. The distance between localized centers enters the exponent of the tunneling factor. Even a slight change in the distance brings about a marked change in the hopping probability and, hence, in the release time from the trap. Thus, a carrier moving over localized states to the opposite electrode sometimes becomes trapped by a "blind" center, where it may remain a long time, and this is what accounts for the decrease in mobility and the buildup of charge. The mobility and accumulated charge depend on temperature, because carrier hopping is a thermally activated process.

Let us consider now a *I–V* curve (curve *3* in Fig. 6) for the case where the sample under study was first cooled in the dark down to 100 K and then was illuminated at this temperature with photons with a maximum energy not exceeding 1.8 eV. We can safely assume that all thermally activated shallow traps are frozen out and do not contribute to the current transport processes. Illumination will release nonequilibrium carriers from the traps whose activation energies do not exceed the maximum photon energy. In view of the spectral range of the incident light, the width of the trap activation energy interval is 1.2 eV. The positive *I–V* branch is more complex in this case. Ohm's law is satisfied within a narrower voltage interval (from 0 to 0.16 eV), after which (from 0.16 to 0.83 eV) the *I–V* branch is sublinear with an exponent $k = 1.6$. The free carrier concentration derives in this case from nonequilibrium carriers only. A comparison of curves *1* and *3* shows that, for the same applied voltage, the current through an illuminated composite maintained at room temperature is substantially higher. Assuming that the shallow traps are frozen out at 100 K and are not involved in generation and recombination processes, we conclude that illumination causes depletion of the traps in the dielectric layer that lie near the midgap and have a 1.2-eV-wide energy distribution. The concentration n_t as calculated from Eq. (4) is in this case not less than 0.29×10^{20} cm^{-2}. The effective carrier mobility μ_{eff} given by Eq. (3) is 0.96×10^{-16} cm^2/(V s).

The current transport mechanism in the sublinear region and in the voltage interval from 0.83 to 1.56 V (where the current scales as $I \approx U^k$ with exponent $k = 2.6$) may be associated with the photostimulated ejection of carriers from shallow traps and their tunneling transport to the electrode.

As the bias increases from 1.56 to 2.0 V, a knee appears in the *I–V* curve and the dependence of current on applied voltage becomes sublinear, $I \approx U^k$, with $k = 1.2$. In this case, most of the shallow traps are already filled and do not participate directly in carrier transport. Carrier transport occurs in these conditions by tunneling over localized states in the bandgap of the dielectric.

A *I–V* curve measured under a negative bias applied to the nanocomposite layer consists of two parts: a linear region and a region with a power-law dependence $I \approx U^{3.4}$. The voltage U_1 is 0.32 V. The concentration n_t as calculated from Eq. (4) is 0.58×10^{20} cm^{-3} in this case. The effective carrier mobility μ_{eff} obtained using Eq. (3) is 1.6×10^{-16} cm^2/(V s). The mechanisms of current transport involved here are similar to those considered earlier for the negative *I–V* branches (curves *1*, *2* in Fig. 6).

5. CONCLUSIONS

(1) It has been shown that the Si–SiO$_2$ nanocomposite can be obtained through the oxidation of porous silicon. The nanocomposite consists of silicon dioxide with embedded inclusions of crystalline silicon of two types: (i) round-shaped particles 5 to 30 nm in size and (ii) a filamentary network structure with filaments about a few nanometers thick.

(2) The concentration of thermally activated traps in the bulk of the nanocomposite is 0.94×10^{20} cm^{-3}. The effective carrier mobility $\mu_{\text{eff}} = 0.45 \times 10^{-16}$ cm^2/(V s). The substantially lower value of the effective carrier mobility as compared with literature data may be assigned to strong carrier capture by the traps and to the long time they remain trapped by the centers localized in the large-area Si : SiO$_2$ interface. The concentration of optically depleted traps is not less than 0.58×10^{20} cm^{-3}. The effective carrier mobility in this case is 1.6×10^{-16} cm^2/(V s).

(3) The strong capture by traps in the nanocomposite and the photosensitivity in the visible region revealed in the present study suggest that this nanocomposite is a promising material for use in functional microelectronic devices.

ACKNOWLEDGMENTS

This study was supported by the Department of Physical Sciences of the Russian Academy of Sciences (program “New Materials and Structures”).

REFERENCES

1. A. I. Gusev and A. A. Rempel, *Nanocrystalline Materials* (Fizmatlit, Moscow, 2001; Cambridge International Science Publishing, Cambridge, 2004).
2. M. S. Ablova, M. V. Zamoryanskaya, V. I. Sokolov, and R. I. Khasanov, Pis’ma Zh. Éksp. Teor. Fiz. **29** (11), 41 (2003).
3. B. Dac and S. P. Mc. Ginnis, Semicond. Sci. Technol. **14**, 998 (1999).
4. L. A. Balagurov, S. C. Bauliss, A. F. Orlov, B. Unal, and D. G. Yarkin, in *Proceedings of International Conference on Porous Semiconductors: Science and Technology, Madrid, 2000*, p. 53.
5. A. G. Cullis, L. T. Ganam, and P. D. J. Calcott, J. Appl. Phys. **82**, 909 (1997).
6. D. Kovalev, H. Heckler, G. Polisski, and F. Koch, Phys. Status Solidi B **215**, 871 (1999).
7. T. Schmidt, K. Lischka, and W. Zulehner, Phys. Rev. B **45**, 8989 (1992).
8. O. Bisi, S. Ossicicni, and L. Pavesi, Surf. Sci. Rep. **38**, 1 (2000).
9. X. L. Wu, S. J. Xiong, D. L. Fan, Y. Gu, X. M. Bao, B. B. Sui, and M. J. Stokes, Phys. Rev. B **62** (12), R7759 (2000).
10. M. Ballucani, V. Bondarenko, G. Lamedica, V. A. Yakovleva, and A. Ferrari, Appl. Phys. Lett. **74**, 1960 (1999).
11. M. Stewart, E. G. Robins, T. W. Geders, M. J. Allen, H. Ch. Choi, and J. M. Buriak, in *Proceedings of International Conference on Porous Semiconductors: Science and Technology, Madrid, 2000*, p. 31.
12. D. Dimova-Malinovska, J. Lumin. **80**, 207 (1998).
13. G. I. Skanavi, *Physics of Dielectrics (Strong Field Region)* (Fizmatgiz, Moscow, 1958) [in Russian].
14. B. E. Deal, E. H. Snow, and C. A. Mead, J. Phys. Chem. Solids **27** (11–12), 1873 (1966).
15. A. M. Goodman, Phys. Rev. **114** (2), 588 (1966).
16. A. P. Baraban, P. P. Konorov, and A. A. Kruchinin, Optoelectron. Poluprovodn. Tekh. **7**, 31 (1985).
17. R. M. Hill, Philos. Mag. **24** (192), 1307 (1971).
18. V. F. Korzo and V. N. Chernyaev, *Dielectric Films in Microelectronics* (Énergiya, Moscow, 1977) [in Russian].
19. M. A. Lampert and P. Mark, *Current Injection in Solids* (Academic, New York, 1970; Mir, Moscow, 1973).

Translated by G. Skrebtsov

Physics of the Solid State, Vol. 47, No. 7, 2005, pp. 1372–1375. Translated from Fizika Tverdogo Tela, Vol. 47, No. 7, 2005, pp. 1323–1326.
Original Russian Text Copyright © 2005 by Akopyan, Gaĭsin, Loginov, Novikov, Tsagan-Manzhiev, Vasil'ev, Golubkov.

LOW-DIMENSIONAL SYSTEMS AND SURFACE PHYSICS

Stabilized High-Temperature Hexagonal Phase in Copper Halide Nanocrystals

I. Kh. Akopyan*, V. A. Gaĭsin*, D. K. Loginov*, B. V. Novikov*, A. Tsagan-Manzhiev*, M. I. Vasil'ev, and V. V. Golubkov****

**Fock Institute of Physics, St. Petersburg State University,*
Ul'yanovskaya ul. 1, Petrodvorets, St. Petersburg, 198504 Russia
*** Institute of Silicate Chemistry, Russian Academy of Sciences, St. Petersburg, 199155 Russia*
e-mail: bono1933@mail.ru

Received September 6, 2004

Abstract—Low-temperature ($T = 4.2$–77 K) absorption spectra of CuCl and CuBr nanocrystals in photochromic glass matrixes are studied. A fine structure of exciton absorption bands (Z_3 band for CuCl and Z_{12} band for CuBr) is discovered and studied as a function of nanocrystal size. It is suggested that the high-energy part of the absorption band is due to the high-temperature hexagonal β phase being stabilized in very small samples; a transition to the stable cubic phase with increasing nanocrystal size is demonstrated. *© 2005 Pleiades Publishing, Inc.*

Despite the full understanding of the quantum-confinement effects in optical spectra of nanocrystals gained over recent years [1], polymorphism is still not understood. However, it is quite evident that, when dealing with the quantum-confinement effects, one should take into account the possibility of very small nanocrystals being formed of nonequilibrium phases [2]. The present work studies the possibility of nonequilibrium phases of copper halides being stabilized in nanocrystals. Copper halides have been studied thoroughly for a long time [1], but their optical properties are still of great interest both for fundamental and applied research. In the present paper, it is demonstrated, for the first time, that a copper halide nanocrystal can be made from either the equilibrium cubic phase or metastable β phase, depending on its size.

We studied low-temperature ($T = 4.2$–77 K) absorption spectra of CuCl nanocrystals of mean radii $a = 5.2$–18.5 nm and CuBr nanocrystals of mean radii 3.5–24.0 nm contained in a sodium alumina-borosilicate glass matrix [3]. Because of the spin–orbital splitting, two exciton bands (Z_{12}, Z_3) are observed in the absorption spectra of the nanocrystals, with Z_3 being the lower energy band for CuCl. We observed doubling of the absorption bands in a certain range of nanocrystal dimensions.

The absorption spectra taken at $T = 77$ K for CuCl nanocrystals with radii ranging from 5.2 to 18.5 nm are shown in Fig. 1. The Z_3 and Z_{12} absorption bands, in agreement with the quantum-confinement effect, shift toward short wavelengths as the nanocrystal size decreases. The Z_3 band is clearly doubled in relatively small samples (curves *1*–*3*). As follows from Fig. 1, the relative intensity of the long-wavelength component (A_1) increases as the mean nanocrystal radius increases.

Its intensity exceeds that of the short-wavelength component (A_2) in the spectrum of 12-nm samples, and further, for $a > 12$ nm, the long-wavelength part becomes dominant.

The absorption spectra of CuCl nanocrystals of the same dimensions taken at $T = 4.2$ K are shifted to lower energies but have the same characteristic features and are virtually identical to the spectra shown in Fig. 1. In the inset to Fig. 1, the energies of the maxima of the A_1 and A_2 bands at $T = 4.2$ K are shown as a function of the inverse square of the nanocrystal radius.

It is clearly seen that, as the nanocrystal size increases, the spectral position of the A_1 band approaches the bulk exciton energy (3.04 eV at $T = 4.2$ K and 3.22 eV at $T = 77$ K).

The energy distance between the components of the Z_3 absorption band is independent of nanocrystal size within the accuracy of our measurements and is equal to ~12 meV.

These results are reproduced well for other families of CuCl nanocrystals, in particular, for thulium-doped nanocrystals. However, it is worth mentioning that the long-wavelength component of the doubled exciton band dominates the spectra of thulium-doped samples starting from appreciably smaller dimensions of the nanocrystals.

The luminescence spectra of CuCl nanocrystals at $T = 4.2$ K consist of emission bands in resonance with absorption bands and an impurity band near 3.18 eV. In accordance with the absorption data, the resonance emission band of a nanocrystal of appropriate dimensions is likewise doubled and the relative intensity of the long-wavelength component increases with nanocrystal size.

The absorption spectra in the region of the Z_{12} band taken at $T = 77$ K for CuBr nanocrystals with radii ranging from 4.4 to 24.0 nm are shown in Fig. 2. Only the A_2 band was observed in the absorption spectra for $a \leq 6$ nm. As the nanocrystal size increases, the long-wavelength component A_1 appears. For CuBr nanocrystals with radii exceeding 7 nm, the Z_{12} absorption band is doubled, as is the exciton absorption band of CuCl in the spectra shown in Fig. 1. For nanocrystals with radii in the range 9–11 nm, the intensities of both components are roughly equal, and for the range 15–24 nm the intensity of the A_1 component becomes higher than that of A_2 (for the largest radius, 24 nm, the spectral position of the long-wavelength component virtually coincides with the position of the Z_{12} band in bulk CuBr [4]). However, in contrast to the case of CuCl, the intensity of the short-wavelength component is still appreciable. In the inset to Fig. 2, the spectral positions of the maxima of both bands at $T = 77$ K are shown as a function of the inverse square of the nanocrystal radius. The energy distance between the components is about 19 meV.

Several possible reasons can be considered for the doubling of the exciton absorption line in the nanocrystals under study.

It was demonstrated in [5] that the halide phase in sodium alumina-borosilicate glass matrices consists of at least two components, CuCl and NaCl (CuBr and KBr in the case of copper bromide). Therefore, after crystallization, each region can contain CuCl crystals and its solid solutions. In this case, the experimental data can be explained assuming that the high-energy component is related to the solid solution and the low-energy component corresponds to a pure copper halide crystal (the energy gap of alkali halides is significantly larger than that of copper halide). It follows that small nanocrystals consist predominantly of the solid solution and that their composition approaches that of the pure compound as the nanocrystal size increases. However, this scenario seems unlikely because, according to [5], the halide fluid composition (approximately 17 mol % NaCl) varies insignificantly with size. Furthermore, a stronger shift to short wavelengths should be expected for a structure consisting of a solid solution of CuCl and NaCl because of the large difference between their energy gaps.

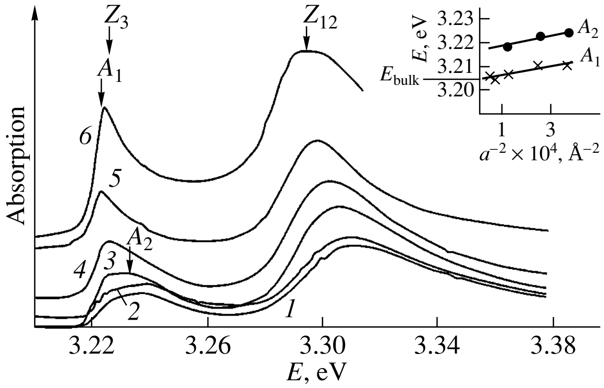

Fig. 1. Absorption spectra of CuCl nanocrystals for various values of their mean radius: (*1*) 5.2, (*2*) 6.0, (*3*) 9.2, (*4*) 12.0, (*5*) 15.0, and (*6*) 18.3 nm; $T = 77$ K. The inset shows the energies of the maxima of the A_1 and A_2 bands at $T = 4.2$ K as a function of the inverse square of the nanocrystal radius.

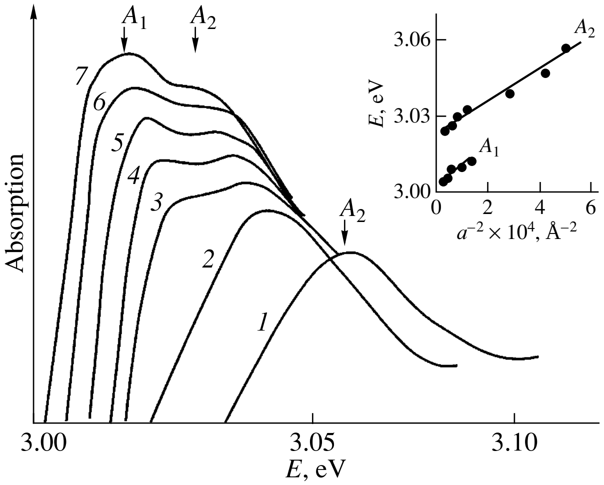

Fig. 2. Absorption spectra of CuBr nanocrystals for various values of their mean radius: (*1*) 4.4, (*2*) 4.8, (*3*) 7.4, (*4*) 9.0, (*5*) 11.0, (*6*) 20.0, and (*7*) 24.0 nm taken at $T = 77$ K in the region of the absorption band Z_{12}. The inset shows the energies of the maxima of the A_1 and A_2 bands at $T = 77$ K as a function of the inverse square of the nanocrystal radius.

The observed phenomenon (the appearance of a short-wavelength component of the absorption band) can be due to deformations of nanocrystals that arise during crystallization, for example, because of compression exerted by the glass matrix. The low-energy component of the absorption band should be linked to the absorption of undistorted nanocrystals because this component tends to the exciton energy in a bulk crystal for large nanocrystals. Therefore, the high-energy component corresponds to absorption in strained nanocrystals. However, the energy distance between A_1 and A_2 depends on the crystal dimensions only weakly; therefore, we have to admit that the stresses in a nanocrystal are independent of its size in this case, which is hard to explain. At the very least, the size effect will be observed for nanocrystals with $a < 16$ nm, in which an inner pore is created during crystallization, whereas for larger nanocrystals the matrix is destroyed and a free surface appears during crystallization [5].

We believe that the most consistent assumption is the following. It is well known [4] that copper halides have a cubic zinc-blende structure (γ phase) at normal pressure and low temperatures (up to 435°C for CuCl and up to 405°C for CuBr). At higher temperatures, up to the melting point for CuCl and up to the temperature of the phase transition to the α phase, (T = 485°C) for CuBr, they are crystallized into a hexagonal wurtzite structure (β phase).

We believe that the observed fine structure of the exciton absorption bands is due to the high-temperature hexagonal phase being stabilized in very small nanocrystals. In optical spectra, the β phase should manifest itself as splitting of the Z_{12} band caused by the trigonal crystal field and as blue shifts of the Z_3 band and Z_{12} doublet. However, the energy distance between the observed A_1 and A_2 lines in CuBr is significantly smaller than the expected values of Z_{12} doublet splitting (50 meV) and shift (65 meV) due to the transition of this compound from the zinc-blende structure to the wurtzite structure [4] (we are not aware of the corresponding data for CuCl). Therefore, we have to assume that we are dealing with structures of an intermediate type [6] consisting of hexagonally and cubically packed layers with uneven alteration along a preferred direction (crystals with one-dimensional disorder). In this case, the splitting of the Z_{12} band and shift of the Z_3 band can be assumed to be linear in a parameter α (the degree of hexagonal ordering) that is proportional to the number of hexagonally packed layers ($\alpha < 1$).

Thus, we believe that the low-energy band in the absorption spectra of CuCl and CuBr nanocrystals, whose position approaches the bulk exciton energy at large nanocrystal sizes, corresponds to the stable cubic phase. The high-energy band dominating the spectra of smaller nanocrystals (only this band is present in the absorption spectrum of CuBr nanocrystals with radii less than 6 nm) can be considered an exciton absorption band of nanocrystals containing hexagonal stacking faults. The parameter α for CuBr nanocrystals can be estimated as $\alpha = 0.38$ in the linear approximation for the exciton energy in crystals with structure disorder. The character of the dependence of the relative intensity of the A_1 and A_2 components in the absorption spectra on the nanocrystal size suggests that the stable cubic phase will arise as the nanocrystal size increases. However, it is noteworthy that we failed to observe the splitting of A_2 in CuBr as expected for the Z_{12} band in a hexagonal crystal. Possibly, this is due to the parameter α being small and the half-width of the bands being large.

As follows from our data, the hexagonal phase of CuCl manifests itself for nanocrystals with radii less than 10 nm. In CuBr, the metastable phase survives in samples with a radius of 24 nm, though the exciton absorption of the stable γ phase appears in spectra starting from radii of >7 nm. We note that, in CuI nanocrystals produced by deposition on a polymer film [7], the hexagonal phase exists up to a radius of 57 nm, and in silver iodide, which is isostructural to copper halides, the cubic and hexagonal phases coexist in bulk samples and form polytypes of various orders.

Preliminary x-ray analysis data confirm that the β phase is present in CuCl nanocrystals: hexagonal reflections were found in a 7.4-nm sample.

Thus, the experimental data obtained suggest that nanometer-sized CuCl and CuBr crystals can exist at low temperatures in the nonequilibrium hexagonal β phase. As the nanocrystal dimensions increase, the stable cubic γ phase arises.

Currently, the formation of nonequilibrium crystal structures in metal nanoparticles is virtually a firmly established fact [8]. For example, Nb, Ta, Mo, and W, which have the bcc structure in bulk, crystallize into either the fcc or the closely packed hexagonal structure in particles 5 to 10 nm in size.

There are data implying that semiconductor nanoparticles also tend to crystallize into metastable forms. For example, small-size CdS and CdSe crystals (<5 nm) have a cubic structure and a stable hexagonal structure arises only when their dimensions increase (see, i.e., [9]). Nanocrystals tending to turn from the wurtzite to the zinc-blende structure with decreasing size show disordered structures containing packing defects. Studies of the formation of the HgI_2 crystal phase on the surfaces of various matrices have shown that a compound emerging on a matrix surface tends to transform into nonequilibrium phases (mainly the high-temperature yellow modification), which gradually convert into the stable red tetragonal phase as the crystals grow [10]. Analysis of the HgI_2 phase composition in various nanocomposites also showed that this semiconductor is in a metastable phase in small samples [10].

The possible variation in the crystal structure of small particles with a decrease in their size is related in most theoretic papers to the size dependence of the surface energy, whose contribution to the free energy of small particles becomes significant. The specific surface energy (the surface tension σ) as a function of the particle radius can be described, in a first approximation, by the Tolman equation $\sigma(R) \approx \sigma_\infty(1 + 2\delta/R)^{-1}$, where σ_∞ is the surface tension of a flat surface and δ is the Tolman length (which is of the order of the interphase boundary thickness). Thus, the surface tension can either decrease (for $\delta > 0$) or increase (for $\delta < 0$) as the particle size decreases. Thermodynamic treatment of the surface tension as a function of the surface radius of curvature in the limit of small radii [11] shows that it decreases as the radius becomes smaller and vanishes when the radius becomes zero.

However, this conclusion is made for spherical and flat surfaces under the assumption that the surface as a whole has the same surface tension. When dealing with single crystals, it is necessary to attribute a specific "linear tension" value to each face and to each edge. The contribution of edges and corners can be neglected for large crystals, but, as the dimensions decrease to the point where the edge width is comparable to the sizes of adjacent faces, it becomes compulsory to take the edge energy into account. Calculations of the equilibrium shape of a single crystal with allowance for the edge energy were performed in [11]. It was shown that the mean surface tension increases and the edge and corner energies become noticeable as the crystal size decreases. In this case, it is energetically favorable for the crystal to change its structure in such a way that the surface tension and the total free energy do not increase. Therefore, structures that are metastable or do not exist at all in bulk samples of a compound can become possible for small sample sizes.

REFERENCES

1. A. Ekimov, J. Lumin. **70**, 1 (1996).
2. Yu. I. Petrov, *Clusters and Small Particles* (Nauka, Moscow, 1986) [in Russian].
3. I. Zh. Bus'ko, V. V. Golubkov, M. I. Vasil'ev, V. V. Pshenitsyna, and V. A. Tsekhomskiĭ, Fiz. Khim. Stekla **28**, 180 (2002).
4. M. Cardona, Phys. Rev. **129**, 69 (1963).
5. V. V. Golubkov and V. A. Tsekhomskiĭ, Fiz. Khim. Stekla. **12**, 206 (1986).
6. A. Yu. Maslov, D. L. Fedotov, L. G. Suslina, V. G. Melekhin, and A. G. Areshkin, Fiz. Tverd. Tela (Leningrad) **25**, 1408 (1983) [Sov. Phys. Solid State **25**, 809 (1983)].
7. A. Tanji, I. Akai, K. Kojima, T. Karasava, and T. Komatsu, J. Lumin. **87–89**, 516 (2000).
8. I. D. Morokhov, V. I. Petinov, and L. I. Trusov, Usp. Fiz. Nauk **133**, 653 (1981) [Sov. Phys. Usp. **24** (4), 295 (1981)].
9. R. Rossetti, S. Nakamura, and L. E. Brus, J. Chem. Phys. **79**, 1086 (1983).
10. I. Kh. Akopyan, M. É. Labzovskaya, and B. V. Novikov, Fiz. Tverd. Tela (St. Petersburg) **44**, 1326 (2002) [Phys. Solid State **44** (7), 1388 (2002)].
11. A. I. Rusanov, *Phase Equilibriums and Surface Phenomena* (Khimiya, Leningrad, 1967) [in Russian].

Translated by G. Tsydynzhapov

Physics of the Solid State, Vol. 47, No. 7, 2005, pp. 1376–1382. Translated from Fizika Tverdogo Tela, Vol. 47, No. 7, 2005, pp. 1327–1332.
Original Russian Text Copyright © 2005 by Voronov, Ivchenko.

LOW-DIMENSIONAL SYSTEMS AND SURFACE PHYSICS

Bragg Solitons in Quantum-Well Structures

M. M. Voronov and E. L. Ivchenko

Ioffe Physicotechnical Institute, Russian Academy of Sciences,
Politekhnicheskaya ul. 26, St. Petersburg, 194021 Russia
e-mail: ivchenko@coherent.ioffe.rffi.ru

Received September 9, 2004

Abstract—Soliton pulse propagation in a periodic quantum-well structure with a period close to one-half the light wavelength corresponding to the exciton resonance frequency was studied. The various kinds of exciton nonlinearity characteristic of a quantum well (P^3- and EP^2-type nonlinearities, biexciton nonlinearity) were included. The characteristic features of the soliton were studied in each of the cases considered. The effect of refractive index mismatch between the barrier and quantum-well materials on the soliton parameters was analyzed. Soliton solutions to the Maxwell–Bloch nonlinear equations are compared with their plane-wave solutions. *© 2005 Pleiades Publishing, Inc.*

1. INTRODUCTION

The current physics of photonic crystals has evolved into an independent branch of solid-state optical spectroscopy where basic research is being actively pursued and ways to apply technologies in practice are being sought. There are three-, two-, and one-dimensional photonic crystals, depending on whether the permittivity of the medium is modulated in three, two, or one dimension. The simplest conceivable realization of a one-dimensional photonic crystal is an …*A*/*B*/*A*/*B*… periodic structure consisting of two materials, *A* and *B*, with different refractive indices. Periodic structures with semiconductor quantum wells and, in particular, resonance Bragg structures make up a specific class of resonance one-dimensional photonic crystals with exciton polaritons as normal waves [1–8]. Most of the research into resonance Bragg structures has been performed in the field of linear optics. However, nonlinear optical phenomena have also been studied in such structures, among them degenerate four-wave mixing [9] and suppression of the superradiant reflection signal with increasing incident light intensity [10].

In this paper, we report on a study of the nonlinear properties of resonance Bragg and quasi-Bragg structures with the aim of verifying whether they can support soliton pulse propagation. Speaking in a broader vein, we have in mind the phenomena of self-induced transparency [11], which can be observed in these structures with quantum wells. It is for this purpose that solutions to the Maxwell–Bloch equations are sought and analyzed. Three different mechanisms of nonlinearity operative in the system are consistently included. It is shown that inclusion of each of them gives rise to a soliton solution similar to that considered earlier for a bulk semiconductor [12] or for a periodic structure with two-level systems [13–15]. In addition to the soliton solutions, we also find plane-wave solutions to the nonlinear Maxwell–Bloch equations. An analysis of these solutions sheds light on the relation between the soliton type and the character of the system nonlinearity.

2. MAXWELL–BLOCH EQUATIONS FOR EXCITONS IN A BRAGG STRUCTURE

We consider the propagation of electromagnetic radiation along the normal (*z* axis) to a periodic layered structure with a period $d = a + b$, which is the sum of the widths of the quantum well (a) and the barrier (b). It is assumed that (i) the background permittivities ε_a and ε_b of the quantum-well and barrier materials are different but the mismatch $|\varepsilon_a - \varepsilon_b|$ is small as compared to the mean value $\bar{\varepsilon} = (\varepsilon_a a + \varepsilon_b b)/d$, (ii) the Bragg frequency of the periodic structure

$$\omega_{\mathrm{B}} = \pi c/(\bar{n} d) \tag{1}$$

(where $\bar{n} = \sqrt{\bar{\varepsilon}}$) is close to the exciton resonance frequency ω_0 in a single quantum well, and (iii) the light wave carrier frequency lies in the vicinity of the frequency $\omega_0 \approx \omega_B$. In these conditions, the electric induction is related to the electric field as

$$\mathbf{D}(z, t) = [\bar{\varepsilon} + \Delta\varepsilon_1 \cos(2kz)]\mathbf{E}(z, t) + 4\pi \sum_j \mathbf{P}_j^{\mathrm{exc}}(z, t). \tag{2}$$

Here, $\mathbf{P}_j^{\mathrm{exc}}(z, t)$ is the dielectric polarization induced by an exciton excited in the *j*th well; $j = 0, \pm 1, \pm 2, \ldots$; $k = \pi/d$; and $\Delta\varepsilon_1 = 2(\varepsilon_a - \varepsilon_b)a/d$. In view of the weak mismatch between the dielectric constants ε_a and ε_b, we expanded the background permittivity in a Fourier series and retained only the first two terms in Eq. (2). The axial symmetry of the system permits us to assume all fields to be similarly polarized and to use the scalar quantities E, P_j^{exc}, etc., rather than vectors.

Because the well width is small as compared to the period of the structure, we can neglect the coordinate dependence of electric field within a quantum well and write the exciton contribution to polarization as a sum of δ-function contributions:

$$P^{\mathrm{exc}}(z,t) = \sum_j \delta(z - jd)\int P_j^{\mathrm{exc}}(z',t)dz'. \tag{3}$$

Taking into account the coherent backscattering, the electric field $E(z, t)$ can be written as a superposition of two types of waves propagating in the direct (>, along the z axis) and reverse (<) directions:

$$\begin{aligned} &E(z,t) \\ &= [\mathcal{E}_>(z,t)e^{ikz} + \mathcal{E}_<(z,t)e^{-ikz}]e^{-i\omega_{\mathrm{B}}t} + \text{c.c.} \end{aligned} \tag{4}$$

We assume that the electric-field envelopes are slowly varying functions. Therefore, the inequalities

$$\left|\frac{\partial\mathcal{E}_>}{\partial z}\right| \ll k|\mathcal{E}_>|, \quad \left|\frac{\partial\mathcal{E}_>}{\partial t}\right| \ll \omega_{\mathrm{B}}|\mathcal{E}_>|$$

are met, as are the analogous inequalities for $\mathcal{E}_<$. Polarization (3) can be rewritten in the form

$$\begin{aligned} &P^{\mathrm{exc}}(z,t) \\ &= d\sum_j (-1)^j P_j^{\mathrm{exc}}(t)\delta(z - jd)e^{-i\omega_B t} + \text{c.c.}, \end{aligned} \tag{5}$$

where, for convenience, we wrote the common factor d and the multiplier $(-1)^j$ under the sum sign. The function $P_j^{\mathrm{exc}}(t)$ is related to the amplitude of the electric field in the jth quantum well by the equation

$$\begin{aligned} &\left[\frac{\partial}{\partial t} + i(\omega_0 - \omega_{\mathrm{B}}) + \Gamma\right]P_j^{\mathrm{exc}}(t) \\ &= i\mu\Gamma_0\mathcal{E}_+(jd,t) + iF_{NL,j}(t). \end{aligned} \tag{6}$$

Here, Γ_0 and Γ are the radiative and nonradiative exciton damping constants in a single quantum well, respectively; $\mu = \bar{\varepsilon}/(2\pi^2)$; and

$$\mathcal{E}_+(jd,t) = \mathcal{E}_>(jd,t) + \mathcal{E}_<(jd,t),$$

where $F_{NL}(t)$ is the nonlinear contribution to the inhomogeneous term of the equation for $P_j^{\mathrm{exc}}(t)$.

We consider two types of exciton nonlinear polarization in a quantum well: nonlinearity of the type EP^2, which is characteristic of a simple two-level system, and nonlinearity of the type P^3, as in the case of a classical anharmonic oscillator. We also take into account the biexciton mechanism of nonlinearity. In this case, the nonlinear contribution to Eq. (6) takes on the form

$$\begin{aligned} F_{NL,j}(t) &= \left|P_j^{\mathrm{exc}}(t)\right|^2[\beta_1 P_j^{\mathrm{exc}}(t) + \beta_2\mathcal{E}_+(jd,t)] \\ &\quad + \gamma_{\mathrm{bi}}B_j(t)\mathcal{E}_+^*(jd,t), \end{aligned} \tag{7}$$

where β_1 and β_2 are real coefficients, B is the amplitude of the biexciton wave function, and the coefficient γ_{bi} is proportional to the matrix element of the induced exciton-to-biexciton transition. The function $B_j(t)$ satisfies the equation

$$\begin{aligned} &\left\{\frac{\partial}{\partial t} + i[2(\omega_0 - \omega_{\mathrm{B}}) - \delta_{\mathrm{bi}}] + \Gamma_{\mathrm{bi}}\right\}B_j(t) \\ &= i\gamma_{\mathrm{bi}}P_j^{\mathrm{exc}}(t)\mathcal{E}_+(jd,t), \end{aligned} \tag{8}$$

where $\hbar\delta_{\mathrm{bi}} \equiv \varepsilon_{\mathrm{bi}}$ and Γ_{bi} are the binding energy and the decay constant of the biexciton, respectively. In [16], the exciton dielectric polarization $\bar{P}$ averaged over the well width a was introduced; this polarization is d/a times larger than the polarization P_j^{exc} used here. Therefore, the constants β_1 and β_2 introduced in [16] differ from those in Eq. (7) by the factors $(d/a)^2$ and d/a, respectively. Note that the dielectric polarization P_j associated with the excitation of an exciton and a biexciton in the jth well includes two terms, P_j^{exc} and P_j^{bi}. The former term satisfies Eq. (6), and the latter can be written as

$$P_j^{\mathrm{bi}}(t) = \frac{\gamma_{\mathrm{bi}}}{\mu\Gamma_0}B_j(t)P_j^{\mathrm{exc}*}(t) \tag{9}$$

and is due to the biexciton decaying into an exciton and a photon.

In this work, we study light waves whose fields $\mathcal{E}_>$ and $\mathcal{E}_<$ and polarization P_j^{exc} vary in space on a scale larger than the period of the structure d, thus permitting us to pass over from discrete sets of $P_j^{\mathrm{exc}}(t)$ and $B_j(t)$ to continuous functions $\mathcal{P}(z, t)$, $\mathcal{B}(z, t)$. In this case, the Maxwell–Bloch equations reduce to a set of equations

$$\begin{aligned} &\left(\frac{\partial^2}{\partial t^2} - \frac{c^2}{\bar{n}^2}\frac{\partial^2}{\partial z^2}\right)\mathcal{E}_+(z,t) \\ &= \frac{4\pi\omega_{\mathrm{B}}}{\bar{n}^2}\left(i\frac{\partial\mathcal{P}(z,t)}{\partial t} - \omega_1\mathcal{P}\right) - \omega_1^2\mathcal{E}_+, \\ &\left(\frac{\partial^2}{\partial t^2} - \frac{c^2}{\bar{n}^2}\frac{\partial^2}{\partial z^2}\right)\mathcal{E}_-(z,t) \\ &= -i\frac{4\pi\omega_{\mathrm{B}}}{\bar{n}^2}\frac{c}{\bar{n}}\frac{\partial\mathcal{P}(z,t)}{\partial z} - \omega_1^2\mathcal{E}_-, \end{aligned} \tag{10}$$

$$\left[\frac{\partial}{\partial t} + i(\omega_0 - \omega_B) + \Gamma\right]\mathcal{P}(z, t)$$
$$= i\mu\Gamma_0\mathcal{E}_+(z, t) + iF_{NL}(z, t),$$

where $\mathcal{E}_- = \mathcal{E}_> - \mathcal{E}_<$ and $\omega_1 = \Delta\varepsilon_1\omega_B/4\bar{n}^2$.

3. SOLITONS IN A RESONANCE BRAGG STRUCTURE

In this section, we neglect the permittivity mismatch by assuming $\varepsilon_a = \varepsilon_b \equiv n^2$ (or $\Delta\varepsilon_1 = 0$) and consider a resonance Bragg structure satisfying the condition

$$\frac{\omega_0 n}{c}d = \pi. \qquad (11)$$

Furthermore, we neglect the nonradiative damping (Γ) and retain only P^3-type nonlinearity, which is accounted for by coefficient β_1 in Eq. (7). In this case, the polarization satisfies the equation

$$\frac{\partial\mathcal{P}(z, t)}{\partial t} = i\mu\Gamma_0\mathcal{E}_+(z, t) + i\beta_1|\mathcal{P}(z, t)|^2\mathcal{P}(z, t). \qquad (12)$$

In the absence of nonlinearity, the solutions to the Maxwell–Bloch equations are plane waves,

$$\mathcal{E}_\pm(z, t), \mathcal{P}(z, t) \propto e^{-i(\omega - \omega_0)t + iKz} \qquad (13)$$

with ω and K meeting the dispersion relation [3]

$$(\omega - \omega_0)^2 = \Delta_0^2 + \left(\frac{cK}{n}\right)^2$$

or

$$\omega = \omega_0 \pm \sqrt{\Delta_0^2 + \left(\frac{cK}{n}\right)^2},$$

where $\Delta_0 = \sqrt{2\omega_0\Gamma_0/\pi}$ is one-half of the bandgap width in the exciton polariton spectrum of the resonance Bragg structure. According to Eq. (4), K is the wave vector reckoned from the extremum point $k = \pi/d$ at the Brillouin zone edge of the periodic structure. In the presence of nonlinearity, there are solutions like Eq. (13) with a z- and t-independent amplitude. The dispersion equation for these waves

$$(\omega - \omega_0)^2 = \Delta_0^2\frac{\omega - \omega_0}{\omega - \omega_0 + \beta_1|\mathcal{P}|^2} + \left(\frac{cK}{n}\right)^2 \qquad (14)$$

depends on the square of the amplitude modulus, $|\mathcal{P}|^2$. This gives rise to the formation of an allowed miniband inside the gap $2\Delta_0$, as is the case in a quasi-Bragg structure with $\omega_0 \neq \omega_B$ [5].

We will show that the inclusion of the P^3 nonlinearity also brings about the appearance of soliton solutions. The solitons are bounded in space, i.e., decay for $z \longrightarrow \pm\infty$ and propagate at a finite velocity while retaining their shape. We first assume that the electric field and dielectric polarization depend on only one variable, $x = t - (z/V)$, where V is the soliton velocity. From the first of equations (10), it follows that the electric field satisfies the equation

$$\frac{d\mathcal{E}_+(x)}{dx} = i\frac{4\pi\omega_0}{n^2}\frac{V^2}{V^2 - (c/n)^2}\mathcal{P}(x).$$

Substituting this expression into Eq. (12) differentiated with respect to x, we arrive at a closed equation for polarization,

$$\frac{\partial^2\mathcal{P}}{\partial x^2} - i\beta_1\frac{\partial}{\partial x}(|\mathcal{P}|^2\mathcal{P}) = \frac{\Delta_0^2 u^2}{1 - u^2}\mathcal{P}, \qquad (15)$$

where we introduced a dimensionless velocity $u = Vn/c$. This equation is essentially a modified nonlinear Schrödinger equation similar to that considered in [12] for a bulk semiconductor. In [12], the coefficient on the right-hand side of the equation for $\mathcal{P}$ is proportional to the velocity V, whereas in Eq. (15) this coefficient is a nonlinear function of V; in particular, at low velocities this function is quadratic. This is where the resonance Bragg structure differs from a uniform bulk semiconductor. In accordance with [12], Eq. (15) has a soliton solution

$$\mathcal{P}(x) = e^{i\phi(x)}\sqrt{\frac{2}{x_0|\beta_1|\cosh(x/x_0)}}, \qquad (16)$$

$$\phi(x) = -3\,\mathrm{sgn}\,\beta_1\arctan(e^{-x/x_0}),$$
$$x_0 = \frac{\sqrt{1 - u^2}}{2\Delta_0|u|}. \qquad (17)$$

This solution describes solitons propagating either at velocity $V = uc/n$ or at $-V = -uc/n$, i.e., in the case where $x = t - (z/V)$ or $x = t + (z/V)$. Solution (16) corresponds to an electric field

$$\mathcal{E}_+ = \frac{8\pi\omega_0}{n^2}\frac{u^2}{1 - u^2}\sqrt{\frac{2x_0}{|\beta_1|}}\frac{-\mathrm{sgn}\,\beta_1 + i\sinh(x/x_0)}{\cosh^{3/2}(x/x_0)}e^{i\phi(x)},$$
$$\mathcal{E}_- = \frac{1}{u}\mathcal{E}_+,$$

which yields

$$\mathcal{E}_> = \frac{1}{2}\mathcal{E}_+\left(1 + \frac{1}{u}\right), \quad \mathcal{E}_< = \frac{1}{2}\mathcal{E}_+\left(1 - \frac{1}{u}\right). \qquad (18)$$

The velocity of soliton propagation is related to the maximum value of the square of the polarization modulus (at $x = 0$) through

$$|\mathcal{P}|^2_{\max} = \frac{4\Delta_0|u|}{|\beta_1|\sqrt{1 - u^2}}.$$

Terms of higher orders in $\mathcal{P}$ in Eq. (12) can obviously be neglected provided $\hbar|\beta_1\mathcal{P}^2| \ll \varepsilon_B$, where ε_B is the exciton binding energy. For comparable values of ε_B and $\hbar\Delta_0$, this condition is met for $|u| \ll 1$. Therefore, the quantity $1 - u^2$ in the above relations can be replaced by unity.

Note that the P^3 nonlinearity considered here plays a significant role in giant polariton–polariton scattering in quantum microresonators, which is observed in the case where the pumping light is incident at a "magic" angle [17–19].

4. STRUCTURES WITH DIFFERENT BACKGROUND PERMITTIVITIES

Let us consider soliton solutions in structures with different ε_a and ε_b with inclusion of the EP^2-type and the biexciton nonlinearity.

3.1. Nonlinearity of the EP^2 Type

In this case, the equation for polarization has the form

$$\left[\frac{\partial}{\partial t} + i(\omega_0 - \omega_B)\right]\mathcal{P}(z, t) = i\mu\Gamma_0\mathcal{E}_+(z, t)w(z, t), \quad (19)$$

where

$$w(z, t) = 1 - Q^2|\mathcal{P}(z, t)|^2, \quad Q^2 = -\beta_2/(\mu\Gamma_0),$$

and it is assumed that $\beta_2 < 0$. Let us introduce dimensionless variables: time $\tau = t/\tau_0$, coordinate $\zeta = \bar{n}z/c\tau_0$, polarization $\tilde{\mathcal{P}}(\zeta, \tau) = \sqrt{2}\,Q\mathcal{P}(\zeta, \tau)$, and electric field $\Sigma_\pm(\zeta, \tau) = -i\sqrt{2}\,Q\mu\Gamma_0\tau_0\mathcal{E}_\pm(\zeta, \tau)$, where

$$\tau_0 = (\pi/\omega_B\Gamma_0)^{1/2} = \sqrt{2}/\Delta_0. \quad (20)$$

In contrast to the P^3 nonlinearity considered above, no exact solution to the set of equations (10) and Eq. (19) could be found. This is not required in this case, however, because the term EP^2 on the right-hand side of Eq. (19) can be considered to be the next term in the expansion of the external force acting on the exciton oscillator in powers of P^2; the subsequent terms of this expansion can be neglected provided $|\tilde{\mathcal{P}}|^2 \ll 1$. Within the same approximation for the function w, we can replace

$$1 - (1/2)|\tilde{\mathcal{P}}|^2 \longrightarrow \sqrt{1 - |\tilde{\mathcal{P}}|^2} \quad (21)$$

after which the EP^2 nonlinearity for the exciton in a quantum well coincides with the nonlinearity for a two-level system. After replacement (21), we can find exact soliton solutions to the Maxwell–Bloch equations, because they reduce to similar equations for a resonantly absorbing Bragg reflector [13–15]; this reflector is specified by a periodic background permittivity $\varepsilon(z) = \bar{\varepsilon} + \Delta\varepsilon_1\cos(\pi z/d)$ and includes an embedded system of thin layers (with the same period d) that contain atoms or quantum two-level systems with a resonance optical-transition frequency $\omega_0 \approx \omega_B = \pi c/(d\sqrt{\bar{\varepsilon}})$. In [13], ε_0, ω_{12}, and ω_{gc} are used in place of $\bar{\varepsilon}$, ω_0, and ω_B.

The set of nonlinear equations obtained after replacement (21) has the following solution for the electric field:

$$\Sigma_+(\zeta, \tau) = \frac{\Sigma_0 e^{i(\alpha\zeta - \Delta\tau)}}{\cosh[\beta(\zeta/u - \tau)]}, \quad (22)$$

which is called a phase-modulated 2π soliton [13]. Here, α, β, and Δ are real parameters; Σ_0 is the amplitude; and $u = \bar{n}V/c$ is the dimensionless velocity of the soliton. The specific features of the semiconductor structure become manifest only through relation (20) established by us here between the time τ_0 and the radiative-decay constant Γ_0 of the exciton in a single quantum well. Out of the five soliton parameters Σ_0, α, β, Δ, and u, one can be chosen to be independent. If the velocity u is chosen as a free parameter, then the remaining four can be expressed in terms of u, the relative detuning from resonance $\delta = (\omega_0 - \omega_B)\tau_0$, and the quantity $\eta = \Delta\varepsilon_1(\omega_B\tau_0/4\bar{n}^2)$ (which is proportional to the permittivity mismatch) in the following way [20]:

$$\alpha = -\frac{\eta}{2u}\frac{1 - 3u^2}{1 - u^2} + \frac{\delta}{2u}, \quad \Delta = \frac{\eta}{2}\frac{1 + u^2}{1 - u^2} + \frac{\delta}{2},$$
$$\beta^2 = \frac{2u^2}{1 - u^2} - \frac{1}{4}\left(\eta\frac{1 + u^2}{1 - u^2} - \delta\right)^2, \quad \beta^2 = \frac{|\Sigma_0|^2}{4}. \quad (23)$$

The exciton contribution to dielectric polarization is given by

$$\tilde{\mathcal{P}}(\zeta, \tau) = \{iC_1 + C_2\tanh[\beta(\zeta/u - \tau)]\}\Sigma_+(\zeta, \tau), \quad (24)$$

where

$$C_1 = \frac{\delta - \Delta}{\beta^2 + (\delta - \Delta)^2}, \quad C_2 = \frac{\beta}{\Delta - \delta}C_1.$$

In this case, we have

$$\sqrt{1 - |\tilde{\mathcal{P}}|^2} = 1 - \frac{\beta^2(1 - u^2)}{u^2\cosh^2[\beta(\zeta/u - \tau)]}.$$

For structures with an EP^2 nonlinearity, replacement (21) is valid and solutions (22)–(24) are applicable under the condition that $|\tilde{\mathcal{P}}|^2 \ll 1$ or $\beta^2(1 - u^2) \ll u^2$. As follows from Eq. (23), the dimensionless exciton velocity satisfying this condition is

$$u = \pm\sqrt{\frac{4+\delta^2-\eta^2+|\Sigma_0|^2-4\sqrt{1+\eta(\delta-\eta)-\eta^2|\Sigma_0|^2/4}}{8+(\eta+\delta)^2+|\Sigma_0|^2}}.$$

For small values of η, δ, and $|\Sigma_0|^2$, we have

$$\begin{gathered} u = \pm u_0\left(1+\frac{|\Sigma_0|^2}{16u_0}\right), \quad u_0 = \frac{|\eta-\delta|}{2\sqrt{2}}, \\ \alpha = \sqrt{2}\,\mathrm{sgn}\left(\frac{\delta-\eta}{u}\right), \quad \Delta = \frac{\eta+\delta}{2}, \\ C_1 = \frac{2}{\delta-\eta}, \quad C_2 = -\frac{4\beta}{(\delta-\eta)^2}. \end{gathered} \tag{25}$$

It follows that this solution is valid only for $|\Sigma_0|^2 \ll (\eta-\delta)^2$.

3.2. Biexciton Nonlinearity

For a resonance Bragg structure ($\omega_0 = \omega_B$, $\varepsilon_a = \varepsilon_b$), there is also plane-wave solution (13),

$$\mathcal{E}_+(z,t) \propto e^{-i(\omega-\omega_0)t+iKz}, \quad \mathcal{B}(z,t) \propto e^{-2i(\omega-\omega_0)t+2iKz}$$

with the dispersion equation

$$(\omega-\omega_0)^2 = \Delta_0^2\left\{\frac{[2(\omega-\omega_0)+\delta_{\mathrm{bi}}](\omega-\omega_0)}{[2(\omega-\omega_0)+\delta_{\mathrm{bi}}](\omega-\omega_0)-\gamma_{\mathrm{bi}}^2|\mathcal{E}_+|^2}\right\}^2+\left(\frac{cK}{\bar{n}}\right)^2.$$

For $\Delta_0 \gg \delta_{\mathrm{bi}}$, the inclusion of nonlinearity brings about the formation of a transparency window of width $\gamma_{\mathrm{bi}}^2|\mathcal{E}_+|^2/\Delta_0$ near the frequency $\omega_0 - \delta_{\mathrm{bi}}/2$. Exactly at this frequency, the solution consists of phase-matched light and biexciton waves with amplitudes satisfying the condition $\mu\Gamma_0\mathcal{E}_+ + \gamma_{\mathrm{bi}}\mathcal{B}\mathcal{E}_+^* = 0$; so the polarizations $\mathcal{P}_X \equiv \mathcal{P}^{\mathrm{exc}}$ and $\mathcal{P}_{XX} \equiv \mathcal{P}^{\mathrm{bi}}$ are zero. W did not succeed in finding a soliton solution of the type of Eq. (16) for this case.

We analyzed the possible existence of a phase-modulated 2π soliton in a quasi-Bragg structure with mismatched permittivities ε_a and ε_b and with a frequency detuning between ω_0 and ω_B. In the case of a weak nonlinearity

$$|P_{XX}| \ll |P_X| \tag{26}$$

and if the condition

$$\delta_{\mathrm{bi}} = 2(\delta-\eta)/\tau_0 \tag{27}$$

is met, the set of three equations consisting of the first of Eqs. (10), the equation

$$\begin{gathered}\left\{\frac{\partial}{\partial t}+i[2(\omega_0-\omega_B)-\delta_{\mathrm{bi}}]\right\}\mathcal{B}(z,t) \\ = i\gamma_{\mathrm{bi}}\mathcal{P}_X\mathcal{E}_+(z,t),\end{gathered} \tag{28}$$

and the equation

$$\begin{gathered}\left[\frac{\partial}{\partial t}+i(\omega_0-\omega_{\mathrm{B}})\right]\mathcal{P}(z,t) \\ = i\mu\Gamma_0\mathcal{E}_+(z,t)+i\gamma_{\mathrm{bi}}\mathcal{B}\mathcal{E}_+^*(z,t),\end{gathered} \tag{29}$$

is satisfied by the field $\Sigma_\pm(\zeta,\tau) \equiv -i\mu\Gamma_0\tau_0\mathcal{E}_\pm(\zeta,\tau)$ in the form of Eq. (22), the polarization $\mathcal{P}(\zeta,\tau)$ in the form of Eq. (24), and the biexciton envelope

$$\mathcal{B}(\zeta,\tau) = \kappa\Sigma_+^2(\zeta,\tau). \tag{30}$$

Here, κ is a constant, which can be expressed in terms of the velocity u as

$$\kappa = \frac{\gamma_{\mathrm{bi}}}{4\mu\Gamma_0}\left(\frac{1}{u^2}-1\right), \tag{31}$$

the parameters α, β, and Δ satisfy Eqs. (23) or (25); and the amplitude Σ_0 is connected with β and velocity u through the relations

$$2\beta^2 = \left(\frac{\gamma_{\mathrm{bi}}}{\mu\Gamma_0}\right)^2|\Sigma_0|^2, \quad u = \pm u_0\left[1+\left(\frac{\gamma_{\mathrm{bi}}}{\mu\Gamma_0}\right)^2\frac{|\Sigma_0|^2}{8u_0}\right], \tag{32}$$

which differ in terms of the coefficient of $|\Sigma_0|^2$ from similar expressions for the case of EP^2-type nonlinearity [see Eqs. (23), (25)]. Condition (26) is met for $|\gamma_{\mathrm{bi}}\kappa\Sigma_0^2/\mu\Gamma_0| \ll 1$.

5. DISCUSSION OF THE RESULTS

In order for the structure to support a soliton, its thickness has to exceed the linear dimensions of the soliton. According to Eq. (16), the extent of the soliton forming with a P^3-type nonlinearity is equal, in order of magnitude, to

$$L_s = \frac{2cx_0}{n} \approx \frac{c}{n\Delta_0|u|},$$

and the duration of the soliton signal at any fixed point z can be estimated as $2x_0 = (\Delta_0 u)^{-1}$. In experimentally studied Bragg multiple quantum-well (MQW) structures CdTe/Cd$_x$Zn$_{1-x}$Te [21] and Ga$_{0.96}$In$_{0.04}$As/GaAs [22], the radiative exciton decay constant is $\hbar\Gamma_0 = 0.12$ and 0.027 meV, respectively, which yields 11 and 5 meV for $\hbar\Delta_0$ and 5×10^{-4} and 10^{-3} cm for the length $c/(\bar{n}\Delta_0)$, respectively. For $u \sim 0.1$, the soliton size is 5×10^{-3} and 10^{-2} cm, respectively, thus extending over several hundreds of periods of the resonance Bragg structure. Therefore, a soliton will form if a structure contains more than a hundred quantum wells (in [4], the number of quantum wells in the structures under study was as high as one hundred). A similar statement applies to the condition of formation of the phase-modulated 2π solitons considered above. Note that estimates made for real quantum-well structures show that $|\eta| \ll 1$ and $|\delta| < 1$; therefore, the soliton pulse velocity is indeed much smaller than the phase velocity and depends on its amplitude only weakly.

The resonance Bragg structure in a heterosystem with $\varepsilon_a = \varepsilon_b$, by definition, satisfies condition (11). In this case, both parameters, η and δ, are zero and from Eq. (23) it follows that $\beta^2(1 - u^2)/u^2 = 2$, i.e., that this quantity is not small and solution (22) is inapplicable to a structure with EP^2 nonlinearity. Thus, a phase-modulated 2π soliton forms only in a quasi-Bragg structure that, in the absence of nonlinearity, already has a narrow allowed miniband near the frequencies ω_0 and ω_B. We attribute the difference in the manifestation of the P^3 and EP^2 nonlinear terms in a resonance Bragg structure with $\varepsilon_a = \varepsilon_b$ to their different influence on solutions like Eq. (13) with a constant amplitude. In contrast to the P^3 nonlinearity, which gives rise to the formation of an allowed miniband in the vicinity of the frequency ω_0 [see dispersion equation (14)], the EP^2 nonlinearity does not create a transparency window for exciton polaritons within the polariton gap but results instead in its narrowing:

$$2\Delta_0 \longrightarrow 2(1-|\tilde{\mathcal{P}}|^2)^{1/4}\Delta_0 \approx 2(1-(1/4)|\tilde{\mathcal{P}}|^2)\Delta_0.$$

From the relations $|u| \approx |\eta - \delta|/\sqrt{8}$ and $|\Sigma_0|^2 \ll (\eta - \delta)^2$, it follows that 2π solitons do not form for $\eta = \delta$. If the difference between n_a and n_b is small and $a \ll d$, then the $\eta = \delta$ condition can be recast in the form

$$\omega_B = \omega_0\left(1 + \frac{n_b - n_a}{n_b}\frac{a}{d}\right), \qquad (33)$$

where $n_a = \sqrt{\varepsilon_a}$ and $n_b = \sqrt{\varepsilon_b}$. Equation (33) is the generalized Bragg condition for a structure with mismatched n_a and n_b [23, 24]. If this condition is satisfied, the two forbidden minibands characteristic of this system merge into one. This condition can be approximated by the expression $d = \pi c/\omega_0 n_b$. Thus, the disappearance of the transparency window in the forbidden miniband in a structure with $\eta = \delta$ prevents the formation of solitons of this kind.

6. CONCLUSIONS

We have shown that a P^3 nonlinearity in a resonance Bragg MQW structure allows the existence of solitons (16) and that the EP^2 and biexciton nonlinearities in a resonance quasi-Bragg structure give rise to the formation of phase-modulated 2π solitons. The main factor responsible for the appearance of soliton solutions has been established to be the formation of a photoinduced transparency window in the forbidden miniband for exciton polaritons in a resonance Bragg structure and the existence of this window in a resonance quasi-Bragg structure. The results obtained can be generalized to allow simultaneous inclusion of two or three types of exciton nonlinearities, as well as inclusion of the polarization dependence of the nonlinear term F_{NL} in Eqs. (7) and (10). Obviously enough, the biexciton nonlinearity is not involved in the formation of circularly polarized solitons by virtue of the selection rules governing two-photon excitation of the biexciton ground state.

The problem of excitation of the above solitons in the case where a light pulse is incident from vacuum onto a semi-infinite MQW structure or a structure of a finite width is beyond the scope of the present study.

We would like to stress that the most serious problem in the experimental observation of solitons is that of soliton stability; namely, the nonradiative exciton damping constant Γ and the inhomogeneous broadening of the exciton resonance frequency have to be noticeably smaller than the reciprocal length of the soliton pulse $\Delta_0 u$.

ACKNOWLEDGMENTS

This study was supported by the Russian Foundation for Basic Research and the Ministry of Science and Education of the Russian Federation.

REFERENCES

1. E. L. Ivchenko, Fiz. Tverd. Tela (Leningrad) **33**, 2388 (1991) [Sov. Phys. Solid State **33**, 1344 (1991)].
2. E. L. Ivchenko, A. I. Nesvizhskiĭ, and S. Iorda, Fiz. Tverd. Tela (St. Petersburg) **36**, 2118 (1994) [Phys. Solid State **36**, 1156 (1994)].
3. E. L. Ivchenko and M. Willander, Phys. Status Solidi B **215**, 199 (1999).
4. C. Ell, J. P. Prineas, T. R. Nelson, Jr., H. M. Gibbs, G. Khitrova, S. W. Koch, and R. Houdré, Phys. Rev. Lett. **80**, 4795 (1998).
5. L. I. Deych and A. A. Lisyansky, Phys. Rev. B **62**, 4242 (2000).
6. T. Ikawa and K. Cho, Phys. Rev. B **66**, 85338 (2002).
7. K. Cho, T. Hirai, and T. Ikawa, J. Lumin. **100**, 283 (2002).
8. L. Pilozzi, A. D'Andrea, and K. Cho, Phys. Rev. B **69**, 205311 (2004).
9. M. Hübner, J. Kuhl, T. Stroucken, A. Knorr, S. W. Koch, R. Hey, and K. Ploog, Phys. Rev. Lett. **76**, 4199 (1996).
10. S. Haas, T. Stroucken, M. Hübner, J. Kuhl, B. Grote, A. Knorr, F. Jahnke, S. W. Koch, R. Hey, and K. Ploog, Phys. Rev. B **57**, 14860 (1998).
11. S. L. McCall and E. L. Hahn, Phys. Rev. **183**, 457 (1969).

12. I. B. Talanina, Phys. Lett. A **241**, 179 (1998).
13. A. Kozhekin and G. Kurizki, Phys. Rev. Lett. **74**, 5020 (1995).
14. A. Kozhekin, G. Kurizki, and B. Malomed, Phys. Rev. Lett. **81**, 3647 (1998).
15. T. Opatný, B. A. Malomed, and G. Kurizki, Phys. Rev. E **60**, 6137 (1999).
16. Y. Fu, M. Willander, E. L. Ivchenko, and A. A. Kiselev, Phys. Rev. B **55**, 9872 (1997).
17. P. G. Savvidis, J. J. Baumberg, R. M. Stevenson, M. S. Skolnick, D. M. Whittaker, and J. S. Roberts, Phys. Rev. Lett. **84**, 1547 (2000).
18. C. Ciuti, P. Schwendimann, B. Deveaud, and A. Quattropani, Phys. Rev. B **62**, 4825 (2000).
19. A. Kavokin, P. G. Lagoudakis, G. Malpuech, and J. J. Baumberg, Phys. Rev. B **67**, 195321 (2003).
20. G. Kurizki, A. E. Kozhekin, T. Opatný, and B. Malomed, cond-mat/0007007.
21. Y. Merle d'Aubigné, A. Wasiela, H. Mariette, and T. Dietl, Phys. Rev. B **54**, 14003 (1996).
22. M. Hübner, J. P. Prineas, C. Ell, P. Brick, E. S. Lee, G. Khitrova, H. M. Gibbs, and S. W. Koch, Phys. Rev. Lett. **83**, 2841 (1999).
23. E. L. Ivchenko, V. P. Kochereshko, A. V. Platonov, D. R. Yakovlev, A. Waag, W. Ossau, and G. Landwehr, Fiz. Tverd. Tela (St. Petersburg) **39**, 2072 (1997) [Phys. Solid State **39**, 1852 (1997)].
24. L. Deych, M. Erementchouk, E. L. Ivchenko, A. Lisyansky, and M. M. Voronov, Phys. Rev. B **70**, 195106 (2004).

Translated by G. Skrebtsov

Physics of the Solid State, Vol. 47, No. 7, 2005, pp. 1383–1387. Translated from Fizika Tverdogo Tela, Vol. 47, No. 7, 2005, pp. 1333–1337.
Original Russian Text Copyright © 2005 by Gan'shina, Kochneva, Podgornyĭ, Shcherbak, Demidovich, Kozlov.

LOW-DIMENSIONAL SYSTEMS AND SURFACE PHYSICS

Structure and Magneto-Optical Properties of "Porous Silicon–Cobalt" Granular Nanocomposites

E. A. Gan'shina*, M. Yu. Kochneva*, D. A. Podgornyĭ, P. N. Shcherbak*,**
G. B. Demidovich*, and S. N. Kozlov*
** Moscow State University, Leninskie gory, Moscow, 119992 Russia*
e-mail: kozlov@vega.phys.msu.ru
*** Moscow State University of Steel and Alloys, Leninskiĭ pr. 4, Moscow, 117936 Russia*

Received October 4, 2004

Abstract—The structural and magneto-optical properties of "porous silicon–cobalt" nanocomposites prepared through electrochemical deposition on silicon substrates of different porosities are investigated. It is revealed that, under galvanostatic conditions, cobalt micrograins are formed only in a surface layer of porous silicon. The greater the pores in silicon, the larger the mean size of the ferromagnetic micrograins. The nanocomposites thus fabricated possess ferromagnetic properties and, at specified compositions, are characterized by anomalously large magnitudes of the equatorial or transverse magneto-optical Kerr effect (TMOKE). The magneto-optical properties of the nanocomposites are simulated in the Bruggeman effective-medium approximation. It is shown that the anomalous negative transverse magneto-optical Kerr effect is associated with the oxidized state of porous silicon in the vicinity of the ferromagnetic metal micrograins. *© 2005 Pleiades Publishing, Inc.*

1. INTRODUCTION

Low-dimensional composite materials are finding ever-widening application in many areas of science and engineering [1]. In particular, low-dimensional magnetic composites of the "dielectric–ferromagnetic metal" type are of considerable interest from both the scientific and practical standpoints. These materials exhibit unusual properties, such as strong nonlinear magneto-optical effects, a negative giant magnetoresistance, an anomalous giant Hall effect, etc. [2–5]. On the other hand, owing to the practical use of its low-dimensional modifications, silicon—a basic material in modern microelectronics—has already often been referred to as an optoelectronic material [6]; however, it has still remained inapplicable as a magnetosensitive material. The design of low-dimensional silicon-based magnetic composites has opened new fields of use in silicon micro- and optoelectronics. This paper reports on the results of investigations into the structural and magneto-optical properties of nanocomposites fabricated from porous silicon and a ferromagnetic metal, namely, cobalt.

2. SAMPLE PREPARATION AND EXPERIMENTAL TECHNIQUE

Porous silicon in the form of 1- to 20-μm-thick layers was prepared on the (100) and (111) surfaces of *p*-silicon single crystals with electrical resistivities ρ = 10.0, 0.03, and 0.005 Ω cm through anodization in an HF–ethanol (1 : 1) solution at an electric current density ranging from 20 to 30 mA cm^{-2}. The porosity of the layers prepared was controlled using the gravimetric method and varied in the range from 60% (low-resistivity silicon) to 80% (high-resistivity silicon) [6, 7]. The pore diameter in the porous layer was equal to 2–4 nm in the case of high-resistivity silicon (ρ = 10.0 Ω cm), 7–15 nm for low-resistivity silicon (ρ = 0.005 Ω cm), and 6–10 nm for silicon with an electrical resistivity ρ = 0.03 Ω cm [8]. Cobalt micrograins were introduced into the layers of porous silicon through electrochemical deposition (under galvanostatic conditions) from an alcoholic solution of cobalt chloride $CoCl_2$. The amount of cobalt introduced into the layers of porous silicon was determined by measuring the electric charge transferred through the silicon–electrolyte interface. The magneto-optical properties of the "porous silicon–cobalt" nanocomposites thus fabricated were investigated using the equatorial or transverse magneto-optical Kerr effect (TMOKE). The dependences of the magnitude of the transverse magneto-optical Kerr effect δ on the photon energy $h\nu$ were measured in the photon energy range $h\nu$ = 1.3–3.8 eV with a light beam incident at an angle of 70° in magnetic fields of up to 2.5 kOe. The structure and composition of the nanocomposites were controlled using scanning electron microscopy and scanning Auger electron spectroscopy on a PHI-680 scanning Auger electron microprobe system (Physical Electronics Co.).

3. RESULTS AND DISCUSSION

Figure 1 displays a typical scanning electron microscope image of the surface of a porous silicon–cobalt nanocomposite. According to scanning Auger electron

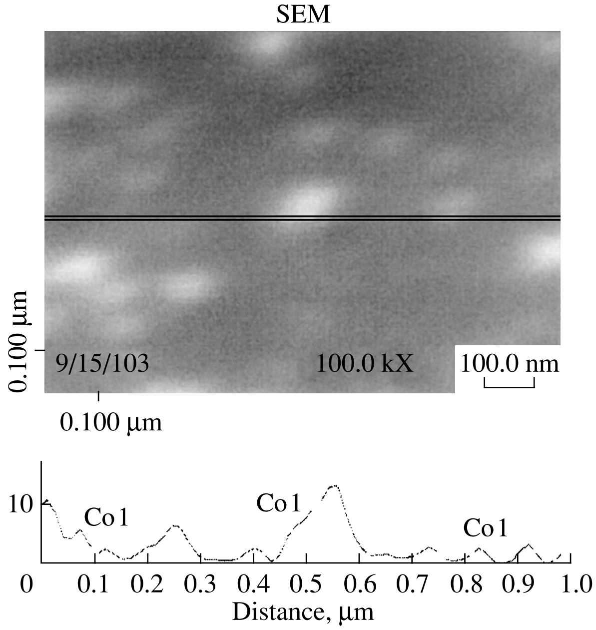

Fig. 1. Scanning electron microscope image of the surface of the porous silicon–cobalt nanocomposite and the cobalt distribution along the specified line. The electrical resistivity of the silicon substrate is $\rho = 10\ \Omega$ cm.

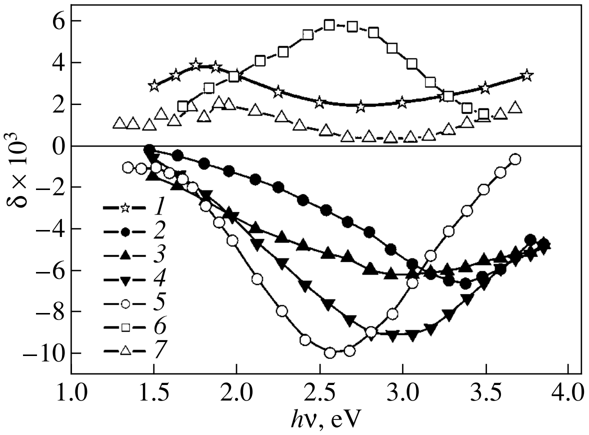

Fig. 2. Dependences of the transverse magneto-optical Kerr effect δ on the photon energy *h*ν for (*1*) pure cobalt and (*2*–*7*) porous silicon–cobalt nanocomposites with a 5-µm-thick porous silicon layer. The electrical resistivity of the silicon substrate is $\rho = 10\ \Omega$ cm. Cobalt concentration: (*2*) 2.5×10^{17}, (*3*, *7*) 5×10^{17}, and (*4*–*6*) 10×10^{17} atoms/cm^2.

spectroscopy, the light spots seen in this micrograph are identified as cobalt grains. It can also be seen from this micrograph that cobalt grains are distributed over the surface of the nanocomposite in a random manner and that the cobalt grain sizes vary in the range from several nanometers to several tens of nanometers.

The behavior and the magnitude of the transverse magneto-optical Kerr effect δ as a function of the photon energy *h*ν strongly depend on the parameters of the porous layer and on the content of the ferromagnetic component in the nanocomposite. It can be seen from Fig. 2 that, as a rule, the dependences of the transverse magneto-optical Kerr effect δ on the photon energy *h*ν for porous silicon–cobalt nanocomposites differ substantially from the dependence δ(*h*ν) for pure cobalt. The sign of the transverse magneto-optical Kerr effect was determined by the conditions used for fabricating the nanocomposites and, in the majority of cases, turned out to be negative (in contrast to the case of pure cobalt). However, some samples exhibited a positive transverse magneto-optical Kerr effect. Nanocomposite samples at a cobalt concentration ranging from $\sim 5 \times 10^{17}$ to 10^{18} atoms/cm^2 are characterized by anomalously large magnitudes of the transverse magneto-optical Kerr effect $\delta \sim 10^{-2}$, which exceed those for pure cobalt by several factors. All the nanocomposites at a cobalt concentration of higher than 2×10^{17} atoms/cm^2 possess ferromagnetic properties; more specifically, the magnitude of the transverse magneto-optical Kerr effect is nonlinear with respect to the magnetic field amplitude and approaches saturation in a magnetic field of ~2 kOe.

Figure 3 shows the transverse magneto-optical Kerr effect δ as a function of the photon energy *h*ν for nanocomposites prepared from low-resistivity silicon with electrical resistivities $\rho = 0.03$ and $0.005\ \Omega$ cm. The dependences of the transverse magneto-optical Kerr effect on the photon energy for these nanocomposites are qualitatively similar to those obtained for the nanocomposites based on high-resistivity silicon. However, the maximum magnitudes of the Kerr effect in the former case, as a rule, are considerably less than those in the latter case. It is worth noting that there is a close similarity between the dependences δ(*h*ν) for the nanocomposites that differ in terms of the thickness of the porous silicon layer by more than one order of magnitude but contain an identical number of cobalt atoms per unit of the geometric surface of silicon (5×10^{17} atoms/cm^2). This finding suggests that, upon electrochemical deposition (under the galvanostatic conditions), the cobalt micrograins are predominantly formed in a thin surface layer of porous silicon and no cobalt species penetrate into the bulk of the micropores. This assumption is confirmed by the fact that the photoluminescence intensity of porous silicon weakly depends on the concentration of the electrochemically deposited metal (Fig. 4).

The formation of cobalt micrograins in surface layers of the porous silicon–cobalt nanocomposites fabricated in this work is directly confirmed by scanning Auger electron spectroscopy in the course of layer-by-layer ion etching of the nanocomposites. As can be seen from Fig. 5, cobalt is revealed only in 10- to 20-nm-thick surface layers of the nanocomposite. The size of cobalt micrograins on the surface of the porous silicon layer depends on the nature of the porosity: in the case

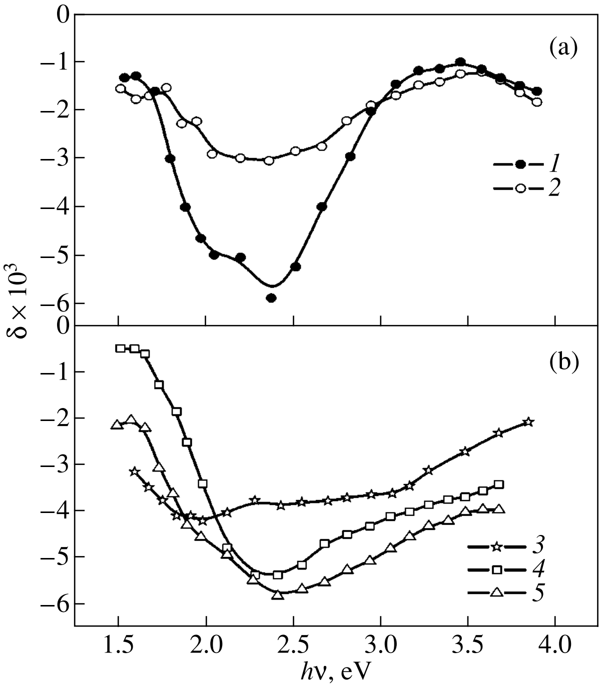

Fig. 3. Spectral dependences of the transverse magneto-optical Kerr effect δ on the photon energy $h\nu$ for porous silicon–cobalt nanocomposites prepared on silicon substrates with electrical resistivities ρ = (a) 0.005 and (b) 0.03 Ω cm. The cobalt concentration in all samples is equal to 5 × 10^{17} atoms/cm^2. Porous layer thickness: (*1*) 20, (*2*) 1, (*3*) 20, (*4*) 10, and (*5*) 5 μm.

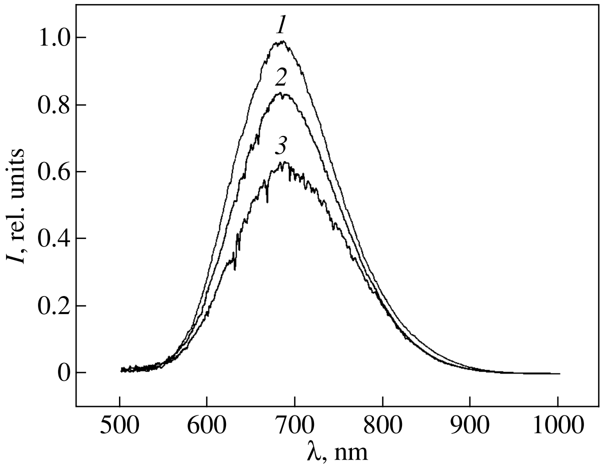

Fig. 4. Evolution of the photoluminescence spectrum of porous silicon with a gradual increase in the cobalt concentration in the porous silicon layer. The porous layer thickness is equal to 5 μm. The electrical resistivity of the silicon substrate is ρ = 10 Ω cm. Cobalt concentration: (*1*) 0, (*2*) 10^{17}, and (*3*) 1.5 × 10^{18} atoms/cm^2.

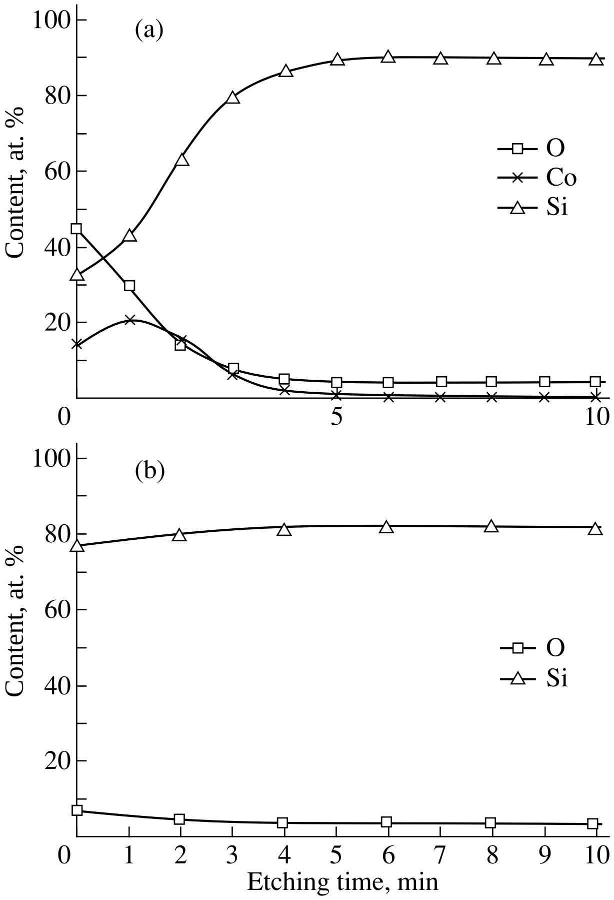

Fig. 5. Concentration distribution of the elements over the depth of (a) the porous silicon–cobalt nanocomposite and (b) the porous silicon layer free of cobalt micrograins. The electrical resistivity of the silicon substrate is ρ = 10 Ω cm. The cobalt concentration is 5 × 10^{17} atoms/cm^2.

of nanocomposites based on microporous silicon prepared on a high-resistivity substrate, the mean size of metal micrograins and, accordingly, the mean distance between the micrograins are significantly less than those for nanocomposites based on mesoporous silicon prepared on a low-resistivity substrate (Fig. 6). This correlates with the experimental spectral dependences of the transverse magneto-optical Kerr effect: the magnitude of the transverse magneto-optical Kerr effect δ for the nanocomposites based on microporous silicon, as a rule, is larger than that for the mesoporous silicon–cobalt nanocomposites (compare Figs. 2 and 3). It seems likely that a decrease in the mean distance between individual clusters leads to an enhancement of the magnetic ordering of the nanocomposite due to the dipole–dipole interaction [9], as is the case in Co–SiO_2 nanocomposites [5].

In order to determine the factors responsible for the behavior of the spectral dependences δ($h\nu$), we performed a simulation of these dependences in the Bruggeman effective-medium approximation [10]. It follows from the results presented in Fig. 7 that the porous silicon–cobalt nanocomposites should exhibit a positive transverse magneto-optical Kerr effect at any content of the ferromagnetic component in the nanocomposite. The negative transverse magneto-optical Kerr effect can be observed only in the regions where

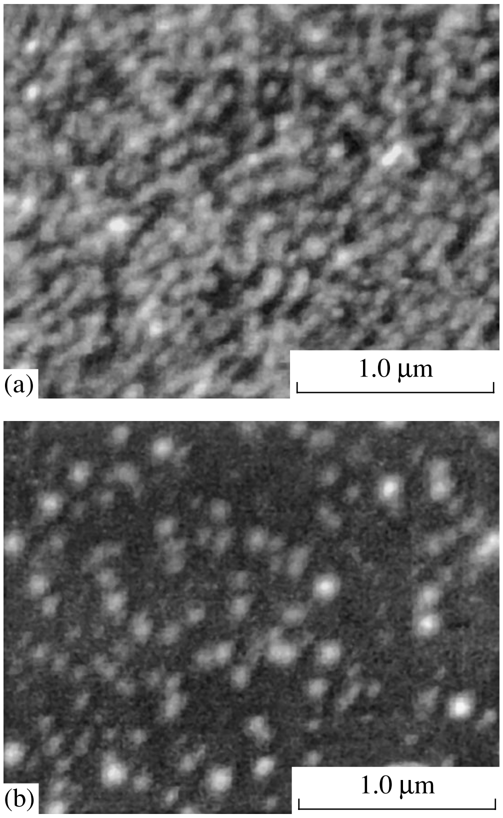

Fig. 6. Scanning electron microscope images of the surfaces of the porous silicon–cobalt nanocomposites on silicon substrates with electrical resistivities ρ = (a) 10.0 and (b) 0.005 Ω cm.

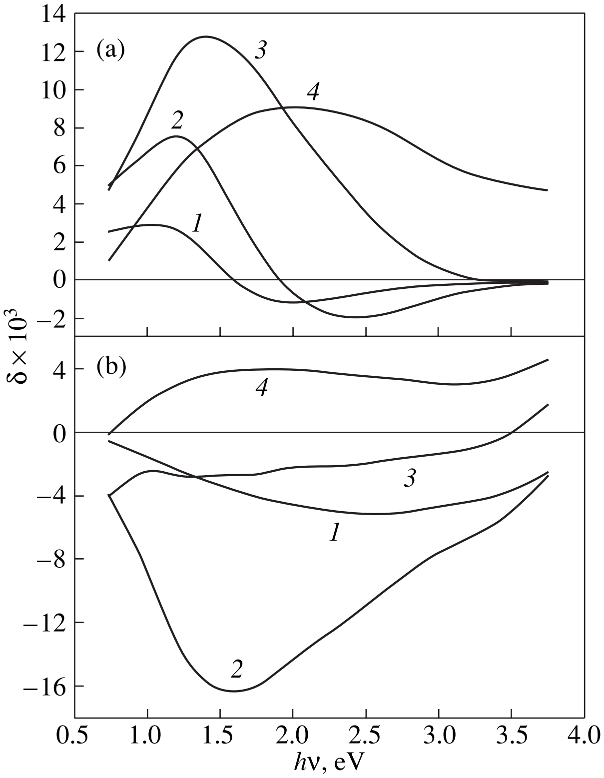

Fig. 7. Calculated dependences of the transverse magneto-optical Kerr effect δ on the photon energy $h\nu$ in the Bruggeman effective-medium approximation for (a) $\mathrm{Co}_x(por\mathrm{Si})_{1-x}$ and (b) $\mathrm{Co}_x(\mathrm{SiO_2})_{1-x}$ at cobalt contents x = (*1*) 5, (*2*) 15, (*3*) 40, and (*4*) 80%.

the cobalt micrograins are surrounded by oxidized fragments of porous silicon. Indeed, according to scanning Auger electron spectroscopy, the oxygen content is usually increased in the vicinity of the cobalt micrograins on the surface of the porous silicon layer (Fig. 6). It seems likely that the incorporation of cobalt micrograins into the mouths of the silicon micropores is accompanied by deformation of the surface layer of the porous matrix and by an increase in the number of weakened Si–Si bonds that readily oxidize upon contact with the environment. Moreover, an increase in the rate of oxidation of porous silicon in the vicinity of the metal micrograins can be caused by the so-called spillover effect [11]. This effect manifests itself in the migration of active (apparently, atomic) oxygen localized at cobalt micrograins into the nearest surface regions of porous silicon with subsequent oxidation of these regions. In the case when the cobalt micrograins penetrate deep into the silicon micropores, the dominant role is played by their interaction with the unoxidized porous matrix and the transverse magneto-optical Kerr effect is positive in sign. As follows from the experimental data, this situation is favored by an increase in the voltage (and, hence, in the electric current) upon the electrochemical incorporation of cobalt micrograins into the porous silicon layer.

4. CONCLUSIONS

(1) It was demonstrated that the porous silicon–cobalt nanocomposites fabricated using the electrochemical method possess ferromagnetic properties and, at specified compositions, are characterized by anomalously large magnitudes of the transverse magneto-optical Kerr effect. The maximum magnitudes of the magneto-optical Kerr effect are observed for the nanocomposites based on microporous silicon (prepared on high-resistivity silicon substrates).

(2) It was established that there is a correlation between the magnitude of the transverse magneto-optical Kerr effect, the size of ferromagnetic micrograins, and the nature of the porosity of the silicon substrate; more specifically, a decrease in the micropore size is accompanied by a decrease in the mean size of the cobalt micrograins, as well as by an increase in the transverse magneto-optical Kerr effect.

(3) The simulation of the magneto-optical properties of porous silicon–cobalt nanocomposites demonstrated that the negative transverse magneto-optical Kerr effect

is caused by the oxidation of fragments of porous silicon in the vicinity of the cobalt micrograins. This conclusion is experimentally confirmed using scanning Auger electron spectroscopy.

(4) It was assumed that the considerable increase in the rate of oxidation of porous silicon in the vicinity of the cobalt micrograins is associated with the spillover of active oxygen from the metal micrograins to the nearest surface regions of porous silicon, as well as with the mechanical stresses arising in the lattice of porous silicon in the vicinity of the cobalt micrograins.

ACKNOWLEDGMENTS

This work was performed within the framework of the program “Universities of Russia” (project no. UR.01.03.071/04) and the Russian federal program “Integration” (project no. I0964/1989).

REFERENCES

1. R. C. Hayward, P. Alberius-Henning, B. F. Chmelka, and G. D. Stucky, Microporous Mesoporous Mater. **44–45**, 619 (2001).
2. A. B. Granovsky, I. V. Bykov, E. A. Gan’shina, V. S. Gushchin, M. Inoue, Yu. E. Kalinin, A. A. Kozlov, and A. N. Yurasov, Zh. Éksp. Teor. Fiz. **123** (6), 1256 (2003) [JETP **96** (6), 1104 (2003)].
3. S. Mitani, H. Fujimori, and S. Ohnuma, J. Magn. Magn. Mater. **165**, 141 (1997).
4. A. N. Vinogradov, E. A. Gan’shina, V. S. Guschin, V. M. Demidovich, G. B. Demidovich, S. N. Kozlov, and N. S. Perov, Pis’ma Zh. Tekh. Fiz. **27** (13), 84 (2001) [Tech. Phys. Lett. **27** (7), 567 (2001)].
5. S. Sankar, D. Dender, J. A. Borchers, D. J. Smith, R. W. Erwin, S. R. Kline, and A. E. Berkowitz, J. Magn. Magn. Mater. **221**, 1 (2000).
6. V. M. Demidovich, G. B. Demidovich, and S. N. Kozlov, Poverkhnost, No. 7, 66 (2001).
7. L. Pavesi, J. Phys.: Condens. Matter **15**, R1169 (2003).
8. V. Lehmann, R. Stengl, and A. Luigart, Mater. Sci. Eng., B **69–70**, 11 (2000).
9. M. F. Hansen and S. Morup, J. Magn. Magn. Mater. **184**, 262 (1998).
10. T. K. Xia, P. M. Hui, and D. S. Stroud, Appl. Phys. **67**, 2736 (1989).
11. V. V. Rozanov and O. V. Krylov, Usp. Khim. **66** (2), 117 (1997).

Translated by I. Volkov

Physics of the Solid State, Vol. 47, No. 7, 2005, pp. 1388–1392. Translated from Fizika Tverdogo Tela, Vol. 47, No. 7, 2005, pp. 1338–1342.
Original Russian Text Copyright © 2005 by Krivolapchuk, Lundin, Mezdrogina.

LOW-DIMENSIONAL SYSTEMS
AND SURFACE PHYSICS

The Role of Built-in Electric Fields in the InGaN/GaN Quantum-Well Emission

V. V. Krivolapchuk, V. V. Lundin, and M. M. Mezdrogina
Ioffe Physicotechnical Institute, Russian Academy of Sciences,
Politekhnicheskaya ul. 26, St. Petersburg, 194021 Russia
e-mail: vlad.krivol@mail.ioffe.ru, margaret.m@mail.ioffe.ru

Received July 26, 2004; in final form, November 9, 2004

Abstract—By analyzing the evolution of time-resolved photoluminescence spectra, it is detected experimentally for the first time that there is a correlated effect of built-in electric fields and of long-lived localized states on the formation of emission in quantum wells based on nitrides of Group III elements. It is shown that light-emitting diode structures can be classified for commercial applications by studying time-resolved photoluminescence spectra. *© 2005 Pleiades Publishing, Inc.*

1. INTRODUCTION

Intensive studies of InGaN/GaN quantum-well heterostructures have culminated in the commercial development of light-emitting diodes designed for operation in various spectral regions [1, 2]. However, it is known that the defect concentration in these materials remains fairly high and that one still cannot, in particular, substantially reduce the density of dislocations caused by stresses originating from the lattice misfit between the substrate (as a rule, Al_2O_3) and GaN and by thermal stresses between the substrate and GaN. It has also been demonstrated that, unlike other semiconductors (GaAs, GaP), in which dislocations act as nonradiative [1, 2] recombination centers and, as a result, an increase in the dislocation density (to 10^4 cm^{-3}) drives the radiation intensity to zero, the concentration of radiative recombination centers in GaN does not depend on the density of structural defects [2]. This specific feature of GaN and of GaN-based structures offers the possibility of designing high-efficiency devices from materials having a lattice defect concentration higher than that in other III–V compounds. Recent studies have revealed a number of remarkable properties of InGaN/GaN heterostructures and of devices based on these structures, which should apparently be assigned to the presence of a spontaneous piezoelectric field [3]. To increase the efficiency of these devices, one needs to estimate the effect exerted by the various parameters of the structures on the mechanisms of their emission. Progress in this area will depend, therefore, on a clear understanding of how and to what extent the spontaneous piezoelectric field and localized states contribute to emission in such structures.

In this paper, we report on a contactless optical spectroscopic study of the characteristics of radiation emitted by InGaN/GaN-based quantum-well structures. This is done by analyzing a possible correlation between the localized states and built-in piezoelectric fields, as well as the role played by this correlation in the onset of efficient emission in these structures. Steady-state and time-resolved photoluminescence spectra were studied for this purpose.

2. EXPERIMENT

We studied radiation spectra of InGaN/GaN-based quantum-well light-emitting structures. The object of study was an array of five (~25-nm-thick) quantum wells MOCVD-grown on a sapphire substrate and separated by 70-nm-thick GaN barriers. The photoluminescence (PL) and electroluminescence spectra of the samples were obtained under both cw and pulsed excitation. Both steady-state and gated (time-resolved) PL spectra were taken. Optical measurements were carried out on an SDL-2 grating spectrometer with a reciprocal linear dispersion of 1.3 nm/mm in the region of GaN edge luminescence. Time-delayed spectra and decay processes were studied with the use of an LGI-21 pulsed nitrogen laser operating at a wavelength λ = 3371 Å and a pulse duration (FWHM) $\tau \approx 10$ ns. The delayed spectra were recorded in gated time windows (5–10 μs wide) delayed by time t_d varied in the interval t_d = 0–80 μs. The measurements were conducted at temperatures T = 300, 77, and 4.2 K. To accurately compare the emission spectra of different InGaN/GaN structures, the variable parameters (the angle of incidence of light, the pump light intensity, the temperature) were held constant.

3. EXPERIMENTAL RESULTS AND DISCUSSION

The PL spectrum of all samples taken under cw pumping has a fairly strong line in the blue region

($\lambda \approx 445$ nm), which is due to quantum-well emission (Fig. 1).

Studies of time-resolved PL spectra revealed that, for comparable emission intensities in the blue region, the PL spectra of samples differ in terms of the shape of the luminescence band measured at zero delay ($t_d = 0$). Note that, in this spectral region, only one sufficiently strong line is generally observed. This line is inhomogeneously broadened (the FWHM dispersion for different samples does not exceed 10 meV) and originates from the recombination of carriers residing in quantum-well levels.

Turning now to the PL spectra, we consider the factors governing the intensity and width of an emission line.

In general, the radiation intensity I_r produced at an excitation level $G = f(I_{ex})$ depends on the total lifetime of nonequilibrium carriers (excitons) τ. The total lifetime, in turn, is determined by the radiative (τ_r) and nonradiative (τ_{nr}) decay times of excitons (carriers): $1/\tau = 1/\tau_r + 1/\tau_{nr}$. Therefore, the radiation intensity can be written as $I_r = G/(1 + \tau_r/\tau_{nr})$. The nonradiative decay time τ_{nr} is determined by the trapping (with a cross section σ_i) of excitons into deep states (present in a concentration N_i), whose existence rests on the presence of various defects: $1/\tau_{nr} = \sum_i v\sigma_i N_i^{nr}$ (v is thermal velocity, i labels the defect type). It follows that the PL intensity for $t_d = 0$ is determined not only by the concentration of nonradiative recombination centers but also by the capability of carriers to move over the crystal so as to eventually reach the nonradiative recombination centers.

Because the photoexcitation energy $E_{ex} = 3.67$ eV > E_g (E_g is the bandgap width), carriers are born free (mobile). They relax to the energy levels in a quantum well involved in emission in times that are, in any case, no longer than τ_r. In the course of relaxation, mobile carriers are captured by various traps with a characteristic trapping time τ_{trap}. The traps act as centers of both radiative and nonradiative recombination; so, $\tau_{trap} \neq \tau_{nr}$. In this case, the luminescence intensity should depend on the ratio τ_r/τ_{trap}. To find the contributions of free and localized states to the formation of the emission line, the PL excitation (PLE) spectra of samples of different types were studied. Figure 2 displays typical PLE spectra obtained for two energies within the emission line profile. One energy is the position of the maximum in the PL line ($E_1 = 2.715$ eV), and the other ($E_2 = 2.565$ eV) lies in the long-wavelength wing of the PL line. As is evident from Fig. 2, the PLE spectra measured at E_1 and E_2 fall off in the same way on the higher energy side (the *a*–*b* interval in Fig. 2). This falloff can be identified with the attainment of a threshold energy $h\omega = E_{thr}$ at which there appear mobile carriers that can be captured efficiently by traps [4].

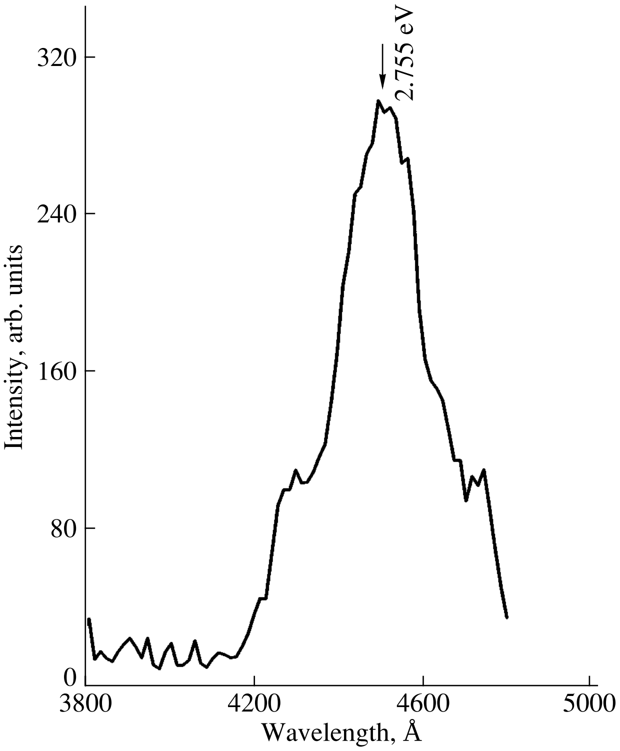

Fig. 1. Photoluminescence spectrum of an InGaN/GaN quantum-well heterostructure taken at $T = 77$ K.

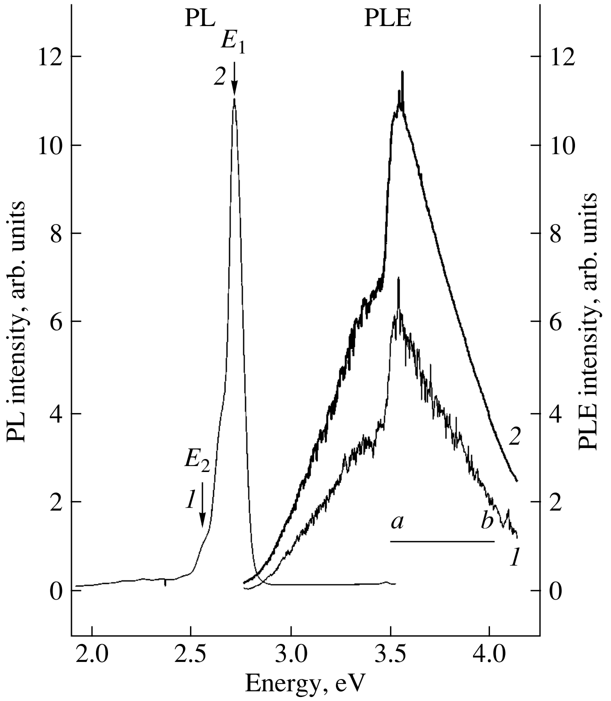

Fig. 2. Photoluminescence excitation (PLE) spectra of InGaN/GaN heterostructures taken for two energy values within the PL line profile, $E_1 = 2.715$ eV and $E_2 = 2.565$ eV, at $T = 77$ K.

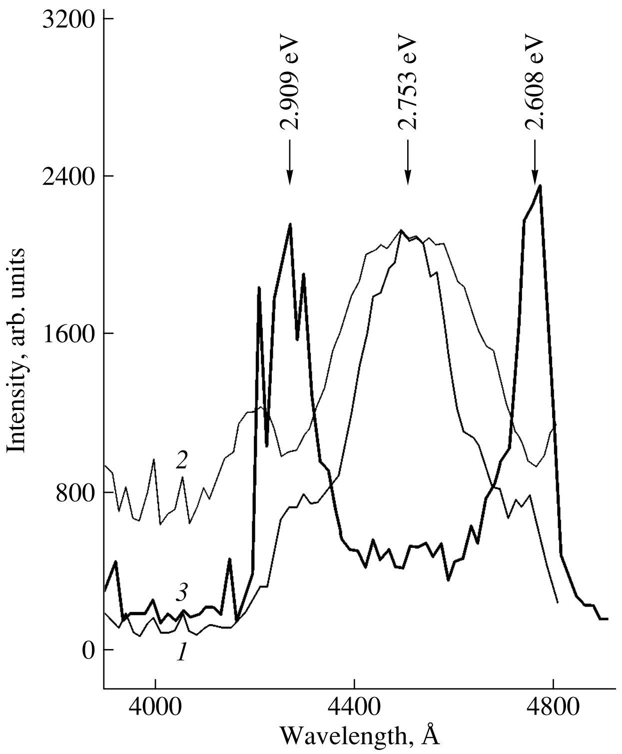

Fig. 3. Time-resolved photoluminescence spectra (T = 4.2 K) obtained at different delay times t_d: (*1*) 0, (*2*) 20, and (*3*) 40 μs.

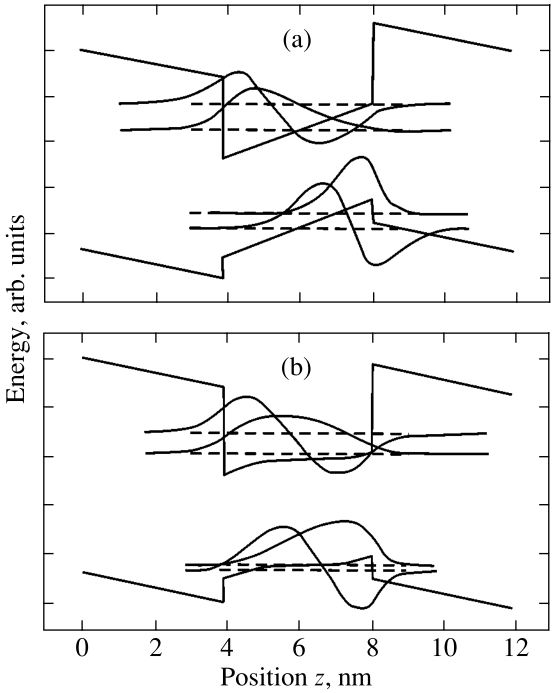

Fig. 4. Energy diagram of quantum-well structures and carrier wave-function envelopes in the presence of (a) weak and (b) strong internal electric fields (according to [8]).

As follows from the shape of the PLE spectra, it is the localized states that contribute heavily to the emission. One may therefore expect the shape of the PL spectra in different samples to be intimately connected with the specific features of the population and depletion of localized states in a given sample. To reveal these features, time-resolved PL spectra were studied (as in [5]).

It was found that the shape of the time-resolved PL spectra is essentially different. Figure 3 shows time-resolved PL spectra measured with $t_d = 0$, 20, and 40 μs at 4.2 K. Two points appear of interest: (i) increasing the delay time still further (up to 80 μs) reduces the intensity but does not affect the shape of the spectra noticeably, and (ii) the overall pattern of the spectra does not change with temperature. Note that the fact itself of the emission persisting for long times (80 μs) implies the existence of nonequilibrium carriers that are trapped into long-lived localized states. One may tentatively assume that such carriers are holes in an n-type material with a sufficiently high electron concentration ($n > 10^{16}$ cm^{-3}). The mechanism responsible for this long line afterglow is phenomenologically similar to that observed in n-GaAs with metastable states (N_{MS}) [6], where part of the photoexcited carriers are trapped into metastable states, to be subsequently ejected from them into the valence band. Due to the interaction between the holes ejected into the valence band and electrons (free or bound in shallow levels), emission lines form in the time-delayed spectra, with the time scale of the gate delay t_d being determined by the hole release time τ_s.

Another point relevant to the line shape is the role played by the complex spatial relief of the potential U_{ph} experienced by the nonequilibrium carriers involved in the formation of this radiation. This random potential is caused both by fluctuations in the thickness of quantum wells and barriers and by the electric field generated by impurities in the barriers. Carriers are localized on potential fluctuations, and the scatter in the energy ΔE_{rad} of photons emitted in radiative recombination is responsible for the inhomogeneous line broadening. A doublet structure consisting of comparatively narrow lines appears within the inhomogeneously broadened emission line (at $t_d = 0$) as a result of a delay for $t_d \geq 20$ μs. This fact indicates that the localized states responsible for the inhomogeneous broadening are metastable. Therefore, as these localized states are depleted (with a characteristic time τ_s), their contribution to ΔE_{rad} decreases. As a result, the quantum-well PL line narrows with increasing delay time t_d (provided $t_d > \tau_s$). In some cases, within the inhomogeneously broadened emission line at $t_d = 0$, delayed spectra for $t_d \geq 20$ μs exhibit a doublet structure consisting of comparatively narrow lines (Fig. 3), which should likewise be attributed to the existence of metastable localized

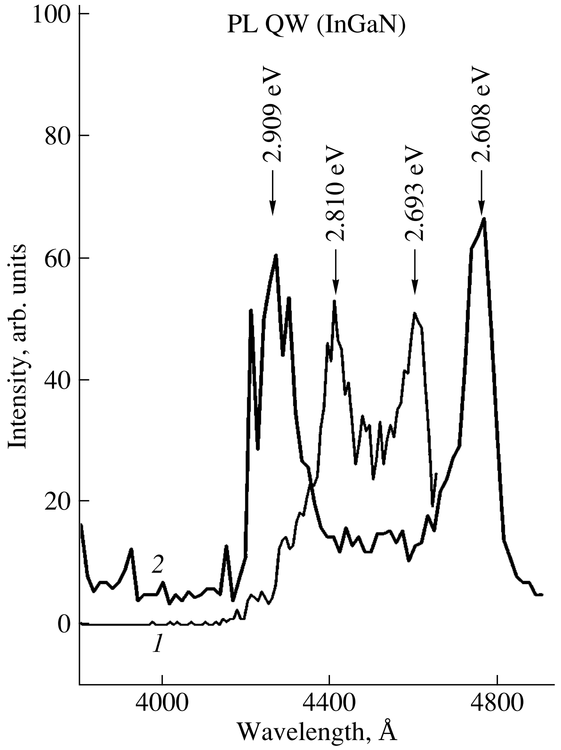

Fig. 5. Effect of temperature on the spectral interval between the doublet components: (*1*) 77 and (*2*) 4.2 K. t_d = 60 μs.

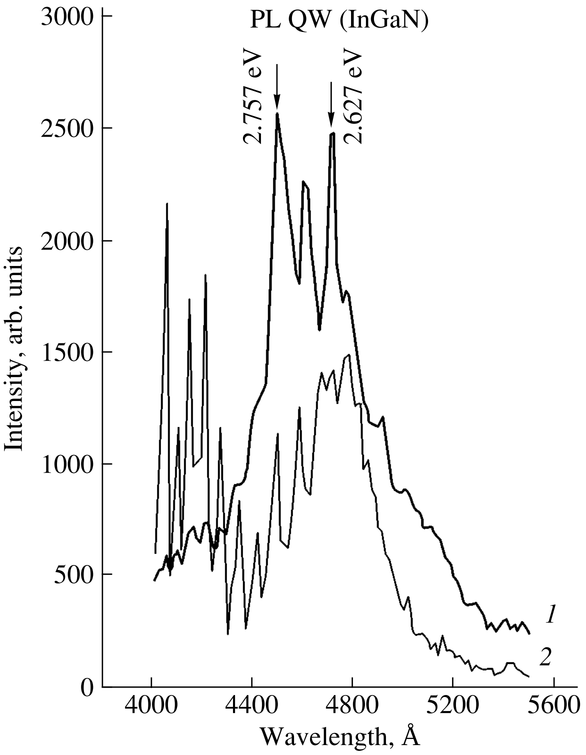

Fig. 6. Intensity of photoluminescence spectrum components measured under (*1*) high and (*2*) low pumping levels.

states. One should, however, identify the factors accounting for such a large difference in the contributions of the localized states to the formation of the quantum-well emission line.

A key to understanding this situation is provided by a well-known property of nitrides of Group III elements, namely, the existence of spontaneous piezoelectric fields [7]. Therefore, prior to turning to an analysis of the spectral evolution in samples with quantum wells, we will first address the general energy diagram of a quantum well in the presence of a transverse electric field (perpendicular to the layers) (Fig. 4 [8]). Figure 4 shows the profile of a quantum well (the *z* axis is the growth direction of the structure) for low and high internal electric fields (Figs. 4a and 4b, respectively). This diagram qualitatively illustrates the situation arising in the structure when the electric field is changed. If the piezoelectric field F_{pz} is high enough, the wave functions are centered close to the interfaces, thus increasing the probability of carriers being localized in the random interface potential U_{ph}. In this case, the doublet shape of the emission line in the time-delayed spectra (Fig. 3) indicates the presence of a built-in electric field and the spectral interval between the doublet lines reflects the effective strength of this field. By definition, the strength of a piezoelectric field depends on the magnitude of stresses in a sample. The stress (piezoelectric field), in turn, depends on the sample temperature. In this case, the variation in stress with temperature may be expected to bring about a change in the delayed PL spectra. Indeed, the samples exhibit an increase of the spectral interval between the doublet components when the temperature is changed from 77 to 4.2 K, which implies an increase in the built-in piezoelectric field $F(pz)$. One may therefore maintain that at T = 77 K the field F_{pz} is lower than at T = 4.2 K (Fig. 5).

In this case (T = 77 K), we studied the behavior of the time-resolved spectra as a function of the photoexcitation intensity and external electric field (reverse bias V_b).

It is known that the field in a quantum well can be varied by properly changing the excitation level I_{ex}. This effect is due to a change in the screening field resulting from the concentrations of injected carriers being different. Figure 6 plots the PL intensities obtained at different pumping levels. We also studied time-delayed PL spectra measured under application of a reverse bias V_b to the quantum-well structure. Figure 7 displays delayed spectra (at t_d = 20 μs) of a sample taken at a zero external field under a bias V_b = 20 V. In both cases, as seen from Figs. 6 and 7, a change in the effective field in a quantum-well structure brings about quenching of the short-wavelength component in the delayed luminescence spectra. Note that this evolution of the spectral shape is a function of both the external field (reverse bias V_b) and photoexcitation intensity.

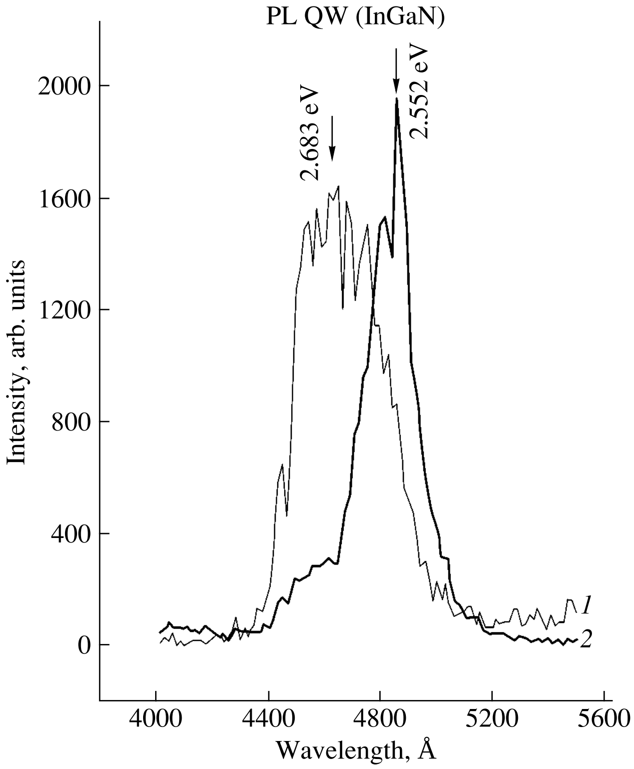

Fig. 7. Time-resolved spectra (*1*) in a zero external field and (*2*) under an external bias V_b = 20 V. T = 77 K.

Therefore, these factors should be properly taken into account when testing devices with these structures by using time-delayed PL spectra.

4. CONCLUSIONS

To sum up, the presence of narrow long-lived doublet components in time-delayed spectra and their dependence on the pumping intensity and reverse bias V_b indicate the involvement of localized metastable states and built-in electric fields in the formation of the emission spectrum; i.e., built-in fields favor carrier localization or delocalization on interface fluctuations caused by a variety of factors (internal field strength, pumping intensity, temperature variations).

ACKNOWLEDGMENTS

The authors are indebted to A.V. Andrianov for his assistance in the experiment.

This work was supported by the Presidium of the RAS (program “Low-Dimensional Quantum Structures”).

REFERENCES

1. A. V. Andriyanov, V. Yu. Nekrasov, N. M. Shmidt, E. E. Zavarin, A. S. Usikov, N. N. Zinov’ev, and M. N. Tkachuk, Fiz. Tekh. Poluprovodn. (St. Petersburg) **36** (6), 679 (2002) [Semiconductors **36** (6), 641 (2002)].
2. X. A. Cao, S. F. LeBoeuf, and L. B. Rowland, Appl. Phys. Lett. **82** (21), 3614 (2003).
3. F. Bernardini and V. Fiorentini, Phys. Rev. B **56** (16), R10024 (1997).
4. V. Yu. Davydov and A. A. Klyuchikhin, Fiz. Tekh. Poluprovodn. (St. Petersburg) **38** (8), 897 (2004) [Semiconductors **38** (8), 861 (2004)].
5. V. V. Krivolapchuk and M. M. Mezdrogina, Fiz. Tverd. Tela (St. Petersburg) **46** (12), 2129 (2004) [Phys. Solid State **46** (12), 2201 (2004)].
6. A. V. Akimov, A. A. Kaplyanskiĭ, V. V. Krivolapchuk, and E. S. Moskalenko, Pis’ma Zh. Éksp. Teor. Fiz. **46**, 35 (1987) [JETP Lett. **46**, 42 (1987)].
7. Y. Narukawa, Y. Kawakami, S. Fujinita, Sh. Fujinita, and S. Nakamura, Phys. Rev. B **55** (4), R1938 (1997).
8. S. Kalliakos, P. Lefebvre, and T. Taliercio, Phys. Rev. B **67**, 205307 (2003).

Translated by G. Skrebtsov